Innovative surface, tunnel, and in-pit geophysical methods for mineral exploration and mine planning: case studies from the Bushveld Complex mines, South Africa

By

Moyagabo Kenneth Rapetsoa

A thesis submitted in fulfilment of the requirements for the degree of

DOCTOR OF PHILOSOPHY

In the

FACULTY OF SCIENCE

UNIVERSITY OF THE WITWATERSRAND,

JOHANNESBURG

School of Geosciences

University of the Witwatersrand, Johannesburg

November 2023

DECLARATION

I declare that this thesis is my own, unaided work. It is being submitted for the Degree of Doctor of Philosophy at the University of the Witwatersrand, Johannesburg. It has not been submitted before for any degree or examination at any other University.

Moyagabo Kenneth Rapetsoa

Student number: 867109

Signed on the 03rd day of November 2023 at University of the Witwatersrand, Johannesburg

ABSTRACT

Innovative geophysical methods were used to study the platinum group element mineralisation and their associated geological structures at Maseve and Tharisa mines, western Bushveld Complex. Four case studies are presented in this thesis that incorporate the use of in-mine or near mine geophysical methods for mineral exploration. The first one being in-mine seismic data acquired in 2020 at Maseve mine using cost-effective seismic source and sensors, followed by innovative seismic experiments acquired in 2022 at Maseve mine to evaluate the viability of using tunnel and surface experiments for mineral exploration in a noisy, logistically difficult mine environment. Thirdly, the 2021 integrated geophysical surveys conducted at Tharisa mine to image fractures that act as water pathways into the pit. Finally, integrated geophysical techniques are used to delineate boulders to enhance future mine planning and designs at Tharisa mine. The acquired geophysical data were processed using modern processing algorithms to enhance the target mineralization and complex geological structures in all the sites.

In-mine reflection seismic datasets acquired in 2020 at Maseve mine proved useful as they provided optimum imaging of the economic Platinum Group Elements (PGEs) such as the Merensky Reef and Upper Group 2 chromitite layers (known as reefs). This is one of the few in-mine seismic experiments to have been conducted in South Africa for mineral exploration. In 2022, 2D reflection seismic profiles were acquired on surface above the Merensky Reef and Upper Group 2 chromitite, together with four 2D reflection seismic profiles acquired along the mine tunnel at ~ 550 m below the surface and tens of meters above known mineralisation: Merensky Reef and Upper Group 2 chromitite layer. Interpretation of the in-mine and surface seismic data were complemented by the use of 3D ray tracing numerical simulations to understand the distribution and out-of-plane reflectivity from the target mineralization. The 2022 Maseve reflection seismic data improved the imaging of geological structures and mineral deposits.

The geophysical data acquired in 2021 at Tharisa mine demonstrated the importance of using near-surface integrated geophysical methods (magnetics, seismics, and electrical resistivity) with other datasets such as borehole logs and physical property measurements to understand the geophysical response of the mineral deposits. Ground magnetic data delineated a major dyke that was identified on the aeromagnetic data and geological mapping. Electrical resistivity tomography, on the other hand, identified linear low resistivity zones that differentiate

fractured and undisturbed hard rock. Seismic methods were important for depth to bedrock imaging. Integration of geophysical methods was encouraged by the need to understand geological structures (e.g., faults, dykes, iron-rich ultramafic pegmatites, boulders) that can have impact on the efficiency, safety and costs of mining in South Africa. Moreover, this approach encourages the implementation of innovative geophysical surveys in brownfield sites for better mine design and planning, and to increase a life of mine (LoM).

DEDICATION

To my late Grandfather, Mokgatla George Shokane, for his endless lessons and inside jokes that we shared when I was growing up. This work will always represent all your undying belief in me.

Robala ka Khutšo Ngoato.

"*Agee Ngwato, Agee Phala, Agee Mohlamatsi wa mmamoriti molalamabotla ke dikgolo di are llela. Ke Mokgatla wa borwatomola mahlo. Maru a hlakana godimo. Bare Mokgatla ga a dule kgorong o tlatlawetša masogana. Ke batho ba le fetša poba ka šololo, wa fetša poba rea goma. O se bone Phala go inama bohlale e tswetswe le bjona. Ke wa bo leshweng lepotonko lebati le legolo la bo Mmahlogo. Bahlamatso weee. Ke morwa kgwahle mahlare mmammutla wa lešia mpša ka lebelo. A re mogwaka tla o nthuše sebata ke a naiwa, ge ele lehu re hwile la thoka la mpša re hwa re kganyetša. Ke morwa Maolela ditlakala moobeledi wa tša kgole. Ke mothupi wa go thopa tša ga matlala a thopa dipitsi le ka dikgong*"

ACKNOWLEDGEMENTS

My sincere gratitude is extended to my academic supervisors, Prof. Musa Manzi and Dr. Michael Westgate. Prof. Musa Manzi, ever since I joined the geophysics department, you have served as both a mentor and a supervisor to me. Your undying support to students does not go unrecognised. You impart many life lessons that not only helped in academics, but life in general. Unfortunatley, the only thing I could not do is get to drink espresso, which is one last thing that I will have to learn to appreciate. Dr. Michael Westgate, you are among the most remarkable people I have ever met. You were patient and passionate and always had time to help. You serve as an inspiration to me.

I apologize in advance if I missed anyone, but I would like to express my gratitude to my encouraging colleagues for their unwavering support and the many conversations we had throughout my PhD journey. I am grateful to Mpofana, Nombuso, Nandipha, Emmanuel, Jureya, Sikelela, Ndamulelo, Salizwa, Nondumiso, Omphulusa, Marcus, Joseph, and Fenitra from the geophysics team. Additionally, I would like to thank Ian James, Bojan Brodic, and Uppsala University stuff and students for their assistance. A special thank you to Prof. Raymond Durrheim, who helped me constantly learn new ideas and work with experts in other fields.

Above all, I want to express my gratitude to my family for their love and support throughout my career: Lemo Patrick, Moyagabo Phina, Matidi Brian, Mokgatla Collen, and Satsela Thato. To my amazing cousins, who have never shied away from supporting me with my academic obsession. You are incredibly loved. George, Pheladi, Gillian, and Makgati.

Thank you to all of my friends and some partners for the food, games, walks, dates, beers, and many other things. - Jacky, Lengana, Nare, Deepak, Thabisile, Veronica, Mahlatse (Shashaki), Ofentse (Mafefe), Maphuti, Mumbi, Manyaku, Semakaleng, Sphelele, Maphala, Mathobela (Tluka), Mapula (J.Q), Snethemba, Nqaba, Ettore, Nomthandazo, Mankuke, and Lischen, Nolwandle, Thokozile, and Manyabe. A special thank you to Sharon Phato Matloga, who never stopped believing in me and being understanding of my insomniac tendencies.

Finally, but just as importantly, I would like to express my gratitude to the Mandela Mining Precinct's Advanced Orebody Knowledge Program (funded by DSI and Minerals Council). Their financial support has enabled me to carry out and complete my doctoral research. We also extend our gratitude to the Royal Bafokeng Maseve and Tharisa mines for granting us permission to use their mine sites for this study. I am appreciative of Mr. Sipho Sithole and the staff at Maseve Mine, especially Michelle Pienaar, the AOK program manager.

Table of Contents

LIST OF FIGURES

LIST OF ABBREVIATIONS

1C	One component
2D	Two dimensional
3C	Three component
3D	Three dimensional
BC	Bushveld Complex
CMP	Common-midpoint
DMO	Dip moveout
FD	Finite difference
f-k	Frequency wavenumber
Ga	Billion years ago
GPS	Global positioning system
Hz	Hertz
IRUPS	Iron rich ultramafic pegmatite
kg	Kilogram
km	Kilometer
m	Meter
m/s	Meter per second
MR	Merensky Reef
ms	Milliseconds
NMO	Normal moveout
PGE	Platinum Group Elements
RMS	Root mean square
SNR	Signal to noise ratio
TWT	Two way travel-time
UG2	Upper Group 2
V_p	Compressional velocity

1. Introduction

1.1.Motivation and objectives

The Bushveld Complex (BC) in north-western South Africa is known for its rich Platinum Group Element (PGE) deposits (locally termed reefs). The Rustenburg facies represents (Figure 1) the southernmost part of the western limb of the Bushveld Complex. It is known for the dominant Pt-Pd sulphides (30%) and four subfacies (rolling reef, chromitite contact reef, non pegmatoidal wide reef, and potholed thin reef) that have regional variations in the geological structures of the Merensky Reef (MR) (Viljoen, 1999). The early discovery research of the PGEs started in the 1906 by William Bettel (e.g., Merensky, 1925; Wagner, 1929; Lehmann, 1955; Scoon and Mitchell, 2005). The Merensky Reef was first discovered in the eastern limb, but mining commenced in the western Bushveld Complex. As a result, the western Bushveld Complex has drawn considerable scientific interest. For example, geophysical studies have been used extensively to understand the structures and geological characteristics of the mineralization (e.g., Cawthorn and Webb, 2001; Campbell, 2011; Manzi et al., 2020; Sehoole, 2020), geological studies for understanding the emplacement and origin of the mineralization and its host rocks (e.g., Hunter, 1978; Schouwstra et al., 2000; Clarke et al., 2009; Basson, 2019). As a result, mining and geological research have been active at the western limb of the Bushveld Complex. The area offers an opportunity to study the surface exposed geology, mineralization and structures, while underground tunnels provide access to in-situ conditions (pressure and temperature) of the geological structures and mineralisation.

High-resolution geophysical techniques have been widely used for mineral exploration and characterisation of deep and shallow deposits. Many of the shallow deposits are nearing exhaustion, therefore mineral exploration shifted its focus to search for new discoveries at greater depths. Imaging of geological structures and mineralisation at greater depths is challenging for conventional geophysical methods (e.g., magnetics, gravity, 2D reflection seismics, and resistivity), owing to the structural complexity of the orebodies and costs of extracting the ore in a safe manner. Furthermore, the increase in mining depth increases the challenges for new mineral exploration. An alternative solution is to look into greenfield exploration for shallower deposits. However, the need to conduct greenfield exploration has not seen an increase over the years due to costs and project lengths. Therefore brownfield exploration has grown in value and many of the brownfields are yet to be fully exploited.

Brownfield exploration also faces challenges, to state a few: obstructions over mineral deposits due to infrastructure, and vibrational noise as a result of active mining and roads.

In this research, several geophysical surveys were conducted between 2020 and 2022 across the Rustenburg Facies section of the western Bushveld Complex, covering two mines: Royal Bafokeng Maseve and Tharisa mines. The principal objective of this thesis was to utilise in-mine and near-mine geophysical methods (2D reflection seismics, magnetics and electrical resistivity tomography) to image geological structures and mineral deposits in environmentally challenging mine sites.

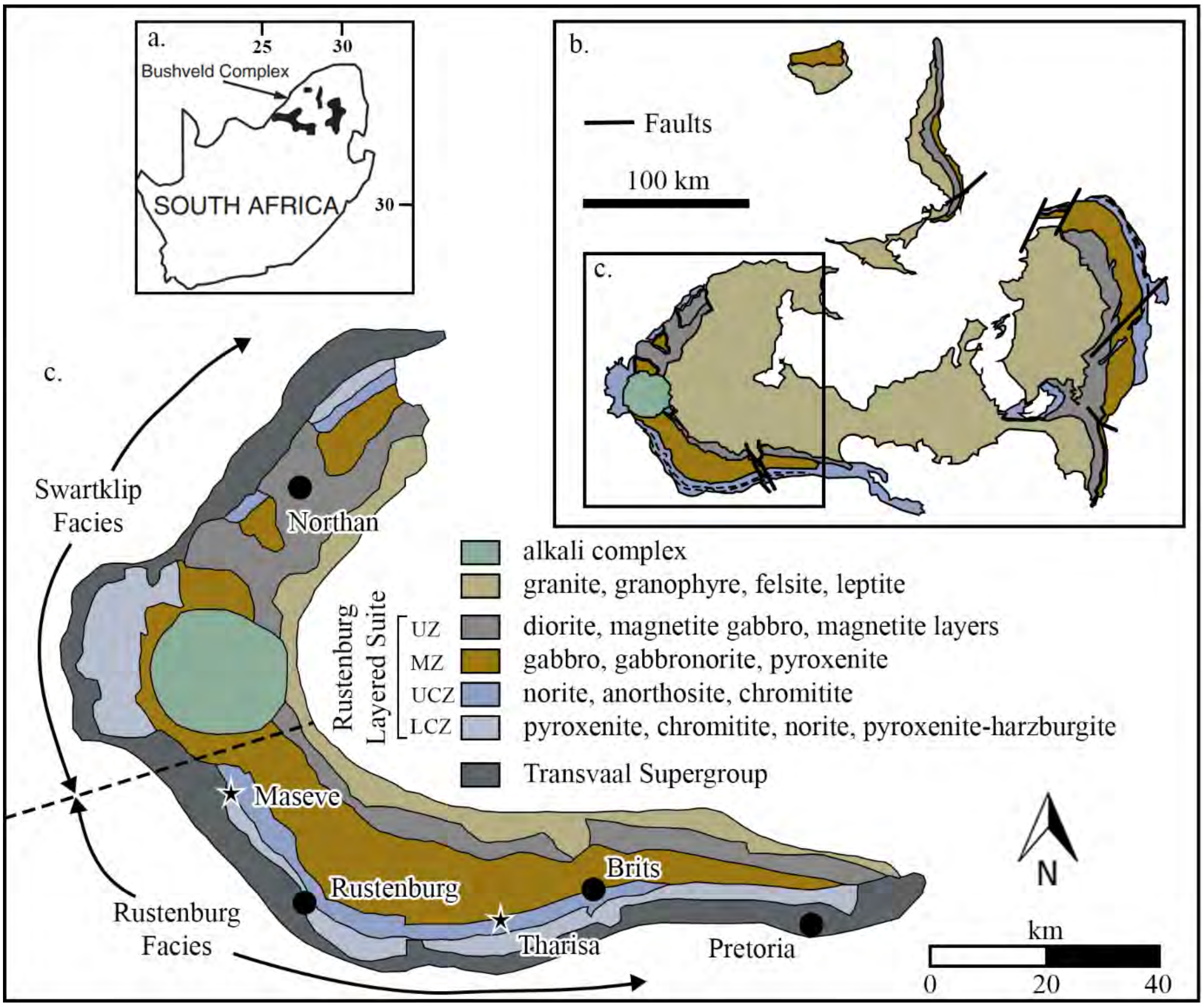

Figure 1.1: *a) Location of the Bushveld Complex within South Africa. b) Geological map of the Bushveld Complex, South Africa. c) Swartklip Facies and Rustenburg Facies, the two primary facies of the Rustenburg Layered Suite that Wagner (1929) described, are depicted on the western limb of the Bushveld Complex. The study areas (stars) are found within the Rustenburg Facies (Modified from Smith et al., 2004).*

Geophysical data acquired in active hard rock mine sites require special attention to processing due to the amount of anthropogenic, vibrational noise and subsurface complex conditions encountered compared to the soft rock environments. Interpretation of 2D reflection dataset is challenging in crystalline hard rock environments that exhibit heterogeneous zones such as faulting and folding, which may cause diffractions and energy scattering. Faults are usually observed as offsets along lateral continuous reflections, and this is rare to encounter in crystalline environments as 2D reflection seismic methods are generally susceptible to revealing sub-horizontal structures, compared to steeply dipping structures (Lundberg, 2014). As a result, the application of multiple geophysical methods (magnetics, electrical tomography resistivity, ground penetrating radar) were utilised in this research together with numerical modelling to improve and constrain 2D seismic interpretation. Geophysical surveys acquired in this research demonstrate that geophysical data can be conducted in unconventional environments in a cost-effective and efficient manner.

While demonstrating the uses of numerical modelling, integrated physical property analyses, and geophysical methods, this thesis has the following objectives:

- To demonstrate the applicability of reflection seismic surveys in cost-effective manner to delineate mineral deposits and their associated geological structures in a noisy mining environment;
- To provide an integrated interpretation of the subsurface and demonstrate the value of geophysical technologies for mineral exploration in noisy crystalline hard rock environments;
- To test seismic response of mineralisation using seismic modelling and physical property studies, and improve the subsurface interpretation of mineral deposits and geological structures.

1.2.Thesis structure

This thesis is based on four case studies and it is divided into 13 chapters. **Chapter 1** highlights the introduction and objectives of the study. **Chapter 2** provides an integrated geological background of the two case studies. The western limb of the Bushveld Complex is described first, along with an overview of its location, tectonic background, and structural layout. Secondly, an overview of mineral deposits found in the BC is presented in case study one to four (Paper I - IV), together with their origin and mining depths. **Chapters 3-4** provide an overview of the theory and methodology of seismic methods for mineral exploration. Firstly, a brief overview of acquisition, processing and interpretation of seismic data in different mining environments is provided. Secondly, modelling algorithms used in all the papers are summarised. Thirdly, the methodologies applied during physical property measurements are presented. **Chapter 5** provides a detailed data acquisition methodologies applied during the study. **Chapter 6** presents the summaries of the scientific papers. **Chapters 7 – 10** contain papers that have been published, and under review. **Chapter 11** provides a brief discussion of the research and synthesis of the manuscripts. **Chapter 12** provides concluding remarks of the research and recommendations. **Chapter 13** provides the list of references used in **Chapters 1-5**.

The main findings in **Chapters 7 - 10** of the research are divided into two case studies:

Case studies 1 - 2: In-mine or tunnel seismics in hard rock environment

- Comparison between spiked and streamer mounted sensors for imaging Platinum Group Elements (PGEs) reefs and complex structures in deep underground mining environments of the Bushveld Complex.
- Testing of conventional (cabled system) seismic equipment inside a mine tunnel.
- Comparison between wireless sensors (1C vertical geophones, 5 Hz), spiked sensors (14 Hz), and streamer mounted sensors (4.5 Hz) in mineral exploration.

The streamer mounted sensors showed considerable advantage over the spiked sensors in mine tunnel seismic surveys in terms of coupling, costs, and deployment time. Application of cabled seismic equipment is discussed as a cheap and an easy-to-deploy exploration technique in noisy mine environment (**Paper I).** The application of wireless sensors was tested as an exploration technique on surface, with a combination of 1C spiked and streamer mounted sensors prior to deployment in underground environments. **Paper II** reports on the results from both surface and tunnel seismic experiments at Maseve mine site. The study served as a pilot study to prepare future work for the simultaneous and time synchronised surface-tunnel data acquisition using a GPS time transmitter developed under the EU-funded Smart Exploration Project.

Case studies 3-4: Open pit geophysical surveys in hard rock environment

Case study 3 demonstrates how integrated seismic, magnetics and electrical resistivity data, combined with borehole data and surface mapping dataset, can characterise geological structures (faults and dykes) and platinum-bearing horizons (reefs) (**Paper III**). Additionally, it demonstrates the challenges faced by the geophysical methods to characterize near-surface fractures and mineralisation in an active mine site with large infrastructure, trucks and electrical powerlines that cause interfering noise during acquisition. The results from case study 1 are integrated with case study 3 (**Paper IV**) that targeted subsurface boulders. Case study 3 demonstrates that integration of geophysical methods can improve mine efficiency and reduce costs. The results from this study are integrated with hydrological and geochemical studies to further unravel and determine the source of water that migrates into the pit (**Appendix C**).

1.3. Contributions

The PhD candidate co-authored several papers during the PhD journey, and also presented at several local and international conferences. However, this thesis presents only the work that is directly linked to his PhD thesis and where he took leadership of the project. Some papers are presented as part of the main chapters, while others listed in the list of appendices. Below is a summary of the authors' contributions to each paper. I am the first author of Chapters 1-12; first author for appendix A, a complementary manuscript to Chapter 7; I am the fourth author for the paper in appendix B and fifth author to appendix C, which is linked to the study conducted in Chapters 9 and 10.

Chapter 7: *Rapetsoa, M. K., Manzi, M. S. D., Westgate, M., Sihoyiya, M., James, I., Onyebueke, E., Kubeka, P., Durrheim, R. J., Kgarume, T., Cost-effective in-mine seismic experiments to image platinum deposits and associated geological structures at Maseve platinum mine, South Africa. Near Surface Geophysics. 2022; 20: 572–589. https://doi.org/10.1002/nsg.12216*

I planned the in-mine seismic experiments and participated in data acquisition in 2020. I processed the seismic data with the help of my supervisors, and compiled the initial draft of the paper and created the majority of the figures. My supervisors helped with the interpretation of the reflection seismic data. Together with the co-authors the manuscript text was improved through a number of iterations and discussions.

Chapter 8: *Rapetsoa, M. K., Manzi, M. S. D., Sihoyiya, M., James, I., Durrheim, R.J., Michelle Pienaar, Innovative seismic imaging of the platinum deposits, Maseve mine – Part II: Surface and In-mine.*

I was involved in the seismic survey design, acquisition and processing of the data. I prepared the figures and wrote the first draft of the manuscript. Discussion of the design, analyses, results and interpretation of the data is conducted over a number of iterations with the authors to improve the manuscript.

Chapter 9: *Rapetsoa, M. K., Gomo, S., Manzi, M. S. D., James, I., Dildar, J., Sihoyiya, M., Mutshafa, N.,* Durrheim, R.J., *Multi-geophysical methods for characterizing fractures in an open pit mine, western Bushveld Complex, South Africa, Geophysical prospecting.*

I was involved in the design and acquisition of seismic, electrical resistivity and magnetics data with S. Gomo, N. Mutshafa, M.S.D. Manzi, and prepared the final data with J. Dildar. The interpretation of the seismic data and electrical resistivity was conducted by myself and was assisted by S. Gomo. I prepared all the figures and wrote the first draft of the manuscript with the assistance from M.S.D. Manzi. The quality of the text was improved by involving all co-authors in discussions.

Chapter 10: *Gomo, S., Rapetsoa, M.K., Manzi, M.S.D., Onyebueke, E., Dildar, J., Sihoyiya, M. et al. (2023) Integrated geophysical methods for boulder delineation to improve mining. Geophysical Prospecting, 00, 1– 21. https://doi.org/10.1111/1365-2478.13322.*

I was involved in the design, acquisition and interpretation of seismic data. I wrote some section of the manuscript, prepared some figures, and was involved in writing the discussion of the results.

1.4. Supplementary material

Supplementary peer reviewed

Appendix A: *Moyagabo K. Rapetsoa, Musa S. D. Manzi, Mpofana Sihoyiya, Michael Westgate, Phumlani Kubeka, Emmanuel Onyebueke, Raymond J. Durrheim; Seismic solutions utilizing existing in-mine infrastructure for mineral exploration: A case study from Maseve platinum mine, South Africa. The Leading Edge 2022; 41 (1): 54–61. doi: https://doi.org/10.1190/tle41010054.1*

I was responsible for the experimental design and data acquisition. I prepared the figures, completed all the analyses, and wrote the first draft of the paper. Discussions of the design and analysis of the data, together with the text, were conducted over a number of iterations with the co-authors.

Appendix B: *Sihoyiya, M., Manzi, M.S.D., James, I., Rapetsoa, M.K., Westgate, M., Nwaila, G., Linzer, L., Durrheim, R.J. and Staley, P. (2022), Seismic delineation of the gold-bearing structures in the South Rand goldfield (South Africa): A comparison of pre-stack time and depth migration approaches on legacy seismic data. Near Surface Geophysics, 20: 697-709. https://doi.org/10.1002/nsg.12209*

My contribution to this manuscript included interpretation of the seismic data and assisted with the revisions of the manuscript.

Supplementary manuscripts

Appendix C: *Dildar, J., Manzi, M., Abiye, T., Gomo, S., Rapetsoa, M. K., Drennan, G. (2023). Groundwater Circulation in the Shallow Crystalline Aquifer of 2 Tharisa Mine, South Africa: Evidence from Environmental 3 Isotopes and Near-Surface Geophysics*

I was involved in preparation of images, interpretation and discussion of the seismic data.

Peer reviewed abstracts and reports

I participated and presented peer-reviewed abstracts in several local and international conferences:

- Berhanu, R., Manzi, M., Westgate, M., Sihoyiya, M., **Rapetsoa, M. K.** (2022). Reprocessing of Legacy Seismic Profile for Shale Gas Exploration in the Karoo Basin (South Africa). Presented at the NSG2022 28th European Meeting of Environmental and Engineering Geophysics, European Association of Geoscientists & Engineers. 18-22 September 2022.
- Dildar, J., Manzi, M., Abiye, T., Gomo, S., **Rapetsoa, M. K.**, Sihoyiya, M. (2022). An Integrated Approach to Characterise the Subsurface Using Near Surface Geophysical Methods. Presented at the NSG2022 4th Conference on Geophysics for Mineral Exploration and Mining, European Association of Geoscientists & Engineers. 18-22 September 2022.
- Mabele, N., Manzi, M., Sekiba, M., **Rapetsoa, M.K.**, Gomo, S., Mutshafa, N., Onyebueka, E. (2022). Delineation of the Sinkhole along R21 Highway in Gauteng (South Africa) Using Integrated Geophysical Methods. Presented at the NSG2022 28th European Meeting of Environmental and Engineering Geophysics, European Association of Geoscientists & Engineers. 18-22 September 2022.
- Manzi, M. S. D., Brodic, B., **Rapetsoa, M. K.** (2022). Tunnel Seismics for Mineral Exploration – Is it Worth The Effort? Presented at the NSG2022 4th Conference on

Geophysics for Mineral Exploration and Mining, European Association of Geoscientists & Engineers. 18-22 September 2022.

- Matamela, J., Manzi, M. S. D., **Rapetsoa, M. K.** (2022). Combined Downhole and Surface Seismic Investigation of the Karoo Basin, South Africa. Presented at the NSG2022 4th Conference on Geophysics for Mineral Exploration and Mining, European Association of Geoscientists & Engineers. 18-22 September 2022.
- Mayipheli, I., Manzi, M. S. D., Sihoyiya, M., **Rapetsoa, M. K.** (2021). Physical property analysis and de-noising of the legacy seismic data: Implication for CO2 storage site characterisation, Zululand basin, South Africa. Presented at the 15th Africa Array Scientific Meeting, Africa Array. 1-3 December 2021.
- Mkhomazi, M. N., **Rapetsoa, M. K.**, Manzi, M. S. D., Gomo, S., Sihoyiya, M. (2022). Delineation of Underground Tunnels Using Seismics and Magnetics at Golden Valley Mine, South Africa. Presented at the NSG2022 4th Conference on Geophysics for Mineral Exploration and Mining, European Association of Geoscientists & Engineers. 18-22 September 2022.
- Onyebueke, E., Manzi, M., **Rapetsoa, M.K.**, Westgate, M. (2021). In-mine Underground Tunnel Seismic Experiment, using High-resolution Reflection Seismic Method at Maseve Mine, Rustenburg, South Africa. Presented at the 82nd EAGE Annual Conference & Exhibition, European Association of Geoscientists & Engineers. 18-21 October 2021.
- **Rapetsoa, M. K.**, Manzi, M. (2021). In-Mine Seismic Method for Platinum Orebody Exploration in Maseve Platinum Mine, South Africa. Presented at the NSG2021 2nd Conference on Geophysics for Infrastructure Planning, Monitoring and BIM, European Association of Geoscientists & Engineers. 29 August – 2 September 2021.
- **Rapetsoa, M. K.**, Manzi, M. S. D., Sihoyiya, M., Westgate, M., Kubeka, P., Onyebueka, E., Durrheim, R. J. (2021). Seismic solutions utilizing existing in-mine infrastructures for mineral exploration: a case study from Maseve Platinum Mine, South Africa. Presented at the 15th Africa Array Scientific Meeting, Africa Array. 1-3 December 2021.
- **Rapetsoa, M. K.**, Manzi, M., Westgate, M., Gomo, S., Sihoyiya, M., Dildar, J. (2022). Multi-Geophysical Characterization of Water Conduits in an Open Pit Mine, Bushveld Complex, South Africa. Presented at the NSG2022 4th Conference on Geophysics for Mineral Exploration and Mining, European Association of Geoscientists & Engineers. 18-22 September 2022.

- Sihoyiya, M., Manzi, M. S. D., **Rapetsoa, M. K.**, Westgate, M. (2021). Re-processing of the 2D legacy seismic data for improved structural imaging and gold exploration in the South Rand Goldfield, South Africa. Presented at the 15th Africa Array Scientific Meeting, Africa Array. 1-3 December 2021.
- Sihoyiya, M., Manzi, M., Westgate, M., Rapetsoa, M.K., James, I. (2022). Reprocessing Legacy Seismic Data for Imaging PGE Mineralisation: Case Studies from the Bushveld Complex, South Africa. Presented at the NSG2022 4th Conference on Geophysics for Mineral Exploration and Mining, European Association of Geoscientists & Engineers. 18-22 September 2022.

2. Study areas

This section provides a brief summary of the geological background of the study areas that are presented in this thesis. The case studies that form part of this thesis are from two mine sites, which are located in the western Bushveld Complex, South Africa (Figure 1.1). **Papers I – IV** focus on the igneous intrusion of the Bushveld Complex (2.1 Ga), in the northwest South Africa, near the city of Rustenburg. A more detailed description is given in the papers (**Chapters 7-10**).

2.1. Maseve mine

Maseve mine, in the North West Province South Africa, is located in the highly mineralised Critical Zone of the Bushveld Complex (Figure 1.1). The province is known for its rich chromite and Platinum Group Element (PGE) deposits that are used in a variety of sectors. Host rocks of the PGE mineralisation are mafic to ultramafic igneous rocks of the Palaeproterozoic age (2.06 Ga) (Eales and Cawthorn, 1996; Kinnaird, 2005).

The deposits are spread across the Bushveld Complex, with the two main economic horizons for PGE deposits being Merensky Reef (MR) and Upper Group 2 (UG2) chromitite. The economic deposits are found in flat layered horizons and are crosscut by multiple intrusions such as the diabase and dolerite dykes. Faults, slump structures (e.g., potholes), and iron-rich ultramafic pegmatites (IRUPs) further disrupt the mineralization. (Lee, 1996; Campbell, 2011; Cawthorn, 2015).

The study area is located about 10 km south of Pilanesburg Alkaline Intrusive Complex and 38 km northwest of the city of Rustenburg. Figure 1.1 shows the location of the study area in near Maseve mine and the details about the main geological units are reported in **Papers I and II.**

2.2.Tharisa mine

Tharisa mine is a chromitite and platinum mine, located in the northwest province of South Africa. The mine is 35 km east of the city of Rustenburg. The mine operates on surface with two open pits, and there are plans to develop underground operations in the future to exploit deeper mineralisations (Lotheringen et al., 2016).

The mine currently exploits the Middle Group (MG) chromitites that are situated in the Critical Zone of the Bushveld Complex (Figure 2.1) with the UG1 being 165 to 18 m above the MG. The deposits have a general thickness ranging from few centimeters to 3 m (Lotheringen et al., 2016). The Bushveld Complex within the study area has been affected by several faults and dykes that coincides with areas of weakness that were reactivated during the emplacement of the Bushveld Complex (Bumby et al., 2012; Hartzenberg and Plessis, 2014). Detailed geological section is provided in **Papers III and IV**.

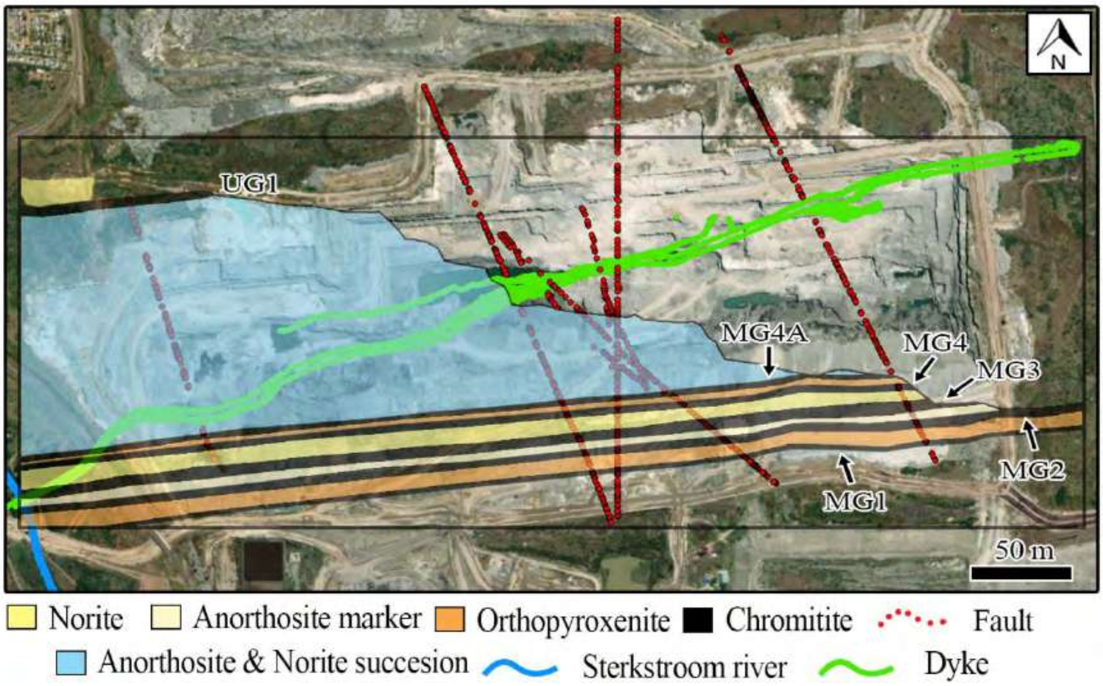

***Figure 2.1**: Overview of mineral deposits that are exploited at Tharisa mine together with the associated geological structures (Dyke: green, Faults: red). Figure adapted from Paper III.*

3. Methods

This section describes the theoretical background for geophysical methods that are relevant to the research presented in this thesis. Papers I and II are concerned with reflection and refraction seismic methods, while Papers III and IV are concerned with seismic, magnetic and electrical resistivity methods. Hand and borehole rock samples of the target ore deposits and host rocks were collected from the sites to conduct physical property measurements such as bulk density and seismic velocities using an ultrasonic system. 2D finite difference modeling was carried out and a 1D synthetic seismogram was generated to help with the interpretation of the seismic data and to study the origin of seismic reflectivity (see Paper I). Furthermore, 3D ray tracing was also conducted to constrain seismic interpretation (Paper II).

3.1. Seismic method

Reflection seismic techniques have been used in hard rock environments for mineral prospecting, due to the high-resolution imaging they provide (Eaton et al., 1996; Manzi et al., 2012; Maliwonski et al., 2012; Ahmadi et al., 2013; Malehmir et al., 2013; Bellefleur et al., 2015; Cheraghi et al., 2015). South Africa has done 2D and 3D high-resolution reflection seismic surveys over the past 30 years to better understand mineral reserves and increase mine safety and planning.

3.1.1. Acquisition

Seismic methods require sources (e.g., vibrational, impact and explosives) to inject seismic energy into the ground. The source can generate three types of seismic waves: P waves (backward and forward particle motion), S waves (side to side particle motion) and boundary waves (complex particle motion). Over the years, seismic surveys utilised high velocity P waves only. However, technological advancement has allowed the use of sources that generate S-waves, which can be recorded through multicomponent sensors that measure all the seismic waves (Manzi, 2014; Cox, 2020).

Prior to a reflection seismic data acquisition, one needs to design a survey using certain acquisition parameters, to state a few, a recording length, sample interval, offset and spread type. The choice of these parameters is controlled by the objective of the survey. Several receivers (seismic spread) can be set up for a seismic survey, with the receivers aligned along a certain direction (Knapp and Steeples, 1986). In this research split spread (Figure 3.1a) and end-on spread (Figure 3.1b: roll along) source-receiver geometry were employed to acquire the seismic data. Multiple shots are taken along the profile at specific locations and the energy generated is recorded by multiple receivers on surfaces. To improve the signal-to-noise ratio (SNR), the traces are then sorted into sets of gathers that have a common midpoint (Figure 3.1c: CMP). The source and receiver are moved in a systematic pattern across the survey, resulting in a coverage area were common midpoint traces are summed up, resulting in a fold coverage (Bjorlykke and Mondol, 2010). Figure 3.1d demonstrates the concept of fold due to multiple shots taken along the same trajectory. In Paper II, the effect of seismic spread to fold coverage is demonstrated. Nominal fold is expressed as:

$$F = \frac{N\Delta g}{2\Delta s}, \qquad (3.1)$$

where N is the number of channels, Δg is the receiver spacing and Δs is the source spacing.

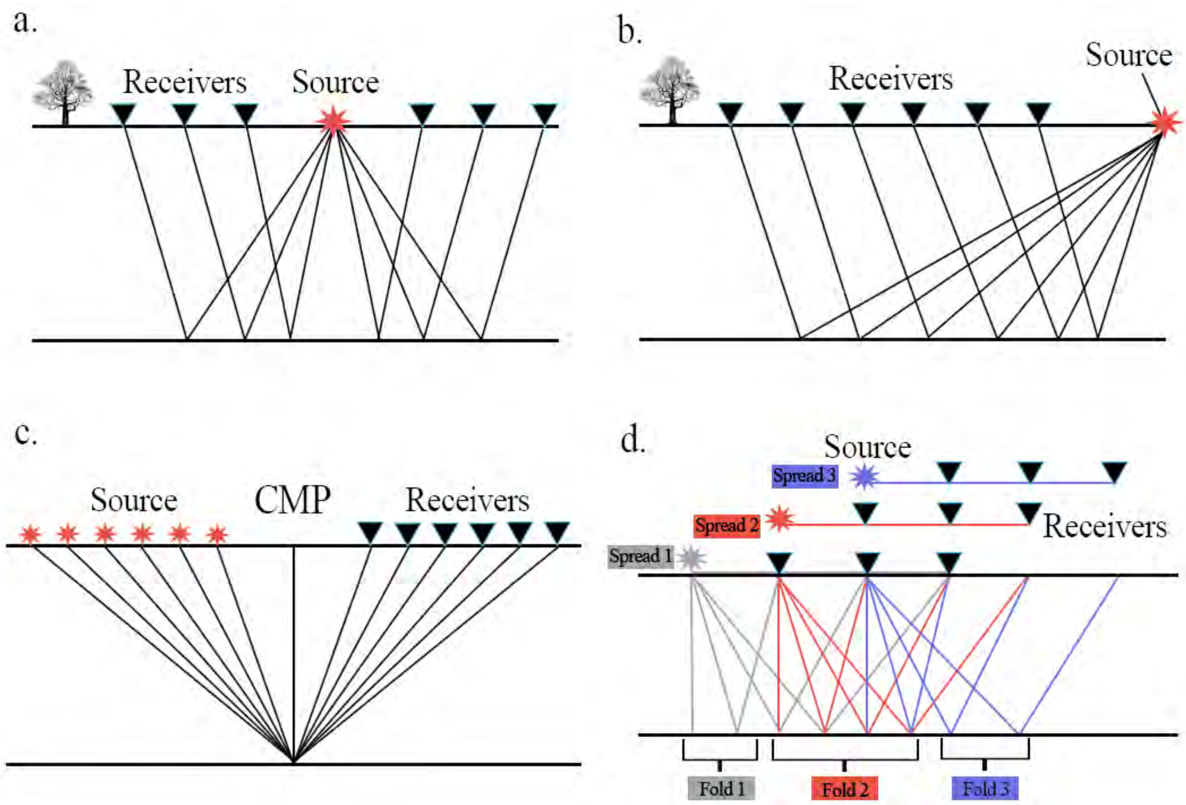

Figure 3.1: *Geometries of the source and receiver in reflection seismic surveys. a) Split spread. b) End-on spread. c) Common midpoint (CMP) gather for a horizontal layer. d) Roll along data acquisition setup showing the increase in fold at the centre of the profile.*

Seismic waves are transmitted, reflected and refracted (Figure 3.2) at boundaries that have a change in physical properties (e.g., velocity, density and young moduli). Receivers (geophones) detect the waves that have travelled through the media and the time taken to travel is referred to as two-way travel time (TWT). The waves propagate through the media at different velocities and the refracted waves are based on Snell's law as expressed by Yilmaz (2001):

$$\frac{\sin \theta_1}{\sin \theta_2} = \frac{V_2}{V_1}, \qquad (3.2)$$

where V_1 and V_2 are the velocities of the first and second medium, while θ_1 and θ_2 are the angles of incident and refraction, respectively. If the incident angle achieves a critical angle, then the ray is refracted such that it runs along the boundary creating a head wave that emits critically refracted waves back to the surface (Figure 3.2). The properties of the different media can be determined using the travel time and wave-motion velocity for the refracted and reflected ray.

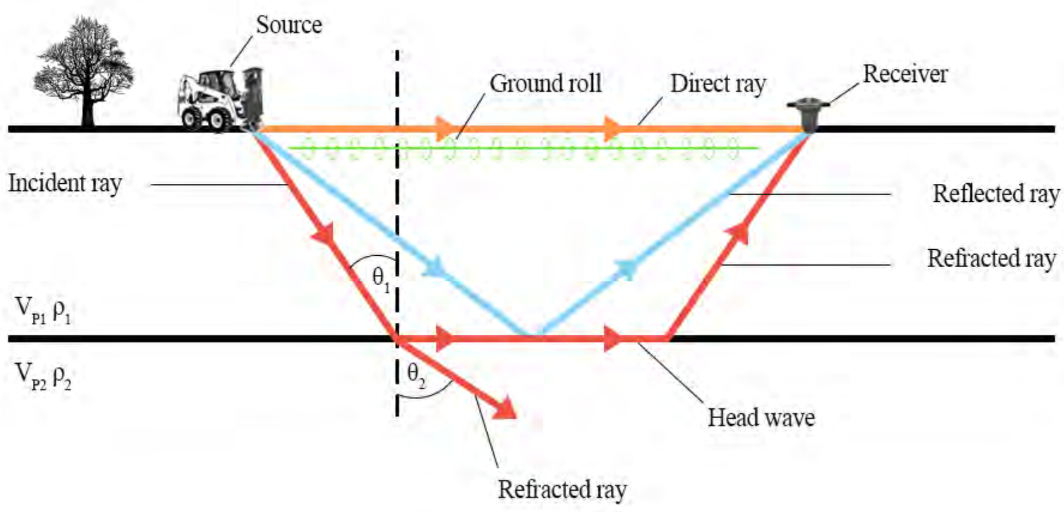

Figure 3.2: *Diagram displaying the seismic wave arrivals from the source (direct, reflection, and refraction) that are reflected or refracted at lithological boundaries and detected by the receivers. V_p: P-wave velocity, ρ: density.*

The strength of reflections are in general influenced by the impedance contrast (the product of seismic velocity and density). The impedance contrast between different media can be influenced by changes in lithology, porosity, diagenesis, to mention a few (Bjorlykke and Mondol, 2010; Alsadi, 2017). The proportion or ability for seismic energy to produce a strong reflection is controlled by the reflection coefficient (the ratio of reflected to incident energy), with a required minimum incident energy of at least 6% needed for the reflection to be detected (Salisbury et al., 2003). The normal incidence P-wave is expressed by (Salisbury et al., 2003):

$$R = \frac{z_2 - z_1}{z_2 + z_1} = \frac{V_{P_2}\rho_2 - V_{P_1}\rho_1}{V_{P_2}\rho_2 + V_{P_1}\rho_1}, \tag{3.3}$$

where $Z = V_P \cdot \rho,$ is the impedance, V_P is compressional-wave velocity, and ρ is the bulk density of the corresponding medium. Some of the energy is transmitted rather than being entirely reflected back to the surface, and this energy is crucial for imaging deeper boundaries.

CMP-sorting

Seismic data are recorded with sequential shots fired at different locations. One shot location has multiple traces that are recorded by active receivers during acquisition. A trace is defined as a time series of reflections for measurement of one shot at one receiver position. The traces are sorted with the distance (offset) between the shot location and receiver (Figure 3.3). The process is repeated for multiple shot locations and stored in the recording instrument. The seismic data are commonly stored and organised in common-shot gathers for logistical purposes. However, for processing purposes it is more convenient to sort the data in common-midpoint (CMP) gathers. Common-midpoint sorting of data involves picking traces that have one midpoint from a shot record (Figure 3.3), with traces sorted with either an increasing or decreasing offset. The midpoint here is defined as the midpoint between the source and receiver position (Yilmaz, 2001, pp93; Denttith and Mudge, 2014). The number of traces that are collected into a gather are equal to the fold and can be calculated using Equation 3.1. CMP - sorting is important for normal moveout (NMO) corrections and stacking of seismic data, which will be discussed later.

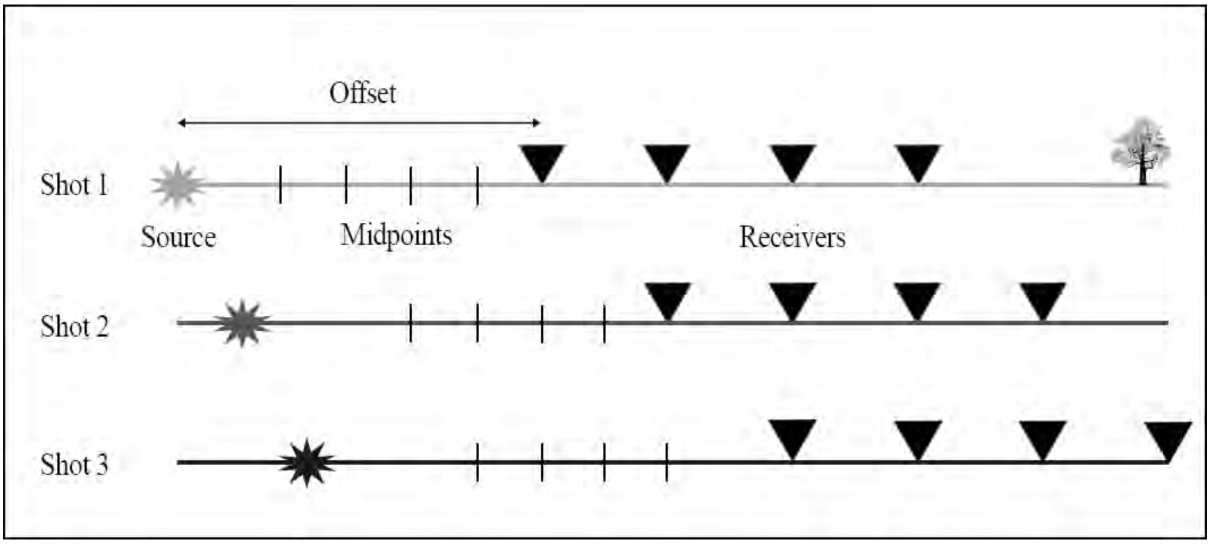

***Figure 3.3**: Diagram illustrating the Common midpoint between sources and receivers (Adapted from Drijkoningen, 2016).*

Seismic resolution

Mineral deposits in the Bushveld Complex have a thickness ranging between 4 cm and 3 m (Lee, 1996). Seismic resolution is the ability to distinguish between closely spaced objects so that they can be seen as two or more rather than one. Geological layers can be very close such that they are indistinguishable on seismic data. Therefore, when designing a survey, it is important to consider parameters that provide the best resolution for the acquired data. Seismic resolution can be divided into two categories: Vertical and horizontal resolution (Chopra et al., 2006). The ability to distinguish between two arrivals that are the result of the top and bottom layer is referred to as vertical resolution (Figure 3.4a), whereas the horizontal resolution is focused on lateral feature distinction on the same interface. Vertical resolution is based on the Rayleigh limit of resolution, which states that the thickness of a layer must be ¼ of the dominant wavelength. Vertical resolution limit is usually taken as $\frac{\lambda}{4}$ in the presence of noise (with $\lambda = \frac{v}{f}$, where λ is the seismic wavelength, ν is the mean velocity and f is the dominant frequency). However, it is possible to detect layers down to $\frac{\lambda}{32}$, for data with high SNR (Widess, 1973; Manzi, 2014; Chopra et al., 2006). Unless the layer thickness is greater than a wavelength, interfaces with close spacing cause seismic arrivals to overlap (Figure 3.4b). Due to absorption, seismic waves lose high frequencies and velocities with depth, therefore vertical resolution decreases with depth.

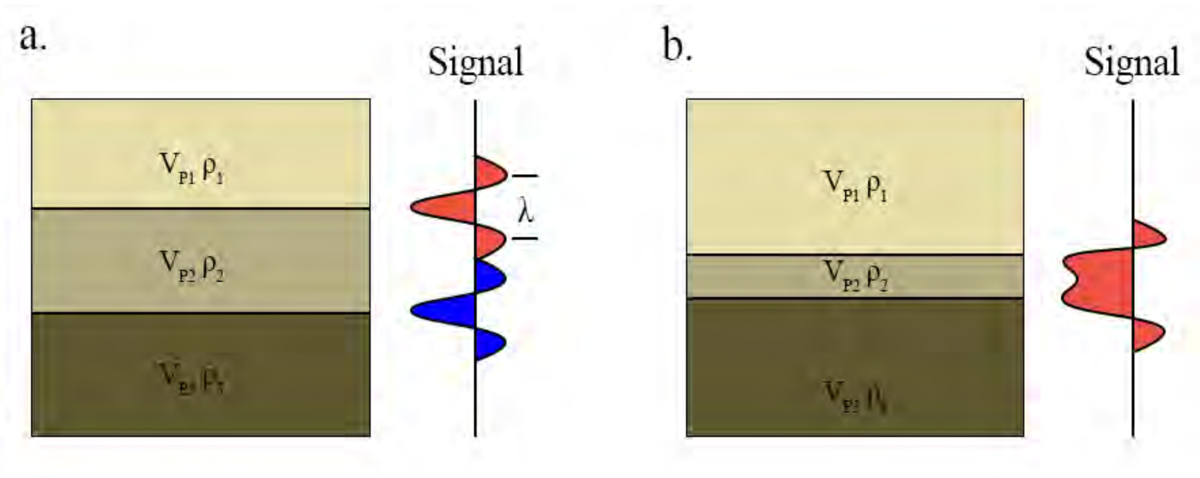

Figure 3.4: *a) Model demonstrating thick layer signals. Layers are easily resolved because their thickness exceeds the dominant wavelength. b) Thin layer model, with layer two having a thickness less than the dominant wavelength. The signal for top and bottom interfaces overlap. λ: wavelength, V_p: P-wave velocity, ρ: density.*

Horizontal resolution is based on the Fresnel zone criterion. The Fresnel zone represents an area (Figure 3.5: A-A*) where seismic energy is returned to the receivers within half the wavelength of the initial reflected arrivals. The size of the Fresnel zone represents the horizontal resolution limit, where reflections that are separated by a distance smaller than the Fresnel zone cannot be separated (Kearey, 2002; Ordońez, 2014). The Fresnel zone width is dependent on the depth to the reflectors, dominant frequency and the velocity above the reflector. It is expressed as (Yilmaz, 2001):

$$w = \sqrt{\frac{z_0 \lambda}{2}} = \frac{V}{2}\sqrt{\frac{t_0}{f_d}}, \tag{3.4}$$

where V is the velocity, t_0 is the two-way travel time, and f_d is the dominant frequency. It is important to note the effect of receiver spacing on the horizontal resolution. In order for reflections from the same layer to be well correlated in complex environments, the distance between receivers needs to be kept to a minimum.

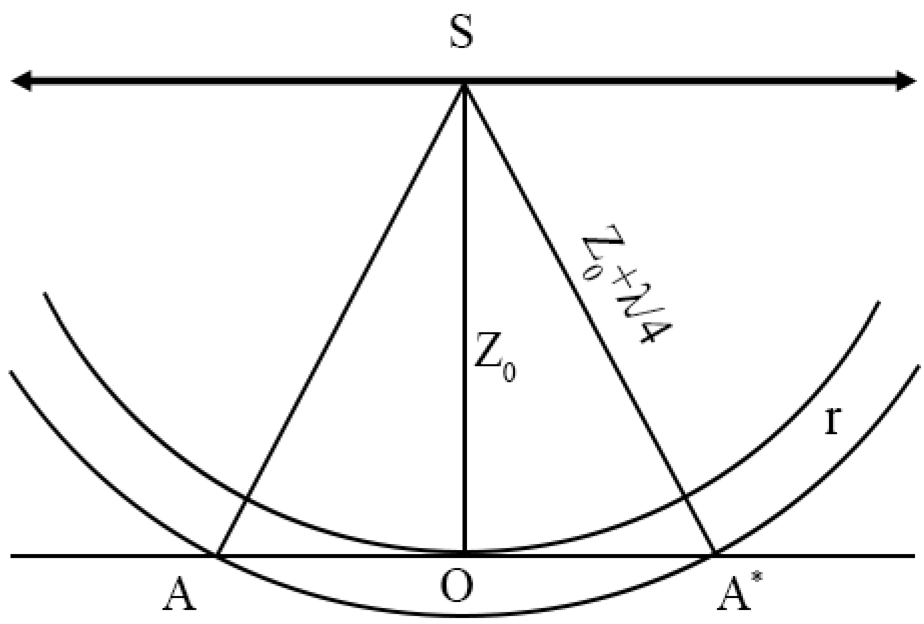

Figure 3.5: *Z_0 is the distance between the reflector and the surface, λ is the wave-front's wavelength, and r is the distance between the first Fresnel zone and the reflection interface O. Z_0 is the distance between the reflector and the surface, λ is the wave-front's wavelength, and r is the distance between the first Fresnel zone and the reflection interface O. (Adapted from Bjorlykke and Mondol, 2010).*

3.1.2. Processing

Seismic processing in 2D and 3D datasets aims to provide a clear 2D or 3D subsurface image while increasing the SNR of seismic data by suppressing the incoherent and coherent noise. Reflection seismic surveys aim at enhancing and exploiting the reflected waves. The reflections are observed as hyperbolic features on a seismic shot gather and can provide information about the geological interfaces. The shot gather is not only populated by reflection features. Ground rolls, direct waves and refracted waves also manifest as linear features on the shot gather (Figure 3.6). This section highlights the processing steps that were predominantly applied in this thesis. Processing parameters are summarized in each paper. It is also important to note that the processing steps cannot be standardized as they are dependent on 1) the objectives of the study and 2) costs of the study versus quality of data required.

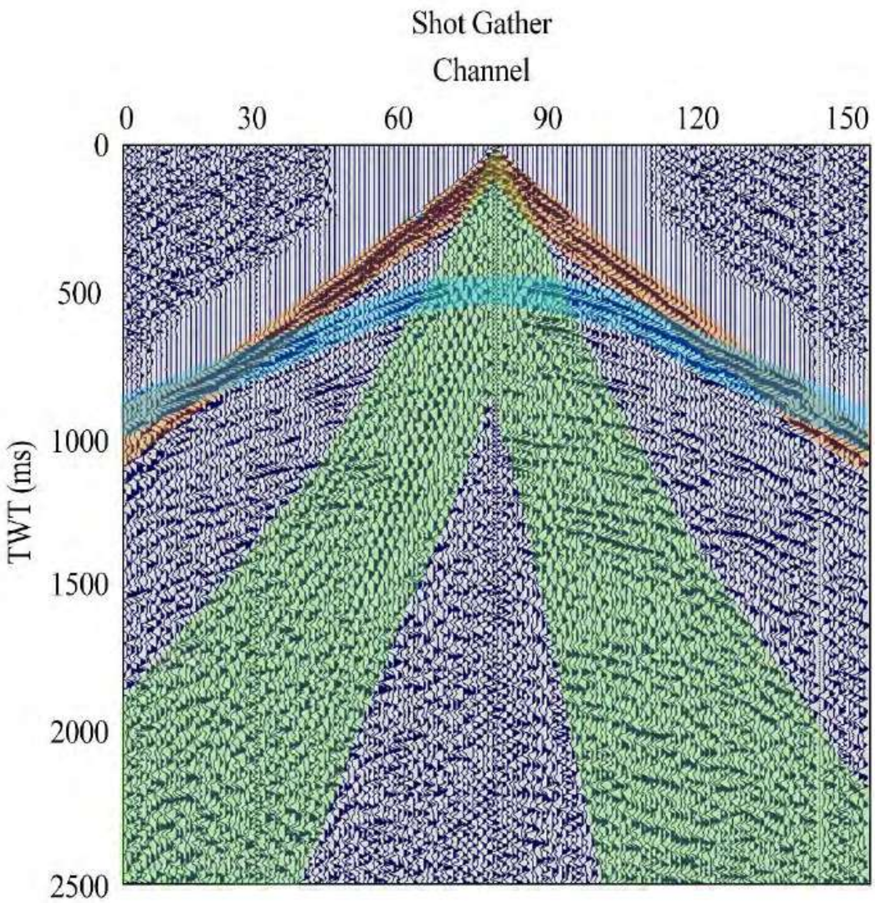

Figure 3.6: *Shot gather showing the seismic wave events (coloured) that correspond with those on Figure 3.1. Blue: reflected waves. Orange: direct and refracted waves. Green: Ground roll.*

Processing of seismic data can be grouped into five corrections: time, amplitude, frequency-phase content, stacking and migration. The above mentioned corrections are important to improve SNR and corrections for physical processes such as the elevation changes and weathered layer.

Static corrections

Seismic wave propagation is theoretically assumed to be conducted on a flat surface and layers of uniform velocity as discussed in velocity analysis section below. However the actual observations can be conducted in terrains that have high variable elevations, resulting in varying reflection times of seismic traces (Figure 3.7a). The time variation introduced by near - surface irregularities can affect the positioning of the reflections and result in the traces in a CMP gather not stacking properly. Therefore static corrections are important to compensate for this effect (Yilmaz, 2001; Kearey, 2002).

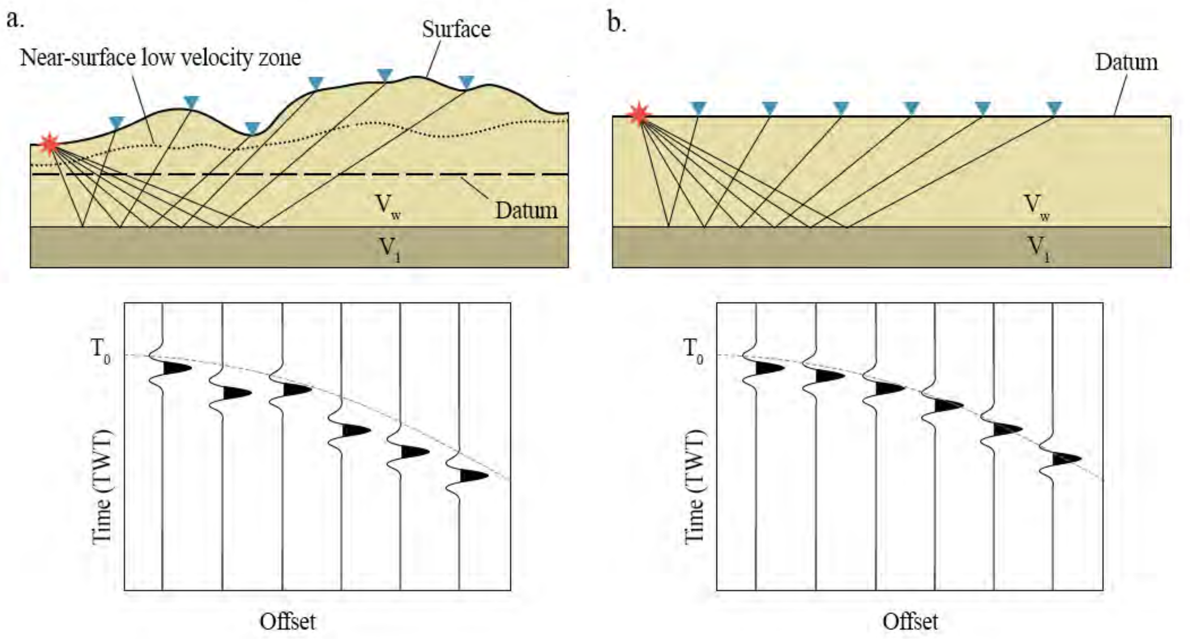

Figure 3.7: *Static corrections. a) The ideal smooth curvilinear moveout (dotted red line) of the reflections is delayed or distorted by static effects due to elevation changes and the near-surface low velocity zone (dotted black line). b) Static corrections applied to the same shot gather, showing good curvilinear alignment of the reflection traces that are equivalent to travel times from a horizontal datum beneath the low velocity zone.* V_W*: P-wave velocity of weathered layers,* V_1*: P-wave velocity of hard rock (Adapted from O'Brien, 1974).*

Static corrections are separated into two components: elevation static corrections and weathering static corrections. The elevation statics are usually applied to correct for surface heights of the geophones and shot points, while weathering static corrections are applied to correct for the low seismic wave velocity layers that spans few to tens of meters thick below the shots and receivers (Kearey, 2002; Cox, 2020). Knowledge of the seismic wave velocity of the weathered layer is important for application of weathering static. Refraction static analysis u to determine the variable velocity and thickness of the top layer and thus used in reflection processing (Opara et al., 2018).

Filtering

Filtering of seismic data can be divided into three components for the purpose of this thesis: 1) Velocity filtering (*f-k*), 2) frequency filtering to enhance the SNR of the data, and 3) inverse filtering (deconvolution) to improve vertical resolution. The choice of a filter and its parameters depends on the targeted events on a seismic shot gather (Yilmaz, 2001; Kearey, 2002). The first filtering technique to be discussed is the frequency-wave number (*f-k*) filter that can be applied to attenuate coherent noise that is introduced during acquisition by the instrument and ground roll. Different seismic events, due to their characteristic velocities, may appear as coherent linear features (Figure 3.8a) with a particular dip angle in the *f-k* plot (Westgate, 2020). The *f-k* spectrum is divided into two panels: the negative panel (Figure 3.8b: red outline) that is characterised by negative wavenumbers and consists of events such as 1) mechanical noise, 2) back scattered events, and 3) aliased energy. While the positive panel (Figure 3.8b: blue outline) is characterized by positive wave numbers and consists mainly of events such as 1) refracted waves, 2) direct waves, 3) reflected waves, and 4) multiple reflections. However, it is possible for the positive wave number events to exist in the negative panel. Different events are easily differentiated and removed in the *f*-k domain compared to the *t-x* domain. This is as a result of each event having amplitudes that arise at different sections of the *f-k* spectrum. The hyperbolic nature of the reflections result in their amplitudes being grouped around the frequency axis on both sides of the panels. Since reflections are our primary target, application of *f-k* is to create a polygon that preserves the signal amplitudes of the reflections (Figure 3.8b: fan shaped polygon) or alternatively create a polygon that discriminates the noise signals that are to be filtered out.

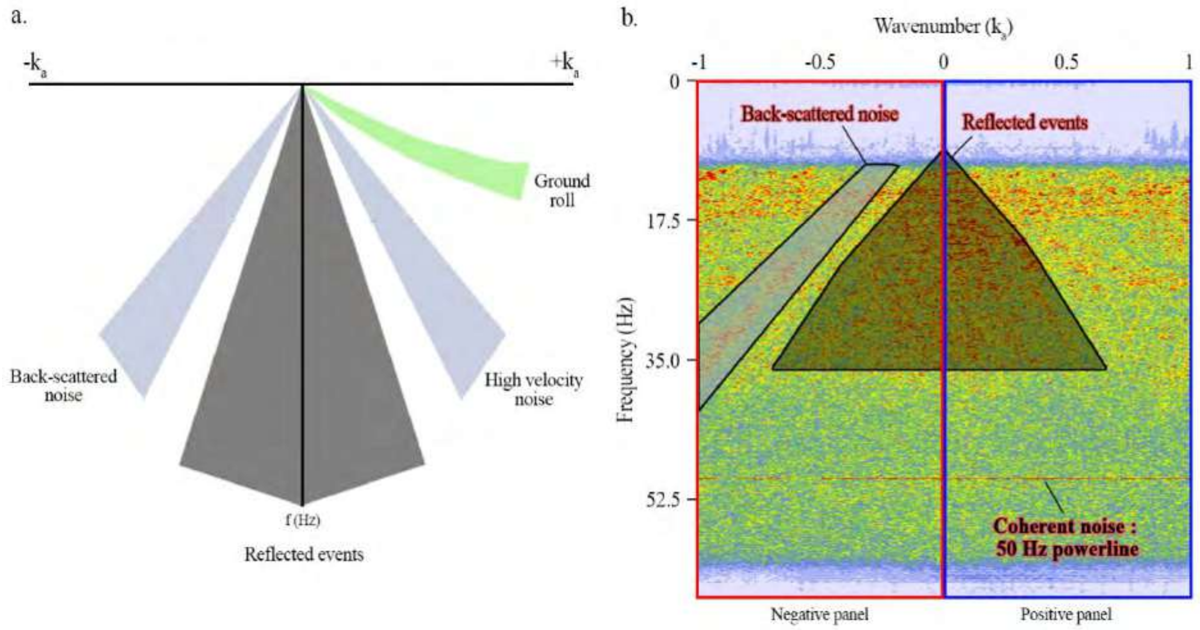

Figure 3.8: *a) f-k plot showing reflection events and different types of noise that can be found in a seismic shot gather. b) An example of f-k spectrum from a shot gather in Figure 3.6. Coherent noise from the 50 Hz power line is noted, with ground roll (light green) linear features noted on the edge of the spectrum and reflection event at the center (grey).*

Figure 3.9a–c illustrates an application of the *f–k* filter to data from Paper II. This shot gather shows strong contamination by the 50 Hz noise and ground roll in both the *t-x* (Figure 3.9a) and *f-k* domain (Figure 3.9c). Figure 3.9b depicts a shot gather with attenuated ground roll following the application of an *f-k* filter. Traditionally, low frequency and high frequency random noise would be removed using a band pass filter before the *f-k* filter was applied. However, through a trial and error approach, the application of an *f-k* filter was more effective to the dataset presented in Paper II. Filters are applied in no particular order, as they are unique to each dataset. For the short seismic profiles from Papers I and III, a band pass filter with frequencies between 3 and 180 Hz was used. The *f-k* spectrum shows a distinct horizontal noise in both panels, and this is the 50 Hz noise from the electrical power cables. This event can either be removed using a notch filter or it can be removed on the *f-k* domain (Figure 3.9d). The ground roll has the largest inclination on the shot gathers and the amplitudes appear closer to the wavenumber axis on the *f-k* spectrum, whereas the S-waves have velocities of 1300 m/s and appear as linear events with a mild inclination on the *f-k* spectrum.

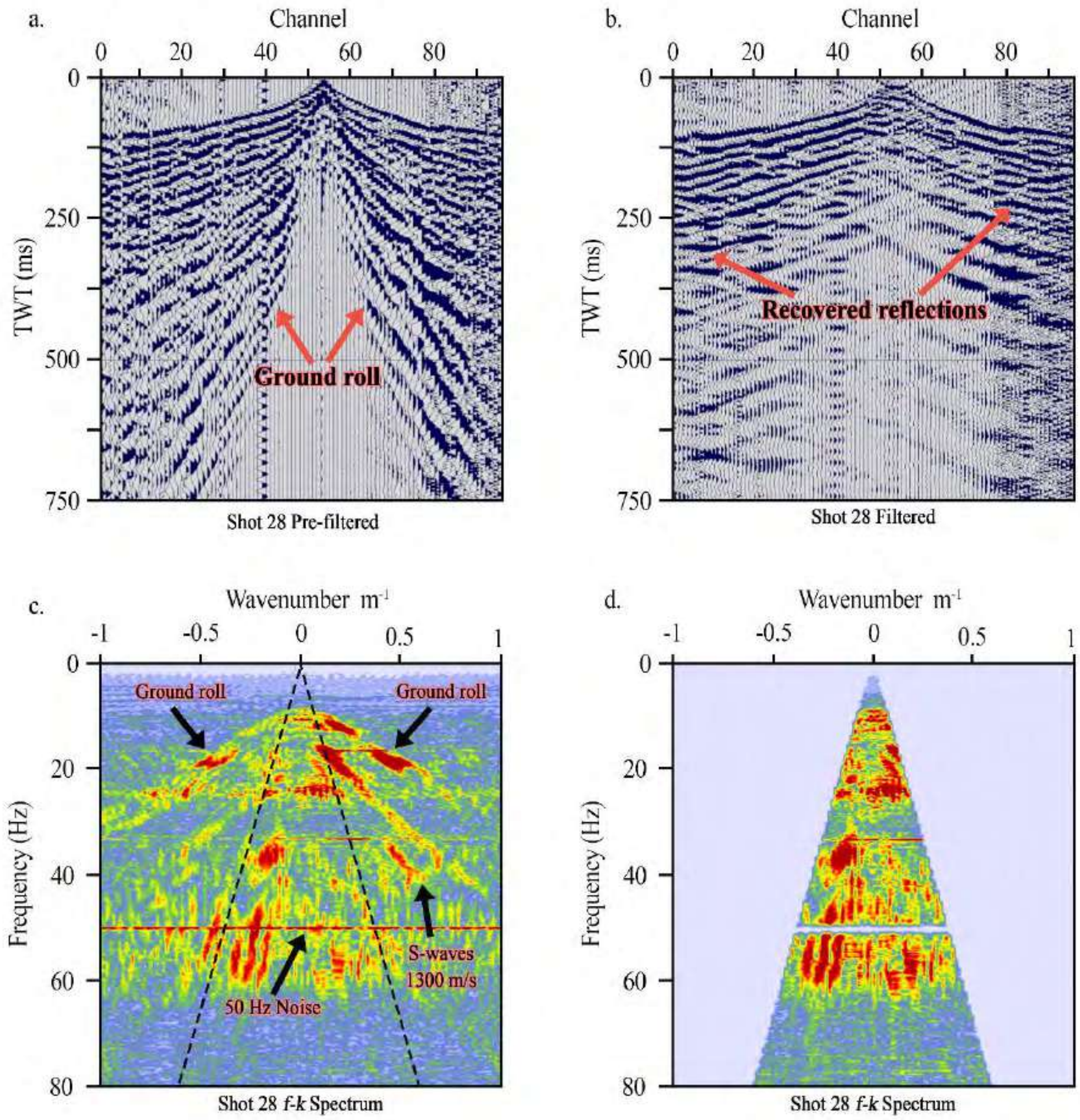

Figure 3.9: *Diagram showing the application of f-k on seismic data from Paper III. a) Raw seismic shot gather. b) Shot gather after application of f-k filter. c) f-k spectrum for raw shot gather. d) f-k spectrum with the removed ground roll.*

Frequency filtering is usually applied to attenuate any coherent or incoherent noise. Multiple sets of filters exists depending on the type of noise targeted. The filters that were applied for this thesis are shown in Figure 3.10 and are described below:

- **High pass (Figure 3.10a):** This filter preserves frequencies above the cut off frequencies (f_c). This filter is usually applied to attenuate low frequency contamination from the equipment sensitivity.

- **Low pass (Figure 3.10b):** This filter is similar to the high pass filter, however it is inverted and preserves frequencies below the cut off frequency (f_c). Low pass filter is useful for to cut off the high frequency signals that are not desired (e.g., spurious frequencies).
- **Band pass (Figure 3.10c):** This filter preserves frequencies between two boundaries – lower bound (f_l) and upper bound (f_u). It is the most commonly used filter in reflection seismics.
- **Band stop (Figure 3.10d):** This filter is similar to band pass filter, However it cuts off frequencies between the lower bound (f_l) and upper bound (f_u).
- **Notch (Figure 3.10e):** This filter targets a specific frequency from the spectrum. It is useful for removing constant consistent frequency. For example the frequency of the AC current carried in South African power cables is ~ 50 Hz. Data collected on surface in Paper II shows evidence of the 50 Hz frequency contaminating the far offset signal.

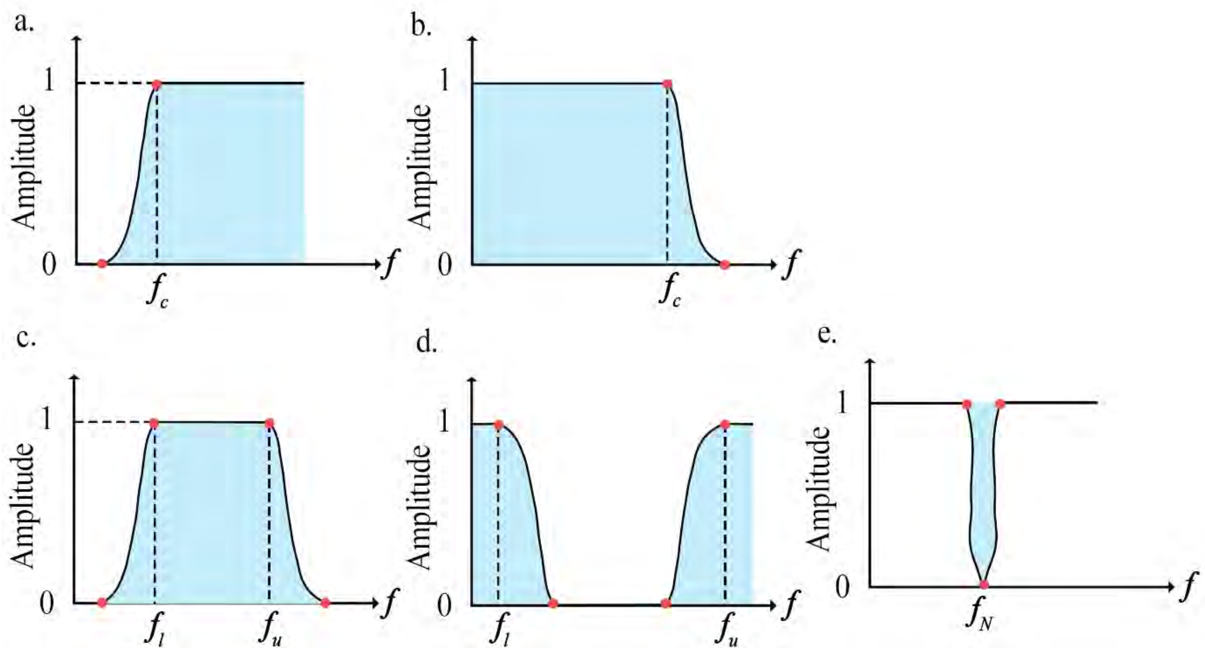

Figure 3.10: *Amplitude spectrum of frequency filters that are usually applied in reflection seismic processing. a) High pass, b) low pass, c) band pass, d) band stop, and e) notch. The filters are tapered at the edges. f_c: Cut off frequency. f_l: lower bound frequency. f_u: Upper bound frequency. f_N: Notch frequency. Red points show the corner frequencies.*

The commonly used filter is the band pass filter for removing the low and high frequencies that populate seismic data. Figure 11a shows the sinc function with oscillations that result in the ringing effect (Figure 3.11b) known as the Gibbs phenomenon (Vretblad, 2003). The filters are tapered on the ends and the resulting sinc function is smoothed (Figure 3.11c). Different sets of tapers are applied, but the most commonly used are the Ormsby filter (zero phase) and Butterworth filter (minimum phase). The Ormsby is characterized by four corner frequencies as shown in Figure 3.11d. Contrarily, the Butterworth filter uses two cutoff frequencies that are 3dB below the maximum power.

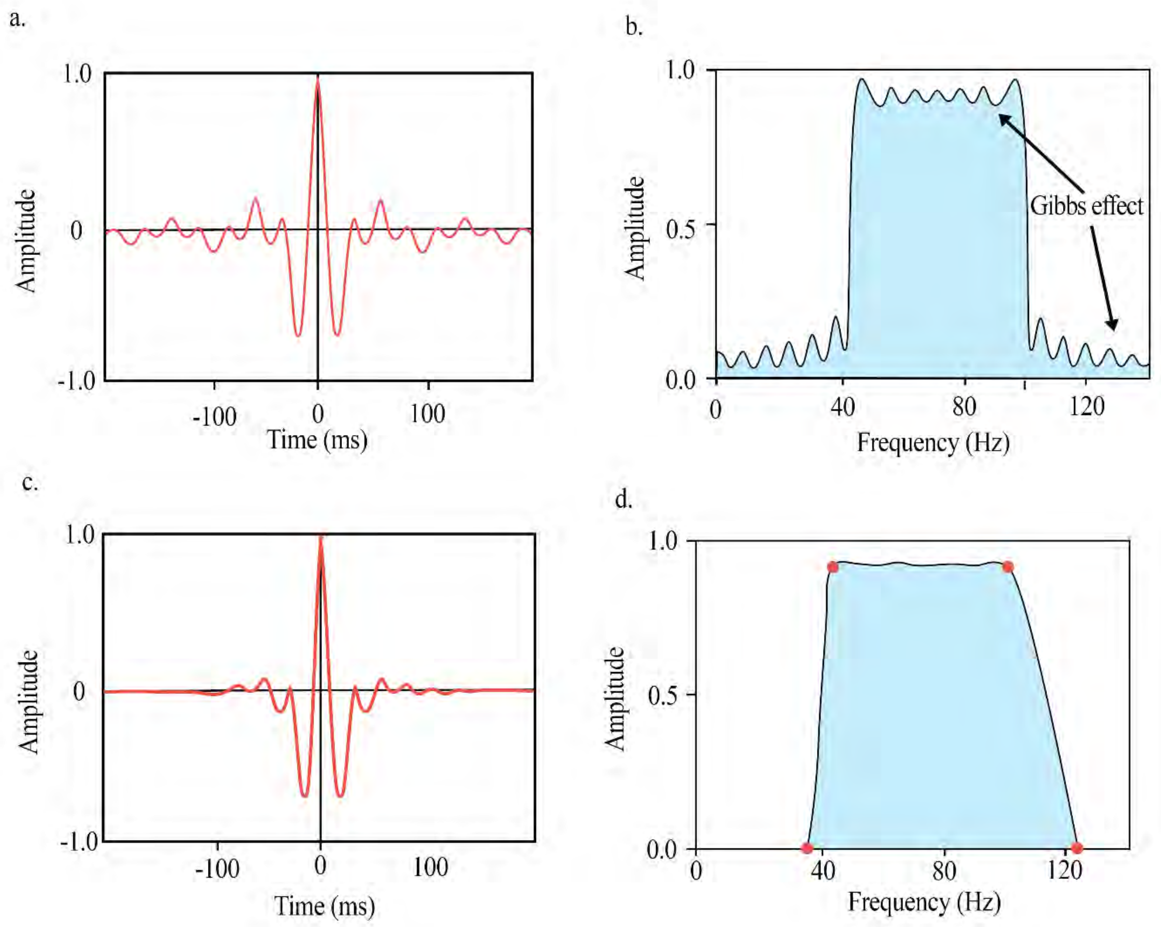

Figure 3.11: *An illustration of the band pass filter with a) sinc function, with its b) time-domain filter operator. Due to the abrupt cutoff, the amplitude spectrum exhibits severe frequency domain ripples. c) Truncated and smoothed narrower filter operator as a result of the smooth edges that remove hard transitions. d) The corner frequencies are used to eliminate the Gibbs effect in the frequency domain.*

The data are inspected for dominant frequencies such that they can be limited within that band, this can be done by applying a set of frequency panels. By inspecting the data from Paper II, the amplitude spectrum of the dataset shows that the highest amplitudes are found between 3 and 70 Hz (Figure 3.12a).

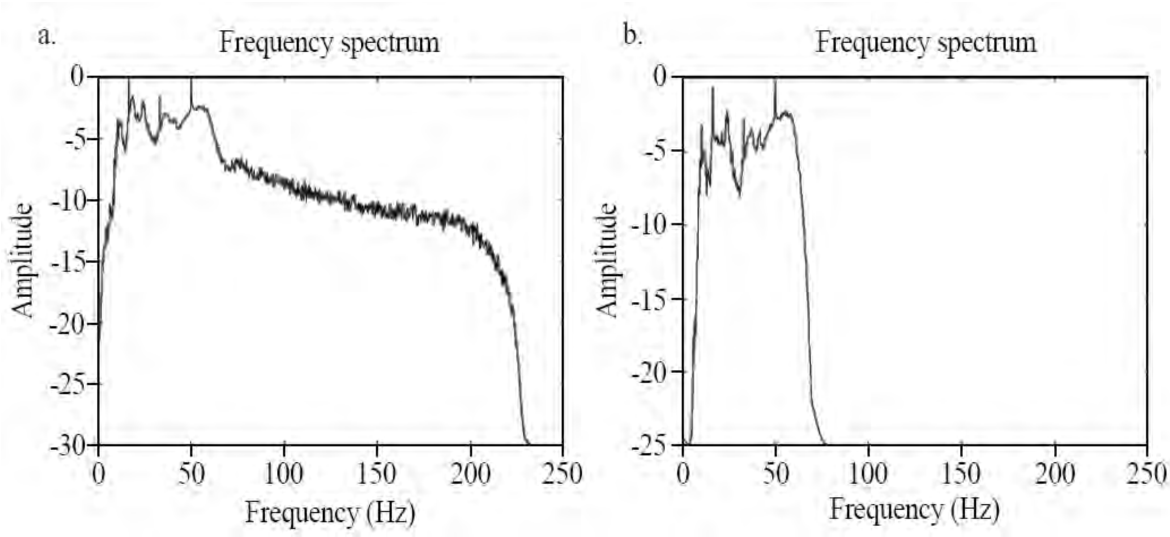

Figure 3.12: *Amplitude spectrum of seismic data from profile SP3 in paper II. a) The raw spectrum without the filter, b) the spectrum with a band pass filter (band pass: 3-13-60-70 Hz).*

An example of frequency panel applied to dataset from Paper II is shown in Figure 3.13. The raw data are shown in Figure 3.13a. The above mentioned filters are applied in the time-distance domain (*t-x*). After applying frequency wave number (*f-k*) filtering, the filters were more effective. The panels started with a narrow band filter (Figure 3.13b) and transitions smoothly into a broad filter starting from the lower end of the spectrum. Consider the portion of the shot gathers and their band pass filters (Figure 3.13). The figures show that the signal of interest is present in the top 500 ms on the gathers. As the band pass rises the seismic energy at maximum depth decrease. The lower frequencies show deeper reflected energy (Figure 3.13a-c) while the higher frequencies improve near-surface energy (Figure 3.13d-f). Further increase in the band pass filter starts to introduce artificial events into the dataset. The 50 Hz is enhanced on the last panel (Figure 3.13f) of the band pass (50-60-220-230 Hz). This is due to the band pass rejecting the dominant energy in the data.

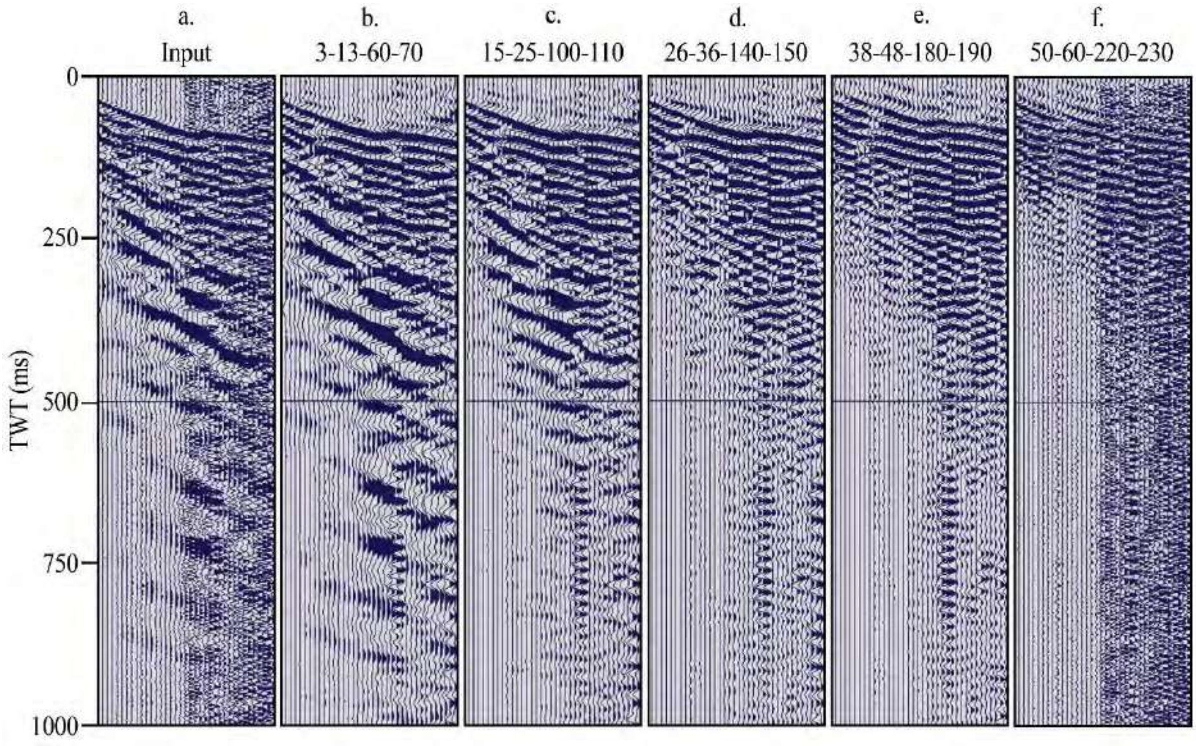

Figure 3.13: *Diagram shows the test of band pass filter on shot gather 28 on seismic profile SP3. The far left pane is a) the input shot gather without filtering. The subsequent panels (b-f) demonstrate the data after applying various frequency band pass filters.*

Inverse filtering (deconvolution), on the contrary, is commonly applied to improve the resolution of the targeted events. Other seismic events have similar frequency spectrum to the target reflections, therefore it is difficult to remove them using frequency filters. This makes inverse filtering the best method to remove noise that have similar characteristics as the target reflections. An example of a signal that has similar characteristics to target reflections that can contaminate seismic data are multiple reflections. Multiples are reflections that have undergone more than one reflection and are observed in seismic data at over double the two way travel time (TWT), twice the dip and reversed polarity (long-path multiples) can also manifest as tails to the primary reflections (shot-path multiples).

Deconvolution is the reverse process of convolution. Prior to discussing deconvolution, it is necessary to describe the convolution Earth model. Different models have been suggested over the years, e.g., the stationary Convolution model described by Robinson (1985) and Ziolowski (1984) described the penetrating treatment convolution models, while the initial convolution model for seismic trace is described by Robinson (1967). The convolution model of seismic methods suggests that the convolution of reflection coefficients of the boundaries and the source wavelet results in recorded seismogram (Dondurur, 2018, 316-318pp). Boundaries that are closely spaced appear as interference on the seismogram, since the source wavelet had a time length set by its dominant frequency. As a result, the source wavelet must be removed in order to obtain the reflectivity series from the recorded seismogram. (Kearey et al., 2002; Dondurur, 2018). Mathematically, the convolution is expressed as (Kearey et al., 2002):

$$s(t) = w(t) * e(t) + n(t) \tag{3.5}$$

Where e(t) is the Earth's reflectivity series, w(t) is the source wavelet, s(t) is the seismogram, and n(t) is random noise. Equation 3.5 has three unknowns, with the recorded seismogram being the only known parameter. To solve Equation 3.5 for the Earth's reflectivity series, multiple assumptions must be considered.

1. **Simple Earth model:** The Earth is made up of horizontal layers with constant lateral velocities. Furthermore it is assumed that only compressional waves with vertical incidence are generated based on the zero offset-data acquisition. The assumption fails in complex geology exhibiting anisotropic nature of seismic velocities. This is because the reflection coefficient will be altered, thus the reflectivity series. More complex solutions will be required to deal with this.

2. **Stationary wavelet:** The source wavelet does not change over time while propagating through the Earth. The pressure wave generated by the source loses its amplitudes, while the high frequencies are absorbed during propagation. Therefore the waveform becomes different from its initial onset. Attempts to remediate this are done by either splitting the deconvolution into time-stages or by use of suitable gain recovery application.

3. **Noise component:** A much simpler assumption of Equation. 3.5 is to consider the noise component negligible, therefore the additional term +n(t) can be removed. Recorded seismic data always include noise that can be generated during acquisition either by the environment, equipment or pre-processing steps. Whilst the noise cannot be completely removed. It is important to make a zero noise assumption as deconvolution performs well under this condition (Russell, 1988).
4. **Source waveform:** This theorem assumes that the w(t) term in Equation 3.5 is known, however in some seismic surveys it is unknown. The applied deconvolution is either deterministic or statistical.

- Deterministic deconvolution: Source waveform is known and the inverse can be determined. The field trace deconvolved contain the zero phase wavelet (Figure 3.14a).
- Statistical deconvolution: Most commonly used deconvolution, where the source waveform is unknown and an assumption is made about both the wavelet and the reflection coefficient series. A minimum phase assumption is made for the wavelet. (Figure 3.14b).

5. **Wavelet causality**: The seismic wavelet's energy is zero at time zero and it is always in the minimum phase. Different seismic sources produce different wavelets. Four different types of wavelets exist: minimum, maximum, mixed, and zero phase. Zero phase wavelets have energy before time zero, therefore they are non-casual, while the maximum (Figure 3.14c), minimum and mixed phase (Figure 3.14d) have zero energy at time zero. An example of a zero phase wavelet is data from a vibroseis, which has to be converted into a minimum phase wavelet to produce stable results when running deconvolution. Majority of the impulse sources that are used in this thesis produce minimum phase source signals.

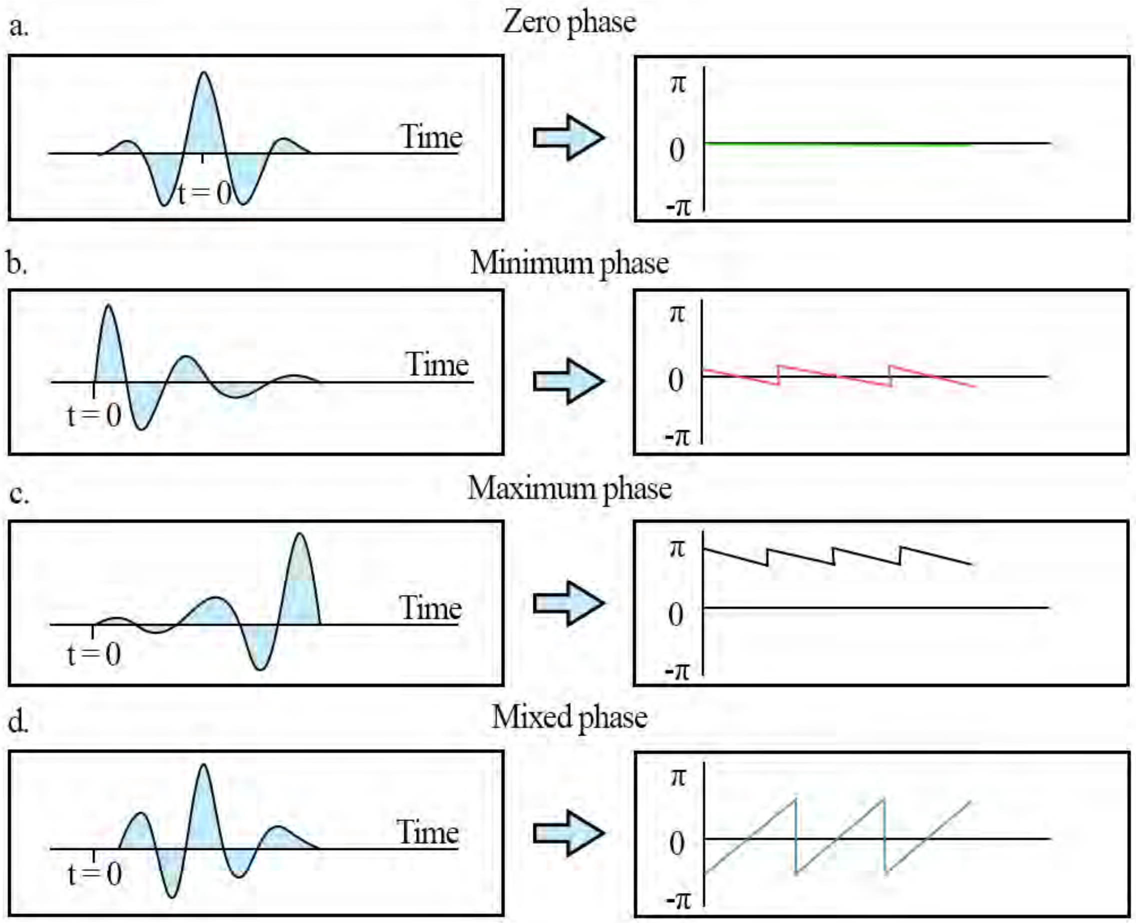

Figure 3.14: *Diagram showing the a) zero, b) minimum, c) maximum, and d) mixed phase wavelets together with their phase spectra. (Adapted from Dondurur, 2018, pp321).*

6. **Random reflectivity**: The reflectivity series is assumed to be random (white spectrum), which is the most crucial assumption.
    - This assumption is important for the statistical extraction of a wavelet. This is an unrealistic assumption as it is almost impossible for the signal to be free of noise. To extract the wavelet from the seismic trace and retrieve the Earth reflectivity, the deterministic deconvolution solves Equation. 3.5:

    $$e(t) = w^{-1}(t) * s(t), \tag{3.6}$$

    where $w^{-1}(t)$ is an inverse input wavelet such that the autocorrelation of the source wavelet $[\phi\{w(t)\}]$ is approximated to a direct delta $[\delta(t)]$ in Equation 3.7.This holds if the reflectivity series is random. Wavelet autocorrelation (autocorrelation of reflectivity series and source wavelet) is equal to the autocorrelation of the seismogram, and it is stated as follows:

    $$\phi\{e(t)\} * \phi\{w(t)\} = \phi\{s(t)\}, \tag{3.7}$$

    Since the source wavelet autocorrelation is equal to the Dirac delta, therefore Equation 3.7 results in:

    $$\phi\{w(t)\} = \phi\{s(t)\}, \tag{3.8}$$

    Therefore, if the reflectivity series is random, the seismogram's autocorrelation can be utilized in place of the source wavelet's autocorrelation.

The wavelet is rarely known, therefore $w^{-1}(t)$ is computed using statistical approach instead of deterministical approach. Supposed the desired output is d_i, where $i = 1, \dots, n$ and the actual output is given as a_i when convolving $w^{-1}(t)$ and $w(t)$, therefore the coefficients (L) of $w^{-1}(t)$ can be determined by mean-squared error between the desired output and actual output:

$$L = \sum_i (d_i - a_i)^2 \tag{3.9}$$

This can be minimized by setting the partial derivative with respect to the filter coefficient, equal to zero and it is expressed as follows:

$$\frac{\partial}{\partial f_i} L = 0 \tag{3.10}$$

Where f_i filter coefficient. The least squares error is given by equation 3.9, and Weiner (1949) provided a generalized matrix form with a filter length n as:

$$\begin{pmatrix} r_0 & r_1 & r_2 & \cdots & r_{n-1} \\ r_1 & r_0 & r_1 & \cdots & r_{n-2} \\ r_2 & r_1 & r_0 & \cdots & r_{n-3} \\ \vdots & \vdots & \vdots & \ddots & \vdots \\ r_{n-1} & r_{n-2} & r_{n-3} & \cdots & r_0 \end{pmatrix} \begin{pmatrix} f_0 \\ f_1 \\ f_2 \\ \vdots \\ f_{n-1} \end{pmatrix} = \begin{pmatrix} g_0 \\ g_1 \\ g_2 \\ \vdots \\ g_{n-1} \end{pmatrix} \tag{3.11}$$

Where r_i is the autocorrelation of the input wavelet w, and g_i is the cross correlation between the desired output d and the input signal w (Robinson and Treitel, 2000; Dondurur, 2018; Westgate, 2020). Figure 3.15 shows the design and use of the Weiner filter.

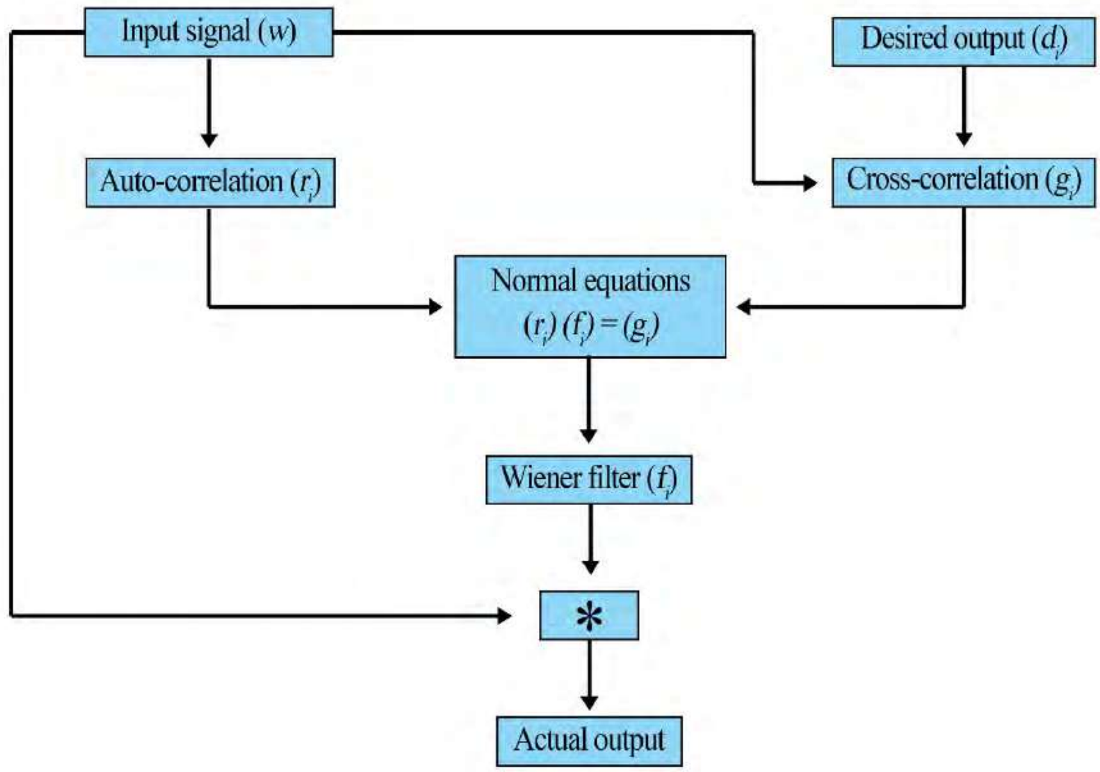

Figure 3.15: *Schematic flowchart illustrating the Weiner filter, calculation and application of deconvolution. * denotes convolution.*

Spiking deconvolution

Spiking deconvolution is the compression of the source wavelet into a zero-lag spike $(1, 0, 0, \cdots, 0)$. To perform the spiking deconvolution, a filter operator coefficient must be determined in order to eliminate the source wavelet from the dataset. The method can be implemented deterministically if the source wavelet is known; otherwise, the method will be implemented statistically. The latter can be written as Equation. 3.11:

$$\begin{pmatrix} r_0 & r_1 & r_2 & \cdots & r_{n-1} \\ r_1 & r_0 & r_1 & \cdots & r_{n-2} \\ r_2 & r_1 & r_0 & \cdots & r_{n-3} \\ \vdots & \vdots & \vdots & \ddots & \vdots \\ r_{n-1} & r_{n-2} & r_{n-3} & \cdots & r_0 \end{pmatrix} \begin{pmatrix} f_0 \\ f_1 \\ f_2 \\ \vdots \\ f_{n-1} \end{pmatrix} = \begin{pmatrix} 1 \\ 0 \\ 0 \\ \vdots \\ 0 \end{pmatrix} \qquad 3.12$$

Weiner spiking deconvolution uses either the least-squares inverse filtering or Wiener filters. Deconvolution with least-squares inverse filtering is performed with a known source wavelet (deterministic), where the recorded seismogram is convolved with the inverse filter operator to produce an estimated series of Earth's reflectivity. (Dondurur, 2018). This is described on assumption 6. The filter operator obtained from inverse input wavelet (Figure 3.16a) is used to convert the wavelet into a spike at $t = 0$. While deconvolution with weiner filter is computed using the input seismic trace (statistical deconvolution) to determine the autocorrelation matrix of the normal equations (Yilmaz, 2001) and it is dependent on the least square approximation (Figure 3.16b).

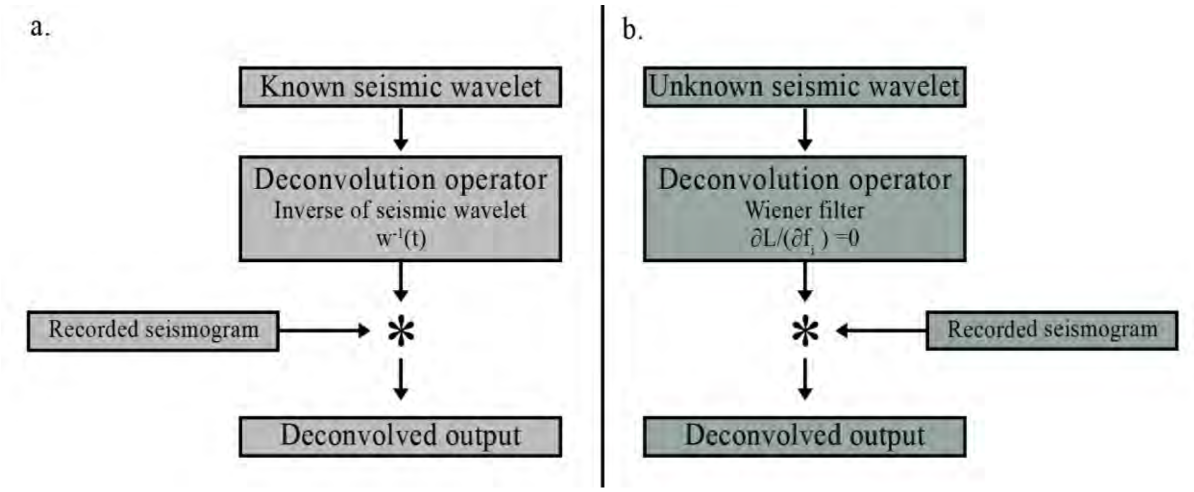

Figure 3.16: *Diagram showing spiking deconvolution application by the a) least-squares inverse filtering versus b) Wiener filter. * denotes the convolution.*

Predictive deconvolution

Predictive deconvolution is the most commonly used and it is applied by using information of the primary reflections to predict and suppress systematic noise such as multiples. A time advanced version of the input wavelet $w(t)$ is predicted when applying prediction convolution, which is $w(t + \alpha)$, where the prediction lag is α. The resulting equation from Equation 3.11 is (Peacock and Treitel, 1969):

$$\begin{pmatrix} r_0 & r_1 & r_2 & \cdots & r_{n-1} \\ r_1 & r_0 & r_1 & \cdots & r_{n-2} \\ r_2 & r_1 & r_0 & \cdots & r_{n-3} \\ \vdots & \vdots & \vdots & \ddots & \vdots \\ r_{n-1} & r_{n-2} & r_{n-3} & \cdots & r_0 \end{pmatrix} \begin{pmatrix} f_0 \\ f_1 \\ f_2 \\ \vdots \\ f_{n-1} \end{pmatrix} = \begin{pmatrix} g_\alpha \\ g_{\alpha+1} \\ g_{\alpha+2} \\ \vdots \\ g_{\alpha+n-1} \end{pmatrix} \qquad 3.13$$

Were f_i is the prediction filter for predicting the advanced input wavelet as described above. Predictive deconvolution can be approached in two manner: 1) we can design the prediction filters similar to Equation. 3.10 and apply it to the input series that yields the predictable components in the seismic input traces that correspond to multiples. 2) Design a prediction error filter (difference between the actual output a_i and the desired output d_i) and convolve it with the input series. The prediction error filter is expressed as $(1, 0, 0, \cdots, f_0, f_0, f_0, \cdots, f_n)$ and gives the prediction process error that corresponds to the primary reflections (Peacock and Treitel, 1969). In order for the convolution of the prediction error filter and the input trace to be able to suppress the multiples and compress the primary reflections, the operator length and prediction lag need to be carefully chosen. Predictive deconvolution is a broad technique that includes spiking deconvolution. (Dondurur, 2018, pp372). In Paper II, predictive deconvolution is manipulated to create a spiking deconvolution for surface seismic data collected at Maseve mine. Predictive deconvolution is applied for more complex subsurface that results in source wavelet varying during acquisition. Different parameters (gap, length and noise level) are changed to design an inverse operator for predictive deconvolution (Ahmadi, 2015, pp23).

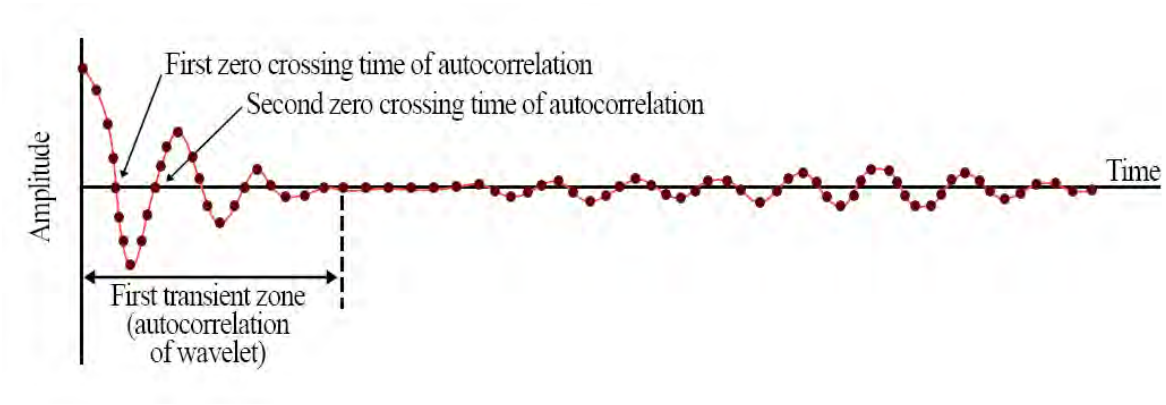

Figure 3.17: *The autocorrelogram's initial transient zone is not far from the operator length. The first or second autocorrelation crossing points for resolution improvement are used to define prediction lag. (Adapted from* Dondurur, 2018).

The choice of the deconvolution parameters (operator length and prediction lag) is dependent on each dataset. The duration of the initial transient zone is the operator length. (Figure 3.17) in the autocorrelation of the seismic trace (Yilmaz, 2001). The ideal operator length is when it roughly matches the wavelet's autocorrelation. The suppression of multiple reflections and the resolution of the autocorrelation are both governed by the prediction lag (Keary et al., 2002). For the purpose of enhancing resolution, it is chosen as either the first or second zero crossing points of the autocorrelation (Figure 3.17).

As part of the prestack processing, predictive deconvolution was applied on seismic data acquired from profiles SP1 and SP3 at Maseve mine site. Figure 3.18 demonstrates the effect of predictive deconvolution in one of the shot gathers from seismic profile SP3. The deconvolution parameters (operator length and the prediction lag) where unique for every shot in the dataset. The filter has recovered and improved the resolution of the dataset when comparing the raw shot gather before deconvolution (Figure 3.18a) and the shot gather after deconvolution (Figure 3.18b).

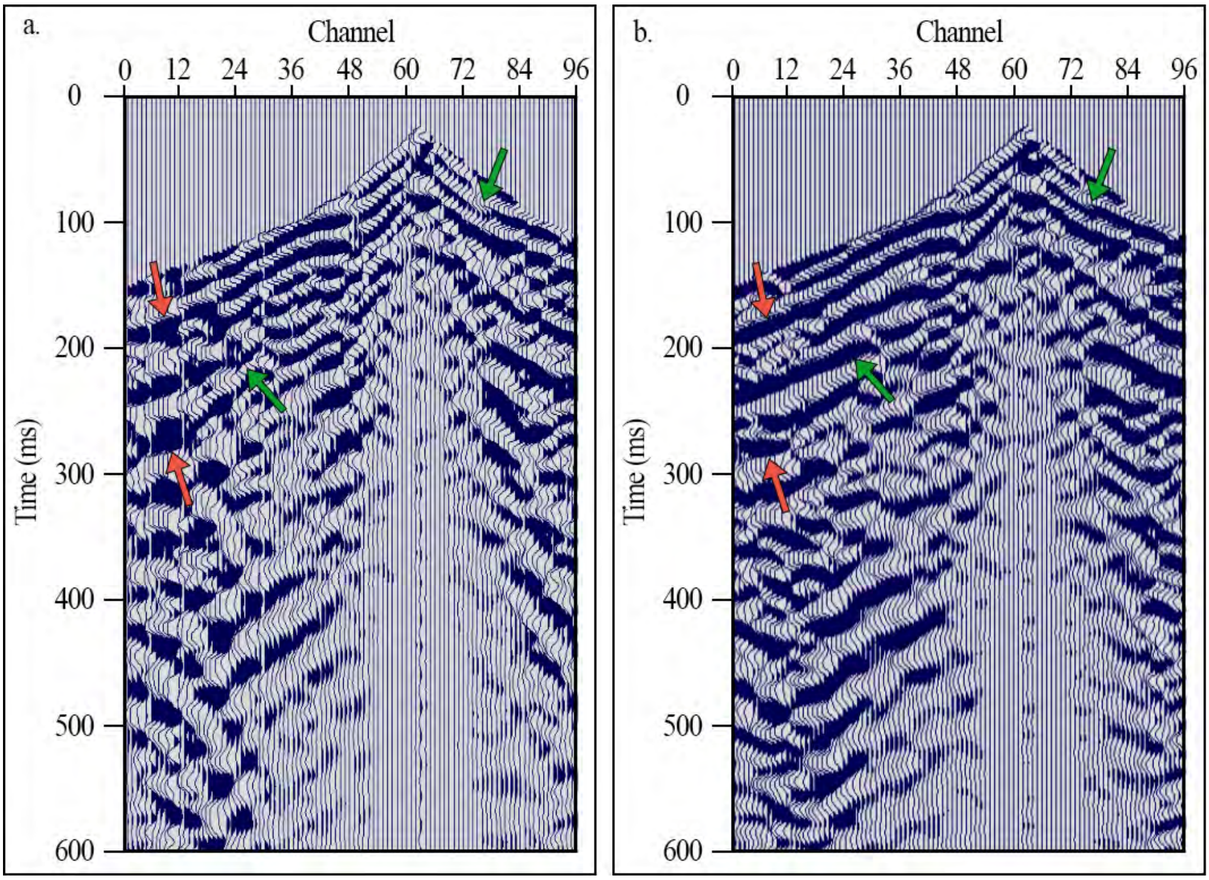

Figure 3.18: *Example of predictive deconvolution applied on a shot gather from Paper II. a) The shot gather before deconvolution, and b) the shot gather after deconvolution. Green arrows show areas that had weak signal and are improved after deconvolution. Red arrows indicate where the wavelets have been compressed and separated.*

Velocity analysis and stacking

CMP stacking

Common-midpoint stacking is a crucial step in seismic processing for increasing signal-to-noise ratio (SNR). The concept of common-midpoint sorting has been discussed in the acquisition section of the thesis. Stacking refers to a summation of seismic traces into a one trace that approximates a zero offset (Figure 3.19: Alsadi, 2017, pp269). Prior to stacking the data, both the static corrections (discussed in previous chapter) and NMO corrections need to be applied. As previously discussed, reflections appear in a shot gather as hyperbolae (Figure 3.6: blue shading), as a result of increasing or decreasing offset. The travel time delay (difference between the slant travel time and the vertical reflection time) is known as the normal moveout.

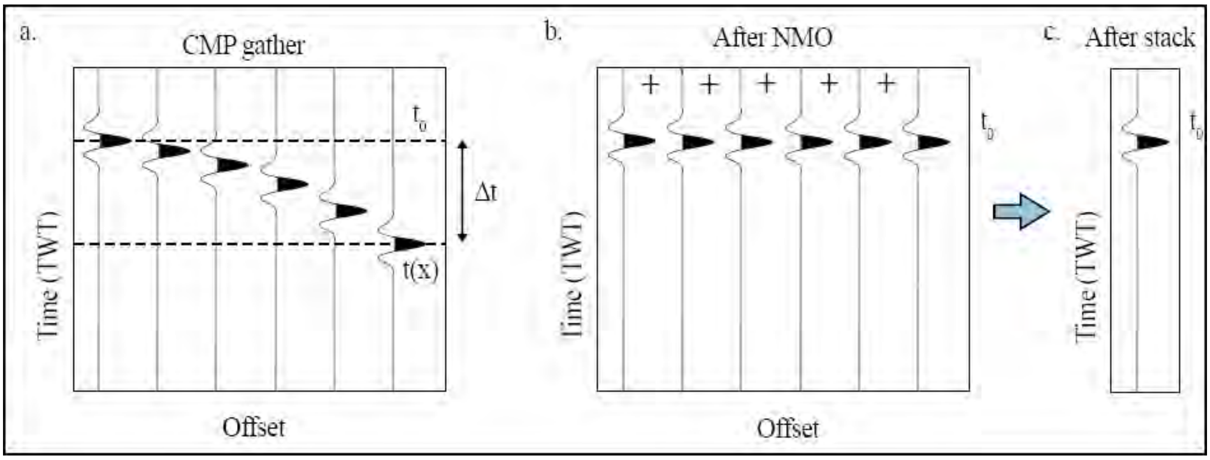

Figure 3.19: *a) CMP gather illustrating 6 traces, b) following NMO-correction. (Adapted from Alsadi, 2017, pp269).*

Normal moveout corrections are applied to account for the travel time differences of the traces that are to be stacked (Figure 3.19a). The traces are time shifted such that the reflected traces are shifted to as if they were acquired with a zero offset (Figure 3.19b). Application of NMO requires the stacking velocities for each zero offset.

Let us consider a reflection from a single layer. The following equation represents the travel time curve of reflections for various source-to-receiver offsets:

$$t(x) = \sqrt{{t_0}^2 + \frac{x^2}{v^2}} \qquad 3.14$$

Where x represent the distance separating the source and receiver, and v denote the velocity of the medium above the interface. The NMO correction is expressed as the difference between the travel time for a receiver located at x away from the source $t(x)$ and the travel time for zero offset distance t_0:

$$\Delta t = t_0 - t(x) \qquad 3.15$$

Substituting 3.13 into 3.14, we get:

$$\Delta t = t_0 - \sqrt{{t_0}^2 + \frac{x^2}{v_{stack}^2}} \qquad 3.16$$

From Equation 3.16, we note that the NMO correction depends on the offset and the stacking velocity (also referred as NMO velocity). Therefore, choosing correct velocities for flattening the reflections is important. Figure 3.20 shows the effect of overcorrected reflections due to low velocities, while under-corrected reflections are due to high velocities (Yilmaz, 2001, p282).

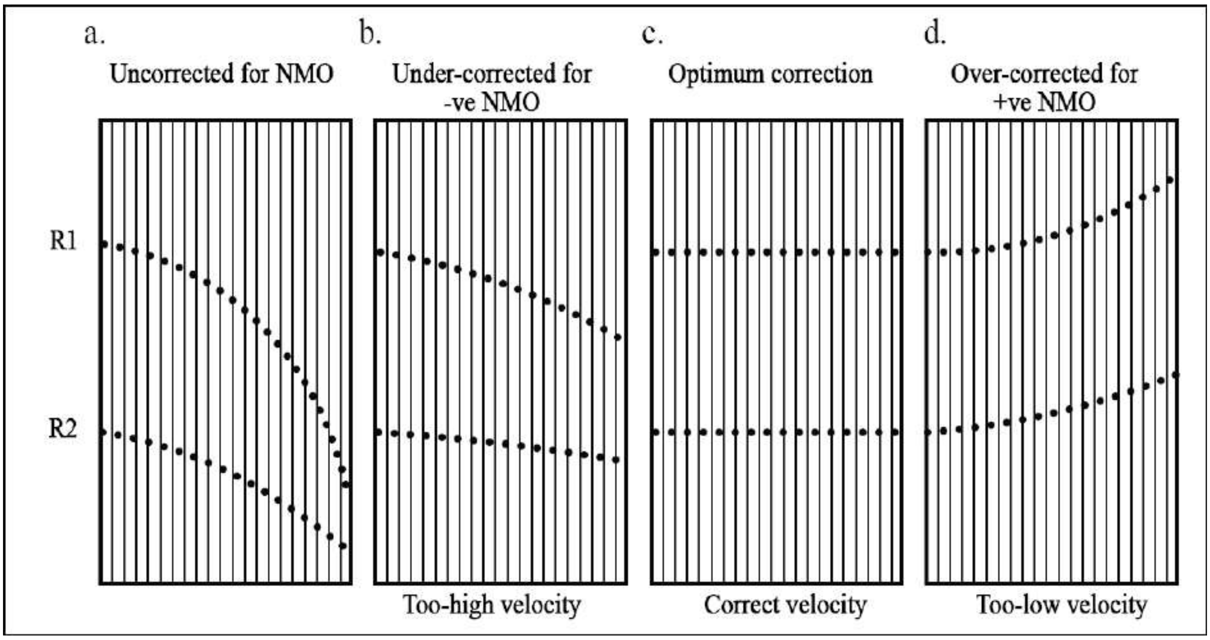

Figure 3.20: *Normal moveout correction (NMO) of reflections. Common midpoint (CDP) gathers with reflections before a) NMO corrections; and after NMO corrections with b) high velocities; c) correct velocities; d) low velocities (Adapted from Yilmaz, 2001, p282).*

In the case of a single horizontal reflector, the optimal moveout velocity for correcting reflection hyperbolae is equal to the velocity of the medium above the reflector. Let us now examine a medium that consists of several horizontal layers with varying thicknesses and velocities. Interval velocities exists between the layers $(v_1, v_2, \cdots, v_n)$, n represents the number of layers. The travel time equation for a ray path that travels along the shortest path between the energy source and reflector and receiver can be expressed as (Taner And Koehler, 1969):

$$t(x) = t_0^2 + \frac{x^2}{v_{rms}^2} + C_2 x^4 + C_3 x^6 + \cdots \qquad 3.17$$

Where coefficients $C_1, C_2, \cdots, C_n$ are dependent on the thickness and interval velocity. The constant velocity of the overlaying medium for one medium is replaced by the root mean square velocity v_{rms} of the layers over the reflector. The v_{rms} and t_0 are expressed as:

$$v_{rms}^2 = \frac{1}{t_0} \sum_{i=1}^{n} v_i^2 \Delta t_i \text{ and } t_0 = \sum_{i=1}^{n} \Delta t_i \qquad 3.18 \text{ and } 3.19$$

where Δt_i is the vertical two way travel time through the ith layer. The approximation for the interfaces below the first layer is made. However, interfaces are more accurate at small offsets for horizontal layers. Arbitrary dipping interfaces have similar travel time approximation (hyperbolic) of multi-layered medium, however the NMO velocity for multiple layers with arbitrary dips below the first reflector is given by (Yilmaz, 2001, pp287):

$$v_{NMO}^2 = \frac{1}{t_0 \cos^2 \beta_0} \sum_{i=1}^{n} v_i^2 \Delta t_i \prod_{k=1}^{i-1} \left(\frac{\cos^2 \alpha_k}{\cos^2 \beta_k} \right) \qquad 3.20$$

Where α and β are the angles of the dipping layers. For a single layered dipping reflector, the NMO velocity collapses to the medium velocity divided by the cosine of the dip angle.

Dip moveout

In the above section the focus was on the application of NMO for stacking flat events, however the Earth comprises of structures with different orientations and geometries. Dipping reflections result in different reflection points in the CMP gather, thus providing different travel time curves and incorrect estimated velocities. An increase in reflection time for a given reflector due to a dipping layer is known as dip moveout (DMO). DMO is a prestack migration (discussed in the next section) principle. Therefore prior to stacking dipping reflectors, a DMO should be applied then followed by NMO. In a dipping reflector model, the reflections are dispersed over the reflection plane, therefore application of DMO moves the dispersed (non-zero offset) reflection points of each trace to true reflection times and zero-offset locations (Hale 1991, p4).

During application of NMO corrections, frequency distortions occur for shallow events and near large offsets in which the dominant frequencies shift to the lower frequencies. The frequency distortions are expressed as (Dondurur, 2018, p470):

$$\frac{\Delta f}{f} = \frac{\Delta t_{NMO}}{t(0)} \qquad 3.21$$

Where f is the dominant frequency and Δf is the change in frequency after NMO. For seismic data affected by frequency stretching, a stretch mute can be applied and it is quantified in percentages. In this thesis, majority of the seismic profiles acquired are short, therefore the effect of stretch mute is not dominant. A 70% stretch mute was used in the data of this thesis as there was no noticeable effects on the frequencies on the gathers.

Velocity estimation

The main objective for velocity estimation is to determine the amount of normal moveout that should be applied to maximize the stacking of events. The velocity applied for stacking may differ with the RMS velocity as the stacking velocity returns the best stacking results of the events, while the root mean square is the actual RMS velocity of the layer. However, for small offsets and horizontal layers, the stacking velocity is similar to the RMS velocity.

Multiple methods of velocity estimation exist, the most conventional ones are briefly described below (Yilmaz, 2001; Drijkoningen, 2016; Dondurur, 2018, p427-436):

$(\boldsymbol{t^2} - \boldsymbol{x^2})$	The square of the travel times $\boldsymbol{t}$ and offset $\boldsymbol{x}$ are plotted as a linear function and the gradient of the linear curve is noted to be $\frac{\mathbf{1}}{\boldsymbol{v^2}_{\boldsymbol{rms}}}$ on Equation 3.16. From this one can extract the stacking velocity. The method can be reliable for estimating stacking velocities, however this is dependent on the quality of the data (signal-to-noise ratio).
Constant velocity scan	This method is based on flattening the reflections using a range of velocities on each CMP gather after NMO corrections are applied. The results of the CDP gathers are then plotted in a series of panels and velocities that flatten a specific reflection at a given time location are picked. A velocity function for the whole recording time is then derived from the multiple velocity functions for specific CDPs. A 2D velocity field of the seismic profile is obtained by repeating the velocity scan over several CDPs along the line.
Constant velocity stack (CVS)	Stack sections consisting of a range of CDPs are stacked at different constant stacking velocities after the application of NMO corrections. The stack sections are then displayed in series, then pick velocities that produce the best stack sections. A velocity function is obtained from a range of CDP gathers and a 2D velocity field is obtained for the entire seismic profile.

Velocity spectra	This process transforms from the two-way travel (TWT) time offset domain $(\boldsymbol{t}-\boldsymbol{x})$ to the zero-offset TWT stacking velocity domain $(\boldsymbol{t_0}-\boldsymbol{v})$. At a particular velocity, the CMP gather is corrected and a coherency measure is applied to the dataset. The process is repeated over several velocities, resulting in a velocity spectrum. The most common coherency measure used is the semblance and it is expressed as (Yilmaz, 2001; Dondurur, 2018, p432): $\boldsymbol{S}=\frac{\boldsymbol{1}}{\boldsymbol{M}}\frac{\sum_t[\sum_{i=1}^{M}\lvert \boldsymbol{f_i}\rvert]^2}{\sum_{i=1}^{M}\boldsymbol{f_i^2}}$ where $\boldsymbol{f_i}$ is the amplitude at an offset and two-way time after NMO correction. M is the number of traces in the CDP gather. The semblance has the value of 1 if the reflection hyperbola is perfectly aligned with constant amplitude for all offsets. Velocity spectrum is most desired for data that are contaminated with multiple reflections as it is able to differentiate between primary reflections and multiples.

The accuracy and resolution of velocity estimation are affected by multiple factors, to state a few (Yilmaz 2001, p302): depth of reflectors, spread length, SNR number of traces, dip of the reflector. The data presented in this research were mainly acquired from short profiles (~ 240 m in length), therefore constant velocity stack was mainly applied to the data. In Paper II, longer seismic profiles were acquired, therefore both the constant velocity stack and velocity spectra (semblance) were tested. An example of CVS method applied to the seismic profile SP3 is shown in Figure 3.21.

The first pass velocity stack is done using interval P-wave velocities (Figure 3.21a), followed by CVS. Reflection packages R0, R1, R2, and R3 (Figure 3.21b) are best stacked at P-wave velocities between 1800 and 2500 m/s (Figure 3.21a), while R4, R5 and R6 are best stacked in velocities 3200 – 4400 m/s. Figure 3.22 shows the application of velocity spectra (Figure 3.22a: semblance) on the dataset. The velocities are adjusted for the primary events (reflections), this aid in creating a suitable 2D velocity field (Figure 3.22b). Figure 3.22c shows reflections that are more coherent compared to those stacked using interval velocities.

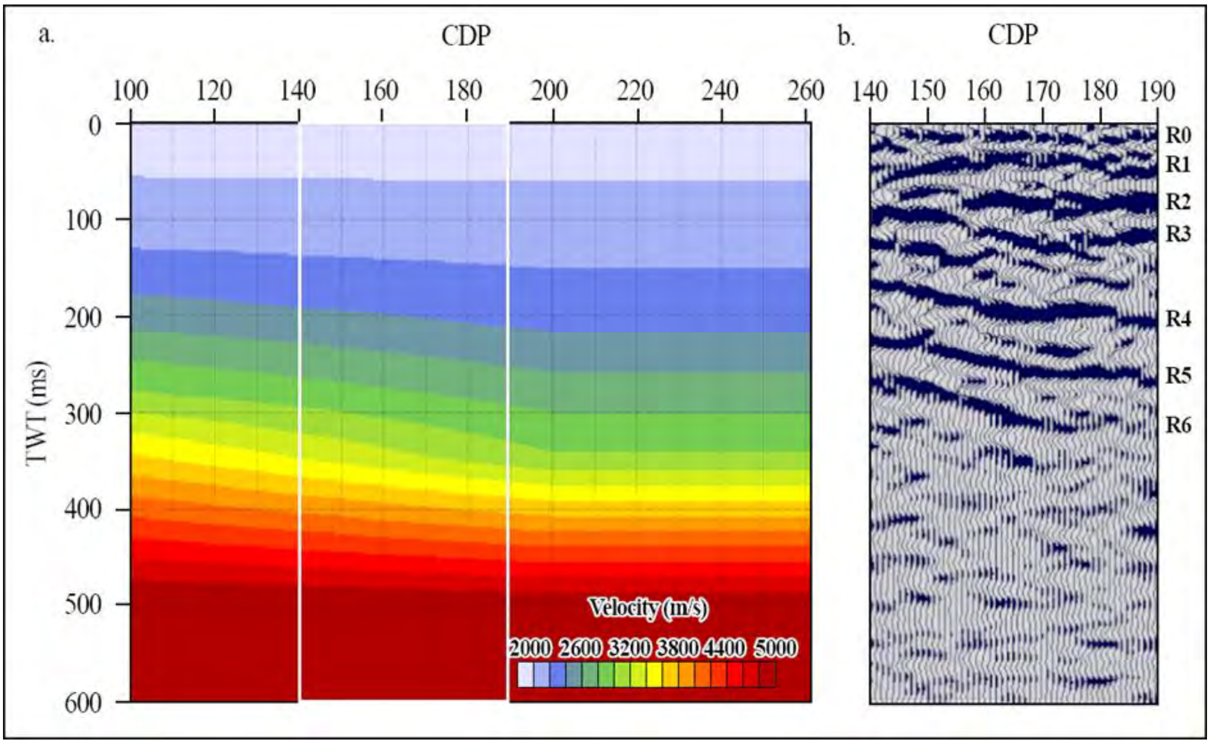

Figure 3.21: *a) 2D root mean square velocity field obtained from iterative constant velocity analysis. b) Stack section from the root mean square 2D velocity field. R0-R6: reflections.*

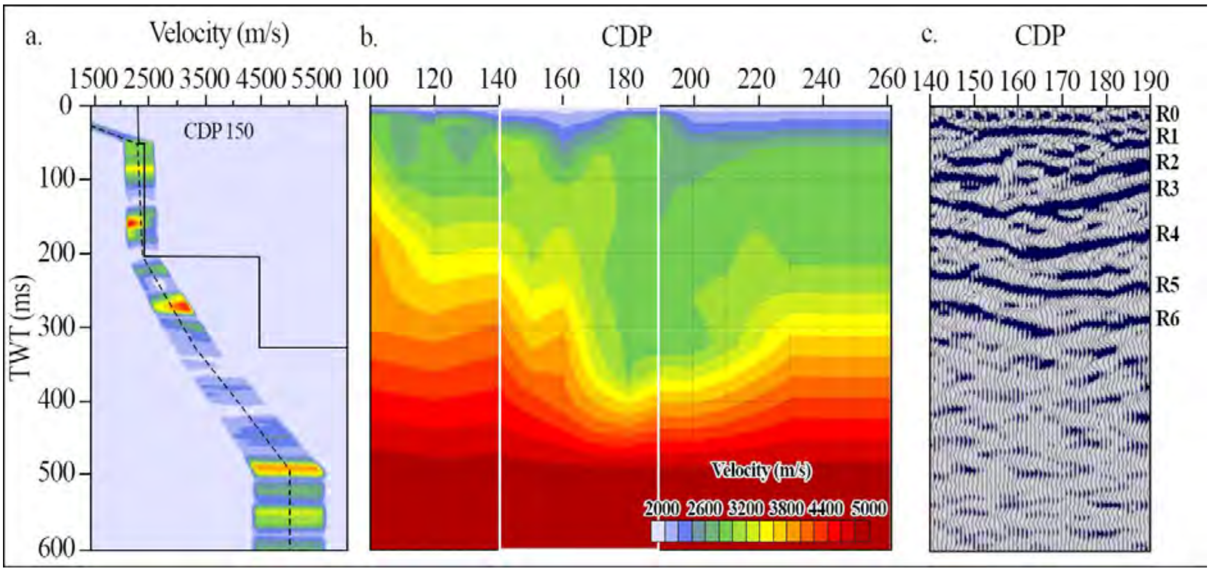

Figure 3.22: *a) An example of semblance plot from seismic profile SP3 presented in Paper II. Dashed black line shows the root mean square (RMS) velocities, while black solid line shows the interval velocity functions picked. b) 2D RMS field obtained from mapping several velocity functions using semblance analysis along the seismic profile. c) Second pass 2D velocity stack from semblance analysis. R0-R6: reflections.*

Migration

One of the most important steps in processing seismic data is migration. This process is applied to seismic data to reposition reflections from their midpoint locations to true subsurface locations at depth (Yilmaz, 2001). Application of migration process targets the primary reflections and diffraction events, while other seismic events that are in the data are smeared, resulting in migration noise. The seismic stack section represents an undistorted subsurface image, provided that the reflection interfaces are horizontal. However, dipping reflectors and terminating reflectors cause distortions in the stack section. Therefore migration is applied to restore the distorted seismic stack section to best represent the subsurface geology (Alsadi, 2017, p272). Dipping reflections are moved to their true positions (Figure 3.23a), while diffractions caused by geological discontinuities (Figure 3.23b: terminating reflectors) such as faults are collapsed. Migrated sections are characterized by migration smiles at depths and near the ends of the seismic sections where there is a low fold and high noise (Telford et al., 1990).

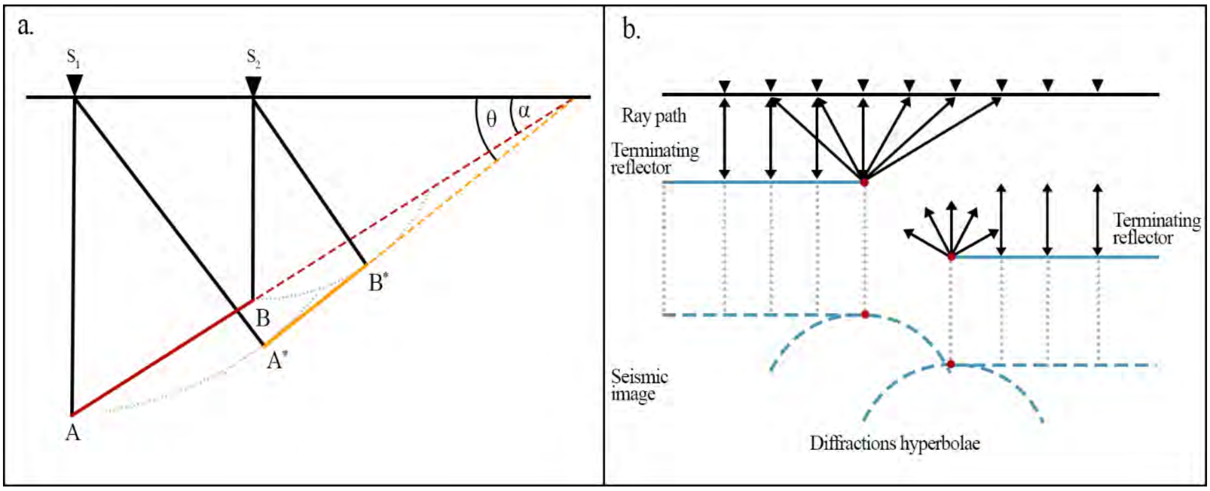

***Figure 3.23**: a) Distortions caused by a dipping reflector. The reflector is recorded to be directly below the receivers. Migration shifts and decrease the dip angle and length of the reflections. b) Distortions caused by terminating reflectors (fault). The reflectors create diffractions (hyperbolic events).*

Migration can be carried out in both time (using RMS velocities) and depth (using interval velocities), however it is commonly preferred to be shown in time domain for comparison with the stacked section (Yilmaz, 2001). However, time migration does not produce accurate subsurface conditions for structurally complex subsurface geology with high lateral velocity variations. Migration can either be conducted before or after stacking. Sihoyiya et al. (2022)

demonstrate the difference and advantages of pre-stack time and depth migration, together with post-stack time and depth migration. The most common migration principles used are Kirchhoff, finite difference, and *f-k* migration techniques. In this thesis the data were mainly migrated using Kirchhoff migration, therefore it is described in detail for this research. A detailed review of the migration principles are discussed by Sheriff and Geldart (1995), Yilmaz (2001), Alsadi (2017), and Krebes (2019).

Kirchhoff migration

Kirchhoff migration, also termed diffraction summation migration, is based on Huygens's principle where each point on the wave-front is itself a secondary wavelet. The diffraction points are located at the apex of the diffraction hyperbola (Figure 3.24a) after the summation of the data values along the diffraction. The closely spaced diffraction points interfere constructively and result in making up a reflection surface (Figure 3.24b). However for a terminating reflector such as a fault, the hyperbola at the terminating point does not interfere with the hyperbolae on the continuous reflector (Figure 3.24c). Therefore, diffractions appear superposed on the seismic stack section (Alsadi, 2017).

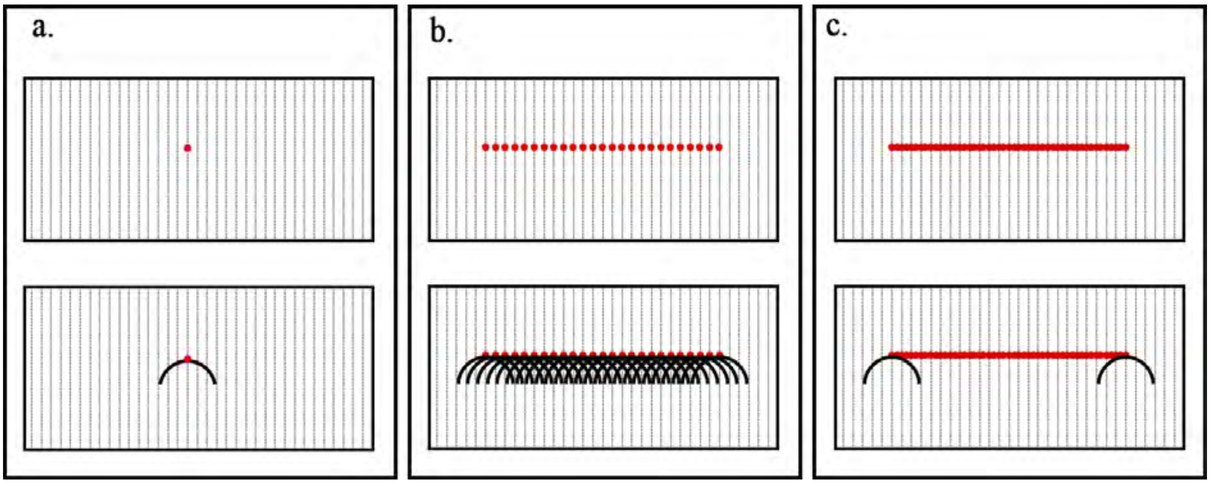

Figure 3.24: *Diffraction summation (adapted from Yilmaz, 1987). a) Diffraction migrates to a point on the apex of the hyperbola. b) A sequence of diffraction points result in a reflector and if they are c) closely spaced, only the reflector and diffractions at the terminating points are superposed.*

The method is based on the Kirchhoff-Rayleigh integrals and it is expressed as (Krebes, 2019):

$$P_{out} = \frac{1}{2\pi}\int dx \left\{\frac{\cos\theta}{r^2} P_{in}\left(x_{in}, x = 0, t - \frac{r}{v_{rms}}\right) + \frac{\cos\theta}{vr}\frac{\partial}{\partial t} P_{in}\left(x_{in}, z = 0, t - \frac{r}{v_{rms}}\right)\right\} \quad 3.22$$

Where P_{out} and P_{in} is the output wavefield at a subsurface location and input zero-offset wavefield at the surface, $r = [(x_{in} - x)^2 + z^2]^2$ is the distance between the input and the output points, and v_{rms} is the RMS velocity at the output points. The integrand is split into two fields: firstly, near field term that is proportional to $\frac{1}{r^2}$, and the field is negligible at large distances (r). Secondly, the far field term is proportional to $\frac{1}{r}$. The Kirchhoff migration has an advantage over other methods as it incorporates three factors prior to summation: 1) the obliquity factor $(\cos\theta)$ that considers the angle dependence of amplitudes. 2) The spherical divergence or spreading factor $\left(\frac{1}{r}\right)$ that considers the amplitude decay by a factor of the root distance. 3) The wavelet shaping factor, which considers the distortions of the amplitude and phase during wavefront propagation, therefor aims at restoring the correct phase to the data. Over the year Kirchhoff migration has proved to be a migration method preferred for structurally complex area, as it handles lateral velocity variation that have steep dips of up to 90° (Yilmaz, 2001; Manzi, 2014) .

3.2. Magnetics

Amongst the geophysical methods, magnetic methods are relatively the cheapest, and easy to use for exploring the Earth's subsurface, with minimal corrections that need to be applied (Telford et al., 1990). The method is applied for a wide variety of near to deep surface geophysical problems such as archaeological and engineering site investigations (i.e., detecting buried targets or geological structures), exploration for economic deposits (directly detecting magnetic minerals) and study the tectonic structures and processes of the Earth (determine the depth to the base of the Earth's crust) (Everett, 2013; Hinze et al., 2013). Magnetic surveys can be conducted on surface or on airborne platforms. Historically, surface magnetic methods have been conducted to image the near-surface with high-resolution and detect local anomalies. However, in recent times the most widely used magnetic survey technique is airborne. This is due to the ability to conduct airborne surveys over larger areas and maintain high-resolution with the use of high precision magnetometers. Airborne magnetic surveys have been conducted in South Africa for the discovery of the Far West Rand Goldfields gold (e.g., Roux, 1967) and kimberlite (e.g., Macnae, 1995). In this research we applied surface magnetic techniques and the procedure is briefly described in the section below.

Prior to discussing the surface magnetic techniques, we briefly discuss the fundamentals of magnetism and the Earth's magnetic field. The magnetic method is a passive exploration method as it is based on using the natural magnetic force of the Earth. The magnetic field of the Earth is made up of multiple magnetic components that are generated within and outside the Earth;

- **Main field**: The main field accounts to the majority (approximately 90%) of the geomagnetic field (Dentith and Mudge, 2014). The remnant and induced magnetism of the rock is as a result of the internal field from the core of the Earth.
- **Small field (External field)**: This originates outside the Earth and it is superimposed on the main geomagnetic field. The field is diurnal in nature and can reach maximum and minimum (Figure 3.25) of 60 nT (local noon) at the geomagnetic equator and mid-latitudes, respectively (Butler, 2005, pp154). The diurnal variations have an effect on the magnetic data, therefore it is carefully monitored and can be accounted for by measuring the field using a base station (stationary magnetometer) nearby the survey area. Rapid variations in small fields are as a result of the solar winds that are emitted by the Sun. Magnetic surveys cannot be conducted during this period as the amplitudes of the anomalies created by the crustal rocks are small (Hinze et al., 2013) .

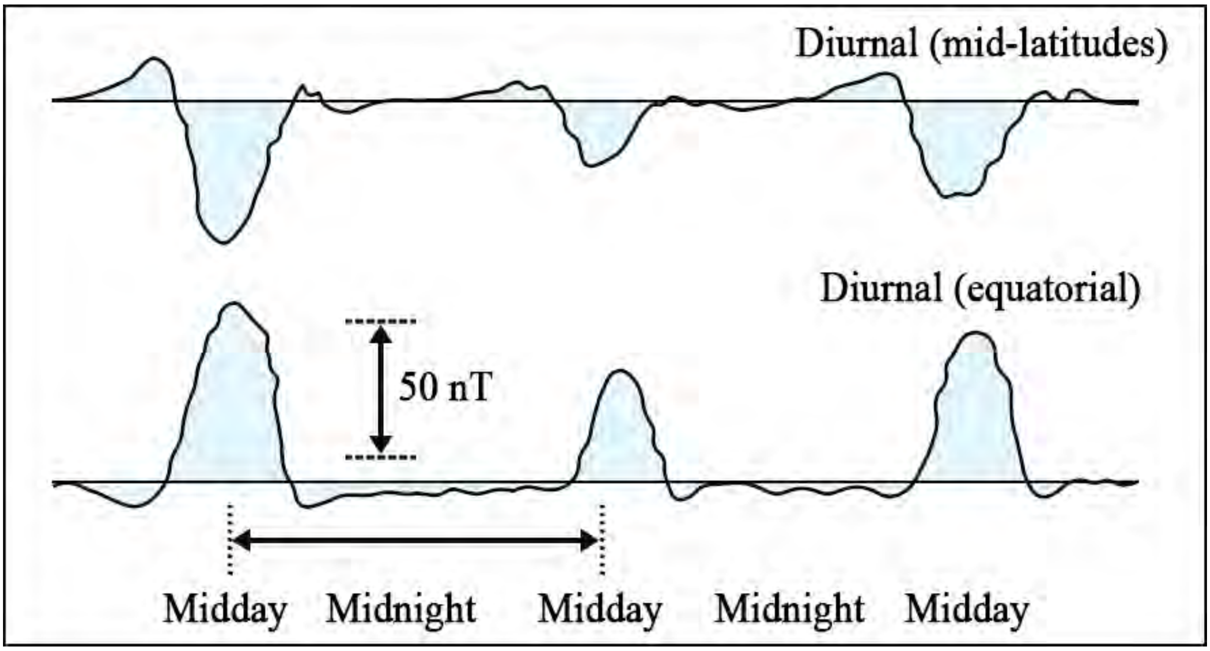

Figure 3.25: *Diurnal variations on thein the total magnetic intensity of the geomagnetic field at mid-latitudes and equatorial regions.*

The rocks in the near-surface crust have induced and remanent magnetism as a result of the main field, thus the near-surface of the Earth's crust has local magnetic anomalies that result in spatial variations of the main field. Magnetic surveys target the spatial changes in the magnetic field due to crustal anomalies (Telford et al., 1990; Dentith and Mudge, 2014).

3.2.1. Acquisition

Ground magnetic surveys are conducted using a sensor mounted on a pole, at regular intervals (sampling) along parallel line to cover a designated study area. The sampling interval is an important field parameter when conducting a magnetic survey, as it is required that at least two measurements need to be within the target anomaly. The depth to target needs to be estimated prior to determining the sampling rate.

Another factor that is important in magnetic surveys is signal-to-noise ratio. It is very common to conduct a magnetic survey in an area that has man-made objects (e.g., steel pipes, wire fence, power transmission lines) that are magnetic and may introduce noise in the dataset. Unless the man-made object is the target, magnetic surveys need to be conducted with the sensor elevated such that the noise signal is attenuated. The field parameters and choice of instrumentation used is influenced by factors such as the size, location, physical characteristics of the study area, objective of the survey and noise levels. Different magnetometers have been developed over the years, with varying advantages. A detailed review of magnetic field instrumentation is given by Telford et al. (1990) and Hinze et al. (2013). In this research, the magnetic surveys were conducted using the proton precession magnetometer as a base station and the cesium vapour magnetometer as a "walking mode"; the rover magnetometer (G859) was carried on a non-magnetic backpack along the profiles. The two magnetometers used in this research are resonance magnetometers. A brief overview of the magnetometers is given below:

- **Proton precession magnetometer:** The magnetometer is based on the Zeeman Effect. The magnetic field (perpendicular to the Earth's field) is applied to protons, then the protons align with the induced magnetic field. The magnetic field is switched off and the protons process at the Larmor precession frequency (Telford et al., 1990). The precession frequency is proportional to the magnetic field and the total magnetic intensity measurement is obtained from the formula:

  $$|H| = \frac{\omega_P}{\gamma_P}. \qquad 3.23$$

  Where |H| is the magnetic field, ω_P is the precession frequency and γ_P is the gyromagnetic ratio. The magnetometer has sensitivity of ~0.1 nT at 0.2 Hz (Nabighian et al., 2005; Butler, 2005).

- **Alkali (cesium) vapour magnetometer:** The alkali vapour magnetometer is also known as optically pumped magnetometer and is based on similar principles as the proton precession magnetometer. However the magnetometer is based on electrons instead of protons (Nabighian et al., 2005). It is more rapid, with cycle rates of 10 Hz and has high sensitivity (0.01 nT).

Accurate Global Position System (GPS) positions need to be acquired using a differential GPS, however magnetic readings are measured rapidly, therefore, survey points need to be marked such that the GPS locations can be obtained with accuracy. The development of newer magnetometers has however allowed the capability to acquire magnetic data continuously with an integrated GPS logging system with an accuracy of 5 cm (Butler, 2005, pp159). As discussed in the previous section, an external magnetic field needs to be corrected by deploying a magnetic base station to monitor the variation. The station is placed in a hidden location such that it cannot be disturbed.

3.2.2. Processing

Prior to interpretation of the data, standard processing steps are taken to remove spatial and temporal variations in the magnetic field measurements. The objectives of processing ground magnetic data can be separated into two sets: 1) Isolate the magnetic signature of the geological source of interest by removing extraneous spatial and temporal magnetic measurements. 2) Enhancement of the magnetic anomaly of interest by applying a variety of filters in the spatial domain or wavenumber domain (Hinze et al., 2013). This section briefly describes some of the processing steps applied to the data acquired for this study such as the effects of the time-varying external field, diurnal variations, removal of the International Geomagnetic Reference Field (IGRF), deculturing, gridding and filtering.

Spatial and Temporal variations

Spatial magnetic variations of the magnetic field include, but not limited to regional variation in the magnetic field, elevation effects, terrain effects, and surface and near-surface effects (Dentith and Mudge, 2014). The magnetic data collected for this thesis was conducted over a small region, therefore spatial magnetic variations such as the difference in observational elevations and magnetic terrain effects were negligible. However, global magnetic variation and the surface and near-surface effects of natural and cultural sources were considered.

- ***Global field models***

Once the positioning errors are removed, the next step is to remove the global field. The magnetic field due to the Earth outer core is much larger than the crustal magnetic field, therefore, it is important to remove the global field in order to improve the resolution of the geological magnetic targets (Hinze et al., 2013). For surveys that cover a large area, the geomagnetic field can be removed by determining the IGRF for the time and location of each measurement (Nabighian et al., 2005). For smaller surveys, variations in the geomagnetic field are not rapid, therefore can be removed together with regional responses (Dentith and Mudge, 2014). The first global field model was released in 1969, with the model being updated every 5 years. This model is important for the removal of the geomagnetic field (Nabighian et al., 2005).

- ***Surface and Near-surface effects***

Ground magnetic surveys are conducted with the sensor being close to the ground, therefore surface and near-surface sources are mapped and can distort the target anomaly. The data for this research were collected in an active mine environment, therefore the presence of cultural noise effect was expected. Cultural noise appears in the data as high frequency and high intensity components, therefore spike filters (e.g., Naudy filter) can be used to remove the noise. However, the filter can also remove the high frequency content of the target anomalies (Naudy and Dreyer, 1968; Nabighian et al., 2005). An alternative method to filter out the noise is to manually inspect the dataset and remove features that are obviously related to cultural objects. Over the years a number of automated methods have been developed to identify cultural magnetic anomalies and their characteristics (e.g., Muszala et al., 2001; Hassan and Pierce, 2005; Salem et al., 2010). Natural magnetic effects arise a result of magnetic mineral content in rocks. Therefore an understanding of the surrounding geological rock is important when conducting magnetic surveys. The effects of natural magnetism can be minimized by avoiding local magnetic material. However, this requires multiple observations to be conducted over time at the site to identify field derived from the anticipated sources (Hinze, 1963). The expected anomaly of interest in this research is located within magnetic rocks of the Bushveld Complex, South Africa. Their magnetic effects were expected on the acquired data.

When isolating the magnetic effect of the geological target, short-term changes in the magnetic field (temporal changes) need to be considered. The changes vary in duration (from a second to a day). Diurnal variations are an example of temporal variations, and can interfere with the magnetic data. The variations must be removed prior to subsurface geological interpretations. Multiple methods have been utilized to remove the variation, with the most precise method for surface surveys being monitoring the continuous variation using a base magnetometer (Dentith and Mudge, 2014). The measurements from the base magnetometer are then subtracted from the station measurements. This correction is effective provided that the base station is located within the survey area, and has a precision of 1 nT or less with an interval of 1 sec to 1 min. The data can also be manually inspected for noise spikes and shot-period variations, which can be edited (Hinze et al., 2013; Dentith and Mudge, 2014).

Filtering

Application of filters for magnetic data processing vary, depending on the data quality. The filters aim to enhance the anomaly of interest. Many filters have been developed over the years, with increased modern computing power as a result of an ever increase in digital data associated with modern magnetic survey techniques.

- ***Reduction to pole (RTP)***

The shape of the magnetic source, the orientation of the magnetic body with respect to the magnetic north, the variation in inclination and declination of the magnetization in the source, and the local Earth's magnetic field influence the shape of the magnetic anomaly. Due to the above mentioned parameters, the magnetic anomaly can be asymmetric, making it difficult to interpret (Baranov, 1957). Therefore a method to overcome this effect was developed, such that any observed anomaly can be transformed (Figure 3.26) into an anomaly that would have been measured at the magnetic pole (vertical magnetization and ambient field). This process is called the reduction-to-pole (Baranov, and Naudy, 1964; Ravat, 2007).

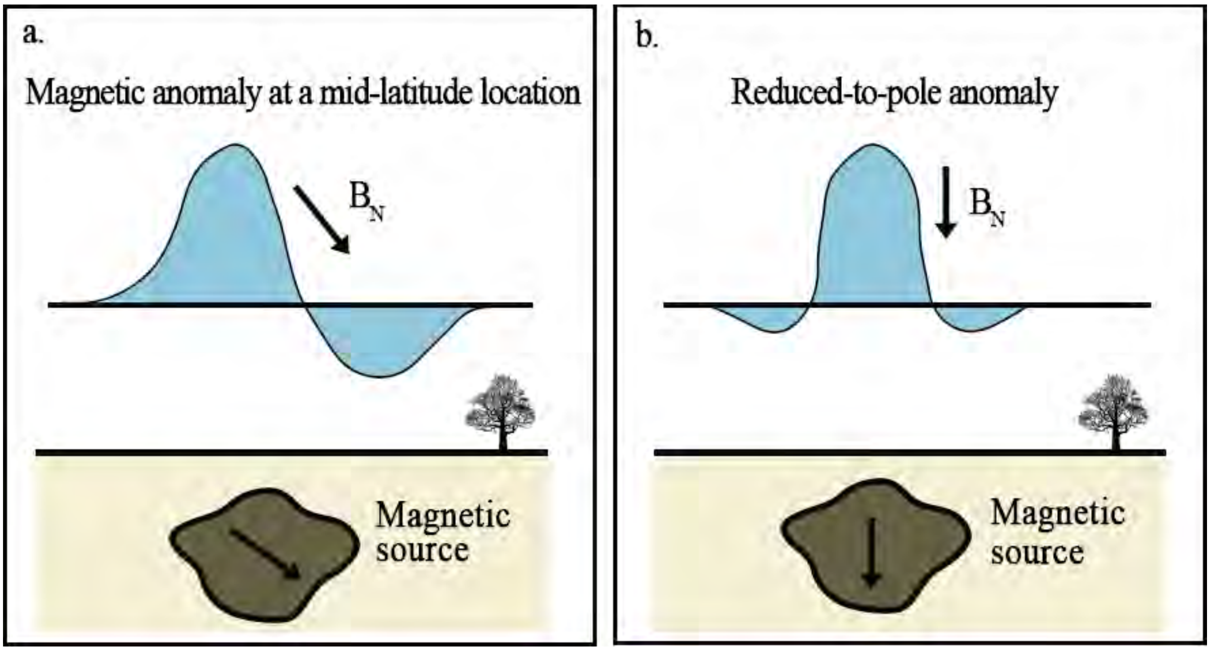

Figure 3.26: *a) Asymmetric magnetic anomaly due to uniform arbitrarily magnetized body below the Earth's surface, with an inclined Earth magnetic field and b) its reduced to pole anomaly in the vertical magnetization and vertical field.*

- ***Tilt derivative***

Over the years, a number of algorithms to enhance features on magnetic data have been developed. The methods are based on first-order derivatives of potential fields to enhance edges and centers of the magnetic source (Dentith and Mudge, 2014). However, this thesis only provides an overview of one of the simplest image enhancement technique applied on magnetic data. The tilt derivative (TD) at a location (x, y, z) is a normalised geometric function of the vertical derivative and horizontal derivative, and it is given by (Miller and Singh, 1994):

$$TD = \tan^{-1}\left(\frac{\frac{\partial F}{\partial z}}{\sqrt{((\partial F/\partial x)^2+(\partial F/\partial y)^2)}}\right) \qquad 3.24$$

where F is the magnetic field. The TD acts as a type of an automatic gain control (AGC) as it is good for enhancing local anomalies at both low and high amplitude. The non-directional tilt derivative (Equation. 3.24) technique is useful as it highlights anomalies with all geometries and orientations. The tilt derivative can be modified to account for specific trending magnetic lineaments that need to be enhanced. The directional tilt derivative (DTD) is given by (Stewart and Miller, 2018):

$$DTD = \tan^{-1}\left(\frac{\frac{\partial F}{\partial z}}{\left|\sin\theta\frac{\partial F}{\partial x}+\cos\theta\frac{\partial F}{\partial y}\right|}\right) \qquad 3.25$$

where θ is the direction of calculation.

3.3. Resistivity

Over the years electrical resistivity method has become one of the widely used geophysical methods for engineering, environmental, hydrological and mining investigations (Loke, 2020). The method is based on the principle of determining the subsurface resistivity distribution by inducing electrical current into the Earth and generates an electromagnetic signal that is monitored on the ground surface (Aizebeokhai, 2010). The resistivity in the ground is related to geological conditions such as water saturation, porosity, mineral and fluid content. Multiple electrical methods with varying setups and configurations have been developed, such as DC resistivity, induced polarization (IP), self-potential (SP), electromagnetic (EM), and magnetotelluric (MT) methods. In this thesis, only the DC resistivity method is used and described (Georgsson and Karlsdóttir, 2010).

Resistivity methods employ the principles of Ohm's Law that governs the current in the subsurface. Loke (1999) describes and derives the relationship between the current density and current (Dey and Morrison, 1979) given by:

$$\nabla \cdot \mathbf{J} = -\nabla \cdot [\sigma(x,y,z)\nabla\phi(x,y,z)] = \left(\frac{I}{\Delta V}\right)\delta(x-x_s)\delta(y-y_s)\delta(z-z_s) \qquad 3.26$$

Where σ is the conductivity of the medium, J is the current density, ΔV elemental volume surrounding the current source *I,* and position(x_s, y_s, z_s). The relationship gives the distribution of potential in the subsurface due to a point source. Equation 3.26 is solved by conducting forward modelling to determine the potential that would be observed at a certain point (Loke, 1999).

Resistivity measurements are conducted by injecting current into the ground using a pair of current electrodes (C_1 and C_2) and measuring the potential using another pair of potential electrodes (P_1 and P_2). The current injected in a homogenous half-space flows radially from the current electrodes (Figure 3.27) and the potential over a homogenous half space at a distance r_1 and r_2 (distance from first and second electrodes, respectively) from the electrodes is given by:

$$V = \frac{\rho I}{2\pi}\left(\frac{1}{r_{c1}} - \frac{1}{r_{c2}}\right) \qquad 3.27$$

The measured potential difference on surface between the two electrodes over a homogenous half space is given by:

$$\Delta V = \frac{\rho I}{2\pi}\left(\frac{1}{r_{c1p1}} - \frac{1}{r_{c2p1}} - \frac{1}{r_{c1p2}} - \frac{1}{r_{c2p2}}\right) \quad 3.28$$

However, field surveys are conducted in a heterogeneous Earth where the subsurface resistivity is anisotropic (Herman, 2001). The apparent resistivity can be calculated using the current and voltage values:

$$\rho_a = \frac{\Delta V}{I} k_{geom} \quad 3.29$$

Where k_{geom} is the geometric correction factor and it is the quotient of cross-sectional area and length of a specimen. The geometric correction factor for a general configuration of electrodes for measurements of resistivity depends on the arrangements of the electrodes and is given as (Aizebeokhai, 2010):

$$k_{geom} = \frac{2\pi}{\left(\frac{1}{C_1P_1} - \frac{1}{C_1P_2} - \frac{1}{C_2P_1} + \frac{1}{C_2P_2}\right)} \quad 3.30$$

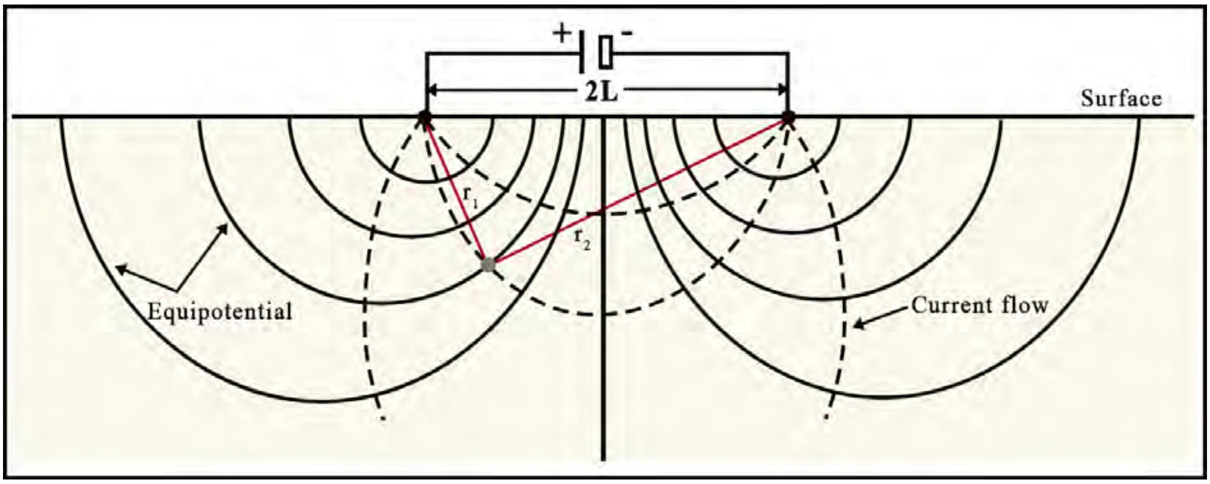

Figure 3.27: *Potential distribution for two point sources of current in a homogenous half-space. L: length of current dipole,* r_1*:distance to first electrode,* r_1 : distance to *second electrode (adapted from* Telford et al., 1990).

3.3.1. Acquisition and inversion

Over the years, a number of resistivity arrays have been developed (Dahlin and Zhou, 2004; Szalai and Szarka, 2008; Martorana et al., 2017). Figure 3.28 shows the array configurations of some of the commonly used arrays together with their geometric factors.

Resistivity surveys were first conducted by the Schlumberger brothers in the 1920s, with the methods divided into two survey techniques: sounding and profiling. Sounding surveys were the first to be used, with four electrodes deployed, the center of the electrodes fixed at one position and the outer electrode spacing being increased to obtain information of the deeper subsurface (e.g., Figure 3.28a: Schlumberger array). Profiling surveys are conducted with the distance between the electrodes fixed and the electrodes are shifted along the profile (e.g., Figure 3.28b). The survey technique is mostly useful for mineral exploration (Telford et al., 1990).

Two-dimensional resistivity imaging surveys are the most commonly used tool for mapping complex geological environments. The imaging technique involves integration of electrical sounding and profiling (Griffiths et al., 1993). The surveys are carried out using multiple electrodes connected to multi-core cables. Apparent resistivity measurements are conducted using a range of different electrode configurations and separation. The most commonly used electrode configurations are Schlumberger, Wenner (alpha), dipole-dipole, pole-pole and pole-dipole arrays. The choice of the array type depends on the type of structure to be mapped as the apparent resistivity observed over the same structure can be different (Loke, 1999; Aizebeokhai, 2010). The Schlumberger, Wenner and dipole-dipole are commonly used for their high vertical resolution and adequate depth of investigation. A description of the array types that are used in this thesis is given below:

- **Schlumberger** (Figure 3.28a) – The Schlumberger array involves four electrodes, with the potential electrodes planted at the center of the array and the current electrodes moved outward for each measurement. Schlumberger is commonly used for vertical electrical sounding (Alfouzan, 2008). The array is sensitive to vertical variations in the subsurface and has a better resolution and depth of penetration to Wenner array (Herman, 2001).
- **Wenner (alpha)** (Figure 3.28b) – The electrodes in this array are equally spaced along the profile, with the array having three different sets of configurations as Wenner-alpha, Wenner-beta and Wenner-gamma. The most commonly used arrangement being the Wenner-alpha (Carpenter and Habberjam, 1956). The Wenner array is sensitive to vertical changes in the subsurface and has a moderate depth of penetration and high signal strength compare to the Schlumberger and dipole-dipole arrays. The high signal strength is important for conducting surveys in areas of high background noise. An increase in electrode spacing results in poor horizontal coverage (Loke 1999; Aizebeokhai, 2009).
- **Dipole-Dipole** (Figure 3.28c) – The array is widely used because of its high sensitivity to resistivity variations, 3D structures, and horizontal changes (Loke 1999). The array is mostly used for imaging vertical structures such as dykes, cavities and fault zones. However, it has poor sensitivity to image horizontal structures (e.g., sills and sedimentary

horizontal layers). The signal strength decreases with increasing distance from the dipole pair (Aizebeokhai, 2009).

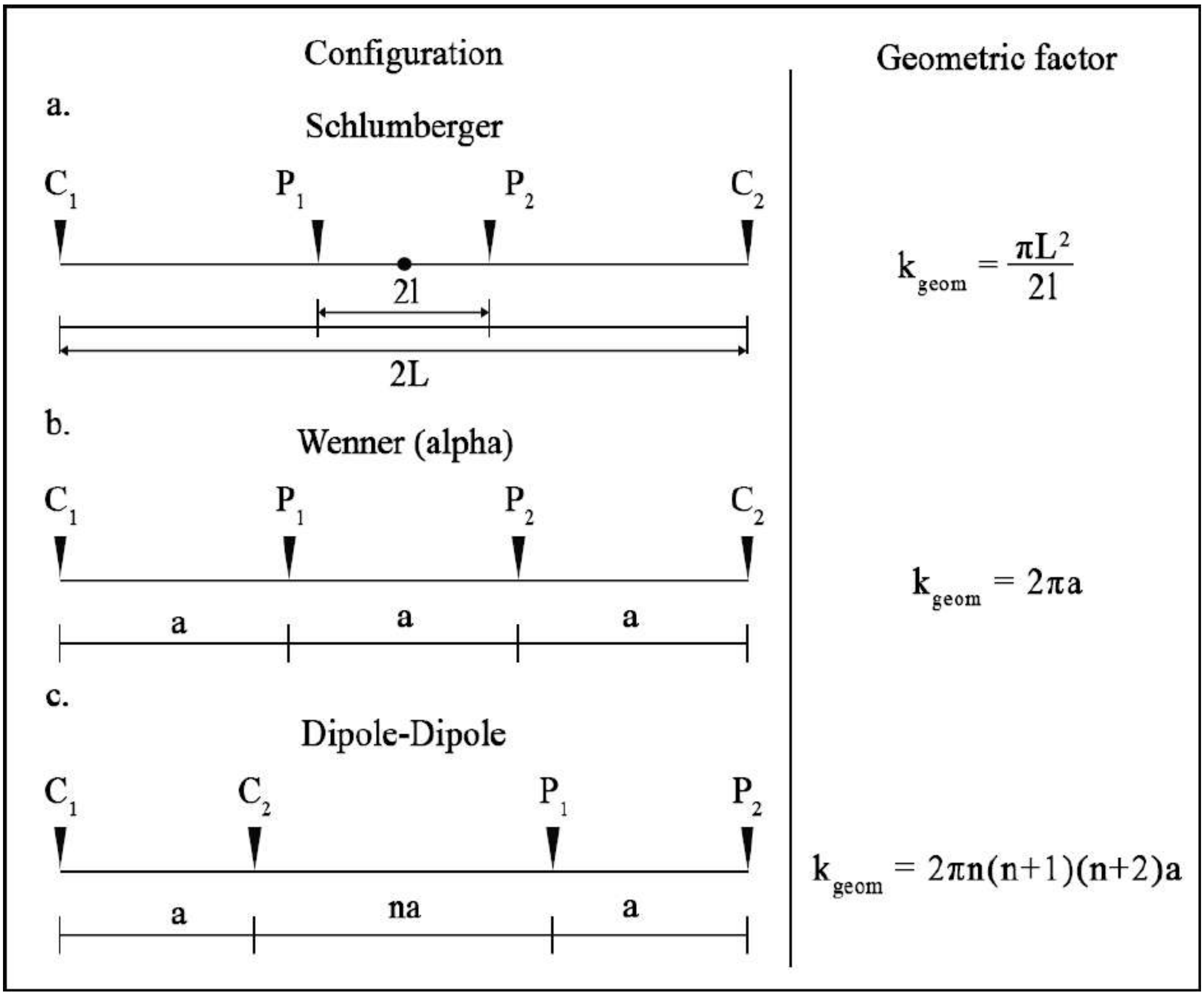

-

Figure 3.28: *Commonly used resistivity arrays (or configurations) and their geometric factors. C_1 and C_2 are current electrodes while P_1 and P_2 are the potential difference electrodes (adapted from* Aizebeokhai, 2010).

Acquisition of resistivity measurements is relatively cost-effective compared to other geophysical methods. Modern resistivity measurements do not require four electrodes to be moved after every measurement, however, multiple electrodes are planted into the ground and the resistivity system automatically acquire the data in arbitrary four electrode configuration (Aizebeokhai, 2010). The development of the automated resistivity systems has greatly improved the efficiency for acquiring the data.

The measured apparent resistivity is normally plotted as a pseudo-section contour map, which provides an approximate picture of the resistivity distribution in the subsurface. The subsurface picture is distorted as the shape depends on the array type and the true subsurface resistivity

(Dentith and Mudge, 2014). Figure 3.29 shows the Schlumberger pseudo-section contouring of a resistivity profile collected as part of this research. The pseudo-section provides the initial picture for qualitative interpretation.

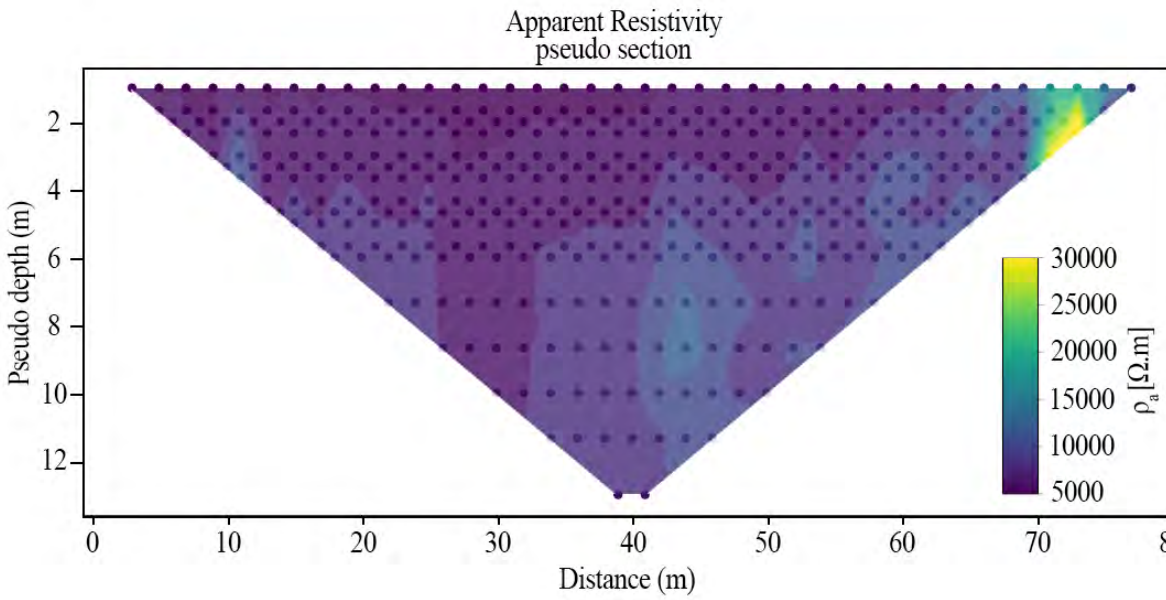

Figure 3.29: *Pseudosection for a Schlumberger array, showing 17-data levels with 41 electrodes. The colour bar shows the apparent resistivity of the median measurement.*

A number of programs have been developed for inversion of apparent resistivity measurements. The quality of data influences the variations in the apparent resistivities on a pseudosection. Poor quality data will have unusual high or low apparent resistivity values. These high and low spots can be identified and picked out as bad apparent resistivity measurements. Numerical methods (finite difference or finite element) are used to calculate the apparent resistivity of the subsurface and produce a desired 2D model (Alfouzan, 2008). The apparent resistivity data are inverted using the modelling software ResIPy. The inverted data are used to produce 2D resistivity sections that can be used to characterise the subsurface geology.

3.4. Ground penetrating radar

Compared to other geophysical methods, Ground Penetrating Radar (GPR) is a relatively a young method. The method was first applied in the 1960s for echo sounding and later expanded into a large number of applications (e.g. geological and environmental studies, mining, geotechnical investigations, archaeological surveys and groundwater exploration) than any other geophysical method (Bailey et al., 1964; Beres Jr. and Haeni, 1991; Neal and Roberts, 2000; Francke and Yelf, 2003; Annan, 2002; Annan, 2005; Venkateswarlu and Tewari, 2014).

GPR surveys are conducted by moving the transducer antenna and the receiver antenna along the surface (Figure 3.30a). The ability to image targets in the subsurface is due to the different electromagnetic properties (i.e. dielectric permittivity, magnetic permeability, and electric conductivity) between subsurface layers or objects. In particular, the propagating wave's velocity and attenuation are significantly influenced by dielectric permittivity (*ε)* and electric conductivity (*σ)*, respectively (Everett, 2013; Catapano et al., 2019). The transducer (Tx) generates high frequency electromagnetic waves (50–500 MHz), some of which are reflected or backscattered and are recorded by the antenna (Rx). The GPR system measures the travel time through the subsurface of the emitted waves and an analysis of the travel time can be used to estimate the depth of the reflecting interface. Figure 3.30b illustrated the A-scan (left) and B-scan (right) images produced when the EM waves are reflected back to the antennas. GPR image (B-scan) is a collection of several A- scans (traces) for each measurements point. The B-scan in Figure 3.30b illustrates a strong, consistent signal that is indicative of both the reflected signal from the air-soil interface and the direct coupling between the transducer and receiver antenna. The signal is regarded as noise that needs to be filtered because of its comparatively large amplitudes (See A-scan in Figure 3.30b) in relation to the target response (diffraction hyperbola), as will be discussed in the following section. In theory, Maxwell's equations, which are discussed in chapter 3.1, govern the physics of GPR (EM waves). The two way travel time is given by:

$$\tau = \frac{2R}{c_0}\sqrt{\varepsilon_r} \qquad 3.31$$

Where R is the distance from antenna to the target, ε_r is the relative permittivity, and c_0 is the speed of light in a vacuum. Due to the nature (high frequency) of the emitted EM waves, GPR has a much rather higher resolution compared to other geophysical methods. However, it falls short in terms of depth of penetration (Bechtel et al., 2007). The penetration depth and resolution of the GPR system is dependent of multiple factors (not limited to) such as: central frequency, electrical properties, size of the antennas, interference and backround noise.

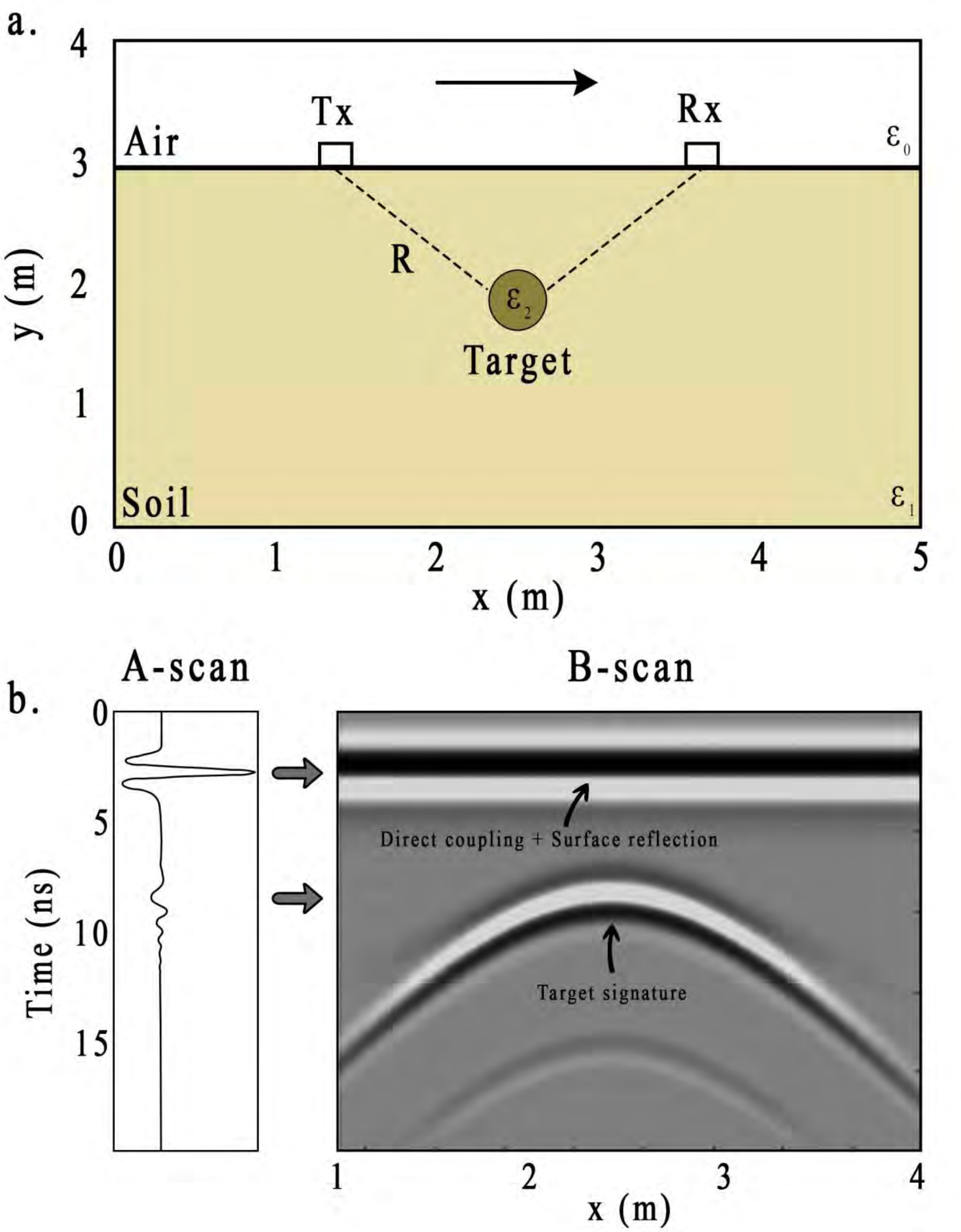

Figure 3.30: *a) a transmitter (Tx) and receiver (Rx) are moved in the x-direction and record traces for each discrete x-position. b) Shows the resultant A-scan (single trace) and B-scan (multiple traces) space-time image, where the backscattered field from the target creating a hyperbolic shape.*

Data Processing

Figure 3.30 shows a simplified version of GPR data. For various reasons, GPR raw data is typically difficult to interpret. The basic processing steps required to enhance the GPR image are described in the section that follows. Depending on the survey scenario, these steps may be fully or partially necessary. It is important to keep in mind that the processing steps listed below may not be all that are necessary for GPR; additional processing steps may be required.

- **Time- Zero correction:** The process of time-zero correction involves removing the initial strong, flat signal originating from the interface between the air and the medium, such as soil. This step is important for comparing the depth and reflection times of targets that are positioned at different locations along the profile. Most of the time, it is challenging to define the precise zero-time cut. However, the first zero following the maximum is the most often selected option (Catapano et al., 2019).
- **Backround removal:** This process involves the removal of horizontal interfaces that are present in the data. Depending on the objective of the study, this processing step might prove to be useful or might not be necessary. Background removal is ineffective, for instance, if the objective is to image the thickness of interfaces. On the contrary, background removal is required if the goal is to image changes in the subsurface. Finally, the process should be used with caution because it has the potential to introduce artifacts into the data (Benedetto et al., 2017).
- **Dewow filtering:** Majority of GPR systems record "wow" data (Figure 3.31a) as part of their raw data recording process. These are the very low-frequency noises that are introduced into the data due to the large amplitudes that overwhelm the electronic instrument. For zeroing (Figure 3.31b) the data, the dewow filter is applied. In essence, the filter is a high pass filter that only allows high frequency component of the data (Maruddani and Sandi, 2019).

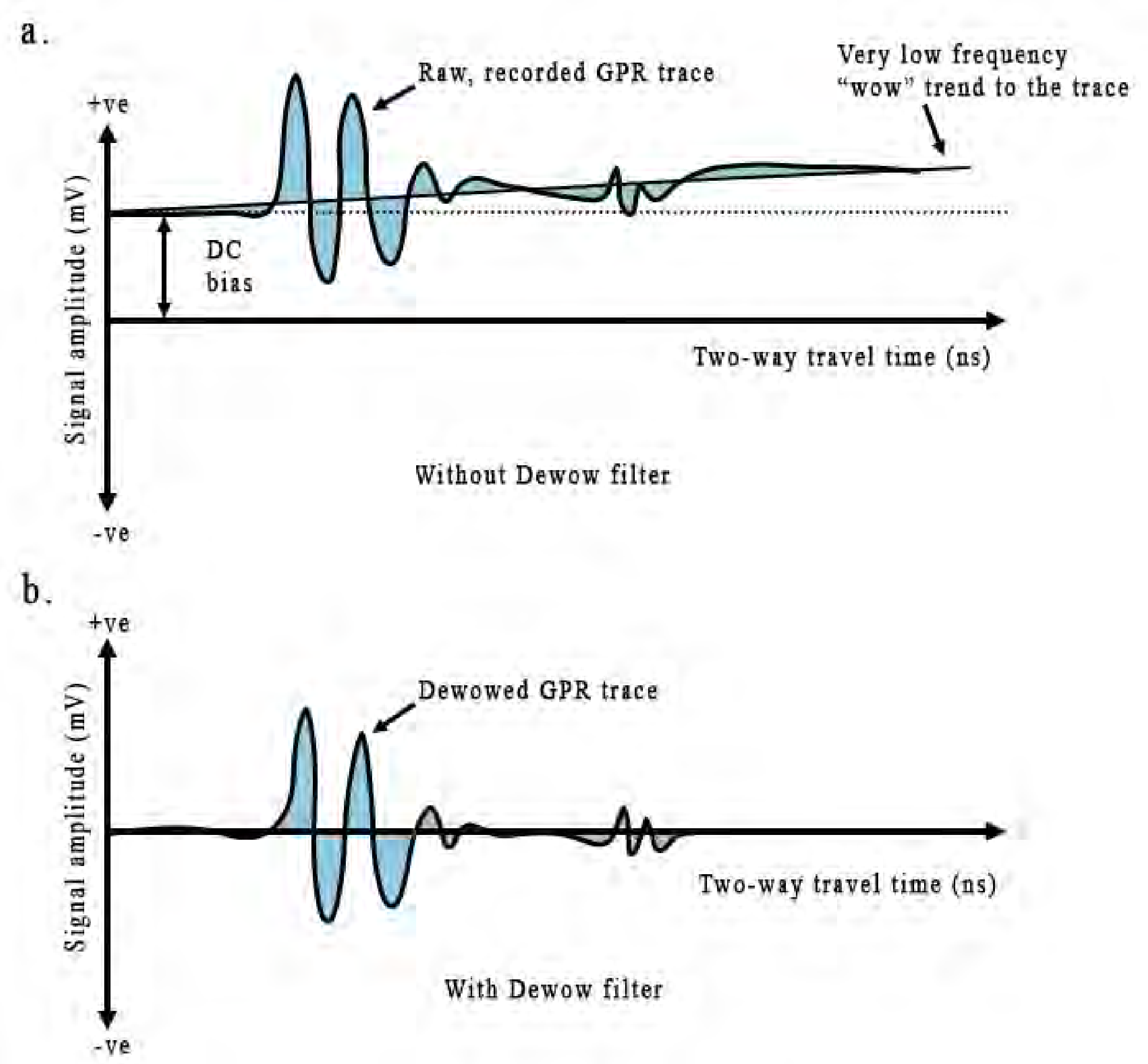

Figure 3.31: *Concept of a dewow filter, with a) the DC bias displayed before and b) after the dewow filter application (adapted from Maruddani and Sandi, 2019).*

- **Velocity corrections:** This process is essential for converting travel time into depth. Moreover velocity analysis is important for migration algorithm application. The most common method to apply velocity analysis is by measuring the velocity of the hyperbolas that are associated with subsurface targets. The other methods is based on survey methodology, where a common midpoint data collection is applied (Reynolds, 2011).Velocity analysis is obtained from the CMP gathered data similar to reflection seismics (Neal and Roberts, 2000).
- **Gain adjustments:** During data acquisition, part of the energy is reflected and some is attenuated, therefore resulting in weak signal recorded for targets that are at greater depths. A gain function is applied to the dataset to improve the signal after it has been

attenuated (Annan, 2005). Different gain controls can be applied to the dataset, with each having its advantages and drawbacks (Benedetto et al., 2017). Below are examples of gain adjustments that can be applied (not limited to):

- **Constant scale:** A multiplier is applied equally over each trace
- **Normalization:** Applied of trace by trace. The data is scaled to its maximum value.
- **Automatic gain control:** Amplitudes distributed equally within a time window
- **Linear gain:** A time varying gain filter that increases linearly with depth.

- **Filtering:** In this step, 1D and 2D filters are used to improve the signal-to-noise ratio and, as a result, the quality of the GPR image. There are many types of filters, just like any other, such as low pass, high pass, band pass, deconvolution, and 2D Fast Fourier transform (FFT) (Szymczyk and Szymczyk, 2013; Maruddani and Sandi, 2019) .
- **Migration:** The primary goal of migration in GPR processing is to collapse subsurface object diffractions into a single point, similar to reflection seismic processing. (Catapano et al., 2019). Detailed GPR migration techniques are described in (Economou et al., 2015).

4. Modelling and physical property measurements

4.1. Seismic modelling

To fully understand the subsurface geology, the final seismic section should be interpreted, integrated with geological maps and borehole information. However, in complex surface and subsurface geology, reflections can be misinterpreted or interpreted with less confidence. Seismic forward modelling can be utilised as a tool to verify and evaluate structural and stratigraphic interpretations. Synthetic seismic sections produced from modelling can be compared to final stacked section for a desired correlation between the modelled results and actual data (e.g., Cheraghi et al., 2011; Bellefleur et al., 2012; Malinowski et al., 2012; Squelch et al., 2013). Moreover, seismic modelling can be utilised for survey design and understanding seismic response of a known geological structure from different sources and receiver setups. In this thesis we apply 1D and 2D synthetic models. 1D Synthetic models are mainly used for testing the reflectivity of the target horizons. The method employs basic one dimensional earth model with specific velocities, thickness and density. The Ormsby, Morlet, Ricker, and minimum phase wavelets are a few examples of the various source wavelets that depict distinct seismic sources (Ryan, 1997). The most common method for computing synthetic seismograms is the 1-D reflectivity method. This method was first developed in the early 1970 by Fuchs and Muller (1971). A more detailed description of the reflectivity method is given by Sen (2011). For 2D synthetic modelling, multiple techniques have been developed to model seismic wave propagation. In this research, finite-difference and ray tracing methods were tested and used.

4.1.1. Finite difference modelling

Finite difference methods (FDM) are the most widely used numerical simulation methods for seismic ground motion. The method is dominant due to its applicability in complex models, relative accuracy and computational efficiency (Moczo et al., 2004). It is a good approximation to the solution of the wave equations. Over the years there have been a number of publications and/or reports on the use of finite difference methods for full waveform inversions (e.g., Dessa et al., 2004; Bleibinhaus et al., 2007), modelling different hard rock environments (e.g., Bohlen et al, 2003; Cheraghi et al., 2011; Ahmadi et al., 2013), wave propagation through random media (e.g., Frankel and Clayton, 1984, 1986; Moczo,1998), and approximating earthquakes as a point source and its associated wave propagation (Moczo et al., 2007).

The wave equation exhibits two modes: acoustic wave and elastic wave equations. Subsurface wave propagation simulations are preferably carried out using elastic or visco-elastic wave equations, due to the nature of acoustic wave equations (e.g., it is only valid in fluid medium) (Robertsson et al., 1994; Saenger and Bohlen, 2004). Acoustic wave equations have an advantage over the elastic wave equations as they are computationally less demanding (Fitchner, 2011). Multiple authors (e.g., Jastram et al., 1992; Wang et al., 2016) have used acoustic wave mode in active source modelling experiments, provided that the S-wave energy is minimal. Most of the modelling work has been conducted for 2D models, however, 3D applications have been considered in geologically complex environment (e.g., Dong and McMechan, 1991; Igel et al., 1991). In this research, 2D and 3D acoustic FD methods are used. The 2D acoustic wave equation in a homogenous media can be expressed as (Zakaria, 2000):

$$\frac{\partial^2 p}{\partial t^2} - c^2 \left\{ \frac{\partial^2 p}{\partial x^2} + \frac{\partial^2 p}{\partial z^2} \right\} = 0 \tag{4.1}$$

Where p is the acoustic pressure, c is the velocity of the acoustic wave, (x, z) are positions in space and t is time. The first expression on the wave equation (Equation 4.1) can be approximated using the second order finite difference approximation as:

$$\frac{\partial^2 p}{\partial t^2} = \frac{p_{i,j}^{k+1} - 2.p_{i,j}^{k} + p_{i,j}^{k-1}}{(\Delta t)^2} = c^2 \left\{ \frac{\partial^2 p}{\partial x^2} + \frac{\partial^2 p}{\partial z^2} \right\}, \tag{4.2}$$

then we have:

$$p_{i,j}^{k+1} = 2(1 - 2\gamma^2) p_{i,j}^{k} - p_{i,j}^{k-1} + \gamma^2 (p_{i+1,j}^{k} + p_{i-1,j}^{k} + p_{i,j+1}^{k} + p_{i,j-1}^{k}) \tag{4.3}$$

The wave equation is approximated in rectangular coordinate system by the second order difference, where $\gamma = \frac{c\Delta t}{\Delta h}$, and $h = \Delta x = \Delta z$ is the grid size in x and y directions and Δt is the time step (Alford et al., 1974; Zakaria et al., 2000).

For the numerical modelling experiments to be stable, certain boundary conditions have to be satisfied; (1) $\gamma = \frac{1}{\sqrt{2}}$, (2) the grid spacing has to be chosen correctly to avoid dispersions in the model and it is expressed as (Amini, 2014):

$$h < \frac{\lambda_{min}}{n}, \tag{4.4}$$

where λ_{min} represents the minimum wavelength and n depends on the order and length of the finite difference operator. (3) Time stepping should fulfil the following condition (Fitchner, 2011):

$$\Delta t < const \frac{h_{min}}{c_{max}} \quad (4.5)$$

The wave propagation problems are conventionally applied to infinite medium. However, the limitation is the finite number of cores of computers available for the model, therefore it is necessary to have boundaries in order to have a finite model. The boundaries can however produce reflections that interfere with the reflections from the interfaces. One way to attenuate this is by introducing boundary conditions. Reynolds (1978) illustrated the usefulness of transparent boundary conditions compared to dirichlet boundary conditions. An example of a transparent boundary condition can be represented as:

Right side boundary:

$$p_{n+1,j}^{k+1} = p_{n+1,j}^{k} + p_{n,j}^{k} - p_{n,j}^{k-1} + c_{i,j}\frac{\Delta t}{\Delta x}\left(p_{n,j}^{k} - p_{n+1,j}^{k} - (p_{n-1,j}^{k-1} - p_{n,j}^{k-1})\right) \quad (4.6)$$

Surface side boundary:

$$p_{i,j}^{k+1} = p_{i,1}^{k} + p_{i,2}^{k} - p_{i,2}^{k-1} + c_{i,j}\frac{\Delta t}{\Delta z}\left(p_{i,2}^{k} - p_{i,1}^{k} - (p_{i,3}^{k-1} - p_{i,2}^{k-1})\right) \quad (4.7)$$

Instead of padding the grid at the edges, transparent boundary conditions replace the wave equation with a one-way wave equation. However, the effectiveness of this boundary condition reduces for waves that strike the boundary at shallow angle (Cerjan et al., 1985). Another boundary condition technique was developed by Cerjan et al. (1985). The non-reflecting boundary condition is applied by multiplying the pressure $P^n(i,j)$ amplitudes outside the boundary lines by the factor (Cerjan et al., 1985):

$$G = \exp -[0.0015(20 - i)]^2, \quad (4.8)$$

where: $1 \leq i \leq 20$.

4.1.2. Ray tracing

Numerical techniques such as finite difference methods have been used for wave propagation solutions, however such techniques are computationally demanding. Therefore high-frequency approximation methods that allow fast numerical models of complex laterally varying layered structures have been developed (Cerveny et al., 1988; Gjøystdal et al., 2002; Cerveny et al., 2007). Asymptotic ray tracing methods have been widely used as high-frequency approximations interpretational tool in numerical modelling of seismic waves (Farra, 1993). The high frequency time-harmonic solution for an acoustic wave propagating (elastic wave equation: $\nabla^2\Phi = \frac{1}{c^2}\frac{\partial^2\Phi}{\partial t^2}$) through an inhomogeneous media can be represented as (Rawlison et al., 2007):

$$\Phi = Ae^{-i\omega(T(x)+t)}\ , \tag{4.9}$$

where Φ represents the pressure field, A is amplitude, ω is angular frequency, and T is a surface of constant phase. Taking the Laplacian and second derivative of Equation 4.9 and substituting in the wave equation yields:

$$\nabla^2 A - \omega^2 A|\nabla T|^2 - i[2\omega\nabla A \cdot \nabla T + \omega A\nabla^2 T] = -\frac{A\omega^2}{c^2}, \tag{4.10}$$

considering the real part only, dividing through by $A\omega^2$ and applying the high frequency approximation ($\omega \rightarrow \infty$), we arrive at the Eikonal equation:

$$|\nabla T|^2 = \frac{1}{c^2}\ . \tag{4.11}$$

Taking the imaginary part of Equation 4.10 and divide by ω, we arrive at the transport equation:

$$2\nabla A \cdot \nabla T + A\nabla^2 T = 0, \tag{4.12}$$

which is used to compute the amplitude of the propagating wave. The Eikonal and transport equations can be expanded for more complex media (e.g., anisotropic media).

Figure 4.1 shows a simple geological model that is crosscut by a near vertical fault with a source located on surface at distance 490 m. Seismic ray traces are overlaid over the model showing the impact the fault plane has on seismic ray traces. Application of ray tracing techniques has been widely used around the world (e.g., Cerveny, 1985; Vlastislav and De Castro, 1993; Gjoystdal et al., 2002; Cerveny et al., 2007), with an expansion into elastic, complex, heterogeneous and three dimensional models.

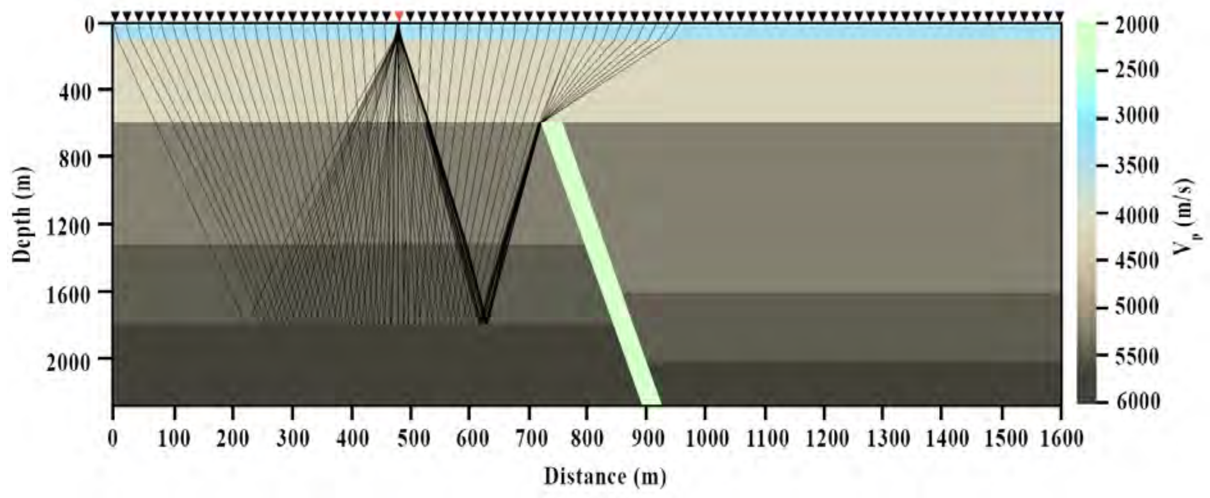

Figure 4.1: *Ray tracing through a simple geological model with a near vertical fault plane. A seismic source is located at 490 m distance on surface (red triangle). 2D ray tracing was conducted using Tesseral pro software.*

4.2. Physical properties

This section provides a brief outline of the techniques used to conduct physical property measurements for the rock samples used in the thesis. Some physical property data used in the thesis were extracted from studies conducted by Sepato (2015) and Nkosi (2017) and from the Council for Geoscience (CGS) database (https://shorturl.at/nGPUV).

To conduct seismic modelling using FD methods and ray tracing, a set of physical property (velocity and density) measurements for the host and target mineralisation needed to be defined. Physical properties can be obtained from a wide range of methods such as downhole logging, surface seismics, or laboratory measurements. The above mentioned methods have their advantages and disadvantages, with the downhole logging giving the best representation of seismic velocities in-situ conditions of the rock formation. However it is not always possible to conduct downhole logging in deep crystalline boreholes (Adams et al., 1997). In situations where borehole data are not available, theoretical estimations can be made based on elastic constants of mineral velocities or by measuring the rock velocities using laboratory techniques. The data used in this thesis were collected using laboratory techniques and to do this, rock samples from the area of interest were collected.

4.2.1. P-wave velocity

Seismic velocities can be measured using ultrasonic instruments (Salisbury et al., 2003; Malehmir et al., 2013; Nkosi et al., 2017). Ultrasonic equipment is made up of a receiver and a source transducer that are connected to a waveform generator as shown in Figure 4.2a. A high frequency signal is produced by the transducers and passes through the rock sample. The signal is observed through the oscilloscope and the waveform is recorded by the computer. Prior to the measurements, the samples need to be prepared by cutting each side to make a flat surface. Borehole core samples are mostly used as they are easy to cut on each side of the core. However irregular shaped samples can be collected and be prepared into a cubic shape. The P-wave velocity measurements for the Bushveld Complex rocks were conducted using a handheld Ultra sonic tester (Figure 4.2b: UK1401 SURFER) at atmospheric conditions. The tester was taken inside the tunnel to measure the P-wave velocity of in-situ rocks (Figure 4.2c). The ultra-sonic tester utilises the same concept as the ultrasonic equipment described above, however it does not have separate components for inducing the signal, and recording the waveform. The samples for using an ultrasonic tester need not to be prepared compared to using the cabled ultrasonic equipment.

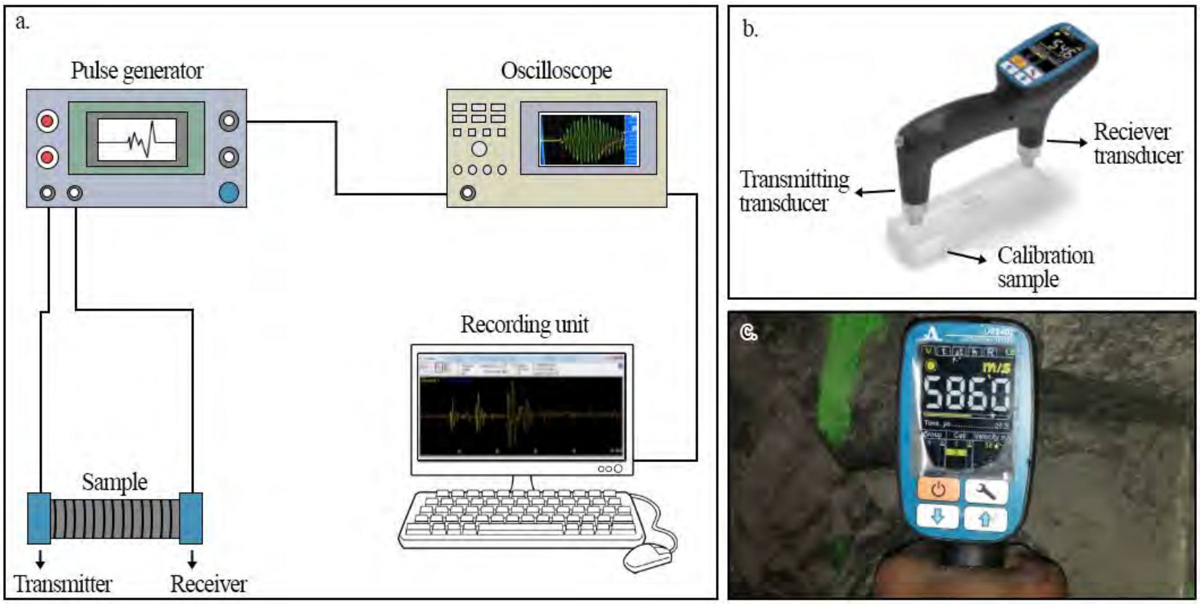

Figure 4.2: *P-wave velocity measurements using ultrasonic equipment. a) Schematic diagram of the ultrasonic equipment. b) UK1401 ultrasonic tester with a calibration sample. c) UK1401 tester used in underground condition on hangingwall.*

4.2.2. Bulk density

Another geophysical property that is important for seismic modelling is bulk density. Density measurements for rock samples that are irregular are tedious as it is difficult to accurately measure the volume of the sample. There are multiple methods for determining the density values of irregular samples such as the suspension, level and overflow methods that are all based on Archimedes principles (Hughes, 2005). As shown in Figure 4.3, the suspension technique involves the immersion of a sample into a container with water and the sample suspended on an electronic scale. According to Archimedes principle, a buoyant force exerted on a body that is submerged in a fluid is equal to the weight of the fluid that the body displaces (Halliday et al., 2000).

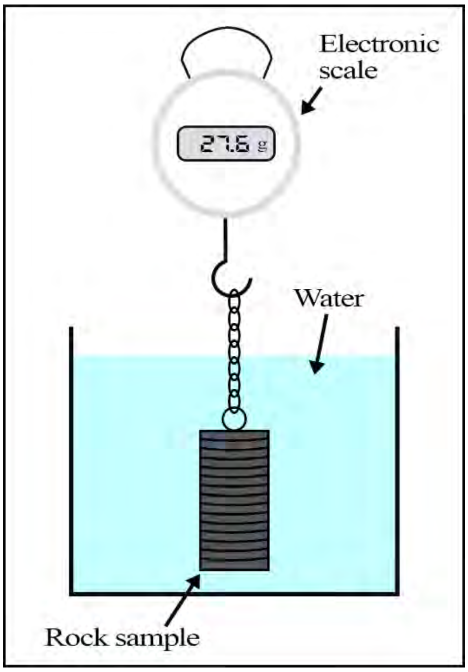

Figure 4.3: *Rock sample hanging on an electronic scale and immersed in a water-filled container. The sample is suspended in the water such that it does not touch the bottom.*

The density measurements reported in this thesis were immersed in pure water, therefore the volume of the sample can be expressed as change in weight divided by the density of the fluid (water with density $of\ 1\ kg/m^3$):

$$V = \frac{\Delta w\ (kg)}{\rho\ (\frac{kg}{m^3})} = \Delta w = w_a - w_w \qquad (4.13)$$

Where V is the volume, w_a is the weight of the dry sample and w_w is the weight of the sample submerged. The density of a body is given by the equation:

$$\rho = \frac{m}{V} \qquad (4.14)$$

$m = w_a$ is the mass of the dry sample measured using an electronic scale. The density is then expressed as:

$$\rho = \frac{w_a}{w_a - w_w} \tag{4.15}$$

4.2.3. Magnetic susceptibility

The magnetic susceptibility logs were measured using a magnetic susceptibility sonde. The sonde is a casing for the emitter and receiver coils that create an oscillating magnetic field which then induces alternating current. The alternating current induces a secondary magnetic field that will spread throughout the surrounding rock and it is then detected by the receiver coil. Using the sonde allows collection of magnetic susceptibility in both water and air-filled boreholes. Sepato (2015) conducted density and magnetic susceptibility measurements of rocks from the Bushveld Complex using downhole logging techniques. In this thesis, the laboratory magnetic susceptibility measurements were conducted using a handheld magnetic susceptibility meter. The SM-30 uses an 8 kHz LC oscillator as an emitter and a pick-up coil (~50 mm in diameter) as a sensor. To make measurements, the coil is placed on the surface of the sample, followed by removing the SM-30 coil away from the sample and a measurement is recorded manually into a sheet. The SM-30 has a sensitivity of 1×10^{-7} SI units, while the downhole magnetic susceptibility logging instrumentation can reach sensitivity of the order 1×10^{-6} SI units.

5. In-mine and surface seismic surveys

Cost-effective in-mine and surface seismic surveys were conducted between 2021 and 2022 at Maseve mine as part of the Advanced Orebody Knowledge (AOK) programme. The in-mine seismic surveys were designed to image geological structures and delineate economic Platinum Group Elements (PGEs). The surface seismic surveys were particularly included to compliment and constrain in-mine seismic experiments.

5.1. In-mine seismic data acquisition

The in-mine seismic surveys comprised of 11 profiles that were designed along the development and entry tunnels. Due to the limited lengths of the tunnels, two orthogonal profiles (Figure 5.1), namely, TP2 (235 m) and TP3 (235 m) had significant spread to be analysed for imaging geological structures and delineate mineralisation. TP2 was conducted with a fixed spread, using 48 1C cabled spike receivers positioned at every 5 m; while TP3 was conducted in two phases, with the first phase (Paper I) consisting of three segments (115 m each) that are collinear using 24 1C spiked geophones (Figure 5.2a: drilled into the tunnel surface) and the second phase (Paper II) consisting of three segments of 48 1C land streamer geophones (Figure 5.2b) that extend from the first phase of seismic profiles. The choice to acquire TP3 in segments was influenced by the length of the cabled system (48 channel, 5 m interval cables) that was available to us.

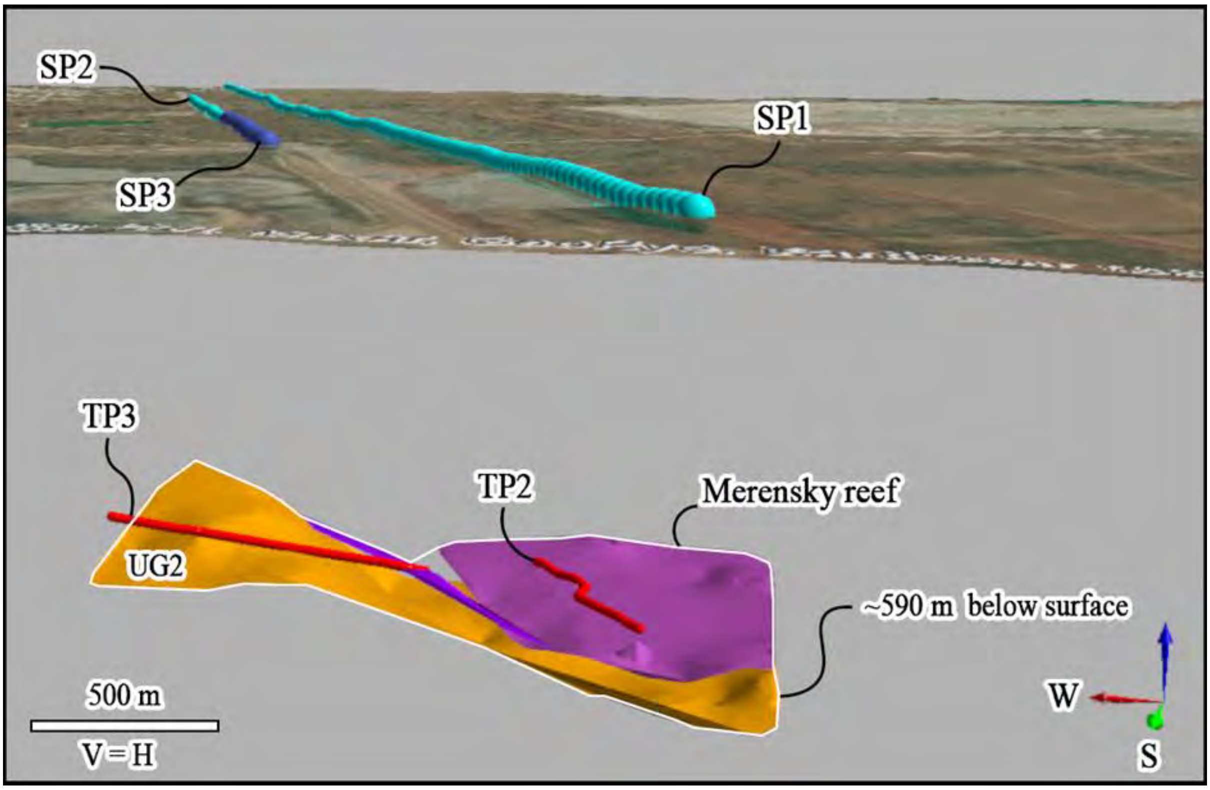

Figure 5.1: *Aerial photo projected on a digital elevation model (DEM) showing the position of the surface (SP1-SP3) and tunnel (TP2 and TP3) relative to the Merensky Reef (purple) and UG2 (orange). The sky blue colour represents nodal receivers on surface. The navy blue and red colour represent the cabled receivers on surface and inside the tunnel, respectively.*

Source points were 2 m apart with four stacks recorded at every shot point to improve the SNR. A 6.3 kg sledgehammer was used as a seismic source over the 24 kg vertically accelerated weight drop (AWD) due to mine restrictions (e.g., low hanging wall and logistically intensive to transport a heavy source to the mine tunnels). Seismic acquisition parameters for both phase one and two surface data are described in detail in Papers I and II.

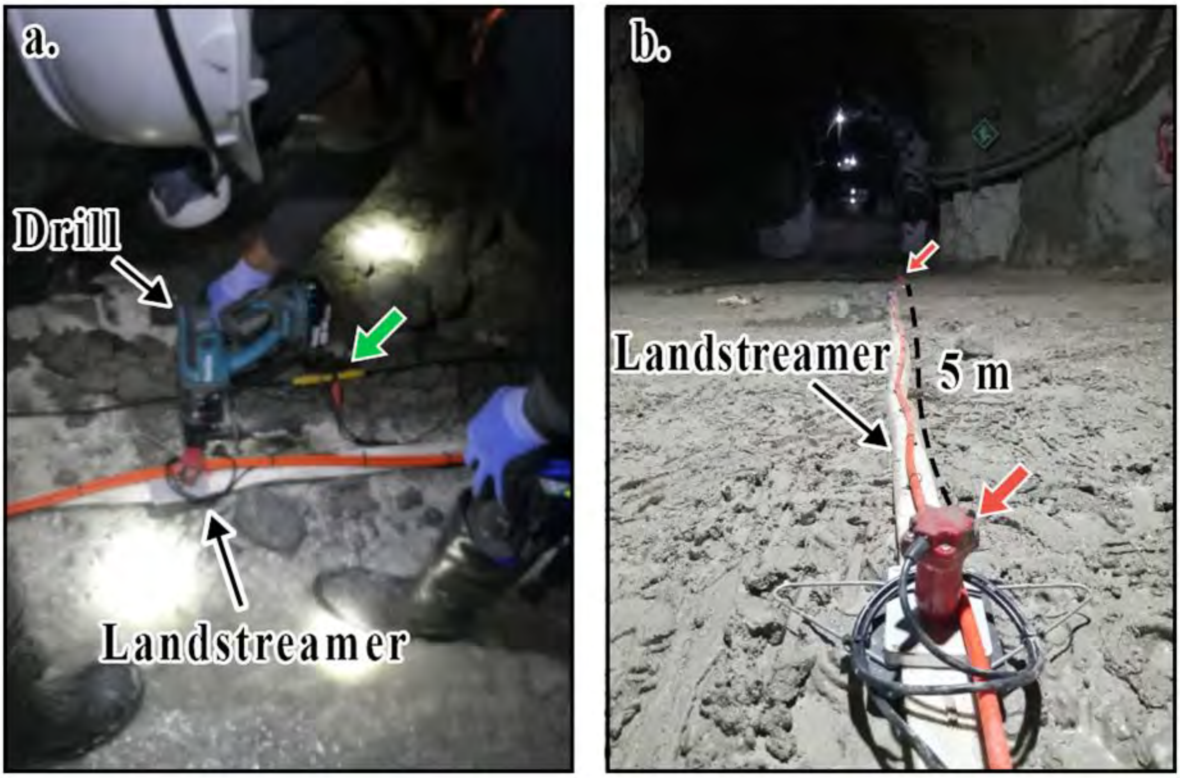

Figure 5.2: *a) Field photo showing the deployment of the spiked geophones by drilling into the hard rock in underground mine tunnel. Green arrow shows spiked geophone cabled system next to the land streamer. b) Photo of the seismic land streamer used to collect seismic data in the tunnel. Red arrows show the 1C 4.5 Hz geophones.*

Maseve mine is placed under care and maintenance, therefore the tunnels are free from mining activities. However, the tunnels are equipped with water pumps (Figure 5.3a) and ventilation (Figure 5.3b) to exchange the air and water intakes for the mining levels. The strength of the noise in the tunnel is rather strong (Figure 5.3c), however the seismic shot gathers (Figure 5.3d) show relatively good SNR.

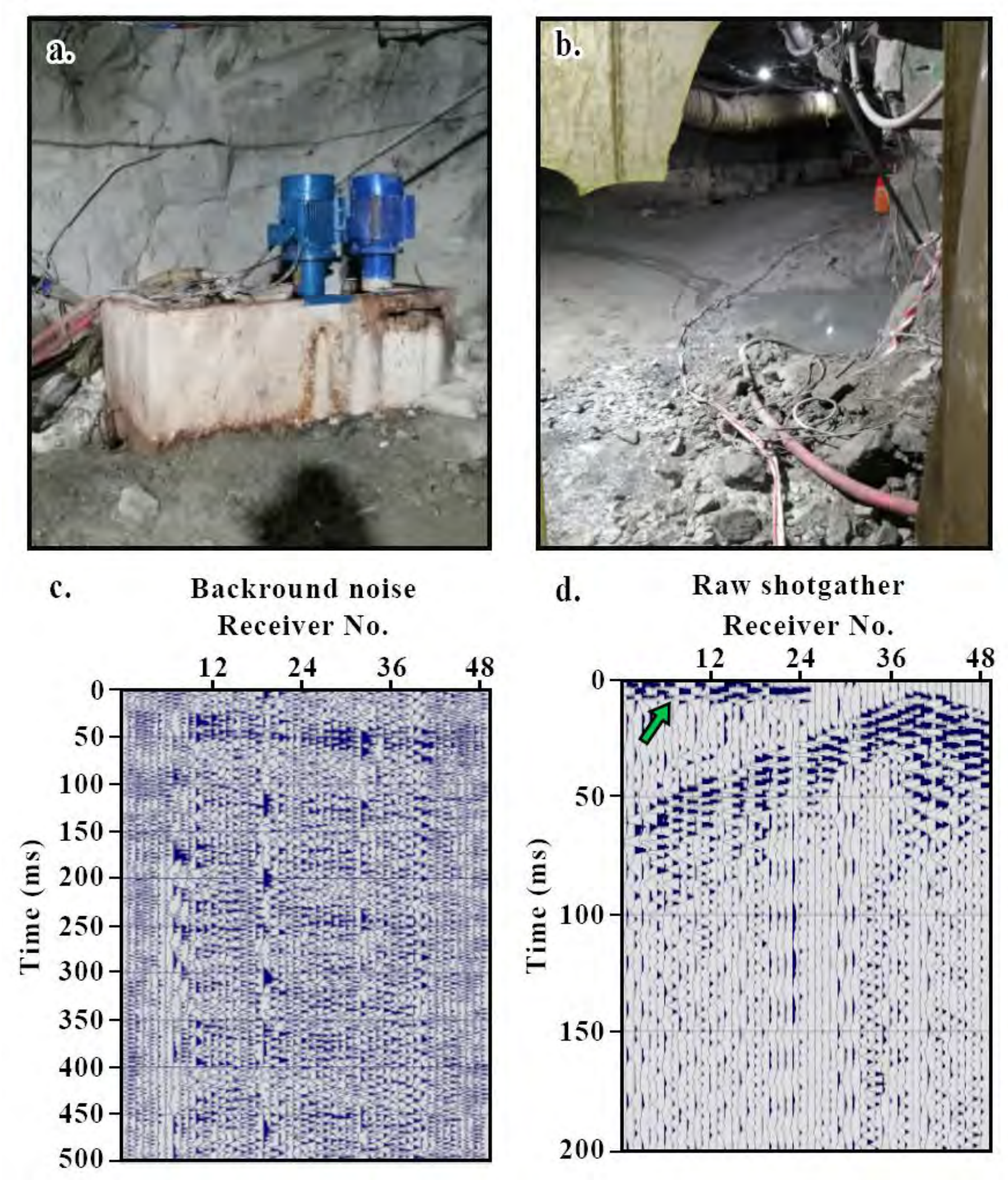

Figure 5.3: *Examples of the sources of noise in underground mining environments include but not limited to a) water pump and b) ventilation and flowing water. c) An example of background noise recorded in mine tunnels. d) Raw shot gather showing the contamination of the data at far offset (green arrow) by background noise.*

*5.2.*Surface seismic data acquisition

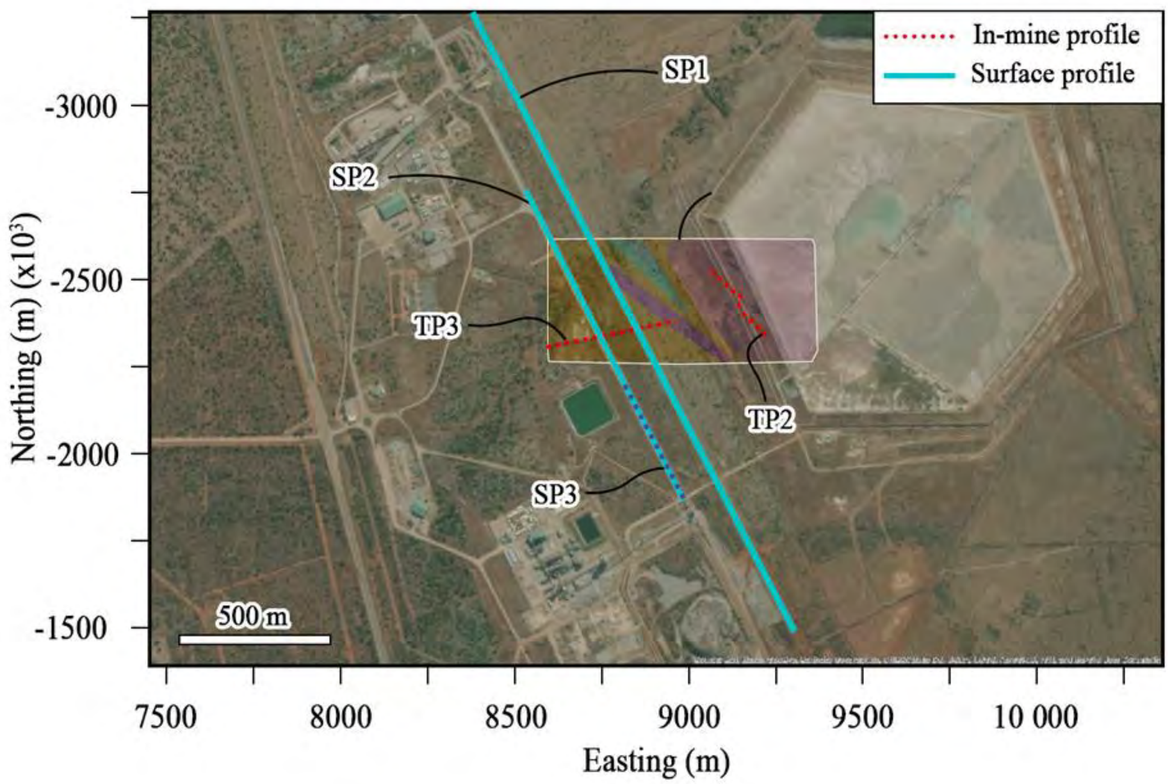

Figure 5.4: *Surface profiles (SP1, SP2 and SP3) and the two long tunnel seismic profiles (TP2 and TP3) collected inside the tunnel, few meters above the Merensky Reef and UG2 deposits (white outline).*

For the surface seismic acquisition, three seismic profiles were distributed parallel to each other along the conveyor belt (Figure 5.4: SP1, SP2 and SP3) approximately 590 m above the Merensky Reef and UG2 deposits. The surface seismic data collection were collected using a combination of nodal receivers (Figure 5.5a) connected to 1C vertical component (5 Hz) geophones and 14 Hz 1C spiked geophones. SP1 (Figure 5.5a) and SP2 (Figure 5.5b) where acquired using the nodal stations spaced at every 10 m. While acquisition along SP3 involved the use of 96 1C cabled geophones (Figure 5.5b) collocated along SP2. A 500 kg drop-hammer (Figure 5.5c: drop-hammer) was deployed as a seismic source, with the impact shot made at every 10 m for all the seismic profiles. The accurate GPS receiver coordinates where collected using a differential GPS for all the seismic profiles. An event recorder (Figure 5.5c) was mounted on the bobcat to GPS time stamp each shot.

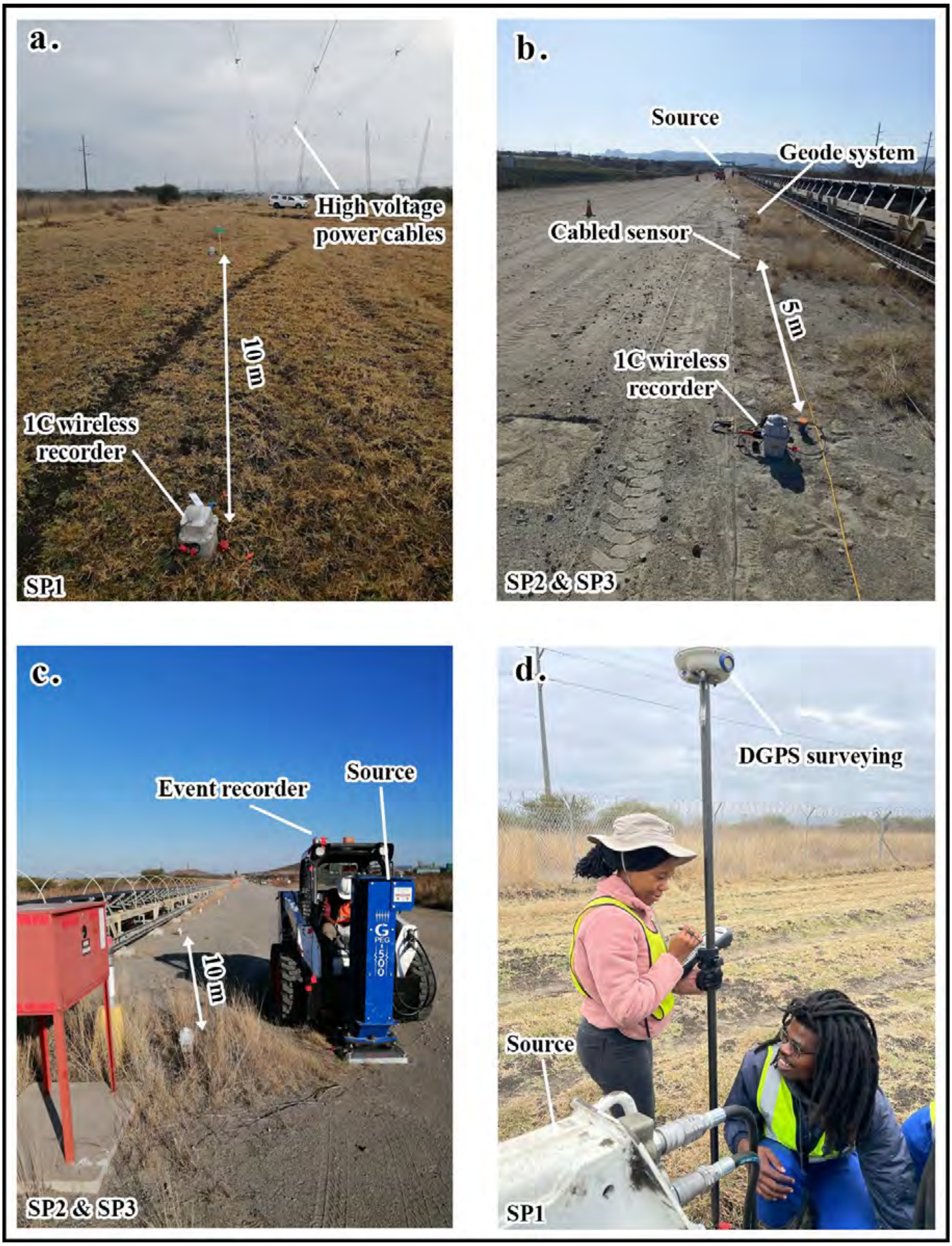

Figure 5.5: *a) Nodal stations connected to 5 Hz 1C geophones spaced at every 10 m for surface seismic data acquisition. b) 1C wireless nodes collocated with the cabled geode system for surface seismic data acquisition of SP2 and SP3. c) 500 kg drop-hammer mounded on a skid steer bobcat used as a seismic source on surfaced. d) Accurate GPS locations of receivers are surveyed using the differential GPS.*

The data acquired on surface are characterized by ambient noise due to the surface infrastructure such as 50 Hz electrical power cables (Figure 5.6a), roads and processing plant (Figure 5.6b). This infrastructure produces coherent noise that is noticeable on active seismic data (Figure 5.6c, d). Surface data were collected to understand the acquisition challenges and innovation aspects required to acquire seismic data in a highly noisy and logistically challenging mine environments. The results were further used to validate the in-mine seismic experiments.

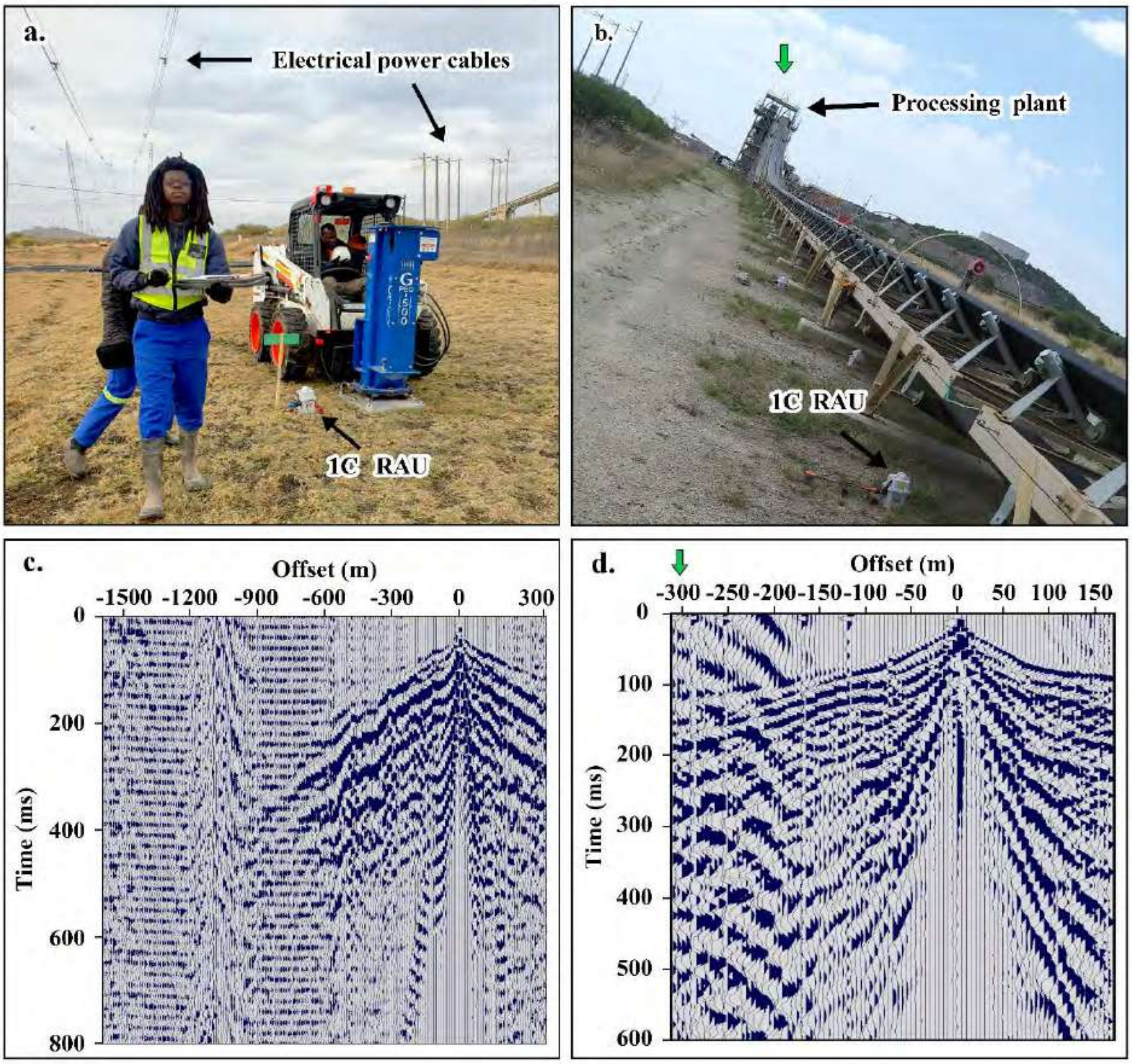

Figure 5.6: *a) Field conditions showing electrical power cables above the survey area and b) processing plant near the seismic profiles. c) Raw shot gather showing the strong coherent noise caused by the 50 Hz frequency from the electrical power cables.*

6. Summary of papers

Paper I: Cost-effective in-mine seismic experiments to image platinum deposits and associated geological structures at Maseve platinum mine, South Africa

Summary

The delineation of mineral deposits and their related geological structures is of great importance to the mining industry, as structures such as dykes and faults can affect the safety, cost and efficiency of mining. Seismic experiments were conducted at Maseve mine tunnels in 2020. The experiments are likely the first in-mine seismic experiments to be conducted in a deep South African platinum mine. The surveys were designed to image geological structures and delineate economic Platinum Group Elements (PGEs) bearing Merensky Reef and Upper Group 2 chromitite layers (known as reefs).

The in-mine seismic surveys consisted of seven 2D reflection seismic profiles in the development tunnels, which were located ~550 m below ground surface and a few tens of metres above known mineralisations: the Upper Group 2 and Merensky Reef. Only the results obtained from active in-mine seismic profiles (P5–P7) are presented. The in-mine seismic experiments involved the use of cost-effective seismic equipment such as the 4.5 Hz land streamer and 6.3 kg sledgehammer, which were easily accessible for surveys. The seismic data were processed using today's standard processing approaches. Despite the fact that the seismic data were acquired in a closed mine, ventilation and dewatering pumps were active and amongst the sources of noise inside the tunnel. An attempt was made during data processing stage to attenuate the noise and enhance the reflections. An *f-k* filter was important in eliminating the airwaves and boosting the amplitudes of the reflections.

The seismic data from the three profiles were stacked and migrated. An improvement in the SNR was observed, therefore the reflections are observed in the final stacked section. In order to constrain the interpretation of the reflections and investigate the source of seismic reflectivity, a 2D acoustic finite difference model was conducted using the geometry of the orebody. The model was based on the borehole data and mine plan provided by the Maseve mine. Rock samples from the orebody and host rocks were collected from the underground workings. Ultrasonic physical property measurements of the rocks were conducted at room temperature. The densities (2700 - 3000 kg/m^3) and velocities (5400 – 5950 m/s) of the rocks are within a narrow range, except for the chromitite (density: 4392 kg/m^3, P-wave velocity: 6118 m/s) sample that is much denser than the host rocks.

A general assessment of the in-mine seismic results reveals that the data, although acquired in a noisy mine environment, are of high quality from which structural interpretation can be drawn. The strong, seismic reflections associated with the MR and UG2, although disrupted by faults and folds, are prominent and reliable indicators of mineralisations throughout the seismic profiles. In general, the geometry of the MR and UG2 orebodies was well defined by seismics. Good correlation between seismics and mine orebodies (derived from boreholes) is mainly observed from the centre of the profile. In terms of structural interpretation, our results confirm the existence of previously known faults and dykes and further constrain their interpretation.

Given the cost-effective nature of the instruments used and the limitation posed by mine infrastructure to properly design in-mine seismic surveys, the results demonstrate that in-mine seismic surveys can be an asset for mineral exploration and mining. Furthermore, these experimental surveys are considered to be cost-effective as the approach was approximately > 60% cheaper than if the survey was acquired by commercial contractors on surface (assuming that there would be no infrastructure limitations, environmental and permitting issues) using more expensive and heavier geophysical equipment (such as vibroseis trucks and 100s of receivers on surface).

Conclusion

2D in-mine seismic profiles were acquired at Maseve mine to image the platinum deposits, host rocks, and geological structures. The data were processed with today's standard processing techniques to attenuate mine-generated noise and enhance the target reflections in the dataset. Despite the challenges faced in the design and processing of the data, the Merensky Reef and Upper Group 2 orebodies were imaged successfully at approximately 55 m and 124 m below the tunnel floor, respectively. Furthermore, faults and dykes crosscutting the mineralisation were imaged, highlighting the importance of cost-effective seismic methods for mineral exploration. The study forms a pilot concept for the mining industry to utilise in-mine seismics development and mine planning. This survey set-up is cost-effective because it uses an affordable energy source and land streamer, which do not require extensive planning and mobilisation.

Paper II: Innovative seismic imaging of the platinum deposits, Maseve mine – Part II: Surface and in-mine (in preparation)

Summary

Paper II focuses on the data acquired on surface and in-mine (SP1, SP3, TP3 and TP4) as part of the Advanced Orebody Knowledge (AOK) programme. With successful experiments conducted as part of phase 2 (Paper I), a pioneer study was conducted in 2022 at Maseve mine to test the feasibility of applying tunnel-surface experiments in a noisy and logistically challenging mine environment. The survey took into account the limitations expected at an operational mine such as limited time, site accessibility and day-to-day operations at Maseve mine. The study forms a pilot study for the experiments that were conducted in the late 2022, under the EU funded ERAMIN-FUTURE project.

The objectives of this paper are as follows:

- To substantiate the use of small scale seismic surveys in highly noisy and logistically challenging mine environments.
- To image the extension of the deep mineralisation and associated geological structures.
- To understand the acquisition challenges and innovation aspects required to acquire seismic data.

Although the dataset was collected in a noisy mine environment, the raw shot gathers generally exhibit high SNR with some minor contamination from mine infrastructural noise. The noise generated by the mine infrasture (e.g., mine pumps, ventilation and flow of water), only overshadows reflections at shot locations that are in the close proximity of the noise sources.

Traditional processing techniques were adopted to remove the coherent noise. Through the application of conventional pre-stack processing techniques, in particular, unmigrated stack sections from profiles TP3 and TP4 were produced. A set of reflections can be observed in all the profiles. A strong seismic reflection is attributed to the Upper Group 2 chromitite (UG2). A 3D constant velocity ray tracing was used to validate the results of the unmigrated profiles. Two migration algorithms such as Kirchhoff and Phase shift migration were tested on the dataset, and both resulted in an introduction of artefacts in the dataset; hence interpretation of the data is conducted using unmigrated depth sections.

The geometry of the seismic reflection attributed to UG2 mineralisation is similar to that of the mine's UG2 orebody model, which is derived from the borehole information and underground mapping. As part of testing the feasibility to conduct tunnel-surface experiments in a noisy and logistically challenging mine, surface seismic profiles were designed to image the ~540 m deep mineralisation. Three surface seismic profiles were collected using a combination of nodal arrays and seismic land streamer. Raw seismic shot gathers show some good reflections associated with mineralisations, but also exhibit noise from the mine infrastructure such as processing plant and electrical power cables.

The secondary objective of this survey was to image the extension of the deep mineralisation and associated geological structures. The surface seismic profiles were processed using conventional processing techniques. Although there is coherent noise in the raw seismic data, the processing steps focused on enhancing the SNR of the pre-stack gathers and enhancing the reflections with the focus on the top 300 ms. Depth-converted migrated sections were produced showing the continuity of the orebody-generated reflections at depths below the mine tunnels (~ 500 m depth). Finally, the mine-modelled structures and surface boreholes, as well as the depth-converted seismic sections, were imported into the 3D visualisation software for final geological interpretation. In general, the shallow reflections were observed on the seismic sections corresponding to the bedrocks, followed by two more disturbed reflections at depth originating from the Merensky Reef and UG2 mineral deposits.

Conclusions

The in-mine surface seismic survey experiments acquired at Maseve mine were processed using today's standard processing techniques. These techniques managed to enhance near-surface reflections associated with the bedrocks. The tunnel seismic experiments demonstrated the application of seismic methods using in-mine infrastructure to image platinum deposits and geological structures. Careful data processing approach proved to be important to enhance high quality reflections and suppress coherent noise generated by mine infrastructure. The simple surface experiments not only proved to be efficient, but illustrated the capability of small scale seismic surveys to image the subsurface geology at an active mine site. The use of small scale seismic surveys can add value in active mining environments for exploration purposes.

Paper III: Multi-geophysical methods for characterising fractures in an open pit mine, western Bushveld Complex, South Africa

Summary

Paper III presents part of a broad study that was conducted at Tharisa mine in the Bushveld Complex. Open pit mines are faced with multiple challenges (e.g., bench slope stability, migration of water and near-surface boulders). The need to delineate the fractures and understand the migration of water into the mine pit has led to the development of multi-geophysical and hydrological acquisition setups for gathering data in the noisy mine environments. In this study, multi-geophysical surveys (seismic, magnetics, and electrical resistivity) were conducted to delineate fractures that act as conduits for water migration into an open pit mine. The study demonstrates the challenges faced by the geophysical methods to characterise near-surface fractures and mineralisation in an active mining environment.

Three seismic profiles were collected in an active open pit mine environment to image deeper discontinuities and mineralisation contacts. Cabled geode system was deployed with a combination of 4.5 Hz spiked geophones and 14 Hz 1C land streamer. The choice to use the two set of sensors is influenced by the ground condition in the mine. The land streamer was used in an area with compact hard rock and high fracturing, while the spike geophones were deployed in areas where they could be planted on to the ground. Three magnetic data grids were collected in the pit targeting a known major dyke that crosscuts the pit. The grids covered a total area of 16 km^2 using the proton precession and cesium vapour magnetometers. Regional aeromagnetic data covering the western Bushveld Complex were used to identify major geological structures around the mine. A section of the dyke was surveyed in great detail with nine parallel N-E ground magnetic lines of 70 m in length, with a line spacing of 10 m. The last geophysical method deployed in the pit was the electrical resistivity, with three profiles cross cutting the mapped dyke and known faults. Forty-one fixed electrodes were used for each of the three profiles, with a spacing of 2 m for RP1 and RP2, while RP3 had an electrode spacing of 6 m.

Processing of the seismic data involved the suppression of the noise from the mine workings to enhance the P-wave reflections that are caused by lithological boundaries. Conventional seismic processing techniques were deployed, targeting near-surface reflections. The *f-k* filter was effective in attenuating coherent noise introduced into the dataset by secondary energy sources (dump trucks and drilling). The phase shift and Kirchhoff migration techniques were

tested to check their capabilities in mapping the fractures systems. In the end, the Kirchhoff migration method with a constant velocity of 3000 m/s produced the best image for final structural interpretation. Longer and wider seismic and magnetic grids are likely the best approach to this type of geology and challenges. However, this will be difficult as a result of the active mining and infrastructures.

The magnetic data were gridded and a total magnetic intensity (TMI) map was produced. Basic magnetic data processing steps were taken to enhance the anomalies. The vertical tilt angle derivative enhanced the edges of the dyke contacts. The resistivity data were inspected for bad data points using an inversion program (ResIPy). The bad data points were eliminated and a tomographic inversion was carried out using a weighted least square function. The topographic effect was not taken into account because the elevation difference was less than 1 m along the profiles. Complex lateral and vertical variations of resistivities were observed on the resistivity models. The Schlumberger and dipole-dipole models were considered for this study due to their sensitivity to horizontal (high resistivity zones: white arrows) and vertical (low resistivity: blue arrows) changes in resistivity, respectively.

The electrical resistivity and P-wave seismic velocity models show inhomogeneous horizons, with sudden resistivity and velocity changes that are attributed to fractures. Integration of the dipole-dipole resistivity and reflection seismic sections revealed that the lithology within the pit is disturbed. The fractured norites exhibit resistivities of $\leq 89 - 213\ \Omega.\mathrm{m}$ and P-wave velocities of $\leq 500 - 1300\ \mathrm{m/s}$. The highly fractured norites are attributed to blasting in the pit.

The data collected at Tharisa mine illustrated that good quality geophysical data can be used to establish regional structural fracture system in an area of interest. This is likely the first multi-geophysical study to be conducted in an open-pit for imaging fractures in the Bushveld Complex. The data were collected without any interruption to mining activity, illustrating the cost and time effectiveness of the surveys inside the pit.

Conclusions

The data show a set of low P-wave velocity zones, low magnetic signatures and high conductive zones that are associated with a fracture system within the pit. Moreover, a set of reflections is imaged that is associated with deeper mineralisation. This is important as the mine is undergoing plans to move underground and mine deeper ore deposits. The importance of such studies is to highlight the benefit of geophysical and geological data integration to image depth to the bedrock, fractures within the host rock and dyke in a complex mining environment. This is critical for future mine planning and designs. The combination of three or more geophysical methods has more advantage in subsurface imaging. The geophysical data were integrated with borehole data and physical property measurements to further constrain the final geological interpretation

Paper IV: Integrated geophysical methods for boulder delineation to improve mining

Summary

Boulders in mining operations pose challenges, affecting productivity, costs, and risks, potentially escalating engineering risks and increased costs. Therefore, locating boulders beforehand is crucial for proper mine planning and minimizing negative impacts on mining and engineering operations. Boulders are rock fragments with a diameter greater than 256 mm, forming from chemical or mechanical processes like spheroidal weathering or blasting respectively. They can be shaped like corestones, concentric shells, or embedded in saprolite (Udden, 1914; Dan et al., 2016; Shao et al., 2020). The boulders are typically separated by fractures and soft cemented materials with lower densities, compaction, and competence. These boulders in the Bushveld Complex of South Africa are exposed by mining operations, and consist of anorthosite to norite boulders embedded in weathered rock. These boulders are more competent and have higher magnetic susceptibility, making them more resistive, dense, and magnetic compared to their surrounding rocks.

This paper presents the results of integrated geophysical surveys conducted at the Tharisa mine in the Bushveld Complex. The primary goal was to delineate and characterize subsurface boulders in saprolite clays. The surveys targeted boulders larger than 4 meters, as smaller ones can be easily disposed of by mining operations. The secondary aim was to map geological features impacting mining operations for effective mine planning and better resource allocation.

Physical properties, such as P-wave velocity and magnetic susceptibility, were measured to assess feasibility and investigate any significant contrast between boulders and host rock. Three portable magnetometers were used to collect the magnetic data: two G856 proton precession magnetometers and one G895 caesium vapour magnetometer with a built-in GPS receiver. Both G856 proton precession magnetometers were employed as base station magnetometers and were positioned in quiet, isolated locations. The G856 and G895 magnetometers had their data collection intervals set to 15 seconds and 30 seconds, respectively. The Caesium vapour magnetometer was utilized as rover magnetometer. The heights of the magnetic sensor and GPS reception antennas on the rover magnetometer (G859) were around 2-3 m and 1.7–2 m from the surface, respectively. The magnetic data were obtained in a walking mode with a sampling rate of 1 s, line spacing of 2 m, across an area of 150 100 m in order to get high-resolution data and prevent spatial aliasing.

Five resistivity survey lines (RL1 to RL4) were conducted using an automated ABEM 1200 system, with an electrode spacing of 1 m and 2 m. A high-resolution resistivity line RL3.1 was collected over profile RL3 due to observations of hard rock boulders on surface. Two seismic profiles were acquired along the resistivity profiles, with 14 Hz vertical geophones. The data were collected using a 2 m geophone and shot spacing for high-resolution near-surface mapping. The survey was conducted using low cost seismic sources (5 kg sledgehammer and 24 kg accelerated weight drop), with 4 shots taken at every position to improve the signal-to-noise ratio. Data were carefully monitored during recording to prevent noise from mining activities like drilling, blasting, and moving vehicles. A ground penetrating radar (GPR) data grid was collected using the GSSI-SIR 4000 GPR system, with a line spacing of 1 m. Additional 2D profiles (GL1 and GL3) were conducted along the seismic and resistivity profiles for integration purpose.

Fast Fourier Transform frequency domain approach was used to process the magnetic data, eliminating diurnal changes, de-spiking, and micro-levelling in order to minimize directional effects and eliminate long wavelength signals. Additionally, the data were corrected and enhanced using magnetic enhancement methods in order to better highlight certain magnetic source features. For ERT to generate the inverted models, the acquired ERT data were manually de-spiked and inverted. The inversion was carried out using a weighted least-squares objective function and linear filtering. While for seismic, first breaks were manually picked to produce P-wave velocity models. Basic GPR processing techniques were applied to the acquisition delay time, attenuate unwanted frequency components and enhance sub-vertical reflectors. The resistivity and seismic inversion results align with borehole BH1 data. A dark to light blue near-surface zone with resistivities below 40 Ω m and P-wave velocities below 1400 m/s is interpreted as the saprolite clay-regolith zone. As depth increases, resistivity and P-wave seismic velocity increase in subsurface rocks. The linear features on the GPR GL1 radargram are structural responses, correlating with resistivity and seismic tomogram.

Conclusion

This study demonstrates the integration of magnetic, electrical resistivity, refraction seismic, and ground penetrating radar methods to improve understanding of subsurface rocks, increasing efficiency in mining and enabling sound engineering decisions. It proposes using integrated geophysical techniques for mining and engineering site characterization to identify geological features like boulders, fractures, and horizons. Successful geological feature identification may be achieved by focusing on weathering, structural, and magnetization impacts in subsurface rocks in magnetic settings. The study successfully maps boulders, fractures, undulating lithological horizons, and remanent igneous features, demonstrating that the integration of various geophysical techniques can improve mine blasting programs, lessen boulder formation brought on by blasting, and help with cost-effective decision-making.

Near Surface Geophysics

EUROPEAN ASSOCIATION OF GEOSCIENTISTS & ENGINEERS

Near Surface Geophysics, 2022 doi: 10.1002/nsg.12216

Cost-effective in-mine seismic experiments to image platinum deposits and associated geological structures at Maseve platinum mine, South Africa

Moyagabo K. Rapetsoa[1], Musa S.D. Manzi[1*], Michael Westgate[1], Mpofana Sihoyiya[1], Ian James[2], Emmanuel Onyebueke[1], Phumlani Kubeka[3], Raymond J. Durrheim[1] and Thabang Kgarume[4]

[1]*School of Geosciences, University of the Witwatersrand, Johannesburg, South Africa,* [2]*Terraspect Geophysics, Perth, Australia,* [3]*Royal Bafokeng Platinum, The Pivot, Fourways, South Africa, and* [4]*Council for Scientific and Industrial Research, Pretoria, South Africa*

Received June 2021, revision accepted May 2022

ABSTRACT

The detection of mineral deposits and their related geological structures is of great importance to the mining industry as structures (such as dykes and faults) can affect the safety, cost and efficiency of mining. With the goal of testing cost-effective seismic methods for mineral exploration and mining, active and passive seismic experiments were conducted at Maseve platinum mine in the Bushveld Complex (South Africa) in 2020. The experiments involved surface-passive (using 5 Hz wireless nodes; single vertical component) and in-mine active reflection seismic surveys (using 4.5 Hz land streamer and 5 kg sledgehammer) to image geological structures and delineate economic platinum-group elements bearing Merensky and Upper Group-2 chromitite layers (known as reefs). This paper presents only the results from the in-mine active seismic experiments. The in-mine seismic surveys consisted of seven 2D reflection seismic profiles in the development tunnels, which were located ~550 m below ground surface and a few tens of metres above known mineralizations: the Upper Group-2 and Merensky Reef. The data were carefully processed to enhance the reflections and suppress noise generated by mine infrastructure (e.g., equipment and ventilation). We successfully imaged the Merensky Reef and Upper Group-2 orebodies approximately 55 m and 124 m below the tunnel floor, respectively, and delineated faults and dykes that crosscut them. Furthermore, the seismic data reveal relatively strong amplitude and faulted reflections below the Upper Group-2 that may represent deeper chromitite-enriched orebodies. However, the economic value of these horizons can only be confirmed through drilling. The processed seismic data were combined with borehole data, synthetic modelling and geological models to constrain the interpretation. This study encourages the use of in-mine seismics for future mineral exploration, mine development and planning.

Key words: Seismic, Imaging, Tunnel, Integration, Near-surface.

INTRODUCTION

The Bushveld Complex, located in the northern parts of South Africa, is the world's largest layered igneous intrusion with an estimated area of 64,000 km^2. It hosts the world's largest

*E-mail: musa.manzi@wits.ac.za

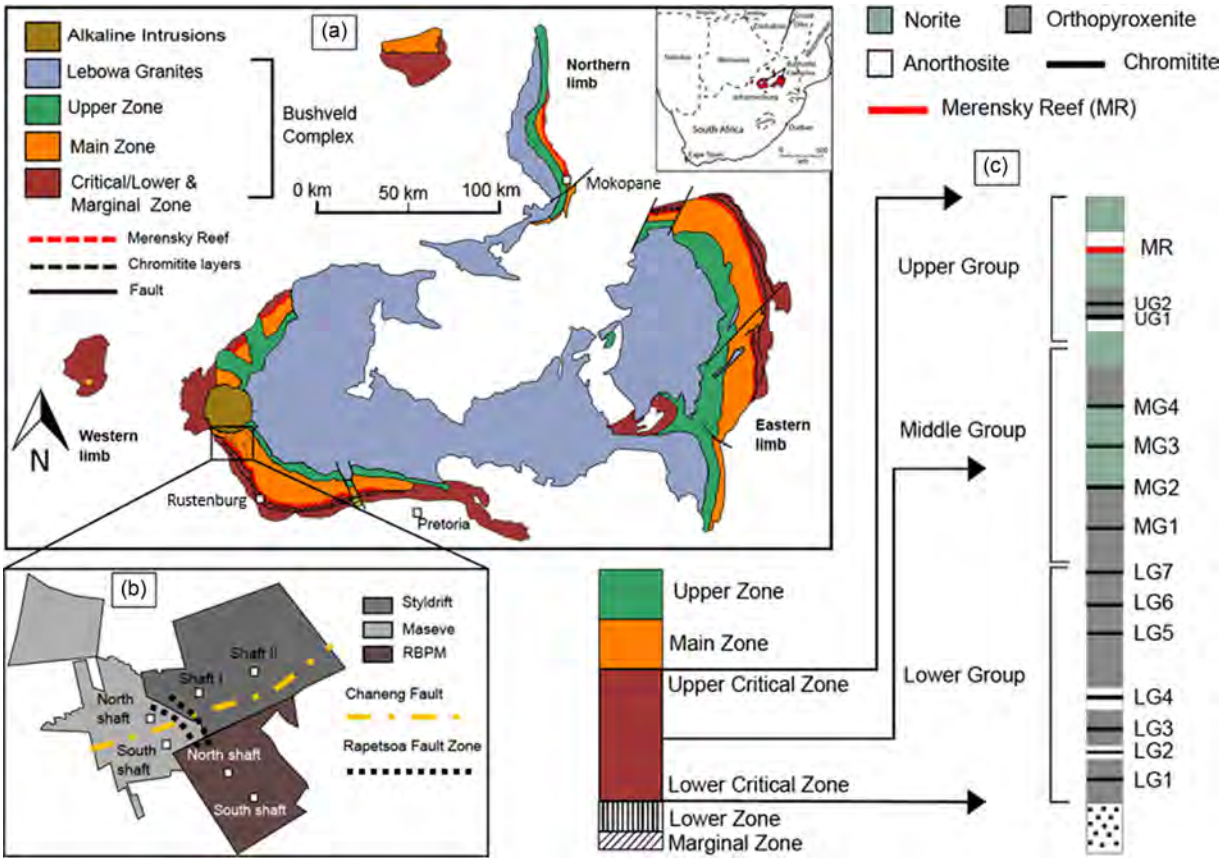

Figure 1 (a) Geological map of the Bushveld Complex (modified from Cawthorn, 2015) showing the location of the Maseve mine site. (b) Map of the Maseve mine showing the location of the study area at the north shaft and the surrounding mines that are used for seismic surveys. The orange dashed lines show the ENE–WSW trending Chaneng fault, while the black dotted lines show the NE–NW trending fault (here termed Rapetsoa Fault Zone (RFZ)). (c) Stratigraphic column of the critical zone showing the chromitite layers and Merensky Reef (MR). RBPM: Royal Bafokeng Platinum Mine; UG: Upper Group; MG: Middle Group; LG: Lower Group.

reserves of platinum-group elements (PGEs) and accounts for almost 80% of all platinum that is mined worldwide (Chistyakova *et al*., 2019).

The PGE deposits occur at various locations around the perimeter of the Bushveld Complex. The Maseve mine is located ∼ 38 km NW of Rustenburg and ∼ 10 km south of the Pilanesberg Alkaline Intrusive Complex in the North West Province, South Africa. The mine is situated on the western limb of the Bushveld Complex, next to the Styldrift and Wesizwe mines (Figs 1 and 2). The mine was placed under care and maintenance in 2017 due to economic reasons and is currently used to test new mining technologies, making it an ideal site for field research.

Underground mining operations in the Bushveld Complex occur between 0.5 km and 2.0 km below surface. Geological structures (e.g., faults, dykes, potholes, and Iron Rich Ultramafic Pegmatites (IRUPs)) are encountered more frequently as mining depth increases (Eales and Cawthorn, 1996; Sehoole *et al*., 2020). These geological structures not only delay development and production, but also threaten the safety of mineworkers by increasing the risk of fall of ground that can result in injuries and fatalities (Guo and Luo, 2014). Furthermore, faults and dykes may act as conduits for flammable gases and groundwater to the mining levels, which may lead to disasters in the mines. These structures can also be re-activated during mining activities and cause rock bursts. The heightened risks compromise the fundamental principles governing South African mining; i.e., safety and optimized ore extraction. These problems highlight the growing need for these geological structures to be identified ahead of mining.

The reflection seismic method is one of the most important geophysical methods because of its ability to detect both large and small-scale subsurface features (Malehmir *et al*., 2012). In South Africa, the reflection seismic method is

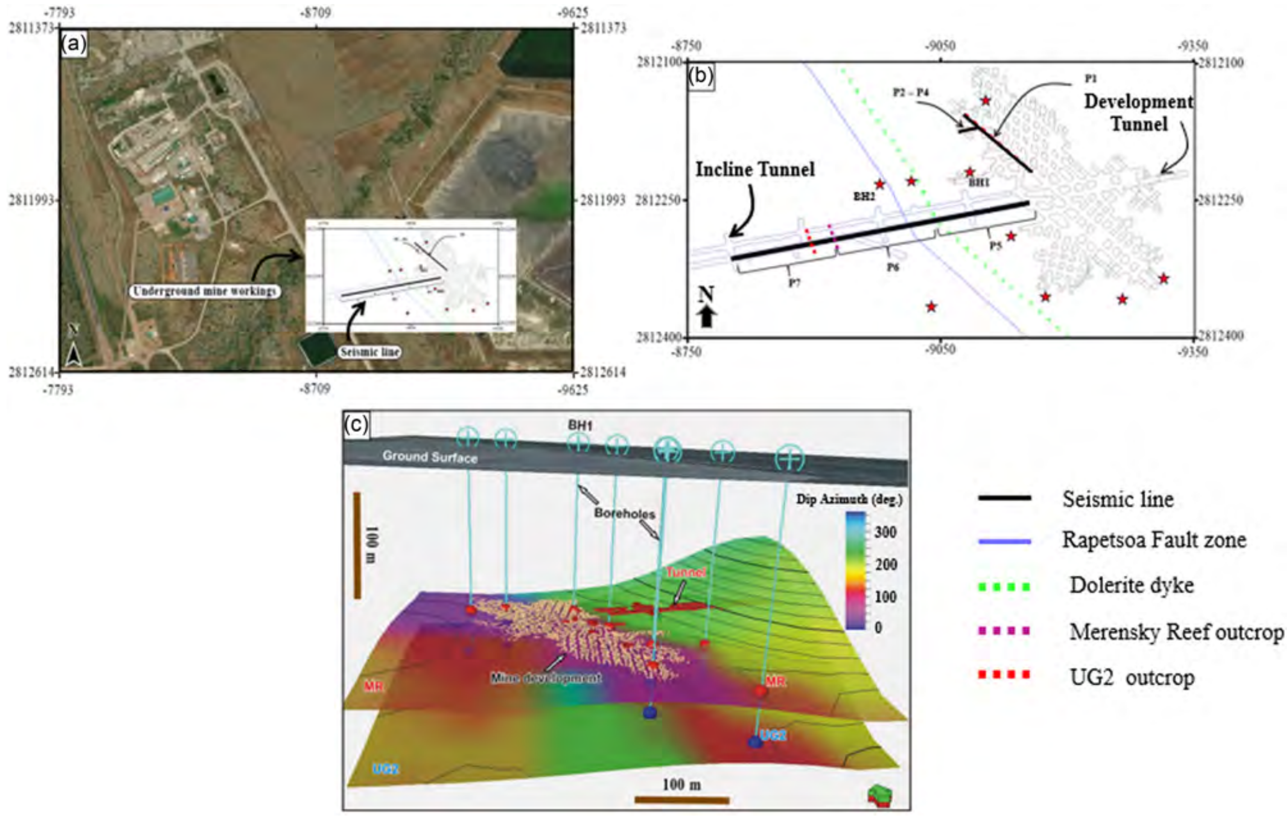

Figure 2 (a) Map view of the Maseve mine surface workings and underground working indicating the seismic profile (black) collected. (b) Underground mine plans, showing the location of the seismic profiles (black) and geological structures such as fault (blue) and dolerite dyke (green) for in-mine seismic experiments. (c) A schematic 3D geological model of the study area, showing the Merensky Reef (MR), Upper Group 2 reef (UG2) and the incline tunnel (red) (the green arrow is pointing to the south). The position of the seismic line is indicated along the incline tunnel. BH1: borehole 1; BH2: borehole 2; P1: profile 1, P2–P 4: profile 2 to profile 4; P5: profile 5; P6: profile 6; P7: profile 7.

mainly used for exploration, mine design, and planning, due to its ability to delineate complex geological features (Stevenson and Durrheim, 1997; Manzi *et al*., 2012; Manzi *et al*., 2019).

Active surface reflection seismic surveys have been conducted since the 1980s in South Africa to address challenges related to deep and near-surface mineral exploration, with the goal of reducing drilling and exploration costs, maximizing mine safety and increasing the possibility of finding new prospects and the life of mine. In the 1990s, exploration and mining companies started conducting high-resolution surface 2D and 3D reflection seismic surveys in the Bushveld Complex to map economic platinum-bearing horizons (known as reefs) and other subsurface features (faults, dykes, folds and potholes). The 3D reflection seismic surveys were particularly designed to map major faults, dykes, potholes (slump structures), and IRUPs. However, the surface seismic surveys were unable to accurately map and provide the geometry of smaller geological structures ahead of mining tunnels (Trickett *et al*., 2004). In the early 2000s, trials were conducted to investigate technologies that can delineate subtle structures with a throw of ∼ 2 m (Stevenson *et al*., 2003). The trials mainly involved borehole seismic techniques (e.g., cross-well reflection seismics, seismic tomography and vertical seismic profiling), which produced resolutions of 1 to 3 m; however, these techniques exhibited low resolutions in noisy mining environments (Stevenson *et al*., 2003; Manzi *et al*., 2012).

As an alternative solution, and despite suffering from noise produced by mine operations such as blasting, ventilation and drilling, in-mine seismics has proven useful in improving the imaging resolution of the mineral deposits and geological structures (Brodic *et al*., 2017, 2021; Donoso *et al*., 2021). The application of in-mine seismic techniques has grown worldwide; however, the techniques are not yet well established in deep South African mines.

In this study, we conducted 2D in-mine seismic surveys at Maseve platinum mine in the Bushveld Complex (South

Africa) to characterize geological structures using different seismic data acquisition techniques. The seismic experiments were conducted in an area covered by ground-penetrating radar (GPR) and electrical resistivity tomography (ERT) surveys for integrated interpretation purposes. Integration of geophysical and geological data has played a key role in mapping; the deep geological structures and obtaining information on/ahead of the tunnel face. GPR and ERT are commonly used to map tunnel roofs and sidewalls, the information of which is in turn utilized to assess and mitigate fall of grounds due to unstable hangingwalls (Kgarume *et al*., 2019). However, in this paper, we present only the results from the in-mine seismic trials.

The extent to which in-mine seismic techniques can image structures depends on multiple factors: acoustic impedance contrast; the geometry and structural characteristics of the target; host rock properties; survey design (receiver and source position); and the mine noise level along the tunnel. To better design in-mine seismic surveys and conduct high-resolution seismic surveys, noise levels need to be assessed and appropriate sources and receivers need to be used. Furthermore, accurate velocity models for the rock mass around the tunnel need to be determined for numerical modelling, seismic processing, interpretation and time-to-depth conversion (Malehmir *et al*., 2013; Manzi *et al*., 2017).

STUDY AREA AND GEOLOGICAL BACKGROUND

The emplacement of the Bushveld Complex has been the subject of academic debate, and its geology has been documented by several authors (Eales and Cawthorn, 1996; Buchanan and Reimold, 1998; Kinnaird, 2005; Hunt *et al*., 2018). The intrusive rocks of the Bushveld Complex were emplaced at ~2.06 Ga into the intra-cratonic sedimentary sequence of the Transvaal Supergroup (Cawthorn and Webb, 2001). The Bushveld Complex is known for its remarkable size, covering an area of about 64 000 km^2. The complex (Fig. 1) is composed of four major limbs, with only the eastern, western and northern limbs outcropping. The southern limb is visible only from gravity data and has been confirmed by drilling. Over the years, several authors have debated about the limbs being connected (Webb *et al*., 2004; Kinnaird, 2005). The successive injections of magma resulted in the geology of the area being divided into three plutonic suites: the Rashoop Granophyre Suite; the mafic to ultramafic Rustenburg Layered Suite (RLS); and the Lebowa Granite Suite (Eales and Cawthorn, 1996; Hunt *et al*., 2018). Based on mineralogical variation, the RLS is further divided into the (from bottom to top): Marginal; Lower; Critical; Main; and Upper Zone (Kinnaird, 2005).

The Critical Zone is about 900–1500 m thick and has been divided into the Lower Critical Zone (LCZ) and the Upper Critical Zone (UCZ) based on the appearance of cumulus plagioclase. The LCZ is characterized by pyroxenites, Lower Group chromitite layers (LG) and Middle Group chromitite layers (MG1 and MG2), whereas the UCZ is characterized by the Merensky Reef (MR; a package of platinum-bearing chromitite-feldspathic orthopyroxenite), Upper Group chromitites (UG1 and UG2), Middle Group chromitites (MG3 and MG4), pyroxenites, norites and anorthosites (Kinnaird, 2005; Seabrook, 2005). The upper limit of the UCZ is marked by the Bastard Reef (referred to as cyclic/rhythmic unit) (Cawthorn, 2015). The MR and the UG2 chromitite are the two major economic horizons for PGE deposits. The thickness of the MR ranges from 0.5 m to 2.0 m, with an average thickness of 1.0 m. The UG2 chromitite layer contains the largest PGE resources on Earth, with a thickness ranging between 0.5 m and 1.0 m. The Middle Group (MG) is made up of four major and minor chromitite layers with a thickness of 0.01-0.05m, whereas the LG consists of seven chromitite layers, with the thickest being 0.8–1.2 m (Lee, 1996; Nex *et al*., 1998; Kinnaird, 2005). The MR and the UG2 are mined at depths greater than 500 m below surface at the Maseve mine, with the UG2 occurring between 15 m and 400 m below the MR in the Bushveld complex (Manzi *et al*., 2020; Sehoole *et al*., 2020).

The Bushveld Complex is crosscut by multiple dykes of different ages and compositions, with diabase and dolerite dykes being dominant in the area. A few dykes at the Maseve mine have been confirmed through drilling and underground mapping. Knowledge of the dykes is important as they reduce the ore reserve and may present mining difficulties. The dykes in the Bushveld Complex are often associated with fault zones (Ledwaba *et al*., 2012; Scheiber-Enslin and Manzi, 2018). Furthermore, the Bushveld Complex is affected by slump structures (locally known as 'potholes') and IRUPs that result in challenges to mining operations. The Bushveld Complex is generally faulted, and the regional structural interpretation suggests that the ENE–WSW trending Chaneng Fault Zone (Fig. 1b) is the most dominant structure in the Maseve area (Basson, 2019). To the south of the Pilanesburg complex, a dense conjugate network of faults and fractures trending NE and NW is displayed on the high-resolution aeromagnetic images (Scheiber-Enslin and Manzi, 2018; Basson, 2019). These geological features have been confirmed through drilling at the Maseve mine and incorporated in the geological model

Table 1 Physical property measurements of Bushveld Complex rocks. Velocity and density of feldspathic and pegmatoidal pyroxenite are adapted from Manzi *et al.* (2020).

Rock type	v (m/s)	ρ (kg/m^3)
Merensky Reef (orthopyroxenite)	5950	2744
UG2 (chromitite)	6118	4392
Anorthosite (pegmatoidal)	5530	2947
Anorthosite (weathered)	3088	2851
Norite	5667	2951
Feldspathic pyroxenite	5400	3000
Pegmatoidal pyroxenite	5900	2700

v = P-wave velocity ρ = density.

(Fig. 2). Most of the faults strike north to northwest and dip at an average of about 70° to 80° (Scheiber-Enslin and Manzi, 2018).

PHYSICAL PROPERTY MEASUREMENTS

Physical property measurements were collected following the procedure described by Nkosi *et al.* (2017). The main objective was to investigate the potential source of seismic reflectivity of the mineralization (Merensky Reef (MR) and Upper Group-2 (UG2)) with respect to their host rocks. The ultrasonic velocity (P-wave) measurements were conducted using a UK1401 SURFER ultrasonic tester, operating at frequencies of 50 kHz. Throughout the seismic P-wave velocity measurements, the repetition frequency of the instrument was kept constant between 2 Hz and 4 Hz, depending on the size of the sample. Five P-wave velocity measurements were taken on each sample and an average was taken as the final velocity value (Table 1). Although the ideal conditions for measuring these samples are at elevated pressures (∼ 20–60 MPa) to mimic the in situ environment, our measurements were conducted at atmospheric temperature and pressure. The bulk density measurements were conducted using the water immersion method (based on Archimedes' principle) (Nkosi *et al.*, 2017). Another factor that affects acoustic impedance is porosity; however, in this study, we did not conduct porosity measurements as the rock samples are from a crystalline environment and have comparable porosity (Malehmir *et al.*, 2013; Nkosi *et al.*, 2017).

Synthetic seismogram

This section presents results of the physical property measurements (bulk density and seismic velocities) of rocks in the Bushveld Complex that make up the hanging wall and footwall of the MR and UG2. Previous studies have reported seismic velocities and densities of rocks in the Bushveld Complex (Campbell, 2011; Manzi *et al.*, 2017); therefore this study reports in detail the individual density and velocity measurements of the hanging wall and footwall in the study area. We used the information to design the seismic experiments to investigate 'near-surface' geological structures, i.e. within 150 m of the mine tunnel in which the survey was conducted. Table 1 summarizes the ultrasonic velocities and density measurements of the MR, MR hanging wall, MR footwall and UG2. While the velocity and density of feldspathic and pegmatoidal pyroxenite are from Manzi *et al.* (2019), the densities and velocities of the rocks are within a narrow range, except for the chromitite sample that is much denser than the host rocks and the water-saturated top layer of norite that has a lower velocity. The average P-wave velocity measurements of the core samples range from 3088 m/s to 6118 m/s and the average density measurements range from 2700 kg/m^3 to 4392 kg/m^3. To compute the synthetic seismograms, we used the measured densities, velocities and depths from borehole 1 (BH1; see Figs 2 and 3). The borehole has a total depth of 577.5 m from the Earth's surface and intersected the MR and UG2 at 515.14 m and 570.94 m, respectively. We used a Ricker wavelet with a dominant frequency of 130 Hz and a sampling rate of 0.25 ms to compute the seismograms for the lower 75 m of the borehole, which covered the ore zones beneath the tunnel (Fig. 3). The acoustic impedance contrast between the hanging wall and footwall of the MR suggests that the interface is associated with a strong reflection, which can be used as a proxy for MR mineralization. The UG2 has a higher acoustic impedance contrast with the host rocks; hence, a noticeable reflection at the interface (Fig. 3), which is in agreement with studies conducted by Scheiber-Enslin and Manzi (2018) and Manzi *et al.* (2020).

2D acoustic modelling and seismic reflectivity

The geology of the Maseve mine is detailed in the mine's resource estimation report (Muller and Visser, 2010). The Bushveld Complex has been well studied (Nex *et al.*, 1998; Webb *et al.*, 2004; Kinnaird, 2005; Cawthorn, 2015), and the geological structures in certain areas make it an ideal place to conduct numerical modelling to investigate the seismic response of mineralizations and other geological structures. However, the Bushveld Complex rocks (anorthosite, norite and pyroxenite) have similar physical properties (mainly seismic velocities). Acoustic impedance contrast in the Bushveld Complex is mainly controlled by noticeable differences in

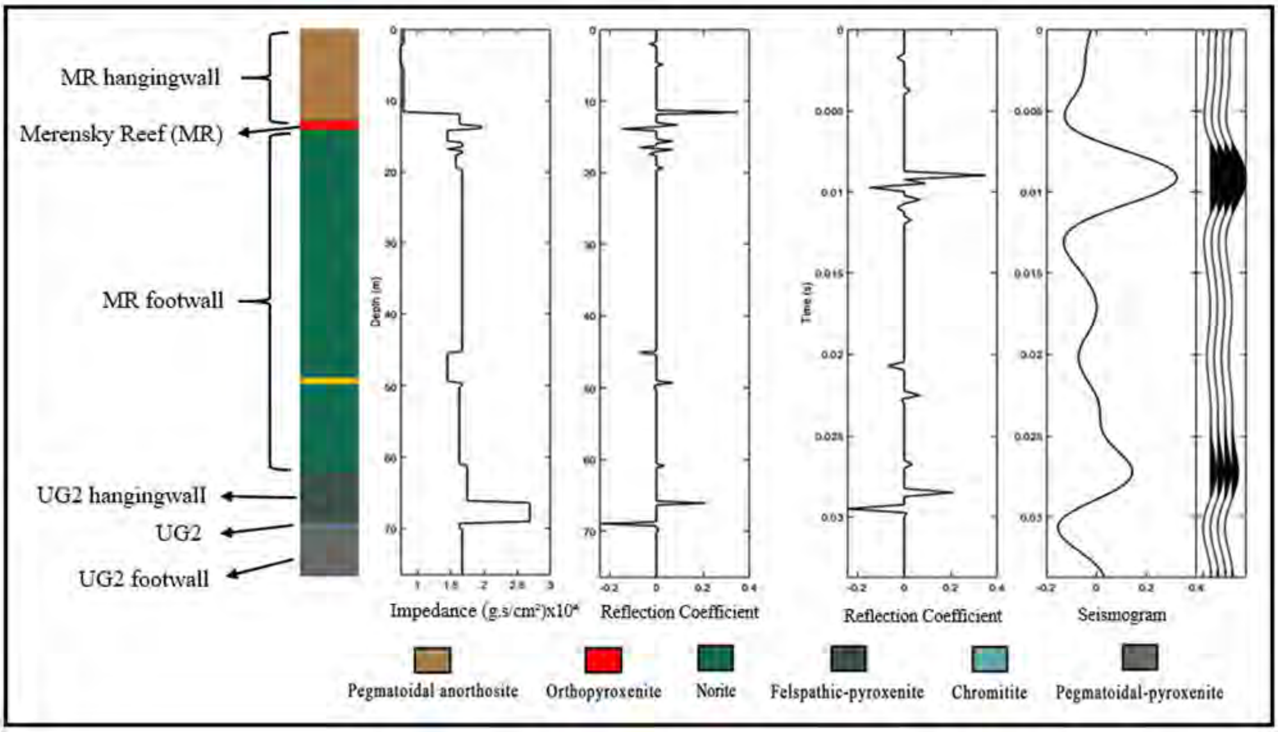

Figure 3 Stratigraphic column derived from borehole 1 (BH1) of the Maseve mine. Reflection coefficients were derived from the acoustic impedance, and synthetic seismograms were generated using the reflection coefficient and a Ricker wavelet (130 Hz). Generated reflections are associated with the two major reefs (Merensky Reef and UG2). The impedance contrast of the Merensky Reef (MR) and its hangingwall is high due to the water-saturated hangingwall and low velocities of the anorthosite rocks in the hangingwall. The acoustic impedance of the Upper Group 2 (UG2) and the surrounding rock is typically high compared to that of the MR (see Manzi et al., 2020).

the densities of the rocks, which in turn provides a strong reflective interface between the mineralization and the host rocks. The MR has a slightly higher seismic velocity than the host rock, while the UG2 has a higher density compared to the host rocks (Table 1). The focus of the study is to image the near-tunnel-floor mineralization and geological structures; therefore, the complex geology of the area is not presented in detail. The thickness and depth of the targeted mineralizations were obtained from the available surface boreholes in the study area (Figs 2 and 3). The MR (∼ 1–2 m thick) and UG2 (∼ 1–2 m thick) were intersected by surface borehole (BH1) at depths of 515 and 571 m, respectively. These horizons are faulted and folded (asymmetrical synclinal fold with a NW–SE trending fold plane), resulting in the MR and the UG2 outcropping on the west-south-west (WSW) side of the seismic line (Fig. 2b). The acquired seismic profiles (mainly P5 and P6) transverse a major dolerite dyke and the fault zone (here termed Rapetsoa Fault Zone (RFZ)) that crosscut the MR and UG2 (Fig. 2). Seismic modelling only considers the rocks beneath the tunnel. The rock between the tunnel and the Earth's surface is considered to be free space. The elevation of the inclined tunnel is used as the datum for reflection seismic processing. Therefore, the complex characteristics of the full 3D wavefield are not analysed in this paper.

The modelling was conducted using Tesseral Pro software. Figure 4 shows the geological model built (Ahmadi *et al.*, 2016; Singh *et al.*, 2020) from borehole data and mine information (Fig. 2). The 2D acoustic finite-difference modelling was conducted to assist with the planning of the in-mine seismic surveys, to investigate the source of seismic reflectivity in the data and to constrain seismic interpretation. The structures identified from the mine plan (Fig. 2b) were used to build a geological model (Fig. 4) of the rock mass beneath the incline tunnel. The finite-difference model was 360 m (horizontal extent) × 140 m (depth), with a grid cell of 1 m in both vertical and horizontal directions. A synthetic 2D seismic survey was designed to generate 2D synthetic shot gathers using acoustic modelling (Fig. 5a) of the first few hundreds of metres for two shot examples (Fig. 5a, d: first and centre shot). The main objective of numerical modelling was to simulate the

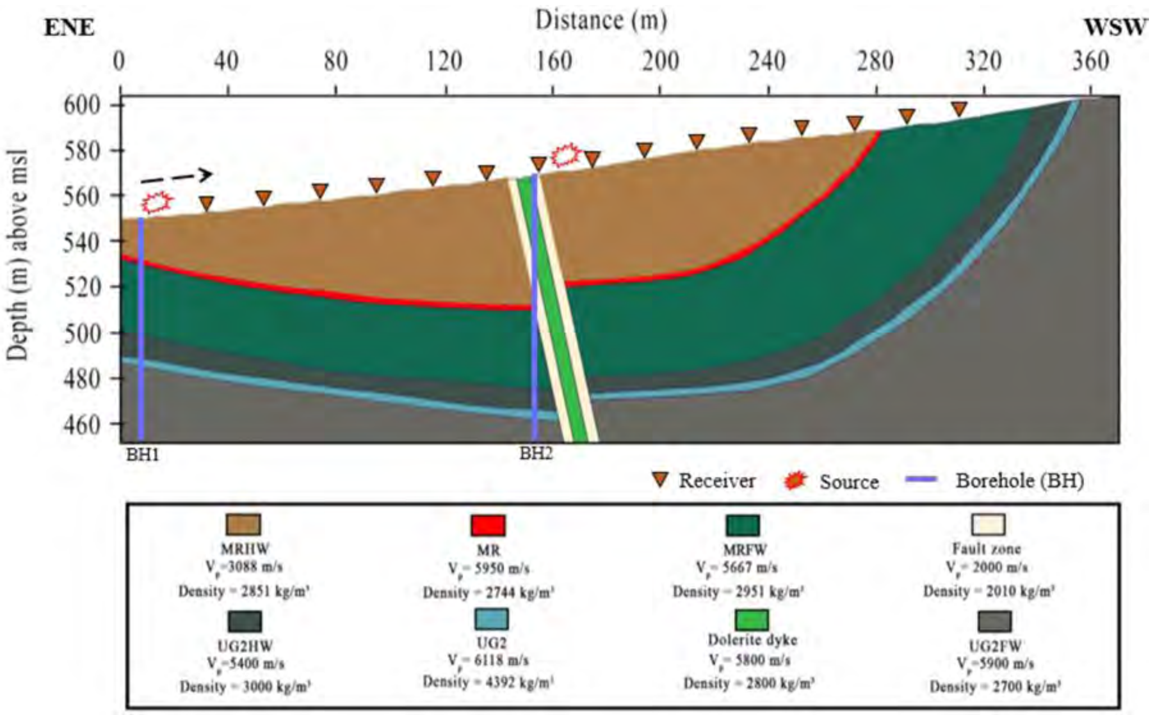

Figure 4 Geological/finite-difference model at the Maseve mine. The model shows the two-target mineralizations (MR and UG2) and geological structures (fault and dyke). The velocity and density of the rocks are noted. The receiver (brown) and shot (red) positions are shown, together with the acquisition direction (ENE–WSW) over an incline. The boreholes used for the model as shown (purple) MRHW: Merensky Reef hangingwall (Weathered Anorthosite; MR: Merensky Reef (orthopyroxenite); MRFW: Merensky footwall (norite); UG2HW: Upper Group 2 hangingwall (feldspathic-pyroxenite); UG2: Upper Group 2 (chromitite); UG2FW: Upper Group 2 footwall (pegmatoidal pyroxenite); msl: mean sea level; BH: Borehole.

seismic response of the targets (MR and UG2) and geological structures (faults and dykes). The synthetic data were generated using the acquisition parameters very close to the ones used for real seismic surveys, except that the model used a single profile (360 m long), while the real survey data had three merged profiles (115 m long). The synthetic seismic modelling had a maximum two-way travel time of 500 ms. A Ricker wavelet of 130 Hz was used for modelling, with a sampling rate of 0.25 ms. The measured average velocities and densities in Table 1 were used in the model. The shot gathers of the synthetic data (Fig. 5a, d) were then compared with those of the acquired data (Fig. 5b, e). The comparison between the synthetic and real data is discussed later.

SEISMIC DATA ACQUISITION

Prior to the seismic surveys, a preparatory mine site visit was made for a few days to check the tunnel conditions and decide on the location of shots and receivers. Information from the ground-penetrating radar and electrical resistivity tomography surveys conducted in the tunnel a few weeks prior assisted in designing our surveys to better delineate the targets (depth and lateral extent of the deposits, as well as geological structures).

In November 2020, seven 2D in-mine seismic profiles were acquired with a total length of about 0.6 km over known orebodies (Fig. 2a, b). The final set-up included: one profile in the development tunnel (P1); two around Michelle's pillar (P2 and P4); one profile in a crosscut (P3); and three profiles (P5, P6 and P7) in the incline tunnel (Fig. 2b). The three incline tunnel profiles, namely P5 (115 m long), P6 (115 m long) and P7 (115 m long), were collected in segments that are collinear to each other, orientated in an east-north-east (ENE) to west-south-west (WSW) direction (Fig. 2b). P5, P6 and P7 profiles are the focus of this paper and were designed to cover the area along the incline tunnel. P1 was collected perpendicular to P5–P7, with the goal of imaging the folded Merensky Reef (MR) and Upper Group-2 (UG2) located at about 20–70 m depths below the incline tunnel (Fig. 2b). P2 and P4 were experimental lines collected around the pillar of interest. The idea being to test the response of the 4.5 Hz geophone (1C)

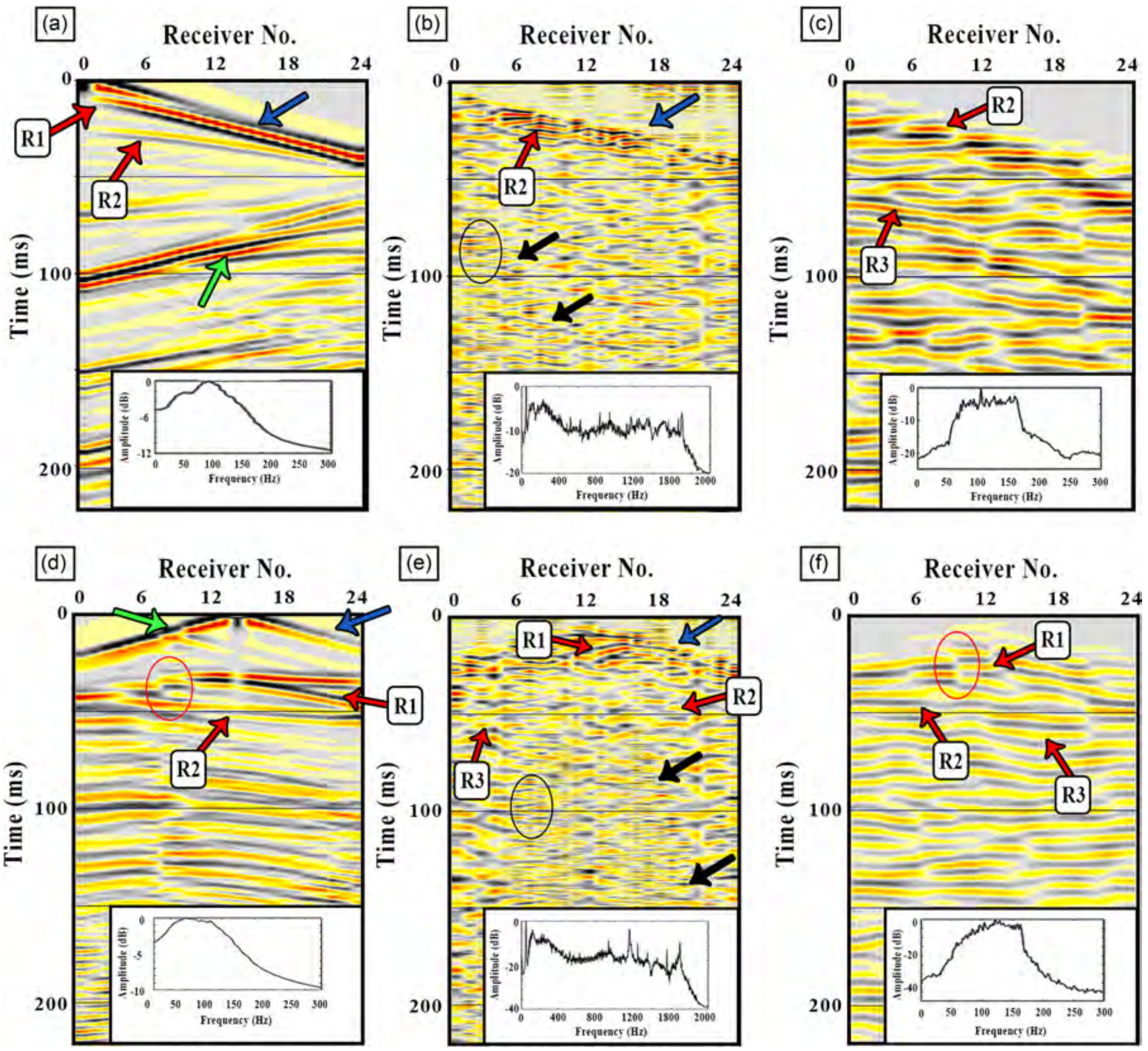

Figure 5 Shot gathers examples from P5 (see Fig. 2b) first shot and middle shot, with their frequency spectra. Shot gathers highlight clear reflections marked by red arrows. (a and d) Synthetic shot gathers modelled from the geological model; (b and d) raw shot gathers; (c and d) processed shot gathers. (a) Clear reflection (R1: 10 ms, R2: 27 ms) from the UG2 and diffractions (green) due to the dyke and fault zone. (b) Raw shot gathers with reflections overshadowed by high frequencies (black circle), airwaves are indicated by black arrows and first breaks are indicated by blue arrows. The frequency spectrum has frequency ranges of 0–1800 Hz as a result of the sampling rate of 0.25 ms. (c) The processed shot gathers showing clear reflections, with one of the reflections not easily identified on the synthetic gather and the raw shot gather. (d) R1 (29 ms) originates from the Merensky Reef and R2 (45 ms) originates from the UG2. The modelled dyke and fault zone disturb R2 (red circle). (e) R1 at 20 ms, R2 at 45 ms and R3 at 55 m are observed on the raw shot gather. (f) The three reflections observed (R1, R2 and R3) are enhanced after pre-stack filtering.

attached to the land streamer along the pillar; the shots were generated horizontally along the pillar using a 5 kg sledgehammer. P2 was conducted at the base of the pillar, whereas P4 had receivers supported on the sidewall. P3 was collected with planted cabled sensors (1C; 4.5 Hz and 14.0 Hz), while the other 5 segments were collected using a 4.5 Hz seismic land streamer. The profiles collected with the land streamer had a receiver spacing of 5 m, providing a total spread of 115 m.

A day was spent testing different sources (24 kg accelerated weight drop (AWD) and a 5 kg sledgehammer), and one-component sensors (cabled 100 Hz horizontal, 14.0 Hz vertical and 4.5 Hz land streamer). We also drilled holes along the tunnel floor to plant the cabled geophones and increase the coupling; however, this process proved time consuming as it took about half a day to plant geophones along one profile. This encouraged the use of the land streamer as re-

Table 2 In-mine seismic acquisition parameters at the Maseve mine

Line	P1	P2	P3	P4	P5	P6	P7
Number of receivers	24	24	24	15	24	24	24
Profile length	115 m	26 m	26 m	28 m	115 m	115 m	115 m
Direction	SW-NE	On Pillar	SE-NW	On Pillar	SE-NW	SE-NW	SE-NW
Recording length	500 ms	300 ms	150 ms	150 ms	500 ms	500 ms	500 ms
Sample interval				0.25 ms			
Vertical stacks				4			
Source spacing	5 m	2 m	5 m	5 m	5 m	5 m	5 m
Source type				5 kg Sledgehammer			
Receiver spacing	5 m	2 m	1 m	2 m	5 m	5 m	5m
Geophone frequency	4.5 Hz	4.5 Hz	4.5&14 Hz	4.5 Hz	4.5 Hz	4.5 Hz	4.5 Hz

ceivers in all seismic profiles because it was quick and provided better coupling with the tunnel surface. Shots were generated with both sources to check the signal-to-noise ratio (S/N) of the data and decide on the most suitable seismic source for the surveys. Although the 24 kg AWD provided a better signal, it was not safe to use due to the conditions of the tunnel sidewall and hanging wall (e.g., loose fragments of the hanging wall). A 5 kg sledgehammer was used as a seismic source instead, with a shot spacing of 5 m. To improve S/N, four shot records were vertically stacked at every shot position. A range of sampling rate parameters were also tested to ensure that guided waves and other mine-related noise, for example, were not contaminating the records. Following the analysis of the shot gathers at various sampling rates, a sampling rate of 0.25 ms was chosen as it provided better results with respect to the limitations of the resonant and spurious frequencies of sensors used in the survey. The survey parameters are detailed in Table 2. One of the advantages of the sledgehammer is its light weight and low cost when compared to other seismic sources. The mine is also prone to flammable gases (e.g., methane), so we carefully ensured that the hammer's impact on a base plate did not generate any sparks that could lead to explosions inside the tunnel.

In addition to the seismic surveys conducted along mine tunnels, five active seismic profiles were collected on the surface, simultaneously with passive seismic surveys using three broadband seismometers and remote acquisition units. The surface experiments were an attempt to test the feasibility of conducting tunnel-surface experiments. In this paper, only the results obtained from active in-mine seismic profiles (P5–P7) are presented.

SEISMIC DATA PROCESSING

Figure 5 shows the comparisons between the synthetic (Fig. 5a, d), raw (Fig. 5b, e) and processed (Fig. 5c, f) shot records. The raw seismic data exhibit a high signal-to-noise ratio (Fig. 5b). However, a few traces exhibit some noise due to airwaves (Fig. 5b, e: black arrows) or poor coupling of geophones on the muddy areas along the tunnel. Table 3 provides the workflow followed in the processing of the data, subdivided into pre-conditioning and processing steps. The main aim of the processing workflow was to preserve primary reflections and remove source-generated and ambient noise (e.g., water pipes, moving vehicles and blasting from neighbouring mines) to improve data quality.

The first step was to fix the coordinates and merge the seismic profiles (P5–P7) before processing because the headers had receiver and shot positions as coordinates. Coordinates from the mine pegs were used to determine the shot and receiver locations, using linear and spline interpolation functions. The second step was to fix the geometry. From the coordinates created, a shell-processing-support file was set up for the geometry. The geometry was then merged with the seismic data. For the seismic profile, we assigned common depth points with a spacing of 2.5 m, followed by removing noisy traces, mainly caused by poor ground coupling.

The data are of fair quality, with clear P-wave first breaks in the raw shot gathers (indicated by blue arrows in Fig. 5b, e). Some reflections (R1 and R2) observed in the raw shot gathers (red arrows in Fig. 5b, e) matched reflections in the synthetic shot gathers (Fig. 5a, d). R1 is interpreted to originate from Merensky Reef (MR) and is not clearly defined in the first shot synthetic gather (Fig. 5a); it is masked by first breaks as

Table 3 Processing steps applied to the Maseve mine, South Africa, in-mine seismic dataset.

Pre-conditioning		Parameters
Create coordinates	√	Linear and spline interpolation
Create SPS files	√	Merge the coordinates of P5–P7
Processing		**Parameters**
Data input + reformat	√	From SEGD to SEGY
Geometry assignment + CDP bin	√	Sources and receivers assigned to each trace + CDP size 2.5 m
Trace editing	√	Kill noisy traces
First break picking	√	Automatic, manual picking
Floating datum statics correction	√	Fixed datum elevation: 602 m (below surface). Replacement velocity: 4000 m/s
Refraction static correction	√	Two-layer model based on the first break picking. Root-mean-square error 1.45–2 ms
Trace muting	√	Top mute using first breaks
Bandpass filtering	√	50–60–160–170 Hz
Automatic gain control	√	Window: 50 ms
Balance	√	500 ms
F–k filtering	√	Surgical muting, dip = 1.2 m/s per trace
Velocity analysis	√	Constant velocity stack
NMO corrections	√	5500–6500 m/s, stretch mute: 70%
Residual statics	√	Repeat NMO corrections twice
DMO	√	Kirchhoff common offset
Stack	√	Normal
Bandpass filtering	√	80–90–150–160 Hz
Post-stack time migration	√	2D Kirchhoff
Time-to-depth conversion	√	Constant velocity: 5500 m/s

the reflecting MR is close to the tunnel floor on the east of the model (Fig. 4). R2, on the other hand, is well defined at 25 ms with a weak reflection compared to R1. Possible reflected refractions from the fault (RFZ) zone and dyke are also observed in the synthetic data (Fig. 5a, d: green arrows). R1 (30 ms) and R2 (45 ms) are clearly observed on the centre synthetic shot gather and the raw shot gather. An additional reflection (R3: 55 ms) is also observed on the raw shot gather.

As one of the most important steps in the pre-stack data processing stage, the P-wave first breaks were picked using an automatic method (envelope threshold) combined with manual picking. The picks were used to compute the refraction statics. A total of 1778 picks were used over 72 receivers and 76 shots across the three profiles. The picks were inverted for the two-layer-based refraction model, with four iterations and an RMS error of 1.45–2.00 ms. Figure 6 shows a refraction tomogram (Fig. 6a) and a ray path model with low ray coverages (white arrows in Fig. 6b). The low ray coverage is as a result of merging the three segments into one profile (Fig. 6b). The refraction tomogram (Fig. 6a) was produced to aid with the interpretation of the data for about 20—50 m depth below the incline tunnel. The maximum elevation along the profile is 602 m (above mean sea level) and was chosen as a matching datum elevation together with a replacement velocity of 4000 m/s for floating datum statics. The next step was to apply refraction, residual (using only short wavelength component) and elevation statics correction to enhance the continuity of the reflections and improve the quality of the final seismic section.

Figure 5(b and c) shows the raw shot gathers and a processed shot gather (trace editing, refraction static, bandpass filter and top mute), respectively. The raw data are contaminated by some noise that could be related to ambient sources (i.e., ventilation and water pumps; Fig. 5b). The frequency of the acquired data ranges from 50 Hz to 1800 Hz. The higher frequencies (> 250 Hz) are most likely related to spurious frequencies of the 4.5 Hz geophones used. A bandpass filter (50–170 Hz) was applied to constrain the data within the source energy frequencies. The amplitudes of the first breaks (Fig. 5b, e) are high, affecting the near-surface reflections. To remedy this, we applied top mutes on the first breaks with care in order to not mute some shallow reflections. The processing steps applied illuminated reflections (R2 and R3) in the shot records (Fig. 5f). Although the above-mentioned processing steps enhanced some of the reflections, some noise (probably related to airwaves) were still present in some shot records (Fig. 5b, e: black arrows) and overshadowed the reflections (e.g., R2). To eliminate these, an *f–k* filter was applied to the data. The *f–k*

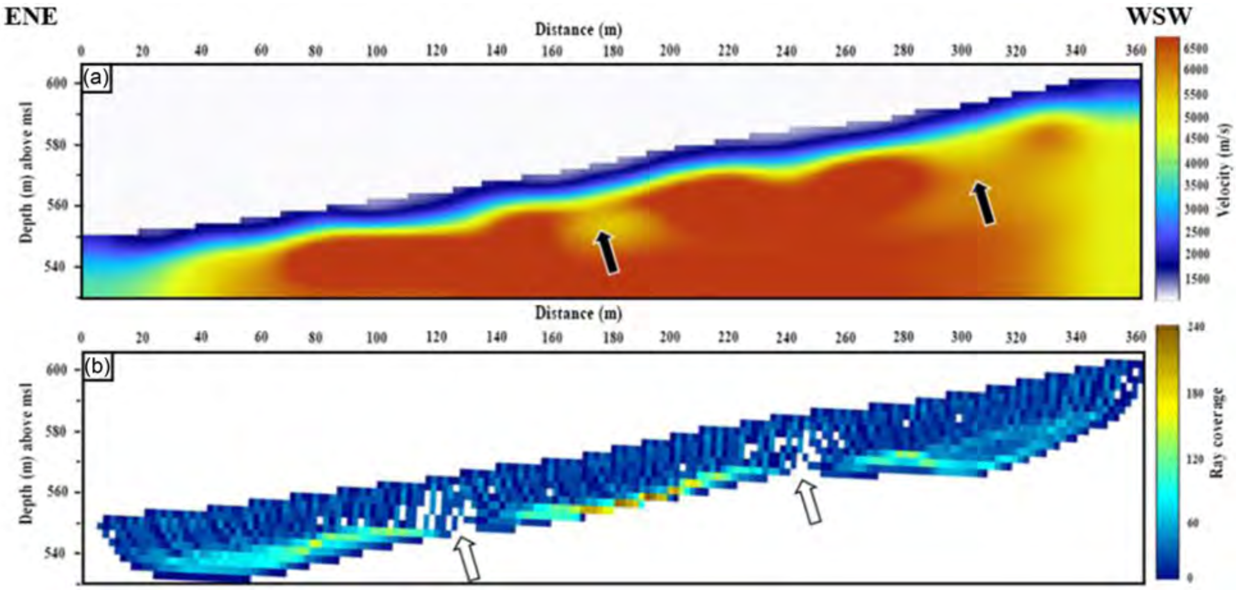

Figure 6 (a) Near-surface P-wave velocity model showing the upper 70 m of the incline tunnel. Black arrows indicated lower velocity zones, which are associated with geological structures intercepted alone the line. (b) Ray path model showing ray coverage of the velocity model. The white arrows indicate an area of low fold and where the three segments were merged. msl: mean sea level.

filter targeted events with velocities below 4100 m/s, in order to enhance the targeted events that have apparent velocities between 5700 m/s and 6400 m/s.

Velocity analysis was conducted using a series of constant velocity stacks generated to select the velocity that showed highest coherency of the reflections. Prior to stacking, Normal Moveout (NMO) corrections were applied to account for the hyperbolic curvature of the reflections and stacked using the NMO velocities of ∼5500 m/s. We calculated and applied residual statics using the updated NMO-corrected gathers, resulting in continuous reflections on the stacked sections. Dip moveout was applied to stack the dipping reflections simultaneously. A second bandpass filter (80–160 Hz) was applied to remove low frequencies that were still present in the data. Figure 7 shows the final unmigrated time (Fig. 7a) and depth-converted (Fig. 7b) stacked sections, respectively. A Kirchhoff migration algorithm was applied using a constant velocity of 5500 m/s, which was decided based on the P-wave velocity distribution on the data and published velocities (Manzi *et al*., 2020). Finally, following a series of tests on velocity fields that provided the best migrated sections, 5500 m/s was used for time-to-depth conversion. Together with mine-modelled structures and surface boreholes, the final depth-converted seismic section was imported into the 3D visualization software package for final geological interpretation and comparison with other geological datasets.

RESULTS AND INTERPRETATION

Seismic processing and interpretation were mainly constrained to the top 100 ms (approximately 275 m depth below the tunnel floor) because the main targets (Merensky Reef (MR) and Upper Group-2 (UG2)) for future mining and exploration at Maseve mine fall within this window (Figs 5–9). The first step was to make a comparison of the synthetic, raw and processed shot gathers (Fig. 5). Clear first arrivals (blue arrows) are seen in the 2D acoustic finite-difference modelled shot record, raw short record and processed shot record (Fig. 5). The airwaves (indicated by black arrows) observed in the raw shot gather (Fig. 5b, e) has been attenuated (Fig. 5c, f) by applying filters (mainly *f–k*) and dip moveout, resulting in a dataset with an improved signal-to-noise ratio. The main reflections observed in the seismic data interpreted to have originated from the mineralizations are MR (R1) at 20 ms, UG2 (R2) at 45 ms and a possibly unknown mineralization (R3) at 55 ms (Fig. 5e, f). MR is shallower toward the ENE on the model. Therefore, the strong reflection (R1) originates from MR and is coupled with the first breaks, while the weak reflection (R2) originates from the UG2. R3 is not modelled in the synthetic data (Figs 4 and 5a) as it was not known, but is visible in Fig. 5(b, e). R3 is interpreted to originate from the UG1, which is a chromitite mineralization that is well known in other mines within the Bushveld Complex. UG1 is, however, not intersected by drilling at the Maseve mine as the drilling

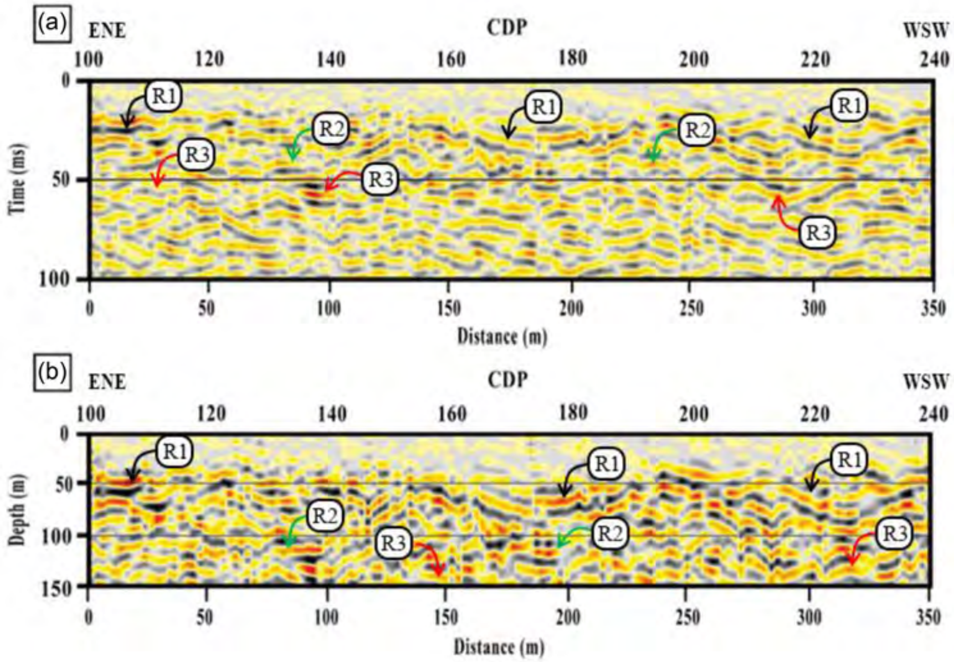

Figure 7 Comparison of unmigrated (time) stack (a) and depth stack (b) sections of incline tunnel profile (P5-P7). Clear reflections (shown with black arrows) are more prominent at the centre of the sections. Time stack section shows strong reflections at 20 ms (black), which correspond to 55 m depth in (b), while the dipping reflections (green arrows) at about 45 ms correspond to 124 m on the depth section. Third reflection (red arrows) is shown at 55 ms and is expected at a depth of 151 m.

only targeted MR and UG2 (Fig. 2c). Our interpretation of this seismic reflection (and others observed in the data) is not conclusive as these events could be associated with complicated wavefield characteristics caused by side tunnels connected to the main exploration tunnel, fracture systems, the rock mass around the tunnel and mine infrastructure (or developments). In addition, there is no borehole information to further constrain our seismic interpretation below the UG2 horizon.

P-wave velocities obtained from the first break tomograms show a good definition of two zones in our area: fractured top layer (~ 10 m thick) exhibiting velocities between 1000 m/s and 4000 m/s and the hard rock exhibiting variable thicknesses (10–40 m) with velocities between 4000 m/s and 6500 m/s. These velocities show a good match with the known velocities from (norite and pyroxenite; Manzi *et al.*, 2020) and borehole stratigraphy and complement P-wave reflectivity observed on the final stacked sections (Figs 7 and 8). Based on the refraction tomograms, existing borehole, geological models (Fig. 2) and tunnel observations (i.e. outcropping MR and UG2 ~ 110 m and ~180 m WSW of the centre of the merged profile, respectively), the stratigraphy generally dips at ~ 10° towards WSW and dips 60° ENE due to folding and faulting (Fig. 4).

The unmigrated time (Fig. 7a) and depth-converted (Fig. 7b) stacked seismic sections suggest that the reflections are well delineated in our study. The strong reflectivity observed at 20 ms (black arrows) on the time stack section corresponds to 55 m depth on the depth stack section. The reflections (Fig. 7a, b: marked with arrows) are more prominent at the centre of the seismic section. The shallow reflection occurring at about 55 m is attributed to the MR, as discussed previously. The far ends of each seismic profile (P5–P7) show reflections that may be related to processing artifacts, while the middle section (CDP: 160-180; 200-230) shows more coherent reflections due to the high fold-of-coverage (Fig. 8a). Overlaying the borehole log and 1D synthetic data onto the depth-converted migrated section (Fig. 8b) confirms that the strong reflections (R1) at about 55 m depth can be attributed to the MR, while the reflection at ~124 m (R2) is associated with the UG2. The reflector (R2) dips towards west-south-west and loses coherency at CDP 130. The area is structurally complex as interpreted in Fig. 9. MR and UG2 are affected by folding (e.g., a synclinal structure is observed between CDP 160 and 200) and crosscut by dykes (dotted green and red lines) and faults (indicated by pink lines) different orientations (Fig. 9). In addition to faults and dykes, the seismic section

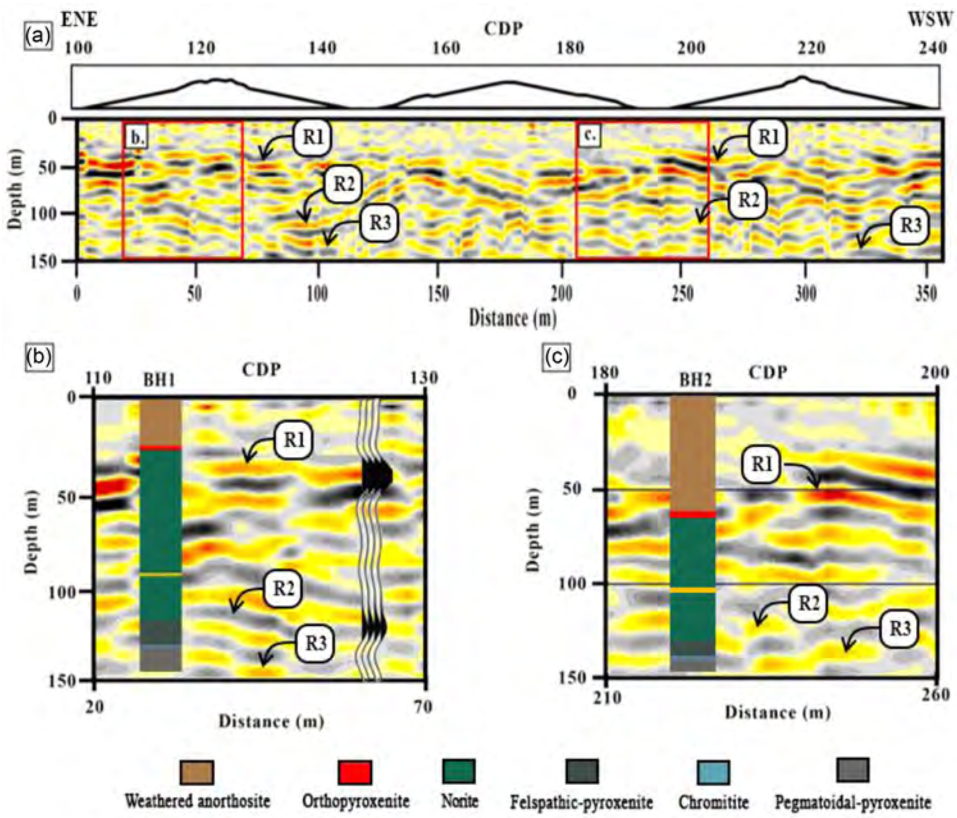

Figure 8 Depth-converted migrated seismic section; red outline shows the focus area where boreholes 1 and 2 are overlaid. (a) Migrated stack section of profiles P5–P7 with (b) Borehole 1 and synthetic seismogram overlaid (BH1; see Fig. 2). Reflection R1 correlates with the Merensky Reef (MR) and reflection R2 correlates with UG2. The arrows mark the identified reflector detailed in the text. (c) Borehole 2 correlated with the migrated section.

exhibits a vertical low-seismic amplitude and chaotic feature along the MR and UG2 horizons, which is interpreted to be associated with the IRUP (Fig. 9; IRUP: dotted brown). Similar to faults and dykes, this feature appears to disrupt both the MR and UG2 (Figs 8 and 9), and it occurs in the vicinity of the fault zone. In particular, the seismic sections show the delineation of F4 that coincides with the RFZ interpreted in the mine geological model and described by several authors. Identification of these structures by the seismic data is important as this information can be used to enhance the existing geological model.

DISCUSSION

To better understand the quality of the data and interpret geological structures, it is important to first address the seismic resolution limit of the data. The quality of the acquired data is dependent on many factors such as the impedance contrast between the target and the host rock, the geometry (e.g., shape) and thickness of the target, survey design, instruments used, tunnel conditions and noise level. The seismic resolution limit is controlled by the dominant wavelength (λ) in the data, seismic velocity of the targets and the dominant frequency of the data. Theoretically, the top and bottom of geological features cannot be resolved if its thickness is less than a quarter of the dominant seismic wavelength (i.e., Rayleigh criteria of the vertical resolution limit). However, smaller features down to λ/32 can still be detected, although the detection will depend on the diffractions, not solely on the seismic amplitude (Manzi *et al*., 2014; Malehmir *et al*., 2018).

The dominant seismic frequency of the reflected signal at the Merensky Reef (MR), for example, is ∼ 130 Hz. By taking into account the stacking velocity (∼ 5500 m/s) used in our processing workflow, the dominant seismic wavelength (λ) is ∼ 42 m. This gives us the vertical resolution limit of ∼ 10.5 m, which is the minimum thickness needed to resolve the top and bottom of a layer. However, the MR (∼1–2 m thick) and Upper Group-2 (UG2) (1–2 m) are too thin to be resolved. Hence,

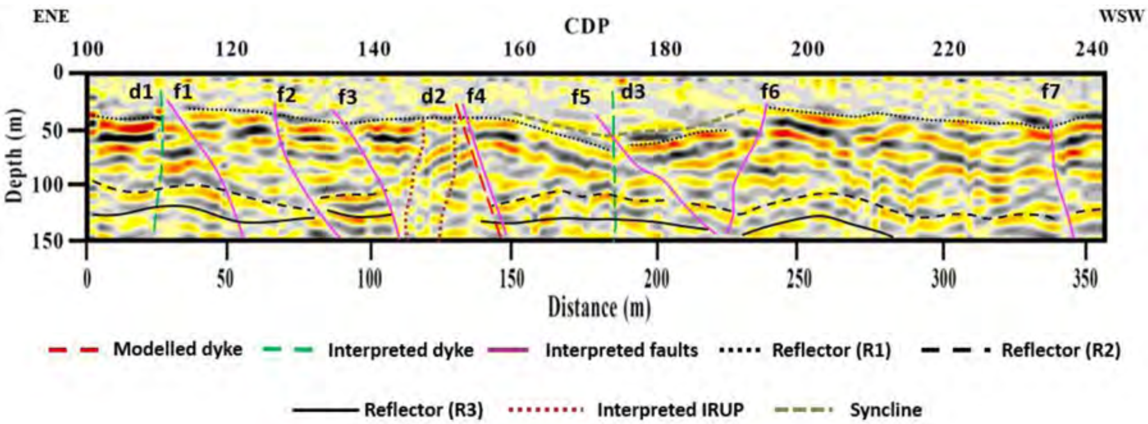

Figure 9 Interpreted migrated section (in depth) of seismic profiles P5-P7. The Merensky Reef (MR) reflector is marked with dotted lines (R1), and UG2 is marked with a dashed line (R2). Third reflection marked with a solid line is linked with the UG1. The reflections are not continuous at areas of the low fold. The reflector is displaced by a combination of normal and reverse faults (purple solid lines). Dashed lines (green) are the interpreted dykes, while the red dashed line is the position of the dyke and fault zone (see Fig. 4). R1 is bent (grey dashed line) between CDP 160 and 190, which is interpreted as a fold, while the brown dotted lines represent an interpreted Iron Rich Ultramafic Pegmatite (IRUP).

the structure of such thin mineralized reefs can be mapped indirectly using the seismic reflective interfaces between hanging wall and footwall rocks as proxies (Manzi *et al.*, 2020). For example, the MR is associated with the reflections arising from the contact between pegmatoidal anorthosite hanging wall and norite footwall. This implies that the MR is not imaged directly because of the low acoustic impedance contrast between the reef (ρ = 2744 kg/m^3; v = 5950 m/s) and the surrounding rocks (norite: ρ = 2951 kg/m^3; v = 5667 m/s; anorthosite: ρ = 2947 kg/m^3; v = 5530 m/s). Due to weathering of the hanging wall, the MR is imaged indirectly due to the high acoustic impedance between the hanging wall (weathered anorthosite: ρ = 2851 kg/m^3; v = 3088 m/s) and the footwall (norite: ρ = 2951 kg/m^3; v = 5667 m/s). The UG2, on the other hand, is directly imaged because of the significant acoustic impedance contrast (mainly controlled by a high density associated with chromitite) between the UG2 (ρ = 4392 kg/m^3; v = 6118 m/s) and the footwall (ρ = 2700 kg/m^3; v = 5900 m/s) (R2 in Fig. 9).

The lateral extent of the geological feature cannot be discerned if it is narrower than the diameter of the first Fresnel zone (i.e., horizontal resolution limit) (Yilmaz *et al.*, 2001), which governs the horizontal positional accuracy of structural information that can be obtained from seismic data. It is worth noting that this horizontal resolution limit assumes that the seismic data are unmigrated. After migration, as is the case with our seismic data, this limit can be enhanced to approximately half the dominant wavelength, i.e. 21 m. Theoretically, this implies that two or more geological features within 21 m of each other will not be resolved as separate features. However, smaller features could still be detected, but this will depend on signal-to-noise ratio of the data, the velocity field and the migration algorithm used for migration (Manzi *et al.*, 2014; Westgate *et al.*, 2020).

A general assessment of the in-mine seismic results reveals that the data, although acquired in a noisy mine environment, are of high quality from which structural interpretation can be drawn. The strong, seismic reflections associated with the MR (~ 20–25 ms in Fig. 7a) and UG2 (~ 45–70 ms in Fig. 7a), although disrupted by faults and folds, are prominent and reliable indicators of mineralizations throughout the seismic profile (see, Figs 7, 8 and 9). The depth position, shape and dips of the interpreted MR and UG2 have been constrained with the geological information. Figure 10(a-d) shows the 3D visualization of the integrated borehole data, seismic data, mine modelled structures (MR, UG2, fault and dyke), seismically defined structures (faults and dykes). Generally, the seismic data has a good tie (within 3 m discrepancy) with the borehole information (Fig. 10a). For example, BH1 intersected the MR and UG2 at a depth of 68 m and 120 m below the tunnel respectively, which correspond to the depth position of reflections R1 and R2 on the migrated section (Fig. 10a). The seismic reflections R1 and R2 show a good correlation with the mine MR and UG2 orebodies, respectively (Fig. 10b). Surface boreholes (e.g., BH2) on the western side of the seismic line (Fig. 2b) intersected the MR at an average depth of 510 m and UG2 at an average depth of 555 m below surface, while the boreholes on the eastern side of the seismic profile

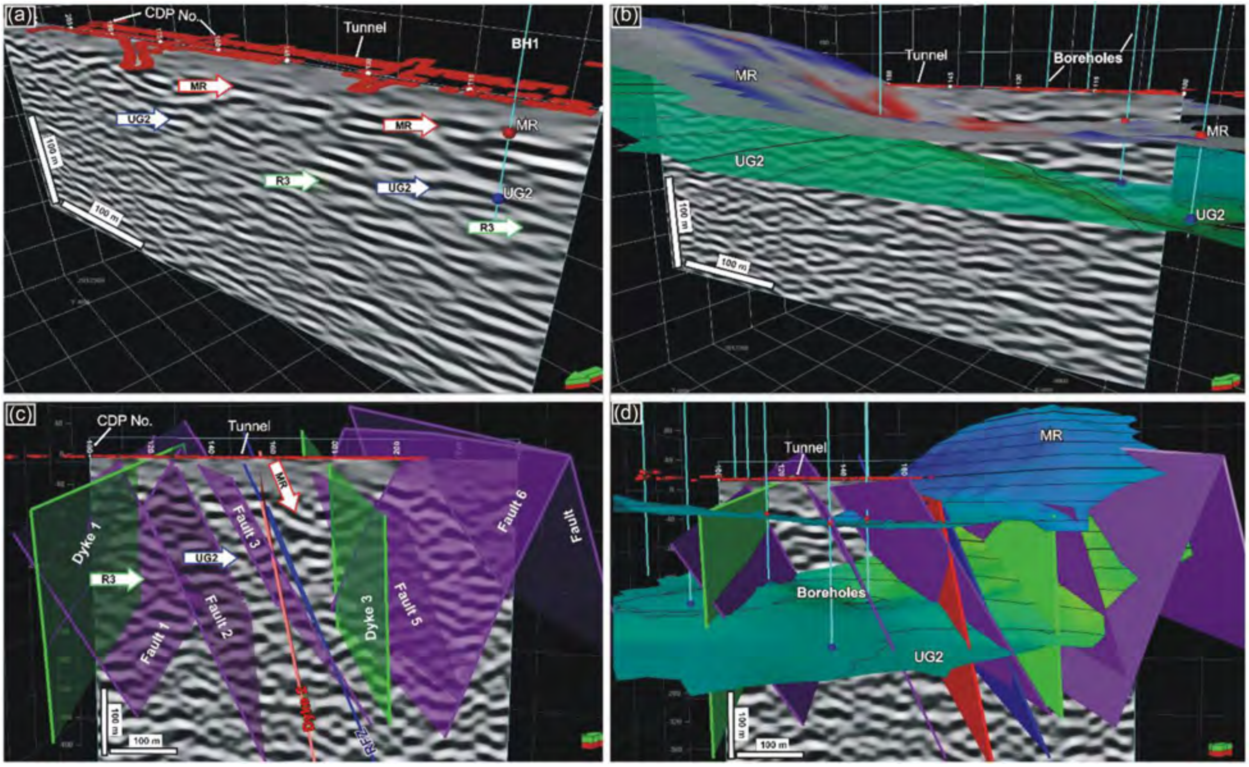

Figure 10 Depth-converted migrated seismic section plotted in 3D view together with the mine tunnel around 550 m below Earth's surface. (a) Correlation between the seismic section and borehole intersections of the MR (red) and UG2 (blue). (b) Correlation between the seismic reflections (R1 and R2) with MR (grey, red, and blue surface) and UG2 (green contoured surface) mine orebodies. (c) Seismic section together with interpreted and mine modelled faults and dykes overlaid. The Rapetsoa Fault Zone (RFZ) is shown in blue, crosscutting the mineralizations (MR, UG2 and R3). (d) Seismic section with boreholes, Merensky Reef (MR) and UG2 mine orebodies, structural interpretations (faults and dykes). The green arrow is pointing to the south.

intersected the MR and UG2 at 515 m and 570 m, respectively, indicating that these two target mineralizations are closer to each other on the western side (Fig. 10b). The boreholes were targeting the MR and UG2, thus did not extend to depths below UG2. Therefore, these boreholes were not used to constrain the source of R3 reflectivity in the seismic data. The minor discrepancies (0–3 m) in depth positions between seismics, orebodies and borehole data might be due to three reasons: (1) the boreholes were projected onto the seismic profile as they were not drilled directly along the seismic line, resulting in the interpreted reflection on the seismic profile having an apparent dip compared to the borehole data, therefore we expect a mismatch of the on a seismic line and the geological model (Fig. 4); (2) the velocity model used to depth convert the seismic sections may be in error; and (3) the mine orebody models are poorly constrained in areas that are not covered by the borehole information (western portion of the study area).

In terms of structural interpretation, our results confirm the existence of previously known faults and dykes (e.g., RFZ and dyke 2 in Figs. 4 and 10c) and further constrain their interpretation. F4 may represent one of the reactivated subordinate faults (e.g. RFZ) associated with the major Rustenburg fault, which has been studied by several authors (e.g., Scheiber-Enslin and Manzi, 2018; Basson, 2019) and confirmed through underground and surface mapping and drilling. Along the fault zone, we have also interpreted a dyke (D2) that corresponds to the one found in the mine model (Fig. 4). Therefore, our results suggest that the RFZ was active (or re-activated) and provided planes of weakness along which dyke 2 intruded. Furthermore, this work has identified more faults (e.g., f1–f7 in Figs 9 and 10c, d) and dykes (dyke 1 and dyke 3 in Fig. 10c, d) that were not incorporated in the existing mine geological model. The majority of the faults in the area are dipping at 60–90° WSW. The faults (Fig. 9; f1, f4, f5 and f7) are mainly reverse faults with a WSW upthrow, displacing the MR and UG2 horizons. F2 and f3 are normal faults dipping WSW, while f6 dips ENE (Fig. 10c).

In general, the geometry of R1 and R2 corresponds with the geometry of the mine MR and UG2 orebodies. Good correlation between seismics and mine orebodies is mainly observed from the centre (common depth point (CDP) no. 160) to the eastern end (CDP no. 100) of the profile (Fig. 10b, d). However, the seismic data suggest that these two horizons (R1 and R2) are faulted towards the far western end of the profile (CDP no. 160–240) with the downthrow in the west. This suggests that MR and UG2 are continuous on the western side of the outcrop position, which contradicts the geometry shown in the mine orebodies (Figs 2c and 10b). If our interpretation is correct, the continuity of these horizons beyond the outcrop position will need to be incorporated in the current mine model to enhance the resource evaluation. The seismic results suggest that faults and dykes crosscut and displace (in the case of faults) the MR, UG2 and R3 horizons, which constrains their timing of activity (i.e., they were active after the reefs depositions). The delineation of these structures is important for future mine planning at Maseve mine as these indicate areas that may not be mineable because of the loss of ground. Although these faults are detected on the seismic section, their throws cannot be determined with confidence as their displacements (throws) are below the seismic resolution limit of the data. In addition to this, the seismic data provide information on a potential chromitite-rich horizon (reflection R3 in Fig. 9) tens of metres in the footwall of the UG2 horizon, which is interpreted as the UG1.

In the future, we plan to overlap (at least by 50% of each profile length) the profiles to avoid obtaining low folds at the end of each profile. In the new data, other processing approaches (such as pre-stack depth and diffraction imaging) will be tested to further improve the imaging of the structures in this area and further investigate the sources of other reflections (including R3). While a longer single profile would have provided better results and allowed deeper imaging, the study was constrained by the available recording system we have (48 channel recording system) and the limited budget to hire a suitable seismic system. In addition to this study, other seismic profiles are being processed and the results will be integrated with the GPR data collected along the same profiles to constrain the geological interpretation.

Given the cost-effective nature of the instruments used and the limitation posed by mine infrastructure to properly design in-mine seismic surveys, the results demonstrate that in-mine seismic surveys can be an asset for mineral exploration and mining. Furthermore, these experimental surveys are considered to be cost-effective as the approach was approximately > 60% cheaper than if the survey was acquired by commercial contractors on surface (assuming that there would be no infrastructure limitations, environmental and permitting issues) using more expensive and heavier geophysical equipment (such as vibroseis trucks and 100s of receivers on surface).

CONCLUSIONS

In-mine seismic experiments were conducted at Maseve mine to image the host rocks, geological structures and the platinum deposits. The surveys involved careful planning through mine visits and using mine geological models and borehole data. This project is a joint effort between South African academic, research, government and mining institutions. While the results of the experiments are encouraging considering they were conducted inside underground mine tunnels in a structurally complex hard rock mining environment, the survey designs and processing of the data were challenging due to flooded mining tunnels causing issues with land streamer sensor-ground coupling; the hard rock environment making it difficult to plant geophones (cabled); loose tunnel hanging wall limiting the use of a heavier energy sources; and fractured tunnel walls and mine infrastructure producing complicated wavefield characteristics (e.g., tunnel guided waves) that are difficult to handle in a 2D scenario.

We demonstrate that the seismic method can be used inside mine tunnels to delineate geological features associated with mineral deposits and improve mining. The processing of the in-mine seismic data provided insight into the location of the Merensky Reef (MR) and Upper Group-2 (UG2) below the mine tunnel, and an additional potential resource below UG2. Despite the challenges faced in the design and processing of the data, the target MR and UG2 orebodies have been imaged with confidence, supported by the geological model. Synthetic data constrained our seismic interpretations, although the model can be improved with more borehole data to constrain the targeted mineralizations. The reported data are only a portion of the full dataset, not including seismic and GPR profiles that are nearly perpendicular to the reported merged profiles. Exploitation of the full dataset will enable the characterization of both the MR and the UG2 in detail. The study forms a pilot concept for the mining industry to utilize in-mine seismics development and mine planning. This survey set-up is cost-effective because it uses an affordable energy source and land streamer, which do not require extensive planning and mobilization.

ACKNOWLEDGEMENTS

This study was sponsored by the Mandela Mining Precinct. Mandela Mining Precinct has received funding from the

Department of Science and Innovation (DSI) together with Minerals Council of South Africa. We thank the staff of Maseve platinum mine, especially Sipho Sithole, for the help during the mine visit and data acquisition. Michelle Pienaar for the coordination and management of the project. PhD and MSc students from the University of the Witwatersrand are thanked for their help during data acquisition. HiSeis Pty Ltd. and Petrosys are highly appreciated for sponsoring the licences for Globe Claritas processing software. We also thank Tesseral Technologies Inc. for supporting us with Tesseral software licences. Finally, we would like to thank the Associate Editor and two anonymous reviewers for providing constructive criticism in their reviews, which improved the quality of this manuscript.

DATA AVAILABILITY STATEMENT

Seismic and borehole research data that support the findings of this study are available on request from the corresponding author. The data are not publicly available due to privacy restrictions. Geological outcrop and open-source borehole data can be found on the website of The Council for Geoscience South Africa (https://maps.geoscience.org.za/portal/apps/sites/?fromEdit=true#/interactivewebmap).

ORCID

Moyagabo K. Rapetsoa https://orcid.org/0000-0003-3275-8994
Musa S.D. Manzi https://orcid.org/0000-0002-1654-5211
Mpofana Sihoyiya https://orcid.org/0000-0003-1956-5223
Ian James https://orcid.org/0000-0002-1655-3529

REFERENCES

Ahmadi, O., Koyi, H., Juhlin, C. and Gessner, K. (2016) Seismic signatures of complex geological structures in the Cue-Weld Range area, Murchison domain, Yilgarn Craton, Western Australia. *Tectonophysics*, 689, 56–66. https://doi.org/10.1016/j.tecto.2016.02.020

Basson, I.J. (2019) Cumulative deformation and original geometry of the Bushveld complex. *Tectonophysics*, 750, 177–202. https://doi.org/10.1016/j.tecto.2018.11.004

Brodic, B., Malehmir, A. and Juhlin, C. (2017) Delineating fracture zones using surface-tunnel-surface seismic data, P-S, and S-P mode conversions. *Journal of Geophysical Research: Solid Earth*, 122(7), 5493–5516. https://doi.org/10.1002/2017JB014304

Brodic, B., Malehmir, A., Pacheco, N.B.M., Juhlin, C., Carvalho, J., Dynesius, L., et al. (2021) Innovative seismic imaging of VMS deposits, Neves-Corvo, Portugal: Part I - In-mine array. *Geophysics*, 1–76. https://doi.org/10.1190/geo2020-0565.1

Buchanan, P.C. and Reimold, W.U. (1998) Studies of the Rooiberg group, Bushveld complex, South Africa: no evidence for an impact origin. *Earth and Planetary Science Letters*, 155(3–4), 149–165. https://doi.org/10.1016/S0012-821X(97)00216-1

Campbell, G. (2011) Exploration geophysics of the Bushveld complex in South Africa. *The Leading Edge*, 30(6), 622–638. https://doi.org/10.1190/1.3599148

Cawthorn, R.G. (2015) The Bushveld complex, South Africa. In: Charlier, B., Namur, O., Latypov, R. & Tegner, C. (Eds.) *Layered intrusions*. Dordrecht: Springer Netherlands, pp. 517–587. https://doi.org/10.1007/978-94-017-9652-1_12

Cawthorn, R.G. and Webb, S.J. (2001) Connectivity between the western and eastern limbs of the Bushveld complex. *Tectonophysics*, 330(3–4), 195–209. https://doi.org/10.1016/S0040-1951(00)00227-4

Chistyakova, S., Latypov, R. and Youlton, K. (2019) Multiple Merensky reef of the Bushveld complex, South Africa. *Contributions to Mineralogy and Petrology*, 174(3), 26. https://doi.org/10.1007/s00410-019-1562-x

Donoso, G.A., Malehmir, A., Brodic, B., Pacheco, N., Carvalho, J. and Araujo, V. (2021) Innovative seismic imaging of VMS deposits, Neves-Corvo, Portugal: Part II. Surface array. *Geophysics*, 1–39. https://doi.org/10.1190/geo2020-0336.1

Eales, H.V. and Cawthorn, R.G. (1996) The Bushveld complex. In *Developments in petrology* (Vol. 15). Elsevier, pp. 181–229. https://doi.org/10.1016/S0167-2894(96)80008-X

Guo, J. and Luo, C. (2014) Application of tunnel seismic image approach to the advanced geological prediction for tunnel. *Journal of Multimedia*, 9(7), 879–886. https://doi.org/10.4304/jmm.9.7.879-886

Hunt, E., Latypov, R. and Horváth, P. (2018) The Merensky cyclic unit, Bushveld complex, South Africa: reality or myth? *Minerals*, 8(4), 144. https://doi.org/10.3390/min8040144

Kgarume, T.E., Van Schoor, A.M. and Nontso, Z. (2019) The use of 3D ground-penetrating radar to mitigate the risk associated with falls of ground in Bushveld Complex platinum mines. *The Journal of the Southern African Institute of Mining and Metallurgy*, 119, 973–982.

Kinnaird, J.A. (2005) *The Bushveld Large Igneous Province, Review Paper*. University of the Witwatersrand, Johannesburg, 39 pp. http://www.largeigneousprovinces.org/sites/default/files/BushveldLIP.pdf [Accessed 11th November 2021].

Ledwaba, L.S., Scheepers, J., and Durrheim, R.J. (2012) Rockburst damage mechanism at impala platinum mine: The Southern African Institute of Mining and Metallurgy, pp. 20.

Lee, C.A. (1996) A review of mineralization in the Bushveld complex and some other layered intrusions. *Developments in Petrology*, 15, 103–145. https://doi.org/10.1016/S0167-2894(96)80006-6

Malehmir, A., Durrheim, R., Bellefleur, G., Urosevic, M., Juhlin, C., White, D.J. et al. (2012) Seismic methods in mineral exploration and mine planning: a general overview of past and present case histories and a look into the future. *Geophysics*, 77(5), WC173–WC190. https://doi.org/10.1190/geo2012-0028.1

Malehmir, A., Andersson, M., Lebedev, M., Urosevic, M. and Mikhaltsevitch, V. (2013) Experimental estimation of velocities and anisotropy of a series of Swedish crystalline rocks and ores: velocities and anisotropy of a series of crystalline rocks and ores. *Geophysical Prospecting*, 61(1), 153–167. https://doi.org/10.1111/j.1365-2478.2012.01063.x

Malehmir, A., Bergman B., Andersson B., Sturk R. and Johansson, M. (2018) Seismic imaging of dyke swarms within the Sorgenfrei–Tornquist Zone (Sweden) and implications for thermal energy storage. *Solid Earth*, 9, 1469–1485.

Manzi, M., Durrheim, R. and Webb, S. (2017) 3D seismic attributes for platinum exploration and mine planning in the Bushveld complex (South Africa). In *International Geophysical Conference, Qingdao, China, 17–20 April 2017* (pp. 665–668). Qingdao, China: Society of Exploration Geophysicists and Chinese Petroleum Society. https://doi.org/10.1190/IGC2017-169

Manzi, M., Malehmir, A. and Durrheim, R. (2019) The value of seismics in mineral exploration and mine safety. In *81st EAGE Conference and Exhibition 2019* (pp. 1–5). London, UK: European Association of Geoscientists & Engineers. https://doi.org/10.3997/2214-4609.201901667

Manzi, M.S.D., Cooper, G.R.J., Malehmir, A. and Durrheim, R.J. (2020) Improved structural interpretation of legacy 3D seismic data from Karee platinum mine (South Africa) through the application of novel seismic attributes. *Geophysical Prospecting*, 68(1), 145–163. https://doi.org/10.1111/1365-2478.12900

Manzi, M.S.D., Durrheim, R.J., Hein, K.A.A. and King, N. (2012) 3D edge detection seismic attributes used to map potential conduits for water and methane in deep gold mines in the Witwatersrand basin, South Africa. *Geophysics*, 77(5), WC133–WC147. https://doi.org/10.1190/geo2012-0135.1

Manzi, M.S.D., Hein K.A.A., Durrheim R.J. and King N., (2014), The Ventersdorp contact reef model in the Kloof gold mine as derived from 3D seismics, geological mapping and exploration borehole datasets. *International Journal of Rock Mechanics and Mining Sciences*, 66, 97–113.

Muller, C.J. and Visser (2010) Resource cut estimation of the western Bushveld joint venture (WBJV) located on the western limb of the Bushveld igneous complex, 7. http://s1.q4cdn.com/169714374/files/doc_downloads/Technical-Report-WBJV-Project-3-10-08-31-filed-10-10-05-Certificate.pdf

Nex, P.A., Ingle, L.J., Kinnaird, J.A., van der Vyver, B.A. and Cawthorn, R.G. (1998) A new stratigraphy for the main zone of the Bushveld complex, in the Rustenburg area. *South African Journal of Geology*, 101(3), 215–223.

Nkosi, N.Z., Manzi, M.S.D., Drennan, G.R. and Yilmaz, H. (2017) Experimental measurements of seismic velocities on core samples and their dependence on mineralogy and stress, Witwatersrand Basin (South Africa). *Studia Geophysica et Geodaetica*, 61(1), 115–144. https://doi.org/10.1007/s11200-016-0804-x

Scheiber-Enslin, S.E. and Manzi, M. (2018) Integration of 3D reflection seismics and magnetic data for deep platinum mine planning and risk mitigation: a case study from Bushveld Complex, South Africa. *Exploration Geophysics*, 49(6), 928–939. https://doi.org/10.1071/EG17083

Seabrook, C.L. (2005) *The upper critical and lower main zones of the eastern Bushveld complex*. PhD thesis, University of the Witwatersrand, Johanesburg, South Africa. p284.

Sehoole, L., Manzi, M.S.D., Zhang, S.E. and Bourdeau, J.E. (2020) An innovative seismic and statistical approach to understand 3D magmatic structures and ore deposits in the western Bushveld Complex, South Africa. *Ore Geology Reviews*, 126, 103784. https://doi.org/10.1016/j.oregeorev.2020.103784

Singh, B., Górszczyk, A., Malehmir, A., Hlousek, F., Buske, S., Sito, Ł. and Marsden, P. (2020) 3D velocity model building in hardrock environment using FWI: a case study from Blötberget Mine, Sweden. In *NSG2020 3rd Conference on Geophysics for Mineral Exploration and Mining* (pp. 1–5). : European Association of Geoscientists & Engineers. https://doi.org/10.3997/2214-4609.202020122

Stevenson, F. and Durrheim, R.J. (1997) Reflection seismics for gold, platinum and base metal exploration and mining in southern Africa. In: Gubins, G. (Ed.) *Proceedings of Exploration 97: 4th Decennial International Conference on Mineral Exploration*, pp. 391–398.

Stevenson, F., Higgs, R.M.A. and Durrheim, R.J. (2003) Seismic imaging of precious and base metal deposits in southern Africa, Chapter 9. In: Eaton, D., Salisbury, M., and Milkereit, B (Eds.) *Hardrock seismic exploration*. Houston, TX: Developments in Geophysics Series, Society of Exploration Geophysicists, pp. 141–156.

Trickett, J.C., Duweke, W.A. and Kock, S. (2004) Three-dimensional reflection seismics: worth its weight in platinum. *Journal of the South African Institute of Mining and Metallurgy*, 105, 257–263.

Webb, S.J., Cawthorn, R.G., Nguuri, T. and James, D. (2004) Gravity modeling of Bushveld complex connectivity supported by Southern African seismic experiment results. *South African Journal of Geology*, 107(1–2), 207–218. https://doi.org/10.2113/107.1-2.207

Westgate, M., Manzi, M.S.D., James, I. and Harrison, W. (2020) New insights from legacy seismic data: reprocessing of legacy 2D seismic data for imaging of iron-oxide mineralization near Sishen Mine, South Africa. *Geophysical Prospecting*, 68(7), 2119–2140. https://doi.org/10.1111/1365-2478.12996

Yilmaz, O., Yilmaz, Ö. and Doherty, S.M. (2001) Seismic data analysis: processing, inversion, and interpretation of seismic data. *Society of Exploration Geophysicists*. Retrieved from https://books.google.co.za/books?id=ceu1x3JqYGUC

8. Paper II: Innovative seismic imaging of the platinum deposits, Maseve mine – Part II: Surface and In-mine

Moyagabo K. Rapetsoa[1*], Musa S. D. Manzi[1], Ian James[1, 2], Mpofana Sihoyiya[1], Raymond J. Durrheim[1], Michelle Pienaar[3].

[1]School of Geosciences, University of the Witwatersrand, Johannesburg, Private Bag, Wits, 2050, Republic of South Africa.

[2]Southern Geoscience Consultants, West Perth, WA, Australia.

[3]Mandela Mining Precinct, Carlow Rd &, Rustenburg Rd, Melville, Johannesburg, 2109, Republic of South Africa.

ABSTRACT

Maseve mine is located in the western limb of the Bushveld Complex, the largest layered igneous intrusion in the world. In this study we present results from phase 2 of the advanced orebody knowledge (AOK) program. We show results from surface (SP1, SP2, and SP3) and tunnel (T3a, T3b, and T4b) reflections seismic profiles with a total distance of 4150 m across the profiles. Tunnel seismic data were acquired using a combination of seismic land streamer and spiked geophones, with a 5 m receiver and shot spacing. Due to space constrains and safety, the shots were acquired using a sledgehammer. The profiles were located 10-50 m above mineral deposits and designed to cross major geological structures. Surface seismic profiles were acquired using both cabled system and wireless recorders with a 5 m and 10 m receiver spacing, respectively. Surface shots were acquired using a 500 kg G-PEG drop-hammer, with a shot spacing of 10 m across the profiles. Although a high noise level due to mine infrastructure and electrical power cables was present, target reflections were enhanced through a careful processing workflow. Interpretation of the data is constrained using borehole data, geological models provided by the mine, and 2D/3D seismic modelling. The geology of the study area is complex, however the processed seismic data exhibit gently dipping reflections that are associated with geological structures in the area such as faults and dykes. The data were able to image the target mineralization (Merensky Reef and Upper Group 2) and provide insight on possible vertical and lateral extension of the mineralization. The tunnel seismic experiments demonstrated the application of seismic methods using in-mine infrastructure to image platinum deposits and geological structures. While the surface experiments not only proved to be efficient, but illustrated the capability of small scale seismic surveys to image the subsurface geology for mining purposes. The use of a small scale seismic survey can add value in active mining environments for exploration purposes.

INTRODUCTION

The South African mineral and mining industry is challenged to provide a high quality and high-resolution deep targeting solution in a cost effective and environmentally effective manner. However, the mineral exploration industry is slow at employing new technologies in comparison to the oil and gas industry, where nearly all up-to-date technologies (e.g., Méndez-Hernández, 2003; Liszicasz et al., 2013; Suotang et al., 2020) are tested and employed. The conservative nature of the mineral exploration industry has resulted in a decline of exploration in geologically complex environments. A number of mineral discoveries have been discovered due to the combination of field geology, geochemistry, drilling and different geophysical methods. However, there is still a great need for innovation and improvement to current exploration methods. Therefore, this has led to an increase in demand to providing the mining industry in South Africa with accurate geological information and knowledge that will contribute to optimal ore extraction and mine safety (i.e., achieving ‘zero harm objectives’). Innovative solutions are also needed to help extend the life of mines but also to provide exploration targets in new places, securing new resources and creating jobs and establishing secure and sustainable access to minerals.

Geophysical methods such as reflection seismics are the most direct and effective way of imaging mineral deposits at depth (Juhlin, Lindgren, and Collini 1991; Eaton, Milkereit, and Salisbury 2003; Ahmadi et al., 2013; Malehmir et al., 2020; Manzi et al., 2020). Furthermore, reflection seismics can provide information about geological structures that host mineral deposits. Surface seismic methods maintain good vertical resolution with depth and, therefore, have been used more routinely for localizing mineral deposits and mine planning in the last decades. However seismic methods, like most exploration technologies, have their own challenges. For example, seismic data collected in brownfield areas can suffer from anthropogenic noise. In some cases, mines can no longer acquire seismic data on surface due to a lack of access to the mining site because of mine infrastructure and environmental issues. In such cases, in-mine seismic surveys are considered a solution. However, further complications and restrictions are introduced if underground spaces (e.g., developmental tunnels, mining stopes, exploration holes, etc.) are used for seismic or other exploration purposes. The nature of these spaces imposes numerous limitations, resulting in conventional active-source seismic imaging being challenging and size limited (small scale). Logistical challenges related to active mining operations, strong vibrational noise, combined with GPS-denied nature of underground spaces preventing accurate time synchronization, are just some factors that have restricted in-mine exploration primarily to drilling and downhole geophysics.

In response to the deep South African mining challenges, the Advanced Orebody Project programme (AOK) was launched. The AOK project is aimed at developing technologies that can be used to obtain information ahead of the mine face. As part of the project, in-mine and surface seismic surveys were acquired in 2020 and 2022 at Maseve mine, which hosts two of the most economic platinum group element deposits in South Africa. The main objectives of this study are to: (1) substantiate the use of small scale seismic surveys in highly noisy and logistically challenging mine environments, (2) image the extension of the deep mineralization and associated geological structures, and (3) understand the acquisition challenges and innovation aspects required to acquire seismic data in active mine sites. Apart from the innovative survey design and processing, our experiments utilized 3D reflection modelling to assist with the interpretation of the seismic sections. The study links the deep reflections imaged on surface with the observed near-surface (below tunnel) in-mine seismic reflections. We show how combined in-mine and surface seismic data can provide key information on mineralization and their associated geological structures such as faults, dykes, potholes, and Iron Rich Ultramafic Pegmatites (IRUPs).

GEOLOGICAL BACKGROUND

Maseve mine is located 38 km NW of Rustenburg town in the largest layered igneous intrusion in the world. The region is well known for hosting the richest platinum group elements (PGEs) (Scheiber-Enslin and Manzi, 2018). A detailed geology of the mine is described in the first phase of this project (Rapetsoa et al., 2022) and it is not repeated here. In summary, Maseve mine exploits two major economic horizons (locally termed reefs) for PGE deposits, namely the Merensky Reef (MR) and Upper Group 2 (UG2). The two reefs are mined at depths greater than 500 m below surface, with the UG2 occurring between 15 and 400 m below the MR in the Bushveld Complex (Manzi et al., 2020; Sehoole, 2020).

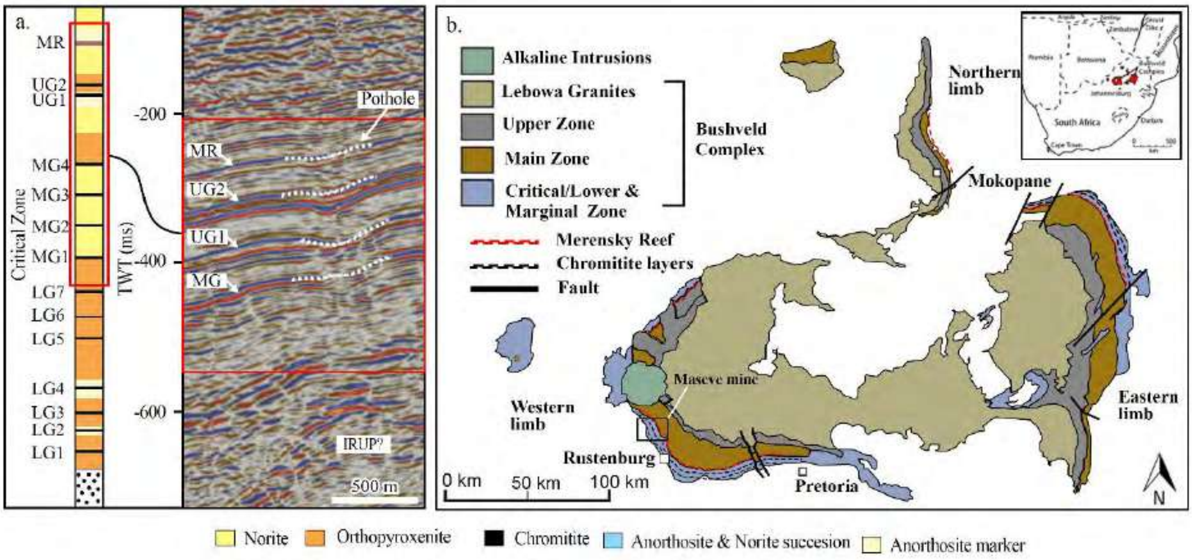

Figure 1: *a) generalized seismic stratigraphy column of the critical zone, highlighting the chromitite layers that are at Maseve and common geological structures such as potholes and Iron Rich Ultramafic Pegmatites (IRUPs) encountered. b) Geological map of the Bushveld Complex, showing the location of Maseve mine and major geological structures.*

Several stages of dyke intrusions of different ages and composition have affected the rocks of the region, with diabase and dolerite dykes being dominant in the area. Underground mapping and drilling is used to confirm the geological structures (faults and dykes) in the area. The dykes in the region are often associated with fault zones (Ledwaba, Scheepers, and Durrheim 2012; Scheiber-Enslin and Manzi, 2018). Other structures that are encountered in the Bushveld Complex include slump structures (Figure 1a: locally termed potholes) and Iron Rich Ultramafic Pegmatites (IRUPs) that can halt mining activities. Regional structural interpretation is described by Basson (2019) and suggests that the dominant structure in the region is the east-northeast – west-southwest Chaneng fault zone.

DATA ACQUISITION

In-mine seismics

Seismic, ground penetrating radar (GPR), and electrical resistivity tomography (ERT) surveys conducted in 2020 (Rapetsoa et al., 2022) assisted us in designing seismic surveys for phase two. The locations of phase two (2022) seismic profiles extended and overlapped with the phase one profiles.

Six seismic profiles, consisting of 4.5 Hz (land streamer) and 14 Hz (planted) geophones, were set up in the mine tunnels with a combined total length of 1.36 km over known geological structures and orebodies (Figure 2). The 2D seismc profiles were acquired using a 6.3 kg sledgehammer and the signal penetration was good for near-surface (~ < 100 m) imaging in the noisy mining environment.

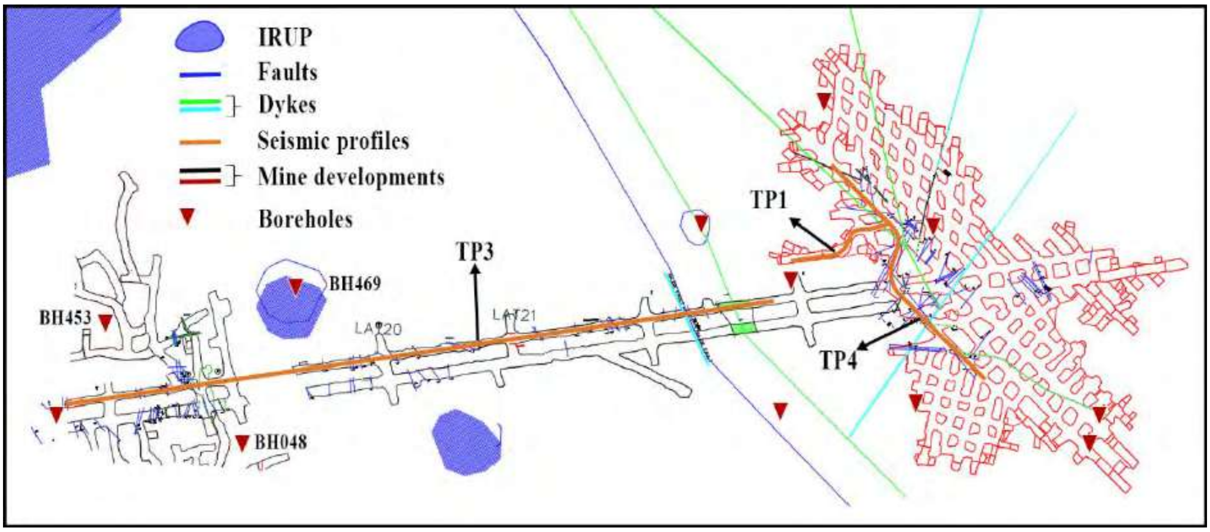

Figure 2: *Underground mine plan, showing the location of the seismic profiles (orange) and geological structures such as fault (blue) and dolerite dyke (green and cyan).TP: Tunnel profile, IRUP: Iron rich ultramafic pegmatites.*

To investigate the effect of the mine noise on the data, the data from the planted geophones and land streamer were compared (Figure 3) to decide on the most suitable sensing technology for acquiring data in the noisy environment. We checked the quality of the data, cost-effictiveness, effect of the tilt and mine infrastructure noise. It was found that the land streamer (Figure 3a) recorded less noise than the planted geophones (Figure 3b). The sources of noise investigated included ventilation, water pumps, and flow of water. The land streamer provided much better results and was used in all the surveys in phase 2.

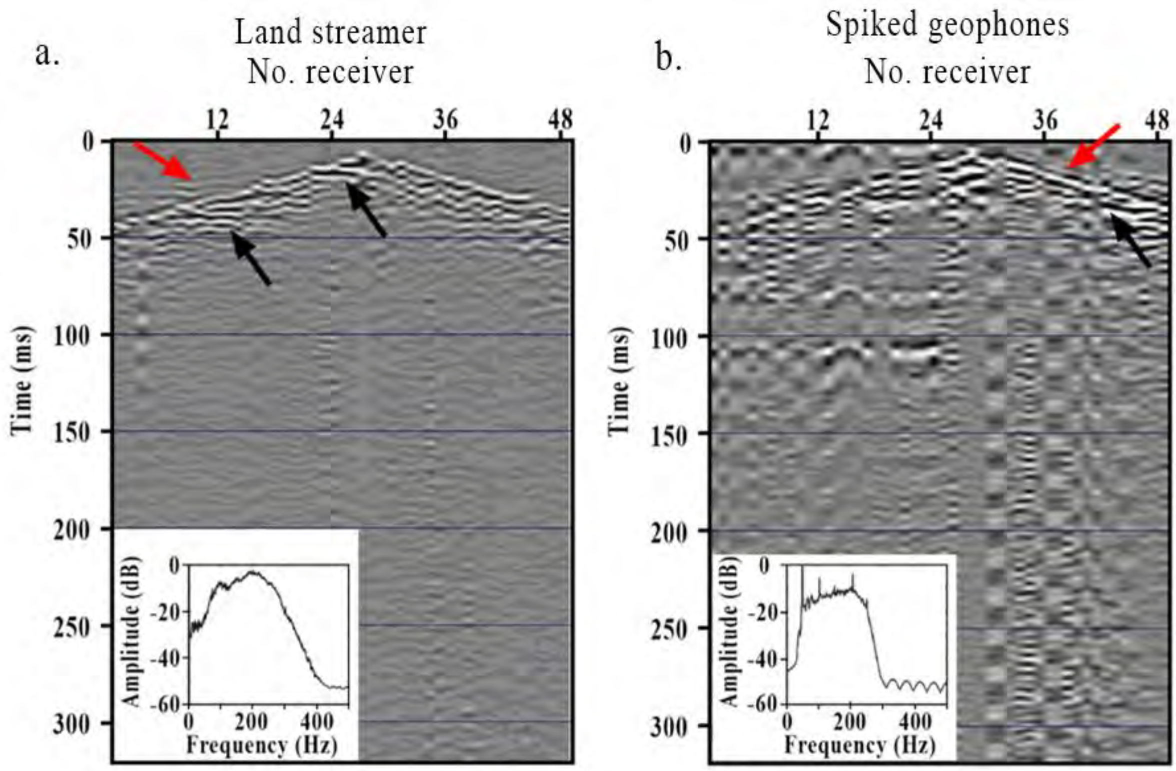

Figure 3: *Shot gathers examples (shots 45 and 73) with frequency spectrum from planted and land streamer receivers. a) the land streamer shot gather, and b) the planted geophone shot gather. Red arrows show first breaks, and black arrows show reflections.*

As the main objective of the phase two surveys was to cover the areas that were not covered in phase one, due to a limited number of receivers and time, a 5 m receiver spacing was used for all the seismic profiles except for profile T1 that had a 2 m receiver spacing. The survey parameters are summarized in Table 1.

***Table 1:** Maseve mine data acquisition parameters for the three 2D seismic profiles (T1, T3a-b and T4b) collected in 2022.*

Profiles	TP3a	TP3b	TP4b
Survey parameters			
Acquisition type	Fixed straight line	Fixed straight line	Fixed crooked line
Acquisition system	Geometric Geode	Geometrics Geode	Geometric Geode
Receiver frequency	4.5 Hz	14 Hz	4.5 Hz
No. of receivers	48	48	48
Receiver spacing	5 m	5 m	5 m
Source	6.3 kg sledgehammer	6.3 kg sledgehammer	6.3 kg sledgehammer
No. of source positions	50	50	50
Source spacing	2 m	2 m	2 m
Profile length	235 m	235 m	235 m
Recording length	500 ms	500 ms	500 ms
Sampling interval	1 ms	1 ms	1 ms

A detailed description of phase one seismic profiles can be found in Rapetsoa et al. (2022). The current work differs from phase one by including a comparison between planted geophones and land streamer data, the meausrement of P-wave velocities (Figure 4a, b) on the footwall and sidewall (weakzones and dykes) inside the mine tunnel, and lastly the knowledge (location) of the geological structures and orebodies. The seismic profiles were shot every 2 m, with an excepion of T1 having a shot spacing of 1 m. Analysis and testing of different sampling rates in phase one led to choosing a sampling rate of 1 ms, as the source was imparting energy from 50 Hz - 120 Hz. While 6 seismic profiles were collected (namely T1,T3a, b, c and T4a, b), this study focuses on the data collectd from T3a, b and T4b due to coverage over the geological structures of interest and comparison of the land streamer and planted geophone dataset. T3a and T3b (west-southwest – east-northeast) profiles were collected adjacent to each other with a total spread of 235 m, using a land streamer and planted geophones, respectively (Figure 4c, d).

Figure 4: *Measurements of the seismic velocities underground using ultrasonic pulse meter over a) a weak zone and b) a dyke. The set-up inside the tunnel of the seismic survey using the seismic land streamer (red arrows) and planned geophone (green arrows) is shown in c) and d)*

The aim of these two seismic profiles was to image the dipping orebodies and geological structures (faults and folds) below the mine tunnel, extend the P5-P7 seismic profiles acquired in phase one (Rapetsoa et al., 2022) and lastly compare the planted geophones and land streamer in mine tunnels. The T4b profile trends southeast – northwest, with a spread of 235 m. A fixed crooked spread with 48 (4.5 Hz) land streamer channels formed this seismic profile with a 5 m receiver spacing. The aim of this profile was to extend P1 from phase one seismic surveys and improve the quality of the data, and to image UG2 below the mine tunnels.

GPS signal is not available in underground mine tunnels, therefore the receiver positions were marked relative to the mine pegs. The elevations of the receivers relative to the tunnel roof were obtained from the LiDAR survey that was conducted concurrently with the seismic surveys.

Surface seismics

In August 2022, high-resolution 2D surface seismic survey was designed and acquired over the Merensky Reef and UG2 deposits. The area is surrounded by mine infrastructure (e.g., tailings, offices, and processing plants), therefore the profiles followed accessible tracks in the area, resulting in a fixed straight line geometry (Figure 5). The entrance to the mine is located on the west side of the profile, while the tailing storage facility (TSF) is on the eastern side of the profiles. Roads on the mine site had frequent heavy traffic generating high levels of background noise during acquisition. The data were acquired using a 500 kg impulse source (Figure 6a: drop-hammer). Aproximatley 400 receiver positions (5-10 m apart) and 330 source positions were deployed and surveyed, using different geophones (Figure 6b-c), with similar recording parameters. As the main objective of the study was to image to a depth of 600 m below surface, a 10 m receiver spacing was used for all the seismic profiles, except seismic profile SP3 that had a 5 m spacing due to the limitation of the cabled system. For SP3, one-component 14 Hz geophones were deployed, while SP1 and SP2 profiles used lower natural frequency (4.5 Hz) geophones. At each source position four shots were recorded and later stacked to improve the signal-to-noise ratio (S/N).

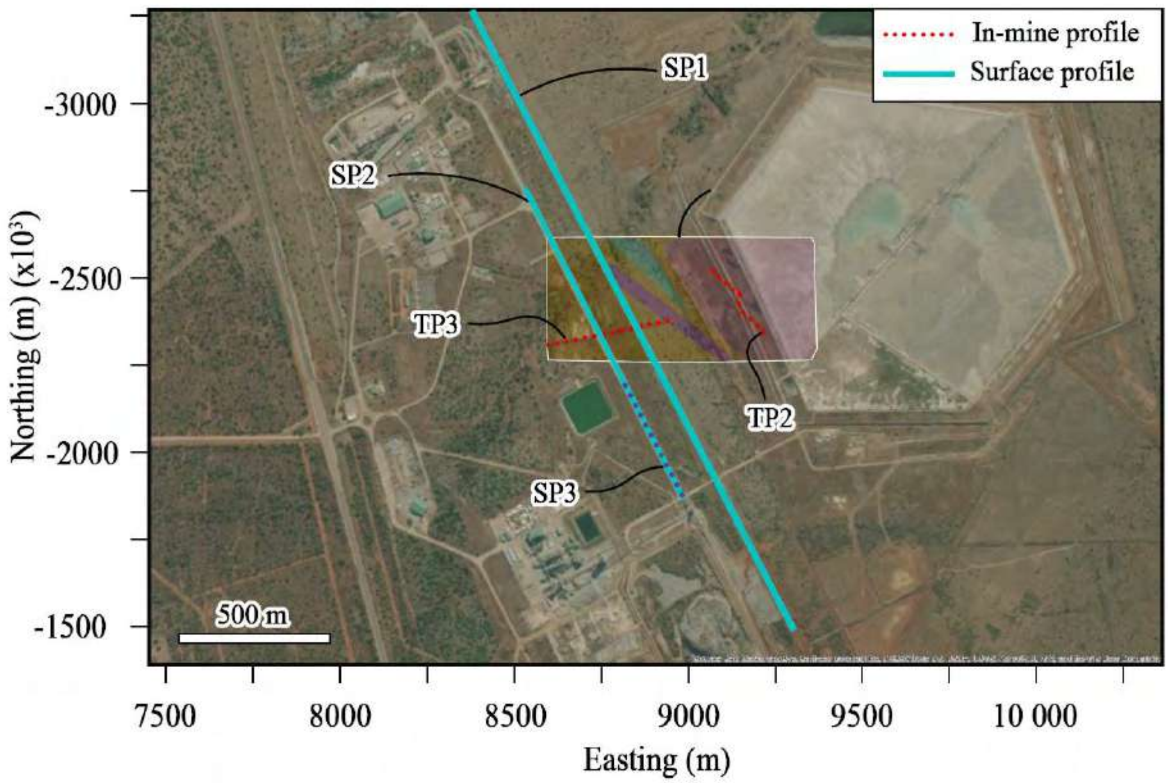

Figure 5: *Surface lines (SP1, SP2 and SP3) and the two underground seismic profiles (TP2 and TP3) collected inside the tunnel, few meters above the Merensky Reef and UG2 deposits (white outline).*

Table 2 lists the main acquisition parameters for the surface seismic survey. The geode cabled system has no form of acquiring GPS locations, therefore accurate GPS receiver coordinates were collected using a differential GPS for all the seismic profiles. An event recorder was mounted on the AWD to record a GPS time stamp that will later be used to harvest the raw shot gathers from the wireless nodes.

Table 2: Summary of the seismic data acquisition parameters of surface seismic profiles (August 2022).

Profiles	SP1	SP2	SP3
Survey parameters			
Acquisition type	Fixed straight line	Fixed straight line	Fixed crooked line
Acquisition system	Sercel UNITE	Sercel UNITE	Geometrics Geode
Receiver frequency	4.5 Hz	4.5 Hz	14 Hz
No. of receivers	198	101	96
Receiver spacing	10 m	10	5 m

Source	500 kg G-PEG drop hammer		
No. of source position	198	101	35
Source spacing	10 m	10 m	10 m
Profile length	1970 m	1000 m	475
Recording length	500 ms	500 ms	500 ms
Sampling interval	2 ms	2 ms	2 ms

DATA PROCESSING

In-mine seismics

Although the four seismic profiles were colleted separately, a similar processing workflow was applied. The processing steps are summarized in Table 3. The data were of good quality, with clear P-wave first breaks and reflections in raw shot gathers. The noise generated by mine pumps, ventilation and water flow proved challenging, overwhelming the signal and obfuscating reflectivity.

Table 3: Processing steps for the reflection seismic datasets of T1, T3a-b and T4b at Maseve mine.

	2D processing flow
1.	Read SEG-Y data
2.	Edit traces, geometry setup T1: Crooked CDP 1 m bin size T3a-b: Crooked CDP 2.5 m bin size T4b: Crooked CDP 2.5 m bin size
3.	Pick first breaks
4.	SNAWT: Surface Noise Attenuation
5.	Refraction and elevation corrections T1: Datum of 537 m below msl, replacement velocity of 5000 m/s T3a-b: Datum of 635 m below msl, replacement velocity of 5200 m/s T4b: Datum of 537 m below msl, replacement velocity of 5000 m/s
6.	Band pass filtering: 16 - 80 - 250 - 300 Hz
7.	Deconvolution: 60 ms filter length, 1 ms gap
8.	Remove first arrivals
9.	NMO corrections: 70% stretch mute, 20 ms taper
10.	*f-k* filter: surgical muting
11.	Velocity analysis

12.	Stack T1: constant velocity of 6000 m/s T3a-b: constant velocity of 6500 m/s T4b: constant velocity of 6000 m/s
13.	Post stack coherency enhancement Spectral weighting: 50 100 150 200 250 Hz Semblance-smoothing
14.	Time to depth conversion using Vp of 6000 m/s and 6500 m/s

Figure 7a-c shows the raw shot gathers, while Figure 7d-e shows shot gathers after pre-stack processing (trace editing, refraction statics, band pass) for signal enhancement. T1 (Figure 7a) shows potential imaging of near-surface reflections with multiple reflections identifiable within the first 25 ms. T3a (Figure 7b) has the potential of imaging the deeper reflections below the mine tunnel with the reflections observed at 50-75 ms. Profile T3b exhibits few noisy traces (Figure 2) probably due to the flow of water against the geophone spikes, therefore careful processing was required for T3b.

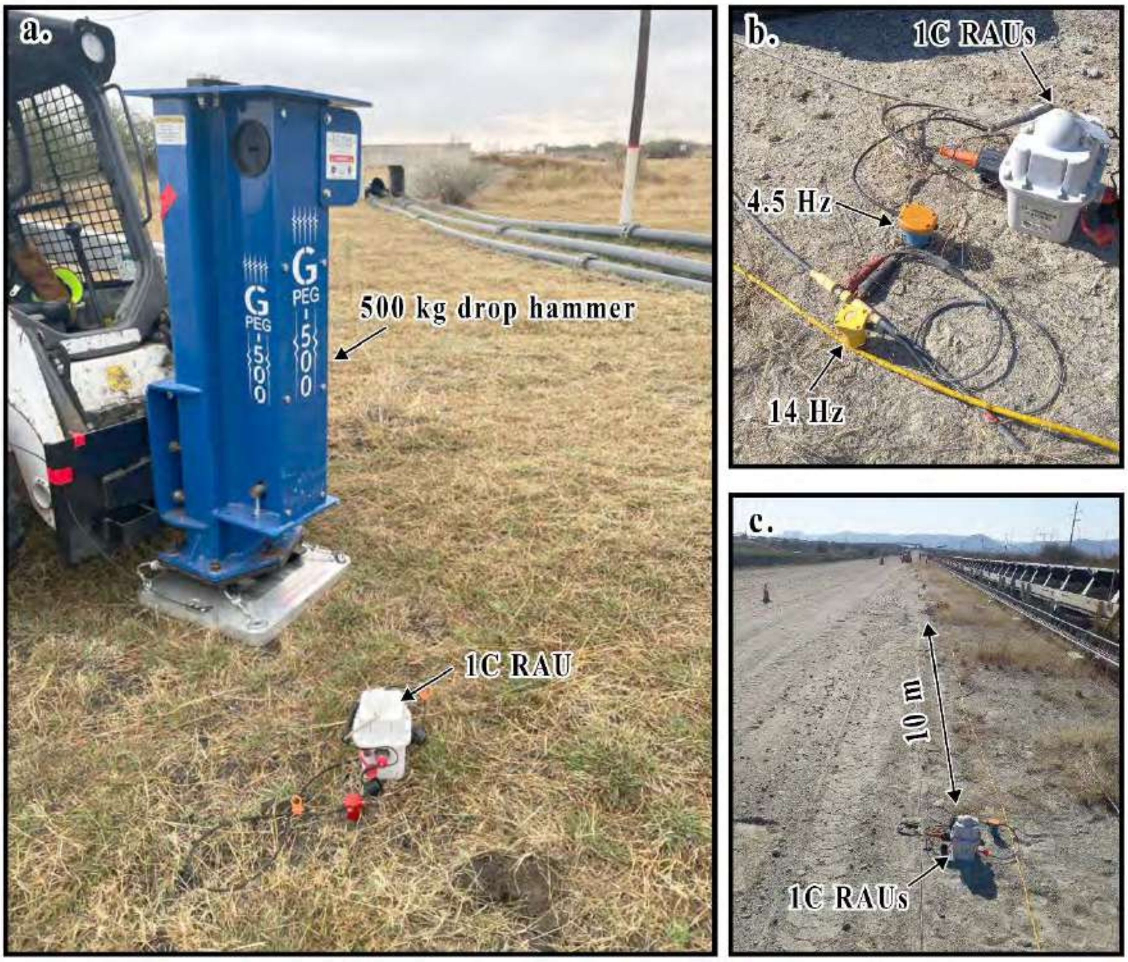

Figure 6: *Seismic source and receivers used during the Maseve surface seismic acquisition (August 2022). a) Photo of the G-PEG 500 drop hammer, and b) Sercel UNITE wireless 1C*

recorders, with a Geometrics Geode cabled system. c) Wireless receivers and 14 Hz cabled system collocated and spaced at 5-10 m from each other along seismic profile SP2 and SP3.

The first processing step was to edit the bad traces, add the geometry that was created from the mine pegs and add CDPs (common depth points) to the traces. The second step was to pick first breaks to assist in refraction static corrections. A total of ~5760 first arrivals were picked manually on each profile to generate a two layered P-wave velocity model. The corrections were estimated using stepwise iterations and changes were made to the geometry and velocity of the first and second layers. Solutions with RMS-misfit lower than 4 were more stable, therefore were used across the different seismic profiles. In general, P-wave velocities obtained from the first break tomograms exhibit a fractured top layer (~ 10 m thick) exhibiting velocities between 1000 m/s and 4000 m/s and the hard rock of variable thickness (10-40 m) with velocities between 4000 m/s and 6500 m/s.

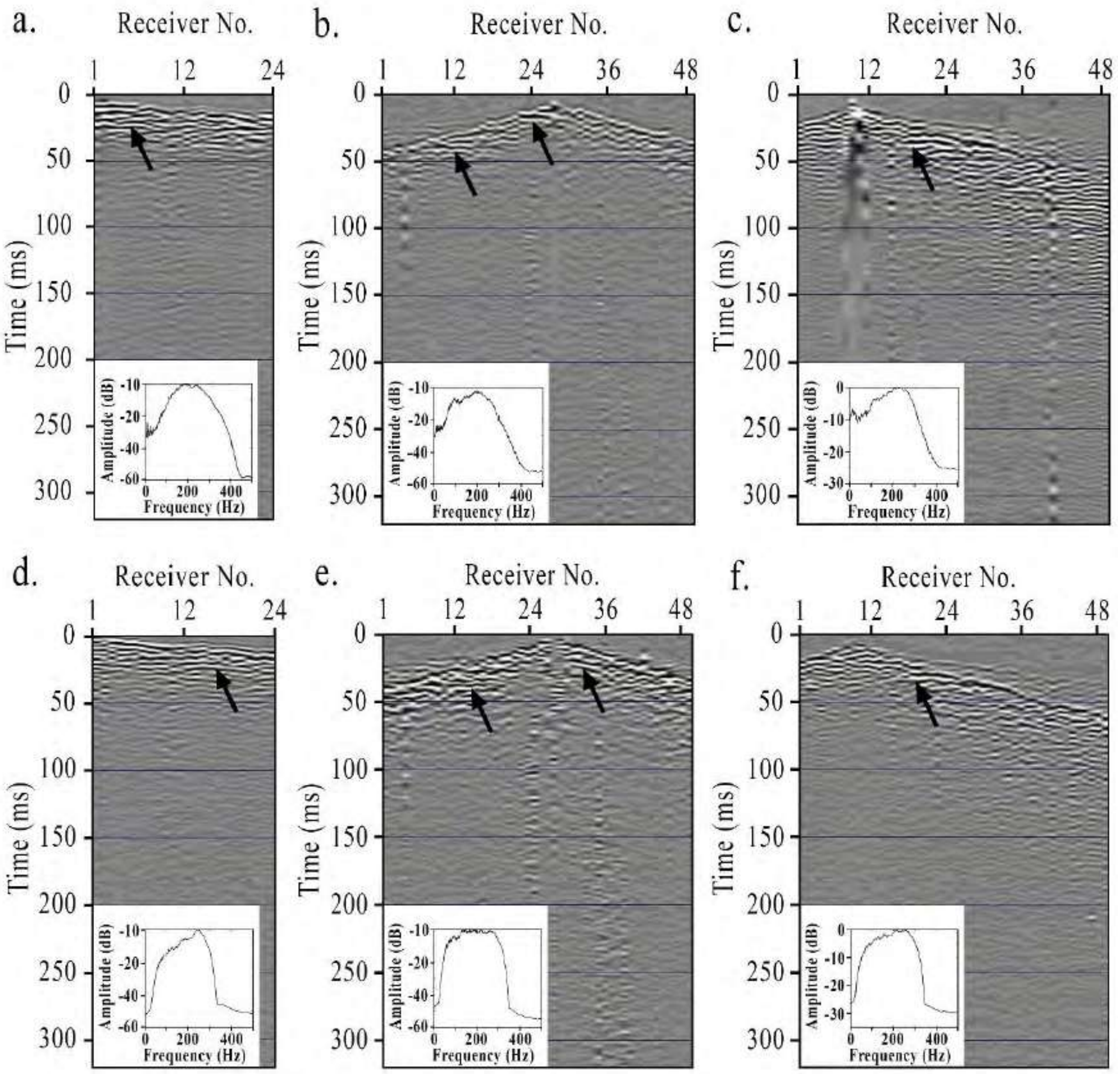

Figure 7: *Three shot gather examples from T1, T3a and T4b, with the corresponding frequency*

spectrum. (a-c) Raw and (d-e) processed shot gathers, with reflections highlighted by the black arrows.

The refraction static corrections improved the quality of the first arrivals and coherency of the identified reflections. The seismic profiles T1 and T4b were collected at the bottom of the incline tunnel, therefore the data were shifted to a reference datum of 537 m below mean sea level (msl), with a replacement velocity of 5000 m/s. While T3a and b where collected along the incline tunnel and the data were shifted to a reference datum of 635 m below msl and a replacement velocity of 5200 m/s. We designed a broad band filter (16 - 300 Hz) to preserve wave energy in that range. The filter reduced low-frequency coherent noise generated by mine infrastructre. The band pass filter and deconvolution were applied, whitening the spectrum and reducing the low-frequency shear wave energy. The last pre-stack process was the removal (top mute) of the direct and refracted arrivals, such that they do not affect the final stack section. A series of constant velocities were tested ranging from 4500 to 8000 m/s with 250 m/s intervals. Through visual inspection, an estimated NMO velocity of 6000 m/s was used for T1 and T4b, while T3a, b used NMO velocity of 6500 m/s for stacking. Spectral weighting was applied to improve the images, together with a semblance based coherency filter to improve the data. Finally the unmigrated stacked data were depth converted with velocities of between 6000 m/s and 6500 m/s.

Surface seismics

Surface seismic profiles were collected to cover and place the known mineral deposit at the centre of the profile. The profiles were located on existing tracks resulting in the seismic profiles being located close to mine infrastructure including electrical power lines (Figure 8a) and mine processing plants (Figure 8b). Identifying reflections on the seismic raw shot gathers was difficult due to electrical noise (Figure 8c) from the power lines. Figure 8d also shows an example of a raw shot gather contaminated by coherent noise from the processing plant along seismic profiles SP2 and SP3. In general, the data along SP2 and SP3 are of good quality with high signal to ratio (S/N), while SP1 is severely contaminated by electrical noise at the far offsets, with 143 of 198 receiver positions having a low signal-to-noise ratio due to the proximity of the power lines. Data processing was difficult for profile SP1, therefore reflection processing focuses on SP2 and SP3.

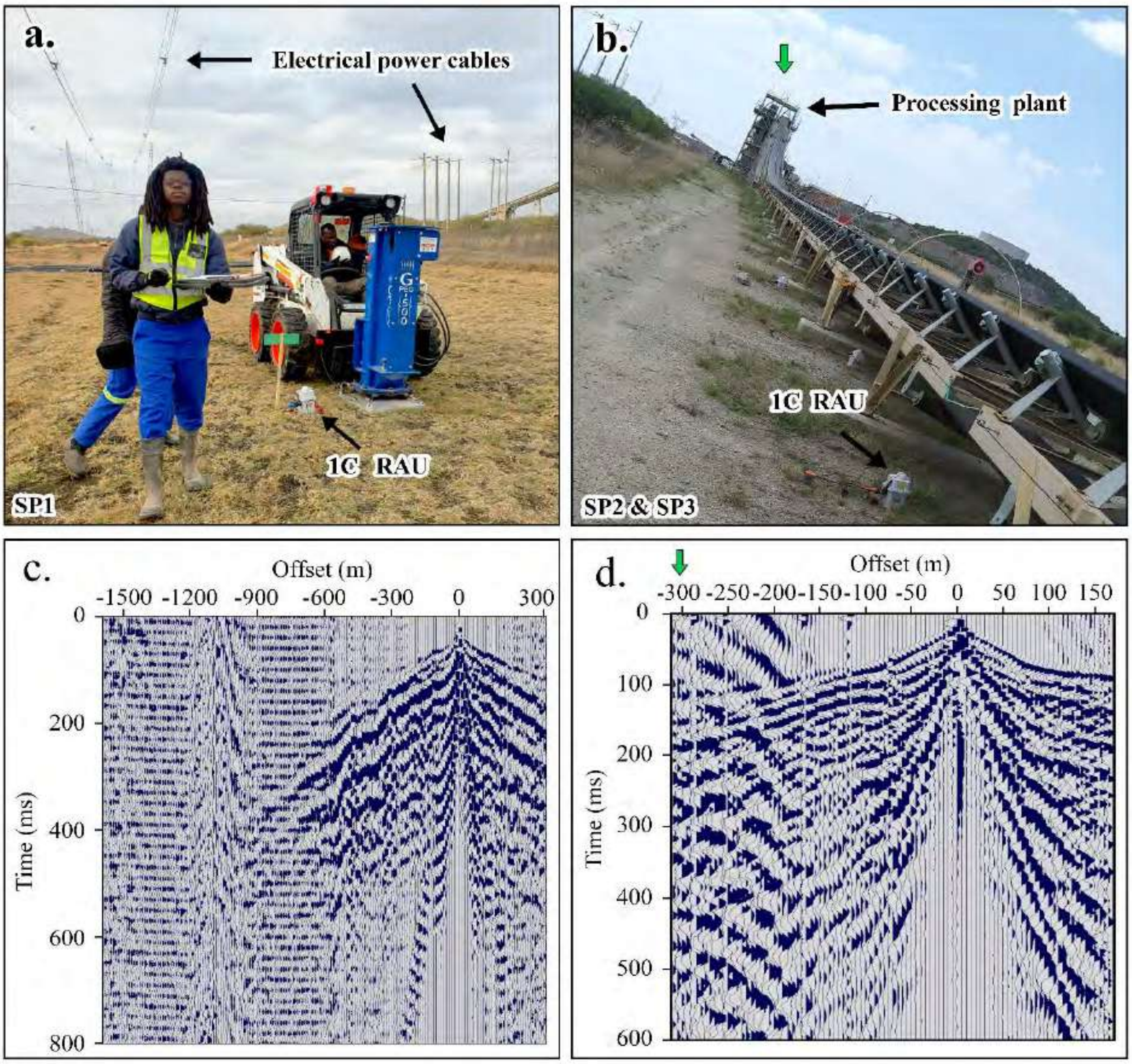

Figure 8: *a) Field conditions showing electrical power cables above the survey area and b) processing plant near the seismic profiles. c) Raw shot gather affected by 50 Hz electrical noise and d) strong coherent noise caused by the processing plant.*

The processing flow is summarized in Table 4. Processing started with building the geometry of the seismic profile, add the shot, receiver and CDP information to the traces. Due to the proximity to the power lines, the first step was to apply a notch filter to remove the 50 Hz harmonic noise. Approximately 23 000 first breaks were manually picked for input to refraction statics. Surface seismic tomography models exhibit velocity ranges between 1000 m/s and 4000 m/s for the top weathered layer, followed by 4000 m/s to 6500 m/s for bedrock. These static corrections improved the continuity of the first breaks and enhanced reflections. Further improvements were made by applying a surface wave attenuation filter. A broad band-pass filter was applied on the dataset to preserve frequencies between 10 and 150 Hz. We then removed the first arrivals using the first break picks, such that they do not appear on the final stack section. Figure 9 shows the comparison of the raw shot gather and pre-stack processing steps (notch filter, refraction statics, and surface wave attenuation) applied.

Table 4: Processing steps for the surface reflection data along SP1, SP2 and SP3 at Maseve mine.

	2D processing flow
1.	Prepare SEG-Y
2.	Geometry setup SP1: Crooked CDP 5 m bin size SP2: Crooked CDP 5 m bin size SP3: Crooked CDP 2.5 m bin size
	Remove 50 Hz Noise: Adaptive notch filter at 50 Hz
3.	Pick first breaks
4.	Refraction and elevation corrections SP1: Datum of 1091 m above msl , replacement velocity of 4500 m/s SP2: Datum of 1084 m above msl, replacement velocity of 4500 m/s SP3: Datum of 1090 m above msl, replacement velocity of 4500 m/s
5.	SNAWT: Surface Noise Attenuation
6.	Band pass filtering: 10 - 20 - 100 - 150 Hz
7.	Surface wave attenuation
8.	Deconvolution: Spiking, 60 ms filter length
9.	Remove first arrivals energy
10.	NMO corrections: 70% stretch mute, 20 ms taper
11.	*f-k* filter: surgical muting
12.	Velocity analysis
13.	Stack T1: constant velocity of 6000 m/s T3a-b: constant velocity of 6500 m/s

	T4b: constant velocity of 6000 m/s
14.	Post-stack coherency enhancement Fx-deconvolution Semblance-smoothing *f-k* filtering
15.	Time-to-depth conversion:

Normal moveout corrections were conducted using velocity ranges between 3000 – 6000 m/s for the three seismic profiles, with a stretch mute between 70 – 80 %. The continuity of the reflections were further improved through the application of FX-deconvolution and semblance based coherency filtering to attenuate random noise. This was followed by *f-k* filtering to remove steeply dipping events in the stack section due to source-generated noise. Finally, migration algorithms were tested and proved to be unsuccessful, therefore unmigrated stack sections were used for interpretation. We then applied time-to-depth conversion using a 1D velocity model that honours the NMO stacking velocities.

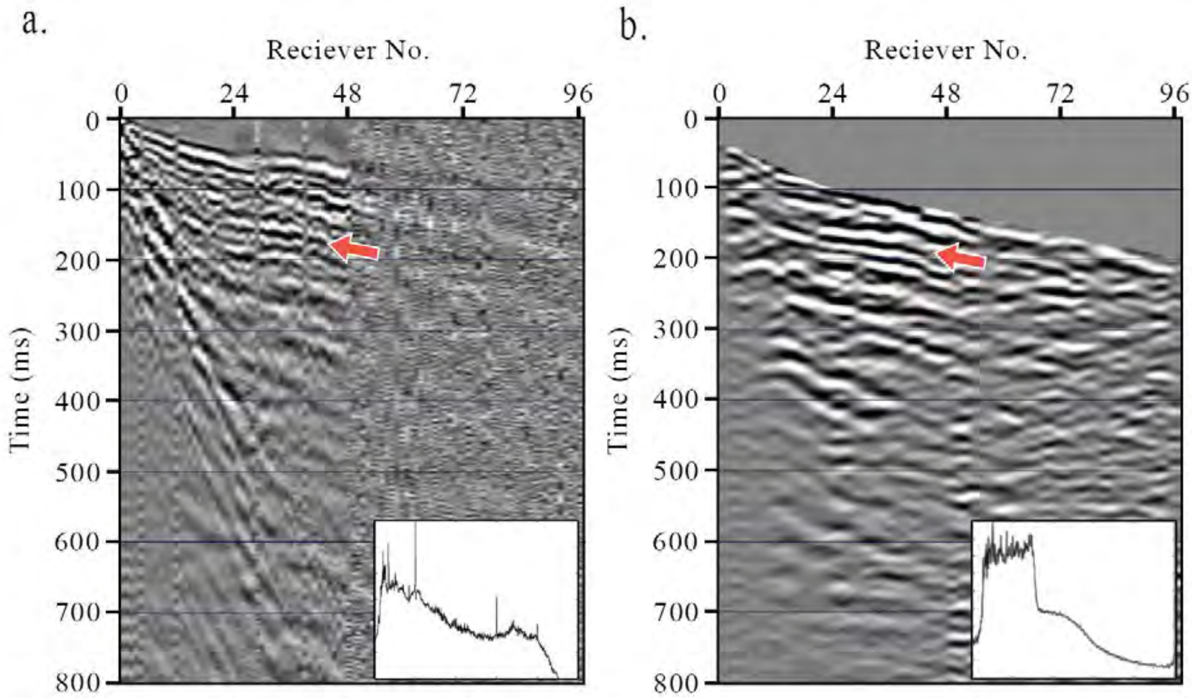

Figure 9: *Shot gather example from SP2, showing a) Raw shot gather and b) processed shot gather with their corresponding frequency spectrum normalized to one and shown for 0 – 250 Hz.Change in frequency content can be observed between channels 1-48 and 49-96 due to the different geophones used (4.5 Hz and 14 Hz). Red arrows indicate observed reflections.*

2D/3D MODELLING AND BOREHOLE DATA

Physical properties and geological information from the mine were used to conduct 2D numerical simulations to investigate seismic reflectivity in the subsurface rocks and to design the seismic acquisition to best illuminate geological structures. Rapetsoa et al. (2022) reports numerical modelling for in-mine seismics.

Two dimensional modelling was conducted using Tesseral Pro^{TM} software. Figure 10a shows the geological models built from borehole data and mine information. A synthetic 2D seismic survey was designed to generate synthetic shot gathers using acoustic modelling. These shot gathers were processed fully to produce a pre-stack time migrated section, which was converted to depth using the velocity model. The main objective of numerical modeling was to simulate the seismic response of the targets (MR and UG2) and geological structures (faults, potholes, dykes and IRUPS). Figure 10b shows an example for the synthetic seismic section produced from the synthetic model. The section shows that the seismic survey is able to detect UG2 and MR as strong reflections, as well image IRUPS, faults and potholes.

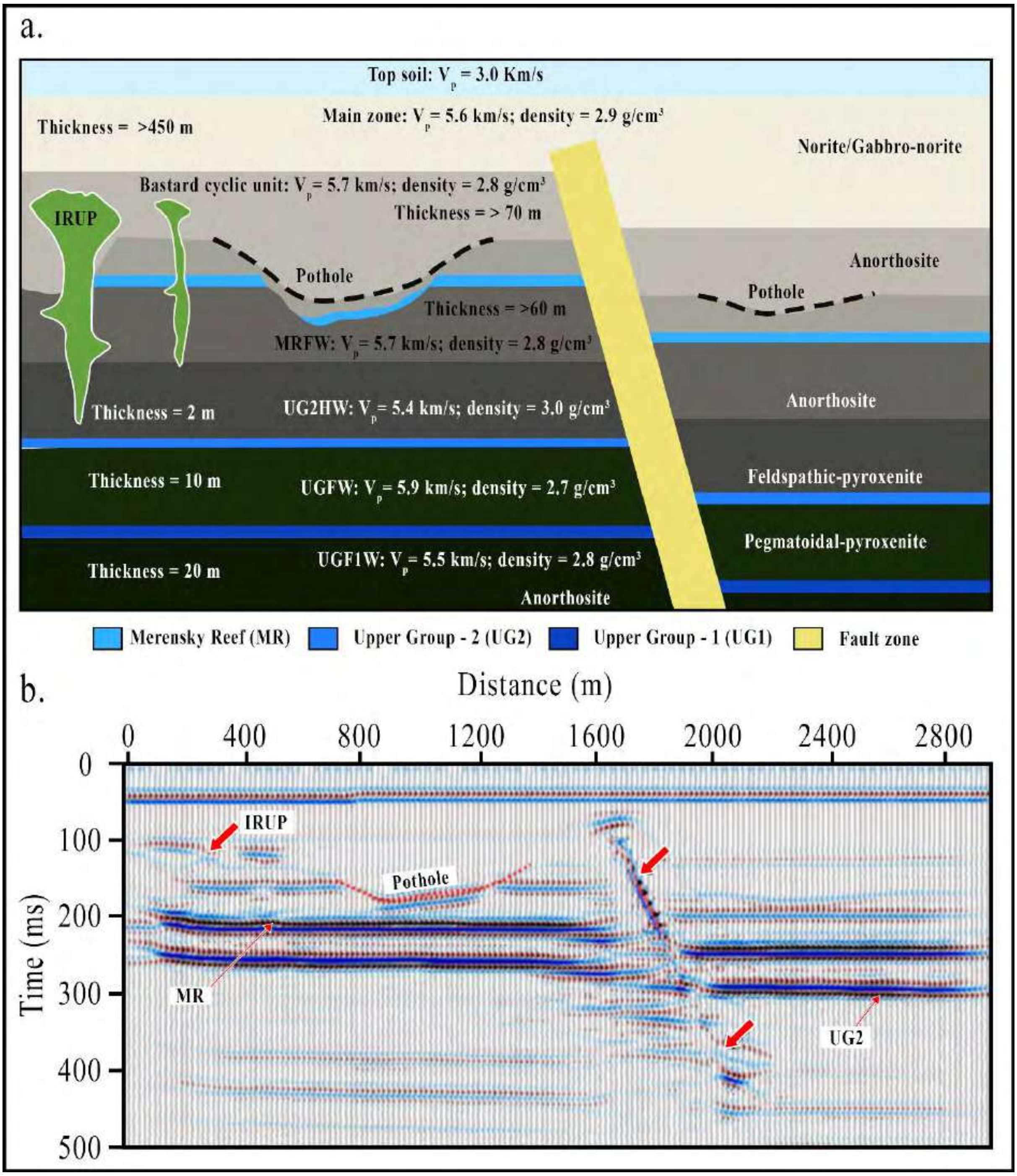

Figure 10: *a) Finite difference model for the Maseve mine. The model shows the two-target mineralisations (MR and UG2) and geological structures (fault, potholes, and IRUP). The velocity and density of the rocks are noted b) Post-stack time migrated section (depth converted) derived from synthetic data showing the imaging of the Merensky Reef, UG2, fault, and IRUP.*

To further constrain the seismic interpretation, we used the densities and velocities measured in phase one to calculate the acoustic impedance contrast and calculate the reflection time series that we further convolved with a 100 Hz Ricker wavelet to generate a synthetic trace (Figure 11).

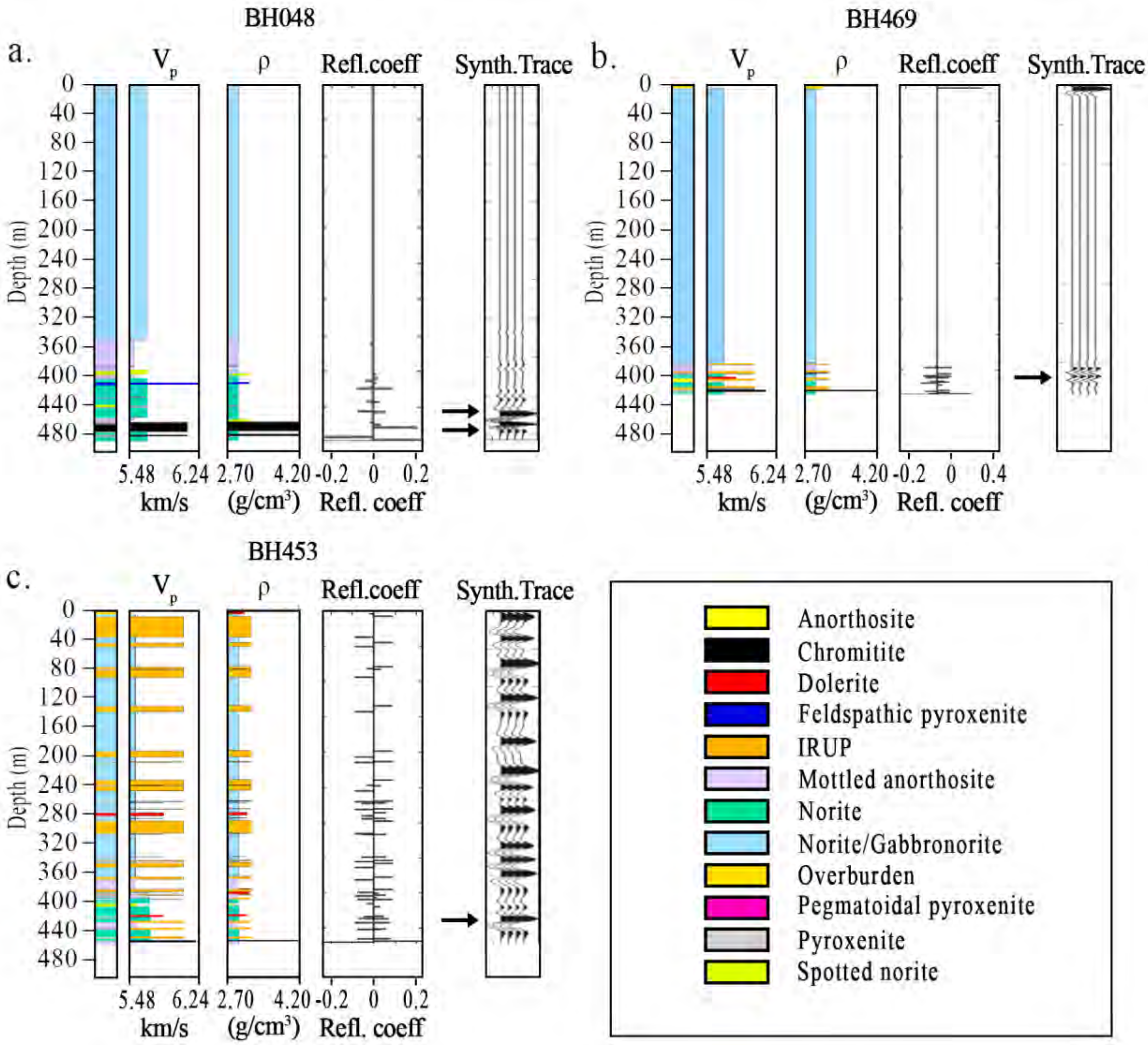

Figure 11: *Borehole data from (see Figure2) a) BH048, b) BH469, and c) BH453 at Maseve mine. Reflection depth series was calculated using the velocity and density. We then produced a synthetic trace by convolving the reflection time series with the Ricker wavelet of 100 Hz. As shown, the Merensky Reef, UG2 and UG1 should be reflective by their hanging wall and footwall due to the sharp acoustic impedance contrasts. MR: Merensky Reef; UG2: Upper Group 2; UG1: Upper Group 1. IRUP: Iron rich ultramafic pegmatite.*

Multiple boreholes were provided by the mine, with this study focusing on the boreholes situated proximal to profile T3. The boreholes (BH048 and BH469) cross the two target deposits (Merensky Reefs and UG2) and the UG1. As stated by Rapetsoa et al. (2022), average velocities down to 500 m are around 5600 m/s and average densities are 3100 kg/m^3. The standout feature is the increase in velocity at 420 m due to interlayered pyroxenite (Merensky Reef), and norite (hangingwall and footwall). This increase causes a change in the acoustic impedance, therefore a point of reflectivity. A more prominent contrast is seen at depths of 480 m and 495 m due to the highly dense chromitite layers of the UG2 and UG1 generating acoustic impedance contrasts, hence noticeable reflections on the synthetic traces. BH453 (Figure 11c) shows evidence of other geological structures (e.g., IRUPs, dolerite dykes and sills) that are expected in the study area.

RESULTS AND INTERPRETATION

Seismic data acquired in phase 2 generated improved results in terms of structural imaging when compared to phase 1. The primary improvement was achieved by altering the seismic designs, with a better set-up of the land streamer, small sampling rate (1 ms), and better understanding of the geology of the area. In general, the seismic data quality is good, and the seismic sections exhibit well-defined reflections (some associated with orebodies) and distinct fault compartmentalization. Numerous faults of many orientations affecting the orebody were clearly mapped below the tunnel floor.

Figures 12a-c show the examples of seismic sections from phase 2. Identifying the geological cause of the reflections seen in seismic sections was challenging as there was no borehole control to constrain the interpretation, especially in the western portion of the study area along the incline tunnel. The side tunnels along the incline and development tunnels where the seismic receivers were located influenced the recorded seismic wave-field. The geologically complex rocks hosting the tunnels may have also resulted in energy contributions coming from the sides and above the mining level where the tunnel profiles are located.

Figure 12a shows the seismic section from profile T3a. The section is dominated by normal and reverse faults with various dips, throws and orientations. The most dominant feature in the section is the north-south trending fold, which is overprinted by steeply dipping (> 60°), north-northwest and north-northeast trending faults. Folding and faulting is interpreted to affect UG2 (indicated by green arrows) and the underlying strata, which is critical for future mining in the area. The seismic section suggests that the throw has displacement less than 20 m, down to 2 m.

Figure 12b is the seismic section from T3b, which was acquired using the planted geophones along.the incline tunnel. The seismic section is less structurally complex than T3a, indicating that the use of planted geophones undersampled a number of structures present in the region. However, the seismic data show good imaging of a major fault (> 150 m throw), which is north-northwest trending. The seismic section shows that the fault is normal and listric in form; crosscutting and offseting the UG2 (green arrows) and underlying horizons, thus constraining the relative age of the fault displacement to post-UG2 deposition.

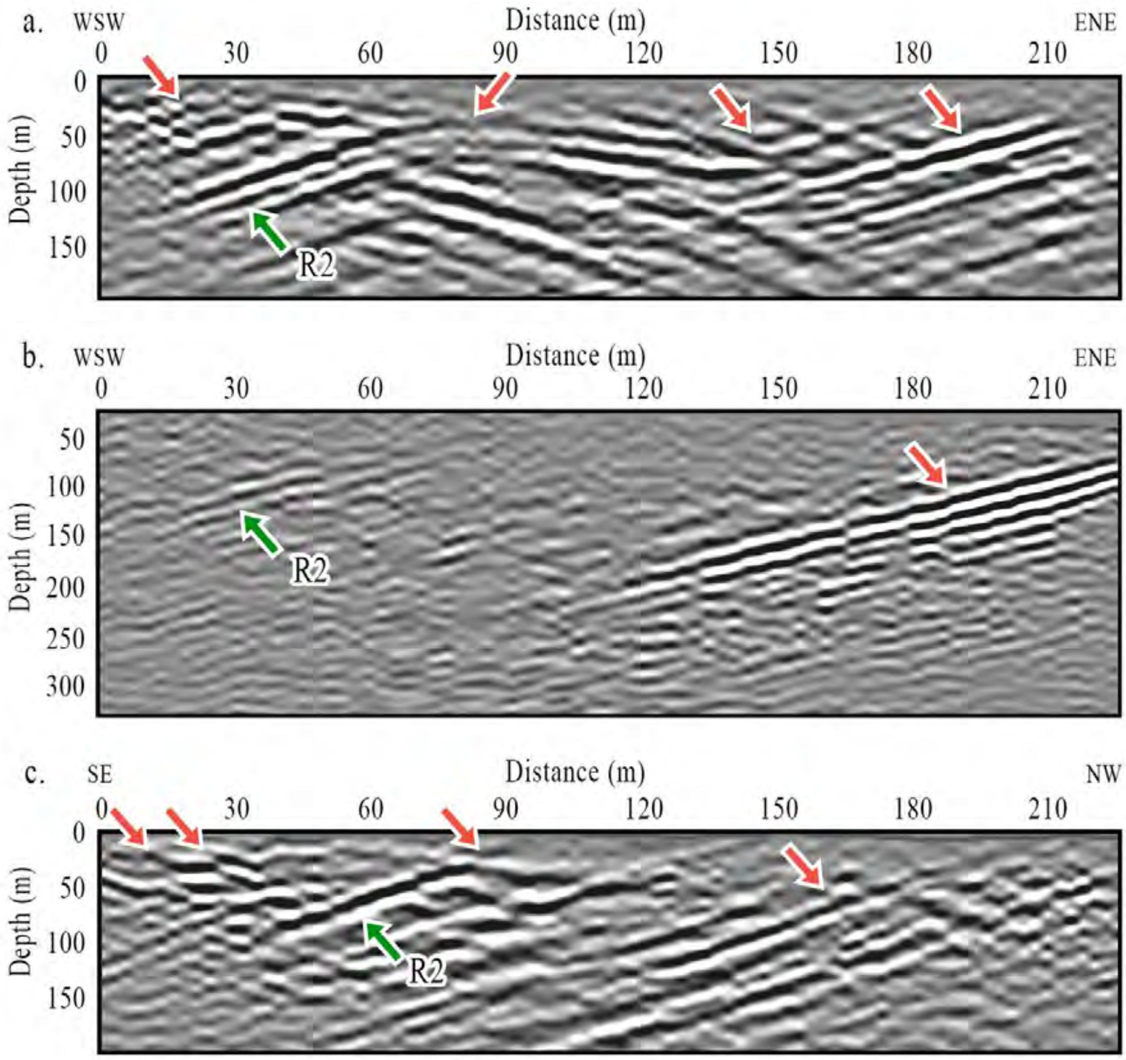

Figure 12: *Depth converted seismic profile a) TP3a acquired using a land streamer, b) TP3b profile acquired using spiked geophones and, c) TP4b profile acquired using a land streamer showing the imaging of the UG2 (green arrows) and geological structures such as faults and dykes (red arrows).*

Figure 12c shows the depth converted seismic section of T4b which has been filtered post-stack to enhance the quality of the data. The seismic section images steeply dipping major (> 10 m throw) and minor (< 10 m) faults cross-cutting and displacing the stratigraphy and orebodies (mainly UG2). The green arrow in Figure 12c indicates the imaging of the UG2 horizon. The dotted and solid lines indicate faults and dykes, respectively. The dykes are interpreted in the data as diffractions or as highly attenuated seismic events that crosscut the strata. Faults, on the other hand, are associated with discontinuities in the data. Dykes are also observed in the fault zones as attenuated high-amplitude events.

Figure 13a, b shows the migrated stack sections of surface profiles (SP2 and SP3) correlated with the downhole logs. R0 correlates with the sharp changes in velocity and density due to contact between the overburden and depth to bedrock. According to BH048 log data, two distinct acoustic impedance contrast regions at 425 and 480 m depth (see Figure 11) correlate with reflections R1 and R2 on the migrated section of SP2 (Figure 13a). The reflections R1 and R2 show a gentle dip northwest of SP2 and are observed at depths between 400 and 450 m. The reflections have an out-of-plane nature as a result of the ~50 m offset of boreholes and seismic profiles. The reflections seen on the synthetic traces and seismic sections are correlated to be of the same origin but are seen at different depth due to the variability of the reflector geometry across the survey area. The mineralisation is visible as a high amplitude reflector in the seismic data. The strong impedance contrasts are associated with the Merensky Reef and UG2.

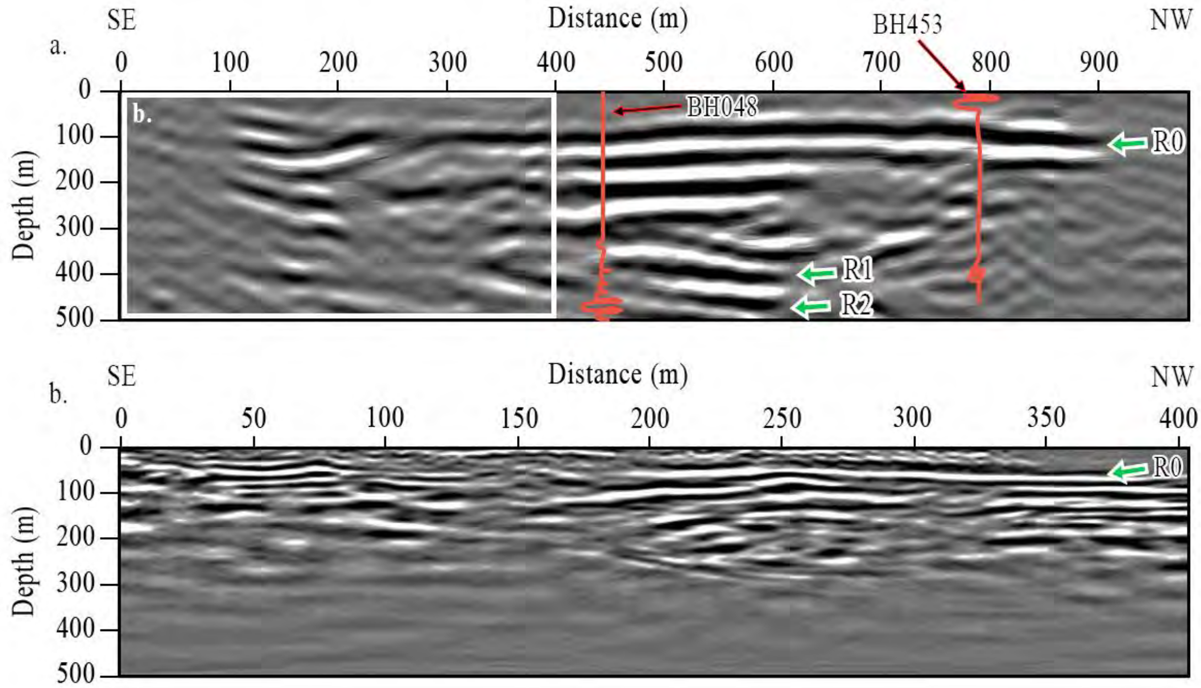

Figure 13: *Depth-converted migrated stack section of a) SP2, with projected synthetic traces from the BH048, showing a depth discrepancy of ~25 m which is as a result of the borehole being ~50 m away from the seismic profile. b) Depth-converted migrated stack section of SP3 showing clear reflections in the first 200 m. Green arrows mark different reflections detailed in the text.*

Figure 14 shows integrated interpretation of in-mine and surface P-wave tomograms and seismic sections. The velocities from the in-mine and surface tomograms (Figure 14a,b) show a good match with the published velocities(e.g., norite and pyroxenite; Manzi et al., 2020), borehole stratigraphy, and complement P-wave reflectivity observed on the final stacked sections (Figure 14c). Figure 14c shows a migrated stack section of surface profile SP2, with the P-wave velocity model imposed. The depth to the bedrock reflection corresponds with the high velocity region (4000 – 6500 m/s) on the P-wave model. In general, the data suggest that the top layer contains low velocities due to fracturing, which is imaged by reflection seismics (Figure 14b). Based on the integrated refraction tomograms, existing boreholes (see Figure 2), geological models (see Figure 10a) and tunnel observations (i.e., outcropping MR and UG2), the stratigraphy exhibits variable dips due to folding and faulting.

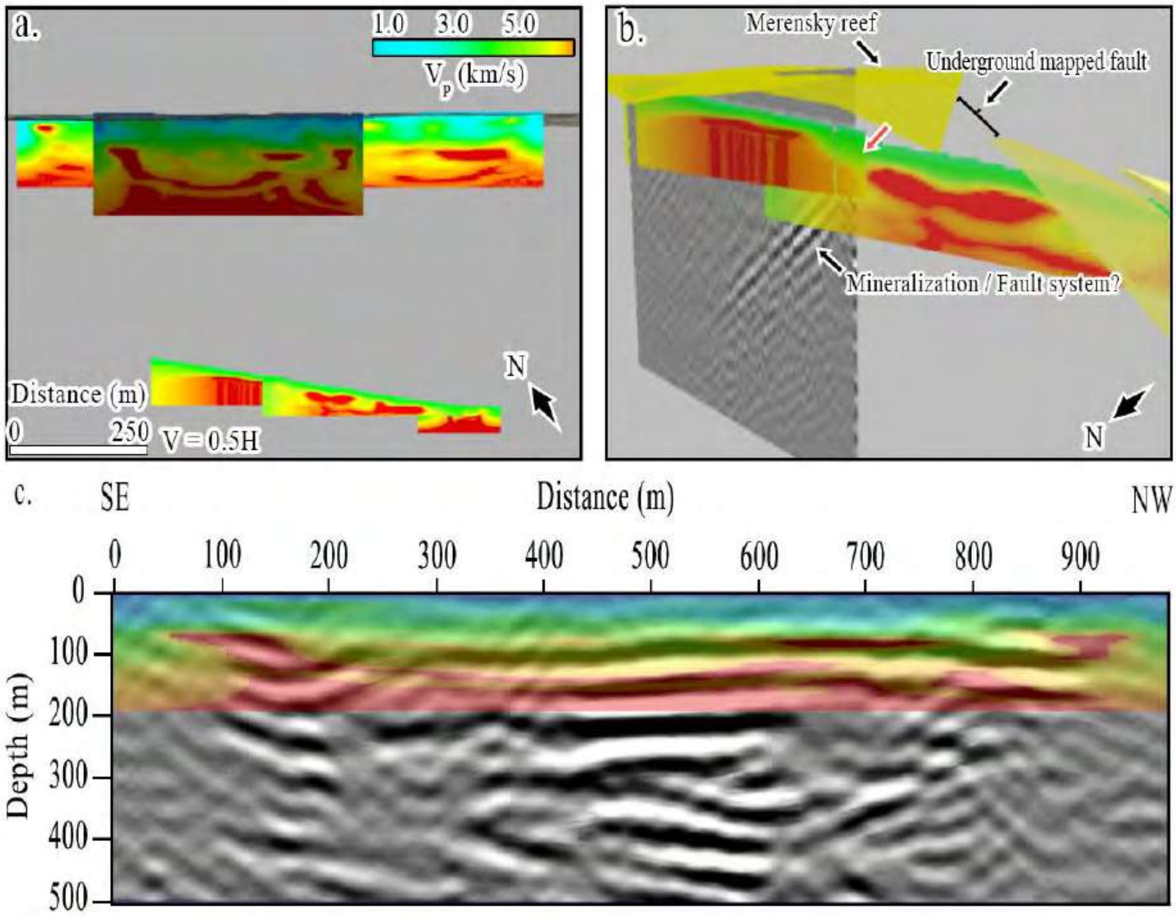

Figure 14: *a) P-wave velocity model for surface and underground seismic experiments. b) P-wave velocity model superimposed on a migrated seismic section and geological model of the Merensky Reef (yellow surface). c) Overlay of P-wave velocity model on top of the migrated seismic section from SP2.*

DISCUSSION

Mineral exploration

The study demonstrated the use of seismic methods to delineate mineralisation and the associated geological structures. The study area is structurally complex with geological features such as faults, dykes, sills, and IRUPs that crosscut the mineralisation. Figure 15 shows 3D views of the seismic sections of surface (SP3) and underground profiles (P5-P7) (Figure 15a) integrated with borehole data (Figure 15b).. The data exhibit strong reflections and geological structures at depths down to 590 m from the surface. The borehole data show the intersections of the Merensky Reef and UG2 at depths of 515 m and 570 m, respectively. It is clear from Figure 15b that the reflections R1 and R2 are generated by the mineralisation, and show possible extensions to the east and west of the study area. This study is encouraging and opens possibilities for reflection seismic to be used for mineral exploration in noisy mining environments.

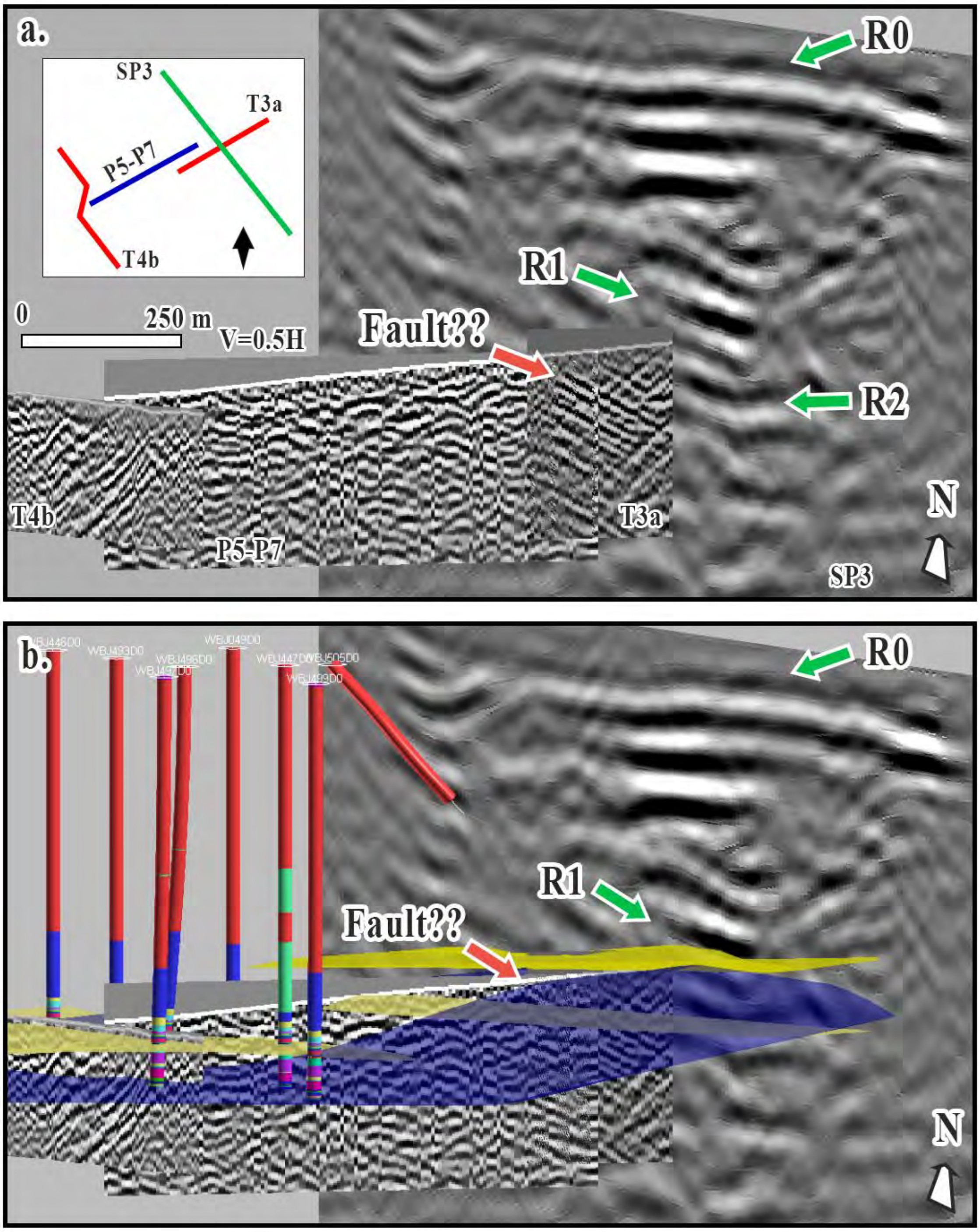

Figure 15: *a) 3D views of the migrated stack section of underground seismic profiles (P5-P7, T3a, and T4b) and surface profile SP2. Insert shows the perspective view of the 3D models. b) 3D views with borehole data and Merensky Reef (yellow surface) and UG2 (blue surface).*

Sensors and seismic source

The use of a seismic land streamer with 4.5 Hz 1C geophones generated clear results, however some traces were still dominated by mine infrastructure generated noise (see Figure 3a). The next step is to use sensors on the land streamer that are less sensitive to electrical noise. One option will be to use a three-component (3C) micro-electromechanical system MEMS-based seismic land streamer (Brodic et al., 2017) . This has three advantages over our land streamer: (1) it records three component data; (2) it provides improved coupling with the tunnel floor; (3) it is MEMS-based, and less sensitive to electrical noise in the noisy environment.

The use of underground mine infrastructure for active-source seismic surveys implies working in restricted spaces, inevitably imposing limitations on the selection of the seismic source. From one perspective, the seismic source selected must be versatile, easy to transport, operate and move in different mine tunnels and drifts at the desired depth. This poses considerable restrictions to the sources that can be used inside the mine, given the need to comply with established mine safety protocols. For example, sources such as vibroseis trucks and those that use gasoline engines, like some accelerated weight drop sources, cannot be used inside the mine. In this study, a sledgehammer hammer was used with success, however the hammer is an impulsive source, and it does not generate broadband frequencies. It also has a limited depth of penetration. For example, the sledgehammer allowed for imaging of structures to depths down to 200 m.

CONCLUSION

The in-mine surface seismic survey acquired at Maseve mine was processed using careful processing approaches to eliminate mine-generated noise. These techniques enhanced near-surface reflections and boosted the signal of the dataset. The tunnel seismic experiments proved that the application of seismic methods using proper designs and adequate seismic equipment can be useful in imaging platinum deposits and geological structures in deep mines. Precise data processing techniques were critical in enhancing the reflections and suppress coherent noise generated by infrastructure. The simple surface experiments not only proved to be efficient but illustrated the capability of small-scale seismic surveys to directly image the subsurface. The use of a small-scale seismic survey can add value in active mining environments for exploration purposes.

In general, the seismic data show the mapping of a large number of faults and dykes with a wide variety of orientations, dips (55° - 88°), and throws (1 - 25 m). These structures crosscut the UG2 and MR horizons, indicating that these structures were active post MR deposition. Comparing the mine geological structures (produced from borehole) with seismically defined geological structures showed that the in-mine seismic data are delineating more structures than the borehole data, suggesting that the borehole data undersampled a number of faults and structures present at the mine site. This implies that taking only a borehole defined model, or mapping model, as a true geological model may be detrimental to mine planning and designs. However, it should be noted that borehole information is critical in confirming the positional accuracy of the MR and UG2. Thus, these two datasets (reflection seismic and geology) should always be integrated for reliable interpretation.

REFERENCES

Ahmadi, Omid, Christopher Juhlin, Alireza Malehmir, and Mie Munck. 2013. "High-Resolution 2D Seismic Imaging and Forward Modeling of a Polymetallic Sulfide Deposit at Garpenberg, Central Sweden." *Geophysics* **78** (6): 339–50. https://doi.org/10.1190/geo2013-0098.1.

Basson, I.J. 2019. "Cumulative Deformation and Original Geometry of the Bushveld Complex." *Tectonophysics* **750** (January): 177–202. https://doi.org/10.1016/j.tecto.2018.11.004.

Brodic, Bojan, Alireza Malehmir, Mehrdad Bastani, Suman Mehta, Christopher Juhlin, Emil Lundberg, and Shunguo Wang. 2017. "Multi-Component Digital-Based Seismic Landstreamer and Boat-Towed Radio-Magnetotelluric Acquisition Systems for Improved Subsurface Characterization in the Urban Environment." *Near Surface Geoscience*, August, 8.

Eaton, David W., Bernd Milkereit, and Matthew H. Salisbury. 2003. *Hardrock Seismic Exploration*. Geophysical Developments Series, no. 10. Tulsa, OK: Society of Exploration Geophysicists.

Juhlin, C., J. Lindgren, and B. Collini. 1991. "Interpretation of Seismic Reflection and Borehole Data from Precambrian Rocks in the Dala Sandstone Area, Central Sweden." *First Break,*. European Association of Geoscientists & Engineers,. https://www.earthdoc.org/content/journals/10.3997/1365-2397.1991002.

Ledwaba, L S, J Scheepers, and R J Durrheim. 2012. "ROCKBURST DAMAGE MECHANISM AT IMPALA PLATINUM MINE." *The Southern African Institute of Mining and Metallurgy*, **20**. https://www.semanticscholar.org/paper/Rockburst-damage-mechanism-at-Impala-Platinum-Mine-Ledwaba-Scheepers/f1bedda21a9fb68c70cd83e17fea41c65bf8a34c.

Liszicasz, George, Azer Mustaqeem, Moin Raza Khan, Muhammad Amir Bhatti, and Abid Hussain. 2013. "SFD® (Stress Field Detection) and Its Integration with Seismic in Kharan Forearc Basin and Its Implications for Hydrocarbon Exploration in a Frontier Area; #90208 (2014)."

Malehmir, Alireza, Musa Manzi, Deyan Draganov, Ute Weckmann, and Esben Auken. 2020. "Introduction to the Special Issue on 'Cost-effective and Innovative Mineral

Exploration Solutions.'" *Geophysical Prospecting* **68** (1): 3–6. https://doi.org/10.1111/1365-2478.12915.

Manzi, Musa S.D., Gordon R.J. Cooper, Alireza Malehmir, and Raymond J. Durrheim. 2020. "Improved Structural Interpretation of Legacy 3D Seismic Data from Karee Platinum Mine (South Africa) through the Application of Novel Seismic Attributes." *Geophysical Prospecting* **68** (1): 145–63. https://doi.org/10.1111/1365-2478.12900.

Méndez-Hernández, Efraín. 2003. "A Brief History and Recent Advances in Seismic Technology for the Petroleum Industry in Mexico."

Rapetsoa, Moyagabo K., Musa S.D. Manzi, Michael Westgate, Mpofana Sihoyiya, Ian James, Emmanuel Onyebueke, Phumlani Kubeka, Raymond J. Durrheim, and Thabang Kgarume. 2022. "Cost-effective In-mine Seismic Experiments to Image Platinum Deposits and Associated Geological Structures at Maseve Platinum Mine, South Africa." *Near Surface Geophysics*, June, nsg.12216. https://doi.org/10.1002/nsg.12216.

Scheiber-Enslin, Stephanie E., and Musa Manzi. 2018. "Integration of 3D Reflection Seismics and Magnetic Data for Deep Platinum Mine Planning and Risk Mitigation: A Case Study from Bushveld Complex, South Africa." *Exploration Geophysics* **49** (6): 928–39. https://doi.org/10.1071/EG17083.

Sehoole, Lebogang Tshepiso Charmaine. 2020. "Application of 3D Seismics to Enhance Mapping of Potholes in the Western Bushveld Complex, South Africa."

Suotang, Fu, Wang Daxing, and Yao Zonghui. 2020. "Progress of 3D Seismic Exploration Technologies and Oil and Gas Exploration and Development Performance in the Loess Tableland Area of the Ordos Basin" **25** (1).

9. Paper III: Multi-geophysical methods for characterizing fractures in an open pit mine, western Bushveld Complex, South Africa

Moyagabo K. Rapetsoa[1*], Sikelela Gomo[1], Musa S. D. Manzi[1], Ian James[2], Jureya Dildar[1], Mpofana Sihoyiya[1], Ndamulelo Mutshafa[1], Raymond J. Durrheim[1]

[1]School of Geosciences, University of the Witwatersrand, Johannesburg, Private Bag, Wits, 2050, Republic of South Africa

[2]Southern Geoscience Consultants, West Perth, WA, Australia

Acknowledgements

We thank Tharisa mine for providing access to the site to conduct the geophysical surveys and granting permission to publish the work. The authors also thank Wits Seismic Research Center for funding this work. We thank several PhD and MSc students from the University of the Witwatersrand, Johannesburg who took part in the data acquisition stage. We also thank Engineering & Exploration Geophysical Services CC for supporting us with the geophysical equipment, and Schlumberger for the continued support with the licences for Petrel. HiSeis Pty Ltd. and Petrosys are highly appreciated for sponsoring the licenses for Globe Claritas processing software.

Conflict of interest

The authors declare that they have no known competing financial interests or personal relationships that could influence the work reported in this paper.

ABSTRACT

In the Bushveld Complex (BC), South Africa, open pit mines are faced with a challenge of rock slope stability due to geological structures (fractures, faults and dykes) that compartmentalise the rock mass. Geophysical surveys (seismics, magnetics and electrical methods) were conducted in a 0.2 km^2 area at Tharisa mine, with the goal to delineate fractures that may be potential conduits for water migration into the pit. Special processing techniques were applied to the dataset to obtain good quality seismic, magnetic and resistivity models. The P-wave velocity models show distinct low velocities in the center of the seismic profile, indicating the presence of weak zones associated with faulting or fracturing. Reflection seismic method was used to image the deeper discontinuities and mineralization contacts. Near-surface reflections are observed throughout the profiles and are correlated with the contact between the chromitite and host rock. Ground magnetic surveys were conducted to delineate dykes and fractures. De-trending and de-culturing techniques were applied on the magnetic data for correcting regional and temporal variations. The low magnetic regions indicate the presence of fracture systems in the subsurface, while the high magnetic region is correlated with the dolerite dyke that crosscuts the pit. The electrical resistivity tomography exhibits linear low resistivity contrast zones that differentiates between the fractured and undisturbed hard rock at an estimated depth of 4 – 10 m. Resistivity shows discontinuities that suggests the presence of fracturing and dyke-host rock contacts. Correlation between magnetics, P-wave velocity models, resistivity section and seismic data is evident when overlaying the different datasets, implying that the low magnetic regions are highly weathered and prone to fracturing. The integration of geophysical data is encouraging, because it was able to image the depth to the bedrock, fractures within the host rock and dyke in a complex mining environment.

Keywords: Fractures, Water migration, Open-pit mine, Groundwater, Imaging

Data availability statement

The data presented in this study are available upon request from the corresponding authors. The data are not publicly available due to privacy restrictions. Petro-physical data can be found on the website of The Council of Geoscience South Africa (https://maps.geoscience.org.za/portal/apps/sites/#/council-for-geoscience-interactive-web-map-1).

INTRODUCTION

Tharisa mine is an open pit (Figure 1a) mine located in the North-west province of South Africa, 35 km east of Rustenburg. The mine is located in a hard rock environment within the Bushveld Complex (BC). The BC exhibits joints of tectonic origin, with varying orientation (planar and non-planar) and intensity across the BC. Joints are often coupled with other geological structures such as dykes, veins and faults (Figure 1b). Systematic joints (planar) are a set of parallel joints spaced evenly apart (Perritt & Roberts, 2007; Roberts & Clark-Mostert, 2010). Majority of the joints in the study area are sub-vertical and can be divided into two sets (Figure 1c), parallel sets (cyan, green and blue) and perpendicular sets (pink, yellow, and red) to a fault zones that crosscut the pit and parallel to a dyke (Figure 1b). Non-systematic joints occur randomly in the study area due to mine blast stress regime. The sub-vertical joints intersect the sub-horizontal interlayering planes of the Middle Group chromitites.

Most open pit mines are faced with a challenge of rock slope stability due to geological structures that cause discontinuities of the rock mass. The fractures introduce mining, engineering and hydrogeological challenges. The development of the mine promotes the increase in fractures through blasting and excavation of the bedrock. Fractures may act as conduits for migration of groundwater (e.g., water from rivers, and aquifers) into the pit, which floods the pit and causes delays in production (Titus et al., 2009; Ofterdinger et al., 2019).

Near-surface geophysical methods have grown widely in addressing mining, engineering and environmental problems, e.g., mineral exploration, detection of buried pipes, sinkholes, and fracture mapping. (Dahlin, 1996; Van Schoor, 2002; Amoush & Mashagbeh, 2009; Kerrigan, 2013; Pazzi et al., 2018). The need to delineate the fractures and understand the migration of water into the mine pit has led to the development of multi-geophysical and hydrological acquisition setups for gathering data in the noisy mine environments. The main objectives of this study are: (1) to use geophysical methods to locate and characterize fractures in an open pit mine, (2) to understand the ground water migration into the pit and associate it with the geological structures around the pit, (3) To delineate the depth of the mineralization and its associated geological structures beyond the mined out areas, (4) to address challenges encountered in geological complex and mine noisy environment when acquiring geophysical data.

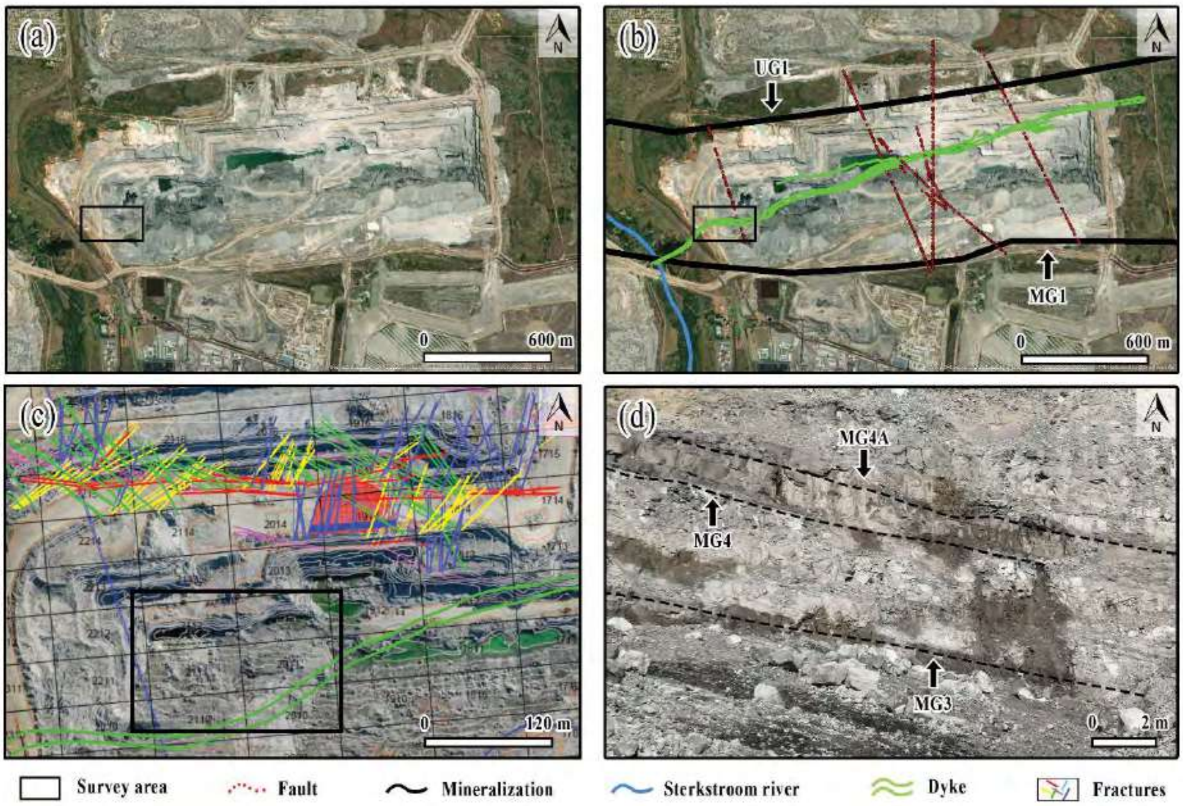

***Figure 1**: (a) Aerial photo of Tharisa mine east pit. (b) Major dyke (green) and faults (red) cross-cutting the west pit at Tharisa mine. Sterkstroom River (blue) divides the mine into a west pit and an east pit. The mineralization (black: UG1 and MG1) runs parallel to the ends of the east pit (c) Mapped fractures (red, blue, green, pink, yellow, and cyan) at the Tharisa mine with varying orientations. (d) Sidewall, showing inter-bedding and cross-cutting joints. Dark areas are areas where water is seeping into the pit.*

The use of multi-geophysical methods (seismics refraction (SRT) and reflection, magnetics and electrical resistivity tomography (ERT)) to image structures depends on multiple factors such as the survey design (receiver and source positions), physical properties of the host rock, geometry (e.g., size and depth), structural characteristics of the target, and the mine noise levels. In this study we also demonstrate the challenges faced by the geophysical methods (i.e. magnetics, SRT and ERT) to characterize near-surface fractures and mineralization in a mining area with large infrastructure, trucks and electrical powerlines that cause interfering noise during acquisition. This study forms part two of the three part integrated geophysical, hydrogeology and geochemical studies to further unravel and determine the source of water that migrates into the pit. Gomo et al. (2023), presents an integrated geophysical approach to delineate boulders in an active open pit mine as part I. Part III of the study (Dildar et al., 2022) focused on integration of the hydrogeology and geochemical data with near-surface geophysical methods.

GEOLOGICAL SETTING AND THARISA MINE

The Bushveld Complex (BC) covers an area of about 65 000 km^2 (Figure 2), typified by a shape of a broad oval, with a long extension of 375 km east-west and 300 km wide to the north-south. The BC is the largest mafic-ultramafic layered igneous intrusion, divided into five limbs that are emplaced on the Transvaal Supergroup at 2058.9 ± 0.8 Ma, with a thickness of 9 km.

The geology and stratigraphy of the Bushveld Complex (Figure 2a,b) is well documented by several authors (e.g., Eales & Cawthorn, 1996; Kinnaird, 2005; Wilson, 2005; Cawthorn, 2015; Basson, 2019).

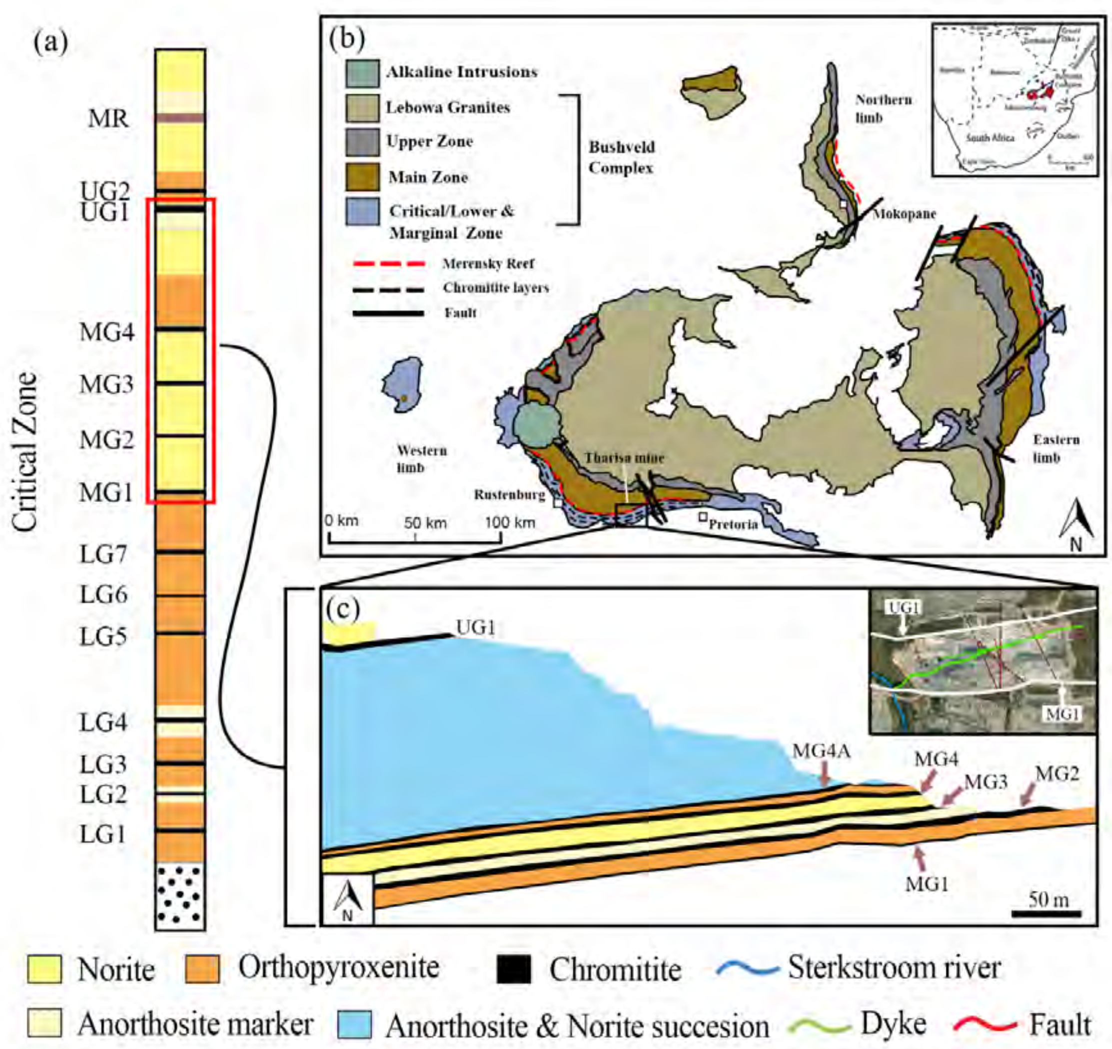

Figure 2: *(a) Stratigraphic column of the critical zone, highlighting the chromitite layers that are exploited at the Tharisa mine. (b) General geological map of the Bushveld Complex showing major faults, economical horizons, and the location of the study area. (c) Simplified geology of the Tharisa mine, with an insert showing the location of the far end mineralizations (white: MG1 and UG1) that are being exploited at the mine, together with geological structures and a river that crosscut the east pit.*

The mineralization at Tharisa mine is situated in the critical zone (CZ) of the Bushveld Complex. The mine is split into two pits (east pit and west pit) by the Sterkstroom River (Figure 1b) and exploits the Middle Group (MG) chromitites (Figure 2c: MG4, MG3, MG2 and MG1). With the UG1 being 165 to 18 m above the MG. Mining of UG1 happened in the past, with the shallow MG1 being mined underground. The mine plans on having underground operations in the future to exploit the deeper MG2 and MG4 mineralizations. The CZ is made up of pyroxenites, anorthosites, norites and stringers of chromitite. The general dip of the mineralization is between 9° and 15° to the north, with the thickness of the MGs and UG1 ranging from few centimetres to 3 m. The geological structures of the Tharisa mine region have been interpreted using aeromagnetic, drilling data and open pit observations (Lotheringen et al., 2016). An approximately 15 m thick, NE-SW trending and near-vertical dyke that crosscuts the west pit is the most dominant feature mapped by the aeromagnetic data (Figure 1b). Multiple faults are mapped within the pit and crosscut the pit with a predominant strike of NNW-SSE, which coincides with the planes of weaknesses that reactivated during the emplacement of the Bushveld Complex. The fractures in the Bushveld Complex are known to be associated with dykes and faults (Bumby et al., 2012; Hartzenberg & Plessis, 2014). The fracturing is observed on the northern part of the pit and our study focuses on characterizing the fractures on the southern part of the pit.

GEOPHYSICAL DATA

In this section we summarize the physical properties, acquisition and processing of the seismic, magnetics and resistivity data that were collected at Tharisa mine.

Data acquisition

Prior to data acquisition, appropriate acquisition parameters need to be assessed, together with the expected response of the target through forward modelling. Forward modelling can also assist in validating the interpretation of the dataset and provide information for mineral exploration and risk assessment (Malehmir et al., 2013; Manzi et al., 2017; Maries et al., 2020; Rapetsoa et al., 2022).

Physical properties

To complement the geophysical data, rock samples and borehole data were collected from the Tharisa mine. To the best of our knowledge the borehole data only include the geological logging. There is no downhole petro-physical data available for the study site. To complement the borehole data, we have gathered more petro-physical data from the Council of Geosciences database and measurements from Sepato (2015). The data used from the above mentioned database were filtered to boreholes that are closer to Tharisa mine. The laboratory measurements in this study were P-wave velocity, bulk density and magnetic susceptibility measurements, while resistivity measurements where sourced from the literature (Maré, 2022). The samples were norites, anorthosites, chromitite and pyroxenites, and the resistivity measurements for pyroxenite were not found in the literature. The collected samples were prepared for bulk density, P-wave velocity and magnetic susceptibility measurements at room temperature and pressure using ultrasonic frequencies. The ideal conditions to measure the samples is under elevated stress (~ 20-60 MPa) to mimic the in-situ environments, but due to a lack of equipment in our laboratory, the measurements were not done at elevated temperature and stress. A high frequency signal is produced by the transducers and passes through the rock sample. The signal is observed through the oscilloscope and the waveform is recorded by the computer. P-wave velocities are estimated from the measured travel times of the high frequency acoustic pulses through the samples. Bulk densities were collected using the immersion techniques, were sampled were suspended in pure water and the density of the sample was estimated by the use of Archimedes principle.

Seismics

The seismic data for this study were collected in October 2021. Two seismic profiles were collected with a total length of 150 m: one of the seismic profiles (SP1 96 m long) was inside the pit, while SP2 (46 m) was collected at the edge of the pit. As the study area is inside the pit, where certain areas are hard rock, a combination of different geophone setup was used.

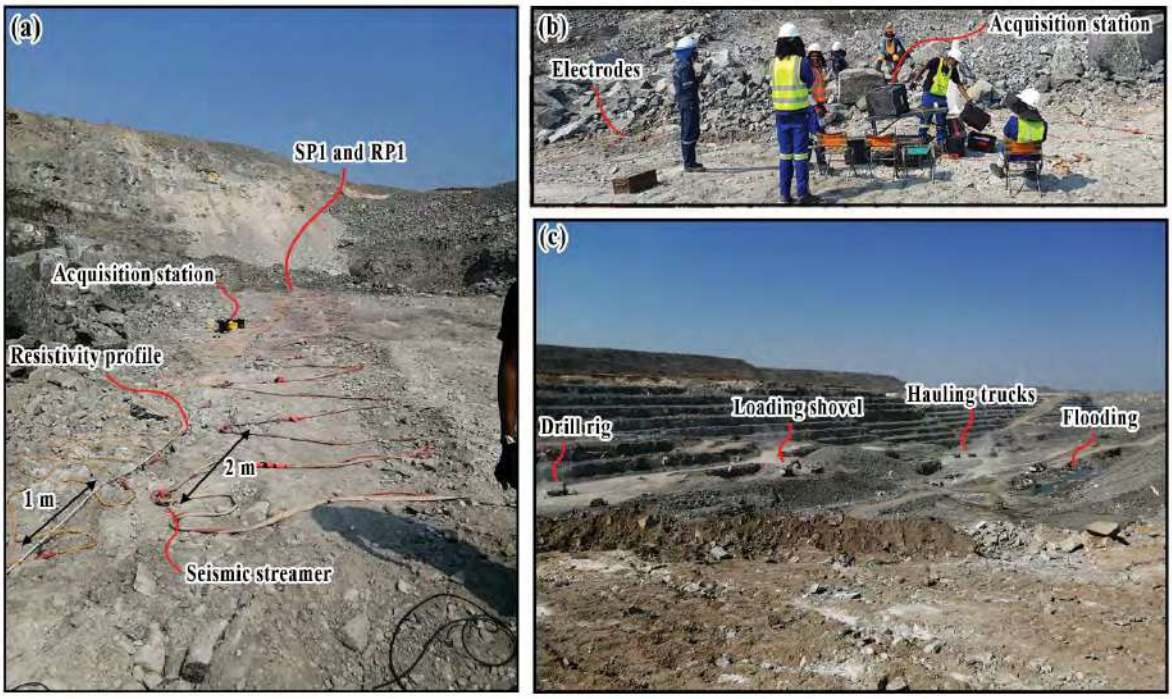

Figure 3: *(a and b) Field photo showing the acquisition setup for seismic and resistivity profiles inside the pit using a seismic land streamer. (c) Field conditions during data acquisition at Tharisa mine, with mining activity near seismic profile.*

A land streamer (4.5 Hz) and spiked geophones (14 Hz) were used along SP1 (Figure 3a and b), with a receiver spacing of 2 m. For SP2, 14 Hz 1C spiked geophones were used, with a receiver spacing of 1 m (Table 1). The seismic profiles (Figure 4a) were setup to be perpendicular to the faults and fractures systems observed on the aeromagnetic data in and around the pit, with the main dyke being parallel to the lines (Figure 4a). For safety reasons, source and receiver positions were limited by the active mine roads, therefore the length of some of the seismic profiles were shorter than desired. Although multiple profiles were collected (named SP1-SP8), this study focuses on the data obtained from SP1 and SP2 due to their location and essential for studying the fracture system of the east pit.

***Table 1**: Main reflection seismic data acquisition parameters*

Profiles	SP1	SP2
Survey parameters		
Acquisition type	Fixed straight line	Fixed straight line
Acquisition system	Geometric Geode	Geometric Geode
Receiver frequency	4.5 Hz and 14 Hz	14 Hz
Type of base	land streamer and 7 cm spike	7 cm spike
No. of receivers	48	48
Receiver spacing	2	1 m
Source	6.3 kg sledgehammer	6.3 kg sledgehammer
Source spacing	2 m	1 m
Profile length	96 m	50 m
Recording length	1000 ms	500 ms
Sampling interval	1 ms	0.25 ms

Prior to collecting the data, we first performed a test to compare the seismic sources (6.3 kg sledgehammer and a 24 kg accelerated weight drop (AWD)). From the test, it was evident that the sledgehammer was suitable for this study, as it preserved the near-offset traces, while the AWD over drives the near-offset geophones by having powerful source impulse. The sledgehammer was also chosen for its applicability in uneven terrains. Noise conditions were different from profile to profile. When acquiring the data in the open pit, there was drilling, dump trucks and loader (Figure 3c) working near the profile. We did not have permission to acquire seismic data during night time, therefore all our seismic profiles were collected during working hours (08:00 and 17:00) where the mining activity and traffic from the main road were high. The receiver and shot positions (eastings, northings and elevation) were surveyed using a real time Differential Global Positioning System (DGPS) device. The shots were recorded at every 2 m for SP1 and 1 m for SP2, four shot records were acquired at every shot position using the sledge hammer and vertically stacked to increase the signal-to-noise ratio (SNR). We analysed and tested different sampling rates, with SP2 being recorded first with a sampling rate of 0.25 ms, while SP1 was recorded with a sampling rate of 1 ms. A sampling rate of 1 ms was chosen for the rest of the seismic profiles, as it provided better results with respect to the high frequencies and spurious frequencies. A total of 96 shots and 4608 traces were generated after vertically stacking the repeated shots.

Magnetics

A three phased five-day field survey in 2021 was conducted to collect total magnetic field data at Tharisa mine. The survey started with an assessment of the pit to locate mine benches that have seepage of water and a dyke, which are a guide to the location of fractures (Figure 1d). The magnetic survey covered a total area of 16300 m^2 using two G856 proton precession magnetometers and a G859 cesium vapour magnetometer. The G856 magnetometers were used as base stations and placed at two different locations (with no cultural noise), mounted on a 2.5 m vertical aluminium pole. The magnetometers (G856) were set to record stationary readings at every 30 seconds interval, the data were then inspected and compared for spikes in the diurnal curve. The G895 magnetometer was used as a rover for acquisition of the magnetic profiles. The GPS antenna was vertically mounted ~ 3 m and the magnetic sensor was mounted ~ 2 m. The three grids (Figure 4b) were surveyed in a fast "walking mode", with the rover magnetometer (G859) carried on a non-magnetic backpack along the profiles. The operator was walking at an approximate speed of 1 m/s on open land, with a sampling rate of 1 s. While certain sections in the pit required a reduction of speed due to deep excavations. The walking mode GPS positioning error is ±1 m. A section of the dyke (Figure 4b: MS1) was surveyed in great detail with nine parallel N-E ground magnetic lines of 70 m in length, with a line spacing of 10 m. Grid 2 and 3 had magnetic lines of over an area of 20 - 70 m x 10 – 70 m and 40 x 70 m. Regional aeromagnetic data (Figure 4c) were used to identify major structures such as dykes and faults. The dyke crosses the pit (Figure 1b) and covers a full length of 2.91 km and have thickness between 10-15 m.

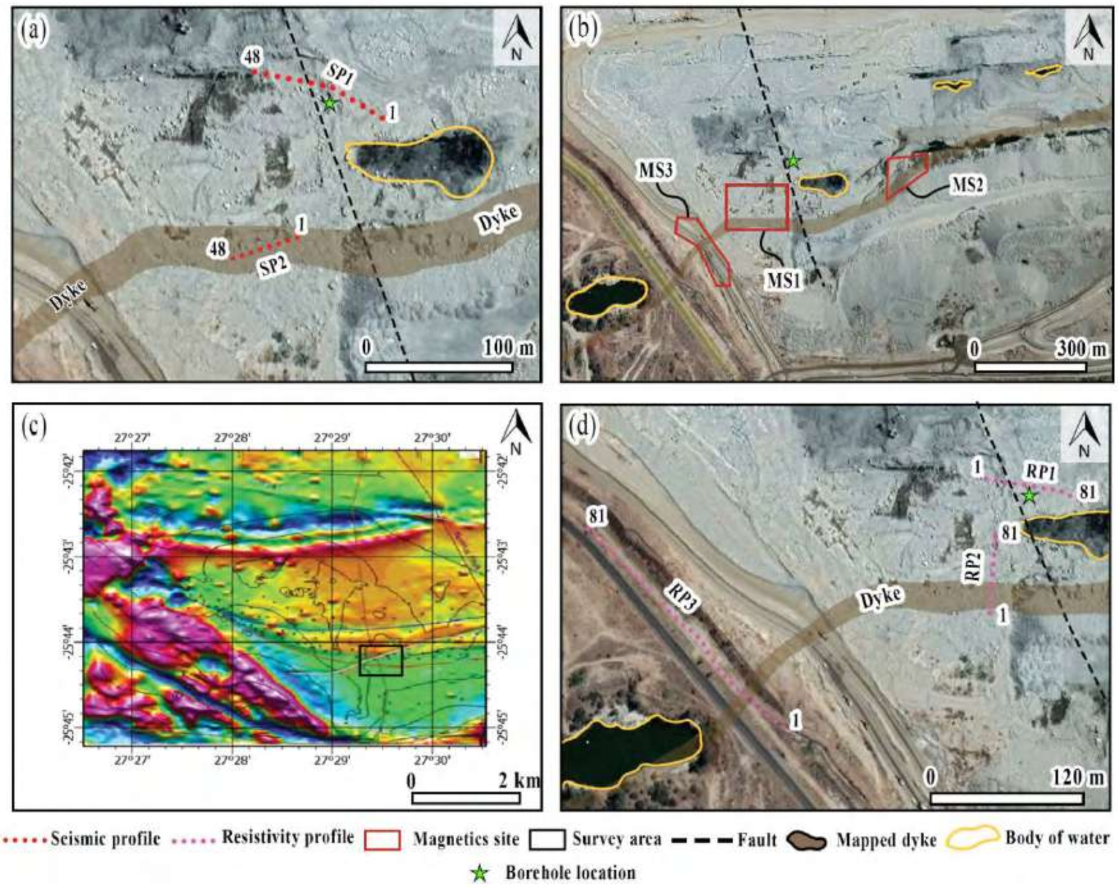

Figure 4: *Aerial photos showing the location of two major geological structures (fault and dyke) and (a) seismic profiles (two seismic profiles inside the pit, with a combination of different sensors), (b) magnetic grids (over the geological structures), (c) Regional aeromagnetic data over the edge of the western Bushveld Complex, showing major geological structures and site location and, (d) resistivity profiles. SP: Seismic profile; RP: Resistivity profile, MS: Magnetic site.*

Resistivity

The electrical resistivity surveys were conducted in two phases. The first phase was for testing the method for imaging and characterizing the chromitite orebody prior to drilling. The second phase was the application of resistivity to locate geological structures (faults, fractures and dykes) that may act as conduit for water migration into the pit.

The first phase involved one profile (Figure 4d: RP1) that was located in the pit over known mineralization, with a strike of E-W. The profile was surveyed using the ABEM Terrameter SAS 1200, with 41 fixed electrodes that are spaced 2 m apart in a Schlumberger, wenner and dipole-dipole array (Reynolds, 2011). All the electrodes (Figure 3a and b) were hammered at least 20 cm into the ground to ensure good coupling. The input current was set to 10 mA and the contact resistance was of the order 200-3000 Ω. The system automatically reports any anomalous contact resistance (negative resistivity readings) and a solution to this was re-planting the electrode or watering the electrode point. The second phase comprised of two resistivity profiles (Figure 4d) with length of 80 m for RP2 and 240 m for RP3. The first profile (RP2), striking S-N, was conducted at the edge of the pit with the aim of imaging the structures that cause seepage (Figure 1d) into the pit. The survey was conducted over an area with fractured rock and a little topographic variation (<1 m). Forty-one fixed electrodes were used for each of the two profiles, with a spacing of 2 m for RP2 and 6 m for RP3. RP2 was perpendicular to the strike of the mineralization and the length was limited by trenches. RP3, on the other hand, had a strike of SE-NW and was designed to delineate water conduits that might be transporting water from the river to the west of the pit. The profile was acquired over an area covered with loose sandy soil, located parallel to the road in the west of the east pit (Figure 4d).

Data processing

Seismics imaging

The collected seismic profiles were designed to cover the east pit of Tharisa mine, particularly the edge of the pit, where the mapped fractures (Figure 1c) are dominant and there is evidence of water flow on the benches (Figure 1d). The profiles were collected on clear tracks and inside the pit for effective shot positions. This resulted in the introduction of noise due to the proximity of the roads and mine workings. Figure 5 shows raw shot gathers and processed shot gathers. The raw shot gathers (Figure 5a and b) were noisy on the far offsets due to, for example, vibrations generated by drilling (Figure 5a: marked with green arrow) and some shots exhibit events that come in later that are due to secondary sources (e.g., dump trucks and loaders). However majority of the shots have good SNR (e.g., SP2) and show strong shallow P-wave reflections. Processing of the seismic data involved the suppression of the noise to further enhance the P-wave reflections that are caused by lithological boundaries. Reflections are observed in the shallow subsurface between 0 and 100 ms (Figure 5c and d). Data processing flow (Figure 6) started with fixing and adding the geometry for all the seismic profiles, and assigning the common depth points (CDP) spacing of 1 m for SP1 and 0.5 for SP2. Approximately 2358 first breaks were carefully picked (manual) on each profile for refraction statics and to generate a two layered P-wave velocity model. The refraction statics improved the continuity of the first arrivals and enhanced the reflections. A constant replacement velocity of 5000 m/s was chosen together with a matching datum of 1109 m, and 1142 m for SP1, and SP2, respectively. Spectral analysis of the seismic profiles show that the data have frequency range of 0-500 Hz for SP1, while SP2 has a frequency range of 0-2000 Hz due to the sampling rate during acquisition. The source energy frequency of the seismic data were in the range of 35 - 125 Hz, therefore we applied band pass filter of 30-45-180-200 Hz.

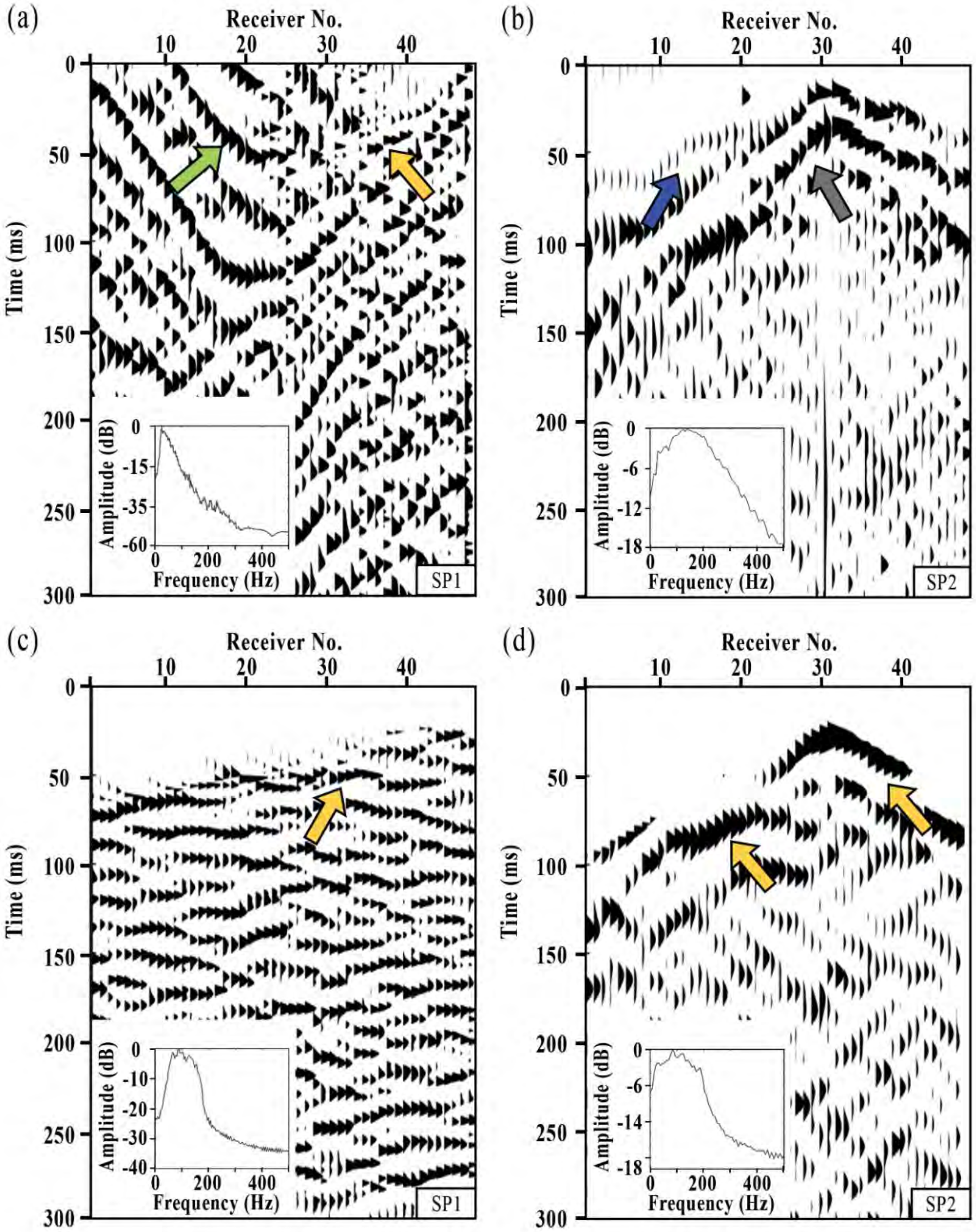

Figure 5: *(a and b) An example of a raw shot gathers from the two seismic profiles (SP1 and SP2), showing the quality of the data inside the open pit, with clear first breaks (blue arrow) on SP2. The green arrow shows noise generated by mine workings. Inserts show amplitude spectra; (c and d) processed shot gathers. The yellow arrows show some reflections recorded in the shot gather, while the grey arrow indicates the surface and guided waves.*

The filter was designed to attenuate the high frequency noise (>300 Hz) introduced during acquisition and also to reduce the low-frequency noise from the ground roll and random noise generated by mine workings. We applied *f-k* filter on the data to remove the steeply dipping air waves and guided waves. The effect of *f-k* filter is clearly demonstrated on SP2 by attenuating the steeply dipping secondary source energy (Figure 5b). A gapped deconvolution with a gap length of 6 ms was applied to broaden the frequency spectrum and reduce source signal. The pre-stack processing flow enhanced the subsurface reflections as shown in Figure 5c and d. Prior to normal moveout (NMO) corrections (60% stretch mute), we applied first break mutes to kill the high amplitude first breaks, such that they do not affect the final stack section and enhance near-surface reflections. A series of constant velocities were tested ranging from 1500 to 5000 m/s with 250 m/s intervals. Through visual inspection, an estimate NMO velocity of 3000 m/s was used for SP1 and 2500 m/s for SP2 for stacking. Post-stack filtering involved fx-deconvolution, spectral weighting and semblance to enhance the continuity of the reflections and improve the final image. We compared the phase shift and kirchoff migration methods, and the kirchhoff migration with constant velocity of 3000 m/s produced the best image. The seismic data were depth converted using 3000 m/s for final interpretation.

2D Travel time tomography

The target fractures within the subsurface can be imaged using seismic tomography. First break picking was conducted with an average of 2358 picks on each profile. A quality check was conducted and bad quality picks were removed prior to the inversion. Following picking of the data, an initial model was created. A non-linear, first-arrival travel time tomographic inversion with Tikhonov regularisation (Zhang & Toksöz, 1998) was run until convergence was achieved. This processes the ray trace synthetic travel times for each shot such that the difference between the input and synthetic first break picks are minimised. Initial analysis of the model was conducted, checking the model misfit on a shot-by-shot and receiver-by-receiver basis. Where a significant misfit was present, the first break picks were checked for consistency. Subsequently the data quality was checked, and, provided there was an acceptable convergence, the tomograms were exported and integrated in the interpretation (James et al., 2019).

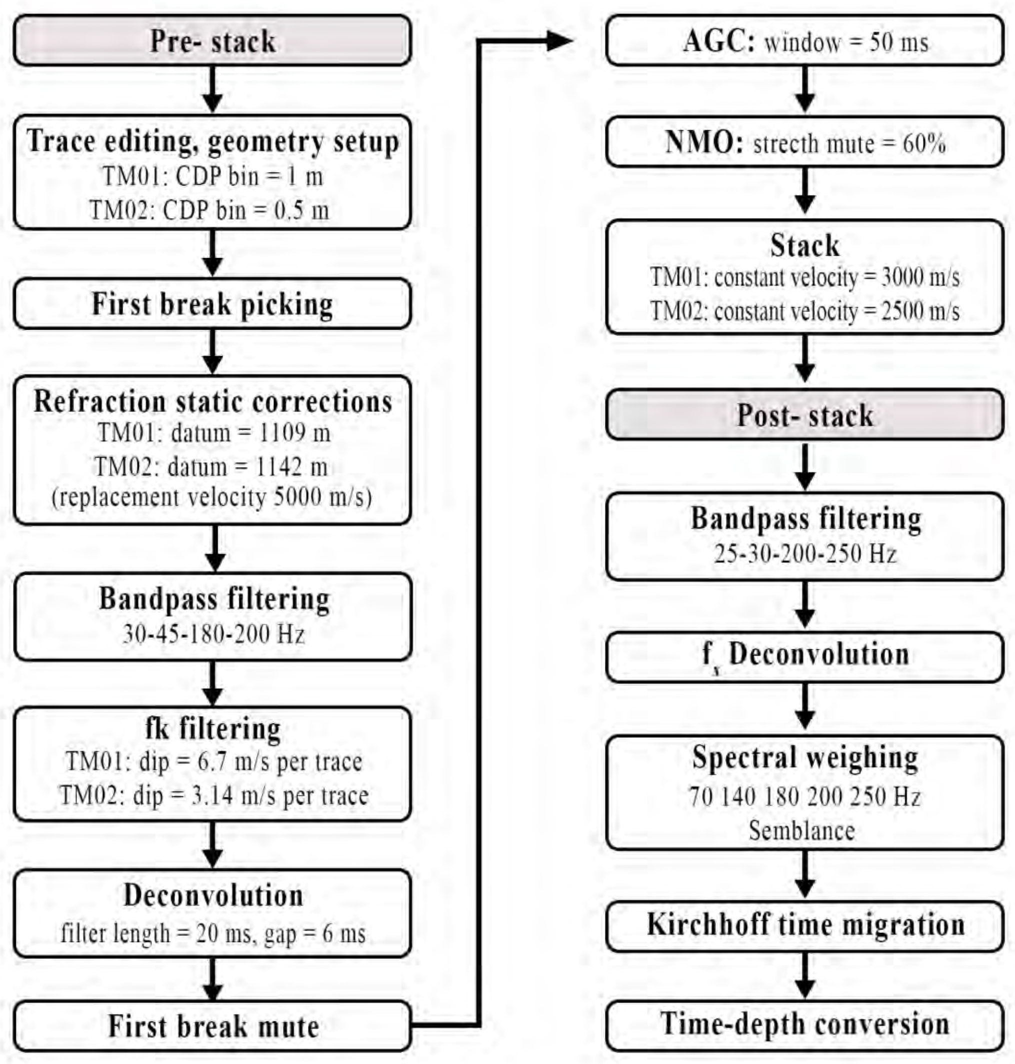

Figure 6: *Processing flow for the reflection seismic datasets of SP1 and SP2, at Tharisa mine.*

The final models for SP1 and SP2 had RMS of about 4 ms and 2 ms after 5 and 10 iterations, respectively. The quality of picks was reasonable considering the noisy environment. The velocities ranging from 500 m/s (loose rocks) to 6500 m/s (bedrock) were considered reasonable for the final model of the two profiles. Refracted arrivals are noticeable in both SP1 and SP2 when inspecting the first arrival vs offset (Figure 7a and b) used for the tomography. Travel time residuals are shown in Figure 7c and d as a function of offset for both profiles. As a result of the near-surface velocity region and maximum offsets between 50 – 100 m, a maximum ray penetration of 16 - 24 m is observed in the velocity models.

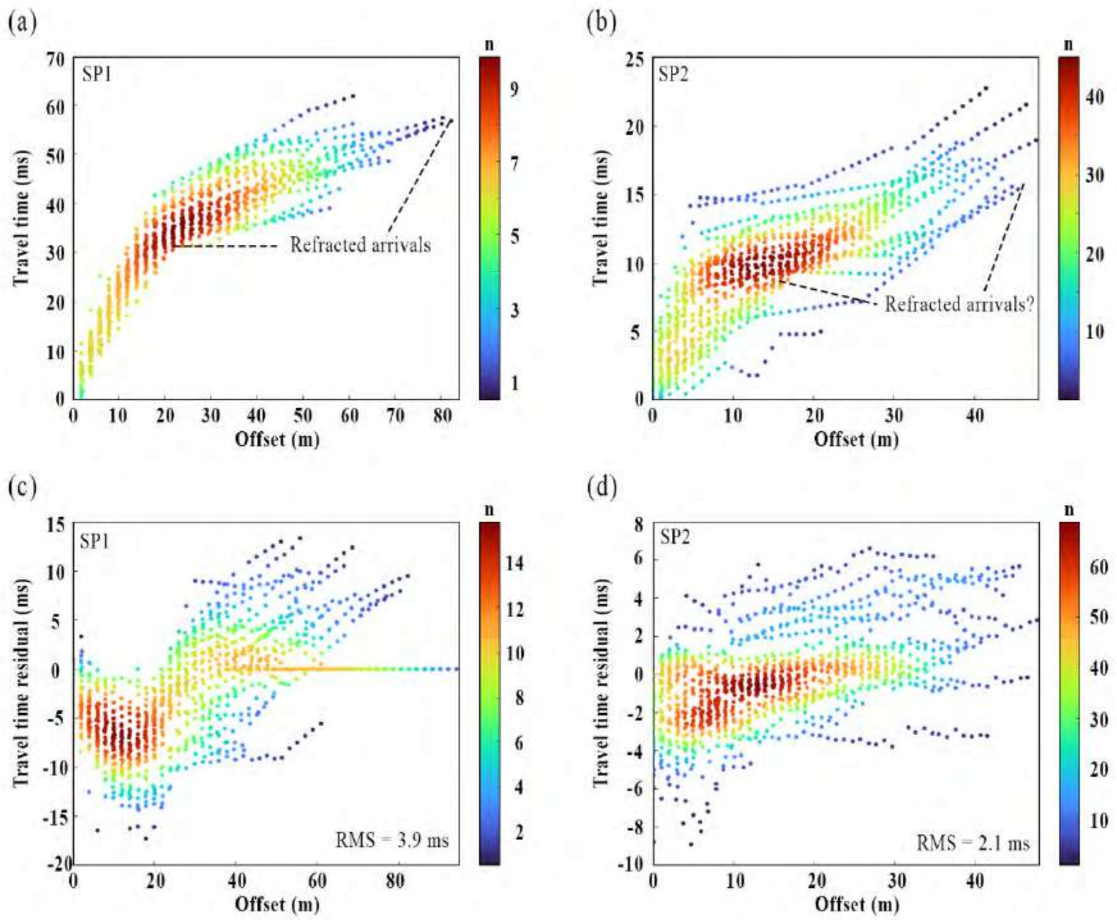

Figure 7: *Quality check of the first breaks and the inverted tomographic models. (a and b) Example of the first break picks for travel time tomogram as a function of offset for SP1 and SP2 respectively. (c and d) Travel time residuals as a function of offset for the same lines after the last iteration of the tomogram, with an RMS value of 3.9 ms and 2.1 ms obtained for the profiles. n: number of points within a range.*

Magnetics

The magnetic data were dumped and corrected for diurnal (temporal) variations. The processing of the data involved the removal of the regional magnetic field (de-trending), manual de-culturing of the original data and interpolating the removed (bad) data points using the minimum curvature technique, which is a favourable gridding technique for gridding potential field data due to its smooth surface approximations (Nabighian et al., 2005; Guo et al., 2012). The Reduction to pole techniques was then applied to reduce the effects of deep magnetization and correct for the positions of the magnetic sources responsible for the observed magnetic signatures. The vertical tilt angle was then applied to enhance the edges of both the shallow and deeper magnetic sources in the data, which in turn enhances the lineaments in the data (Miller & Singh, 1994).

Resistivity

The first step in processing the electrical resistivity data is to edit (eliminate) bad points caused by current deficit at large offsets or bad contact with the ground. The tomographic inversion was carried out using ResiPy with a regularized (weighted least square function) inversion with linear filtering. Prior to the inversion, a triangular finite element mesh was constructed to account for any complex model geometry (Binley & Kemna, 2005; Blanchy et al., 2020). The maximum length, electrodes and data points for the resistivity data is 400 m, 123 and 2110 respectively, therefore the overall calculation time was 114.24 seconds for all the profiles and arrays. The forward modelled apparent resistivity was calculated until the RMS error between the apparent resistivity and modelled resistivity are below 1.5. Table 2 shows the data acquisition and processing parameters. The topographic effect was not taken into account because the elevation difference was less than 1 m along the profiles.

***Table 2:** Resistivity acquisition and processing parameters*

Profiles	**RP1**	**RP2**	**RP3**
Acquisition			
Array type	Schlumberger, Dipole-Dipole, Wenner array		
Acquisition system	ABEM Terrameter SAS 1000		
No. of electrodes	41	41	81
Electrode spacing	2 m	2 m	6 m
Strike	E-W		
Profile length	80 m	80 m	240 m
Inversion			
Inversion method	Weighted least square function		
Iterations	Schlumberger: 4 Dipole-Dipole: 7	Schlumberger: 3 Dipole-Dipole: 3	Schlumberger: 2 Dipole-Dipole: 1
RMS	Schlumberger: 0.92 Dipole-Dipole: 1.07	Schlumberger: 0.97 Dipole-Dipole: 1.25	Schlumberger: 1.2 Dipole-Dipole: 1.03

Results

The P-wave velocity, density, resistivity and magnetic susceptibility measurements showed a narrow range of values within the same samples, with a larger variation observed on P-wave velocities compared to density, resistivity and magnetic susceptibility. Physical properties measurements show that anorthosites (5087.5 m/s) have the lowest P-wave velocities and norites (5670 m/s) have intermediate values, while pyroxenites (5950 m/s) and chromitites (6117.5 m/s) have the highest velocities. We paid more attention to the contrast over the actual velocities and density, as the aim of the physical property measurements was to test if we can seismically distinguish the different rock types within the study area. To present the physical property measurements, we used the lithological data and the physical property measurements to recreate downhole-logging results (Figure 8). To better understand the seismic response of the different rock units, we conducted 1D-synthetic seismogram using a MATLAB script (Westgate, 2020) by calculating the reflection coefficient and convolving it with a 130 Hz ricker wavelet. Pyroxenites show the highest magnetic susceptibility (0.014224524 SI) and the lowest density (2744.5 kg/m^3) (Figure 8). They are known to contain > 20% magnesium oxide as reported by (Sepato, 2015). Although the resistivity measurements of pyroxenites are not available, it is expected to have high resistivity, due to the presence of oxide minerals (Parkhomenko, 1982).

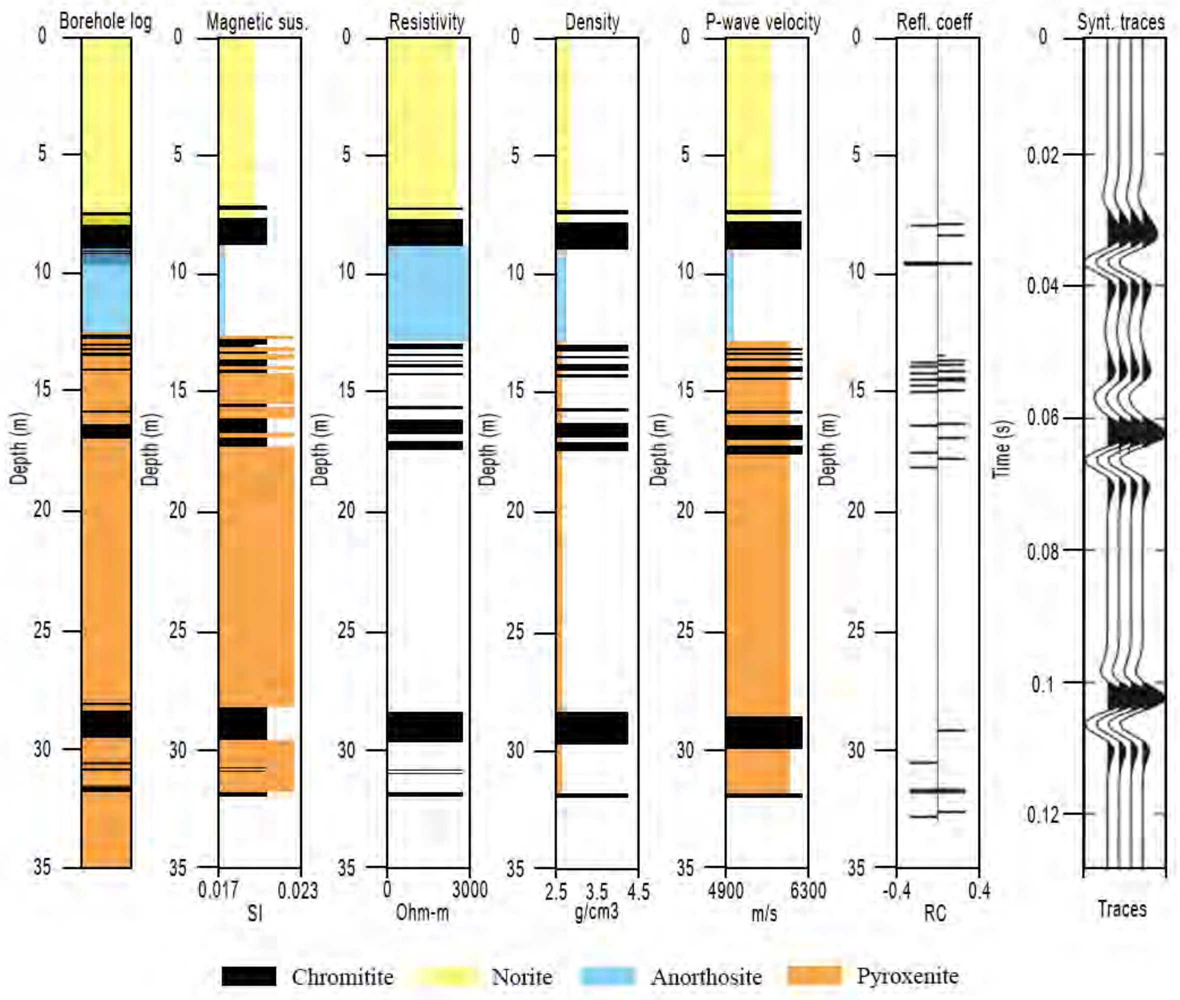

***Figure 8**: Downhole logging and core-logging data that was reconstructed from borehole 1 (BH1) of Tharisa mine. The data shows the contact between the mineralization and the host rock (norites, anorthosites and pyroxenites). Chromitites show a significant density and velocity contrast, making them recognizable from the host rocks. The resistivity log shows less variations in resistivity values across the rocks, with no resistivity data available for pyroxenites. Reflection coefficients were convolved with a 130 Hz ricker wavelet to generate a synthetic seismogram. The colours used for the rock types are consistent throughout the paper.*

Reflection seismic processing focused on cleaning the top 100 ms from ambient and coherent noise in order to enhance target reflections. Although the data were collected in a noisy mine environment, good quality first breaks are observed in all the profiles. Examples of shot gathers from SP1 and SP2 are shown in Figure 5. Note the different noise levels in the profiles. The first profile (SP1) shows evidence of coherent noise (green arrows) on the far offset from drilling. Due to these noise levels in the shot gathers, a significant amount of time was spent on reflection processing with different approaches. The shot gather showed reflections, although it was not convincing. Figure 7 shows the first breaks that were used in the tomography for the profiles in the study area. The plots (Figure 7a and b) show the presence of refracted arrivals on all the seismic profiles, with a root mean square (RMS) between 2 and 4 ms. Given that the seismic data were collected in a noisy area of the mine, the RMS is quite good. Comparing the raw shot gathers and processed shot gathers (Figure 5), the observed noise in the raw gathers has been attenuated and the reflections have been enhanced. A series of reflections are observed in the processed shot gathers at ~55 ms and 100 ms for SP1. Figure 9a, b show 2D velocity models of SP1 and SP2. Note that the seismic tomograms show the presence of three distinct P-wave velocity zones across the two seismic profiles. The near-surface P-wave velocities (dark blue zone) exhibit velocities between ~500 and 1300 m/s at varying depths of ~ 0 - 8 m across the profiles. The dark blue zone is underlain by a thin light blue P-wave velocity zone of relatively higher velocities ($\sim 1300 - 2100$ m/s). The thickness of this zone varies across the profiles. The third P-wave velocity zone (light yellow to brown) is characterized by velocities between ~ 2100 and 6500 m/s, with variable depth from surface.

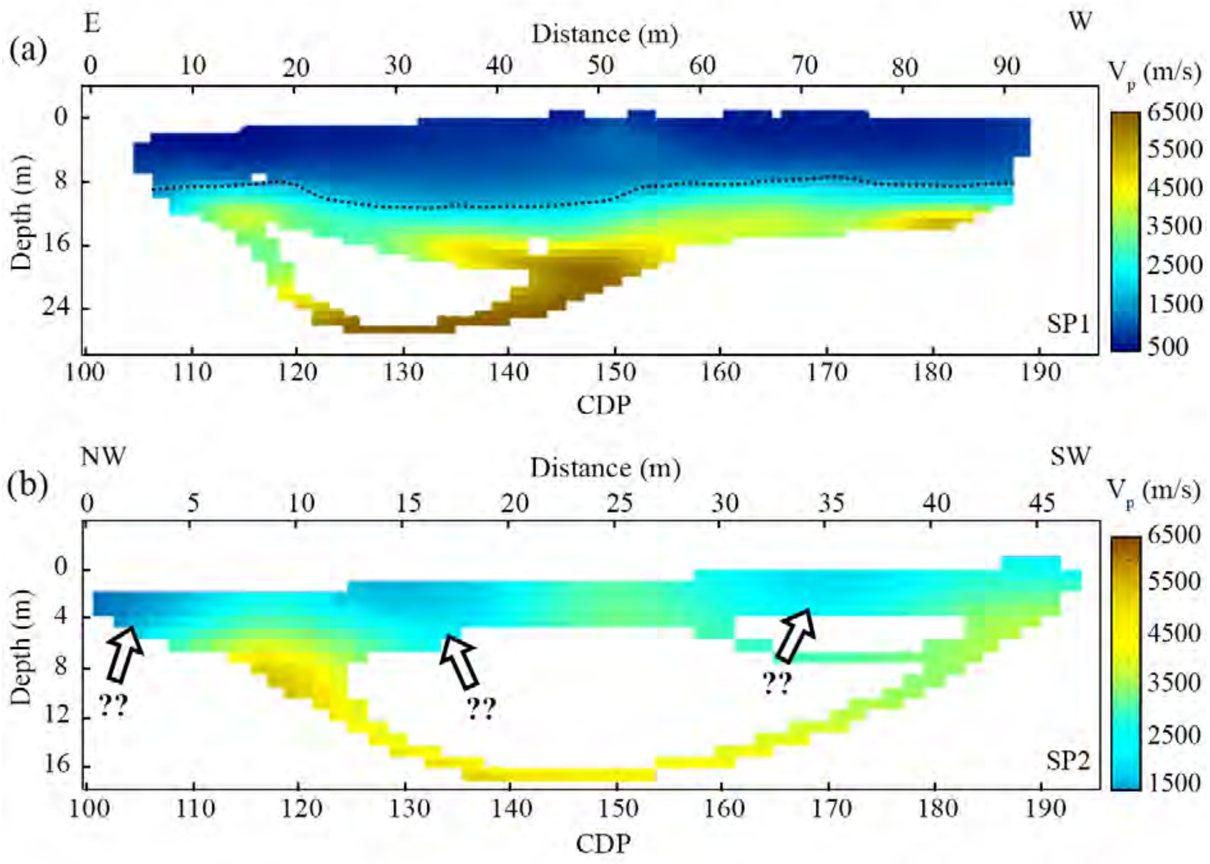

Figure 9: *2D travel time tomography results, with low velocity depressions marked with white arrows. (a) Seismic profile SP1 and (b) profile SP2. Results show ray coverage of approximately 25 m depth.*

The velocity zone consists of abrupt low velocity depression within it, possibly caused by fracturing (Figure 9b: white arrows). However, this is inconclusive as we observe poor ray coverage on SP2. We observe a maximum ray penetration of 20 - 25 m in the velocity models, due to maximum offsets of 98 m. The length of the second profile (SP2) was approximately half the length of the first profile (SP1), thus the depth of penetration for SP2 is lower (~16 m).

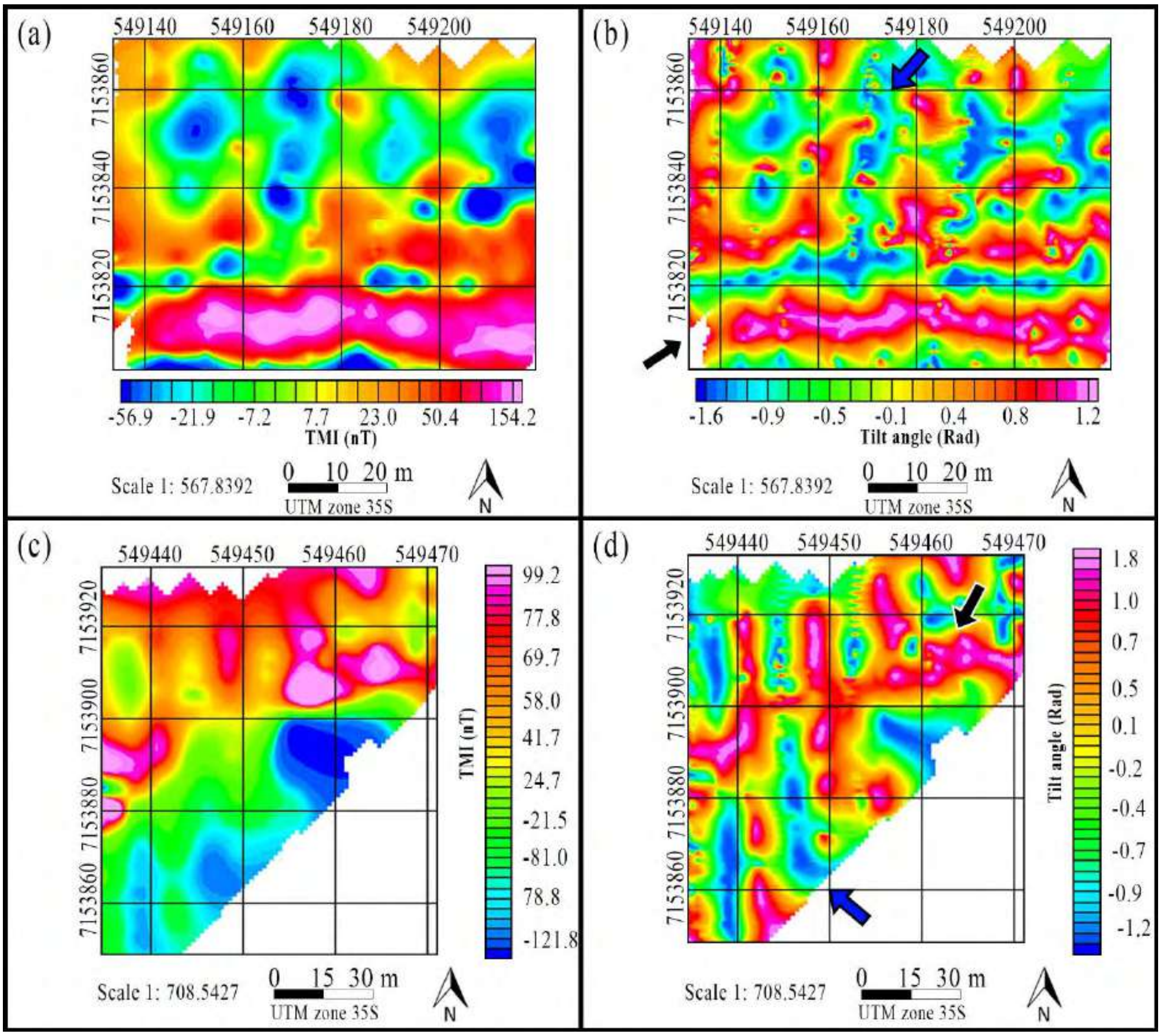

Figure 10: *(a and c) Total magnetic intensity (TMI) map of Tharisa mine after de-culturing, micro-levelling, and residual de-trending. (b and d) Vertical tilt angle derivative of the TMI maps. The black and blue arrows highlight zones of magnetic highs and lows respectively.*

The total magnetic intensity (TMI) map of the study area is presented in Figures 10a and c. Magnetic data processing focused on enhancing linear features within the open pit. Figures 10b and d are the vertical tilt angles. Features on the TMI are pronounced after the removal of the regional magnetic field and reduction to pole (RTP). The pattern of magnetic anomalies indicates the geological structures of the study area. The positive magnetic anomaly (Figure 10b: black arrow) trending east-west on the southern section of G1. This anomaly is correlated with the dyke (Figure 4b) that crosses the open pit. The negative magnetic anomalies (Figure 10b: blue arrows) are attributed to fracture zones, where a reduction in magnetic susceptibility of the rocks occurs due to the reduction in magnetite grains and alteration of magnetite into hematite (a mineral with less magnetic susceptibility) by water occurs (Lapointe et al., 1986; Harding et al., 1988). The vertical tilt angle was applied to enhance linear features observed on the TMI. The edges of the strong positive magnetic anomaly, due to the mapped dyke, is enhanced together with the negative magnetic signatures that are linked to fracturing. The same process was applied to G2 and G3, with the negative magnetic signatures (Figure 10d: blue arrows) enhanced and attributed to fracturing. The positive magnetic signature (Figure 11) continues into G3 and follows the trend of the mapped dyke.

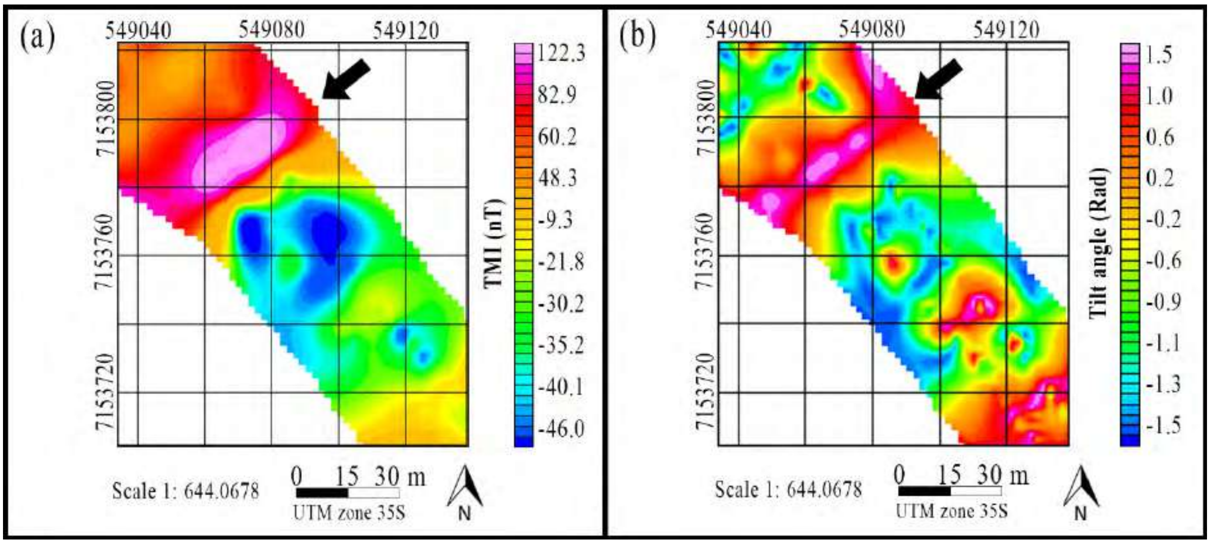

Figure 11: *(a) Total magnetic intensity (TMI) map of Tharisa mine after de-culturing, micro-levelling, and residual de-trending. (b) Vertical tilt angle derivative of the TMI maps. The black arrows highlight zones of magnetic highs.*

Inversion of the electrical resistivity data provided us with possible resistivity models. Complex lateral and vertical variations of resistivities are observed on the resistivity models. The Schlumberger (Figure 12) and dipole-dipole (Figure 13) models are considered for this study due to their sensitivity to horizontal (high resistivity zones: white arrows) and vertical (low resistivity: blue arrows) changes in resistivity respectively.

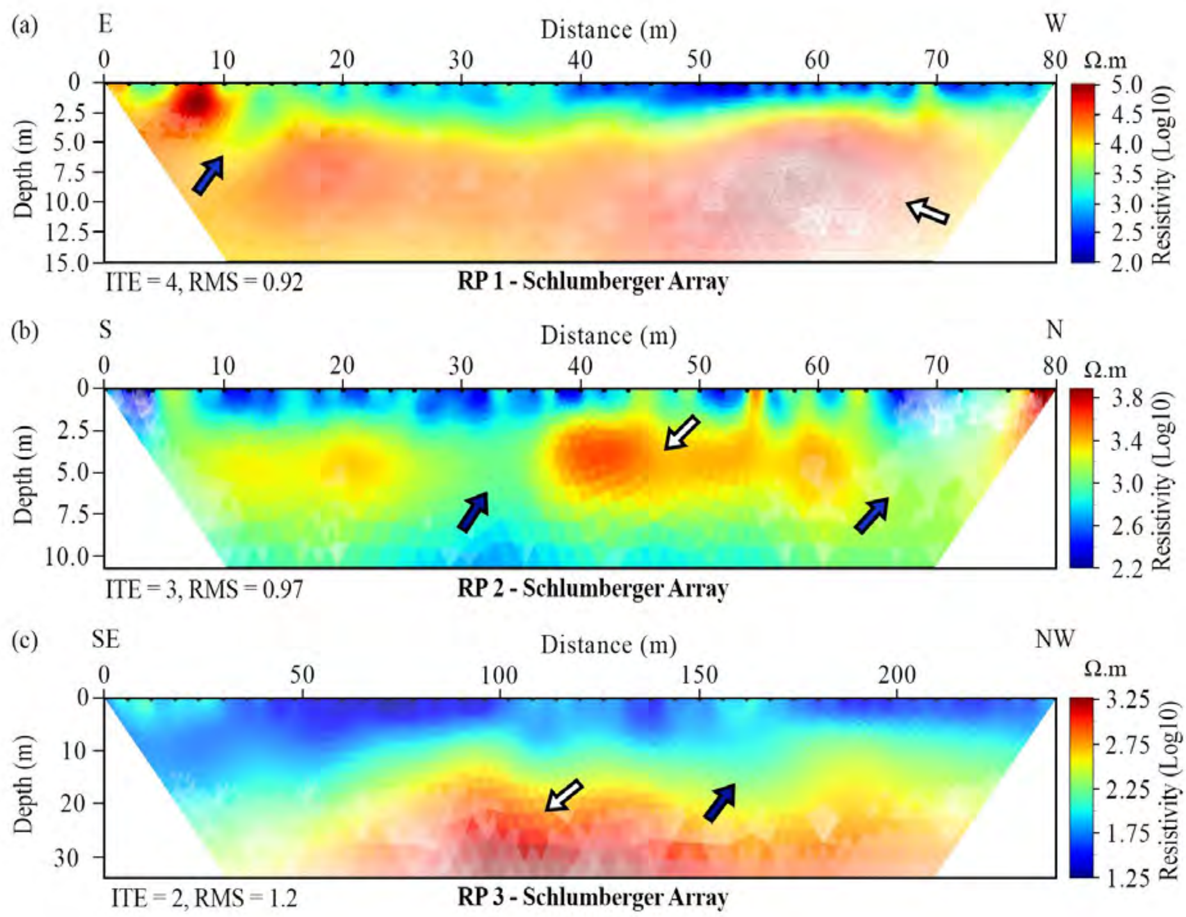

Figure 12: *Schlumberger electrical resistivity inverse sections for profile (a) RP1, (b) RP2, and (c) RP3. The white arrows indicate areas with high resistivity, while the blue indicates low resistivity areas.*

RP1 and RP2 were collected inside the pit, with the top layer of the ground dominated by highly fractured rock (Figure 14a), then followed by fractured bedrock (Figure 14b). This is visible on the resistivity model as a low resistivity zone (blue zone: ~89 – ~213 Ω.m), followed by an intermediate resistivity zone (light green to yellow: ~213 – ~3274 Ω.m). The intermediate resistivity zone is underlain by a zone of much higher resistivities (~3274 – ~20000 Ω.m), coloured as light orange to red zone (Figure 14c: Fresh bedrock). RP3 has the greatest highly conductive layer that has thicknesses ranging between 8 - 20 m towards south-eastern side of the profile. These are attributed to the loose sandy-clay soil (Figure 14c) that is close to the river. The Schlumberger models show conductive layers (low resistivity, blue coloured zone) thickness between 2.5 – 14 m across the profiles.

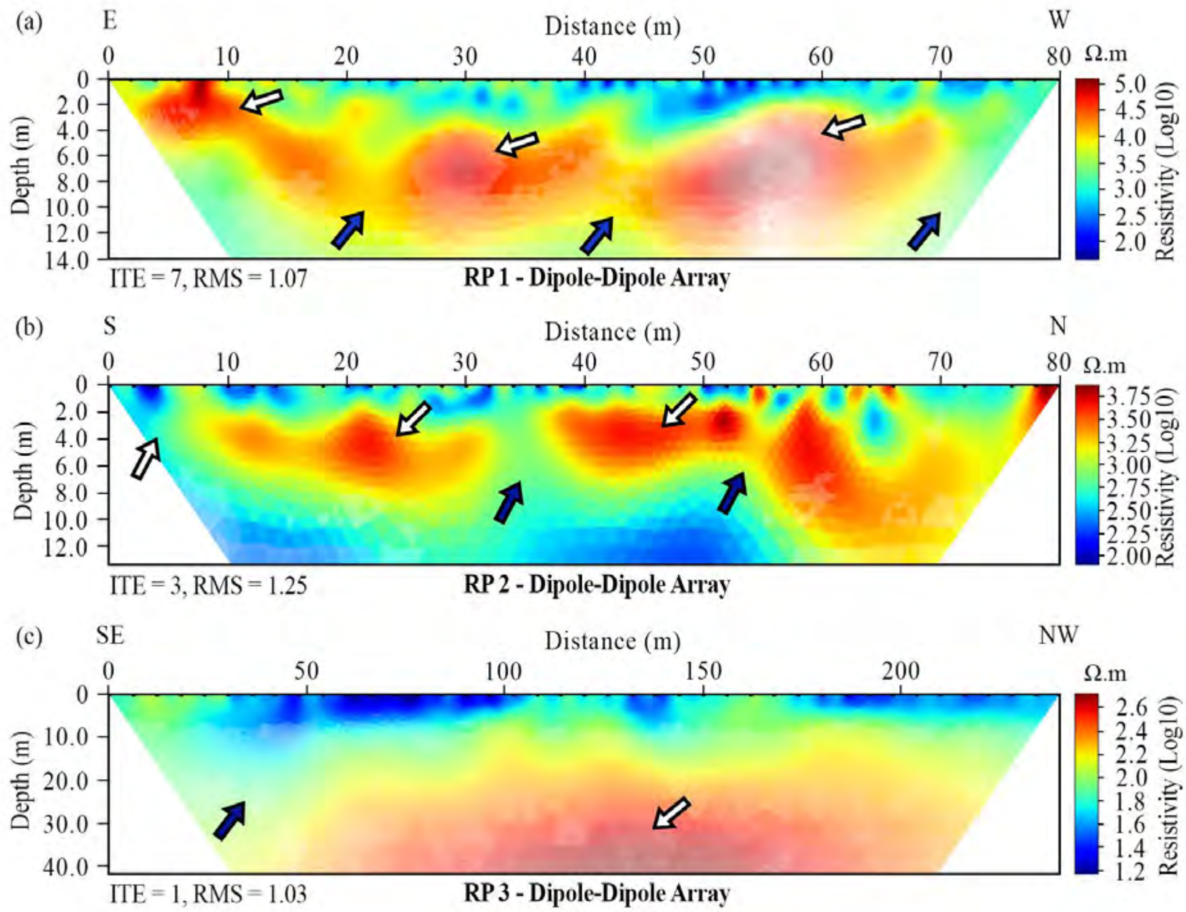

Figure 13: *Dipole-dipole electrical resistivity inverse sections for profile (a) RP1, (b) RP2, and (c) RP3. The white arrows indicate areas with high resistivity, while the blue indicates low resistivity areas.*

Interpretations

Figure 15 compares and correlates the resistivity models, seismic tomograms and seismic reflection data across SP1 and RP1, together with the lithological data from borehole 1 (Figure 4). Both the resistivity model and seismic velocity model results correlate with the borehole (BH1) data.

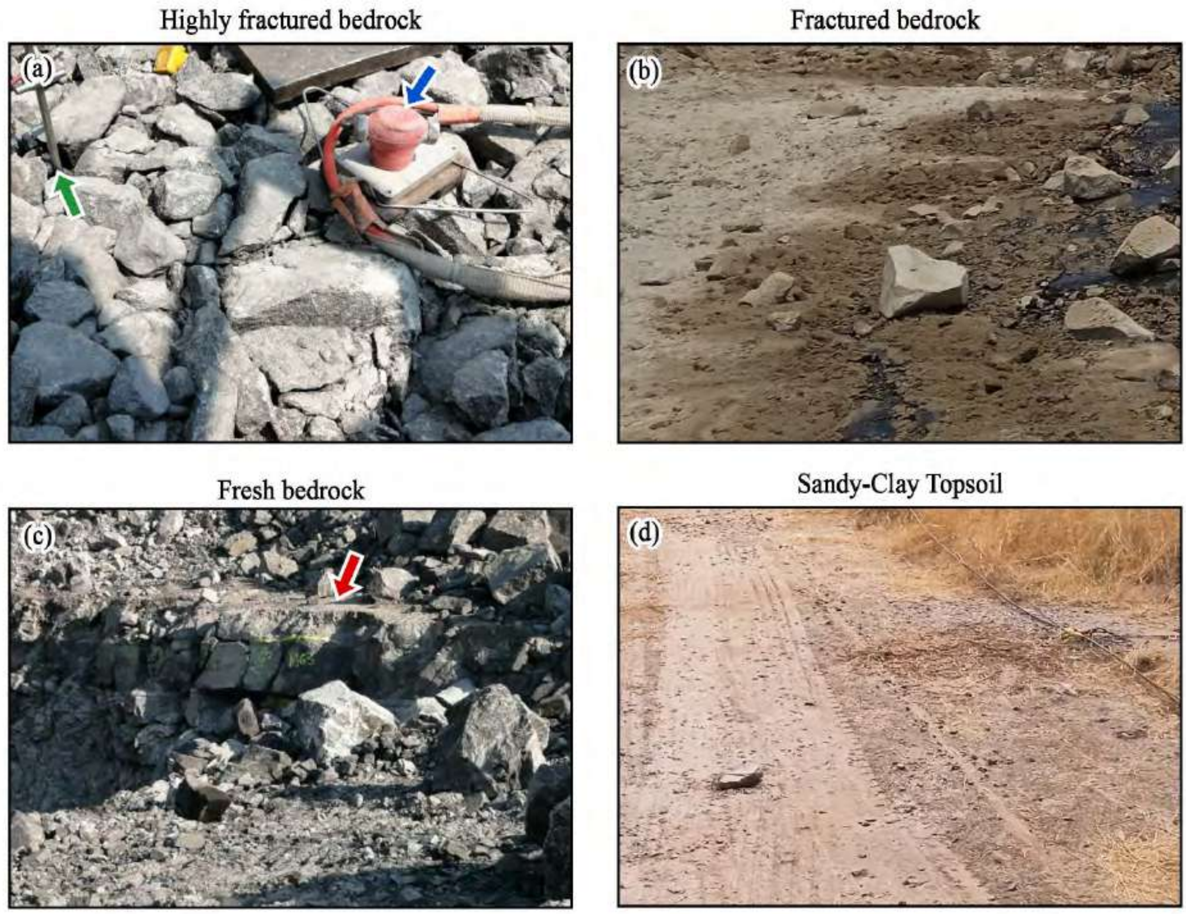

Figure 14*: Field ground conditions. Resistivity and seismic profiles were collected in an active mine. Diagrams show a) highly fracture rock, b) fractured rock and c) fresh bed rock (red arrow) inside an open pit. d) Sandy-clay weathered topsoil outside the pit. Green arrow indicates the resistivity electrodes, while the blue arrows show the land streamer used to collect seismic data*

The top 6 m on the borehole (Figure 15a, b) corresponds with the light blue and dark blue zones, that represent the low resistivity and seismic velocity zones, respectively. The dark blue to light green zones on the resistivity model is characterized by resistivities of $\leq 89 - 213\ \Omega.\text{m}$ and P-wave velocities of $\leq 500 - 1300\ \text{m/s}$. This zone is interpreted to be the top highly fractured norites, due to blasting in the pit. An increase in resistivity and P-wave velocity of the subsurface rocks is observed with increasing depth. The transition between the highly fractured and fresh bedrock at depths of 6 – 8 m is characterized by the higher resistivities and P-wave velocities of $213 - 3274\ \Omega$.m and $1300 - 2100\ \text{m/s}$.

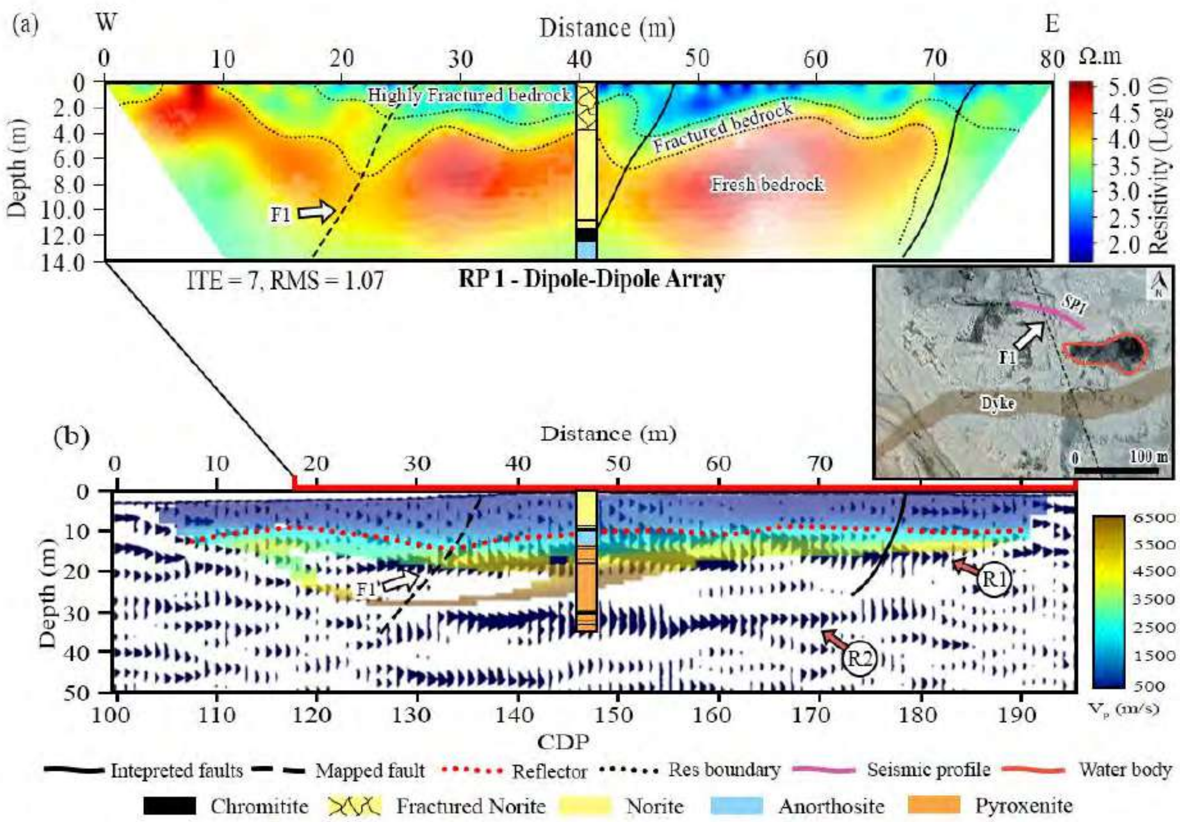

Figure 15: *Integrated and interpreted results of resistivity and seismic refraction and reflection stack. (a) Resistivity tomogram (RP1). (b) Seismic tomogram overlaid on migrated depth stack section for input seismic profile (SP1). The dotted lines show the lithological boundaries between the top weathered rock and fresh bedrock. The solid black lines represent*

the interpreted joints and fractures. Insert shows the location of the resistivity and the seismic profile with the cross-cutting fault pointed with a white arrow.

The layers situated beneath the transition zone, starting with the fresh norite at depths of about 8 m and extending to greater depths, are characterized by higher resistivities of $\sim 3274 - 20000\ \Omega.\mathrm{m}$ and P-wave velocities of $\sim 2100 - 6500\ \mathrm{m/s}$. This layer is interpreted to be the fresh bedrock made up of the norite, anorthosite and chromitite rocks that have not been affected by blasting (Figure 15a, b). The electrical resistivity and seismic velocity models show inhomogeneous horizons, with sudden resistivity changes that are attributed to fractures. However, the P-wave velocity model (Figure 9a) show less lateral velocity changes, therefore no interpretation of lateral P-wave velocity changes can be made. The dipole-dipole resistivity and reflection seismic sections reveal that the lithology within the pit is disturbed. The inversion model (Figure 16a) shows a depression at the center of the profile which can be attributed to the highly fractured bedrock. However, the interpretation of the fracture systems along the bench of the pit is inconclusive as the ray coverage on SP2 is poor. The seismic profiles need to be expanded and improve the ray penetration and coverage before any interpretation can be made. A series of reflections (Figure 16b) observed in SP2 are interpreted to be contacts between highly fractured, fractured bedrock and fresh bedrock. Reflection seismics was mainly used to image the deeper discontinuities and the mineralization contacts. On SP1, a near-surface reflection is observed (Figure 15b). The reflection (R1) is generally flat throughout the seismic profile and can be correlated with the subsurface mineral contact between the chromitites and its host rock at depth (Figure 15b). The origin of the reflections are further confirmed by the sidewall mapping (shown in Figure 1d) of the chromitite layers. The continuity of the reflection is disturbed at 30 – 40 m on the migrated stack section, and this correlates with the resistivity discontinuity observed in Figure 15a (dashed line). This discontinuity is associated with the mapped fault (F1) within the pit (shown on insert of Figure 15).

A similar package of reflections (R2) are observed at 30 m depth, and this can be attributed to the lower mineralization (MG2), however the interpretation of this is inconclusive as there is no borehole information that can constrain the depth of the MG2 mineralization. The two identified reflections are not clear at the edges of the seismic sections and exhibits multiple discontinuities, due to low fold coverage. SP2 was conducted perpendicular to RP2, with the first section of the resistivity profile covering the dyke, while the seismic profile is entirely within the dyke. The dyke is covered by highly fractured rock from the mine workings. This is evident on SP2, as it shows low velocity regions towards the south-western side of the profile at varying depths (Figure 16a).

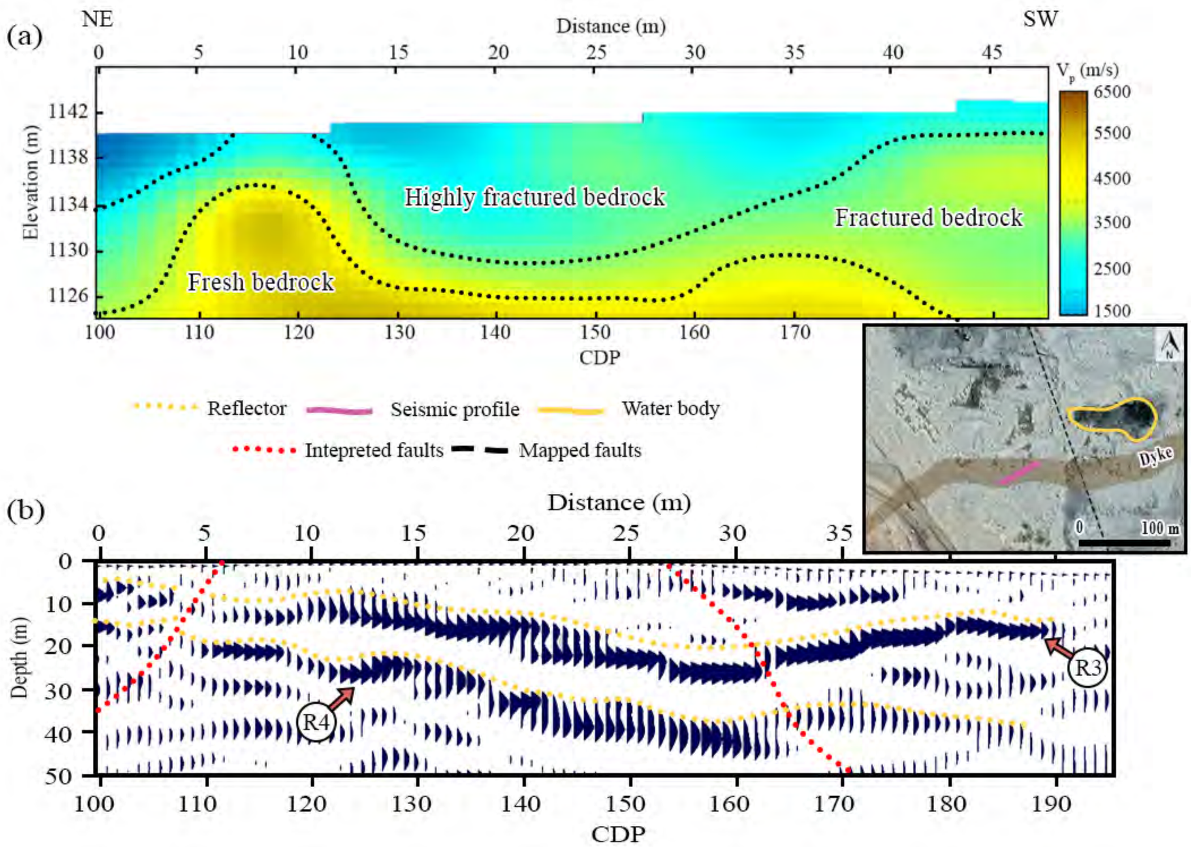

Figure 16: *(a) Tomography results and (b) migrated depth reflection section of SP2 showing reflections dipping to the south west, interpreted as a series of anorthosites and norite succession (grey arrows), that are markers for chromitite mineralization. Low velocity zones are indicated with red arrows and correspond with interpreted faults on the stack section. Insert shows the location of the seismic profile with the cross-cutting dyke (brown) and fault (black dashed line).*

The migrated depth sections (Figure 16b) shows continuous reflections (R3) that can be followed to the surface towards the north-eastern side of the profile. The top reflection (R3: starting from ~ 8 m in the north east to ~ 25 m in the south west) is associated with the contact between the highly fractured and the weathered dyke, the following reflection (R4: starting from ~ 15 m in the east to ~ 40 m in the west) is associated with the contact between the weathered dyke zone and a fresh rock dyke. The low velocity depression (Figure 16a) at the centre of the profile corresponds to the syncline nature of the reflections in Figure 16b between 10 and 40 m. Resistivity values over the dyke range from 3 000 to $> 10\ 000\ \Omega.\mathrm{m}$. Significant differential weathering of the host rock is observed at the contacts with the host rock. Such areas are potential for hosting ground water, therefor exhibit low resistivity zones (Figure 13b: beginning of the profile and between 30 – 40 m). The tomographic results are presented in a series of 3D views (Figure 17 and 18) to present them in their real location, together with other geophysical data (resistivity and magnetics) and geological data from the mine. Figure 17b shows the low P-wave velocity depression together with the faults (white lines) that were interpreted from regional aeromagnetic data (Figure 4c). The low depressions are thick on the far ends of the profiles and correlate with the projected faults. Further interpretation of the tomography velocity zones resulted in an addition of more fault planes (Figure 17c) that can be associated with fracture systems (Figure 1c) that are mapped in the pit. The interpreted fracture system is evident on the magnetic data (Figure 17d) as low magnetic depressions and correlates well. A high magnetic signatures (Figure 18a) is observed on the southern part of the magnetic data and the seismic profiles. The signatures is in relation to the dolerite dyke that intruded through the center of the pit (Figure 18b). The low magnetic regions are correlated with weathered host rock at the contacts.

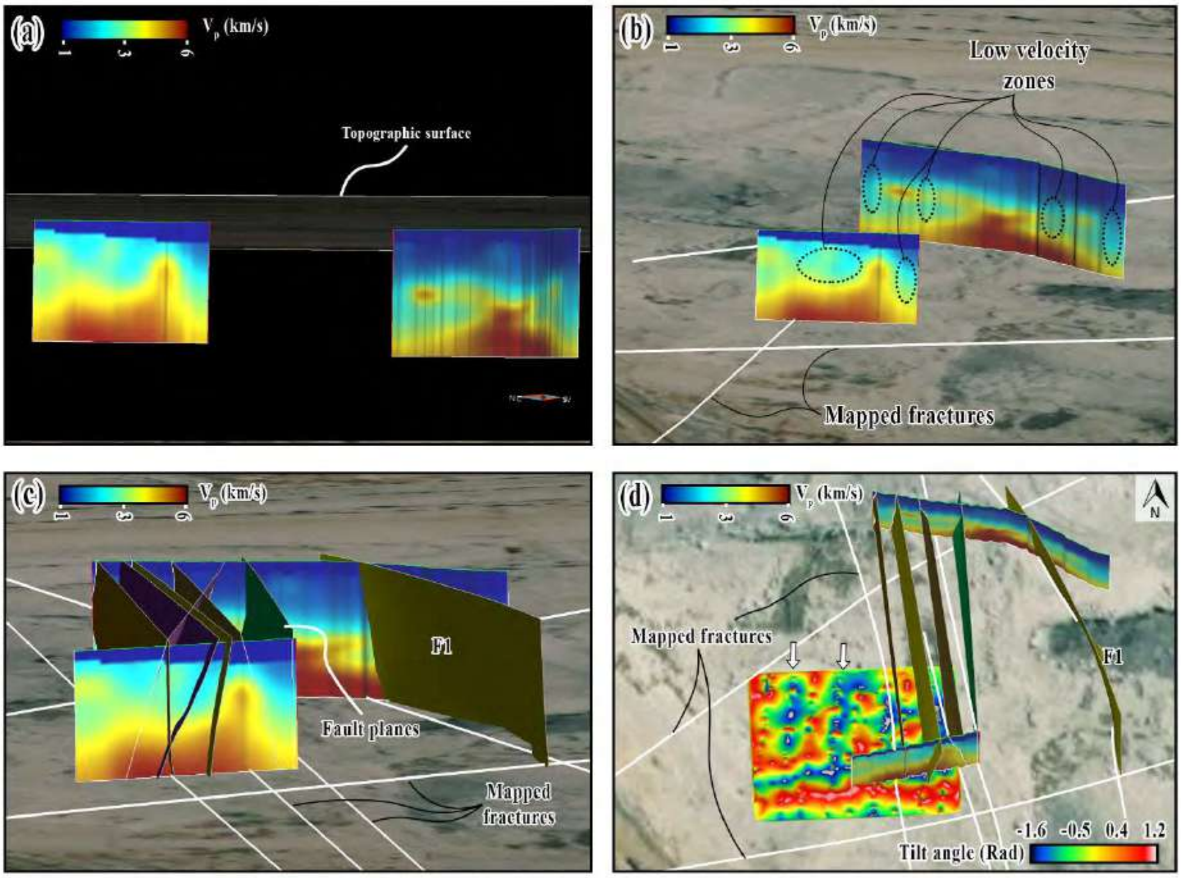

Figure 17: *A series of 3D views showing seismic tomography results with the location of the seismic lines, interpreted major faults from (Figure 3a) aeromagnetic data. (a) Position of seismic profiles, relative to the open pit, (b) tomographic results, with low velocity zones indicated along SP1 and SP2, (c) shows the relationship between the interpreted low velocity zones with the fault structures that where mapped within the pit, (d) Top view: relationship between the tilt angle derivative magnetic map and the interpreted fault structures. White arrows indicate areas of low magnetics. White line indicated mapped faults within the pit.*

Discussion

The geophysical data collected at Tharisa mine illustrate that good-quality geophysical dataset can be used to establish regional structural fracture system in an area of interest. This is likely the first multi-geophysical study to be conducted in an open-pit for imaging fractures in the Bushveld Complex. The data were collected without any interruption to mining activity, illustrating the cost and time effectiveness. The most notable reflection, low magnetic and low resistivity zones originate from the fractures within the open pit. This reflection, magnetic and resistivity zone suggests multiple factors that contributed to the fracture system: (1) Geologically induced fractures that were reactivated during dyke intrusion; (2) induced fractures due to mine blasting. The fracture systems could act as conduits for water from the water table and the river. A good correlation between magnetics, P-wave velocity models, resistivity section and seismic data is evident when overlaying the different datasets (Figures 16 and 17). For example, the low magnetic regions correlate with low P-wave velocity or low resistivity zones. This implies that the areas with low magnetics are highly weathered and prone to fracturing. This is supported by the identification of the dyke contact with the host rock exhibiting a low magnetic and resistivity values (Figure 18b). The use of multiple geophysical methods was useful in the interpretation and imaging of structures within a few meters, demonstrating the potential for high-resolution geophysical methods in mine noisy environment. The quality of the data is attributed to proper survey design, acquisition and processing. This opens up opportunities for the application of multiple geophysical methods in exploration and mine development. Longer and wider seismic and magnetic grids are likely the best approach to this type of geology and challenges. However, this will be challenging as a result of the active mining and infrastructures.

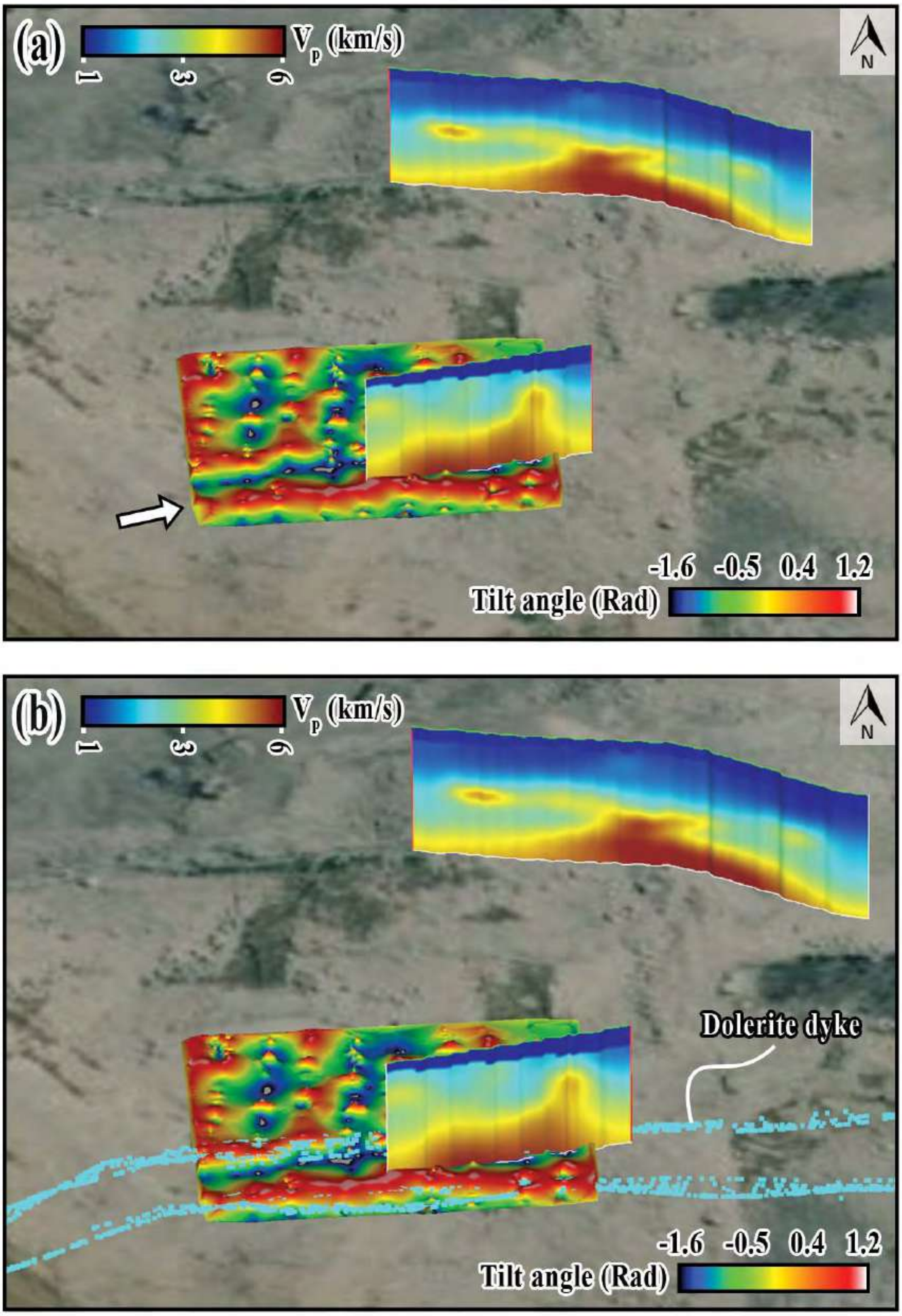

Figure 18: *(a) 3D views showing seismic tomography results with the location of the seismic lines, tilt angle derivative magnetic map. (b) Relationship between the tilt angle derivative magnetic map and the mapped dyke (Figure 1b).*

Conclusion

This study has demonstrated that multi-geophysical methods can be utilized to delineate fractures and faults in an active open-pit mine. The combination of three or more geophysical methods has more advantage in subsurface imaging. The geophysical data were complemented by borehole data and physical property measurements of rock samples. The use of geophysical data in a noisy mining environment proved to be challenging, however seismic data showed good quality first arrivals and refracted arrivals, and this allowed the imaging of the mineralization and host rock along the profiles. Furthermore, the P-wave velocity tomogram provided information about the near-surface rock conditions with the highly fractured rock showing as depression zones. Ground magnetic data provided high-resolution delineation of a major dyke that was previously identified through aeromagnetic data and geological mapping. Ground magnetic further showed that the dyke is crosscut by a series of fractures and faults that may be potential conduits for water migration into the pit. Electrical resistivity tomography identified linear low resistivity zones that differentiate the fractured and undisturbed hard rock. These results will be integrated with hydrological and geochemical studies to further unravel and determine the source of water that migrates into the pit.

Reference

Amoush, H. A., & Mashagbeh, A. (2009). Using Geophysical Methods to Image Near-Surface Cylindrical Pipeline: A Case Study on Engineering Applications, Jordan. *Jordan Journal of Civil Engineering*, *3*(2), 13. Retrieved from https://core.ac.uk/download/pdf/234698299.pdf

Basson, I. J. (2019). Cumulative deformation and original geometry of the Bushveld Complex. *Tectonophysics*, *750*, 177–202. https://doi.org/10.1016/j.tecto.2018.11.004

Binley, A., & Kemna, A. (2005). DC Resistivity and Induced Polarization Methods. In Y. Rubin & S. S. Hubbard (Eds.), *Hydrogeophysics* (Vol. 50, 129–156). Dordrecht: Springer Netherlands. https://doi.org/10.1007/1-4020-3102-5_5

Blanchy, G., Saneiyan, S., Boyd, J., McLachlan, P., & Binley, A. (2020). ResIPy, an intuitive open source software for complex geoelectrical inversion/modeling. *Computers & Geosciences*, *137*, 104423. https://doi.org/10.1016/j.cageo.2020.104423

Bumby, A. J., Eriksson, P. G., Catuneanu, O., Nelson, D. R., & Rigby, M. J. (2012). Meso-Archaean and Palaeo-Proterozoic sedimentary sequence stratigraphy of the Kaapvaal Craton. *Marine and Petroleum Geology*, *33*(1), 92–116. https://doi.org/10.1016/j.marpetgeo.2011.09.010

Cawthorn, R. G. (2015). The Bushveld Complex, South Africa. In B. Charlier, O. Namur, R. Latypov, & C. Tegner (Eds.), *Layered Intrusions* (517–587). Dordrecht: Springer Netherlands. https://doi.org/10.1007/978-94-017-9652-1_12

Dahlin, T. (1996). 2D resistivity surveying for environmental and engineering applications. *First Break*, *14*(7), 275–283. https://doi.org/10.3997/1365-2397.1996014

Dildar, J., Manzi, M., Abiye, T., Gomo, S., Rapetsoa, M. K., & Sihoyiya, M. (2022). An Integrated Approach to Characterise the Subsurface Using Near Surface Geophysical Methods. Presented at the NSG2022 4th Conference on Geophysics for Mineral

Exploration and Mining, European Association of Geoscientists & Engineers. Retrieved from https://www.earthdoc.org/content/papers/10.3997/2214-4609.202220173

Eales, H. V., & Cawthorn, R. G. (1996). The Bushveld Complex. In *Developments in Petrology* (Vol. 15, pp. 181–229). Elsevier. https://doi.org/10.1016/S0167-2894(96)80008-X

Gomo, S., Rapetsoa, M. K., Manzi, M. S. D., Onyebueke, E., Dildar, J., Sihoyiya, M., et al. (2023). Integrated geophysical methods for boulder delineation to improve mining. *Geophysical Prospecting*, 1365-2478.13322. https://doi.org/10.1111/1365-2478.13322

Guo, L., Meng, X., & Shi, L. (2012). Gridding aeromagnetic data using inverse interpolation. *Geophysical Journal International*, *189*(3), 1353–1360. https://doi.org/10.1111/j.1365-246X.2012.05448.x

Harding, K. L., Morris, W. A., Balch, S. J., Lapointe, P., & Latham, A. G. (1988). A comparison of magnetic character and alteration in three granite drill cores from eastern Canada. *Canadian Journal of Earth Sciences*, *25*(8), 1141–1150. https://doi.org/10.1139/e88-112

Hartzenberg, A. G., & Plessis, M. D. (2014). The influence of regional structures associated with the Bushveld Complex on the mechanism driving the behaviour of the UG2 hangingwall beam and in-stope pillars at Lonmin’s Marikana Operations, 10. Retrieved from https://repository.up.ac.za/bitstream/handle/2263/71695/Hartzenberg_Structural_2019.pdf?sequence=1

James, I., Hird, G., & Fitzpatrick, A. (2019). Refraction tomography at the Nova Ni-Cu mine. *ASEG Extended Abstracts*, *2019*(1), 1–3. https://doi.org/10.1080/22020586.2019.12073152

Kerrigan, N. P. (2013). *Using shallow geophysical methods to locate a buried stream channel at a stream restoration site in the burd run waterhed, Shippensburg, pa*. SHIPPENSBURG UNIVERSITY, Shippensburg, PA. Retrieved from https://www.ship.edu/globalassets/geo-ess/kerrigan_thesis_131213.pdf

Kinnaird, J. A. (2005). The Bushveld Large Igneous Province. *The Review Paper, The University of the Witwatersrand, South Africa*, 39. Retrieved from http://www.largeigneousprovinces.org/sites/default/files/BushveldLIP.pdf

Lapointe, P., Morris, W. A., & Harding, K. L. (1986). Interpretation of magnetic susceptibility: a new approach to geophysical evaluation of the degree of rock alteration. *Canadian Journal of Earth Sciences*, *23*(3), 393–401. https://doi.org/10.1139/e86-041

Lotheringen, J., James, J., Lomberg, K., & Bornman, H. (2016). *Tharisa Chrome and PGM Mine, South Africa. Competent Persons Report* (Competence report No. JTHA011) (190). Retrieved from https://www.tharisa.com/pdf/investors/annual-reports/2016/cpr-2016.pdf

Malehmir, A., Andersson, M., Lebedev, M., Urosevic, M., & Mikhaltsevitch, V. (2013). Experimental estimation of velocities and anisotropy of a series of Swedish crystalline rocks and ores: *Velocities and anisotropy of a series of crystalline rocks and ores*. *Geophysical Prospecting*, *61*(1), 153–167. https://doi.org/10.1111/j.1365-2478.2012.01063.x

Manzi, M., Durrheim, R., & Webb, S. (2017). 3D seismic attributes for platinum exploration and mine planning in the Bushveld Complex (South Africa). In *International*

Geophysical Conference, Qingdao, China, 17-20 April 2017 (665–668). Qingdao, China: Society of Exploration Geophysicists and Chinese Petroleum Society. https://doi.org/10.1190/IGC2017-169

Maré, L. P. (2022). Council for Geoscience Petrophysical Properties Atlas. Council for Geosciences. Retrieved from https://maps.geoscience.org.za/download/petrophysics-map-package.php

Maries, G., Malehmir, A., & Marsden, P. (2020). Cross-profile seismic data acquisition, imaging, and modeling of iron-oxide deposits: A case study from Blötberget, south-central Sweden. *GEOPHYSICS*, *85*(6), B233–B247. https://doi.org/10.1190/geo2020-0173.1

Miller, H. G., & Singh, V. (1994). Potential field tilt—a new concept for location of potential field sources. *Journal of Applied Geophysics*, *32*(2), 213–217. https://doi.org/10.1016/0926-9851(94)90022-1

Nabighian, M. N., Grauch, V. J. S., Hansen, R. O., LaFehr, T. R., Li, Y., Peirce, J. W., et al. (2005). The historical development of the magnetic method in exploration. *Geophysics*, *70*(6), 33-61. https://doi.org/10.1190/1.2133784

Ofterdinger, U., MacDonald, A. M., Comte, J.-C., & Young, M. E. (2019). Groundwater in fractured bedrock environments: managing catchment and subsurface resources – an introduction. *Geological Society, London, Special Publications*, *479*(1), 1.1-9. https://doi.org/10.1144/SP479-2018-170

Parkhomenko, E. I. (1982). Electrical resistivity of minerals and rocks at high temperature and pressure. *Reviews of Geophysics*, *20*(2), 193. https://doi.org/10.1029/RG020i002p00193

Pazzi, V., Di Filippo, M., Di Nezza, M., Carlà, T., Bardi, F., Marini, F., et al. (2018). Integrated geophysical survey in a sinkhole-prone area: Microgravity, electrical resistivity tomographies, and seismic noise measurements to delimit its extension. *Engineering Geology*, *243*, 282–293. https://doi.org/10.1016/j.enggeo.2018.07.016

Perritt, S., & Roberts, M. (2007). Flexural-slip structures in the Bushveld Complex, South Africa? *Journal of Structural Geology*, *29*(9), 1422–1429. https://doi.org/10.1016/j.jsg.2007.06.008

Rapetsoa, M. K., Manzi, M. S. D., Westgate, M., Sihoyiya, M., James, I., Onyebueke, E., et al. (2022). Cost-effective in-mine seismic experiments to image platinum deposits and associated geological structures at Maseve platinum mine, South Africa. *Near Surface Geophysics*, nsg.12216. https://doi.org/10.1002/nsg.12216

Reynolds, J. M. (2011). *An Introduction to Applied and Environmental Geophysics*. New York: John Wiley & Sons. Retrieved from https://www.wiley.com/en-sg/An+Introduction+to+Applied+and+Environmental+Geophysics%2C+2nd+Edition-p-9780471485353

Roberts, M. K. C., & Clark-Mostert, V. (2010). Is there some commonality between the geological structures in the Bushveld Complex and the Great Dyke? In *The 4th International Platinum Conference* (149–153). The Southern African Institute of Mining and Metallurgy. Retrieved from https://www.saimm.co.za/Conferences/Pt2010/149-156_Roberts.pdf

Sepato, O. (2015). *Statistical and wavelet analysis of density and magnetic susceptibility data from the Bushveld Complex, South Africa.* University of the Witwaterrand, Johannesburg. Retrieved from http://hdl.handle.net/10539/18528

Titus, R., Witthüser, K., & Walters, B. (2009). Groundwater and Mining in the Bushveld Complex. *International Mine Water Conference*, 7. Retrieved from https://www.imwa.info/docs/imwa_2009/IMWA2009_Titus.pdf

Van Schoor, A. M. (2002). Detection of sinkholes using 2D electrical resistivity imaging. *Journal of Applied Geophysics*, *50*(4), 393–399. Retrieved from http://hdl.handle.net/10204/1474

Westgate, M. C. (2020). *Reappraisal of legacy reflection seismic data using advanced processing techniques and seismic attributes*. University of the Witwatersrand, South Africa. Retrieved from https://hdl.handle.net/10539/31030

Wilson, A. H. (2005). Rock-strength and physical properties of Norites of the Merensky and Bastard Units, western Bushveld Complex. *South African Journal of Geology*, *108*(4), 525–540. https://doi.org/10.2113/108.4.525

Zhang, J., & Toksöz, M. N. (1998). Nonlinear refraction traveltime tomography. *Geophysics*, *63*(5), 1726–1737. https://doi.org/10.1190/1.1444468

Received: 2 September 2022 | Accepted: 18 January 2023
DOI: 10.1111/1365-2478.13322
Geophysical Prospecting EAGE EUROPEAN ASSOCIATION OF GEOSCIENTISTS & ENGINEERS
ORIGINAL ARTICLE

Integrated geophysical methods for boulder delineation to improve mining

Sikelela Gomo[1] | **Moyagabo K. Rapetsoa**[1] | **Musa S. D. Manzi**[1] | **Emmanuel Onyebueke**[1] | **Jureya Dildar**[1] | **Mpofana Sihoyiya**[1] | **Ndamulelo Mutshafa**[1] | **Wesley Harrison**[3] | **Julie E. Bourdeau**[2,4,5] | **Oleg Brovko**[1] | **Ian James**[1,5] | **Gordon R. J. Cooper**[1] | **Stephanie Scheiber**[1] | **Raymond J. Durrheim**[1]

[1]School of Geosciences, University of the Witwatersrand, Johannesburg, Republic of South Africa
[2]Geological Survey of Canada, Ottawa, Ontario, Canada
[3]SRK Consulting, Johannesburg, Republic of South Africa
[4]Wits Mining Institute, University of the Witwatersrand, Johannesburg, Republic of South Africa
[5]Southern Geoscience Consultants, West Perth WA, Perth, Australia

Correspondence
Musa S. D. Manzi, School of Geosciences, University of the Witwatersrand, Private Bag, Wits, 2050, Johannesburg, Republic of South Africa.
Email: musa.manzi@wits.ac.za

Funding information
National Research Foundation; DSI-NRF CIMERA (Centre of Excellence for Integrated Mineral and Energy Resource Analysis)

Abstract
Near-surface boulders can pose serious challenges to opencast mining. They often introduce complexities, delays in drilling, blasting and excavation programmes, which subsequently decrease mining efficiency, increase mining risks and costs. The location of subsurface boulders and the identification of other geological features that may impact mining activities (e.g. fractures, the presence of iron-rich ultramafic pegmatites and the variation in weathering across a mining region) are necessary to reduce the challenges posed by these geological features, therefore optimizing mining efficiency. In this study, magnetics, electrical resistivity tomography, seismic refraction tomography, ground penetrating radar and borehole data are integrated for boulder delineation and mapping of other geological features that may impact mining using an unmined section at Tharisa Mine, Bushveld Complex (South Africa), as a test site. The results obtained from the different geophysical techniques are found to complement each other and successfully delineate boulders, fractures, iron-rich ultramafic pegmatites and the variation in weathering and layering across the area. The incorporation of geophysical results can thus improve mining efficiency, while reducing mining risks and costs.

KEYWORDS
GPR, magnetics, resistivity, seismics, tomography

INTRODUCTION

The development of mines and the optimum exploitation of mineral resources are paramount factors for the economic, societal and environmental development of countries. The presence of boulders in mining operations is problematic as these represent obstacles that may decrease productivity (e.g. delay blasting, drilling and excavation), as well as increase mining and engineering costs and risks (Dan et al., 2016; Felletti & Beretta, 2009; Shao et al., 2020). Boulders are defined as rock fragments with a diameter greater than 256 mm, which may occur in different sizes and shapes, and appear as a corestone surrounded by concentric shells and/or embedded in saprolite. They are formed by chemical (spheroidal weathering) and/or mechanical processes (e.g. blasting) (Dan et al., 2016; Shao et al., 2020; Udden, 1914).

Boulders formed by chemical processes are referred to as subterranean boulders, whereas those caused by mechanical processes are referred to as subaerial boulders (Twidale & Romani, 2005).

It is therefore important to locate boulders beforehand to adequately plan and, thus, minimize any deleterious effects on mining and engineering operations. Although there is a paucity of integrated geophysics studies to detect and map boulders, Jee and Ha (2007) discussed the viability of using electrical resistivity tomography (ERT), ground penetrating radar (GPR), seismic refraction tomography (SRT) and magnetics to delineate boulders during tunnelling. Several other case studies, though not based on boulder delineation, also demonstrate the successful mapping of boulders and boulder zones using various geophysical techniques. For instance, Musil et al. (2002) employed seismic reflection and refraction combined with drilling to map the internal structure, including suspended boulders, of the lower boundary of the Muragl rock glacier (Switzerland). Cardarelli et al. (2010) applied that both ERT and SRT to locate cavities in the near subsurface, which, when filled with air, have a response similar to boulders. Ettinger et al. (2014) used GPR to study the internal geometry of a volcaniclastic fan produced by aggradation during a lahar event from the Cotopaxi volcano (Ecuador). Interestingly, GPR results resolved boulders hosted within the volcaniclastic fan. In a similar study, Gomez et al. (2018) utilized GPR, along with other geospatial techniques, to study the spatial distribution of boulder-size clasts at the Semeru volcano (Indonesia), gaining insights on how their distribution relates to valley morphology and the dynamic deposition of lahars.

Subterranean boulders (corestones) in the weathered zone are often by-products of chemical weathering, appearing as more competent and less altered than the host rock (Dan et al., 2016; Durgin, 1977). These boulders are normally separated or compartmentalized by fractures (joints and/or fault zones) and soft cemented materials with lower densities, compaction and competence (Jee & Ha, 2007). A number of such boulders have been observed in the Bushveld Complex of South Africa, where they became exposed by mining operations. The area of interest consists of anorthosite to norite boulders embedded in saprolite clays (weathered rock). The boulders are more competent and have higher magnetic susceptibility compared to the surrounding weathered rocks. As a result, the boulders are more resistive, dense and magnetic as compared to the surrounding weathered rocks.

In this paper, we present the results from integrated geophysical surveys (i.e. magnetics, ERT, SRT and GPR) that were conducted at an unmined section at the Tharisa Mine in the Bushveld Complex. The main aim of the integrated surveys was to delineate and characterize subsurface (or subterranean) boulders in saprolite clays. Generally, boulders measure between 1 and 2 m across; however, in this study, we designed our surveys to target boulders larger than 4 m as smaller boulders can easily be disposed of by mining operations. A secondary aim was to map geological site features (e.g. lithologies and fractures) that could have a direct impact on mining operations which would ultimately facilitate effective mine planning (Onyebueke et al., 2018). The most significant feature that geophysical methods bring to mineral exploration and mining is the ability to map complex and

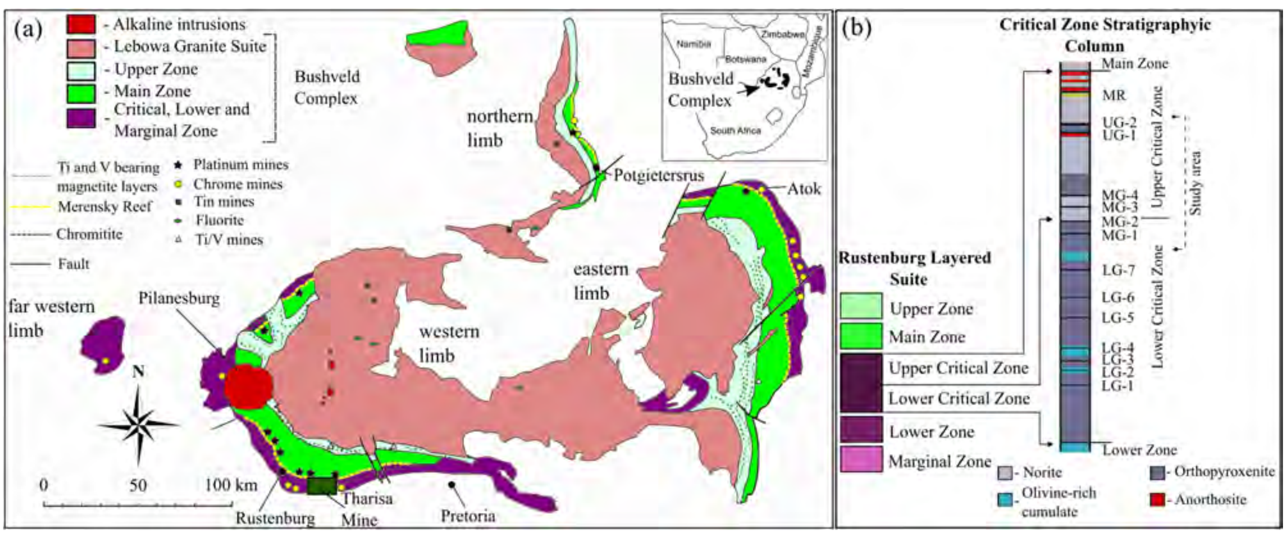

FIGURE 1 (a) Simplified geological map of the Bushveld Complex. (b) Simplified schematic stratigraphic column of the Critical Zone with its position within the Rustenburg Layered Suite. Included in the stratigraphic column is the location of Tharisa Mine, the Merensky Reef (MR), Upper Group (UP), Middle Group (MG) and Lower Group (LG) chromitite layers. *Source*: (a) Modified from Taylor et al. (2009); (b) modified from Hunt et al. (2018).

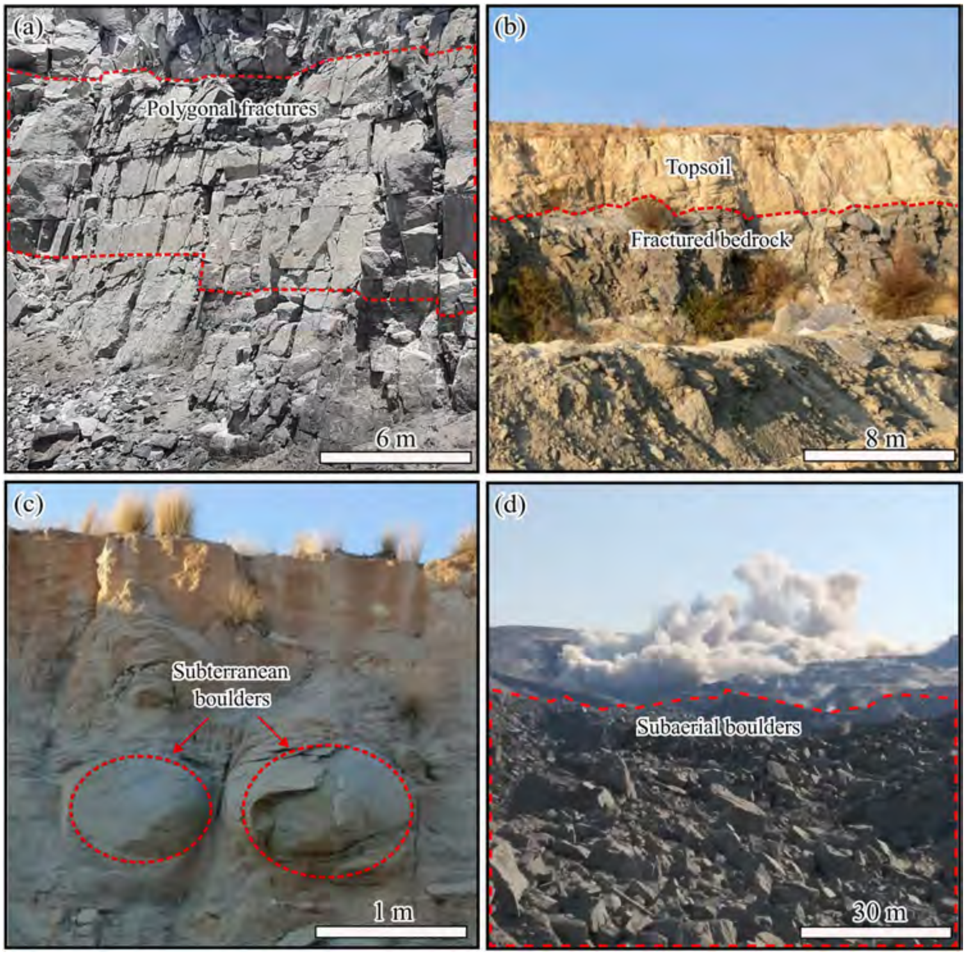

FIGURE 2 (a) Polygonal fractures in the norite and anorthosite rocks at Tharisa Mine, this image was taken inside the opencast mine pit. The red dotted line highlights a highly fractured zone. (b) Highwall face near the study area showing topsoil (highly weathered top zone) and fractured bedrock. (c) Subterranean boulders showing on the highwall face near the study area. (d) Subaerial boulders (blasting induced boulders) inside the pit, at Tharisa Mine. The red dotted line highlights the zone with the subaerial boulders. *Source*: The presented photos were taken by Hloniphani Hlongwa (11/10/2021).

subsurface geological features at greater resolution than any other geological method (Malehmir et al., 2012).

GEOLOGICAL BACKGROUND

The research was carried out at Tharisa Mine, an opencast Platinum Group Metals (PGMs) and chrome mine, situated in the south-western limb of the Bushveld Complex, which itself is located in the northern portions of the Kaapvaal Craton (Figure 1a). The Bushveld Complex hosts the largest ultramafic–mafic layered intrusion in the world, with an aerial extent of about 66,000 km^2 and a thickness between 7 and 9 km (Cawthorn, 2015). The complex formed about 2.05 Ga and hosts stratiform PGM, chromium and vanadium deposits (Scoates et al., 2021). The Bushveld Complex was emplaced through a series of magma injection events, intruding at the unconformity separating the Transvaal Supergroup (Pretoria Group) sedimentary rocks and the Rooiberg Group volcanic rocks (Cawthorn, 2015; Kruger, 2005; Perritt & Roberts, 2007). The complex is subdivided into three major magmatic units: the (1) Rustenburg Layered Suite (RLS), (2) Rashoop Granophyre Suite, and (3) Lebowa Granite Suite, and is split up into five limbs, that is, four outcropping limbs (western, far-western, eastern and northern limbs) and one buried limb (south-eastern limb) (Cawthorn & Webb, 2001; Eales & Cawthorn, 1996). The mafic–ultramafic rocks of the RLS host most of the PGM mineralization of the Bushveld Complex.

The RLS is subdivided into five zones known as the (from bottom to top): (1) Marginal (norites), (2) Lower (cyclic pyroxenite–harzburgite–dunite), (3) Critical (cyclic pyroxenite–norite–anorthosite–chromitite), (4) Main (gabbronorites) and (5) Upper zones (ferrogabbro–anorthosite–magnetite and apatite-bearing diorites) (Figure 1b; Barnes & Maier, 2002; Cawthorn, 2015). The economically significant PGM deposits are found in the Critical Zone, of which the

TABLE 1 Weathered and fresh rock physical property measurements from samples collected in the study area

Weathered norite rock measurements (Sample X)			Fresh norite rock measurements (Sample Y)		
Number of measurements taken	Magnetic susceptibility (×10^{-3} SI)	P-wave seismic velocity (m/s)	Number of measurements taken	Magnetic susceptibility (×10^{-3} SI)	P-wave seismic velocity (m/s)
Sample-X 1	0.128	950	Sample-Y 1	5.84	5710
Sample-X 2	0.137	1090	Sample-Y 2	4.52	5630
Sample-X 3	0.124	1047	Sample-Y 3	5.09	5610
Sample X average	0.127	1029	Sample Y average	5.15	5650
Weathered anorthosite resistivity			**Fresh anorthosite resistivity**		
Rock type		Resistivity (Ω m)	Rock type		Resistivity (Ω m)
Weathered anorthosite		~1000–3000	Fresh anorthosite		~5000–10,000

Note: The resistivity measurements were taken from a study conducted by van Schoor and Fourier (2015) of rocks in South Africa.

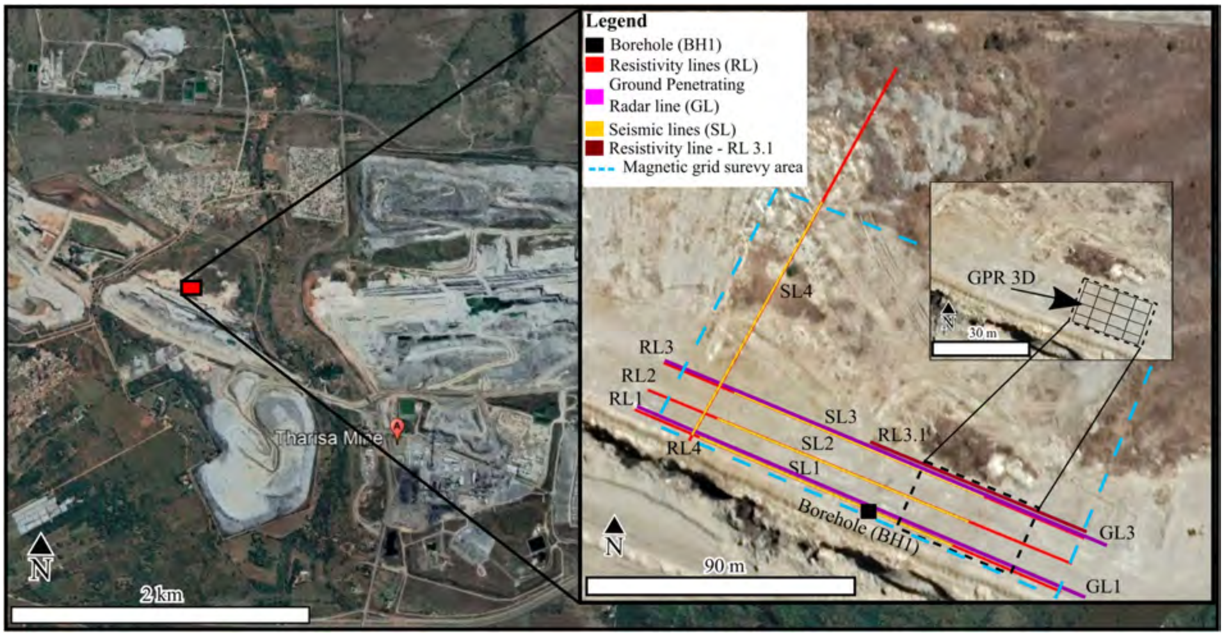

FIGURE 3 Google Earth image showing the location of the study area (marked with a red square) at Tharisa Mine and that of the magnetic, resistivity (RL), seismic (SL) and ground penetrating radar (GL and ground penetrating radar [GPR] 3D) grids collected over the study area (on the zoomed-in image of the study area).

Merensky Reef and Upper Group 2 chromitite (UG2) units define two of the world's largest platinum-bearing orebodies (Cawthorn et al., 2005; Figure 1b). The Critical Zone is further subdivided into the Upper (cyclic orthopyroxenite, norite and anorthosite units) and Lower Critical zones (cyclic chromitite, harzburgite and pyroxenite units) (Figure 1b; Barnes & Maier, 2002; Hunt et al., 2018). The transition zone between the Upper and Lower Critical zones occurs where cumulus plagioclase first appears (Barnes & Maier, 2002; Cawthorn, 2015; Eales & Cawthorn, 1996).

Layered rocks of the RLS were subsequently disrupted by the intrusion/infiltration of iron-rich ultramafic pegmatite bodies (IRUPs) which crystallized from iron-rich intercumulus and residual melts (Reid & Basson, 2002; Scoon & Mitchell, 1994). IRUPs are coarse-grained rocks that occur in the form of pipes, veins and, occasionally, sub-concordant sheets. Furthermore, IRUPs are normally accompanied by numerous fractures and are predominantly found in the Upper Critical, Main and Upper zones. Tharisa Mine is stratigraphically located in the Critical Zone and is underlain by the Middle Group (MG) chromitite layers (Figure 1a,b). The MG chromitite layer package is a deposit of five tabular chromitite layers named MG0, MG1, MG2, MG3 and MG4 (Figure 1b). The main economic horizons of interest at Tharisa Mine are: MG1, MG2, MG3, MG4 and MG4A. In the past, the UG1 was also extracted at the mine, as both the UG2 and UG1 outcrop nearby. The major metal components mined by Tharisa Mine are platinum, followed by palladium and ruthenium.

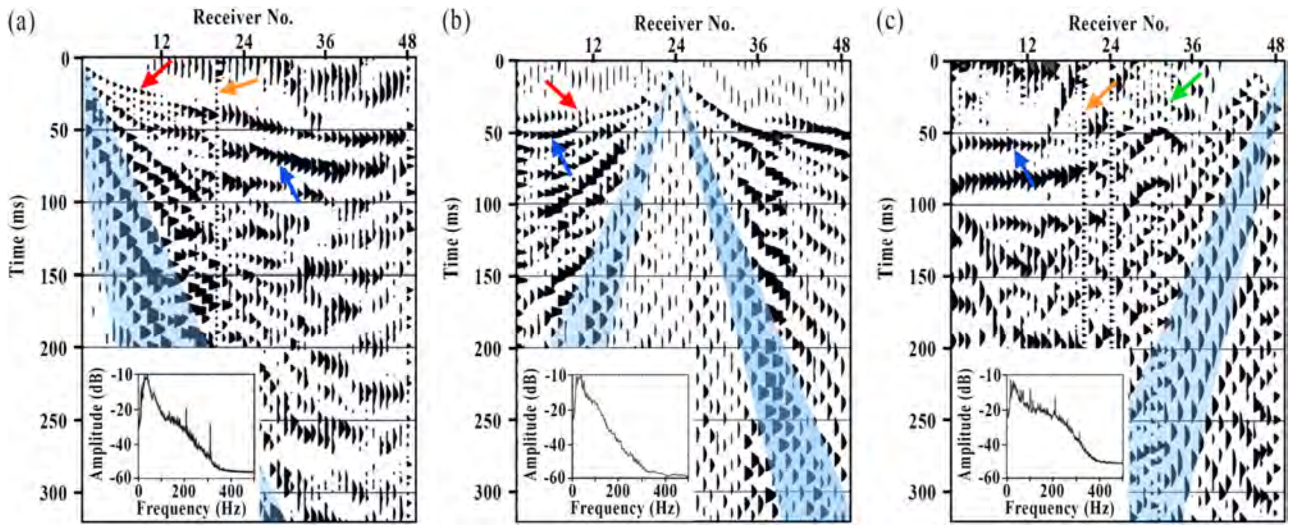

FIGURE 4 Raw seismic shot gathers (a–c) with corresponding frequency spectra. Bad traces (orange arrow) were removed from the shot gathers. The raw shot gathers show first arrivals (red arrows), and reflections (blue arrow) that are masked by the surface waves and air waves (blue shaded areas). The green arrow in part (c) corresponds to noise introduced by a secondary source, whereas the blue shaded area highlights the groundroll (surface wave) zone.

TABLE 2 Seismic data processing parameters

Step	2D processing flow
1.	Read SEG-Y data
2.	Edit traces, add geometry (*X*, *Y*, *Z*)
3.	Pick first P-wave breaks Travel-time–distance curve Inversion
4.	Refraction and elevation corrections Survey lines 1, 2, 3 and 4: datum 1224 m above mean seal level (msl)

OCCURRENCE AND FORMATION OF BOULDERS

Igneous rocks often contain several fracture types (e.g. net, oblique, vertical and horizontal fractures) of variable origin (e.g. tectonic, thermal, epigenetic and anthropogenetic) (Jinghong et al., 2011; Vitale & Isaia, 2014). Fractures in the Bushveld Complex often consist of planar and non-planar joints, that is fractures or cracks with no characteristic shear displacement (Figure 2a–d). The joins are ubiquitous, often planar in nature and occur in sets with approximately the same orientation. Their intensity varies widely across the complex and is largely attributed to tectonic stress (Roberts & Clark-Mostert, 2010; Twidale & Romani, 2005; Wilson et al., 2005). Some fractures observed in the Bushveld Complex (e.g. the prevalent layer-parallel faults and ramps) are interpreted to have formed due to crustal flexure (folding) caused by the intrusion of high-density mafic–ultramafic rocks (isostatic readjustment) (Cawthorn & Webb, 2001; Eales et al., 1993; Perritt & Roberts, 2007). According to Perritt and Roberts (2007), the Critical Zone commonly displays layered-parallel and ramp faults (duplex, frontal and lateral ramps) with prominent striations or corrugations, which are subsurface features often exploited by near-surface weathering processes to break down subsurface rocks.

Joint sets of varying orientation (cross cutting joint sets) often break down large masses of rock into separate fracture-bounded blocks (Figure 2a). In subsurface environments, spheroidal weathering exploits these fractures (along with other rock features, such as crystal boundaries and cleavages) to break down the bedrock and initiate the formation of boulders (Figure 2b,c; Fletcher et al., 2006; Twidale & Romani, 2005). The process is mainly driven by moisture from infiltrating meteoric waters, which contains gases, chemicals and biota that altogether break down fresh bedrock into regolith (saprolite and boulders; Figure 2c). The weathering process decays the bedrock starting from the joints and moves inwards into the core of the fracture-bounded blocks, forming boulders (called subterranean boulders) embedded in saprolite. The amount of weathering, and thus the boulder size and shape, all depend on prevalent fracture systems, shallow ground water chemistry, duration and intensity of weathering, as well as the rheology of the rock (Dan et al., 2016; Twidale & Romani, 2005). Along with subterranean boulders, subaerial boulders (blasting and excavation-induced boulders) are often present in opencast mining environments, including in the study area (Figure 2d).

GEOPHYSICAL SURVEYS

Prior to acquiring geophysical data, we collected rock samples and measured their physical properties, such as P-wave seismic velocity and magnetic susceptibility, to examine the

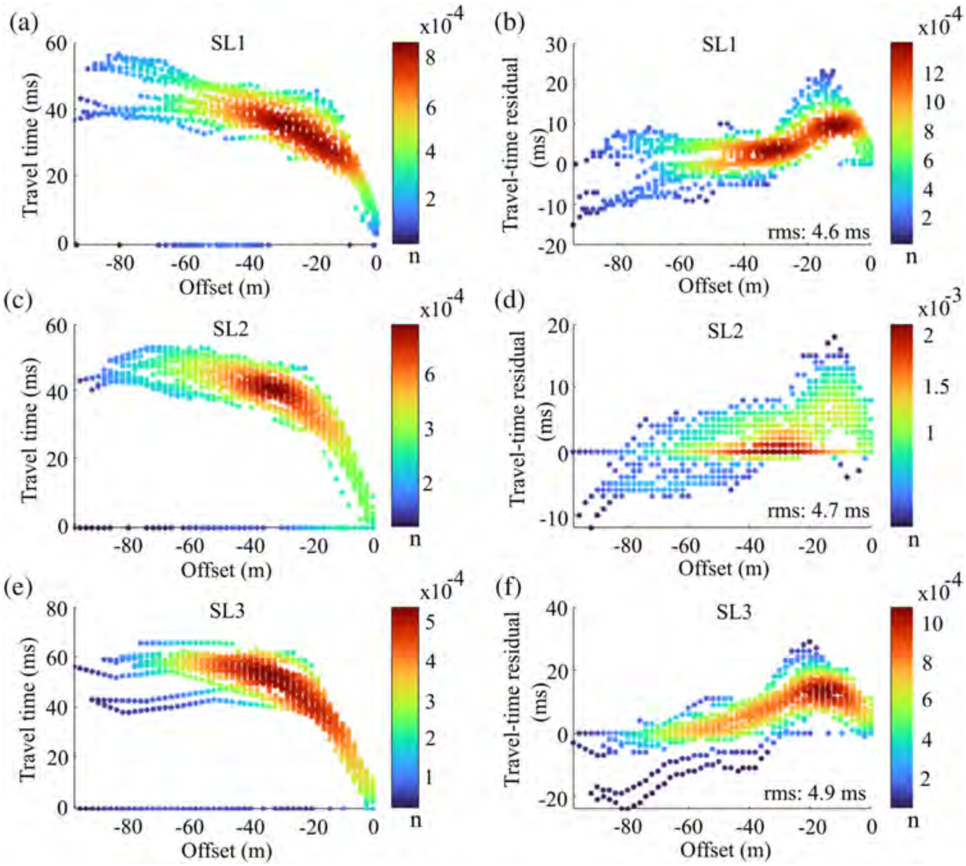

FIGURE 5 First break (a, c, e) and travel-time residuals (b, d, f) plots for seismic profiles SL1, SL2 and SL3. Both the first breaks and travel-time residuals are plotted as a function of offset, the colour scale used to illustrate the data represent the data density, where '*n*' is the number of points within a range.

feasibility of the study, and investigate if there is any significant physical property contrast between the boulders (fresh anorthosite and norite) and host rocks (weathered anorthosite and norite) (see Table 1). We conducted magnetic, electrical resistivity tomography (ERT), seismic refraction tomography and ground penetrating radar (GPR) surveys to map boulders, weathered zones, fresh bedrock zones and other subsurface geological features (i.e. overburden, fractures and iron-rich ultramafic pegmatites in the top 10–40 m). Figure 3 shows the survey locations of the different geophysical techniques.

Geophysical data acquisition and processing

Magnetic data

The magnetic data were acquired using three portable magnetometers, two G856 proton precession magnetometers and one G895 caesium vapour magnetometer with an integrated GPS receiver (WGS 84, accuracy of ±1 m). Both the proton precession magnetometers (G856) were used as base station magnetometers and were placed in separate areas with minimal noise. One of the magnetometers was set to collect data every 15 s and the other at every 30 s. The magnetometer with the best (least spikes) diurnal curve was used to correct the acquired field data. The caesium vapour (G859) magnetometer was used as a rover magnetometer. In order to reduce the effect of near-surface magnetic materials and minerals, the proton precision magnetometers were mounted on 2.5 m high vertically positioned, non-magnetic, aluminium poles. The rover magnetometer (G859) was carried on a non-magnetic backpack, with magnetic sensor and GPS receiver antenna heights of approximately 2–3 and 1.7–2 m from surface, respectively. To obtain high-resolution data and avoid spatial aliasing, the magnetic data were acquired in a walking mode using a sampling rate of 1 s, line spacing of 2 m, over an area of 150 × 100 m. Seventy-five SSW–NNE magnetic survey grid lines were collected over the magnetic grid survey area (Figure 3).

Processing of the magnetic data involved removing diurnal variations, de-spiking and micro-levelling using the Fast Fourier Transform frequency domain technique (which involves using the directional cosine filter and Butterworth filters) in order to reduce directional effects and remove long wavelength signals (detrending). Manual deculturing, as to

TABLE 3 Ground penetrating radar (GPR) acquisition parameters

Acquisition item	3D Grid/line number parameters GPR 3D	GL1 and GL3
Instrument	GSSI-SIR 4000 GPR system	
Grid size/line length	12 m × 15 m (*X*, *Y*)	200 m
Grid and trace spacing	1 m × 0.02 m	0.02 m
Survey direction:	N–S	W–E
Survey pattern	Zigzag	Along the profile
Dielectric	9 F/m	
Processing steps		
Energy decay	0–150 ns time window	
Bandpass filter	80–400 MHz	
Subtract-mean (dewow)	1–2 ns time window	
Subtracting average/background removal	10–20 average traces	
Diffraction stack	Summation width (10–20 traces); velocity (0.1–0.2 ns)	
Time-depth conversion	0.1–0.2 m/ns	

prevent the removal of important shallow geological signals, of the original total magnetic intensity grid and interpolation of the removed data points, using the minimum curvature technique, was subsequently carried out.

Magnetic enhancement techniques were applied to the data so as to correct and enhance specific characteristics of magnetic sources (e.g. magnetization, position, limits and discontinuities). The reduction to magnetic pole technique was applied to correct the position of the magnetic sources and their induced magnetization. The vertical tilt angle filter was applied to sharpen the edges of the magnetic sources (Cooper & Cowan, 2008; von Dobeneck et al., 2021).

Electrical resistivity tomography data

The resistivity survey consisted of five survey lines (RL1 to RL4), with line RL3.1 being a high-resolution resistivity line collected over a smaller section of profile RL3 due to the observation of hard-rock anorthosite to norite boulders at the surface (Figure 3). Four of the five resistivity lines (RL1, RL2, RL3 and RL3.1, WNW-ESE trending lines) were acquired on a graded sandy road, situated on the original surface of the opencast mine, close to the highwall. The lines were acquired perpendicular to the dip of the Bushveld Complex rocks in the area. Profile RL4, an SSW–NNE trending line, was acquired largely on partly loose sandy sediments, north of the road and parallel to the dip of the rocks in the area (Figure 3). The data were acquired using an automated ABEM 1200 resistivity system and an electrode spacing of 1 and 2 m. The profile length of the survey lines (excluding RL3.1) was 160 m, and that of RL3.1 was 80 m. The dipole–dipole and Schlumberger methods were used to acquire the data. The area along which profiles RL1, RL2, RL3 and RL3.1 were collected was a flat graded area with negligible topographic variation. Survey RL4 was acquired over an area with slightly more sand cover and topographic variation (∼1 m), especially in the northern side of the profile. Due to the effects of metal cased boreholes along profile RL4, the resistivity results of RL4 are not presented in the text.

The collected ERT data were first manually de-spiked and inverted to produce their inverted models. A weighted least-squares objective function coupled with linear filtering was used to carry out the inversion. Furthermore, an unstructured triangular finite element mesh, which allows for complicated model geometry, was used to produce the inverse models (Binley & Kemna, 2005; Blanchy et al., 2020). All the calculated resistivity inverse models reached the target root square mean error of ∼1 in three to four iterations.

Seismic refraction tomography data

The seismic data, SL1 to SL4, were acquired along the resistivity survey lines for integration purposes (Figure 3). The data were acquired using 48 (14 Hz) geophones connected to two 24-channel Geometric geode seismographs. To obtain high near-surface resolution, the data were collected using a geophone spacing of 2 m, yielding a common midpoint of 1 m. Shots were taken at every receiver. An asymmetric split-spread geometry with fixed receiver location, at a sampling

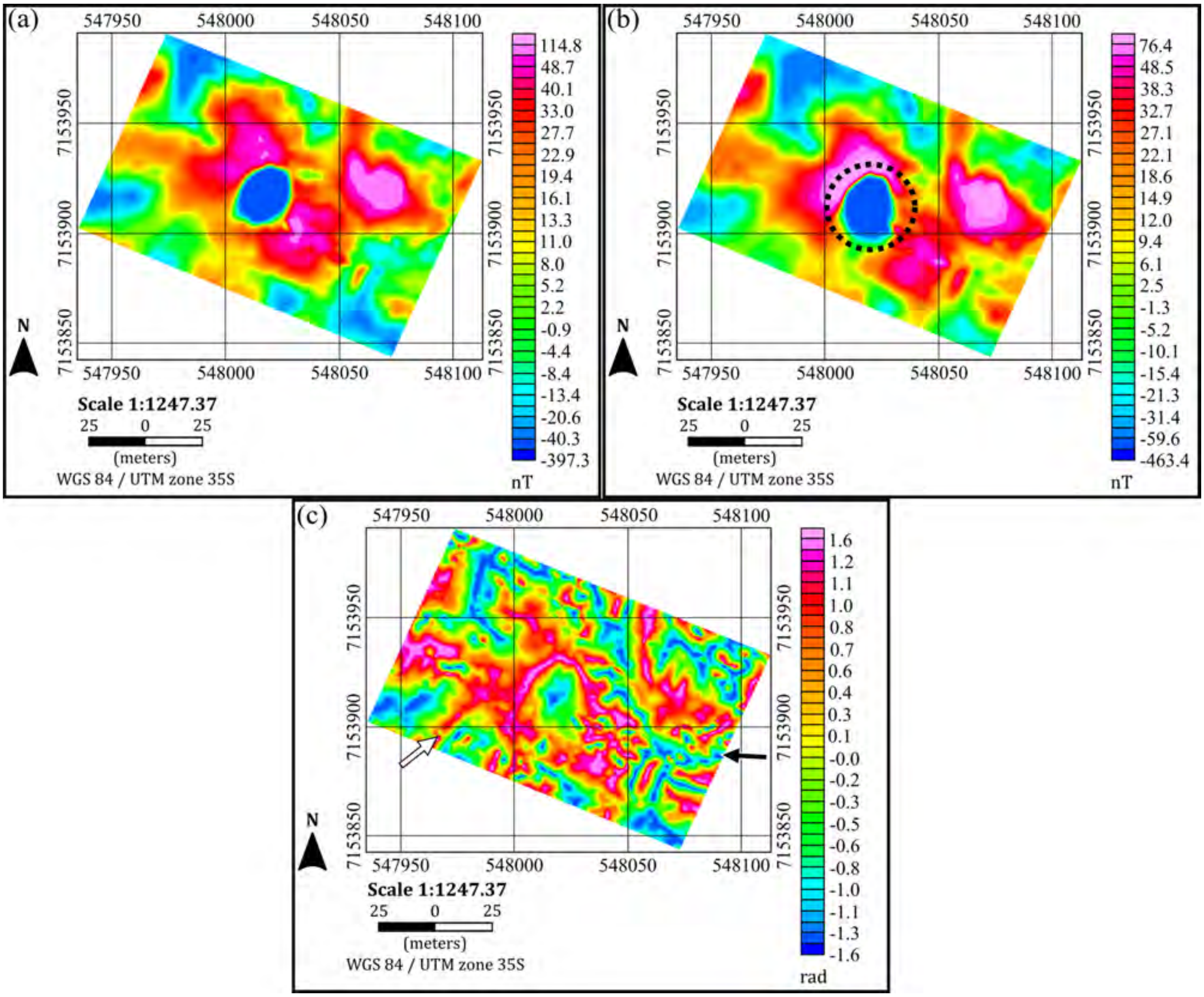

FIGURE 6 (a) Decultured, micro-levelled and detrended residual total magnetic intensity (TMI) map. (b) Reduced to magnetic pole (RTP) map, the black dotted circle shows the position of a body with remanent magnetization found in the study area. (c) Vertical tilt angle of the RTP map. The black and white arrows show connected magnetic low zones and magnetic high zones.

interval of 1 ms and a recording length of 1.5 s, was used to acquire the data. The ESS MINI Base Systems (weight-drop) mounted on a vehicle and/or 5 kg sledgehammer were used as seismic energy sources, and a 20 × 20 × 20 cm^3 aluminium metal base coupling plate was used to improve the source-to-ground coupling. A stack value of four was used to improve the signal-to-noise ratio. A high-cut filter of 250 Hz was used to eliminate the high frequencies that distort the acquired data. During the recording process, the acquired data were carefully monitored to avoid the introduction of noise generated by mining activities (e.g. drilling, blasting, moving vehicles and water pumps).

Figure 4a–c shows the comparison of raw seismic shot gathers of survey lines SL1, SL3 and SL4. The marked-on raw shot gathers are refracted (red arrows), possibly reflected (blue arrows) that appear to be masked by surface waves and air waves (blue shaded areas). Across all the gathered seismic data, the P-waves first breaks are present within the first 75 ms. Figure 4c (green arrow) shows an example of noise generated by drilling (between receivers 24 and 36) in seismic profile SL4. To construct the 2D P-wave refraction models, we used the 7200 first arrival picks across profiles SL1, SL2 and SL3. The processing steps are summarized in Table 2. The first break data were picked manually. First break picks and travel-time residuals for the P-wave velocity tomograms are given in Figure 5(a,c,e) and (b,d,f), respectively. Both the first break and travel-time residuals are illustrated as a function of offset. After 10 iterations, the final models for SL1, SL2 and SL3 profiles had an rms error of 4.6, 4.7 and 4.9, respectively (Figure 5b,d,f). Data acquired along the SL4 survey line are not presented in the text due to poor sensor-ground coupling caused by loose soil dumps along the survey line.

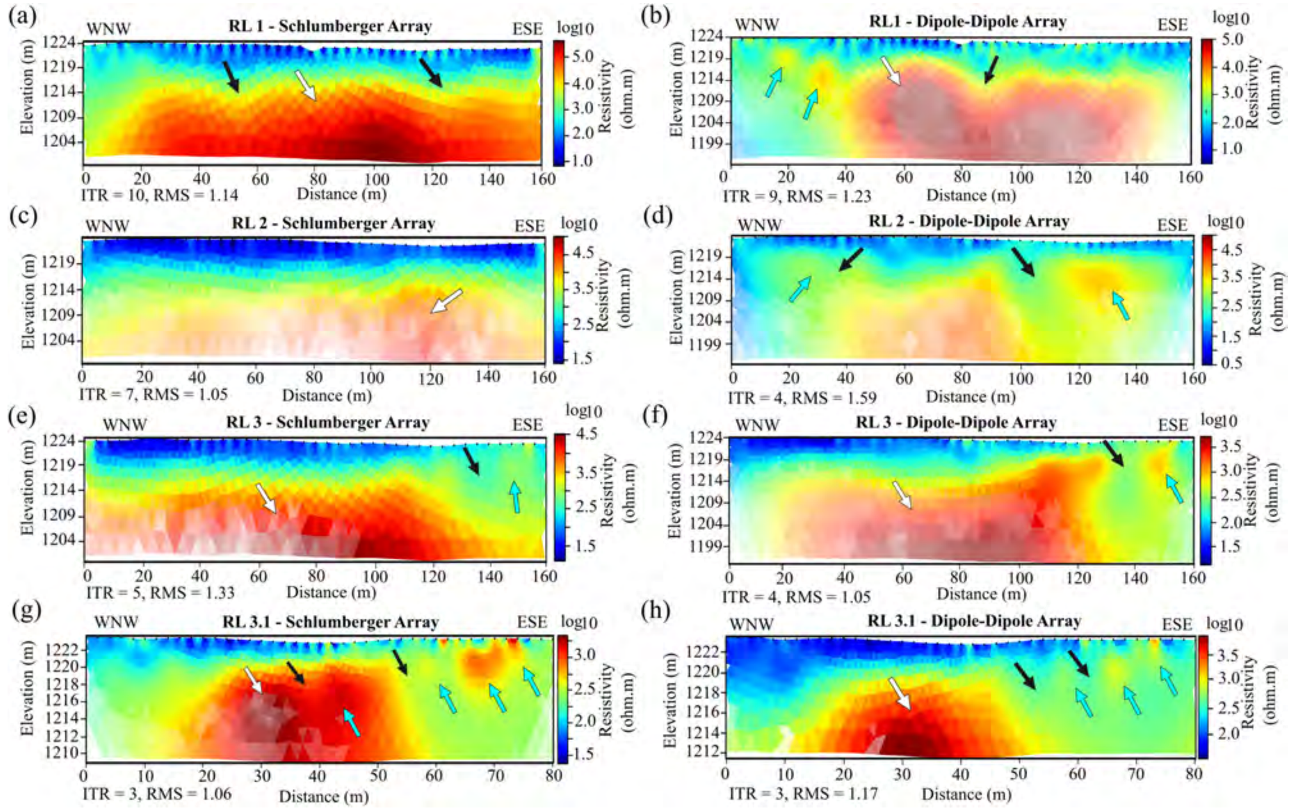

FIGURE 7 Schlumberger (a, c, e, g) and dipole–dipole (b, d, f, h) resistivity inverse models for electrical resistivity tomography survey RL1–RL3.1. The white, black and blue arrows in the plots indicate the high resistivity, low resistivity and potential boulders, respectively. The elevation used to produce the resistivity tomographs is the elevation above sea level, whereas the resistivity variation is measured in Ω m.

Ground penetrating radar

Table 3 shows the geometry parameters used to acquire GPR data. The GPR data were acquired using the GSSI-SIR 4000 GPR. The acquisition procedures involved moving the GPR cart across the 3D grid (GPR 3D) in zigzag direction and along the 2D lines GL1 and GL3 (Figure 3). Common-offset reflection survey mode was used for data acquisition with 0.02 m trace spacing, 0.2 ns sampling interval and 120 ns listening time. To improve the signal-to-noise ratio, 10 vertical radargrams were stacked at each sampling point.

The processing of the GPR data involved removing the acquisition delay time, applying energy decay gain to correct for the spherical spreading and intrinsic attenuation of the signal. A bandpass filter (80–400 MHz) was used to attenuate unwanted frequency components. The dominant frequency is approximately 300 MHz. Subtract-mean (dewow) and subtracting average/background removal filters were applied to enhance the sub-vertical reflectors as well as suppressing the background noise and the direct arrivals. The synthetic reflection hyperbolas were matched with observed diffraction patterns emanating from underlaying boulders, so that a 2D velocity field can be created. The GPR profiles were migrated and converted to depth with a constant velocity of 0.1/0.2 m/ns.

RESULTS

Magnetics

Figure 6 presents the detailed total magnetic intensity (TMI) map of the study area, including the results of the magnetic enhancement techniques. Specifically, Figure 6a–c presents the TMI, reduced to magnetic pole (RTP) and the vertical tilt angle maps of the study area, respectively. The TMI map, Figure 6a, shows the variation and distribution of positive and negative magnetic anomalies in the study area. The application of the RTP technique provides the corrected position of the magnetic sources and their induced magnetization (Figure 6b). From the computation of the RTP conversion, it is observed that a circular feature with remanent magnetization is present (indicated by a black dotted circle). The vertical tilt angle filter sharpens the variation between the low and high magnetic intensity zones (Figure 6c). The vertical tilt angle map reveals that both the high and low magnetic intensity zones are largely interconnected (indicated by arrows in

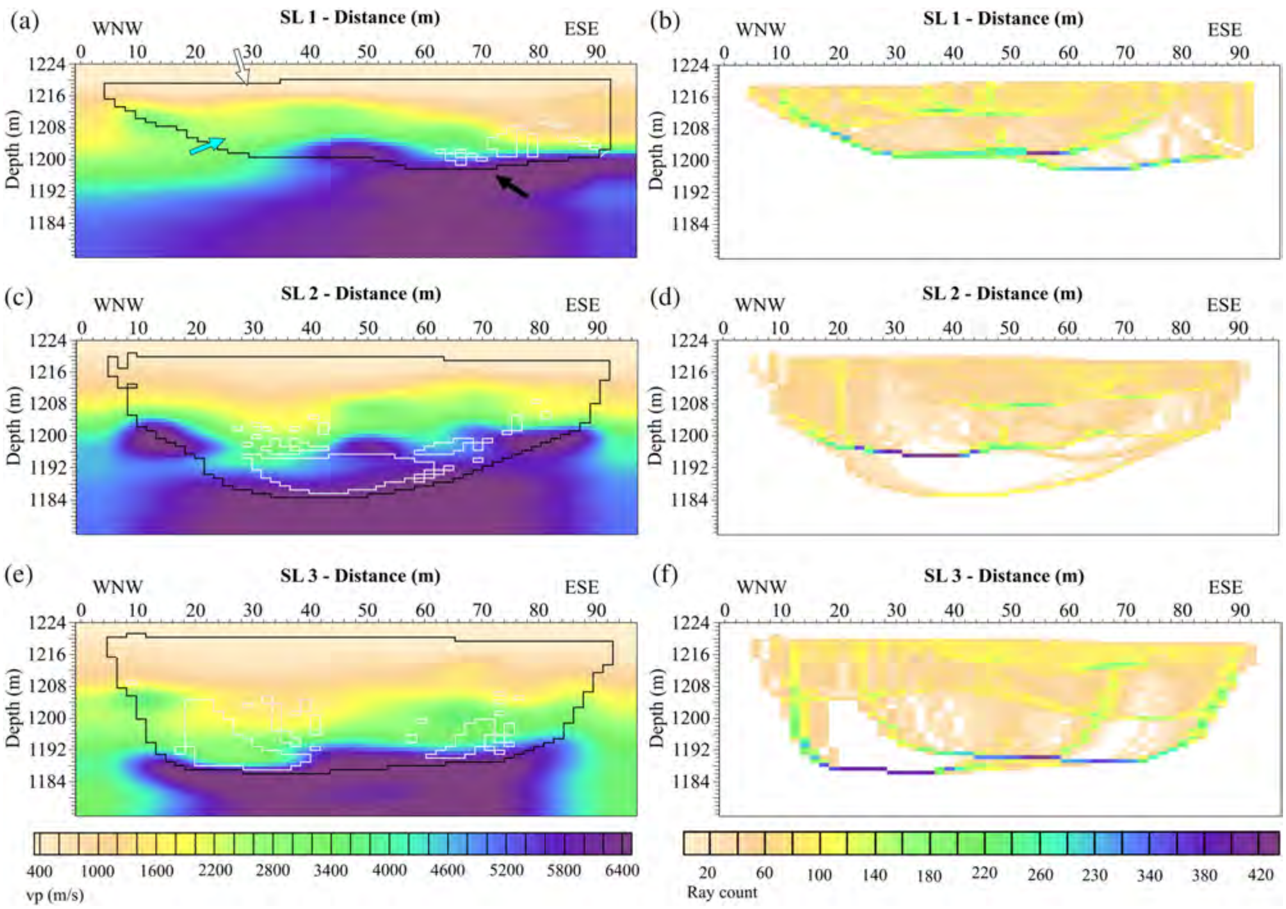

FIGURE 8 First break travel-time tomography model and their corresponding ray paths along profiles SL1 (a and b), SL2 (c and d) and SL3 (e and f). The outlines of the raypaths are drawn on the tomograms, and the zones within the white borders are zones in which ray paths did not travel through. The tomograms display near-linear (top) to distorted (middle and bottom) seismic variations with increasing depth. The white, blue and black arrows show the three identified seismic velocity layers, starting from the layer characterized by the lowest velocities to the layer with the highest velocities, respectively.

Figure 6c). The black and white arrows in Figure 6c each demonstrate an example of a magnetic low and high zone, respectively. The effects of weathering (gradual variation in magnetic intensity moving from the magnetic low to high regions), the presence of fractures (zones that separate the red zones, also appearing as blue) and of a feature with remanent magnetization are well captured in Figure 6a–c.

Electrical resistivity tomography

The 160 m long survey lines acquired across the study area (Figure 3) are observed to reach depths between 21 and 30 m, depending on the type of array used. The resistivity tomography results, shown in Figure 7, show a progressive increase of the resistivities of the rocks with depth. The near-surface (top ~6–5 m) is demarked by a conductive zone (low resistivity, blue coloured zone) with resistivities of ~3–40 Ω m. The thickness of this low resistivity zone is observed to vary from one resistivity profile to another, but it is between 6 and 7 m (Figure 7). This top resistivity low zone is underlain by a zone of much higher resistivities (~40–3162 Ω m), coloured as light green to yellow zone. The contrast observed between these two layers is representative of the sharp contrast observed at the topsoil-fractured bedrock interface, visible on the highwall present a few meters away from the study area (see Figure 2b). Underlying the green to yellow zone is the light to dark red zone, a zone of much higher resistivity (~3162–~10,000 Ω m). The variation in the resistivity of these three observed zones is complex, both moving along and across the profiles (Figure 7). The Schlumberger array is observed to best demonstrate the resistivity variation across depth and the bedrock (high resistivity zones, indicated by white arrows) (Figure 7a,c,e,g), whereas the dipole–dipole array (Figure 7b,d,f,h) best demonstrates potential fractures, highly weathered zones (low resistivity zones separating high

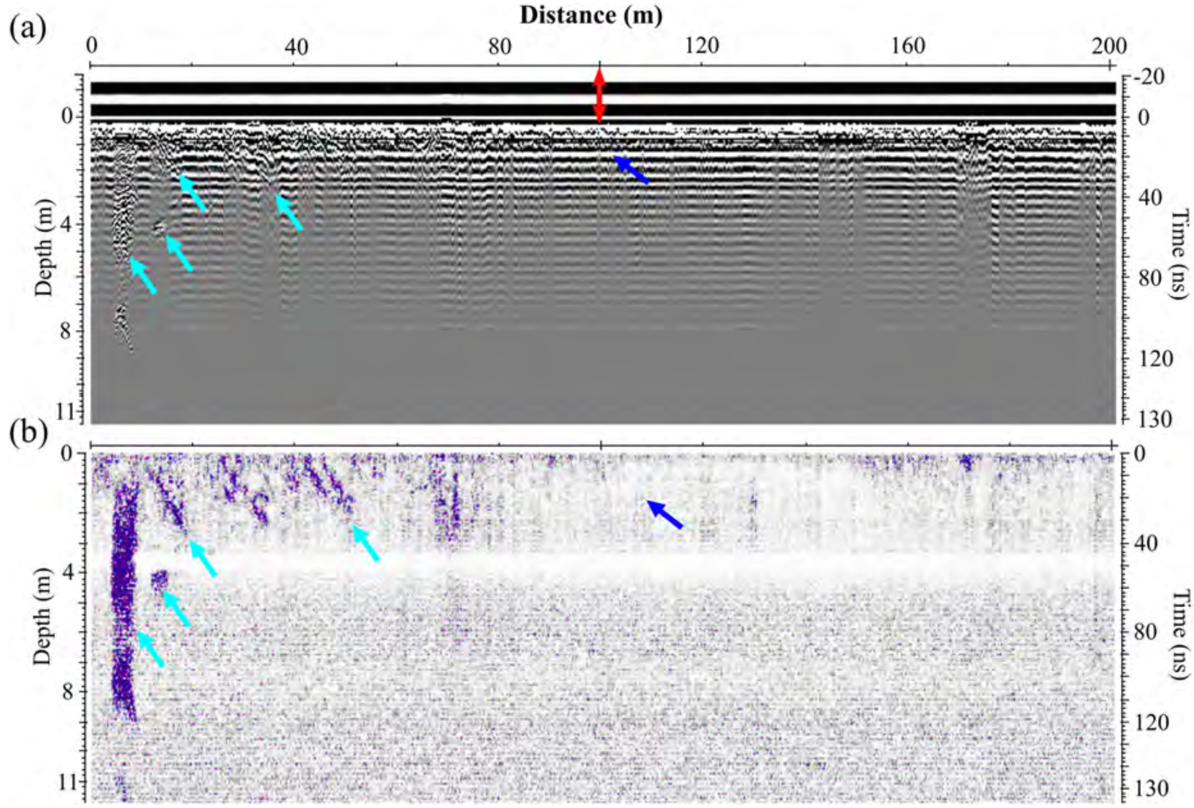

FIGURE 9 A sample of a raw (a) and processed 2D ground penetrating radar (GPR) sections (b) of profile GL1. The double headed red, light blue and dark blue arrows show the delay time, reflection and diffraction and background noise, respectively. The observed reflection and diffraction events are possibly events originating from the contact of different lithologies and boulders.

resistivity zones, indicated by black arrows) and boulders (semicircular, high resistivity features in low resistivity zones, indicated by blue arrows).

Seismic refraction tomography

The P-wave refraction tomograms largely demonstrate an increase in P-wave seismic velocities with increasing depth. Figure 8 illustrates the final P-wave refraction models (Figure 8a,c,e) for profiles SL1, SL2 and SL3, and their ray paths (Figure 8b,d,f). The tomograms reveal the presence of roughly three P-wave seismic velocity zones (layers) of varying thickness, both along and across the seismic profiles (Figure 8). The near-subsurface seismic velocity zone, light brown zone (indicated by a white arrow), exhibits the maximum P-wave velocity of ~1400 m/s. Based on the inversion models, the depth extent of the velocity low zone varies from surface to a maximum depth of about 20 m (Figure 8). This top light brown layer is underlain by a yellow to green seismic P-wave velocity zone (indicated by a light blue arrow) of relatively higher velocities (~1400–~4000 m/s). The thickness of this layer varies across the profiles. The layer consists of semicircles/ellipses of higher velocities embedded within it, which are interpreted as boulders. Underlying this second velocity zone is a light to dark blue seismic velocity zone of higher P-wave velocities (~4000–~6400 m/s, indicated by a black arrow). This light to dark blue seismic velocity zone exhibits variable depth from the surface. The observed seismic velocity zones consist of zones of disturbed layering, possible fracture (jointing and faulting) and boulder zones (Figure 8).

Ground penetrating radar

The ground penetrating radar sections show radar traces (radargram) plotted against time and distance (Figure 9). The *x*-axis represents the distance along the survey line, whereas the *y*-axis represents the travel-time of the radar pulses. The radargrams show several reflections (dark blue arrows) and diffraction events (light blue arrows), probably emanating from buried boulders and loose soil cover, as well as from the background noise (Figure 9).

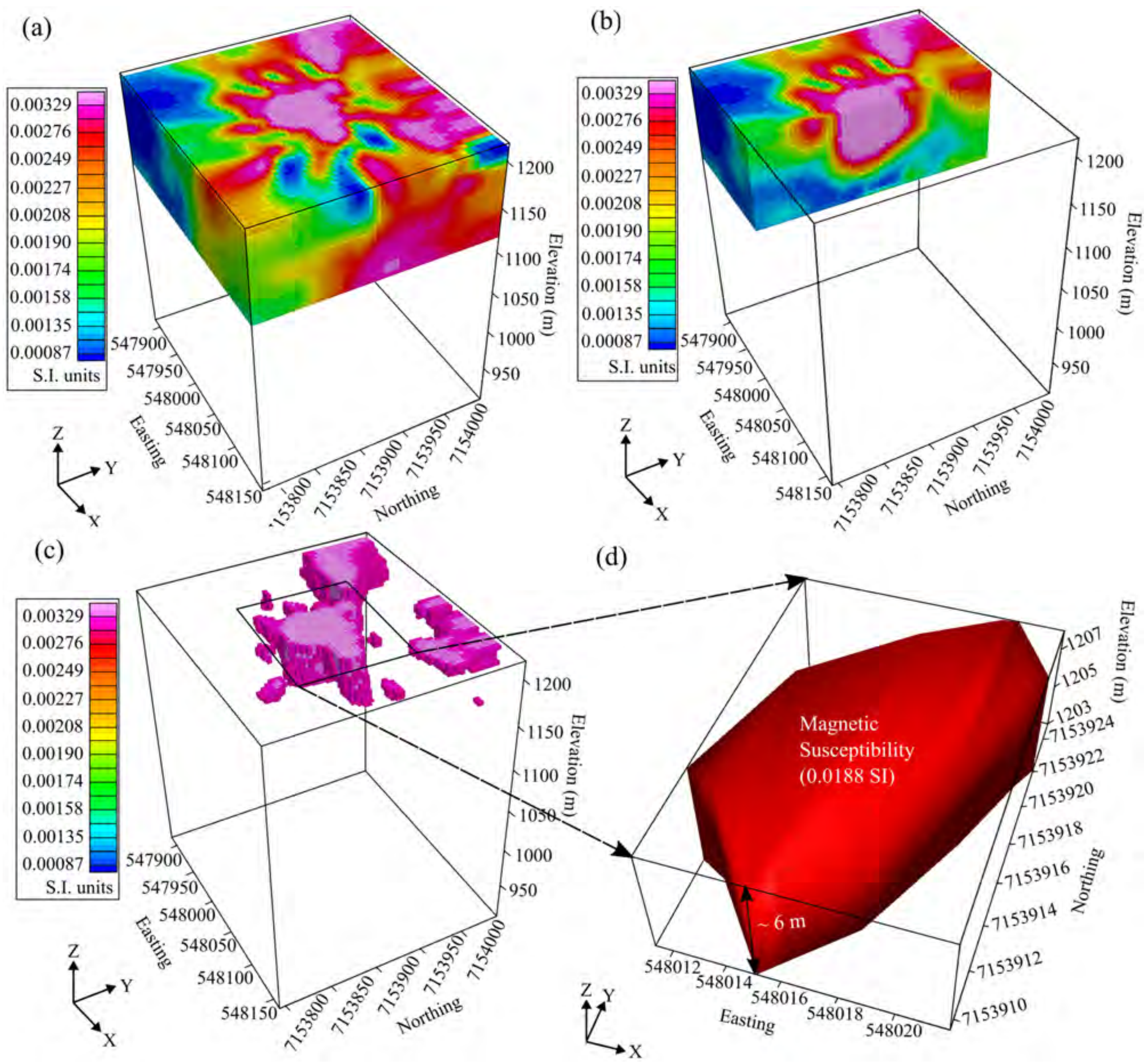

FIGURE 10 Susceptibility Magnetic Vector Inversion (MVI) model of the acquired TMI data in our study area. (a) Full MVI model of the magnetic data displaying the magnetic susceptibility of the rocks, including that of the iron-rich ultramafic pegmatite (IRUP) (centre). (b) Clipped 3D susceptibility model showing the vertical nature of the IRUP. (c) Zones of high magnetic susceptibility around the IRUP are interpreted as potential boulders. (d) 3D best-fit ModelVision model of the IRUP.

INTERPRETATIONS AND DISCUSSION

Magnetic susceptibility inversion models

Noritic and anorthositic rocks can be magnetic due to the presence of accessory minerals such as magnetite and ilmenite (Dunlop et al., 2010; Soumya et al., 2017). The weathering of such mafic rocks, that is, norites and anorthosites, ultimately results in the formation of soil, with silicate minerals breaking down into clay minerals (conductive minerals), and iron-bearing minerals (e.g. magnetite and ilmenite) breaking down into iron oxides of varying magnetic susceptibility (Lu et al., 2008; von Dobeneck et al., 2021). The weathering of magnetite initially forms oxidized ferrimagnetic Fe-minerals, such as maghemite, followed by antiferromagnetic minerals, such as hematite and goethite, which are far less magnetic (Lu et al., 2008; von Dobeneck et al., 2021). Both maghemite and hematite are observed at the mine site. In magnetic soils, however, magnetite can be weathered directly to hematite (Santana et al., 2001). Overall, there is a gradual loss of inherited thermoremanent and/or acquired chemical magnetization with progressive weathering, mainly associated with the alteration and the reduction of grain sizes of magnetic minerals in rocks (Harding et al., 1988; Lapointe et al., 1986; von Dobeneck et al., 2021). The reduction in magnetization with weathering is observed in the magnetic susceptibility measured on hand samples in the laboratory (Table 1). Therefore, magnetic high zones (red- and pink-coloured zones) are interpreted to represent least-weathered areas, whereas low magnetic zones are interpreted to represent highly weathered areas (Figure 6). The high magnetic zones are caused by a shallow, fresher and less fractured bedrock component, and thus, these zones are likely to form blasting-induced boulders when blasted inadequately. The surrounded high magnetic zones are lower magnetic intensity zones (green to dark blue-coloured zones; Figure 6). The lower magnetic intensity zones represent highly weathered and fractured areas. The blue-coloured zones are thought to be the most weathered zones, where fractures in the rock accelerate chemical weathering processes. Thus, blue-coloured zones are where fresh rock was broken-down (e.g. formation of hematite and clay minerals) at a faster rate. The probability of finding isolated subterranean boulders surrounded by regolith should therefore be higher in such highly weathered zones.

The semicircular, low magnetic intensity feature at the centre of the magnetic maps (blue-coloured; Figure 6) is thought to be a weathered remnant of a magnetized iron-rich ultramafic pegmatite (IRUP) (Scoon & Mitchell, 1994). IRUPs are typically weakly magnetic bodies (either positive or reverse magnetization) that preferentially replace anorthosite–leuconorite lithologies (Campbell, 2006; Reid & Basson, 2002; Scoon & Mitchell, 1994). Such lithologies are noted at the Tharisa Mine. Furthermore, the semicircular shape (when viewed perpendicular to layering) of the feature is consistent with the pipe-like shape (when viewed parallel to layering) often noted for IRUP bodies (Scoon & Mitchell, 1994). 3D models of the low magnetic susceptibility feature are presented in Figure 10a–d and confirm that the feature is indeed pipe-shaped. The models also reveal that the feature is shallow (Figure 10b), at a depth of about 10 m from surface with a vertical extent of roughly 6 m (Figure 10c,d), and has a magnetic susceptibility of 0.0188 SI units. Given that the feature terminates at depth (Figure 10b,d) suggests that it is of a replacement nature, which also corresponds to the hypothesized origin for IRUPs (Scoon & Mitchell, 1994). However, amplitude inversion models are often biased towards high amplitude anomalies, which in this case corresponds to the IRUP body. This existing bias results in the attenuation of lower amplitude features, meaning that they may not be well resolved. Thus, although Figure 10c appears to resolve small-scale semi-spherical features (possible boulders), it is possible that additional small-scale features are missed because of their lower magnetic susceptibility compared to the high amplitude IRUP. Considering the high level of weathering encountered in the top subsurface (10–30 m depth), combined with the presence of an IRUP, which is commonly accompanied by numerous fractures, these are promising factors for the presence of boulders in the area.

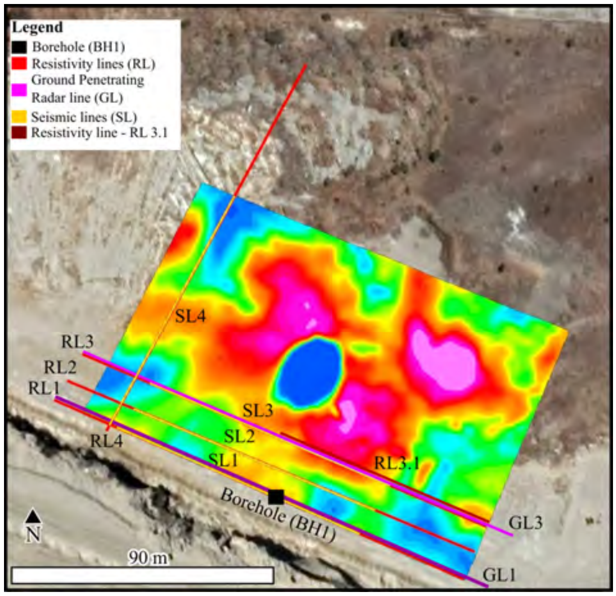

FIGURE 11 Seismic (SL), resistivity (RL) and ground penetrating radar (GL) 2D line locations overlain on the total magnetic intensity map of the study area. The seismic and resistivity profiles were placed on a zone with varying TMI to try map the observed magnetic variation in the subsurface rocks with depth.

Integration of resistivity, seismic and ground penetrating radar results

The electrical resistivity tomography (ERT), seismic refraction tomography and ground penetrating radar (GPR) surveys acquired in this study were collected over an area of varying total magnetic intensity, thus, over an area of variable weathering and magnetic susceptibility (Figure 11). Figure 12 compares and correlates the inverted ERT, SRT and GPR sections across survey profile 1 (profile along which SL1, RL1 and GL1 where acquired) along with lithological data from a borehole (BH1) (Figures 3 and 11). Both the resistivity and seismic inversion results for profile 1 correlate with the borehole BH1 data. At the location of BH1, in both the resistivity and seismic sections, the dark to light blue and light brown zones corresponding to a low resistivity and seismic velocity zone, respectively, represent the top 6 m section (core-loss zone) of BH1 (Figure 12b,c). The dark to light blue near-surface zone is characterized by resistivities of ≤40 Ω m and P-wave velocities of ≤1400 m/s. This zone is interpreted to be the saprolite clay–regolith zone, a zone of high weathering activity. With increasing depth, a large increase in resistivity and P-wave seismic velocity of the subsurface rocks is observed.

The overburn norite and leuconorite (anorthosite-norite) layers, situated below the core-loss zone at depths between

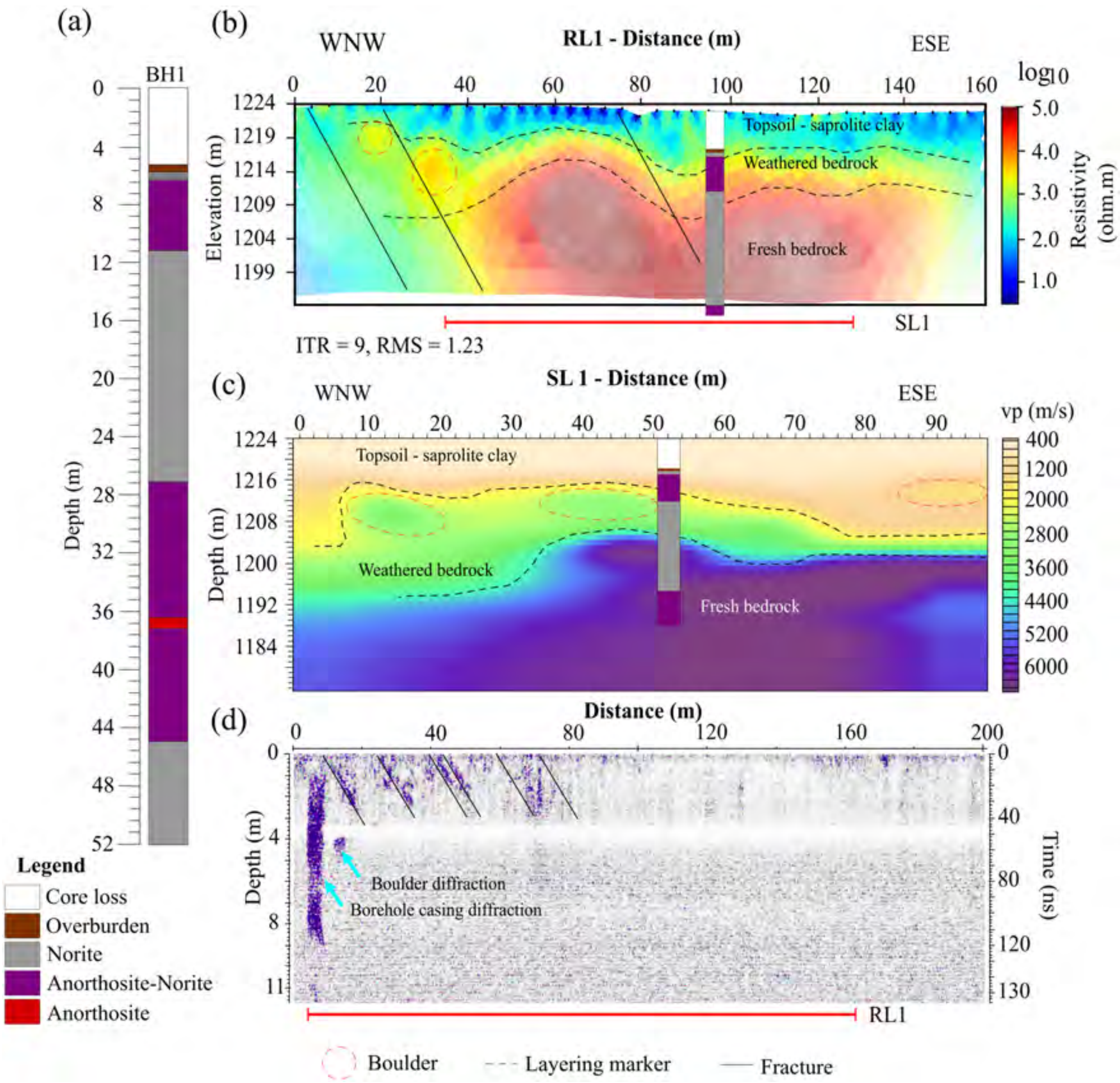

FIGURE 12 Interpretation and integration of methods for profile 1 (profile where SL1, RL1 and GL1 were acquired). (a) Borehole (BH1) lithology along profile 1. The lithological log has been correlated with RL1 and SL1. (b) BH1 overlain on the electrical resistivity tomogram of RL1. (c) BH1 overlain on the seismic refraction tomogram of SL1. (d) Ground penetrating radar section of profile GL1. The dotted lines show the lithological boundaries among saprolite clay, weathered bedrock and fresh bedrock. The solid black lines correspond to joints, fractures or fault lineaments.

6 and 11 m, are characterized by higher resistivities and P-wave seismic velocities of ~40–3162 Ω m and ~1400–3600 m/s, respectively (Figure 12). These layers, that is the overburn, norite and leuconorite, along with the top portion of the norite rock appearing at a depth of 11 m and greater are interpreted to constitute the weathered bedrock zone. The layers situated below the weathered bedrock zone, starting with the norite layer at a depth of about 11 m and extending to greater depths, are characterized by much higher resistivities and seismic velocities of ~3162–10,000 Ω m and ~3600–6400 m/s, respectively. These high resistivity and seismic velocity zones are interpreted to represent fresh bedrock zones, fresh norite to anorthosite zones, that have been least affected by near-surface weathering processes (Figure 12b,c).

The linear features on the GPR GL1 radargram are responses from structural features (joints and faults), which are correlatable with both the resistivity and seismic tomograms (Figure 12b–d).

The resistivity, seismic inverted models and the GPR radargram for profile 3 (line with RL3, SL3, GL3 and RL3.1) are presented in Figure 13. In both the ERT and SRT depth sections, horizons (i.e. saprolite clay, weathered bedrock and fresh bedrock) are inhomogeneous and present abrupt changes that can be attributed to fracture-related distortions (Figure 13a–c). The ERT, SRT and GPR sections reveal that the lithology along profile 3 is highly disturbed (Figure 13a–d). At a distance of about 145 –160 m, along RL3 and about ~0.5–1 m next to the line, exposed rocks (outcrops),

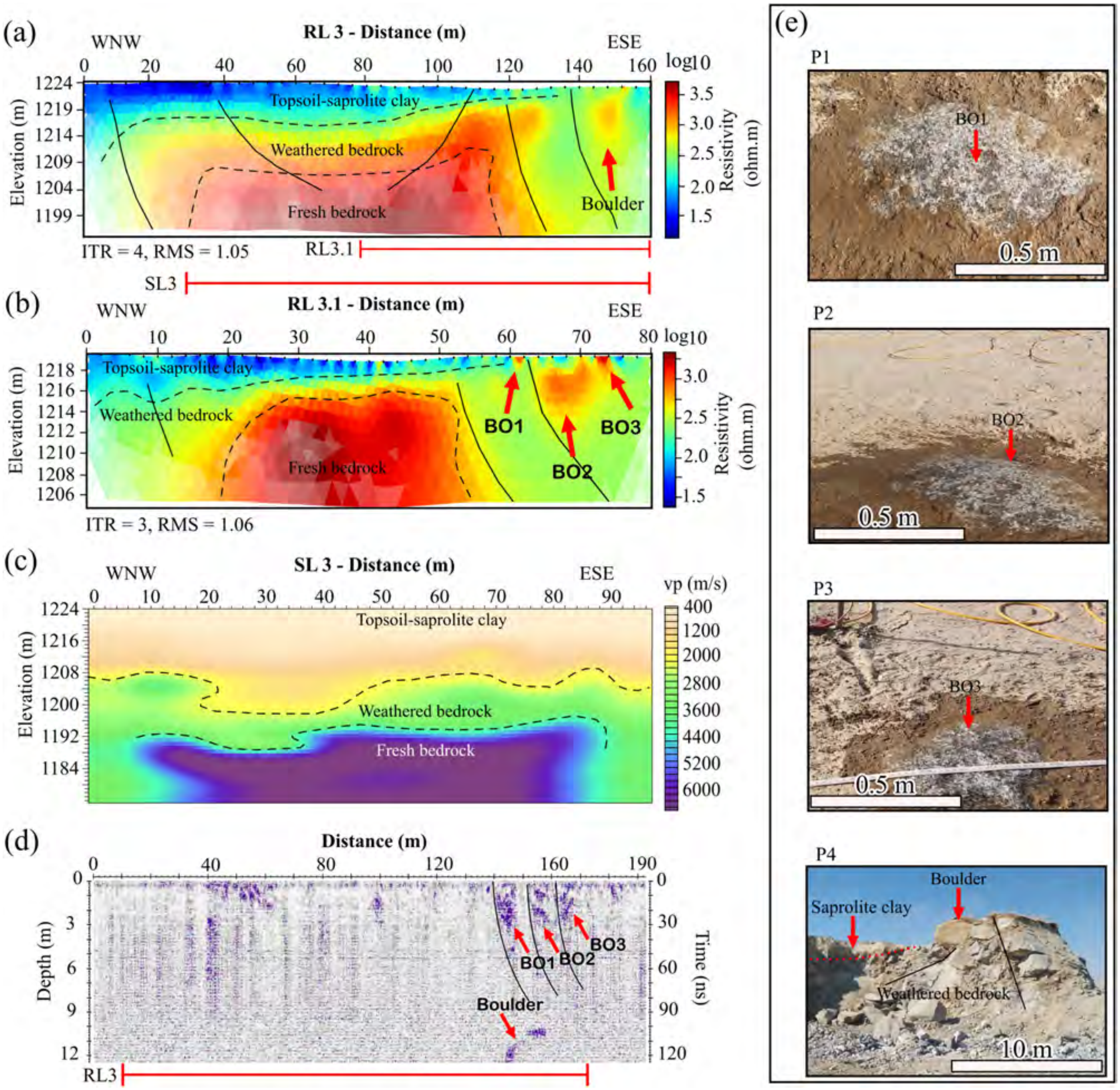

FIGURE 13 Interpretation and integration of methods for profile 3 (profile where SL3, GL3, RL3 and RL3.1 were acquired). (a) Electrical resistivity tomogram of profile RL3. (b) Electrical resistivity tomogram of profile RL3.1, high-resolution line mapping the outcropped region along RL3. (c) Seismic refraction tomogram for profile SL3. (d) Ground penetrating radar section of profile GL3. (e) Images of the outcropping rocks along profile 3 (pictures P1, P2, P3 and P4). The dotted lines show lithological boundaries among saprolite clay, weathered bedrock and fresh bedrock zones. The solid black lines show joints, fractures or fault lineaments. BO, boulder outcrops.

likely corresponding to norite boulders, were observed. A high-resolution (1 m) electrical resistivity depth section of the area adjacent to the outcrops, along RL3 and RL3.1, is presented in Figure 13b. Notably, the high-resolution resistivity depth section shows several high resistivity features (boulders) embedded in a zone of low resistivity along the eastern edge of the section. Some of these boulders were outcropping on surface (BO1, BO2 and BO3 in Figure 13e), which provided confidence in our interpretation. Furthermore, the high-resolution section (RL3.1) details a central high resistivity zone (orange to dark red-colours), interpreted as fresh bedrock, embedded in a low resistivity zone (green to dark blue coloured), which corresponds to weathered/altered rock (Figure 13b). The central high resistivity zone is suspected to be an underground extension of the norite bedrock, based on outcrops near where profile 3 was conducted. The presence of buried boulders is also seen in the GPR radargram as diffractions. The location and depth of the boulders match relatively well between the resistivity tomograms and GPR radargram (Figure 13a–d).

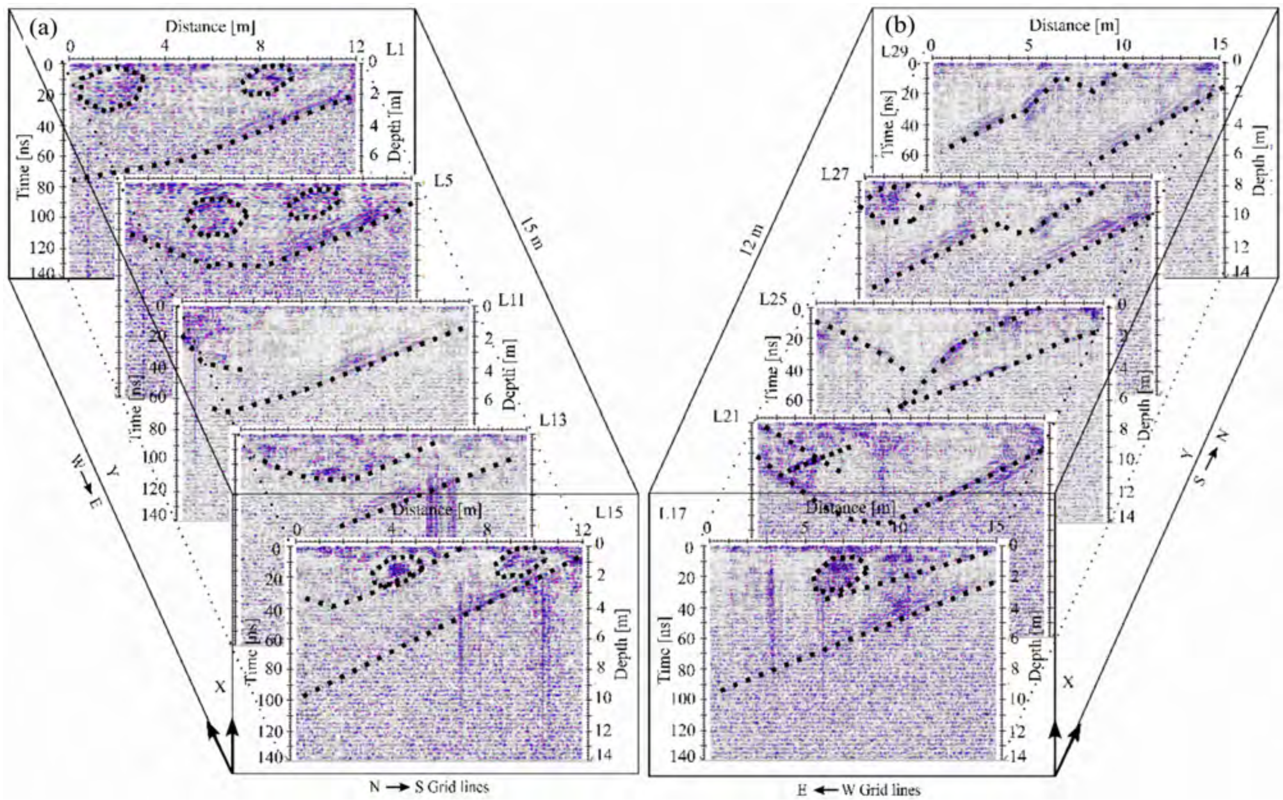

FIGURE 14 (a) and (b) 3D view interpretation of ground penetrating radar (GPR) 3D grid radargram lines along the north–south (*X*) and east–west (*Y*) directions, respectively. *Note*: *Y*-axes are not drawn to scale and the dotted black lines and circles in all sections correspond to different geological features.

The GPR radargram interpretations of grid GPR 3D (Figure 3) are shown in Figure 14. The maximum depth of penetration of the electromagnetic wave is ~10 m. Figure 14a,b shows the 3D view interpretation of GPR 3D grid lines along the north–south (*X*) and east–west (*Y*) directions, respectively. The steeply dipping linear features observed in the radargram sections likely correspond to reflections emanating from joints and fractures. These structural features have variable dips (~30°–50°). The formation of these structures could be as a result of gradual mechanical/chemical weathering or recent mining activity (e.g. rock blasting). The linear features could also correspond to boulder interfaces within the saprolite clay horizon (e.g. Figure 14b). The gentle dipping (~10°–15°) reflections in GPR 3D data likely correspond to responses emanating from the saprolite clay-boulder and weathered bedrock interface. Several diffractions on GPR data are interpreted as boulders, ranging between 2 and 4 m wide at ~1–7 m depth. In future, we plan to process the reflection seismic surveys acquired along these boulders to enhance the detection of these boulders and constrain their 3D geometry through diffraction imaging approaches (Moser & Howard, 2008). The results will be compared to diffraction patterns observed on the GPR data to constrain their interpretation. Several authors (e.g. Khaidukov et al., 2004) have demonstrated the effectiveness of analysing seismic response of similar features through diffraction imaging. Diffraction analysis on the seismic data has the potential to detect even small boulders that are beyond the resolution of other geophysical methods used in this study (Moser & Howard, 2008).

Geological model

By overlaying the electrical resistivity and seismic depth sections on Google Earth maps, we observe that there is strong correlation among the magnetic intensity, P-wave seismic velocity and resistivity variations (Figure 15). Specifically, the magnetic intensity is higher in regions with a thin low seismic velocity and low resistivity zone. The opposite is also true, whereby magnetic intensity is lower in regions with a thick low seismic velocity or low resistivity zone (Figure 15a–f). The thicker the low velocity or conductive zone, the less magnetic the area. Thus, there is a strong depth correlation among magnetic intensity, seismic velocity and resistivity (Figure 15). The correlation is better observed on the TVDR projected images (Figure 15b,d,f). This may imply that where magnetic highs are prominent, the ground is

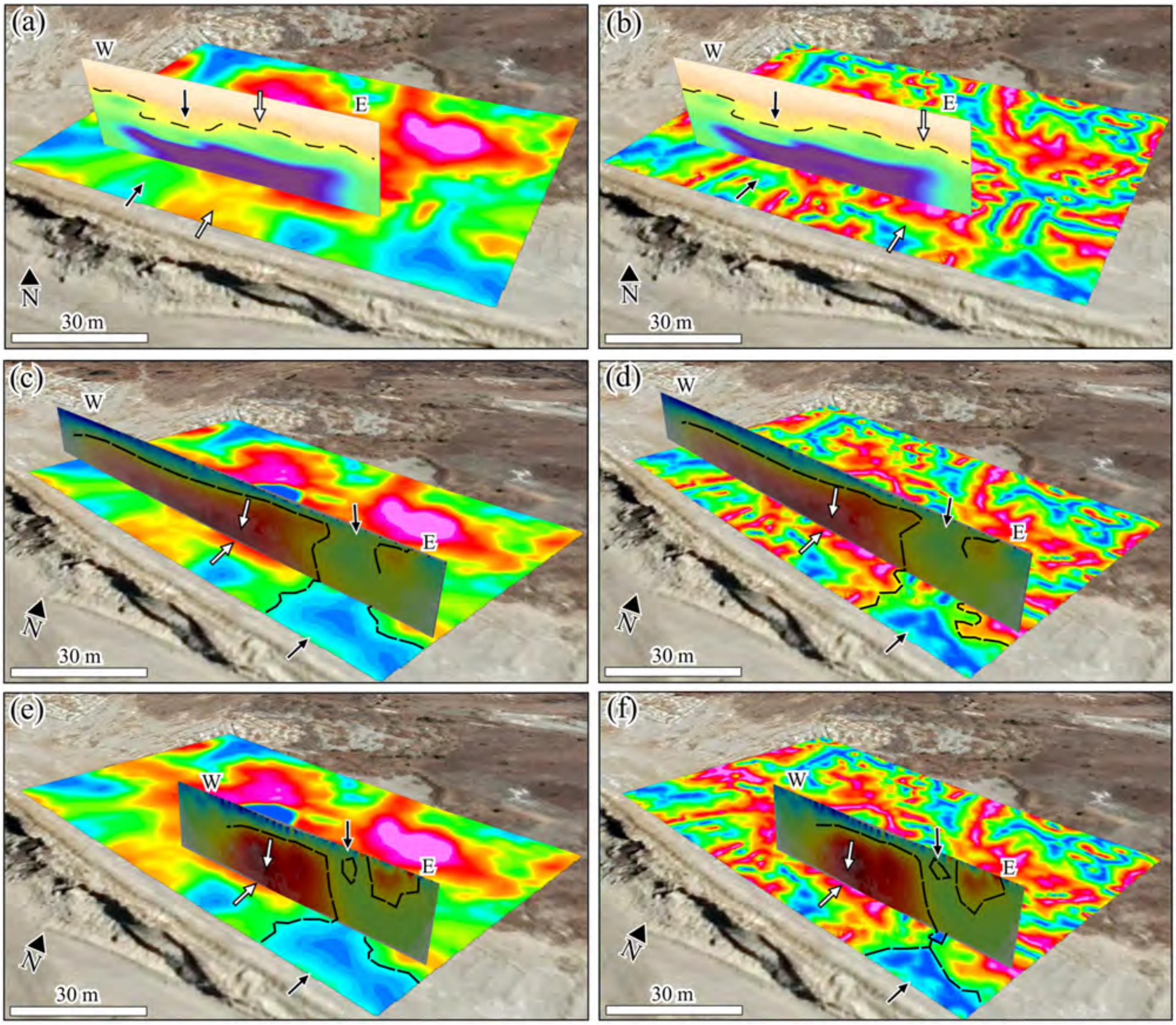

FIGURE 15 Profile SL3 seismic depth section projected on the TMI (a) and TVDR magnetic (b) maps. Profile RL3 resistivity depth section projected on the TMI (c) and TVDR (d) magnetic maps. Profile RL3.1 resistivity depth section projected on TMI (e) and TVDR (f) magnetic maps. The white and black arrows indicate areas where there is high and low correlation, respectively.

relatively less weathered, and the depth of the fresh bedrock is closer to the surface. In regions where the magnetic low is prominent, the thickness of the saprolite clay and weathered horizons is larger, and thus, the depth to the fresh bedrock is greater (excluding regions where remanently magnetized bodies are present, e.g. above the IRUP). In areas where boulders were identified (i.e. Figures 12 and 13a–d), a magnetic high anomaly in a magnetic low zone is observed, which is interpreted to be associated with the less-weathered nature of the boulders as compared to the host rock (Figure 15c–f). These observations demonstrate that electrical resistivity and magnetic surveys can be successfully used to infer the presence of subterranean boulders in magnetic environments. The integrated geophysical data (Figures 12–14), combined with surface geological observations and borehole lithological data, were used to generate a 3D geological model of the study area (Figure 16a,b).

The integration of the data is of significant interest for exploration and planning mining activities (e.g. blasting, extraction of ore and slope/ground stability). Interestingly, not all boulders found at Tharisa Mine are subterranean boulders, some are subaerial boulders caused by blasting activity (Figure 2d). In open-pit mining, subaerial boulders are large rock fragments often formed during excavation and bench blasting, due to inefficient rock breakage. These types of boulders are a recognized by-product of the drill-and-blast techniques (Leng et al., 2020). The drill-and-blasting technique is a cost-effective scheme often used in mines to quickly excavate large areas and break down benches. Oversized boulders are typically formed when

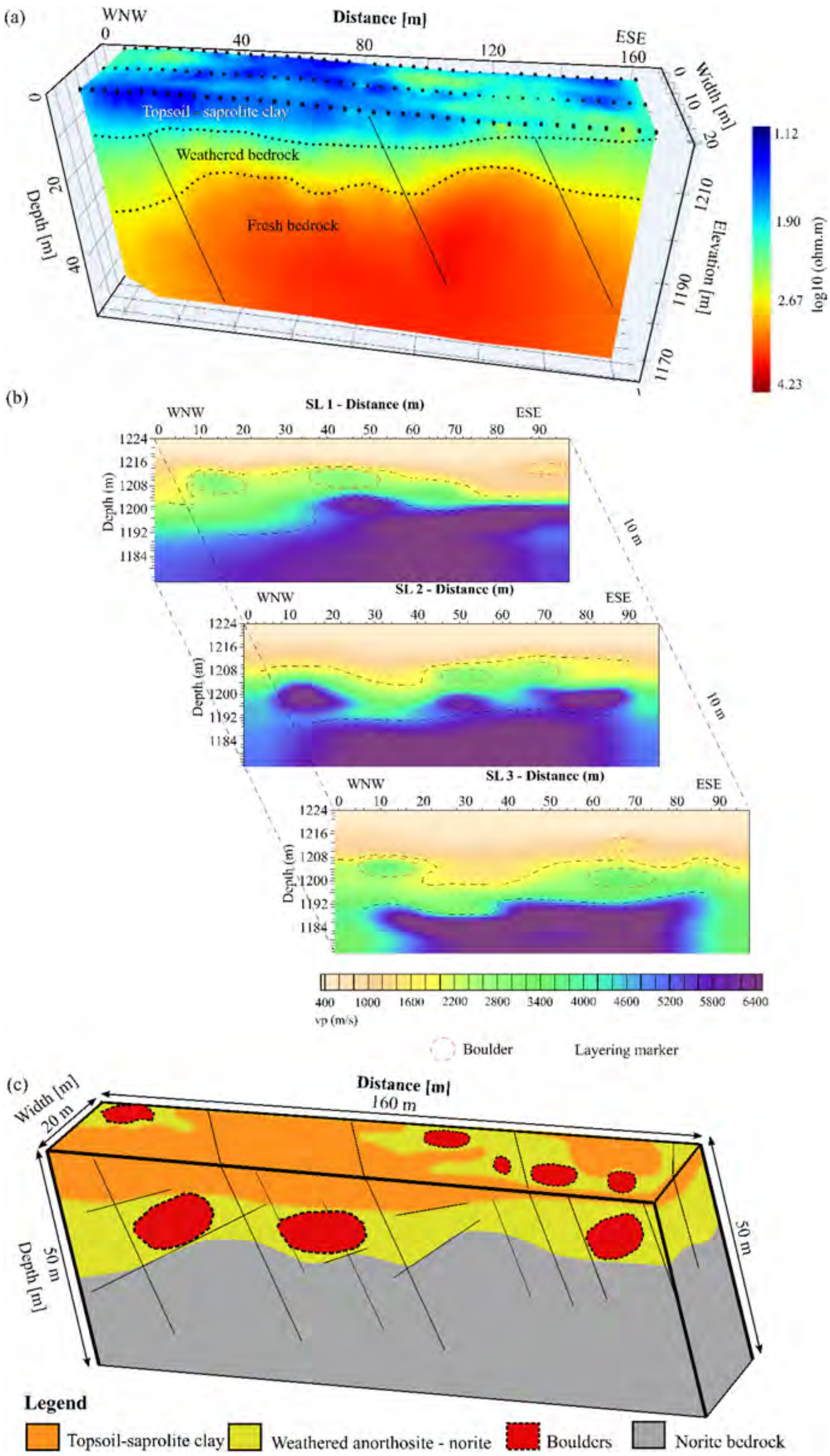

FIGURE 16 (a) 3D electrical resistivity model of survey lines RL1, RL2 and RL3. (b) 3D view of seismic refraction tomograms of survey line SL1, SL2 and SL3. (c) 3D geological model generated from the combined geophysical methods employed in this study.

the blasting energy is not enough to cause sufficient rock breakage.

The efficiency in rock breakage is affected by several factors, including: (1) uneven distribution of energy, (2) structural features (discontinuities), (3) intact rock properties, and (4) the type of blasting (design) used to break down the rock (Leng et al., 2020; Park & Kim, 2020; Yang et al., 2018). Often, the formation of subaerial boulders is an indication that the drill-and-blast technique used at a mine is not optimized to reduce the formation of boulders or produce sufficient rock breakage. Unoptimized blasting produces large fragments (boulders), which will require extra resources to remediate.

Dealing with boulders might necessitate drilling and/or blasting again, which ultimately slows down production.

Additionally, when blasting is not optimized (designed) adequately, excessive throw and fly-rocks occur. Throw and fly-rocks are a by-product of blasting that occur when blasting activity is not designed adequately, and the blasting energy is misdirected (Monjezi et al., 2011; Raina et al., 2015). Fly-rocks pose a huge safety hazard, as they may cause property damage and injuries at mines. Thus, by using intact rock property and structural discontinuity information obtained from integrated geophysical survey results, one can be able to design optimized drill-and-blasting programmes that result in more efficient rock breakage (less boulders), while also reducing throw and fly-rocks (which translates to a safer working environment), thus leading to increased productivity and reduced mining activity costs.

CONCLUSION

This study demonstrates that the integration of magnetic, electrical resistivity, refraction seismic and ground penetrating radar methods can be successfully used to gain a better understanding of the subsurface in order to increase efficient mining and enable sound engineering decisions. We propose the use of integrated geophysical techniques for mining and engineering site characterization to best identify geological features such as boulders, fractures and horizons (i.e. regolith to fresh bedrock). The results presented here demonstrate that by targeting weathering, structural and magnetization effects in subsurface rocks in magnetic environments, geological features that characterize and complicate mining processes can be successfully identified. By mapping the inherent loss of magnetization, presence of remanent magnetization, the degree of weathering, the competence and structural features of subsurface rocks, we were able to successfully map boulders, fractures, undulating lithological horizons and remanent igneous features (i.e. iron-rich ultramafic pegmatites). From these findings, it can be concluded that the integration of numerous geophysical methods can be used to improve mine blasting programmes, reducing the formation of blasting related boulders, and assisting in making cost-effective decisions.

ACKNOWLEDGEMENTS

We would like to acknowledge Tharisa Mine for funding this project and giving us permission to publish this work. The authors also thank the NRF (National Research Foundation) and DSI-NRF CIMERA (Centre of Excellence for Integrated Mineral and Energy Resource Analysis) for funding this research project. Special thanks go to the postgraduate students from the School of Geosciences at the University of the Witwatersrand who assisted with the data collection and the Tharisa Mine staff, especially Hloniphani Hlongwa and Robey Labuschagne, for assisting us during the data acquisition. Special thanks to Nathi Mntungwa from Tharisa Mine for scientific discussions and support. The authors would also like to acknowledge the constructive comments from two anonymous reviewers which have greatly improved the readability of this manuscript. Chief Editor, Tijmen Jan Moser, and Associate Editor, Alireza Malehmir, are also greatly appreciated for the editorial handling.

DATA AVAILABILITY STATEMENT

The data were acquired by the Wits seismic research centre team and are available on request from the corresponding author, subject to the approval from the mine owners.

ORCID

Moyagabo K. Rapetsoa https://orcid.org/0000-0003-3275-8994
Musa S. D. Manzi https://orcid.org/0000-0002-1654-5211
Julie E. Bourdeau https://orcid.org/0000-0003-1670-4363
Ian James https://orcid.org/0000-0002-1655-3529
Gordon R. J. Cooper https://orcid.org/0000-0003-2864-2542

REFERENCES

Barnes, S.J. & Maier, W.D. (2002) Platinum-group element distribution in the Rustenburg Layered Suite of the Bushveld Complex, South Africa. In: Cabri, L.J. (Ed.) *The geology, geochemistry, mineralogy and mineral beneficiation of platinum-group elements*, special vol. 54. Montreal: Canadian Institute of Mining, Metallurgy and Petroleum, pp. 431–458.

Binley, A. & Kemna, A. (2005) DC resistivity and induced polarization methods. In: Rubin, Y. & Hubbard, S.S. (Eds.) *Hydrogeophysics, water science and technology library*, vol. 50. Dordrecht: Springer, pp. 129–156. https://doi.org/10.1007/1-4020-3102-5_5.

Blanchy, G., Saneiyan, S., Boyd, J., McLachlan, P. & Binley, A. (2020) ResIPy, an intuitive open source software for complex geoelectrical inversion/modeling. *Computers & Geosciences*, 137, 104423.

Campbell, G. (2006) High resolution aeromagnetic mapping of "loss-of-ground" features at platinum and coal mines in South Africa. *South African Journal of Geology*, 109, 439–458. https://doi.org/10.2113/gssajg.109.4.439.

Cardarelli, E., Cercato, M., Cerreto, A. & Di Filippo, G. (2010) Electrical resistivity and seismic refraction tomography to detect buried cavities. *Geophysical Prospecting*, 58, 685–696. https://doi.org/10.1111/j.1365-2478.2009.00854.x.

Carollo, A., Capizzi, P. & Martorana, R. (2020) Joint interpretation of seismic refraction tomography by cluster analysis to detect buried cavities. *Journal of Applied Geophysics*, 178, 1–21. https://doi.org/10.1016/j.jappgeo.2020.104069.

Cawthorn, R.G. (2015) The Bushveld Complex, South Africa. In: Charlier, B., Namur, O., Latypov, R. & Tegner, C. (Eds.) *Layered intrusions*. Berlin: Springer, pp. 517–587. https://doi.org/10.1007/978-94-017-9652-1.

Cawthorn, R.G. & Webb, S.J. (2001) Connectivity between the western and eastern limbs of the Bushveld Complex. *Tectonophysics*, 330, 195–209. https://doi.org/10.1016/S0040-1951(00)00227-4.

Cawthorn, R.G., Barnes, S.J., Ballhaus, C. & Malitch, K.N. (2005) Platinum Group Element, Chromium, and Vanadium Deposits in Mafic and Ultramafic Rocks. One Hundredth Anniversary Volume. https://doi.org/10.5382/av100.09

Cooper, G.R.J. & Cowan, D.R. (2008) Edge enhancement of potential-field data using normalized statistics. *Geophysics*, 73, H1–H4. https://doi.org/10.1190/1.2837309.

Dan, M.F.M., Mohamad, E.T. & Komoo, I. (2016) Characteristics of boulders formed in tropical weathered granite: a review. *Jurnal Teknologi*, 78, 23–30. https://doi.org/10.11113/jt.v78.9635.

Dunlop, D.J., Ozdemir, O. & Alvarez, V.C. (2010) Magnetic properties of rocks of the Kapuskasing uplift (Ontario, Canada) and origin of long-wavelength magnetic anomalies. *Geophysical Journal International*, 183, 645–658. https://doi.org/10.1111/j.1365-246X.2010.04778.x.

Durgin, P.B. (1977) *Landslides and the weathering of granitic rocks*. Geological Society of America III, pp. 127–131.

Eales, H.V., Botha, W.J., Hattingh, P.J., De Klerk, W.J., Maier, W.D. & Odgers, A.T.R. (1993) The mafic rocks of the Bushveld Complex: a review of emplacement and crystallization history, and mineralization, in light of recent data. *Journal of African Earth Sciences*, 16, 121–142. https://doi.org/10.1016/0899-5362(93)90163-K.

Eales, H.V. & Cawthorn, R.G. (1996) The Bushveld Complex. In: *Layered* i*ntrusions*. Amsterdam: Elsevier, pp. 181–229. https://doi.org/10.1016/S0167-2894(96)80008-X.

Ettinger, S., Manville, V., Kruse, S. & Paris, R. (2014) GPR-derived architecture of a lahar-generated fan at Cotopaxi volcano, Ecuador. *Geomorphology*, 213, 225–239. https://doi.org/10.1016/j.geomorph.2014.01.013.

Felletti, F. & Beretta, G.P. (2009) Expectation of boulder frequency when tunnelling in glacial till: a statistical approach based on transition probability. *Engineering Geology*, 108, 43–53. https://doi.org/10.1016/j.enggeo.2009.06.006.

Fletcher, R.C., Buss, H.L. & Brantley, S.L. (2006) A spheroidal weathering model coupling porewater chemistry to soil thicknesses during steady-state denudation. *Earth and Planetary Science Letters*, 244, 44–457. https://doi.org/10.1016/j.epsl.2006.01.055.

Gomez, C., Lavigne, F., Hadmoko, D.S. & Wassmer, P. (2018) Insights into lahar deposition processes in the Curah Lengkong (Semeru Volcano, Indonesia) using photogrammetry-based geospatial analysis, near-surface geophysics and CFD modelling. *Journal of Volcanology and Geothermal Research*, 353, 102–113. https://doi.org/10.1016/j.jvolgeores.2018.01.021.

Harding, K.A., Morris, W.A., Balch, S.J., Lapointe, P. & Latham, A.G. (1988) A comparison of magnetic character and alteration in the three granitic drill cores from Eastern Canada. *Canadian Journal of Earth Sciences*, 25, 1141–1150. https://doi.org/10.1139/e88-112.

Hunt, E., Latypov, R. & Horvah, P. (2018) The Merensky cyclic unit, Bushveld Complex, South Africa: reality or myth? *Minerals*, 8, 1–35.

Jee, W.W. & Ha, S. (2007) Feasible boulder treatment methods for soft ground shielded TBM. In: Underground *s*pace – the 4th Dimension of Metropolises. pp. 217–22.

Khaidukov, V., Landa, E. & Moser, T.J. (2004) Diffraction imaging by focusing-defocusing, an outlook on seismic superresolution. *Geophysics*, 69(6), 1478–1490. https://doi.org/10.1190/1.1836821.

Kruger, F.J. (2005) Filling the Bushveld Complex magma chamber: lateral expansion, roof and floor interaction, magmatic unconformities, and the formation of giant chromitite, PGE and Ti-V-magnetitite deposits. *Mineralium Deposita*, 40, 451–472. https://doi.org/10.1007/s00126-005-0016-8.

Lapointe, P., Morris, W.A. & Harding, K.L. (1986) Interpretation of magnetic susceptibility: a new approach to geophysical evaluation of the degree of rock alteration. *Canadian Journal of Earth Sciences*, 23, 393–401. https://doi.org/10.1139/e86-041.

Leng, Z., Fan, Y., Gao, Q. & Hu, Y. (2020) Evaluation and optimization of blasting approaches to reducing oversize boulders and toes in open-pit mine. *International Journal of Mining Science and Technology*, 30, 373–380. https://doi.org/10.1016/j.ijmst.2020.03.010.

Lu, S.-G., Xue, Q.-F., Zhu, L. & Yu, J.-Y. (2008) Mineral magnetic properties of a weathering sequence of soils derived from basalt in Eastern China. *Catena*, 73, 23–33. https://doi.org/10.1016/j.catena.2007.08.004.

Malehmir, A., Durrheim, R., Bellefleur, G., Urosevic, M., Juhlin, C., White, D.J., Milkereit, B. & Campbell, G. (2012) Seismic methods in mineral exploration and mine planning: a general overview of past and present case histories and a look into the future. *Geophysics*, 77, WC173–WC190. https://doi.org/10.1190/geo2012-0028.1.

Monjezi, M., Bahrami, A. & Varjani, A.Y. (2011) Prediction and controlling of flyrock in blasting operation using artificial neural network. *Arabian Journal of Geosciences*, 4, 421–425. https://doi.org/10.1007/s12517-009-0091-8.

Moser, T.J. & Howard, C.B. (2008) Diffraction imaging in depth. *Geophysical Prospecting*, 56, 627–641. https://doi.org/10.1111/j.1365-2478.2007.00718.x.

Musil, M., Maurer, H., Green, A.G., Horstmeyer, H., Nitsche, F.O., Muhll, D.V. & Springman, S. (2002) Shallow seismic surveying of an Alpine rock glacier. *Geophysics*, 67, 1701–1710. https://doi.org/10.1190/1.1527071.

Onyebueke, E.O., Manzi, M.S.D. & Durrheim, R.J. (2018) High-resolution shallow reflection seismic integrated with other geophysical methods for hydrogeological prospecting in the Nylsvley Nature Reserve, South Africa. *Journal of Geophysics and Engineering*, 15, 2658–2673. https://doi.org/10.1088/1742-2140/aadbe3.

Park, J. & Kim, K. (2020) Use of drilling performance to improve rock-breakage efficiencies: a part of mine-to-mill optimization studies in a hard-rock mine. *International Journal of Mining Science and Technology*, 30, 179–188. https://doi.org/10.1016/j.ijmst.2020.03.010.

Perritt, S. & Roberts, M. (2007) Flexural-slip structures in the Bushveld Complex, South Africa? *Journal of Structural Geology*, 29, 1422–1429. https://doi.org/10.1016/j.jsg.2007.06.008.

Raina, A.K., Murthy, V.M.S.R. & Soni, A.K. (2015) Flyrock in surface mine blasting: understanding the basics to develop a predictive regime. *Current Science*, 108, 660–665.

Reid, D.L. & Basson, I.J. (2002) Iron-rich ultramafic pegmatite replacement bodies within the Upper Critical Zone, Rustenburg Layered Suite, Northam Platinum Mine, South Africa. *Mineralogical Magazine*, 66, 895–914. https://doi.org/10.1180/0026461026660066.

Roberts, M.K.C. & Clark-Mostert, V. (2010) Is there some commonality between the geological structures in the Bushveld Complex and the Great Dyke? In: *The 4th international platinum conference, platinum in transition 'Boom or Bust'*, The Southern African Institute of Mining and Metallurgy.

Santana, G.P., Fabris, J.D., Goulart, A.T. & Santana, D.P. (2001) Magnetite and its transformation to hematite in a soil derived from steatite. *Revista Brasileira de Ciencia do Solo*, 25, 33–42. https://doi.org/10.1590/S0100-06832001000100004.

van Schoor, M. & Fourie, C.J.S. (2015) *A guide for applying geophysics to coal mining problems in South Africa*. South Africa: Struik Nature.

Scoates, J.S., Wall, C.J., Friedman, R.M., Weis, D., Mathez, E.A. & VanTongeren, J.A. (2021) Dating the Bushveld Complex: timing of crystallization, duration of magmatism, and cooling of the World's largest layered intrusions and related rocks. *Journal of Petrology*, 62, egaa107. https://doi.org/10.1093/petrology/egaa107.

Scoon, R.N. & Mitchell, A.A. (1994) Discordant iron-rich ultramafic pegmatites in the Bushveld Complex and their relationship to iron-rich intercumulus and residual liquids. *Journal of Petrology*, 35, 881–917. https://doi.org/10.1093/petrology/35.4.881.

Shao, J., Zhang, Q., Wu, X., Lei, Y., Wu, X. & Wang, Z. (2020) Investigation on the water flow evolution in a filled fracture under seepage-induced erosion. *Water*, 12(11), 3188. https://doi.org/10.3390/w12113188.

Sherrod, L., Schlosser, K., Kozlowski, A., Bird, B., Werkema Jr, D.D. & Swiontek, J. (2014) Geophysical characterization of the Keene valley landslide in New York state. *Journal of Environmental and Engineering Geophysics*, 19, 139–155. https://doi.org/10.2113/JEEG19.3.139.

Soumya, G.S., Asanulla, R.M. & Radhakrishna, T. (2017) Rockmagnetism in relation to magnetic mineralogy of anorthosites in the southern granulite region of the Indian shield. *Geophysical Journal International*, 209, 1768–1778. https://doi.org/10.1093/gji/ggx134.

Taylor, C.D., Schulz, K.J., Doebrich, J.L., Orris, G.J., Denning, P.D. & Kirschbaum, M.J. (2009) Geology and nonfuel mineral deposits of Africa and the Middle East. U.S. Geological Survey Open-file Report 2005-1294-E, pp. 1–246.

Twidale, C.R. & Romani, J.R.V. (2005) *Landforms and geology of granite terrains*. London, United Kingdom: Taylor & Francis Group.

Jinghong, W., Caineng, Z. & Rukai, Z. (2011) Characteristics and controlling factors of fractures in igneous rock reservoirs. *Petroleum Exploration and Development*, 38, 708–715. https://doi.org/10.1016/S1876-3804(12)60005-6.

Udden, J.A. (1914) Mechanical composition of clastic sediments. *Bulletin of the Geological Society of America*, 55, 655–744. https://doi.org/10.1130/GSAB-25-655.

Wilson, A.H., Jermy, C.A. & Ridgeway, M. (2005) Rock strength and physical properties of Norites of the Merensky and Bastard Units, western Bushveld Complex. *Geological Society of South Africa*, 108, 525–540. https://doi.org/10.2113/108.4.525.

van School, M. (2002) Detection of sinkholes using 2D electrical resistivity imaging. *Journal of Applied Geophysics*, 50, 393–399. https://doi.org/10.1016/S0926-9851(02)00166-0.

Vitale, S. & Isaia, R. (2014) Fractures and faults in volcanic rocks (Campi Flegrei, southern Italy): insight into volcano-tectonic processes. *International Journal of Earth Science*, 103, 801–819. https://doi.org/10.1007/s00531-013-0979-0.

von Dobeneck, T., Muller, M., Bosbach, B. & Klugel, A. (2021) Ground magnetic susceptibility and mapping across weathered basalt dikes reveal soil creep and pedoturbation. *Frontiers in Earth Science*, 8, 1–8. https://doi.org/10.3389/feart.2020.592986.

Yang, X., Zeng, X., Pu, C. & Xiao, D. (2018) Effects of the pre-existing fissures with different fillings in PMMA on blast-induced crack propagation. *Advances in Materials Science and Engineering*, 17, 1–17. https://doi.org/10.1155/2018/7378282.

Zhihui, W., Xiangmin, C., Jiayong, Y., Jiming, W., Yu, L. & Lei, Z. (2018) Using the integrated geophysical methods detecting active faults: a case study in Beijing, China. *Journal of Applied Geophysics*, 156, 82–91. https://doi.org/10.1016/j.jappgeo.2017.01.030

How to cite this article: Gomo, S., Rapetsoa, M.K., Manzi, M.S.D., Onyebueke, E., Dildar, J., Sihoyiya, M. et al. (2023) Integrated geophysical methods for boulder delineation to improve mining. *Geophysical Prospecting*, 1–21. https://doi.org/10.1111/1365-2478.13322

11. Discussion

To support the increase in production and safety of workers in underground and surface mining environments, several geophysical surveys were designed to test the feasibility of conducting small-scale geophysical surveys in active and logistically challenging mine environments. This thesis compared the results from two sites with varying geological conditions and operations. As mines expand their mining operations to greater depths and surface area means may encounter complex geological environments such as seismicity, stress increase, methane explosion, and seismicity (in case of underground mining), as well boulders and flooding (in case of open pit mining). These conditions pose a risk to infrastructure and mine workers and decrease production of the mine. The papers making up this thesis address the technical advantages and disadvantages of different geophysical equipment used and mine conditions. The papers also compare the contrast between surface and tunnel seismic data.

In Paper I, seismic results acquired in underground mine tunnels to image geological structures and their associated mineral deposits are presented. 2D high-resolution (2 m - 5 m shot and receiver spacing) reflection seismic data were acquired over the Merensky Reef and UG2 deposits at Maseve mine, Bushveld Complex (South Africa). From inspection, the raw data were noisy due to mine infrastructure such as ventilation and water pumps. This paper exploited a portion of the dataset collected in phase one of the project and provided insight on the location of the two economic mineral deposits (Merensky Reef and UG2) below the tunnel. The study utilised both the spiked geophones and seismic land streamer for seismic data recording inside the mine tunnel. The data from the spiked geophones were too noisy to be utilised due to poor coupling to the ground. Therefore, the manuscript presents only the data collected using the seismic land streamer. The poor coupling of the spiked geophones was due to the fact that the geophone had to be planted on hard rock environment. An attempt to drill holes into the hard rock (tunnel floor) to plant the geophones was done to provide good coupling. However, the logistics to drill the geophones into the rock proved to be difficult and time-consuming. Furthermore, the survey set-up was cost effective as it managed to deploy affordable energy sources and land streamer, which do not require extensive planning and mobilisation.

Seismic data from the land streamer showed good signal quality compared to the spiked geophones. This is as a result of the good ground coupling of the land streamer due to the weight of the plate. Drilling of the spiked geophones into the ground was expected to provide good coupling of the geophones. However, the land streamer showed good results as a result of the weight of the streamer plate keeping contact with the ground stable. Mine infrastructure such as ventilation and water pumps proved to be problematic as they introduced noise into the data set.

Paper II is an extension to the work done in **Paper I.** The study presents data acquired on surface and tunnel using both wireless sensors and cabled system. Furthermore, it demonstrates the need for innovative seismic technologies to image geological structures that affect mineralisation, which may have a direct impact on ore resource evaluation. After careful processing, the final surface and tunnel seismic sections presented clear reflections originating from the orebodies. A comparison of data from phase one (**Paper I**) and phase two (**Paper II**) was conducted, with the purpose of testing the tunnel to surface seismic acquisition for deep (~ 3 km) mineral exploration. Similar study was conducted by Donoso et al. (2021) and Brodic et al. (2021) for tunnel – surface imaging using the E-Vib, cabled and wireless sensors (1C and 3C), and 250 kg drop-hammer. Conducting active seismic surveys in mine tunnels introduces limitations to the choice of equipment to be deployed and utilised. From a safety perspective, the use of a drop hammer needs to be carefully monitored for the presence of sparks from the weight and the plate, as this poses a hazard due to the presence of methane in the tunnels. Another aspect that influences the choice of seismic equipment is the logistical difficulties encountered in an active mining environment. Transportation of equipment to and from underground spaces is limited due to the size of the shaft (locally termed cage). This then imposes limitation on the size of sources and number of receivers one can have in underground spaces. To address the aforementioned, a choice to use a light source (6.3 kg sledgehammer) and portable cabled system with 48 channels was used for the underground experiments. Moreover, the use of cabled system increases the amount of time required to deploy the system as one needs to prepare (drilling of the rock to plant the sensors) the site beforehand. To the best of our knowledge, the tunnel acquisition is the first in South Africa to utilize small-scale seismic method to image the known mineral deposits.

Geological complexities and mine infrastructures resulted in a complex seismic wave-field, making it difficult to identify the origin of target reflections on the shot gathers. Moreover, the side tunnels and infrastructure above the location of the seismic profiles contribute to the complex wave-field. This was carefully inspected in our dataset to isolate the correct events as a result of available geological structures. The data also faced difficulties in offset coverages due to limited space in the tunnel, resulting in limited target coverage and low fold distribution. Another aspect that influences the target reflections is the geometry (dip and fold) of the target. This results in out-of-plane reflections that can be observed on the final stack sections. Brodic et al. (2021) discussed a method to correct the out-of-plane reflections on both the pre- and post-migration processing. Out of plane reflections were not considered during processing of the data in this thesis, however is something to consider in future tunnel seismic surveys.

In Paper III, the use of multi-geophysical methods (seismics, magnetics and electrical resistivity) to delineate fractures in an active open-pit mine is demonstrated. Geophysical data were integrated with borehole data and physical property measurements of rock samples to understand the geophysical signature of the orebody and constrain the final geological interpretations. P-wave velocity models provide insight into the near-surface rock conditions. Conventional reflection seismic processing was carried out, and the final stack section delineates the shallow, relatively flat bedrock. The ground magnetic data provide high-resolution delineation of a major dyke that was identified on the aeromagnetic data and geological mapping data. The ground magnetic data also show a series of low magnetic regions that are attributed to fractures that may be potential pathways for water to migrate into the pit. Electrical resistivity tomography identifies linear low resistivity zones that differentiate fractured and undisturbed hard rock. Integrated geophysical methods were able to image the depth to bedrock, fractures within the host rock, and a major dyke that crosscuts the mineralisation at the center of the pit. This was all achieved in a noisy and active mine environment. Apart from imaging fractures within the mine boundaries, the mine also faces a challenge with subsurface boulders that delay production.

Paper IV presents results addressing the challenges and imaging of subsurface boulders using integrated geophysical surveys. Attempts for the mine to expand further north are faced with a challenge to haul and break down boulders that are encountered around the pit. The boulders have a negative impact on the day to day mine operations, therefore small-scale geophysical surveys were designed to delineate and characterise the subsurface. The experiments were conducted on an unmined section compared to the surveys discussed in Paper III. The difference in site can be observed through the seismic data, with high noise content on data acquired inside the pit. The low mine activity of site 2 is evident in the data with good signal-to-noise ratio. Another contrast between data in Paper III and Paper IV was the soil response. Site 1 was on direct hard rock (highly fractured), while site 2 surveys were conducted on loose overburden. This resulted in difficulties in planting the geophones for site 1. The experience gained from data collected in Paper I and II played a role in proper designing and acquiring the seismic profiles in a way to maximise imaging of the structures using cost effective equipment. The near-surface irregularities encountered on both sites meant that careful datum static corrections needed to be applied to correct lateral near-surface changes (Cox, 1999). A low velocity layer (LVL) can be observed in both sites due to the top highly fractured norites of site 1 and highly weathered topsoil in site 2. The presence of the highly fractured norites and weathered layers resulted in the data exhibiting high amplitude and low frequency signals (e.g., ground roll) due to the nature of a weathered layer acting as a high cut filter. To combat these effect, the first shot was not recorded, but taken as a compaction shot. Moreover, where possible, the geophones were buried with an attempt to reduce ground rolls.

The studies presented in this thesis complemented each other. The processing methods deployed in **Paper I and III** allowed for the removal of noise introduced by mine infrastructure. Reflection seismic data from **Paper I** was compared with that of **Paper II** and an improved imaging of geological structures and mineralisation was observed. This highlighted the importance of testing and deploying newly developed technologies in such environments. Integration of 2D modelling, borehole log, and geological information assisted in the final interpretation of the seismic data.

It is imperative to acknowledge that the methodologies presented in this thesis are not without limitations. One important limitation is access to a broadband source for the seismic experiments. The mine tunnels are limited to deploying small portable impact sources, compared to vibrational sources. The use of single or dominant frequencies enabled us to image geological structures and infer mineralization from proxy contacts. However, the conclusions from this research are limited, as they can only detect the structures and not resolve them adequately. The utilization of broadband sources would allow us to obtain more detailed and sharp images of shallow (e.g., thin beds) features and enable us to image deeper targets using the lower frequencies. Future research can benefit from engineering a vertical and horizontal shaker with broadband frequencies similar to the E-vib described by Brodic et al. (2021). However, this seismic source would need to be portable and easy to deploy in deep underground mines, as previously discussed.

Another significant shortcoming to notice was the thesis's approach to data integration. Integration of the dataset relied mainly on joint interpretation (e.g., Ogaya et al., 2016) of the data that is inverted separately, resulting in a lack of resolution. The dataset integration undertaken in this thesis can be developed further. For instance, one of the techniques that can be used to compensate for the lack of resolution in each of the independent datasets used in the research is joint inversion. Joint inversion techniques usually produce better-resolved and reliable results. Yari et al. (2021), for example, used a joint inversion technique of P-wave travel time and electrical resistivity data to image low velocity thin layers embedded between high velocity layers. This technique is now a common practice in geophysics for inverting different datasets such as magnetics, gravity, electromagnetic, and seismic data (Coutant et al., 2012; Zheglova et al., 2018; Zhang and Li, 2019).

The current study did not thoroughly investigate the costs of conducting this research in an operational mine. As previously mentioned, the cost of applying geophysical methods differs depending on (not limited to) the equipment used, type of method, mobilization, and duration taken in the field. The analysis of the costs was beyond the scope of this thesis. However, by examining the literature, we can make an estimate with regard to the costs incurred by different geophysical methods. For example, Fritz (2000) conducted a comparison between the cost and area covered by various geophysical techniques of investigation and the cost and area of drilling a 300 m borehole. The detection and resolution capabilities of the various geophysical techniques vary. Airborne geophysical methods can cover larger areas over a short period of time (reducing costs) and are later used as a guide for ground methods. For example, in Paper III, the ground-based magnetic and seismic data were guided by regional airborne magnetic data. When comparing the costs of ground and airborne geophysical methods, it is important to note that ground geophysical methods are relatively expensive, considering the area they cover (Hajnal et al., 2020).

12. Conclusions and recommendations

12.1. Conclusions

This thesis has applied novel in-mine and surface geophysical methods to image geological structures and mineralisation in active mine environments. The thesis is comprised of three papers; in each case study a set of unique challenges associated with hard rock mining environments was encountered and necessary steps were taken to address them. In general, the thesis shows that geophysical surveys can be successfully acquired in active mines and noisy environments, however the seismic design and processing of the data need to be done in a novel approach. Throughout the PhD research, the limitations and logistical challenges expected at operational mines were taken into account to properly design geophysical surveys.

Although the studies presented here were successful, simultaneous acquisition of tunnel and surface data was not possible as underground mine tunnels are GPS-denied. The next step is to acquire a GPS-time system developed under the Smart Exploration Project and conduct time-synchronised surface-tunnel seismic surveys for deep mineral explorations at the same mining sites used in this study. One of the main lessons from this study that one needs to spend enough time to process in-mine acquired seismic data such that the final results represent the true geology.

12.2. Recommendations

Following the successful experiments in the Bushveld Complex in imaging the platinum orebodies, it is recommended that these experiments should be conducted at gold mine sites. Additionally, the experiments will exploit the tunnel-borehole, active-passive seismic experiments for gold exploration incorporating distributed acoustic sensing (DAS) and nodal array. The aim of these experiments would be to synchronize acquisition of the dataset in all settings mentioned above using the ultra-accurate GPS-time transmitter developed under the Smart Exploration Project (Malehmir et al., 2020).

Through careful analysis of the findings in the thesis, there is a gap in which further research would be beneficial. Several research questions were raised in the introduction section to address research gaps. While some of the research questions were addressed by the research conducted in this thesis, others remain in question. Specifically, the lack of resolution in some geophysical methods and datasets might have helped in characterizing the subsurface. Ground-based geophysical methods are not able to uniquely define the anomalies that are recorded, thus resulting in ambiguities. While seismic data has significantly higher resolution than other ground-based geophysical methods, borehole data remains more reliable. For instance, the general velocity of the rock within the Bushveld complex is around 5700 m/s, with the observed dominant frequency of seismic surveys in the area having a median of ~120 Hz (mainly controlled by the source and geological conditions encountered in the area), which yields resolutions of ~12 m. With electrical resistivity, the resolution and depth of imaging are influenced by electrode spacing. For example, reducing the electrode spacing results in a small depth of investigation but increases the resolution (Greggio et al., 2018). Future work might look to improve the data resolution and repeatability of the geophysical methods.

The study carried out in this research has also highlighted additional areas that can be exploited further. These involve further investigation of the full wave field and noise in mining areas. Can we take full advantage of the seismic wave field to characterize the subsurface? How can we derive meaningful information from the noise signature encountered in operational mines? This would assist in reducing the costs of applying geophysical methods in mine areas, as described in the discussion. In addition, using active seismic creates environmental issues, whereas passive seismic is non-invasive. As a result, passive seismic methods can be used in many areas without causing environmental problems.

13. Reference

Adams, D.C., Miller, K.C. and Kargı, H., 1997. Reconciling physical properties with surface seismic data from a layered mafic intrusion. *Tectonophysics*, *271*(1-2), 59-74.

Ahmadi, O., 2015. *Application of the Seismic Reflection Method in Mineral Exploration and Crustal Imaging: Contributions to Hardrock Seismic Imaging* (Doctoral dissertation, Acta Universitatis Upsaliensis).

Ahmadi, O., Juhlin, C., Malehmir, A. and Munck, M., 2013. High-resolution 2D seismic imaging and forward modeling of a polymetallic sulfide deposit at Garpenberg, central Sweden Seismic imaging at Garpenberg. *Geophysics*, *78*(6), 339-350.

Aizebeokhai, A.P., 2009. Geoelectrical resistivity imaging in environmental studies. *Appropriate Technologies for Environmental Protection in the Developing World: Selected Papers from ERTEP 2007, July 17–19 2007, Ghana, Africa*, 297-305.

Aizebeokhai, A.P., 2010. 2D and 3D geoelectrical resistivity imaging: Theory and field design. *Scientific Research and Essays*, *5*(23), 3592-3605.

Alford, R.M., Kelly, K.R. and Boore, D.M., 1974. Accuracy of finite-difference modeling of the acoustic wave equation. *Geophysics*, *39*(6), 834-842.

Alfouzan, F.A., 2008. Optimiation strategies of electrode arrays used in numerical and field 2D resistivity imaging surveys. *Universiti Sains Malaysia, Penang, Malaysia*.

Alsadi, H.N., 2017. Seismic Hydrocarbon Exploration. *2D and 3D Techniques, Seismic waves*. https://doi.org/10.1007/978-3-319-40436-3_2

Amini, H., 2014. *A pragmatic approach to simulator-to-seismic modelling for 4D seismic interpretation* (Doctoral dissertation, Heriot-Watt University).

Annan, A.P., 2002. The history of ground penetrating radar. *Subsurface Sensing Technologies and Applications*, *3*(4), 303-320.

Annan, A. P., 2005. 11. Ground-Penetrating Radar, in Near-Surface Geophysics. Investigations in *Geophysics Society of Exploration Geophysicists*, 357–438.

Bailey, J. T., Evans, S., and Robin, G. de Q., 1964. Radio Echo Sounding of Polar Ice Sheets: *Nature*, 204, 420–421.

Baranov, V. and Naudy, H., 1964. Numerical calculation of the formula of reduction to the magnetic pole. *Geophysics*, *29*(1), 67-79.

Baranov, V., 1957. A new method for interpretation of aeromagnetic maps: pseudo-gravimetric anomalies. *Geophysics*, *22*(2), 359-382.

Basson, I.J., 2019. Cumulative deformation and original geometry of the Bushveld Complex. *Tectonophysics*, *750*, 177-202.

Bechtel, T., Bosch, F., and Gurk, M., 2007. Geophysical Methods, in Methods in Karst Hydrogeology, 171–199.

Bellefleur, G., Malehmir, A. and Müller, C., 2012. Elastic finite-difference modeling of volcanic-hosted massive sulfide deposits: A case study from Half Mile Lake, New Brunswick, Canada. *Geophysics*, 77(5), 25-36.

Bellefleur, G., Schetselaar, E., White, D., Miah, K. and Dueck, P., 2015. 3D seismic imaging of the Lalor volcanogenic massive sulphide deposit, Manitoba, Canada. *Geophysical Prospecting*, *63*(4-Hardrock Seismic imaging), 813-832.

Benedetto, A., Tosti, F., Bianchini Ciampoli, L., and D'Amico, F., 2017. An overview of ground-penetrating radar signal processing techniques for road inspections: *Signal Processing*, 132, 201–209.

Beres Jr., M., and Haeni, F. P., 1991. Application of Ground-Penetrating-Radar Methods in Hydrogeologie Studies: *Groundwater*, 29, 375–386.

Bjorlykke, K. and Mondol, N.H., 2010. Seismic exploration. *Petroleum Geoscience: From Sedimentary Environments to Rock Physics*, 375-402.

Bleibinhaus, F., Hole, J.A., Ryberg, T. and Fuis, G.S., 2007. Structure of the California Coast Ranges and San Andreas Fault at SAFOD from seismic waveform inversion and reflection imaging. *Journal of Geophysical Research: Solid Earth*, *112*(B6).

Bohlen, T., Giese, R., Müller, C. and Landerer, F., 2003, June. Modeling of seismic waves around a tunnel with irregular wall. In *65th EAGE Conference & Exhibition* (pp. cp-6). European Association of Geoscientists & Engineers.

Brodic, B., Malehmir, A., Pacheco, N., Juhlin, C., Carvalho, J., Dynesius, L., Van Den Berg, J., De Kunder, R., Donoso, G., Sjölund, T. and Araujo, V., 2021. Innovative seismic imaging of volcanogenic massive sulfide deposits, Neves-Corvo, Portugal—Part 1: In-mine array. *Geophysics*, *86*(3), 165-179.

Bumby, A.J., Eriksson, P.G., Catuneanu, O., Nelson, D.R. and Rigby, M.J., 2012. Meso-Archaean and Palaeo-Proterozoic sedimentary sequence stratigraphy of the Kaapvaal Craton. *Marine and Petroleum Geology*, *33*(1), 92-116.

Butler, D.K., 2005. Near-surface geophysics. *Society of Exploration Geophysicists*, 151-171.

Campbell, G., 2011. Exploration geophysics of the Bushveld Complex in South Africa. *The Leading Edge*, *30*(6), 622-638.

Carpenter, E.W. and Habberjam, G.M., 1956. A tri-potential method of resistivity prospecting. *Geophysics*, *21*(2), 455-469.

Castro, F.R., Oliveira, S.P., de Souza, J. and Ferreira, F.J.F., 2018. Combining tilt derivative filters: New approaches to enhance magnetic anomalies. *Revista Brasileira de Geofísica*, *36*(3), 335-343.

Catapano, I., Gennarelli, G., Ludeno, G., Soldovieri, F., and Persico, R., 2019. Ground-Penetrating Radar: Operation Principle and Data Processing, in J. G. Webster, ed., Wiley Encyclopedia of Electrical and Electronics Engineering, 1st ed.Wiley, 1–23.

Cawthorn, R.G. and Webb, S.J., 2001. Connectivity between the western and eastern limbs of the Bushveld Complex. *Tectonophysics*, *330*(3-4), 195-209.

Cawthorn, R.G., 2015. The Bushveld Complex, South Africa. In *Layered intrusions* (pp. 517-587). Springer, Dordrecht.

Cerjan, C., Kosloff, D., Kosloff, R. and Reshef, M., 1985. A nonreflecting boundary condition for discrete acoustic and elastic wave equations. *Geophysics*, *50*(4), 705-708. https://doi.org/10.1190/1.1441945.

Cerveny, V., 1985. The application of ray tracing to the numerical modeling of seismic wavefields in complex structures. *Seismic Shear Waves*, *15*, 1-124.

Červený, V., Klimeš, L. and Pšenčík, I., 1988. Applications of dynamic ray tracing. *Physics of the Earth and planetary interiors*, *51*(1-3), 25-35.

Cerveny, V., Klimes, L. and Psencik, I., 2007. Seismic ray method: Recent developments. *Advances in Geophysics*, *48*, 1-126.

Cheraghi, S., Malehmir, A. and Bellefleur, G., 2011. 2D seismic reflection imaging in the Brunswick no. 6 massive sulphide and iron deposits, Bathurst Mining Camp, Canada: Implications for crustal architecture and mineral potential. *Tectonophysics*, *506*, 55-72.

Cheraghi, S., Malehmir, A. and Bellefleur, G., 2011. Crustal-scale reflection seismic investigations in the Bathurst Mining Camp, New Brunswick, Canada. *Tectonophysics*, *506*(1-4), 55-72.

Chopra, S., Castagna, J. and Portniaguine, O., 2006. Seismic resolution and thin-bed reflectivity inversion. *CSEG recorder*, *31*(1), 19-25.

Clarke, B., Uken, R. and Reinhardt, J., 2009. Structural and compositional constraints on the emplacement of the Bushveld Complex, South Africa. *Lithos*, *111*(1-2), 21-36.

Coutant, O., Bernard, M. L., Beauducel, F., Nicollin, F., Bouin, M. P., and Roussel, S., 2012. Joint inversion of P -wave velocity and density, application to La Soufrière of

Guadeloupe hydrothermal system: Traveltime and gravity joint inversion: *Geophysical Journal International*, 191, 723–742.

Cox, M., 1999. Static corrections for seismic reflection surveys. Society of Exploration Geophysicists.

Cox, D.R., Newton, A.M. and Huuse, M., 2020. An introduction to seismic reflection data: Acquisition, processing and interpretation. In *Regional Geology and Tectonics* (571-603). Elsevier.

Dahlin, T. and Zhou, B., 2004. A numerical comparison of 2D resistivity imaging with 10 electrode arrays. *Geophysical prospecting*, *52*(5), 379-398.

Dan, M.F.M., Mohamad, E.T. and Komoo, I., 2016. Characteristics of boulders formed in tropical weathered granite: a review. *Jurnal Teknologi*, *78*(8-6), 23-30.

Dentith, M. and Mudge, S.T., 2014. *Geophysics for the mineral exploration geoscientist*. Cambridge University Press.

Dessa, J.X., Operto, S., Kodaira, S., Nakanishi, A., Pascal, G., Virieux, J. and Kaneda, Y., 2004. Multiscale seismic imaging of the eastern Nankai trough by full waveform inversion. *Geophysical Research Letters*, *31*(18).

Dey, A. and Morrison, H.F., 1979. Resistivity modelling for arbitrarily shaped two-dimensional structures. *Geophysical prospecting*, *27*(1), 106-136.

Dondurur, D., 2018. *Acquisition and processing of marine seismic data*. Elsevier.

Dong, Z. and McMechan, G.A., 1991. Numerical modeling of seismic waves with a 3-d, anisotropic scalar-wave equation. *Bulletin of the Seismological Society of America*, *81*(3), 769-780.

Donoso, G.A., Malehmir, A., Brodic, B., Pacheco, N., Carvalho, J. and Araujo, V., 2021. Innovative seismic imaging of volcanogenic massive sulfide deposits, Neves-Corvo, Portugal—Part 2: Surface array. *Geophysics*, *86*(3), 181-191.

Drijkoningen, G., 2016. Introduction to Reflection Seismics: *Chapter 5 Processing of Seismic Reflection Data*, TU Delft. 22 February 2016 Available at: https://ocw.tudelft.nl/courses/introduction-reflection-seismics/ (Accessed: 08 March 2023).

Eales, H.V. and Cawthorn, R.G., 1996. The Bushveld Complex. In *Developments in petrology* (Vol. 15, 181-229). Elsevier.

Eaton, D., Guest, S., Milkereit, B., Bleeker, W., Crick, D., Schmitt, D. and Salisbury, M.H., 1996. Seismic imaging of massive sulfide deposits; Part III, Borehole seismic imaging of near-vertical structures. *Economic Geology*, *91*(5), 835-840.

Economou, N., Vafidis, A., Benedetto, F., and Alani, A. M., 2015. GPR Data Processing Techniques, in A. Benedetto and Pajewski, L., eds., Civil Engineering Applications of Ground Penetrating Radar, Springer Transactions in Civil and Environmental Engineering Springer International Publishing, 281–297.

Everett, M. E. (2013) *Near-Surface Applied Geophysics*. Cambridge: Cambridge University Press. doi: 10.1017/CBO9781139088435.

Farra, V., 1993. Ray tracing in complex media. *Journal of Applied Geophysics*, *30*(1-2), 55-73.

Fichtner, A., 2011. *Full seismic waveform modelling and inversion*. Springer Science & Business Media.

Francke, J. C., and Yelf, R., 2003. Applications of GPR for surface mining: Proceedings of the 2nd International Workshop on Advanced Ground Penetrating Radar, 115–119.

Frankel, A. and Clayton, R.W., 1984. A finite-difference simulation of wave propagation in two-dimensional random media. *Bulletin of the Seismological Society of America*, *74*(6), 2167-2186.

Frankel, A. and Clayton, R.W., 1986. Finite difference simulations of seismic scattering: Implications for the propagation of short-period seismic waves in the crust and models of crustal heterogeneity. *Journal of Geophysical Research: Solid Earth*, *91*(B6),6465-6489.

Fritz, F., 2000. Economics of geophysical applications. *Practical Geophysics III for the Exploration Geologist*. (eds. R.B. Ellis, R. Irvine and Fritz). Northwest Mining Association.

Fuchs, K., and Muller, G., 1971. Computation of Synthetic Seismograms with the Reflectivity Method and Comparison with Observations: *Geophysical Journal International*, 23, 417–433.

Georgsson, L.S. and Karlsdóttir, R., 2010. Resistivity methods-DC and TEM with examples and comparison from the reykjanes peninsula and Öxarfjördur, iceland. *Short Course V on Exploration for Geothermal Resources, organized by UNU-GTP, GDC and Kengen, Kenya*.

Gjøystdal, H., Iversen, E., Laurain, R., Lecomte, I., Vinje, V. and Åstebøl, K., 2002. Review of ray theory applications in modelling and imaging of seismic data. *Studia geophysica et geodaetica*, *46*(2), 113-164.

Greggio, N., Giambastiani, B., Balugani, E., Amaini, C., and Antonellini, M., 2018. High-Resolution Electrical Resistivity Tomography (ERT) to Characterize the Spatial Extension of Freshwater Lenses in a Salinized Coastal Aquifer: *Water*, 10, 1067.

Griffiths, D.H. and Barker, R.D., 1993. Two-dimensional resistivity imaging and modelling in areas of complex geology. *Journal of applied Geophysics*, *29*(3-4), 211-226.

Hajnal, Z., Takács, E., Annesley, I. R., and Pandit, B., 2020. Effective utilization of seismic reflection technique with moderate cost in uranium exploration: *Geophysical Prospecting*, 68, 129–144.

Hale, D., 1991. Dip moveout processing. *Society of Exploration Geophysicists*. https://doi.org/10.1190/1.9781560802204

Halliday, D., Resnick, R. and Walker, J., 2013. *Fundamentals of physics*. John Wiley & Sons.

Hartzenberg, A.G. and Du Plessis, M., 2014. The influence of regional structures associated with the Bushveld Complex on the mechanism driving the behaviour of the UG2 hangingwall beam and in-stope pillars at Lonmin's Marikana Operations. In *The 6th International Platinum Conference*.

Hassan, H.H. and Peirce, J.W., 2005. SAUCE: A new technique to remove cultural noise from HRAM data. *The Leading Edge*, *24*(3), 246-250.

Herman, R., 2001. An introduction to electrical resistivity in geophysics. *American Journal of Physics*, *69*(9), 943-952.

Hinze, W. J., von Frese, R. R. B. and Saad, A. H., 2013. *Gravity and Magnetic Exploration: Principles, Practices, and Applications*. Cambridge: Cambridge University Press. doi: 10.1017/CBO9780511843129.

Hinze, W.J., 1963. *Regional gravity and magnetic anomaly maps of the Southern Peninsula of Michigan.* Department of Conservation, Geological Survey Division Report of Investigations 1.

Hughes, S.W., 2005. Archimedes revisited: a faster, better, cheaper method of accurately measuring the volume of small objects. *Physics education*, *40*(5), p.468.

Hunter, D., 1978. The Bushveld Complex and Its Remarkable Rocks: The Bushveld Complex in South Africa, which contains some of the world's most precious resources, is itself a precious resource for geologists studying the crystallization of magmas. *American Scientist*, *66*(5), 551-559.

Igel, H., Mora, P. and Rodrigues, D., 1991. 3-D wave propagation using finite differences. In *SEG* Technical Program Expanded Abstracts *1991* (pp. 1577-1579). *Society of Exploration Geophysicists*.

Jastram, C. and Behle, A., 1992. Acoustic Modelling on a Grid of Vertically Varying SPACING1. *Geophysical prospecting*, *40*(2), 157-169.

Juhlin, C., Dehghannejad, M., Lund, B., Malehmir, A. and Pratt, G., 2010. Reflection seismic imaging of the end-glacial Pärvie Fault system, northern Sweden. *Journal of Applied Geophysics*, *70*(4), 307-316.

Kearey, P., Brooks, M. and Hill, I., 2002. *An introduction to geophysical exploration* (Vol. 4). John Wiley & Sons.

Kinnaird, J.A., 2005. The Bushveld large igneous province. *Review Paper, The University of the Witwatersrand, Johannesburg, South Africa, 39*.

Knapp, R.W. and Steeples, D.W., 1986. High-resolution common-depth-point reflection profiling: Field acquisition parameter design. *Geophysics*, *51*(2), 283-294.

Krebes, E.S., 2019. *Seismic wave theory*. Cambridge University Press. https://doi.org/10.1017/9781108601740.009

Lee, C.A., 1996. A review of mineralization in the Bushveld Complex and some other layered intrusions. *Developments in petrology*, *15*, 103-145.

Lehmann, O., 1959. *Look Beyond the Wind: (the Life of Dr. Hans Merensky)*. Timmins. 183

Loke, M., 1999. Electrical imaging surveys for environmental and engineering studies: A Practical Guide to 2D & 3D Electrical Imaging Surveys. *Technical Reports*.

Loke, M.H., Rucker, D.F., Chambers, J.E., Wilkinson, P.B. and Kuras, O., 2020. Electrical resistivity surveys and data interpretation. In *Encyclopedia of solid Earth geophysics* (1-6). Cham: Springer International Publishing.

Lotheringen, J., J. James, K. Lomberg, and H. Bornman, 2016, Tharisa Chrome and PGM Mine, South Africa. *Competent Persons Report.*

Lundberg, E., 2014. *2D and 3D Reflection Seismic Studies over Scandinavian Deformation Zones* (Doctoral dissertation, Acta Universitatis Upsaliensis).

Macnae, J., 1995. Applications of geophysics for the detection and exploration of kimberlites and lamproites. *Journal of Geochemical Exploration*, *53*(1-3), 213-243.

Malehmir, A., Andersson, M., Lebedev, M., Urosevic, M. and Mikhaltsevitch, V., 2013. Experimental estimation of velocities and anisotropy of a series of Swedish crystalline rocks and ores. *Geophysical prospecting*, *61*(1), 153-167.

Malinowski, M., Schetselaar, E., & White, D. J. (2012). 3D seismic imaging of volcanogenic massive sulfide deposits in the Flin Flon mining camp, Canada: Part 2: Forward modeling. *Geophysics,* 77(5), 81–93. https://doi.org/10.1190/geo2011-0474.1

Manzi, M.S., Cooper, G.R., Malehmir, A. and Durrheim, R.J., 2020. Improved structural interpretation of legacy 3D seismic data from Karee platinum mine (South Africa) through the application of novel seismic attributes. *Geophysical Prospecting*, *68*, 145-163.

Manzi, M.S., Gibson, M.A., Hein, K.A., King, N. and Durrheim, R.J., 2012. Application of 3D seismic techniques to evaluate ore resources in the West Wits Line goldfield and portions of the West Rand goldfield, South AfricaApplication of 3D seismic techniques. *Geophysics*, *77*(5), 163-171.

Manzi, M.S.D., 2014. *Application of 3D Seismic Analysis Techniques to Evaluate Ore Resources on Kloof, South Deeps and Driefontein Gold Mines, Witwatersrand Basin, South Africa* (Doctoral dissertation, University of the Witwatersrand, Faculty of Science, School of Geosciences).

Martorana, R., Capizzi, P., D'Alessandro, A. and Luzio, D., 2017. Comparison of different sets of array configurations for multichannel 2D ERT acquisition. *Journal of Applied Geophysics*, *137*, 34-48.

Maruddani, B., and Sandi, E., 2019. The Development of Ground Penetrating Radar (GPR) Data Processing: International Journal of Machine Learning and Computing, 9, 768–773.

Merensky, H., 1925. How we discovered platinum. *Mining and Industrial Magazine of Southern Africa*, *1*, 265-266.

Miller, H.G. and Singh, V., 1994. Potential field tilt—a new concept for location of potential field sources. *Journal of applied Geophysics*, *32*(2-3), 213-217.

Moczo, P., 1998. *Introduction to Modeling Seismic Wave Propagation by the Finite-Difference Methods*. Disaster Prevention Research Institute, Kyoto University.

Moczo, P., Kristek, J. and Halada, L., 2004. The finite-difference method for seismologists. *An Introduction*, 161.

Moczo, P., Kristek, J., Galis, M., Pazak, P. and Balazovjech, M., 2007. The finite-difference and finite-element modeling of seismic wave propagation and earthquake motion. *Acta physica slovaca*, *57*(2).

Muszala, S., Stoffa, P.L. and Lawver, L.A., 2001. An application for removing cultural noise from aeromagnetic data. *Geophysics*, *66*(1), 213-219.

Nabighian, M.N., Grauch, V.J.S., Hansen, R.O., LaFehr, T.R., Li, Y., Peirce, J.W., Phillips, J.D. and Ruder, M.E., 2005. The historical development of the magnetic method in exploration. *Geophysics*, *70*(6), 33-61.

Naudy, H., and H. Dreyer, 1968. Essai de filtrage non-lineaire applique aux profils aeromagnetiques. *Geophysical Prospecting*, *16*(2), 171-178.

Neal, A., and Roberts, C. L., 2000. Applications of ground-penetrating radar (GPR) to sedimentological, geomorphological and geoarchaeological studies in coastal environments: *Geological Society, London, Special Publications*, 175, 139–171.

Nkosi, N.Z., Manzi, M.S., Drennan, G.R. and Yilmaz, H., 2017. Experimental measurements of seismic velocities on core samples and their dependence on mineralogy and stress; Witwatersrand Basin (South Africa). *Studia Geophysica et Geodaetica*, *61*, 115-144.

O'Brien, P.N.S., 1974. Aspects of seismic research in the oil industry. *Geoexploration*, *12*(2-3), 75-96.

Ogaya, X., Alcalde, J., Marzán, I., Ledo, J., Queralt, P., Marcuello, A., Martí, D., Saura, E., Carbonell, R., and Benjumea, B., 2016. Joint interpretation of magnetotelluric, seismic, and well-log data in Hontomín (Spain): *Solid Earth*, **7**, 943–958.

Opara, C., Adizua, O.F. and Ebeniro, J.O., 2018. Application of static correction in the processing of 3D seismic data from onshore Niger Delta. *Universal Journal of Geoscience*, *6*(1), 1-7.

Ordońez, E.S.O.S., 2014. *Seismic imaging of the structure of the central Ecuador convergent margin: relationship with the inter-seismic coupling variations* (Doctoral dissertation, Université Nice Sophia Antipolis).

Peacock, K.I. and Treitel, S., 1969. Predictive deconvolution-theory and practice. *Geophysics*, *34*(2), 155-169.

Ravat, D., 2007. Reduction to Pole. *Encyclopedia of Geomagnetism and Paleomagnetism.* Switzerland: Springer, 856-857.

Rawlinson, N., Hauser, J. and Sambridge, M., 2008. Seismic ray tracing and wavefront tracking in laterally heterogeneous media. *Advances in geophysics*, *49*, 203-273.

Reynolds, A.C., 1978. Boundary conditions for the numerical solution of wave propagation problems. *Geophysics*, *43*(6), 1099-1110.

Reynolds, J. M., 2011. An Introduction to Applied and Environmental Geophysics: John Wiley & Sons.

Robertsson, J.O., Blanch, J.O. and Symes, W.W., 1994. Viscoelastic finite-difference modeling. *Geophysics*, *59*(9), 1444-1456.

Robinson, E.A. and Treitel, S., 2000. Geophysical signal analysis. *Society of Exploration Geophysicists*, 238.

Robinson, E.A., 1967. Predictive decomposition of time series with application to seismic exploration. *Geophysics*, *32*(3), 418-484.

Robinson, E. A., 1985, Seismic time-invariant convolutional model: *Geophysics*, 50, 2742–2751.

Roux, A.T., 1967. The application of geophysics to gold exploration in South Africa. *Mining and groundwater geophysics*, 425-438.

Russell, B.H., 1988. *Introduction to seismic inversion methods* (No. 2). *Society of Exploration Geophysicists* Books.

Ryan, H., 1997. Ricker, Ormsby, Klander, Butterworth – A Choice of Wavelets: *CSEG Recorder*, 19.

Saenger, E.H. and Bohlen, T., 2004. Finite-difference modeling of viscoelastic and anisotropic wave propagation using the rotated staggered grid. *Geophysics*, *69*(2), 583-591.

Salem, A., Lei, K., Green, C., Fairhead, J.D. and Stanley, G., 2010. Removal of cultural noise from high-resolution aeromagnetic data using a two stage equivalent source approach. *Exploration Geophysics*, *41*(2), 163-169.

Salisbury, M.H., Harvey, C.W., Matthews, L., Eaton, D.W. and Milkereit, B., 2003. The acoustic properties of ores and host rocks in hardrock terranes. *Hardrock seismic exploration: Society of Exploration Geophysicists,* 9-19.

Schouwstra, R.P., Kinloch, E.D. and Lee, C.A., 2000. A short geological review of the Bushveld Complex. *Platinum Metals Review*, *44*(1), 33-39.

Scoon, R.N. and Mitchell, A.A., 2005. The platiniferous dunite pipes in the eastern limb of the Bushveld Complex: review and comparison with unmineralized discordant ultramafic bodies: reply to comment by RG Cawthorn. *South African Journal of Geology*, *108*(4), 587-589.

Sehoole, L., Manzi, M.S., Zhang, S.E. and Bourdeau, J.E., 2020. An innovative seismic and statistical approach to understand 3D magmatic structures and ore deposits in the western Bushveld Complex, South Africa. *Ore Geology Reviews*, *126*, 103784.

Sen, M. K., 2011. Seismic, Reflectivity Method, in H. K. Gupta, ed., *Encyclopedia of Solid Earth Geophysics*, Springer Netherlands, 1269–1279.

Sepato, O., 2015. *Statistical and wavelet analysis of density and magnetic susceptibility data from the Bushveld Complex, South Africa* (Masters Dissertation, University of the Witwatersrand, Faculty of Science, School of Geosciences).

Shao, J., Zhang, Q., Wu, X., Lei, Y., Wu, X. and Wang, Z., 2020. Investigation on the water flow evolution in a filled fracture under seepage-induced erosion. *Water*, *12*(11), 3188.

Shearer, P. M., 2019. *Introduction to Seismology*. 3rd edn. Cambridge: Cambridge University Press. doi: 10.1017/9781316877111.

Sheriff, R.E. and Geldart, L.P., 1995. *Exploration seismology*. Cambridge University Press. https://doi.org/10.1017/CBO9781139168359.

Sihoyiya, M., Manzi, M.S., James, I., Rapetsoa, M.K., Westgate, M., Nwaila, G., Linzer, L., Durrheim, R.J. and Staley, P., 2022. Seismic delineation of the gold-bearing structures in the South Rand goldfield (South Africa): A comparison of pre-stack time and depth migration approaches on legacy seismic data. *Near Surface Geophysics*, *20*(6), 697-709. https://doi.org/10.1002/nsg.12209

Smith, D.S., Basson, I.J. and Reid, D.L., 2004. Normal Reef subfacies of the Merensky Reef at Northam platinum mine, Zwartklip facies, western Bushveld Complex, South Africa. *The Canadian Mineralogist*, *42*(2), 243-260.

Squelch, A., Madadi, M. and Urosevic, M., 2013. A reproducible framework for 3D acoustic forward modelling of hardrock geological models with Madagascar. Australian Society Of Exploration Geophysicists, *Extended Abstracts*, *2013*(1), 1-4.

Stewart, I.C. and Miller, D.T., 2018. Directional tilt derivatives to enhance structural trends in aeromagnetic grids. *Journal of Applied Geophysics*, *159*, 553-563.

Szalai, S. and Szarka, L., 2008. On the classification of surface geoelectric arrays. *Geophysical Prospecting*, *56*(2), 159-175.

Szymczyk, M., and Szymczyk, P., 2013. Preprocessing of GPR data: *Image Processing & Communication*, 18, 83–90.

Taner, M.T. and Koehler, F., 1969. Velocity spectra—Digital computer derivation applications of velocity functions. *Geophysics*, *34*(6), 859-881.

Telford, W. M., Geldart, L. P. and Sheriff, R. E., 1990. *Applied Geophysics*. 2nd edn. Cambridge: Cambridge University Press. https://doi.org/10.1017/CBO9781139167932.

Udden, J.A., 1914. Mechanical composition of clastic sediments. *Bulletin of the geological society of America*, *25*(1), 655-744.

Venkateswarlu, B., and Tewari, V. C., 2014. Geotechnical Applications of Ground Penetrating Radar (GPR).

Viljoen, M.J., 1999. The nature and origin of the Merensky Reef of the western Bushveld Complex based on geological facies and geophysical data. *South African Journal of Geology*, *102*(3), 221-239.

Vlastislav, Č. and De Castro, M.A., 1993. Application of dynamic ray tracing in the 3-D inversion of seismic-reflection data. *Geophysical Journal International*, *113*(3), 776-779.

Vretblad, A., 2003. *Fourier analysis and its applications* (Vol. 223). New York: Springer. 93

Wagner, P.A., 1929. The platinum deposits and mines of South Africa. 1973 edition. *Struik (Pty), Ltd, Cape Town, South Africa, 338*.

Wang, E., Liu, Y. and Sen, M.K., 2016. Effective finite-difference modelling methods with 2-D acoustic wave equation using a combination of cross and rhombus stencils. *Geophysical Journal International*, *206*(3), 1933-1958.

Westgate, M., 2020. *Reappraisal of legacy reflection seismic data using advanced processing techniques and seismic attributes* (Doctoral dissertation, Ph. D. Thesis. University of the Witwatersrand, South Africa).

Widess, M.B., 1973. How thin is a thin bed?. *Geophysics*, *38*(6), 1176-1180.

Wiener, N., 1949. *Extrapolation, interpolation, and smoothing of stationary time series: with engineering applications* (Vol. 113, No. 21, 1043-54). Cambridge, MA: MIT press.

Yari, M., Nabi-Bidhendi, M., Ghanati, R., and Shomali, Z., 2021. Hidden layer imaging using joint inversion of P-wave travel-time and electrical resistivity data: *Near Surface Geophysics*, 19, 297–313.

Yilmaz, Ö., 2001. *Seismic data analysis: Processing, inversion, and interpretation of seismic data*. Society of exploration geophysicists.

Zakaria, A., Penrose, J., Thomas, F. and Wang, X., 2000, November. The Two Dimensional Numerical Modeling of Acoustic Wave Propagation in Shallow Water. In *Proceedings of the Australian Acoustical Society Conference, Joondalup, Australia*, 15-17.

Zhang, R., and Li, T., 2019. Joint Inversion of 2D Gravity Gradiometry and Magnetotelluric Data in Mineral Exploration: *Minerals*, 9, 541.

Zheglova, P., Lelièvre, P. G., and Farquharson, C. G., 2018. Multiple level-set joint inversion of traveltime and gravity data with application to ore delineation: A synthetic study: *Geophysics*, 83, 13–30.

Ziolkowski, A. 1984 *Deconvolution:* International Human Resources Development Corp. Publications.

Seismic solutions utilizing existing in-mine infrastructure for mineral exploration: A case study from Maseve platinum mine, South Africa

Moyagabo K. Rapetsoa[1], Musa S. D. Manzi[1], Mpofana Sihoyiya[1], Michael Westgate[1], Phumlani Kubeka[2], Emmanuel Onyebueke[1], and Raymond J. Durrheim[1]

https://doi.org/10.1190/tle41010054.1

Abstract

We demonstrate the application of seismic methods using in-mine infrastructure such as exploration tunnels to image platinum deposits and geologic structures using different acquisition configurations. In 2020, seismic experiments were conducted underground at the Maseve platinum mine in the Bushveld Complex of South Africa. These seismic experiments were part of the Advanced Orebody Knowledge project titled "Developing technologies that will be used to obtain information ahead of the mine face." In these experiments, we recorded active and passive seismic data using surface nodal arrays and an in-mine seismic land streamer. We focus on analyzing only the in-mine active seismic portion of the survey. The tunnel seismic survey consisted of seven 2D profiles in exploration tunnels, located approximately 550 m below ground surface and a few meters above known platinum deposits. A careful data-processing approach was adopted to enhance high-quality reflections and suppress infrastructure-generated noise. Despite challenges presented by the in-mine noisy environment, we successfully imaged the platinum deposits with the aid of borehole data and geologic models. The results open opportunities to adapt surface-based geophysical instruments to address challenging in-mine environments for mineral exploration.

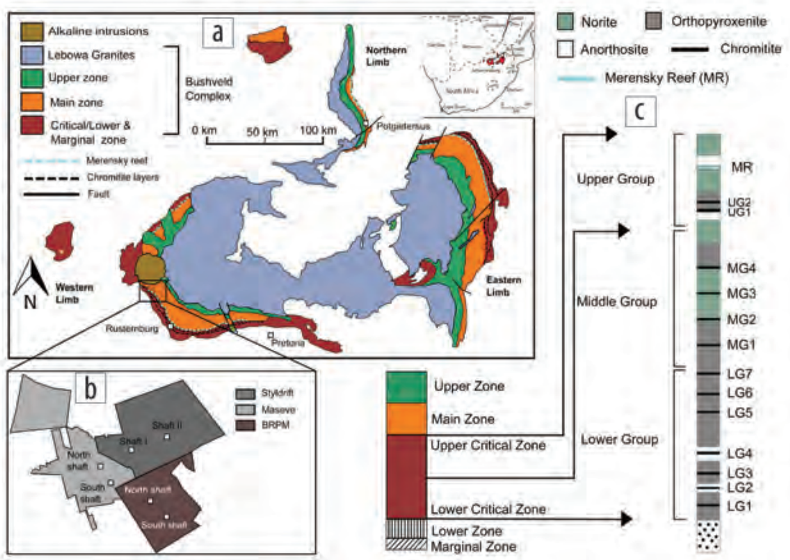

Figure 1. (a) Geologic map of the Bushveld Complex (modified from Cawthorn, 2015) showing the location of the Maseve mine site. (b) Map of the Maseve mine showing the location of the study area at the north shaft and the surrounding mines that are used for passive seismics. (c) Stratigraphic column of the critical zone showing the chromitite layers and Merensky Reef (MR).

Introduction

The Bushveld Complex of South Africa hosts the richest source of platinum group elements (PGEs) reserves, accounting for almost 75% of all globally mined platinum (Scheiber-Enslin and Manzi, 2018). The PGEs are hosted in two major economic horizons (locally termed "reefs") — the Merensky Reef and Upper Group-2 (UG2) chromitite layers. Starting from surface exploitation in the early 1900s, mining operations in the Bushveld Complex have increased in depth (between 0.5 and 2 km) over the years. The increase in depth is associated with complex geologic features such as faults, dykes, potholes, voids, and iron-rich ultramafic pegmatites (IRUPs) intrusions that complicate mining activities (Eales and Cawthorn, 1996; Nkosi et al., 2017; Sehoole et al., 2020). The complex geologic environments cause stoppages to production and mine construction and threaten the safety of mineworkers. With the goals of better understanding some of these geologic structures and improving production and safety, seismic studies were conducted at the Maseve mine, located approximately 38 km northwest of Rustenburg and approximately 10 km south of the Pilanesberg Alkaline Intrusive Complex in the Northwest Province, South Africa (Figures 1a–1c).

In South Africa, the reflection seismic method is used mainly for exploration, mine design, and planning due to its ability to resolve complex geologic features (Stevenson and Durrheim, 1997; Manzi et al., 2012, 2019). The method has played an important role in imaging the deep-seated gold and platinum deposits and geologic structures (Manzi et al., 2012, 2019). In the Bushveld Complex, the use of 2D and 3D reflection seismics started in the 1990s to map the platinum-bearing horizons and complex geologic structures. The 3D reflection seismic surveys were conducted particularly to map major faults, dykes, and IRUPs. However, the surface seismic surveys were unable to resolve geologic structures in detail ahead of mining tunnels (Trickett et al., 2004). Borehole seismic techniques (e.g., crosswell reflection seismics, seismic tomography, and vertical seismic profiling) were used to image structures within resolutions of 1 to 3 m. However, these techniques exhibited low resolutions in noisy mine environments (Manzi et al., 2012). In-mine seismic techniques have proven useful in improving the imaging resolution

[1]University of the Witwatersrand, School of Geosciences, Johannesburg, South Africa. E-mail: 867109@students.wits.ac.za; musa.manzi@wits.ac.za; 1284606@students.wits.ac.za; michael.westgate@wits.ac.za; emmanuel.onyebueke@wits.ac.za; raymond.durrheim@wits.ac.za.
[2]Royal Bafokeng Platinum, Johannesburg, South Africa. E-mail: phumlanik@bafokengplatinum.co.za.

of the mineral deposits (Brodic et al., 2021; Donoso et al., 2021). The progression of in-mine seismic techniques has grown in Europe, but the techniques are not yet well adopted for deep mineral exploration. The key limitation to in-mine seismics is the high noise level produced by mine operations such as blasting, cleaning, and drilling, among others. To improve in-mine seismic designs, a better understanding of the acoustic impedance contrast, geometry, and structural characteristics of the target and the host rock is necessary. One of the important aspects is obtaining accurate velocity information, which needs to be determined both for numerical simulations and to constrain seismic processing, interpretation, and time-to-depth conversion (Malehmir et al., 2013; Manzi et al., 2017).

The Advanced Orebody Knowledge program was launched by several South African research institutions with the aim of addressing some of the aforementioned issues. The program involved collection of not only reflection seismic but also multigeophysical data sets including ground-penetrating radar and electrical resistivity tomography data at Maseve mine. Integration of the geophysical and geologic data has played a key role in mapping the deep seismic reflectors and obtaining information on/ahead of the tunnel face. The main objective of this study is to characterize geologic structures using in-mine seismic experiments in deep (greater than 500 m) platinum mines (Figure 1b).

Geologic background

The Bushveld Complex is in the northwestern part of South Africa and is known for its vast PGEs, complex geology, and remarkable size, covering an area of about 64,000 km^2 (Eales and Cawthorn, 1996). The Bushveld Complex has been a subject for abundant research documented by several authors (Eales and Cawthorn, 1996; Buchanan and Reimold, 1998; Kinnaird, 2005; Hunt, 2006). The complex can be divided into the eastern, western, far western, northern, and southern limbs (visible on gravity and magnetic data) (Cawthorn and Webb, 2001; Kinnaird, 2005). The western limb is the focus of our study (Figure 1a). Several mines currently are in operation in the Bushveld Complex, extracting PGEs, chromium, and vanadium deposits. The economic horizons are found in the mafic to ultramafic cumulate rocks of the complex, termed the Rustenburg Layered Suite (RLS), with an average thickness of 6 km. The RLS forms part of the successive magma intrusions that intruded the Transvaal Supergroup and the Rooiberg Group volcanics at approximately 2.06 Ga (Cawthorn and Webb, 2001). The intrusions resulted in the RLS being divided into five mineralogically varying zones (Figure 1c), namely the marginal, lower, critical, main, and upper zones (Eales and Cawthorn, 1996; Kinnaird, 2005; Scheiber-Enslin and Manzi, 2018). The RLS is overlaid by felsic rocks belonging to the Lebowa Granite and the Rashoop Granophyre Suite.

The focus is on the critical zone that makes up 15%–25% of the RLS in thickness and is subdivided into the lower critical zone and the upper critical zone. The zones are characterized by the layering of norites and anorthosites, together with ultramafic layers of pyroxenite and chromitite. The Merensky Reef and the UG2 chromitite are the two major economic horizons hosting PGE deposits (Trickett et al., 2004; Cawthorn, 2015). The thickness of the Merensky Reef ranges from 0.5 to 2 m, and the UG2 forms part of the chromitite layers that are divided into an Upper Group (UG), Middle Group (MG), and Lower Group (LG) with thicknesses of 0.5–1 m, 1–5 cm, and 0.8–1.2 m, respectively (Lee, 1996; Nex et al., 1998; Kinnaird, 2005). The two major horizons are mined at average depths of 500 m below the surface, with the UG2 occurring 15–400 m below the Merensky Reef (Manzi et al., 2020).

The Bushveld Complex is highly faulted, and the regional structural interpretation suggests that rocks may be flat-lying due to the reaction of the northwest–southeast-trending Rustenburg Fault (Campbell, 2011). The majority of faults are striking north to northwest and dipping at an average of about 70° to 80°. Existing faults gave way for intrusion of multiple dykes of different ages and composition crosscuting the Bushveld Complex stratigraphy. Diabase and dolerite dykes are the most common in the area. Several dykes in the complex have resulted in the loss of ground of the reef. Furthermore, the Bushveld Complex has slump structures (e.g., potholes) and IRUPs that result in blockages to mining operations.

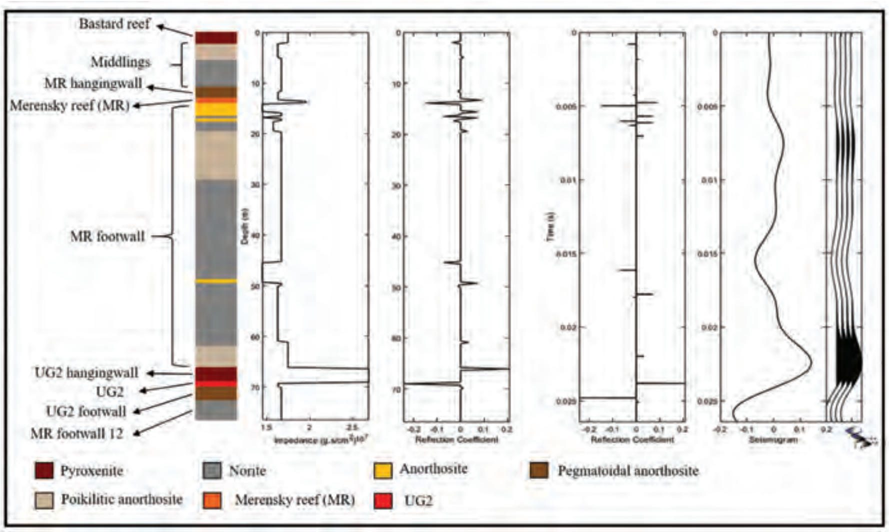

Figure 2. Stratigraphic column derived from borehole 1 of Maseve mine. Reflection coefficients were derived from the acoustic impedance, and synthetic seismograms were generated using the reflection coefficient and a Ricker wavelet (130 Hz). Strong reflections observed are associated with the two major reefs (Merensky Reef and UG2). The acoustic impedance of the UG2 and the surrounding rock is expected to be higher than that of the Merensky Reef (see Manzi et al., 2018).

Seismic modeling and data acquisition

Evaluation of reflection response at Maseve mine area. To investigate the seismic reflectivity response of the mineralizations (MR and UG2) and constrain our seismic interpretation, zero-offset synthetic seismograms were computed (Figure 2) using the borehole (BH1) information provided by the mine. The synthetic seismogram was computed using the ultrasonic (P-wave velocities) and bulk density measurements of the host rock and ore samples collected at Maseve mine. The ultrasonic measurements of P-wave velocities were conducted at atmospheric temperature using 0.5 MHz P-wave transducers. The average P-wave velocity measurements of the collected samples range from 5088 to 6118 m/s, and the average density ranges from 2744 to 4392 kg/m^3. The measured velocity and density values are in agreement with previously published values (see Campbell, 2011; Manzi et al., 2017). Borehole BH1 reached depths of 577.5 m, and it intersected the Merensky Reef and UG2 at 515 m and 571 m, respectively. The seismogram (Figure 2) was computed using a Ricker wavelet with a dominant frequency of 130 Hz and a sampling rate of 0.25 ms. The Merensky Reef and the UG2 are too thin (approximately 1 m thick) to be directly resolved, while the acoustic impedance contrast (bulk density × seismic velocity) of the hanging wall and the footwall is large enough to provide significant reflection response. The seismic reflection from UG2 is more prominent because its acoustic impedance contrast with the host rock is higher (Manzi et al., 2017; Scheiber-Enslin and Manzi, 2018; Manzi et al., 2020).

2D acoustic modeling as a guide for survey design and final interpretation. Seismic reflections in the study area are guided by the interfaces between the hanging wall and the footwall of the mineralization. The Merensky Reef has similar physical properties to the host rock, while the UG2 is much denser compared to the host rock. To build the geologic model, we used information obtained from borehole BH1 and geologic reports from the mine. The thickness of the Merensky Reef in the study area is 0.63 m, while that of the UG2 is 0.84 m, with a dip of approximately 7°. The area exhibits faults and dolerite dykes that crosscut the mineralization; therefore, we included the dyke in the fault zone of the model. Modeling in the tunnel is conducted with the assumption that the tunnel floor is the surface.

Figure 3 shows the model built using Tesseral software, with the information obtained from the mine and the borehole. Two-dimensional acoustic finite-difference modeling was conducted to investigate the seismic reflectivity of the mineralization and constrain the seismic interpretations. The model had a depth of 140 m and a spread of 360 m, with a grid cell of 1 m in both the vertical and horizontal directions. The target on the model was the first few meters of the lithology, with the target being the Merensky Reef and the UG2. The synthetic model parameters were kept the same as the acquisition parameters of our data, with a recording length of 500 ms and sampling interval of 1 ms. Given that the tunnel seismic surveys in hard-rock environments exhibit rather low attenuation, while the surveys conducted with impact seismic sources have demonstrated rather high dominant frequency (e.g., Brodic et al., 2016), a 130 Hz Ricker wavelet was chosen.

Data acquisition. In November 2020, we acquired multiple seismic lines on the surface and inside mine tunnels at the Maseve mine. The data acquisition parameters for the tunnel surveys are summarized in Table 1. A dense array of 2D seismic lines was collected on the surface using Sercel 1C wireless units connected to 5 Hz vertical geophones and a broadband seismometer (Figures 4c and 4e). In this paper, we only present the results obtained from three seismic profiles acquired inside the mine tunnels. The in-mine surveys consisted of seven experimental profiles acquired along exploration tunnels, covering about 0.6 km over known platinum deposits and geologic structures. The surface data were acquired using a 48 kg accelerated weight drop (Figure 4a), while a 5 kg sledgehammer (shot spacing of 2–5 m) was used as the in-mine seismic source (Figure 4b) due to underground conditions (loose fragments of the hanging wall). Signal penetration was fair for near-surface imaging considering the abundance of mining-induced noise. To improve the signal-to-noise ratio, four hammer hits were

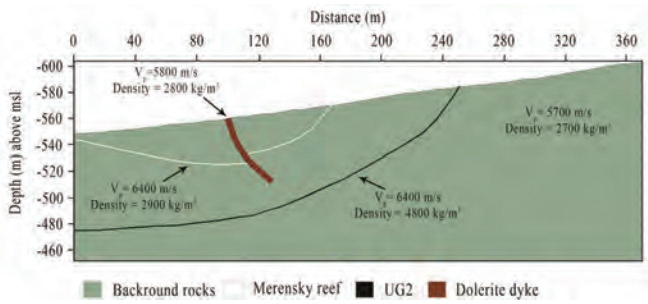

Figure 3. Geologic/finite-difference model at the Maseve mine. The model shows the two-target mineralizations and geologic structures. The P-wave velocity and density of structures are noted.

Table 1. Maseve mine seismic data acquisition parameters of the seven profiles along the incline tunnel.

Line	P1	P2	P3	P4	P5	P6	P7
Number of receivers	24	24	24	15	24	24	24
Profile length	115 m	26 m	26 m	28 m	115 m	115 m	115 m
Direction	SW–NE	On pillar	SE–NW	On pillar	SE–NW		
Recording length	500 ms	300 ms	150 ms	150 ms	500 ms		
Sample interval	0.25 ms						
Vertical stacks	4						
Source spacing	5 m	2 m			5 m		
Source type	5 kg sledgehammer						
Receiver spacing	5 m	2 m	1 m	2 m	5 m		
Geophone frequency	4.5 Hz	4.5 Hz	4.5 Hz	4.5 Hz 14 Hz	4.5 Hz		

made at every shot location and then were stacked vertically. The accurate in-mine coordinates of source and receiver positions were extrapolated using the mine pegs due to inviability of reliable GPS readings underground. The underground experiments had different objectives, so a different receiver spacing was used for the profiles (Table 1). Profiles P1, P5, P6, and P7 were collected using the 4.5 Hz vertical component geophone-based land streamer with a 5 m receiver spacing to cover a large area and image the subsurface mineralization (Figure 4d). Profiles P2 and P4 were collected around the pillar using 14 Hz vertical geophones with an objective to image the structures around the pillar. Profile P3 had a receiver spacing of 1 m, with a combination of two different types of vertical geophones (4.5 and 14 Hz). The 14 Hz geophones were planted in drill holes, while the 4.5 Hz geophones were attached to the land streamer. The aim of P3 was to image mineralizations and geologic structures (faults and dykes) below the tunnel floor. During data acquisition, special attention was given to both data quality control and land streamer deployment to ensure good coupling with the ground. The profiles were designed based on the limited geologic information provided before data acquisition, ensuring that the main geologic structures were perpendicular to the profiles such that the target mineralization (Merensky Reef and UG2) could be imaged. Although seven profiles were collected underground, this paper presents the data obtained from P5, P6, and P7 due to the location and extension, which is essential to image the geologic structures and the dipping UG2. P5, P6, and P7 were collected collinear to each other, trending northeast–southwest and covering 350 m. Data were collected at a 0.25 ms sampling interval with a recording length of 0.5 s.

Figure 4. Seismic sources and the different receivers that were used during the Maseve mine acquisition (November 2020). (a) A 48 kg accelerated weight drop mounted on a vehicle along remote acquisition units. (b) Data acquisition in the mine tunnels using a sledgehammer as a source and 4.5 Hz receiver landstreamer. (c) Sercel Unite wireless 1C receivers used for passive seismic studies. (d) Underground mounting of the 4.5 Hz receiver landstreamer on the sidewall supported by roof bolts. (e) Photo of a broadband seismometer buried in the ground to record mine induced events.

Data processing

Seismic profiles P5, P6, and P7 covered the bottom part (block 11) of the incline tunnel at Maseve mine. This is a few meters above the dipping Merensky Reef and the UG2. The processing steps are summarized in Table 2. The data were of good quality with few noisy traces due to low coupling of the land streamer in the muddy ground of the tunnel. The P-wave first breaks were clearly distinguishable along entire profiles lengths, while P-wave reflections in some of the shot gathers were masked by noise. The first step was to add the coordinates to headers, as the data were collected without coordinates. The mine pegs did not cover every shot or receiver position. We placed receivers 5 m apart using the land streamer cable between the known points, and we interpolated the coordinates using a linear and spline function to estimate the coordinates of each receiver and shot. The geometry of the shots and receivers, including a straight common-depth point (CDP) line with bin spacing of 2.5 m, was created and added to the seismic profiles. The next step was to edit the bad traces and apply residual, refraction (using only the short wavelength component), elevation static corrections. The topography varied over a large distance, and it was corrected using elevation statics. The first breaks were of fair quality; therefore, we combined automatic and manual picking. A total of 1778 picks were used to generate a two-layered P-wave velocity model, which was used for refraction static correction. The refraction tomograms were produced to aid with the interpretation of the data down to about 30 m depth. A bandpass filter (50–170 Hz) was applied to constrain the data within the source energy frequency and remove significant portion of mine-generated noise. The amplitudes of the P-wave first-break picks are relatively high, therefore affecting any near-surface reflections. A top mute was applied on the first breaks to ensure that they do not affect the events in the final stack section. Figures 5a–5c show the synthetic shot gather, raw shot gather, and a processed shot gather (trace editing, refraction statics, bandpass, and top mute), respectively. The ground roll remained dominant in the data, despite the prestack processing. To attenuate these, we applied *f-k* mute to target velocities below 4100 m/s. Velocity analysis was conducted using a series of constant velocity stacks generated to select the velocity field that shows the greatest coherency of reflections. The dipping reflections were stacked coherently with normal moveout (NMO) velocities of 5500 m/s. The data exhibited steep and gently dipping reflections; therefore, we applied dip moveout (DMO) to stack the reflections simultaneously and enhance any dipping events. The consistent low-frequency events were removed by the second pass of frequency filtering (bandpass: 80–160 Hz). The stack data were migrated using a 2D Kirchhoff algorithm to collapse diffractions and place reflections to their correct geologic positions. Finally, the poststack time-migrated data were depth converted using a constant velocity of 5500 m/s.

Results and discussion

The shot gathers (Figure 5) show steeply dipping (R1) and gently dipping reflectors (R2). The two reflections are identified confidently on the processed shot gather (Figure 5c). The synthetic shot gathers (Figure 5a) and raw shot gather (Figure 5b) have high amplitude of the first arrivals, masking near-surface reflections. Application of filters, DMO, and first-break muting resulted in the enhancement of the near-surface reflections at about 25 ms. Additional steeply dipping reflections are observed. These may be associated with the deeper chromitite mineralizations that are not intersected by the boreholes in the study area. The shot gathers demonstrate that in-mine seismic studies have the potential to image near-tunnel geologic features, despite noisy mine environments.

The reflections are interpreted based on geologic observation and data. The results of the 2D reflection modeling and seismic tomograms (Figure 6) are also used to constrain the interpretation. The seismic tomogram shows the top layer to have P-wave velocities ranging between 2300 and 3400 m/s and an average thickness of 3 m. The hard rock is observed at depths of about 10 m, with P-wave velocities ranging between 4500 and 6700 m/s. The velocity of the top layer corresponds to the loose rocks and mud regions in the mine, while the hard-rock velocities match the velocities of the footwall rocks (norites and anorthosites). Merging the three segments has resulted in areas of low ray coverage (see Figure 6).

Figure 7 shows the unmigrated stack section and the processed shot gather section. The reflections appear to be crosscut along the line due to the data being collected as three separate profiles. Therefore, merging them into one profile resulted in a low CDP fold

Table 2. Processing steps applied to reflection seismic data set from Maseve mine.

	Process	Parameters	
1	Data input + reformat	From SEGD to SEGY	✓
2	Geometry assignment + CDP bin	Sources and receivers assigned to each trace + CDP size 2.5 m	✓
3	Trace editing	Kill noisy traces	✓
4	First-break picking	Automatic, manual picking	✓
5	Floating datum static correction	Fixed datum elevation: −602 m Replacement velocity: 5500 m/s	✓
6	Refraction short wavelength static correction	Two layers model based on first-break picking. Root-mean-square error 1.45–2 ms	✓
7	Trace muting	Top mute using first breaks	✓
8	Bandpass filtering	50–60–160–170 Hz	✓
9	Automatic gain control	Window: 50 ms	✓
10	Balance	500 ms	✓
11	*f-k* filtering	Surgical muting, dip = 1.2 m/s per trace	✓
12	Velocity analysis	Constant velocity stack	✓
13	NMO corrections	5500–6500 m/s, stretch mute: 70%	✓
14	Residual statics	Repeat NMO corrections twice	✓
15	DMO	Kirchhoff common offset	✓
16	Stack	Normal	✓
17	Bandpass filtering	80–90–150–160 Hz	✓
18	Post time migration	2D Kirchhoff	
19	Time to depth conversion	1D Constant velocity: 5500 m/s	✓

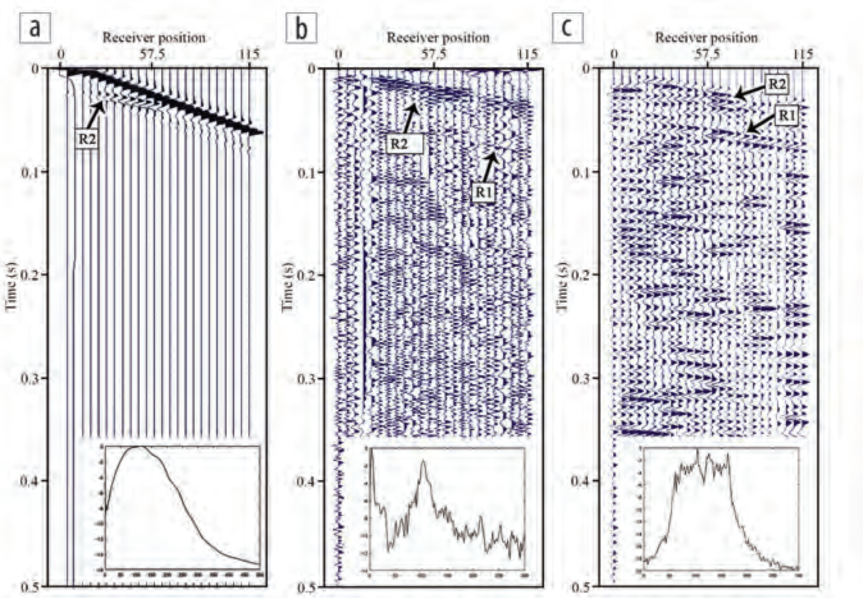

Figure 5. Shot gather examples from P5 shot-5, with their frequency spectra. Shot gathers highlight clear reflections marked by black arrows. (a) Synthetic shot gather modeled from the geologic model, showing one clear reflection (R2) correlating to the UG2. (b) Raw shot gathers, with reflections overshadowed by high frequencies. The frequency spectrum has frequency ranges of 0–1800 Hz as a result of the sampling rate of 0.25 ms. Spurious ringing can be observed on the raw shot gather. (c) The processed shot gathers, showing clear reflections, with one of the reflections not easily identified on the synthetic gather and the raw shot gather.

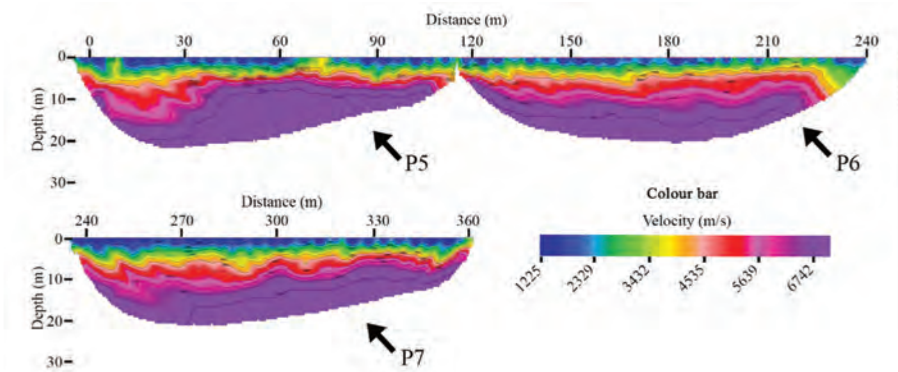

Figure 6. Near-surface P-wave refraction tomogram showing the upper 30 m of P5–P7. The average top velocities match those of the rock in the area. The tomogram has low confidence at areas where P5, P6, and P7 were merged and at the edges of the seismic profiles due to low fold of coverage.

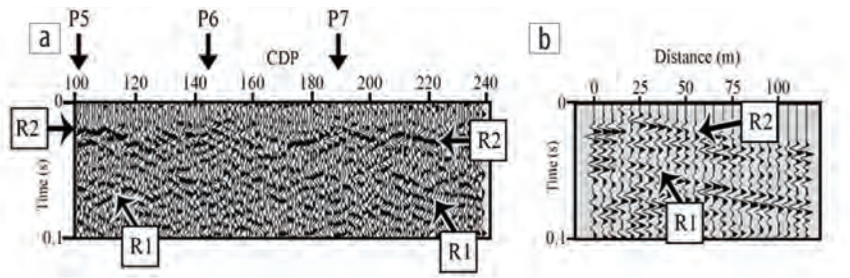

Figure 7. (a) Unmigrated time stack section and (b) a processed shot gather along P5. The reflections identified on the processed shot gather are observed on the unmigrated stack section.

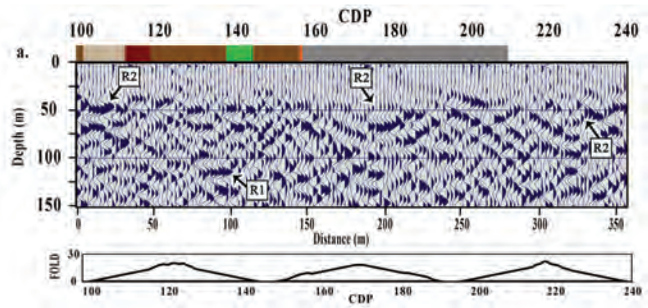

Figure 8. Unmigrated depth stack section of P5–P7 showing horizontal to dipping reflectors. Prominent reflections are observed at the edges of the survey and the coherency decrease at areas of low fold.

(see Figure 8). Two reflections are identified: R1 is associated with possible deeper mineralization below the UG2, while R2 is associated with the UG2. The R1 reflection may be associated with some mineralizations from either Upper Group 1 (UG1) or Middle Group 4 (MG4) (see Figure 1). The reflection (R2) that was hidden by the first arrivals is preserved by stacking, making it more prominent. The steeply dipping reflection (R1) is disturbed by the low fold areas; therefore, the continuous reflection observed on the processed shot gather appears to be interrupted.

The depth of the stack section (Figure 8) honors lateral variations of velocity, and the reflections are more continuous compared to the stack section in time domain. Multiple reflections can be observed in Figure 8. The shallow reflection (R2) occurring at about 70 m corresponds to the depth of UG2 on borehole BH1 (Figure 9). The stack section resolves reflections below 30 m; therefore, the Merensky Reef cannot be identified easily as it falls within this region. The first 30 m is resolved by the seismic tomograms, showing high velocity rock starting at a depth of 6–10 m (see Figure 10).

The seismic data depict clear reflections that can be attributed to the Merensky Reef and the UG2. The two reefs are closer at the edges, as the UG2 creates a syncline structure. The two mineralizations cannot be directly resolved as the vertical resolution is limited to an average of 25 m. The delineation of the mineralization depends on the rock packages surrounding it. The reflection (R2) is due to the interbedding of the hanging wall and the footwall. The interbedding is consistent throughout the line. The Merensky Reef is associated with reflections that arise from the contact between the pegmatoidal anorthosites and the norites, while the UG2 is imaged due to the contact between the orthopyroxenite rocks (2700 kg/m^3) and the chromitite (4800 kg/m^3). The UG2 contact has a higher acoustic impedance contrast compared to the Merensky Reef (see Figure 2). The Merensky Reef package has an average thickness of 7 m, while the UG2 package has an average thickness of 12 m. The migrated section shows that the interbedded reflections of the UG2 have a thickness between 15 and 20 m, which is higher than the thickness intersected by borehole BH1. The differences in thickness between the seismic data and the borehole might be due to the borehole not being directly on the seismic line and the low fold areas. However, the borehole intersected the UG2 at a depth of 72 m from the tunnel floors, which corresponds to the depth of the UG2 package (R2). The unmigrated stack section (Figure 7) shows other reflections that can be attributed to possible deeper mineralization packages below the UG2.

The geologic model shows the presence of dykes and faults in the study area. There is no clear indication of the presence of dykes in our final seismic section. This may be because the dykes have an average thickness of 3 m, which is below the seismic resolution limit of the data (approximately 12 m). However, the data show clear detection of displacements along the reflections that could be attributed to faulting in the area. The interpretation of faults is in agreement with the geologic model from the study area. The displacements of the reflections can be linked to the faults. However, the displacement observed on the data is likely due to the low fold areas; therefore, the interpretation is inconclusive.

Conclusion

Twelve reflection seismic profiles have been acquired successfully at Maseve mine. Seven profiles were acquired along the mine tunnels to image the host rock, geologic structures, and the platinum orebody. Three seismic lines have been processed successfully for the purpose of this study. The profiles show

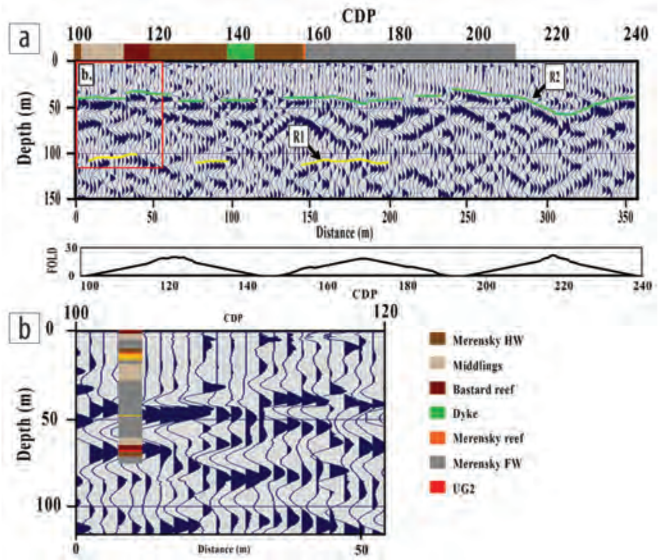

Figure 9. (a) Migrated stack section of P5–P7 with borehole BH1 overlaid (b) showing how reflection R2 correlates with the UG2 package. The arrows mark the identified reflections detailed in the text. Red outline shows the focus area where the seismic tomograms are overlaid.

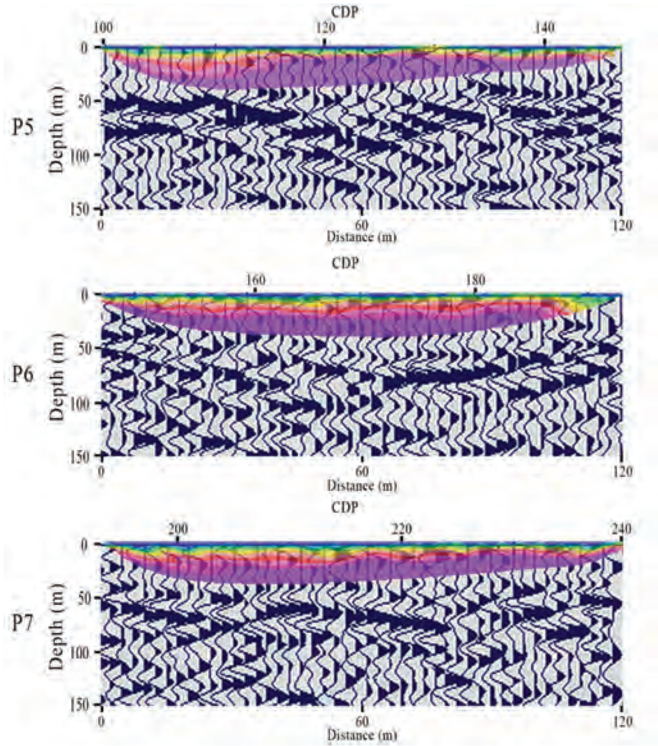

Figure 10. Seismic sections of P5, P6, and P7 showing a depth of 150 m, overlaid by velocity tomograms to correlate the reflections. The tomograms reach a maximum depth of 30 m, which is above the first prominent reflection (approximately 70 m).

high-quality reflections and noisy reflections due to the guided tunnel waves. In this paper, we have focused on introducing in-mine seismic experiments to South African mines. Careful processing, setup, and parameters of the seismic profiles allowed us to observe clear reflections on the data. Despite the challenges faced due to the interference from mining infrastructure, the combination of 2D modeling, borehole log, and geologic information assisted in the interpretation of the seismic data. One reflection is interpreted to originate from the UG2 package (contact between the hanging wall and footwall) where the chromitite layers are hosted. The seismic data clearly depict mineralization and illustrate the potential for in-mine seismics to resolve the targets. The presented data only used a minor part of the full data, neglecting surface, passive, and other underground seismic profiles. Exploitation of the data and integration with borehole information will enable us to characterize the Merensky Reef, UG2, and geologic features in detail. This study shows how high-resolution in-mine reflection seismic data can be used for development and mine planning. It opens the possibilities of using reflection seismics for exploration in difficult in-mine environments. TLE

Acknowledgments

This study was sponsored by the Mandela Mining Precinct. Mandela Mining Precinct has received funding from the Department of Science and Innovation together with Minerals Council of South Africa. We thank the staff of Maseve platinum mine, especially Sipho Sithole, for the help during mine visit and data acquisition. Students from Wits University (South Africa) are appreciated for their help with data acquisition. Michelle Pienaar is thanked for the coordination and management of the project. HiSeis Pty Ltd is highly appreciated for sponsoring the licenses for Globe Claritas processing software. We also thank Tesseral Technologies Inc. for supporting us with Tesseral software.

Data and materials availability

Seismic and borehole research data that support the findings of this study are available on request from the corresponding author. The data are not publicly available due to privacy restrictions. Geologic outcrop and open-source borehole data can be found on the website of The Council for Geoscience, South Africa (https://tinyurl.com/yckw2s2z).

Corresponding author: musa.manzi@wits.ac.za

References

Brodic, B., A. Malehmir, N. Pacheco, C. Juhlin, J. Carvalho, L. Dynesius, J. van den Berg, et al., 2021, Innovative seismic imaging of volcanogenic massive sulfide deposits, Neves-Corvo, Portugal — Part I: In-mine array: Geophysics, **86**, no. 3, B165–B179, https://doi.org/10.1190/geo2020-0565.1.

Buchanan, P. C., and W. U. Reimold, 1998, Studies of the Rooiberg Group, Bushveld Complex, South Africa: No evidence for an impact origin: Earth and Planetary Science Letters, **155**, no. 3–4, 149–165, https://doi.org/10.1016/S0012-821X(97)00216-1.

Campbell, G., 2011, Exploration geophysics of the Bushveld Complex in South Africa: The Leading Edge, **30**, no. 6, 622–638, https://doi.org/10.1190/1.3599148.

Cawthorn, R. G., 2015, The Bushveld Complex, South Africa, *in* B. Charlier, O. Namur, R. Latypov, and C. Tegner, eds., Layered intrusions, Springer Netherlands, 517–587, https://doi.org/10.1007/978-94-017-9652-1_12.

Cawthorn, R. G., and S. J. Webb, 2001, Connectivity between the western and eastern limbs of the Bushveld Complex: Tectonophysics, **330**, no. 3–4, 195–209, https://doi.org/10.1016/S0040-1951(00)00227-4.

Donoso, G. A., A. Malehmir, B. Brodic, N. Pacheco, J. Carvalho, and V. Araujo, 2021, Innovative seismic imaging of volcanogenic massive

sulfide deposits, Neves-Corvo, Portugal — Part II: Surface array: Geophysics, **86**, no. 3, B181–B191, https://doi.org/10.1190/geo2020-0336.1.
Eales, H. V., and R. G. Cawthorn, 1996, The Bushveld Complex, *in* R. G. Cawthorn, ed., Developments in petrology, **15**: Elsevier, 181–229, https://doi.org/10.1016/S0167-2894(96)80008-X.
Hunt, J. P., 2006, Geological characteristics of iron oxide-copper-gold (IOCG) type mineralisation in the Western Bushveld Complex: MSc dissertation, University of the Witwatesrand.
Kinnaird, J. A., 2005, The Bushveld Large Igneous Province: Review paper, the University of the Witwatersrand.
Lee, C. A., 1996, A review of mineralization in the Bushveld Complex and some other layered intrusions, *in* R. G. Cawthorn, Ed., Developments in petrology, **15**: Elsevier, 103–145, https://doi.org/10.1016/S0167-2894(96)80006-6.
Malehmir, A., M. Andersson, M. Lebedev, M. Urosevic, and V. Mikhaltsevitch, 2013, Experimental estimation of velocities and anisotropy of a series of Swedish crystalline rocks and ores: Geophysical Prospecting, **61**, no. 1, 153–167, https://doi.org/10.1111/j.1365-2478.2012.01063.x.
Manzi, M., R. Durrheim, and S. Webb, 2017, 3D seismic attributes for platinum exploration and mine planning in the Bushveld Complex: International Geophysical Conference, SEG Global Meeting Abstracts, 665–668, https://doi.org/10.1190/IGC2017-169.
Manzi, M., A. Malehmir, and R. Durrheim, 2019, The value of seismics in mineral exploration and mine safety: 81st Conference and Exhibition, EAGE, Extended Abstracts, https://doi.org/10.3997/2214-4609.201901667.
Manzi, M. S. D., R. J. Durrheim, K. A. A. Hein, and N. King, 2012, 3D edge detection seismic attributes used to map potential conduits for water and methane in deep gold mines in the Witwatersrand basin, South Africa: Geophysics, **77**, no. 5, WC133–WC147, https://doi.org/10.1190/geo2012-0135.1.
Manzi, M. S. D., G. R. J. Cooper, A. Malehmir, and R. J. Durrheim, 2020, Improved structural interpretation of legacy 3D seismic data from Karee platinum mine (South Africa) through the application of novel seismic attributes: Geophysical Prospecting, **68**, no. 1, 145–163, https://doi.org/10.1111/1365-2478.12900.
Nex, P. A., J. A. Kinnaird, L. J. Ingle, B. A. van der Vyver, and R. G. Cawthorn, 1998, A new stratigraphy for the Main Zone of the Bushveld Complex, in the Rustenburg area: South African Journal of Geology, **101**, no. 3, 215–223.
Nkosi, N. Z., M. S. D. Manzi, G. R. Drennan, and H. Yilmaz, 2017, Experimental measurements of seismic velocities on core samples and their dependence on mineralogy and stress; Witwatersrand Basin (South Africa): Studia Geophysica et Geodaetica, **61**, 115–144, https://doi.org/10.1007/s11200-016-0804-x.
Scheiber-Enslin, S. E., and M. Manzi, 2018, Integration of 3D reflection seismics and magnetic data for deep platinum mine planning and risk mitigation: A case study from Bushveld Complex, South Africa: Exploration Geophysics, **49**, no. 6, 928–939, https://doi.org/10.1071/EG17083.
Sehoole, L., M. S. D. Manzi, S. E. Zhang, and J. E. Bourdeau, 2020, An innovative seismic and statistical approach to understand 3D magmatic structures and ore deposits in the western Bushveld Complex, South Africa: Ore Geology Reviews, **126**, 103784, https://doi.org/10.1016/j.oregeorev.2020.103784.
Stevenson, F., and R. J. Durrheim, 1997, Reflection seismics for gold, platinum and base metal exploration and mining in Southern Africa: Proceedings of Exploration 97: Fourth Decennial International Conference on Mineral Exploration, 391–398.
Trickett, J. C., W. A. Duweke, and S. Kock, 2004, Three-dimensional reflection seismics: Worth its weight in platinum: First International Platinum Conference, Southern African Institute of Mining and Metallurgy, 257–264.

Near Surface Geophysics

Seismic delineation of the gold-bearing structures in the South Rand goldfield (South Africa): A comparison of pre-stack time and depth migration approaches on legacy seismic data

Mpofana Sihoyiya[1], Musa S.D. Manzi[1], Ian James[1,2], Moyagabo K. Rapetsoa[1], Michael Westgate[1], Glen Nwaila[1], Linzer Lindsay[1,3], Raymond J. Durrheim[1] and Philip Staley[4]

[1]*School of Geosciences, University of the Witwatersrand, Johannesburg, Republic of South Africa,* [2]*Terraspect, Bayswater, Western Australia,* [3]*SRK House, Johannesburg, Republic of South Africa, and* [4]*Sibanye-Stillwater, Waltevredenpark, Roodepoort, Republic of South Africa*

Received June 2021, revision accepted March 2022

ABSTRACT

To better image complex geological structures and explore for the gold-bearing quartz pebble conglomerate (locally termed Kimberley Reef) near Burnstone mine in the South Rand goldfield (South Africa), we reprocessed legacy 2D reflection seismic data using up-to-date seismic processing algorithms. The mining region is dominated by steeply dipping normal and reverse faults, as well as dolerite intrusions that crosscut the tabular gold mineralization and complicate the extraction of the ore. The legacy seismic data were acquired in 1993 in the South Rand goldfield as part of the gold exploration programme by the Gold Division of Anglo-American Corporation. The pre-stack data quality was improved by cautiously removing noise and applying static corrections to enhance the continuity of the reflection events. Improved structural imaging was then achieved using pre-stack time migration and pre-stack depth migration through careful velocity analysis. In particular, pre-stack depth migration provided better imaging of near-surface stratigraphic units and deep-seated complex structures, relative to older post-stack migrated images produced in 1993. Other reprocessing improvements included accurate imaging of key seismic reflective interfaces that can be used as proxies to 2D map the gold deposit, its dip variations, and geological structures (faults/dykes) crosscutting it. Synthetic shot gathers data computed using a 2D finite-difference algorithm provided some insight into the source of seismic reflectivity observed on the reprocessed seismic data. The new structural information from reprocessing is essential for enhancing ore resource evaluation and guiding future exploration projects in the region.

Key words: Exploration, Imaging, Processing, Seismics.

INTRODUCTION

The Mesoarchaean Witwatersrand Basin in South Africa hosts some of the world's largest gold deposits and has produced more than one-third of the gold ever mined (Coward et al., 1995; Manzi et al., 2013; Frimmel, 2019). The gently dipping tabular gold orebodies mainly occur in pebble-conglomerate beds (known as reefs). The majority of these deposits are concealed beneath cover rocks and mining takes place more than a kilometre below the surface (Durrheim, 1986; Manzi et al., 2012a,b). During the 1930s, exploration drilling and potential field methods (mainly magnetics and gravity) were

Email: musa.manzi@wits.ac.za

successfully used to map the extent of the Witwatersrand Basin. However, these methods were unable to adequately and accurately delineate the deeply buried gold-bearing strata. In the 1980s, the reflection seismic method was introduced in the Witwatersrand Basin for brownfields and greenfields exploration (Durrheim, 1986). By the late 1990s, the Gold Division of Anglo-American Corporation had already acquired more than 26,000 km line of the 2D reflection seismic data in the Witwatersrand Basin. The 2D seismic surveys provided information about the down-dip extensions of the orebody below thick cover rocks and delineated complex structural styles, such as folds and faults that might have controlled gold mineralization and brought the reefs to mineable depths. These surveys represented the first reflection seismic surveys to be acquired for mineral exploration in hard rock environment worldwide. Following these successes, 2D and 3D reflection seismic surveys have been conducted for gold exploration and mine planning in the Witwatersrand Basin and contributed to the discovery of new Witwatersrand goldfields (Pretorius et al., 2003; Manzi et al., 2018).

Generally, the gold-bearing conglomerate units of the Witwatersrand Basin are interbedded with other metasedimentary rocks, such as shales and quartzites, of which some have similar seismic velocities and densities, making direct imaging of these deposits with reflection seismics difficult. However, previous studies (e.g., Durrheim, 1986; Manzi et al., 2012a,b) have shown that these gold deposits can be targeted using seismic methods because they are overlain by basaltic rocks and underlain by shale units, thus providing strongly reflective interfaces that can be used as proxies to map these reefs.

Decades after the original processing of the legacy seismic in Witwatersrand Basin, computational power has increased and understanding of the hard rock seismic imaging has improved; new advanced approaches of seismic signal processing and depth imaging have been introduced. Moreover, a better understanding of the velocity fields from hard rock environment has shown significant improvement in depth imaging of complex geological structures. Several authors (e.g., Malehmir et al., 2019; Manzi et al., 2019; Westgate et al., 2020) have demonstrated, through various case studies from hard rock environments, how legacy reflection seismic data can be revisited and reprocessed to improve the quality of the data and delineate the complex geological structures that host mineral deposits. The objective of this study is to reprocess the 18 km long, 6 s two-way time (TWT), legacy 2D reflection seismic profile acquired in 1993 near Burnstone mine in the South Rand goldfield of the Witwatersrand Basin (South Africa). The main aim of the study is to improve the quality of the final seismic images through careful reprocessing of the data for further understanding of the complex geometry of the gold-bearing quartz pebble conglomerate (locally termed Kimberley Reef) near Burnstone mine, as well as providing more details of complex structures and their relationship with the orebody. To the author's knowledge, there are no publications regarding the 1993 legacy 2D seismic profile near Burnstone mine. The mine is still in the developmental stages, and our new reprocessing results could contribute to the development of the mine and the evaluation of its resources.

Velocity information obtained from the latest 2D and 3D seismic surveys in the basin and geological information obtained from the drilling and geological mapping can help to produce synthetic models that can be used to constrain our seismic processing and interpretation.

Herein, we show the improvements of the seismic images through reprocessing of the 1993 data by applying up-to-date seismic processing approaches. We also propose some geological interpretations using the new results. Then, we discuss the new processing and imaging results by comparing them with the 1993 legacy seismic data. We also tested and compared pre-stack time migration and pre-stack depth migration approaches, and the results were compared against the post-stack time migration results achieved in 1993. Finally, we discuss the improvement of structural imaging using updated velocity information.

BURNSTONE MINE AND SOUTH RAND GOLDFIELD

General information

The Burnstone mine is a relatively new gold mine in the South Rand goldfield, the north-eastern edge of the Mesoarchaean Witwatersrand Basin in the Kaapvaal Craton. Figure 1 shows a simplified geological map of the Witwatersrand Basin (Fig. 1a) as well as the location of the Burnstone mine and surrounding areas in the South Rand goldfield (Fig. 1b). The mine commenced exploration under Great Basin Gold in 2011 until placed under care about a year later, and in 2014 it was bought by Sibanye Stillwater. Pretorius (1964) outlined a detailed history of mining operations in the South Rand goldfield. In summary, exploration in the South Rand goldfield commenced in 1886, yielding 4.8 g of gold per ton, a minimum amount of gold in comparison with the other goldfields (Pretorius, 1964; Spencer, 1992). Small-scale mines were being explored in the area for ∼70 years until they came to

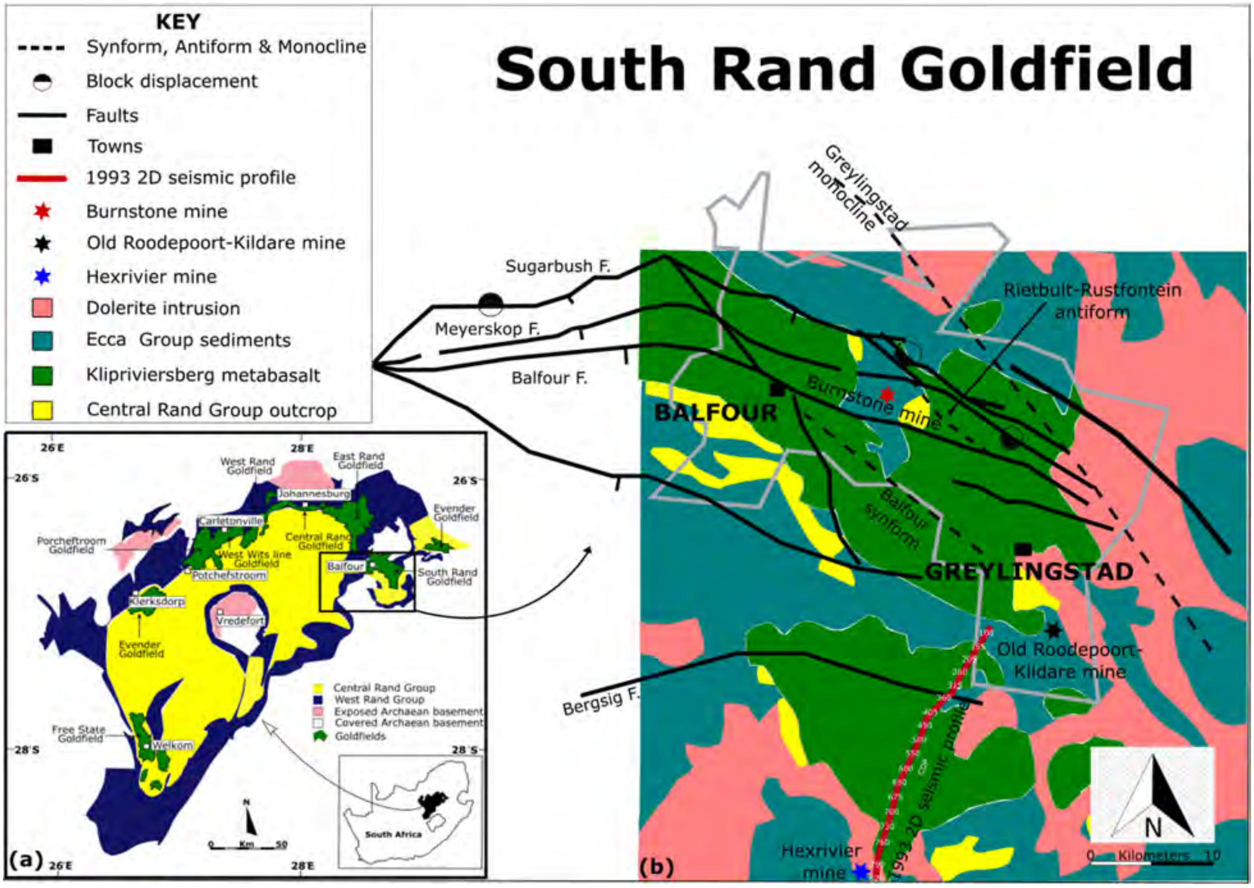

Figure 1 Simplified geological map of the Witwatersrand Basin (a) as well as the location map of the Burnstone mine (red star) and the surrounding areas in the South Rand goldfield (b). The geological structures are overlain on the geological map of the South Rand goldfield (b) (modified from Dankert and Hein, 2010).

a halt in 1962. Amongst these mines, the old Roodepoort-Kildare mine (Fig. 1b) was one of the largest producers of gold in the area. Burnstone mine is currently the only mine being explored for gold in the South Rand goldfield, yielding approximately 6–23 g of gold per ton (Frimmel and Nwaila, 2020). Sibanye Stillwater is assessing the feasibility of deepening the Burnstone mine to access gold reserves up to a depth of 1.3 km below surface. The new project, covering Burnstone mine and surrounding areas, aims to access the Kimberley reefs (known as UK9A) located approximately 200 m below the basaltic rocks of the Ventersdorp Supergroup and approximately 100 m above the Chloritoid Shale Marker (MK1) of the Kimberley Formation (Figs 2 and 3). Sibanye Stillwater is concerned about structural complexity of the lease area around the mine. Therefore, we envision that the reprocessing of the legacy seismic data could provide improved structural information and minimize geological risks during drilling.

Geological and structural setting

There is a vast amount of literature on the geology and stratigraphy of the Witwatersrand goldfields, including Dankert and Hein (2010), Tucker et al. (2016) and Manzi et al. (2013). However, due to the thinness of the basin edge, the South Rand goldfield has not attracted a lot of studies as it is believed to comprise only one economically viable gold-bearing horizon (UK9A) (Spencer, 1992; Van der Heever et al., 2009; Frimmel, 2019). The simplified stratigraphy of the South Rand goldfield is presented in Figure 2. In summary, the Witwatersrand Supergroup is subdivided into the West Rand Group (lower) and Central Rand Group (upper) (Dankert and Hein, 2010). The West Rand Group comprises the lower Hospital Hill Subgroup, middle Government Subgroup and upper Jeppestown Subgroup. The Central Rand Group, hosting 93% of the gold deposits being currently mined in the Witwatersrand Basin, is divided into the lower Johannesburg Subgroup and upper

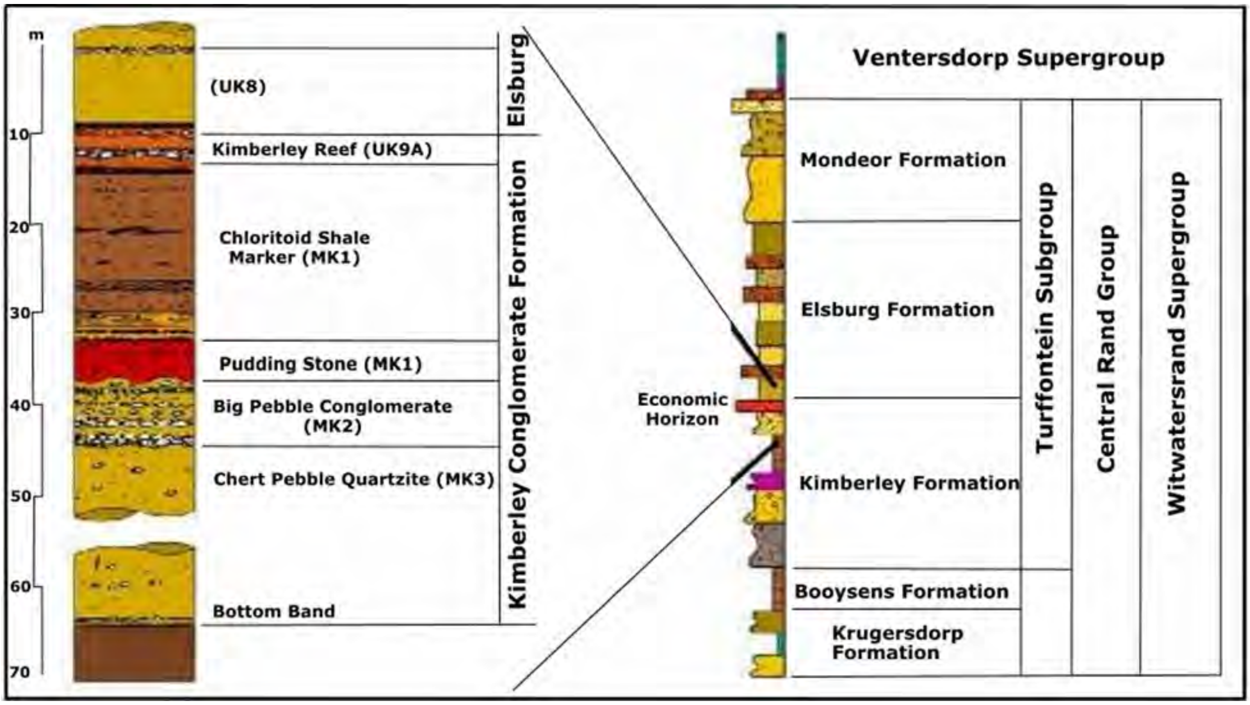

Figure 2 The simplified stratigraphy of the South Rand goldfields (modified from Van der Heever et al., 2009).

Turffontein Subgroup. The upper Central Rand Group is overlain by the basaltic lavas (Klipriviersberg Group) of the Ventersdorp Supergroup (Tucker et al., 2016).

The target orebody (UK9A) is a narrow gold-bearing conglomerate band (up to 2-m thick) and hosted within the quartzites and conglomerates of the Kimberley Formation of the Turffontein Subgroup. It is the only economically viable orebody in the South Rand goldfield; it is considered a composite reef and it is part of a group of multi-conglomerate bands that were previously regarded as secondary reefs due to their low grade (Tucker et al., 2016; Frimmel and Nwaila, 2020). The Kimberley Formation unconformably overlies the Booysens shales and is overlain by the Elsburg Formation, which is in turn overlain by the Mondeor Formation in the upper portion of the Turffontein Subgroup (Tucker et al., 2016). The Economic Horizon of the Kimberley Formation is divided into four members, the basal MK3, overlain by the pudding stone (MK2), which is in turn overlain by the Chloritoid Shale Marker (MK1) (Spencer, 1992).

Structurally, the South Rand goldfield is characterized by major east–west trending fault systems that bound the area of interest in the north and south. The most dominant structures include Sugarbush, Meyerskop, Balfour and Bergsig faults, as well as their associated drag folds (e.g., Greylingstad monocline and Rietbult-Rustfontein antiform), which are attributed to extensional tectonics (Frimmel and Nwaila, 2020) (Fig. 1b). The Sugarbush fault is downthrown to the south by a maximum displacement of up to 3 km and is the reason for the preservation of the South Rand goldfield (Pretorius, 1964; Spencer, 1992; Van der Heever et al., 2009). The regional faults and folds in the area deform the Witwatersrand Supergroup and the overlying Ventersdorp Supergroup (Pretorius, 1964; Spencer, 1992; Van der Heever et al., 2009). The east–west trending Bergsig Fault (Fig. 1b) is particularly interesting since is crosscut by the 1993 seismic profile. The delineation of this structure through reprocessing of the legacy seismic is important for future mine planning and safety in this region.

LEGACY 2D SEISMIC DATA AND 2D SEISMIC MODELLING

Seismic data acquisition

We received the 18-km-long legacy 2D seismic profile as raw shot gathers, stacked and post-stack migrated data with the acquisition parameters in the observer's report as a hard copy. The raw shot gathers were in SEG-Y format with the geometry information saved in the header files. The profile is located within the vicinity of the Burnstone project area, approximately 20 km south of the Burnstone mine (see, Fig. 1). Table 1 provides the summary of the acquisition parameters of the profile.

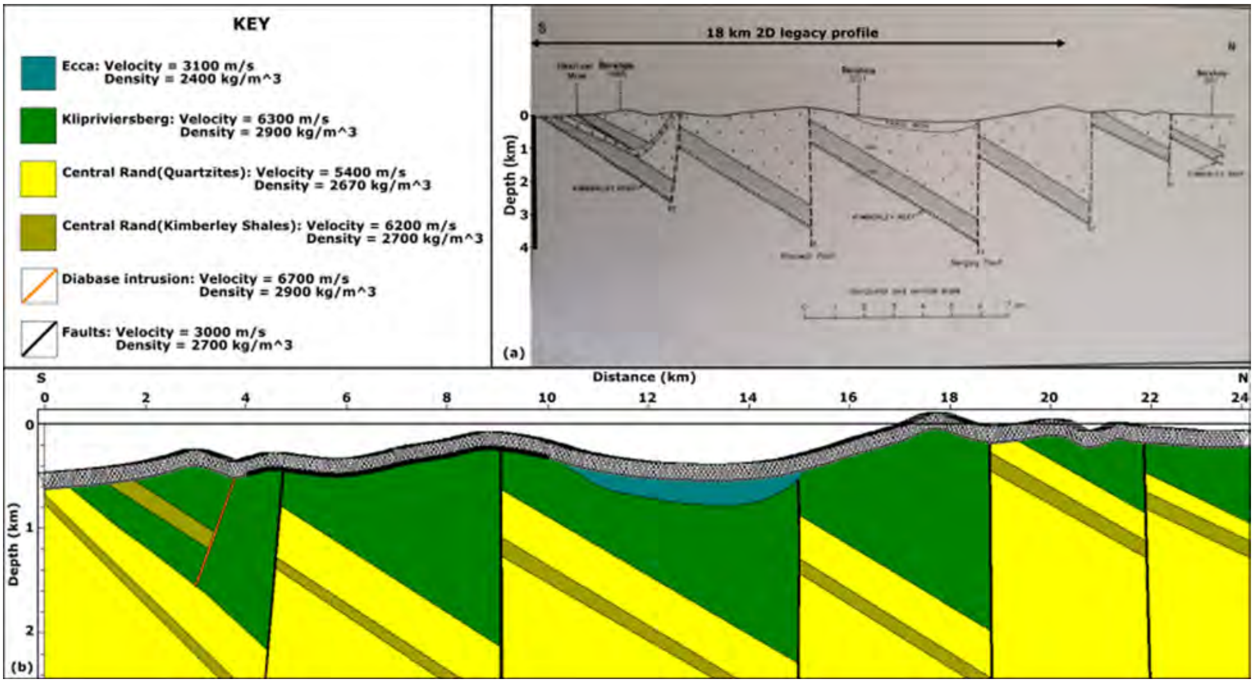

Figure 3 The geological model along the 2D legacy seismic profile as presented by Antrobus (1986) (a) and the model used for 2D acoustic finite-difference calculation (b).

Table 1 Acquisition parameters

Survey Parameters	
Survey type	2D crooked line
Year	1993
Length	18 km
Direction	NE–SW
Spread	2975-25-X-25-2975
Nominal fold	56
Recording System	
Recording device	Sercel SN368
Stacking device	CS2502
Sample Rate	2 ms
Recording length	6 s
Sweep length	16 s
Sweep frequency range	10–61 Hz
Source Information	
Source device	Vibroseis
Vibrator controller	P II
Source spacing	50 m
Receiver Information	
Receiver spacing	50 m
Geophone type	SM4U

In summary, the 2D seismic legacy profile was acquired in 1993 using a vibroseis truck as the energy source. The survey was designed with a sweep length of 16 s and a linear sweep frequency of 10–61 Hz, sampling at a rate of 2 ms. The receiver traces for each shot record were cross-correlated with the sweep signal during the acquisition process. The data were initially stored in SEG-D format and later converted to the SEG-Y format. The line has an orientation that exhibits a NE–SW trend over the Klipriviersberg metabasalt outcrop. It runs from the centre of the goldfields near the old Roodepoort-Kildare mine to the southern edge of the South Rand goldfield near the old Hexrivier mine (see, Fig. 1b). The profile was collected along the dirt road using a crooked seismic line geometry due to the variation of the terrain along the length of the line (Fig. 1b).

The seismic line has a total of 358 shots spaced at 50 m, using a fixed receiver geometry with 120 receivers active for each shot bringing the nominal fold to 56. The survey geometry was a split spread with 60 receivers on either side of the shot spaced at 50 m. The data were recorded using the recorder SN368, correlator-stacker CS 2502 and the vibrator controller P II equipment. The equipment allowed for the seismic data quality control to be conducted in the field during acquisition.

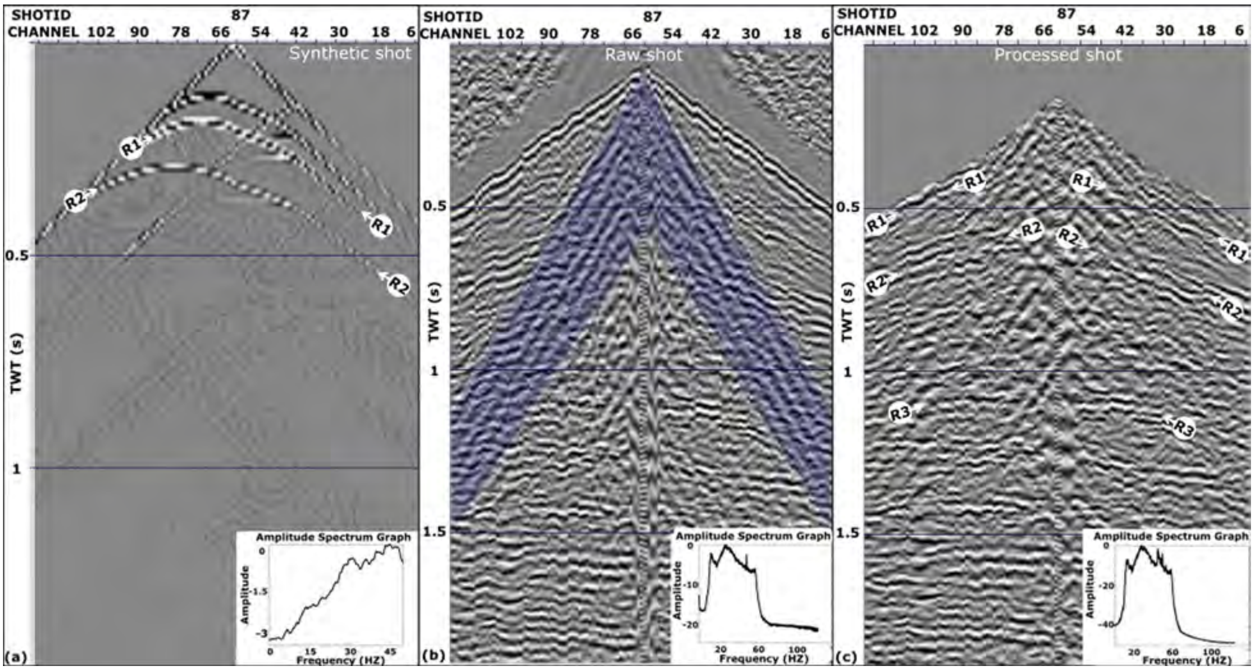

Figure 4 Comparison between s ynthetic shot gather (a), raw shot gather (b) and reprocessed shot gather (c) with the corresponding amplitude spectrum graphs. The shaded area demonstrates the attenuated surface waves, and the arrows show preserved and amplified reflections. R1 highlights the reflections from the contact between the Klipriviersberg metabasalt and the Central Rand quartzites. R2 highlights the reflections from the contact between Booysens shales and the overlying Central Rand quartzites. R3 highlights the deeper West Rand Group reflections.

2D seismic modelling and source of seismic reflectivity

Pretorius (1964), Antrobus (1986) and Spencer (1992) provided a detailed geological model of the South Rand goldfield. The seismic data cover the area south of the town of Greylingstad parallel to the geological model created by Antrobus (1986) from exploration drilling results. Figure 3(a) shows the geological model along the 1993 2D legacy seismic profile. To investigate the potential source of reflectivity in our legacy seismic data, 2D acoustic finite-difference modelling was performed using the geological information from Pretorius (1964) and Antrobus (1986) and physical properties (density and seismic velocities) obtained from Manzi et al. (2013) (Fig. 3b). There is a wide range of successful applications of this approach in hard rock environment (e.g., Ahmadi et al., 2016 and references therein).

The method was only used to model the reflections that span the economic orebody (UK9A). Therefore, the model comprises the first major lithological boundaries and major faults in the area. It has a length of 24 km and a maximum depth of 2500 km (Fig. 3b). To generate the synthetic shot gathers, a Ricker wavelet with a dominant frequency of 60 Hz was used. A seismic velocity of 3100 m/s was assigned to the thin Karoo cover, 6300 m/s assigned to the Klipriviersberg metabasalt, 5400 m/s assigned to Central Rand Group quartzites and 6200 m/s assigned to the Kimberley shales. The Karoo cover, basaltic lavas, quartzites and shales were also assigned densities of 2400, 2900, 2670 and 2700 kg/m^3, respectively. The acquisition geometry for the synthetic data was set to be similar to that of the legacy seismic data for better comparisons. The synthetic model had a 24 km profile length and maximum depth of 2.5 km, with a grid cell size of 4.2 m (vertical and horizontal directions) and a time increment of 0.29 ms. Figure 4(a) shows the generated synthetic shot gather versus real shot gathers (Fig. 4b, c). The synthetic and real shot gathers show strong seismic reflections that originate from major lithological contacts (R1–R3), with a shift of approximately 200 ms due to non-collocation nature of real and synthetic data.

2D seismic processing

The processing workflow of the 2D seismic profile is outlined in Figure 5. The raw data had an outdated and incompatible format with the processing software, which necessitated several pre-processing steps. Firstly, some header names

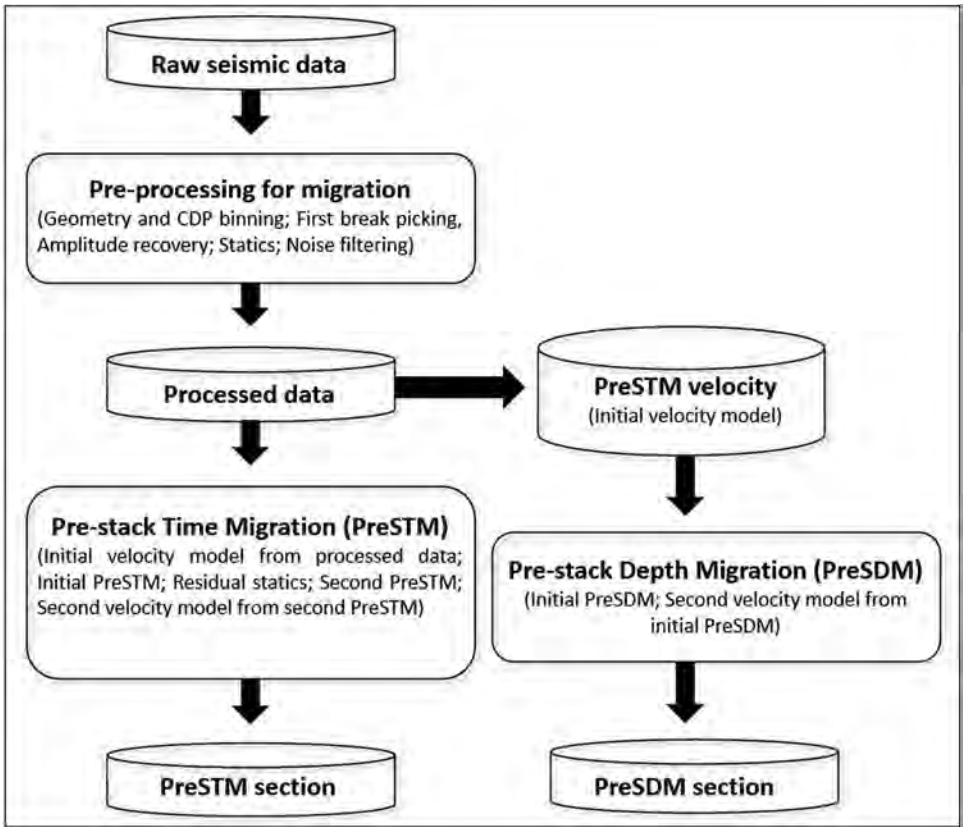

Figure 5 The processing workflow of the 2D seismic profile.

were stored in nonconventional byte locations and were subsequently extracted to their correct locations. Secondly, the geometry stored in the headers was edited since the shot and receiver elevations were offset. As per the Shuttle Radar Topography Mission data, the source elevation honoured the true topography of the line; therefore, the receiver elevation was interpolated from the shot elevation. To finalize the geometry, the traces were stored in common midpoint (CMP) bins spaced 25 m apart using a spline curve fitting.

Pre-stack, the raw shot gathers were contaminated by a 50-Hz spiking noise, most likely from the AC power lines in the area, which was cut-off by a notch filter. The raw short gathers had clear first breaks as shown in Figure 4(b). The attenuated amplitudes in the data were recovered using an automatic gain control (AGC) window of 250 ms. The target strata were mostly dominated by the surface waves (shaded with the blue colure) because of their shallow location in the shot gathers (Fig. 4b). The surface waves were attenuated using an *f–k* filter designed to mute lineaments with an S-wave velocity of 3200 m/s or less and a bandpass filter of [0–10, 60–70] Hz. Figure 4(c) processed shot gather shows the successfully attenuated surface waves. In the final step of the pre-stack processing sequence, a spiking deconvolution with 4 ms gap length and 180 ms filter length was used to broaden the spectrum. Following deconvolution, a series of constant velocities were used to create the velocity model during velocity analysis.

The aim of reappraising the legacy seismic data was to illuminate the reflective strata that span the UK9A reef between 200 ms and 1000 ms two-way time (TWT). The pre-stack processing steps show improvement of the raw shot gathers as illustrated in Figure 4(c). For example, the ground roll noise (shaded blue on the raw shot in Fig. 4b) was successfully eliminated while preserving the target reflections (indicated by the white arrows on the processed shot in Fig. 4c). The first break muting improved the AGC amplitude recovery and illuminated the target shallow reflections on the reprocessed shot gather. Before stacking the refraction top mute was removed to preserve the very near-surface reflections. Appropriate statics were calculated and applied to the data by, firstly, manual picking a total of 32,846 P-wave first breaks and calculating the floating datum using the maximum elevation of 1700 m as the fixed datum with the replacement velocity of 6000 m/s

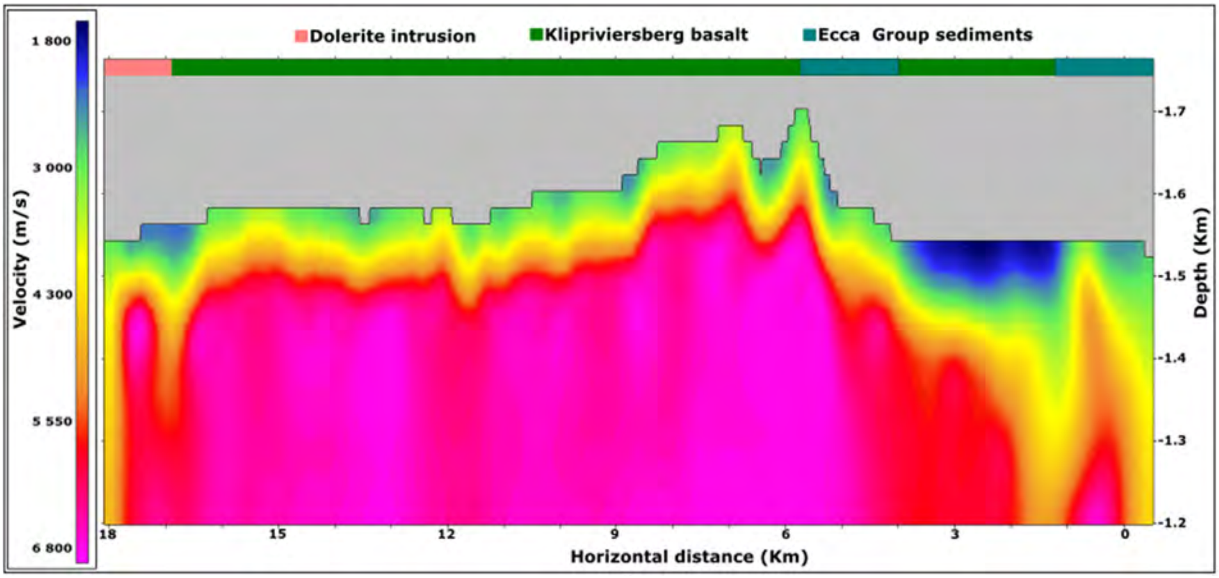

Figure 6 Refraction tomography of the 2D legacy seismic profile. The top rectangles show the geological outcrop along the profile as seen on the geological map.

(Fig. 6). The statics were calculated using least-squares inversion for first arrivals with the RMS error less than 6.5 ms. The weathered layer and the bedrock were modelled with velocities of 3000 ms and above 5500 ms (± 50 ms), respectively. Refraction tomography was calculated to constrain the interpretation of the line at a maximum depth of 1300 m (Fig. 6).

A significant amount of effort was invested in creating a velocity model that honours the complex geology of the area. In addition to this, a series of passes of residual statics were conducted to improve the coherency of reflections. A series of interactive velocity analysis were conducted for pre-stack migration computation. Both Kirchoff pre-stack time migration (PreSTM) and pre-stack depth migration (PreSDM) were applied on the data. A series of passes of the velocity analysis were done on the PreSTM and PreSDM outputs to improve the quality of the stacked data, with Residual Moveout (RMO) analysis applied following the Kirchhoff migrations. The data were then stacked and processed (post-stack) to suppress the surface waves and enhance the continuity of the reflections. Finally, the PreSTM data were converted to depth using the stacking velocities.

Generally, the 2021 PreSTM and 2021 PreSDM data provide much better imaging of the structures when compared to the 1993 legacy PostSTM data (Figs 7 and 8). Furthermore, the PreSDM data exhibit high signal-to-noise ratio than PreSTM (Fig. 7). For example, the results from the PreSTM missed the very near-surface reflection (U1) as shown in Figure 8(a), which is well defined by PreSDM (Fig. 8b). The PreSDM was applied with velocity ranges of 4000–6900 m/s, choosing the velocity model with the most coherent reflections. The velocities used were derived from the physical properties studies conducted in the Witwatersrand Basin (Manzi et al., 2015). The effectiveness of PreSDM in complex hard rock environment is well documented by various authors (e.g., Bradford et al., 2006; Buske et al., 2009; Hu and Stoffa, 2009; Manzi et al., 2012b; Storch et al., 2021).

RESULTS AND INTERPRETATION

According to the surface geological map (Fig. 1) the 1993 2D seismic profile was collected over an outcrop of the Klipriviersberg metabasalts. The low fold Common Depth Points (edges of the profile) were sitting on the thin Karoo cover, with the Karoo dolerite intrusion covering the south-western edge and the Ecca group sediments covering the north-eastern edge. The strata dipping to the north is supported by the presence of the overlying Karoo (Ecca group sediments) on the northern edge of the 1993 2D seismic profile. This supports the documented dip direction of the strata on the 1986 geological model (see, Fig. 3).

Analysis and comparison between the synthetic shot gather from 2D acoustic finite-difference modelling and the reprocessed 1993 2D seismic profile sample shot gather are shown in Figure 4. The main lithological contacts are mapped as strong reflections due to a significant acoustic impedance contrast between the overlying and underlying rocks

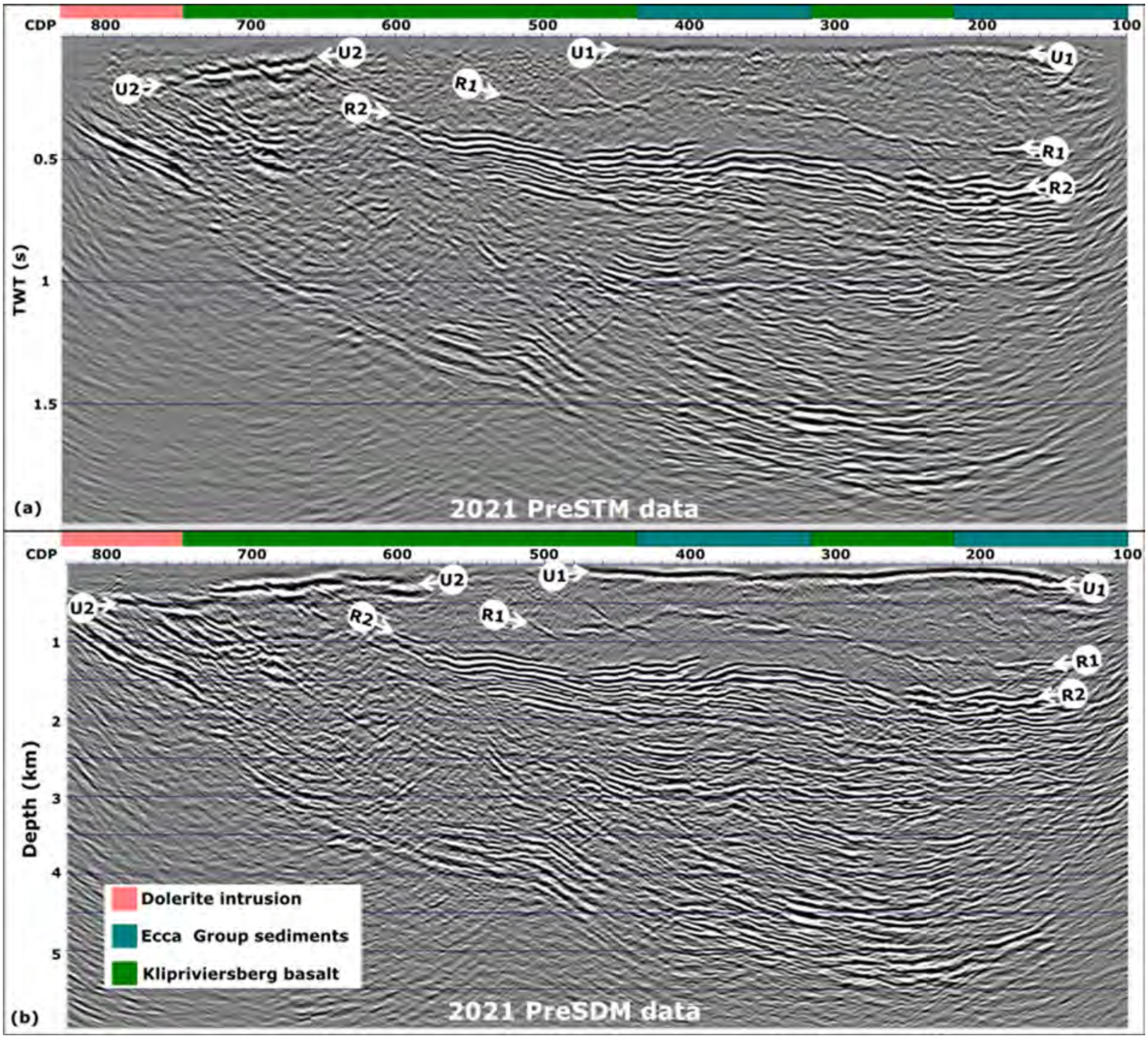

Figure 7 Comparison between PreSTM (a) and PreSDM (b), with the main lithological contacts: Karoo sediments-Ventersdorp basaltic lavas (U1), dolerite sill (U2), Ventersdorp basaltic lavas-Central Rand Group quartzites (R1) and Central Rand Group quartzites-top of MK1 (R2), and the geological outcrop along the profile.

(Figs 7–8): Karoo sediments-Ventersdorp metabasalt (U1), dolerite sill (U2), Ventersdorp metabasalt-Central Rand Group quartzites (R1) and Central Rand Group quartzites-top of MK1 (R2). These results concur with the synthetic modelling results, with a shift of approximately 200 ms due to non-collocation nature of the synthetic model and real data (see Fig. 4a).

Figure 8 shows the comparison between the 1993 legacy post-stack time migrated (PostSTM) section and the 2021 reprocessed PreSTM up to 2 s two-way time, with the outcrop data along the profile. The U1, U2 and R1 reflections are clearly defined by both 2021 PreSTM (Fig. 7b) and pre-stack depth migration (PreSDM; Fig. 8b) reprocessing results when compared to 1993 legacy data (Fig. 7a). In fact, these reflections are completely missed by the 1993 legacy data (see Fig. 8a). The final interpreted PreSDM seismic section is shown in Figure 9(b) with the velocity model overlain (Fig. 9a).

DISCUSSION

The two unconformities (U1 and R1) are clearly mapped due to the high acoustic impedance contrast between the overlying Karoo strata with low velocities (~4000 m/s) and

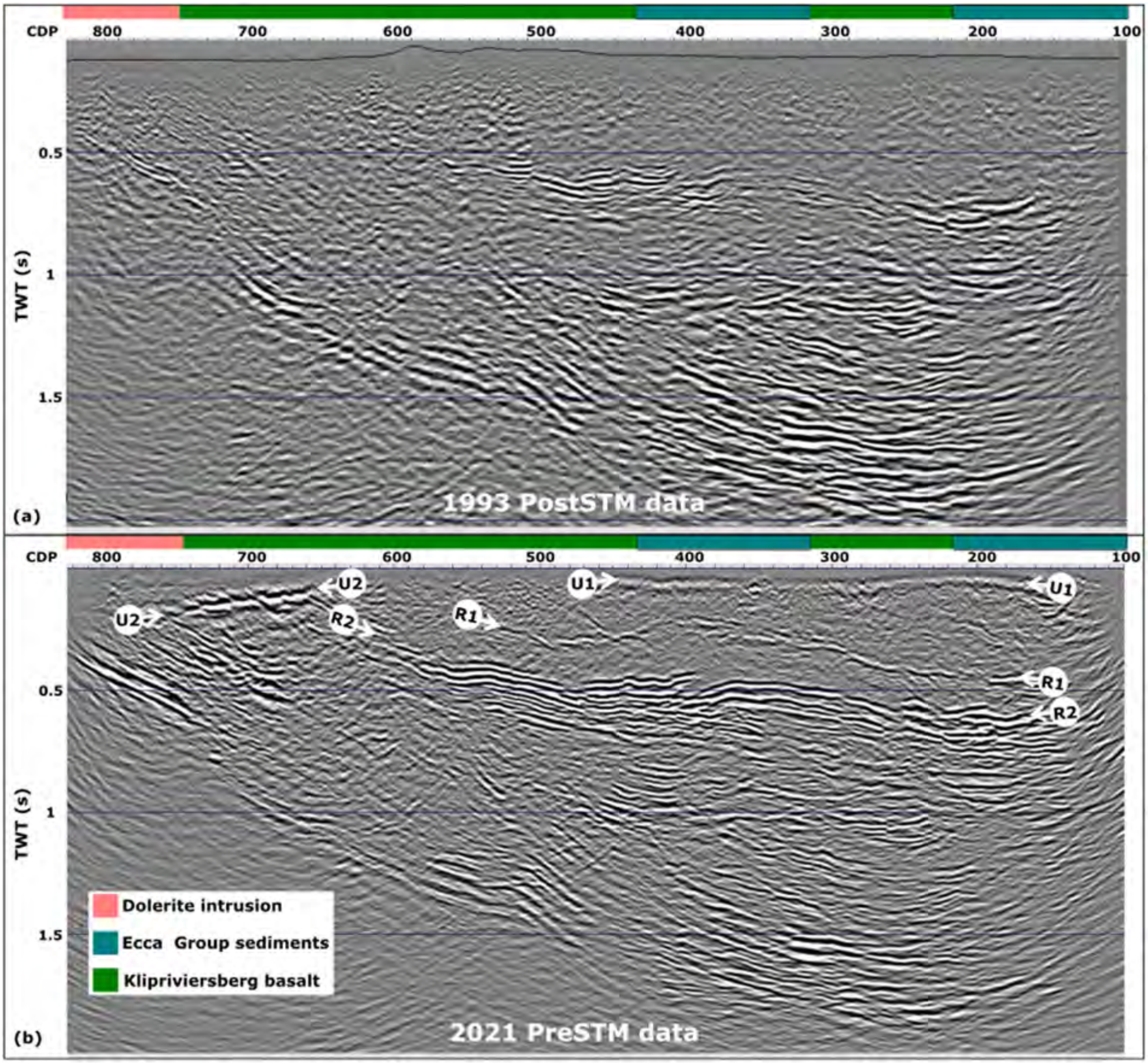

Figure 8 Comparison between 1993 legacy PostSTM data (a) and the 2021 reprocessed PreSTM data (b), with the main lithological contacts: Karoo sediments-Ventersdorp basaltic lavas (U1), dolerite sill (U2), Ventersdorp basaltic lavas – Central Rand Group quartzites (R1) and Central Rand Group quartzites – top of MK1 (R2), and the geological outcrop along the profile.

densities (~2.10 g/cm^3) and the underlying Ventersdorp basaltic lavas with high velocities (~6400 m/s) and densities (~2.90 g/cm^3) (Westgate et al., 2020). The contact between the Ventersdorp basaltic lavas and the underlying Central Rand Group quartzite with relatively lower velocities (~5400 m/s) and densities (~2.67 g/cm^3) also exhibit a significant acoustic impedance contrast (Manzi et al., 2015). MK1 (R2 reflector) is imaged as a strong reflector due to its relatively high densities (~3.01 g/cm^3) and velocities (~5800 m/s) as compared to quartzites (Manzi et al., 2015). The thin gold orebody (UK9A) overlying the MK1 is seismically transparent because it is embedded between quartzite and conglomerates with similar physical properties. However, for mining purposes, its orebody model can be derived from its closest overlying R1 and underlying R2 reflections.

Previous publications and recorded exploration drilled cores show the thickness of the Witwatersrand Supergroup to be approximately 5 km (Manzi et al., 2015). The thickness of the layers associated with the Witwatersrand Supergroup package on the reprocessed 2021 pre-stack depth migration (PreSDM) data has a thickness of ~4.5 km, which corresponds to the expected thickness of the supergroup. The borehole

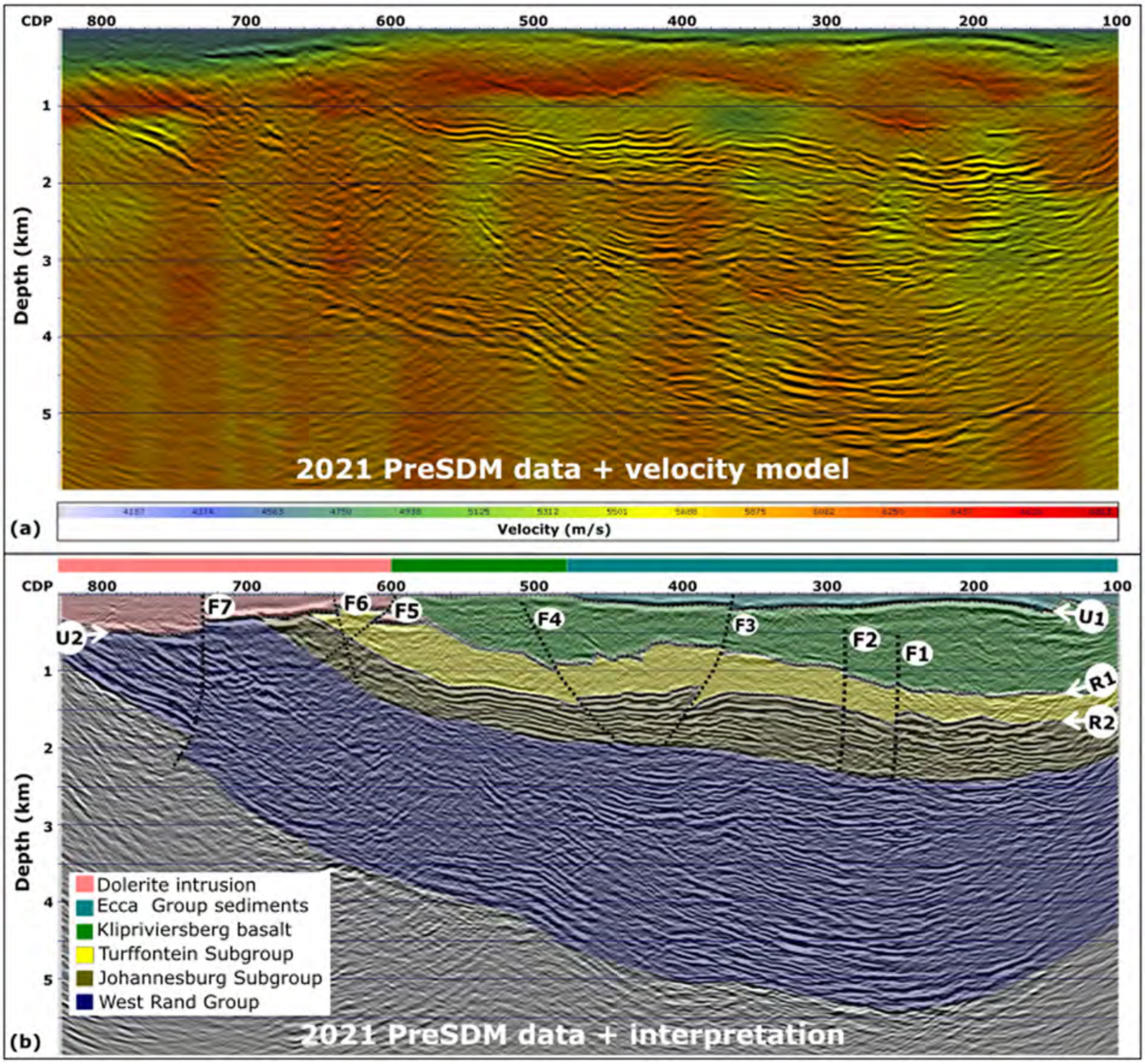

Figure 9 The reprocessed PreSDM section with the velocity model overlain (a) and the final interpreted section (b).

(SD1) information published by Antrobus (1986) intersected the reflector R1 at a depth of 1042 m, which corresponds to the observed position of the reflection on the PreSDM data. Reflector R2 is associated with the shales underlying the gold-bearing orebody (UK9A) intersected by a borehole (SD1) approximately 750 m below R1. The underlying reflections are interpreted to be associated with the West Rand Group strata. The West Rand Group strata are not interpreted in detail as there is no published borehole information from this area.

The faulting (see, Fig. 9b) in the area clearly displaces the Turffontein Subgroup strata as observed by the displacement on reflection R2. The publications from Pretorius (1964), Antrobus (1986) and Spencer (1992) on the structural geology of the study area had no conclusive results on the geometry of the faults in the study area. Fault F1 is interpreted in this study as a normal fault downthrown to the south, displacing reflection packages associated with shales with a near-vertical dip. Fault F3 (corresponding to Bergsig Fault in Fig. 1b) is interpreted as a reverse fault, downthrown to the north and is moderately dipping to the south. F3 displaces the reflection package associated with R2 and the overlying reflections R1 and U1. Fault F4 is a reverse fault, downthrown to the north and is dipping to the south. It displaces the strata associated with the R2 reflections and the overlying R1 reflections. Minor faulting (F2, F5 and F6) in the section is not conclusively interpreted as the reflections do not have clear vertical displacements.

The geological model documented by Antrobus (1986) (Fig. 3a) does not correspond to the interpretation model from the reprocessed 2021 PreSDM data (Fig. 9), with an exception of the southern edge of the data which resemble the same dipping nature as the 1986 model. The thin Karoo cover is observed to be continuous towards the south of the profile as shown by the well-defined unconformity (U1) (Fig. 9b). The reflectors R1 and R2 are seen to be near horizontal with a minor dip to the north. The major faulting documented in the 1986 geological model, Bergsig and Rooiwal faults (Fig. 3a), correspond to the imaged faults (F3 and F4) on the 2021 reprocessed PreSDM section (Fig. 9b).

CONCLUSIONS

We significantly improved the quality of the 1993 legacy seismic data through reprocessing using up-to-date processing algorithms and updated velocity models. Reprocessing using pre-stack depth migration, in particular, delivered improved imaging of shallow and deeper complex geological features such as multiple normal and reverse fault segments that bound orebody blocks. This high-resolution structural imaging may lead to the discovery of resources in faulted areas of the mining lease. In summary, reprocessing of the data has provided:

1. Unconformity (U1) at the base of the Karoo sediments, which is completely missed by the 1993 legacy seismic data.

2. Dolerite sill above the orebody (UK9A). The sill is mapped as a strong reflection, and its close proximity to the orebody could have a direct impact on mining in the region.

3. MK1 (R2) reflection, located a few hundred metres below the orebody (UK9A). The imaging of this shale unit is important because it can be used as a proxy to map the seismically transparent orebody, its dip variations and geological structures crosscutting it.

4. Unconformity (R1) at the base of the Ventersdorp Supergroup, located hundreds of metres above the orebody, could assist in depth positioning the orebody. Similar to R2, this R1 could be used to derive the structural model of the orebody.

5. Geological structures (mainly faults) beneath the Karoo sediments that crosscut and displace the orebody. The delineation of these faults is important for both mine safety and planning. These faults can be associated with a series of smaller faults that are likely to cause poor ground conditions during mining. These faults (in the case of normal faulting) can also bring the orebody to mineable depths, thus enhancing the resource evaluation.

ACKNOWLEDGEMENTS

We are thankful for the financial support from DST-NRF CIMERA and Wits Seismic Research Centre. We appreciate the sponsorship of Globe Claritas seismic processing licences by HiSeis Pty Ltd and the academic MATLAB license through the University of the Witwatersrand. Tesseral Technologies is acknowledged for sponsoring the licences for Tesseral seismic modelling software. We gratefully acknowledge Sibanye Stillwater for the donation of the legacy 2D seismic data that were used in this study. Finally, we would like to thank the Associate Editor and two anonymous reviewers for providing constructive criticism in their reviews, which improved the quality of this manuscript.

DATA AVAILABILITY STATEMENT

The data that support the findings of this study are available from the corresponding author upon reasonable request.

ORCID

Mpofana Sihoyiya https://orcid.org/0000-0003-1956-5223
Musa S.D. Manzi https://orcid.org/0000-0002-1654-5211
Ian James https://orcid.org/0000-0002-1655-3529
Moyagabo K. Rapetsoa https://orcid.org/0000-0003-3275-8994

REFERENCES

Ahmadi, O., Koyi, H., Juhlin, C. and Gessner, K. (2016) Seismic signatures of complex geological structures in the Cue-Weld Range area, Murchison domain, Yilgarn Craton, Western Australia. *Tectonophysics*, 689, 56–66. https://doi.org/10.1016/j.tecto.2016.02.020

Antrobus, E.S.A. (1986) The South Rand goldfield. In: Anhaeusser, C.R. and Maske, S. (Eds.) *Mineral deposits of Southern Africa*, vol. 1. Johannesburg: Geological Society of South Africa, pp. 689–703.

Buske, S., Gutjahr, S. and Sick, C. (2009) Fresnel volume migration of single-component seismic data. *Geophysics*, 74(6), WC47–WC55. https://doi.org/10.1190/1.3223187

Bradford, J.H., Liberty, L.M., Lyle, M.W., Clement, W.P. and Hess, S. (2006) Imaging complex structure in shallow seismic-reflection data using prestack depth migration. *Geophysics*, 71, (6), B175–B181. https://doi.org/10.1190/1.2335659

Coward, M.P., Spencer, R.M. and Spencer, C.E. (1995) Development of the Witwatersrand Basin, South Africa. *Geo-*

logical Society, London, Special Publications, 95(1), 243–269. https://doi.org/10.1144/GSL.SP.1995.095.01.15

Dankert, B.T. and Hein, K.A.A. (2010) Evaluating the structural character and tectonic history of the Witwatersrand Basin. *Precambrian Research*, 177(1–2), 1–22. https://doi.org/10.1016/j.precamres.2009.10.007

Durrheim, R.J. (1986) Recent reflection seismic developments in the Witwatersrand Basin. In: M. Barazangi and L. Brown (Eds.). *Geodynamics Series*, Vol. 13. Washington, DC: American Geophysical Union, 77–83. https://doi.org/10.1029/GD013p0077

Frimmel, H.E. (2019) The Witwatersrand basin and its gold deposits. In: Kroner, A. and A. Hofmann (Eds.) *The Archean Geology of the Kaapvaal Craton, South Africa*. https://doi.org/10.1007/978-3-319-78652-0_10

Frimmel, H.E. and Nwaila, G.T. (2020) Chapter 31 geologic evidence of syngenetic gold in the Witwatersrand goldfields, South Africa. In: Sillitoe, R.H., R. J. Goldfarb, F. Robert and S.F. Simmons (Eds.). *Geology of the world's major gold deposits and provinces*, vol 23. Littleton, CO: Society of Economic Geologist. https://doi.org/10.5382/SP.23.31

Hu, C. and Stoffa, P.L. (2009) Slowness-driven gaussian-beam prestack depth migration for low-fold seismic data. *Geophysics*, 74(6), WCA35–WCA45. https://doi.org/10.1190/1.3250268

Malehmir, A., Donoso, G., Markovic, M., Maries, G., Dynesius, L., Brodic, B., et al. (2019) Smart Exploration: from legacy data to state-of-the-art data acquisition and imaging. *First Break*, 37(8), 71–74. https://doi.org/10.3997/1365-2397.n0049

Manzi, M.S.D., Cooper, G.R.J., Malehmir, A., Durrheim, R.J. and Nkosi, Z. (2015) Integrated interpretation of 3D seismic data to enhance the detection of the gold-bearing reef: Mponeng Gold mine, Witwatersrand Basin (South Africa). *Geophysical Prospecting*, 63(4), 881–902. https://doi.org/10.1111/1365-2478.12273

Manzi, M.S.D., Durrheim, R.J., Hein, K.A.A. and King, N. (2012b) 3D edge detection seismic attributes used to map potential conduits for water and methane in deep gold mines in the Witwatersrand basin, South Africa. *Geophysics*, 77, WC133–WC147. https://doi.org/10.1190/geo2012-0135.1

Manzi, M.S.D., Malehmir, A. and Durrheim, R.J. (2018) 3D reflection seismics for deep platinum exploration in the Bushveld complex, South Africa. *2nd Conference on Geophysics for Mineral Exploration and Mining*, 1–5. https://doi.org/10.3997/2214-4609.201802751

Manzi, M.S.D., Malehmir, A. and Durrheim, R.J. (2019) Giving the legacy seismic data the attention they deserve. *First Break*, 37(8), 89–96. https://doi.org/10.3997/1365-2397.n0050

Manzi, M.S.D., Gibson, M.A.S., Hein, K.A.A., King, N. and Durrheim, R.J. (2012a) Application of 3D seismic techniques to evaluate ore resources in the West Wits Line goldfield and portions of the West Rand goldfield, South Africa. *Geophysics*, 77(5), WC163–WC171. https://doi.org/10.1190/geo2012-0133.1

Manzi, M.S.D., Hein, K.A.A., King, N. and Durrheim, R.J. (2013) Neoarchaean tectonic history of the Witwatersrand Basin and Ventersdorp Supergroup: New constraints from high-resolution 3D seismic reflection data. *Tectonophysics*, 590, 94–105. https://doi.org/10.1016/j.tecto.2013.01.014

Pretorius, C.C., Muller, M.R., Larroque, M. and Wilkins, C. (2003) A review of 16 years of hardrock seismics on the Kaapvaal Craton, Hardrock Seismic Exploration. In: Eaton, D., Salisbury, M. and Milkereit, B. (Eds) *Developments in Geophysics Series*. Houston: SEG, pp. 247–268. https://doi.org/10.1190/1.9781560802396.ch16

Pretorius, D.A. (1964) The geology of the South Rand Goldfield. In: Haughton, S.H. (Ed.) *The Geology of Some Ore Deposits in Southern Africa*. Johannesburg: Geological Society of South Africa, pp. 219–282.

Spencer, R.M. (1992) Late Archaean tectonics and sedimentation of the South Rand Area, Witwatersrand Basin. PhD Thesis, University of the Witwatersrand, Johannesburg.

Storch, I., Buske, S. Victor, P. and Oncken, O. (2021) Seismic images of the Northern Chilean subduction zone at $19^{0}45$'S, prior to the 2014 Iquique earthquake. *Geophysical Journal International*, 225(2), 1048–1061. https://doi.org/10.1093/gji/ggab035

Tucker, R.F., Viljoen, R.P. and Viljoen, M.J. (2016) A review of the Witwatersrand Basin: the world's greatest goldfield. *Episodes*, 39, 104–133. https://doi.org/10.18814/epiiugs/2016/v39i2/95771

Van der Heever, D., Oelofse, J. and Bentle, P. (2009) Revised technical report update of the June 21, 2007, Technical Report (Optimized Feasibility Study), inclusive of updated. Mineral resource and reserve estimates for the Burnstone gold project. Unpublished Company Report to Great Basin Gold Limited.

Westgate, M., Manzi, M.S.D., James, I. and Harrison, W. (2020) New insights from legacy seismic data: reprocessing of legacy 2D seismic data for imaging of iron-oxide mineralization near Sishen Mine, South Africa. *Geophysical Prospecting*, 68(7), 2119–2140. https://doi.org/10.1111/1365-2478.12996

water

MDPI

Article

Groundwater Circulation in the Shallow Crystalline Aquifer of Tharisa Mine, South Africa: Evidence from Environmental Isotopes and Near-Surface Geophysics

Jureya Dildar *, Musa Siphiwe Doctor Manzi, Tamiru Abiye, Sikelela Gomo, Moyagabo Kenneth Rapetsoa and Gillian Drennan

School of Geosciences, University of the Witwatersrand, Johannesburg 2050, South Africa; musa.manzi@wits.ac.za (M.S.D.M.); tamiru.abiye@wits.ac.za (T.A.); 1488846@students.wits.ac.za (S.G.); 867109@students.wits.ac.za (M.K.R.); gillian.drennan@wits.ac.za (G.D.)

* Correspondence: 1442390@students.wits.ac.za

Abstract: For underground mining, efficient groundwater management is one of the critical mining economics components. The region of interest, known as Tharisa Mine, is situated on the western limb of the Bushveld Igneous Complex, which is home to South Africa's premier platinum-group metal resources. This work aimed to provide the findings from the investigation and imaging of the near-subsurface hydrogeological architecture in a shallow profile using stable isotopes of water (^{18}O and ^{2}H) and radioactive water isotopes (^{3}H). Regarding isotope data, ^{18}O varied from −3.5 to 1.5‰; ^{2}H from −24 to 4.7‰; and ^{3}H from 2.0 to 3.4 T.U. Utilizing combined geophysical techniques, the results were verified. Additionally, the geophysical methods, including seismic refraction tomography, multichannel analysis of surface waves, electrical resistivity tomography, and magnetics, helped identify the fluid's pathways and lineaments during migration to verify the isotope results. The groundwater inflow volumes into the open pit were initially determined by integrating the following findings: the delineation of fracture systems/zones and fluid migration pathways; mining activities enhance the storage and transmission ability of the aquifer; and the main sources of water in the mine include mixing of surface and deep water sources, recycling of water possibly via lineaments, and tailings dam seepages.

Keywords: groundwater; environmental isotopes; geophysical methods; fluid migration; active mine

check for updates

Citation: Dildar, J.; Manzi, M.S.D.; Abiye, T.; Gomo, S.; Rapetsoa, M.K.; Drennan, G. Groundwater Circulation in the Shallow Crystalline Aquifer of Tharisa Mine, South Africa: Evidence from Environmental Isotopes and Near-Surface Geophysics. *Water* **2023**, *15*, 2876. https://doi.org/10.3390/w15162876

Academic Editor: Yeshuang Xu

Received: 25 June 2023
Revised: 1 August 2023
Accepted: 3 August 2023
Published: 9 August 2023

1. Introduction

Effective groundwater management is one of the most problematic parts of mining economics. A thorough understanding of groundwater flow dynamics is essential for a mining operation to be profitable [1]. Large land tracts are disturbed by mining activities, exposing additional eroded material. For hard-rock mining sites, especially open pit regions, waste rock dumps, tailings dams, and exploration areas, subsequent erosion of this material is a serious problem [2]. This is because sediments are chemically contaminated as a result of eroded material. Groundwater and surface water effects are caused by chemically contaminated sediments, especially those that contain heavy metals [2]. This includes acidification of the pH or metal loading in surface runoff due to the mobilization of heavy metals infiltrating the nearby subsurface or surface waters [2]. Flooding and structural damage are two examples of the physical effects connected to higher runoff volumes and velocities caused by disruption from mining activities [2]. Waste rock dumps and wet tailings impoundments negatively affect the water quality as surface waterways and the groundwater underneath these facilities are also impacted [3]. The groundwater may subsequently be contaminated by the leaching of harmful materials from these operations [3]. Groundwater enters an open pit when it is in contact with the water table. To facilitate the recovery of the ore when the mine is in operation, mine water must be continuously withdrawn from the mine [3]. The accompanying groundwater decrease may also impact surface water quality and flow rates.

Furthermore, the pumped groundwater's return to surface waters downstream from the dewatered area may impact the water's quality or quantity [3]. Because of this, effective mine water management design, which is both economically and ecologically sustainable, may minimize ineffective and expensive dewatering strategies with a complete understanding of the mine's groundwater storage and flow direction [4]. Studies [5–7] have considered and reported impacts related to the author's findings.

In previous hydrogeological studies, the physicochemical characteristics of groundwater were used to comprehend the hydrogeochemistry of water and the variables that affect ion concentration in aquifers [8–12]. Ref. [8] made the argument that hydrogeochemistry can be used to pinpoint the source of ion concentration in groundwater. Rock weathering and evaporation are responsible for determining the ion concentration of primary hydrochemical facies, according to [10]. To determine the main hydrogeochemical processes (silicate and carbonate weathering, ion exchange processes, and dissolution processes) responsible for groundwater chemistry and specify the groundwater quality parameters, [11] employed hydrogeochemical modeling. Ref. [12] investigated the silicate and carbonate weathering, evaporation, dissolution, and ion exchange in groundwater as well as its quality, origin, and chemistry. To define groundwater quality, origin, evolution, and aquifer chemical processes, the research mentioned above confirmed the use of hydrogeochemistry. Due to the complexity of groundwater flow, conventional hydrological methods and flow models are typically unable to characterize groundwater flow in open pit mining circumstances [13]. Hydrogeological approaches such as hydrogeochemistry must thus be used.

Groundwater evaluation requires geophysical investigations because they offer spatially broad, non-invasive, non-destructive subsurface investigative techniques that may address groundwater potentiality. Groundwater and vadose zone hydrology are the key fields where geophysical techniques have been used to map geological structures, define aquifer borders, and map fracture zones. These techniques are regarded as the most effective and appropriate for groundwater prospecting [14–17] and have been utilized often for mapping aquifer geometry. The techniques have been extensively applied in groundwater-related research in arid and semiarid locations, such as in the estimation and monitoring of groundwater levels [18,19], general groundwater exploration [15,20,21], and groundwater potential assessment [22]. Geophysics has also been employed extensively to characterize the groundwater–surface water interaction, as shown in several case studies [23–26]. However, only a small number of studies simultaneously combined geophysical and isotopicinvestigations.

Geophysical techniques have significantly advanced over the past few decades for near-surface and hydrogeophysical applications [23,27]. While seismic methods are infrequently used to discover and enhance groundwater resources, electrical resistivity methods are widely acknowledged for characterizing aquifers and groundwater salinity. This may result from the high prices, ambiguous outcomes, and challenging interpretive issues. The use of S- and/or P-wave seismic reflections in northern Germany, Denmark, and Canada has been extensively studied and presented in studies [28–30], as well as in studies [31–34], which incorporated airborne electromagnetic surveys with direct-push technology (DPT) and combined these two technologies with S- and/or P-wave seismic reflections.

In this work, groundwater pathways in the Tharisa Mine, one of South Africa's platinum mines, are characterized using combined hydrogeological and geophysical methods. The mine's main concern is determining the water infiltration in the region that has flooded the open pit. The mine intends to explore underground mining in the future. However, water leaking into underground mines/adits may obstruct mining operations in the future. The maximum predicted inflows are:

1. East Pit: 2698 m^3/day (31 L/s);
2. West Pit: 1432 m^3/day (17 L/s).

Sump pumping is a viable management method for the anticipated groundwater inflows because they are not regarded as large inflows. However, seepage water is what causes a problem during mining since it often forms undesirable ponds in the pit and does not quickly gather in the pit sump.

We sampled the water for hydrogeochemical and geophysical investigations to ascertain the connection between groundwater chemistry and the water source. The primary focus was to assess the groundwater's quality and environmental features, as well as its movement and water sources in the mining region. To conduct stable environmental isotopes (^{18}O and ^{2}H) and radioactive water isotopes (^{3}H), we collected water samples from the pit and monitoring boreholes. To further delineate the shallow (50 m deep) subsurface geological features and fluid migration pathways connected to the potential water source in the study area, the use of integrated geophysical methods, such as electrical resistivity tomography (ERT), multichannel analysis of surface waves (MASW), and ground magnetic surveys, was required. In the shallow aquifer, we examined and imaged the near-subsurface architecture (weathered and non-weathered zones and fluid migration channels).

Study Area

The Tharisa Mine is situated in the Marikana section of the Bushveld Igneous Complex (BIC) on its southwest limb (Figure 1). The Critical Zone's chromite packages (Figure 1a) are the major economic prospects of interest for Tharisa Mine [35]. The periodic layering of well-defined cumulus chromite and pyroxenites, olivine-rich rocks, and plagioclase-rich rocks (norites, anorthosites; Figure 1c) defines the Critical Zone [36–39]. The Critical Zone includes deposits for platinum-group metals (PGMs), which are significant economically (Figure 1c). There are up to fourteen identified chromitite layers in the Bushveld Complex, all of which are found in the Critical Zone [36–39]. From the base up, the next three chromitite cycles are significant [36–39]:

1. Lower Group (LG) Chromitite Layers;
2. Middle Group (MG) Chromitite Layers;
3. Upper Group (UG) Chromitite Layers [36–39].

These chromitite layers are notable because they have high concentrations of chromite and PGMs [40]. The Merensky and Bastard units are the topmost units in the Critical Zone [36–39]. Based on the latest occurrence of cumulus feldspar (between the UG and MG Chromitite Layers), the Critical Zone may be further separated into the Upper and Lower Critical Zones [36–39]. The MG and UG Chromitite Layers at Tharisa Mine are mined (Figure 1e).

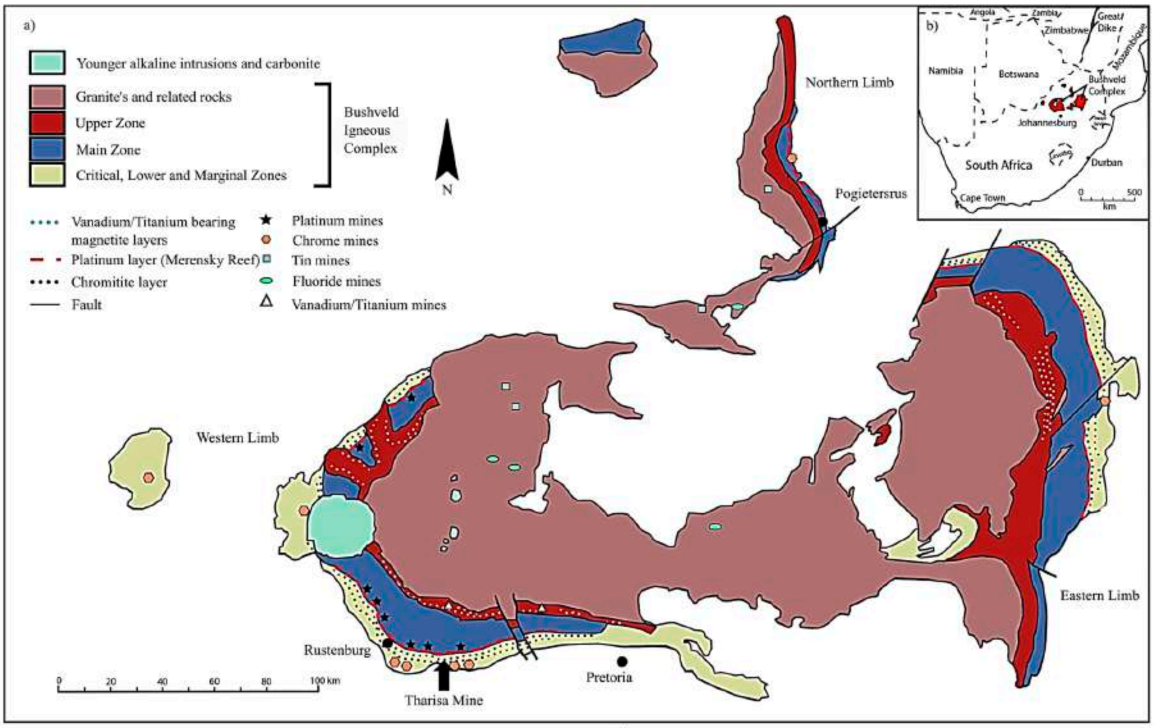

Figure 1. *Cont.*

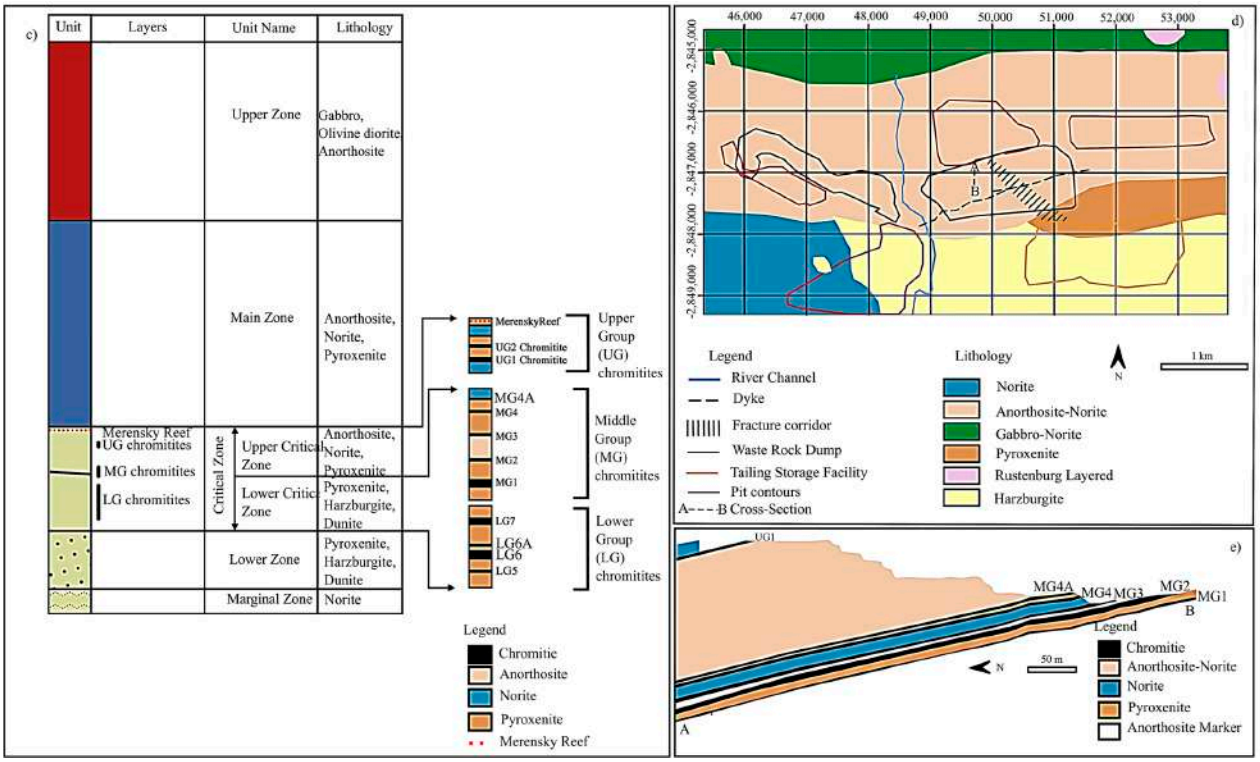

Figure 1. (**a**) Geological map illustrating the relations of the Tharisa Mine on the western limb of the Bushveld Igneous Complex, South Africa (modified from [41]). (**b**) Location of the Bushveld Igneous Complex in South Africa. (**c**) Generalized stratigraphic column of Rustenburg Layered Suite (RLS) (modified from [42]). The Tharisa Mine's main economic horizons are those of the Critical Zone's Middle Group (MG) Chromitite Layers: MG1, MG2, MG3, MG4, and MG4A. (**d**) Local geological map of Tharisa Mine with cross section A–B labeled. (**e**) Local geology of Tharisa summarized in a north–south cross section (A–B) showing the main horizons of economic interest. UG1 crops out further north of the Middle Group Chromitite Layers.

Intergranular and fractured crystalline systems are the different types of aquifers found in the Bushveld Igneous Complex. The intergranular aquifer of the Bushveld Igneous Complex is confined inside the weathered zone, which has a thickness that varies between 12 and 50 m [43]. The fractured and unweathered aquifer extends to depths where increased overburden pressure has sealed the fractures [43]. Under the weathered zone is where it is located. The groundwater flow between the shallow fractured aquifer and the deeper weathered aquifer is controlled by mining voids, fast vertical inflow, and coupled fracture networks [44]. Additionally, the shear zone and areas affected by regional tectonics are involved in this groundwater flow. The Rustenburg Layered Suite of the Bushveld Igneous Complex, which makes up the norites, anorthosites, and pyroxenites in the Tharisa mining region, is composed of:

1. Unweathered rock matrix with minimal porosity and permeability;
2. Rock matrix with discontinuity planes, including faults and joint planes (together referred to as fractures) [45].

The Tharisa aquifer system might initially be categorized as a shallow bedrock with intergranular porosity and permeability [45]. The norites, anorthosites, and pyroxenites underwent extensive in situ weathering, which led to the formation of the shallow unconfined to semi-confined water table aquifer [45]. It is regarded as a single weathered aquifer unit and includes the variably weathered and fractured bedrock underneath the regolith. The second option is a deeper bedrock aquifer system that is unweathered and cracked [45]. Norites, anorthosites, and pyroxenites with faults and fractures make up the unweathered bedrock aquifer [45]. It is considered that the complete bedrock matrix has a relatively low matrix permeability, but faults and mine voids increase the bedrock's effective permeability [45].

To avoid any hydraulic interference with the hydraulic stress elements, such as open pits, waste rock dumps, tailings storage facilities, and boreholes, the preliminary hydrogeological model domain for the Tharisa Mine was chosen exclusively based on catchment areas and divided between the catchments [45]. The main river system at Tharisa Mine is the Sterkstroom River. The Sterkstroom River is a tributary of the Crocodile River (West) and is considered a perennial river with an average flow rate of less than 0.5 m/s. The Tharisa Mine site is divided between the East Pit and West Pit, which are situated on each side of the Sterkstroom River (Figures 1d and 2). The watercourse and the nearby infrastructure that runs parallel to the river are both protected by the pits.

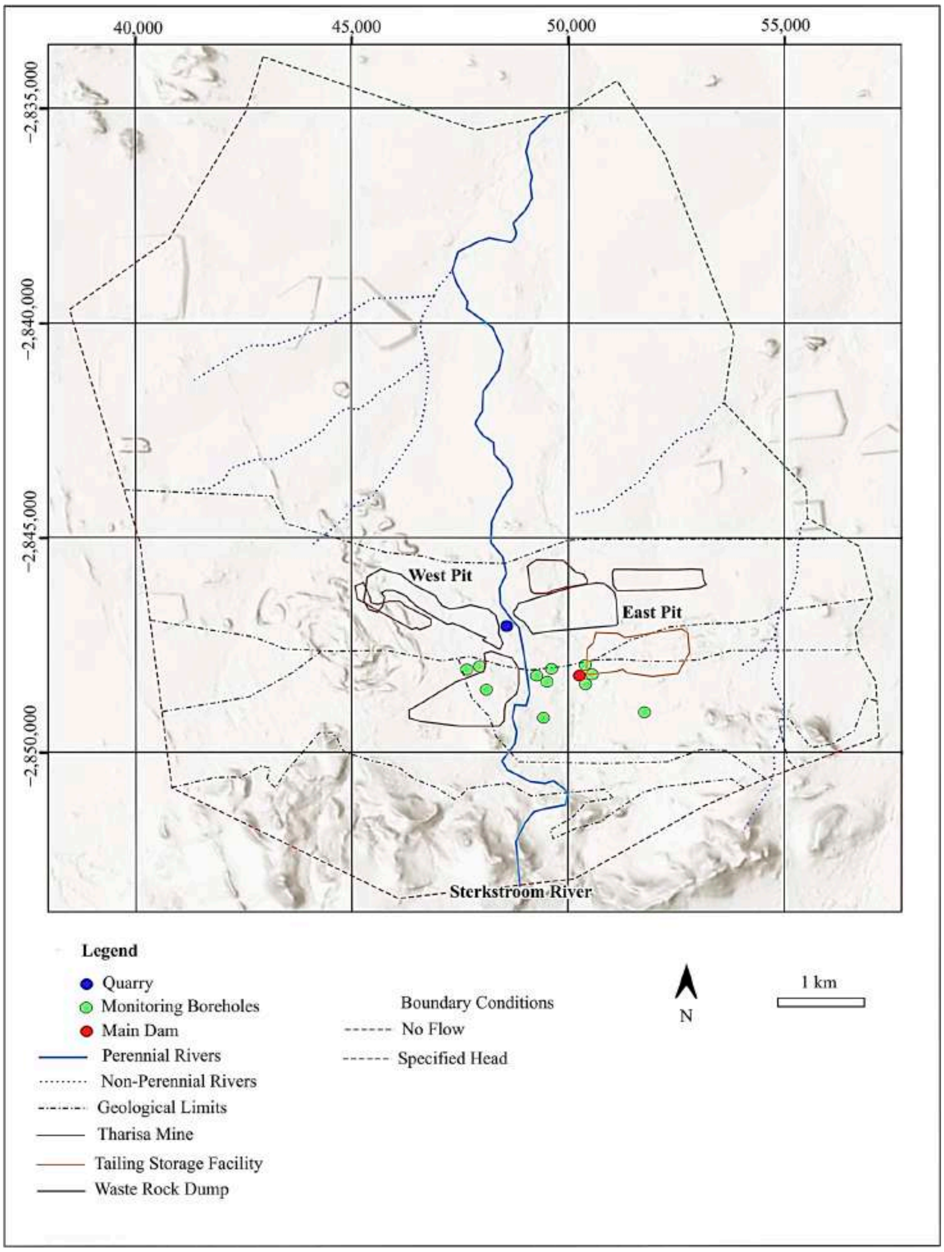

Figure 2. Preliminary Tharisa groundwater model illustrating the various boundary conditions.

Figure 2 depicts the model domain and the primary hydraulic stress components used by the groundwater model. The following are the boundaries established for the Tharisa groundwater model:

1. No-Flow Boundary: Along this portion of the model borders, there is no fluid exchange (into or out of the groundwater system). The no-flow boundary was chosen to be along the lines of high elevation that represent watershed boundaries on the southern and western edges of the model domain;
2. Specified Head Boundary: Fluid exchange happens both within and outside the model area, ensuring that the hydraulic head boundaries are kept at their initial values:
    a. External Boundary: along the low-elevation river on the eastern side and partially on the northern side of the model domain limits;
    b. Internal Boundary: established along the rivers that are a part of the model domain for the groundwater domain [45].

Based on drilling and aeromagnetic data, the current structural interpretation of the Tharisa Mine region is presented in [46]. In August 2007, an aeromagnetic survey was conducted over the Tharisa Mine region to map regional structures (Figure 3). The distance traveled was 900 km, with a line spacing of 100 m at 0 degrees (true north). Tie lines were set 500 m apart and parallel to the survey lines. The ground clearance was 40 m, and the sample spacing along the flight lines was 6.5 m. A steeply sloping NW–SE trending normal fault is the significant fault in the mining region. Only the extreme northeastern part of the land is affected by the fault. The main lineation on the aeromagnetic data is a low-angled WNW–ESE trending thrust fault. The aeromagnetic survey was used to interpret a NE–SW striking sub-vertical dyke with a thickness of around 10 m. In the far eastern pit, a NE–SW running sub-vertical shear zone was seen. In the aeromagnetic data, it is visible as a lineation. Around the shear, the thickness of the MG1 Chromitite Layer decreases. Aeromagnetic anomalies are considered to be the anorthosite and norite in the UG1 Chromitite Layer footwall and are located north of the MG Chromitite outcrops, following the strike's northwesterly flexion.

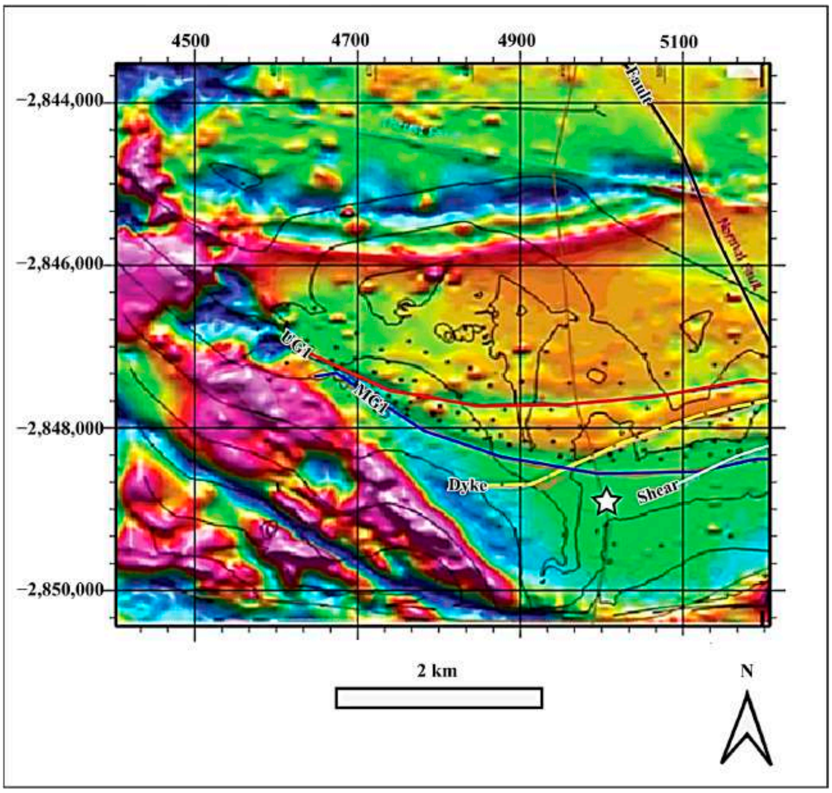

Figure 3. Interpreted aeromagnetic survey map [46]. The black line indicates a normal thrust fault. The Upper Group 1 (UG1) outcrop and Middle Group 1 (MG1) outcrop are represented by a red and blue line, respectively. The main dyke is shown by a yellow dashed line whilst the shear zone is defined as a white line. The white star indicates the location of Tharisa Mine. Magnetic high zones are indicated by the pink color sections, whilst, magnetic low zones are indicated by the dark blue color sections.

The region has a typical summer rainy climate with a mean annual precipitation of around 680 mm and evaporation of about 1800 mm yearly; summer rain is primarily thunderstorms [46]. In the summer, between November and January, the region often has a high S-pan evaporation rate [46]. There is a high relative humidity as a result. Additionally, more water evaporates because the ambient temperature is higher in the summer than in the winter [46].

Winds are light and come mostly from the northwest [46]. Dry and chilly winters prevail. Frost, which happens between two and twenty times a year, and rare hailstorms are examples of extreme meteorological conditions [46].

The average annual temperature for the year is roughly 19 °C, with average maximum temperatures ranging between 22 °C and 32 °C and average minimum temperatures ranging between 2 °C and 18 °C [46]. December through February has the most heat. Winter officially begins when the temperature falls in April and May [46]. June and July have the lowest temperatures [46].

2. Materials and Methods

2.1. Water Sampling Methods (Physicochemical Field Parameters): Electrical Conductivity, Total Dissolved Solids, pH, and Temperature

Since they directly detect the dissolved ionic matter in the water, electrical conductivity measurements are useful in aquatic investigations [3]. High values denote salinity and eutrophic issues, whereas low values indicate waters with high quality and low nutrient levels. If extremely high readings are noted, they can indicate potentially contaminated sites [3]. Water with a pH below 7 suggests an acidic solution, whereas water with a pH over 7 indicates an alkaline solution [3]. The bioavailability of heavy metals is another factor possibly influenced by pH [3].

The aforementioned field characteristics may be used in hydrogeological research to analyze subsurface water flow through strata or lineaments (e.g., groundwater intrusion) and show a potential relationship between water chemistry and preferential weathering [8–12]. Therefore, confirming groundwater circulation and quality can help shed light on the genesis of subsurface features and open the door to suggest several mitigating measures.

After calibration, physicochemical variables such as temperature, pH, electrical conductivity, and total dissolved solids were measured outdoors using a Crison MM40 Multiparameter Instrument (Figure 4). The process for the hydrogeological field sample parameters (Figure 4) is summarized in Table 1.

Table 1. Field sampling procedures.

Collection technique	A Crison MM 40 multimeter is used to take an in situ reading. Allow it to stabilize. Samples are to be stored in a cooler box to avoid fractionation.
Collection	A sample bottle is used as a means of direct collection of an unfiltered sample. Pre-rinse the sample bottle with sample water before the final collection.
Filling technique	The container is tightly capped to the brim to exclude air (air bubbles).
Analysis method	The electrode is stored in a KCl solution (electrolyte). Dip the electrode in deionized water and then into the beaker with the water to be measured. Let it stabilize before recording the data. Then, dip the electrode back into the deionized water before storing it in the KCl solution.

2.2. Environmental Isotopes of Water

Groundwater flow patterns are revealed by studying water isotopes. They are frequently used to conceptually map out a groundwater flow pattern, pinpoint recharge and discharge zones, and determine the mixing and salinization processes that occur in groundwater [47]. Hydrogen and oxygen isotope fractionation results from several hydrologic cycle events, including evaporation, condensation, recharge, mixing, and water–rock interaction [47]. As a result, the processes to which the water is subjected may be determined by methodically sampling the isotopic ratio of different water sources [48,49].

Figure 4. (**a**) An example of how the field sampling was carried out in the study area using the Crison Multimeter. (**b**) Tailings Storage Facility 1 (TSF 1) sample location (indicated by the white star). (**c**) Tailings Storage Facility 2 (TSF 2) sample location (indicated by the white star).

The water samples collected for environmental isotope analysis ($\delta^{18}O$, δ^2H, and ^3H) were used to understand the inter-relationship between water points, interconnection, water source, and mixing. Water samples were collected from different lithologies in the area for this task. All available monitoring wells were sampled for isotopes. All the samples were collected in one day (11 August 2021) and then submitted to the lab on the same day (18 August 2021).

2.2.1. $\delta^{18}O$ and δ^2H

Water samples were collected in 10 mL glass bottles with screw-top lids, washed with sample water before filling, ensuring there were no air bubbles, and properly labeled for measurement of the ^{18}O and ^2H values. While being transported to the lab, samples were placed in a cooler box to keep them from being exposed to light. The Liquid Water Isotope Analyzer model 45-EP was used at the University of the Witwatersrand in South Africa to analyze the stable isotopes of ^{18}O and ^2H. When testing liquid water samples with dissolved salt concentrations up to 1000 mg/L, the laser apparatus can deliver precise results with an accuracy of around 1‰ for ^2H and 0.2‰ for ^{18}O [50].

2.2.2. Tritium ^3H

Bottles with 500 mL volume with screw-top lids were used and washed with sample water before filling, ensuring there were no air bubbles. Each bottle was properly labeled as tritium for sampling. For examination, tritium samples were delivered to the iThemba Labs in Gauteng. A 0.2 T.U detection limit analyzer was used for the electrolytic enrichment technique of tritium analysis [50].

2.3. Electrical Resistivity Tomography (ERT)

Numerous ERT surveys with varying spread lengths (80–300 m) and electrode spacings (1–3 m) were conducted in the mine using the automated ABEM 1200 multielectrode resistivity unit, which is a multi-core cable system. The resistivity data were acquired by injecting direct current into the ground using a pair of current electrodes (A and B) and measuring the resulting potential difference using a second pair of electrodes (M and N) called potential electrodes. To reasonably map horizontal and vertical subsurface changes, the resistivity data were acquired using multiple array types, i.e., Wenner, Dipole–Dipole, and Schlumberger arrays. The collected data were manually de-spiked and then inverted in RES2DInv to obtain 2D resistivity inverse models using a least-squares regression. Gomo et al. (under review) further detail the ERT data acquisition.

Each geological material has a characteristic resistivity value enabling easy delineation of lithological boundaries [51–53]. Therefore, resistivity was a valuable method for this study as it allows for characterizing geological subsoil conductive anomalies using the spatial distribution of the underground electrical resistivity [53–55]. Furthermore, resistivity methods allow geological mapping of structures, groundwater flows, and fracturing by delineating respective geological boundaries and detecting zones of low resistivity associated with water saturation [51–55].

2.4. Multichannel Analysis of Surface Waves (MASW)

The MASW surveys were acquired using a standard MASW roll-along technique [53]. This entailed using a 24-channel seismic system with a 46 m profile length, 2 m spaced receivers (14 Hz, 1-component geophones), a 12 m source to the nearest receiver offset, and a roll-along shift of 2 m and 4 m at sites one and two, respectively. A 6 kg sledgehammer was used as an impact source, and an aluminium base plate was used to improve the seismic source–ground coupling. The data were acquired using five shot stacks, a sampling interval of 1 ms, and a recording length of 1000 ms. The MASW data processing involved converting the acquired data into the phase velocity–frequency domain, picking the fundamental mode to obtain a dispersion curve from the produced phase velocity–frequency spectrum, and inverting the dispersion curves to obtain a 1D shear wave (Vs) velocity profile at each shot location. The process was repeated for each shot location, and the obtained 1D Vs profiles were then integrated to obtain a 2D Vs section of the MASW profiles.

MASW is useful in imaging shear wave velocity structure, low-velocity zones, and fractures [51,53,56]. Moreover, it can map the shear wave velocity profile of an upper weathered aquifer and subsequent water table/saturated zone to a depth of about 15 m [51,53,56].

2.5. Seismics

Multiple profiles with varying lengths (46–96 m) and receiver/shot (1–2 m) spacings were collected with a combination of 14 Hz (1 component) geophones and a land streamer set up to accommodate the hard-rock environment in the mine. The seismic sources used included an accelerated weight drop (24 kg) and sledgehammer (6.3 kg) with an aluminium plate to improve the seismic source coupling. The data processing flow started with fixing and adding the geometry for all the seismic profiles and assigning the common depth points (CDP). The P-wave first breaks were manually picked on each profile for refraction statics and to generate a two-layered P-wave velocity model. Rapetsoa et al. (under review) further detail the seismic data acquisition.

Rock and structural qualities can be determined with the use of seismic studies. The subsurface's velocity and density structure can be detected using seismic techniques [27]. The field design is based on transmitting seismic signals from an energy source and measuring the signals at geophone receivers located at various distances [28,29,33]. When propagating through the earth's crust, P and S waves behave differently regarding the motion of the wave's constituent particles. Given the same frequency content, S waves' having shorter wavelength and slower propagation velocities than P-waves enables them to resolve tiny subsurface features more effectively [27–29,33]. The primary prerequisite for reflected seismic waves at a layer boundary is that the layers must have distinct impedance values calculated using the seismic velocity and density of the layers [27]. Porosity affects density and seismic velocity; both decrease as porosity rises [27]. As observed, velocities may correlate to physical qualities, compaction and saturation levels, and strength in the bedrock; this aids in discovering lithological and hydrological limits in the subsurface [52]. Reflection seismics is a common geophysical exploration method, particularly for applications in hydrogeology and the environment (such as determining aquifer depth or the water table) [57–60].

2.6. Magnetics

Two G856 proton precession magnetometers were used as base stations to acquire the ground magnetic data. A G859 cesium vapor magnetometer was used as a rover to collect the data for a total area of 16,300 m^2. The collected data were then inspected and compared for spikes in the diurnal curve. The regional magnetic field was corrected for diurnal variations, despiked, and interpolated using the minimum curvature technique to produce a total magnetic intensity (TMI) map (further processing is given in Rapetsoa et al. (under review)). Finally, the vertical tilt angle filter was applied to enhance the edges of magnetic sources influencing the data. Rapetsoa et al. (under review) further detail the magnetic data acquisition and processing.

Each subsurface material displays a characteristic magnetic signature [61]. Metal materials within the substrate contain an induced field of force superimposed on the Earth's magnetic field at that location, creating a magnetic anomaly [62]. The location of these magnetic anomalies allows for the analysis of regional geological trends or mineralization (e.g., may indicate the presence of dykes) [63]. This also allows for delineating subsurface features such as faults or intrusive features. Figure 5 demonstrates the location of the respective geophysical profiles used in this study at the sampling points.

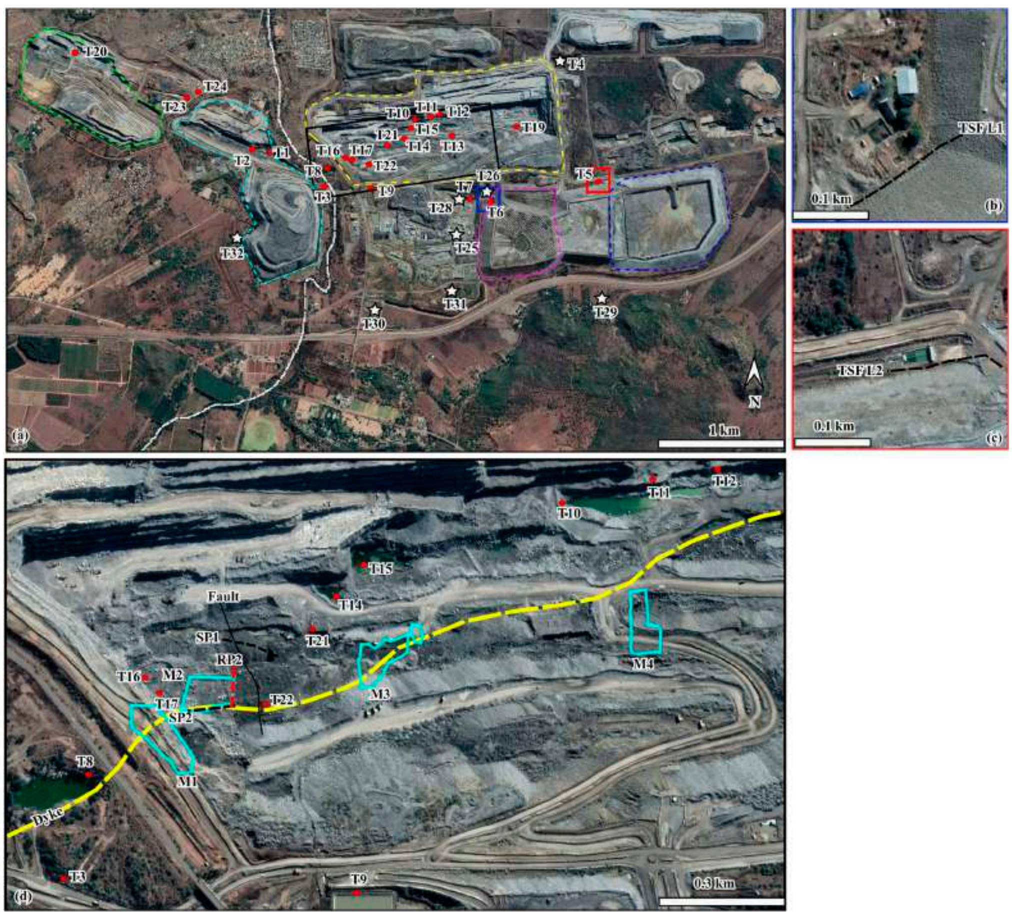

Figure 5. (**a**) Locality map of the study area with in situ field sampling locations. Red dots are sampled surface water; white stars are sampled boreholes. A green dashed line indicates Far West Pit;

West Pit indicated by a light-blue dashed line; East Pit by a yellow dashed line; Tailings Storage Facility 1 (TSF 1) by a pink dashed line; and Tailings Storage Facility 2 (TSF 2) by the dark-blue dashed line. The white dashed line represents the river separating the East and West Pits. (**b**) Tailings Storage Facility 1 is represented by the dark-blue square, and the survey position of Tailings Storage Facility Line 1 (TSF L1) is indicated by a black dashed line. Electrical resistivity tomography (ERT) and multichannel analysis of surface waves (MASW) were conducted along this line. (**c**) Tailings Storage Facility 2 is represented by the red square, and the survey position of Tailings Storage Facility Line 2 (TSF L2) is indicated by a black dashed line. Along this line, both electrical resistivity tomography (ERT) and multichannel analysis of surface waves (MASW) were conducted. (**d**) Main East Pit surveyed area is indicated by the black square. Light-blue polygons indicate magnetic grids (M1, M2, M3, and M4). Seismic Profile 1 (SP1) and Seismic Profile 2 (SP2) are indicated by black dashes (note: Resistivity Profile 1 (RP1) is located along SP1). A red dashed line indicates Resistivity Profile 2 (RP2). The surveyed dyke is indicated by a yellow dashed line. A solid black line indicates a surveyed fault.

3. Results

3.1. Hydrogeological Results

Table 2 summarizes the physicochemical and isotope results. The overall pH of the mine water lay within the suitable range for healthy water: 6.5–8.5 [64]. However, this may be subject to change due to chemicals associated with human waste and mining activities.

Total dissolved solids (TDS) and electrical conductivity (EC) are two parameters that are closely related; both are indicators of salinity. Natural water has a TDS value ranging from ~0.1 to ~528,000 mg·L^{-1} and EC values of 500 to 3000 μS·cm^{-1} [65]. The average TDS value and EC measured in the mine site were 785.4 mg·L^{-1} and 1225.1 μS·cm^{-1}, respectively. This suggests the majority of mine samples were saline.

There was evidence of mixing in certain samples, as shown in Figure 6a–c, which shows decreasing ^{18}O, ^{2}H, and tritium with increasing salinity (TDS). Salinity may result from mixing fresh water that has been isotopically enhanced with water depleted of isotopes, which has a greater salinity [66]. This indicates that most of these liquids were likely connate waters mixing with meteoric water from the contemporary hydrological cycle. In addition to mixing, the dispersion of the points on the plots of TDS vs. ^{18}O, ^{2}H, and tritium (Figure 6a–c) may also indicate that the samples were affected by water–rock interaction processes such as leaching, dissolution, and precipitation, to mention a few [66].

The plot of δ^{18}O vs. EC (Figure 6d) was used to establish the degree of mineralization, i.e., whether the salinization was due to evaporation (high EC), causing enriched δ^{18}O. Due to evaporation, the heavy isotopes are enriched in surface waters. Low EC values may depend on the recharging rainfall (e.g., T3). Due to variations in seasonal recharge, high EC water contains a depleted δ^{18}O value (e.g., T4). As the depth of the water table increases, limited external processes affect the isotope signature. Only water–rock interaction via fractures/migration pathways affect water at depth and therefore display a high EC value (possibly due to mixing). Groundwater undergoing evaporation positively correlates with δ^{18}O and conductivity (e.g., T6, T7, and T29).

In the diagram of δ^{18}O vs. EC (Figure 6d), it can be observed that a negative correlation was obtained with R^2 = 0.005; furthermore, in most samples, an increase in electrical conductivity (EC) values took place without a significant change in isotopic composition, which may be due to mineralization. Few of the groundwater samples and all the surface water samples showed an enrichment of the heavier isotopes without a simultaneous increase in EC; this confirms that some of the groundwater was recharged by evaporated (isotopically enriched) water on the surface or in the unsaturated zone.

This indicates the possibility of repumping, as the water is observed in the pit. The water is pumped via pumps used for dewatering and enters the river. The fault and dyke that run through the pit may bring the water back into the pit. This may be further justified by the high flow rate (~1 L/min) observed at the interaction point of the dyke and fault along the northern East Pit face (T22, Figure 7). A high flow rate is concerning/unlikely in an arid area with a mean annual rainfall of ~680 mm/year, which cannot recharge an area with such a rate. The suggested reasoning is thus that water is being repumped back into the subsurface. The river water sample (T3), on the other hand, was different from that from the mine. Evidence for this is shown at point T3 in Figure 6d; it displayed a depleted EC and $\delta^{18}O$. This suggests that the water sampled was rainwater (as it was more enriched in lighter/depleted isotopes).

Table 2. Physiochemical and isotope parameters.

Description	X	Y	Sample	pH	Temperature (°C)	TDS (mg/L)	EC (µS/cm)	δ^2H (‰)	δ^{18}O (‰)	^{3}H (T.U)
River	−48,920.47	2,847,915.65	T3	6.8	13.3	179.4	283	−18	−3.37	1.8
Dissipator Dam 2	-52,223.74	2,846,645.34	T5	7.5	16.4	886	1379	−5.4	−1.12	2.5
Dissipator Dam 1	−50,657.04	2,846,434.29	T6	7.5	15.1	589	915	0.5	0.58	0.3
Main Dam	−50,470.18	2,848,066.6	T7	8.1	16.5	755	1193	4.7	1.5	3.4
Stormwater Dam	−49,453.15	2,847,951.97	T9	7.6	15.9	812	1268	−8.1	−1.41	1.0
West Pit (Dyke)	−48,426.07	2,847,589.44	T1	6.2	14.5	390	609	−16.6	−3.15	0.3
West Pit	−48,261.84	2,847,524.26	T2	6.4	15.7	556	873	−16.8	−3.2	1.6
East Pit	−50,026.53	2,847,308.23	T10	7.4	19.3	949	1480	−13.8	−2.66	2.2
East Pit	−50,023.6	2,847,287.17	T11	7.2	19.2	941	1474	−17.2	−3.37	2.0
East Pit	−50,146.09	2,847,268.8	T12	7.4	20.8	946	1475	−17.1	−3.41	1.6
East Pit	−50,171.71	2,847,392.87	T13	8	18.3	798	1248	−7.6	−1.75	3.2
Est Pit	−49,773.92	2,847,504.48	T14	7.7	18.7	886	1383	−12.8	−2.42	2.9
East Pit	−49,914.75	2,847,413.06	T15	7.8	19.2	848	1323	−11.5	−2.26	1.8
East Pit (Dyke)	−49,184.37	2,847,564.54	T16	8.1	18	784	1222	−14.5	−2.74	2.0
East Pit (Dyke)	−49,240.63	2,847,627.68	T17	7.7	20.1	799	1247	−12.7	−2.42	1.7
East Pit (Dyke)	−49,211.54	2,847,624.25	T18	7.9	20.6	800	1247	−11	−2.11	2.2
East Pit	−50,687.21	2,847,441.03	T19	8.2	16.7	806	1260	−11.4	−2.4	2.3
Far West Pit	−46,531.23	2,846,628.66	T20	7.3	12.8	609	950	−22.8	−4.63	1.4
East Pit	−49,524.01	2,847,516.84	T21	7.5	13.5	872	1366	−10.3	−1.98	2.1
East Pit	−49,424.98	2,847,702.59	T22	7.36	22.3	947	1295	−9.2	−2.15	2.1
Quarry	−48,941.16	2,847,746.22	T8	7.7	16.7	837	1303	−11.2	−1.92	1.0
Samancor Borehole	−52,223.74	2,846,645.34	T4	6.7	21.6	1450	2230	−18.8	−3.79	1.1
Monitoring Borehole (TM GW FW BH 24)	−47,662.66	2,846,946.1	T24	6.84	23.5	537	839	−24	−3.5	2.0
Monitoring Borehole (TM GW FW BH 25)	−48,480.54	2,847,484.17	T25	7.5	20.1	669	1046	−17.4	−3.77	2.1
Monitoring Borehole (TM GW Dissipater 1)	−50,603.6	2,848,077.08	T26	6.67	21.3	684	1067	−5.9	−0.17	1.1
Monitoring Borehole (TM GW Dissipater 2)	−50,591.71	2,848,037.15	T27	6.98	21.9	693	1082	−6.6	−0.83	1.5
Monitoring Borehole (TM GW RPM)	−50,431.98	2,848,085.29	T28	7.29	20.9	714	1115	−11.5	−1.83	1.5
Monitoring Borehole (TM GW COMM 02)	−51,747.65	2,849,061.98	T29	7.14	21.3	332	519	−0.8	0.61	1.9
Monitoring Borehole (TM GW COMM 01)	−49,472.5	2,849,217.25	T30	7.33	21.9	367	575	−15.9	−2.9	1.5
Monitoring Borehole (TM GW TSF 01)	−50,127.44	2,849,013.64	T31	7.32	21.3	344	536	−12.5	−2.04	1.3
Monitoring Borehole (TM GW COMM 06)	−48,075.45	2,848,504.16	T32	7.15	22.6	296	464	−11.8	−1.93	1.9

Multiple source interpretations are shown in the stable isotope map (Figure 8). Environmental stable isotope measurements for ^{2}H ranged from the most depleted value of −24‰ in a borehole that draws water from a deeper aquifer to 4.7‰ in surface water from a tailings dam, while values for ^{18}O ranged from −4.63‰ to 1.5‰. Surface water and seepage water are shown on a plot of the data against the Pretoria Local Meteoric Water Line (PLMWL), which also reveals a substantially enriched isotopic signal brought on by fractionation during evaporation. The shallow waters were more enriched than the deeper waters and may indicate a substantial mixture of surface waters with recent recharge infiltrating into relatively deep water systems in addition to possible water recycling. Isotopically depleted waters signified the third type of water, hence deeper water systems. However, borehole T20 (Far West Pit borehole) was particularly depleted isotopically, suggesting a different flow/aquifer system. There was also evidence of mixing in the tailings dam (e.g., T5 from TSF 2), and, consequently, tailings dam seepage, as a tailings sample (T6 from TSF 1) had a similar isotope signature to Monitoring Borehole T29 (TMGW COMM 02). Clustering the stable isotope data revealed a similarity in the water source that may not have occurred simultaneously.

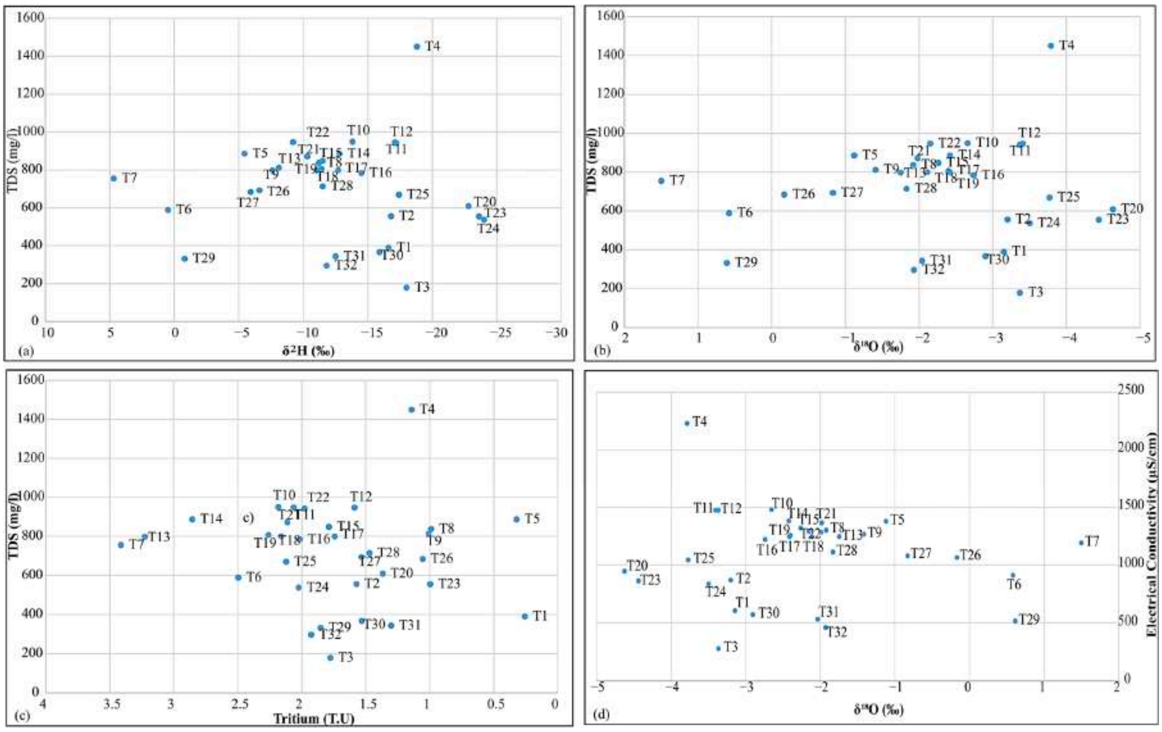

Figure 6. (**a**) Total dissolved solids (TDS; mg/L) vs. δ^{2}H (‰) for all Tharisa Mine samples with R^2 = 0.0011. (**b**) Total dissolved solids (TDS; mg/L) vs. δ18O (‰) for all Tharisa Mine samples with R^2 = 0.0057. (**c**) Total dissolved solids (TDS; mg/L) vs. ^{3}H (T.U) for all Tharisa Mine samples with R^2 = 0.0091. (**d**) Electrical conductivity (µS/cm) vs. δ^{18}O (‰) for all Tharisa Mine samples. A negative correlation was obtained with R^2 = 0.005; furthermore, in most samples, an increase in electrical conductivity (EC) values occurred without many changes in isotopic (δ^{18}O) composition.

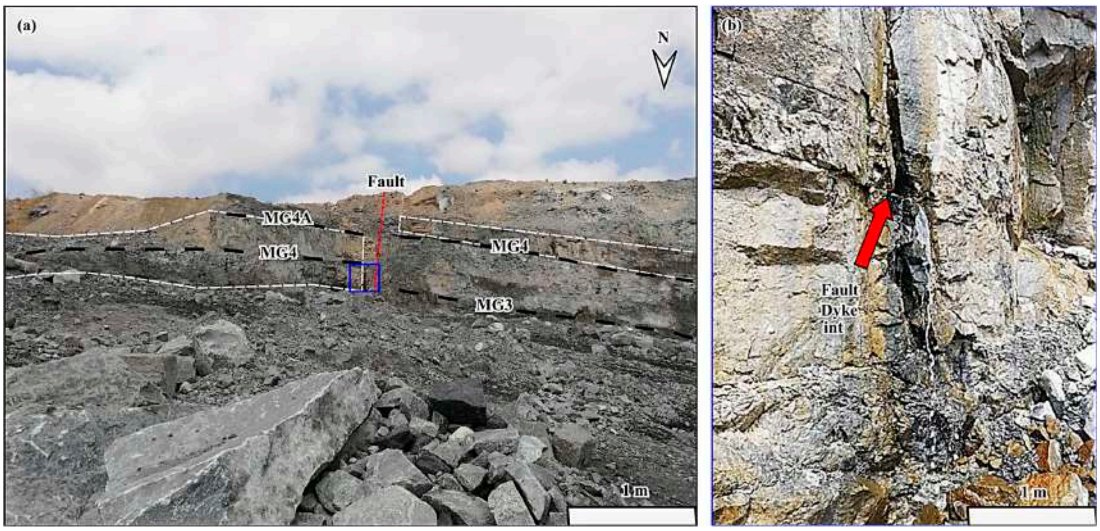

Figure 7. (**a**) East Pit northern wall face. The Fault Zone (indicated by the red dashed line) intersects with the E–W trending dyke (white dashed line). Example of Middle Group (MG) chromitite reefs (MG3, MG4, and MG4A) indicated by black dashed line. Chromitite reefs are young towards the south. (**b**) Fault–dyke intersection zone (Fault Dyke int) is indicated by the blue square in (**a**). A high flow rate (~1 L/min) was observed at the northern East Pit wall face (sampled point T22—East Pit surface water sample).

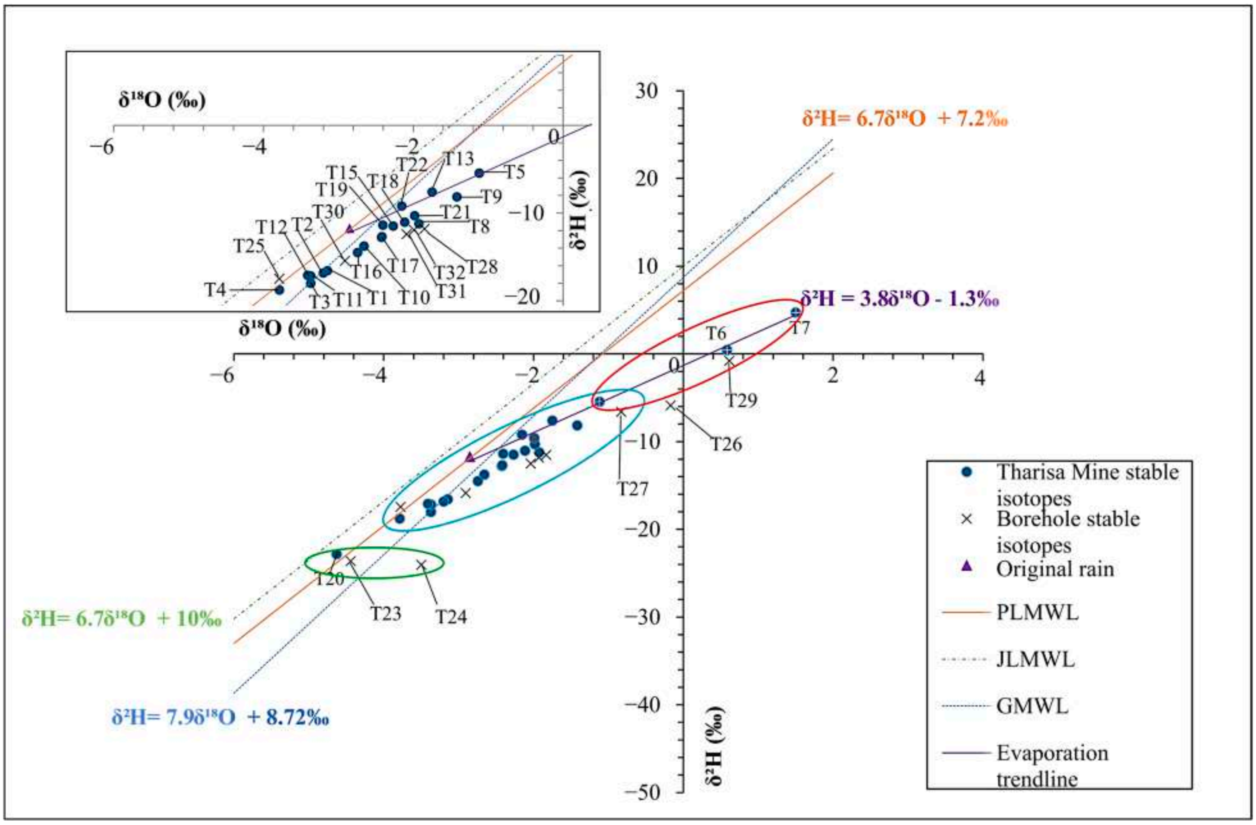

Figure 8. Stable isotopes ($\delta^{18}O$; $\delta^{2}H$) of Tharisa Mine surface water vs. Pretoria Local Meteoric Water Line (PLMWL), Johannesburg Local Meteoric Water Line (JLMWL), and Global Meteoric Water Line (GMWL). Red circle: highly enriched isotopic signal caused by fractionation during evaporation. Blue circle: mixture of surface waters with recent recharge infiltrating deep and possible water recycling. Green circle: isotopically depleted waters, hence deeper water systems.

Generally, the ^{3}H results (Figure 9) supported recent water recharge or an active zone of shallow groundwater and surface water mixing. The mine water samples' higher tritium levels compared to rainwater and lower ^{18}O and ^{2}H values than the corresponding data from shallow boreholes could be explained by the fact that the mine water contains a significant amount of deep circulating groundwater that is drawn from a larger hydrogeological basin and mixes with recharging rainwater. A suggestion of active mixing was not anticipated as mining activity dynamically adds substantial recharge to the local aquifer. However, the highly depleted stable isotope sample (T20) exhibited an elevated ^{3}H level, alluding to a recent recharge from a depleted moisture (rainfall) source but a geographically isolated area of influence. This was similarly seen for samples T4 (Samancor Borehole), T24 (TMGWFW BH 24), and T26 (TMGW Dissipater 1).

Given that most of the baseflow samples (groundwater) were collected near the water table or at the bottom of the pits, the water was anticipated to show the same depleted stable isotope and ^{3}H values as deep groundwater. As a result, the stable isotope data demonstrated and validated the existence of a short-cycle circulation zone or active surface water mixing (circled in red). It should be noted that samples grouped based on ^{18}O and ^{2}H but differing ^{3}H values suggest that comparable properties were recharged at separate periods (years), even though the samples came from the same source. The difference between stable and radiogenic isotopes may be caused by mixing.

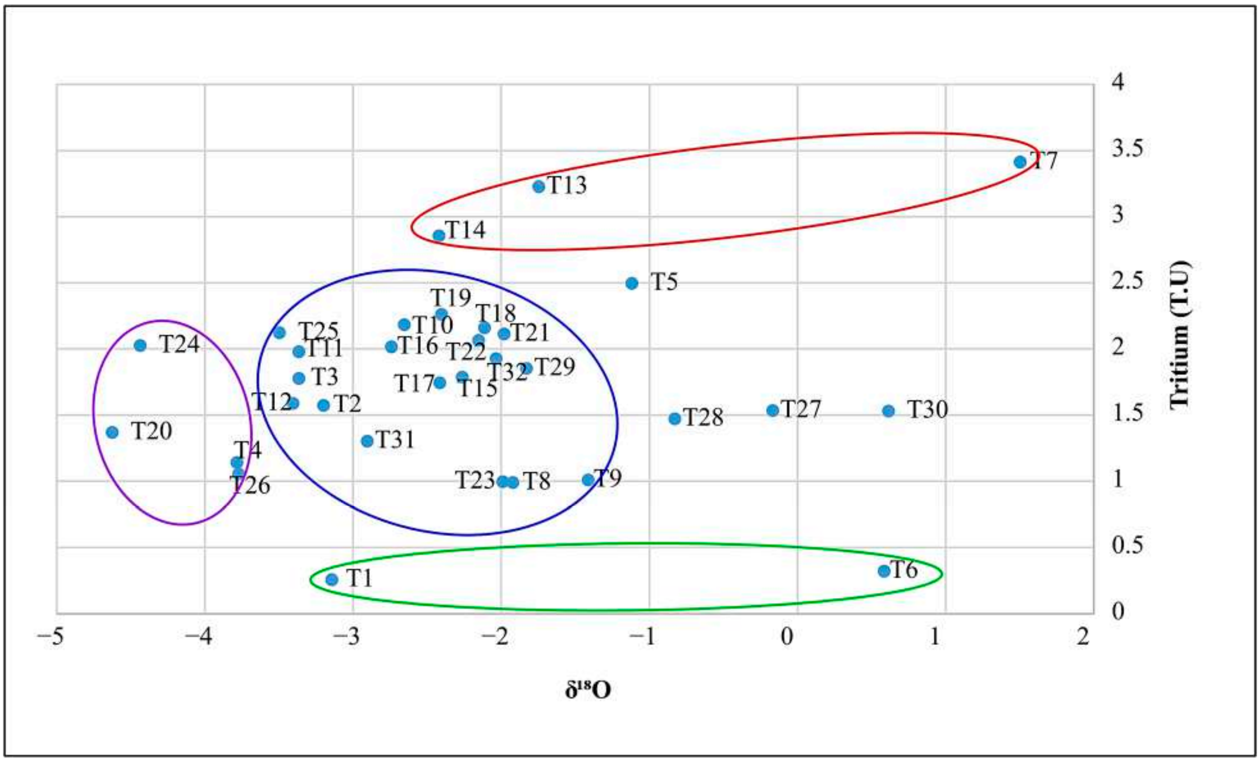

Figure 9. $\delta^{18}O$ (‰) vs. tritium (T.U) of Tharisa Mine surface water. Red circle: recent recharge, enriched isotopes, or possible rainfall. Purple circle: highly depleted $\delta^{18}O$ with an elevated *δ3H* level, alluding to a recent recharge from depleted moisture (rainfall) source but a geographically isolated area of influence. Blue circle: active mixing. Green circle: deep circulating water, depleted isotopes.

Generally, samples with a lower T.U content are older deep circulating waters, whereas samples with a higher T.U content are younger and shallower waters. From the tritium data (Figure 9), it was evident that there was a mixing of deep circulating water with young surface water. Most of the groundwater samples collected displayed characteristics of this mixing signature. Young surface waters may also have rainwater mixing, accounting for the relatively recent recharge. Figure 10a illustrates a surface contour map joining areas of equal tritium value and, therefore, showing a similar recharge period. When these values were plotted as a function of elevation (Figure 10b), it was noted that higher elevation areas displayed more enriched isotope signatures than lower elevation areas. An active mixing surface was also apparent along the descent from higher to lower elevations.

Equation (1) [49] states that when mixing happens in isotopically different water, the process proceeds according to isotopic proportion:

$$\delta\text{sample} = X\delta A + (1 - X)\delta B \quad (1)$$

where X represents the sample's specific mixing fraction from end members A and B. This suggests that the isotopic signature may adjust per the proportionate mixing when A and B combine in the aquifer. Regarding seepages (interflow), we may consider the mixing proportion of T22, where the seepage occurs through a fault/dyke fracture zone in the East Pit. T22 displayed mixing of T2 (West Pit) and T21 (East Pit). T22 comprised 13% of T2 and 87% of T21; this further suggests the possible recycling of water throughout the mine and via lineaments. Similarly, T5 (TSF 2) displayed the mixing of T7 and the original rain signature calculated from Figure 6. T5 comprised 62% of the original rain and 38% of T7.

The mixing may further be attributed to diffuse recharge in the high elevation undergoing deep circulation through tectonically induced fractures. Increased water–rock interaction makes the water more depleted. When this depleted water mixes with surface water (enriched due to evaporation), it signifies an intermediate isotope value between the two sources. This further implies the possibility of recycling along lineaments such as fractures or faults (Figure 10b).

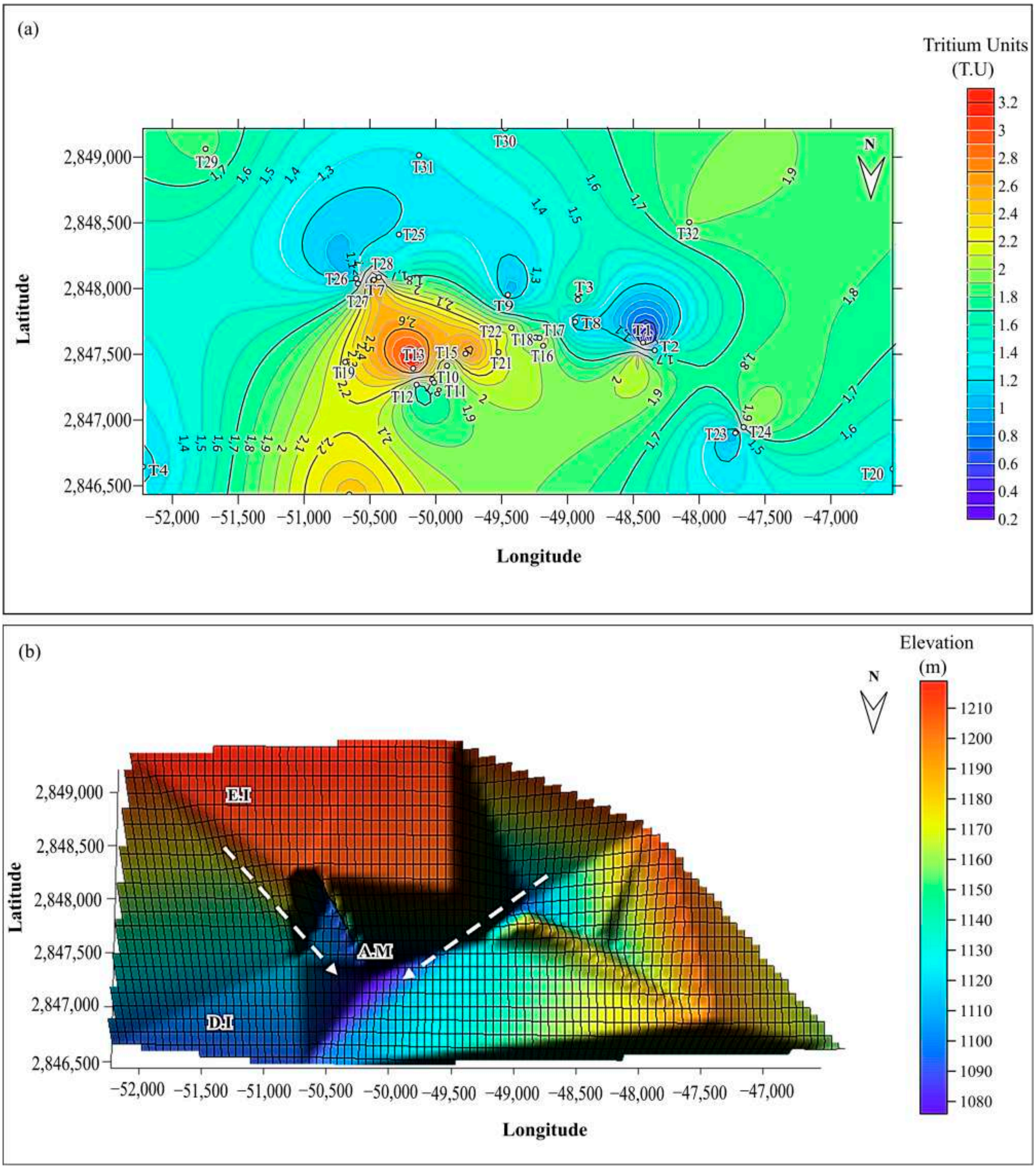

Figure 10. (**a**) Surface contour map joining areas of equal tritium value (T.U), thus showing a similar recharge period. (**b**) Elevation map of areas sampled for isotope analysis. Enriched isotopes (E.I) were more concentrated on higher elevations, whilst depleted isotopes (D.I) were concentrated on lower elevations. In addition, active mixing (A.M) was observed along the descent from the higher to lower elevations (indicated by the white dashed arrows), suggesting possible mixing through lineaments.

3.2. Geophysical Results

Along Tailings Storage Facility Line 1 (TSF L1; Figure 5b), the ERT line (Figure 11a) displays a high resistivity zone (of ~168–447 ohm.m) that extends from the surface to a depth of approximately 6 m and laterally from 0 to ~40 m; this zone is indicated by a solid white arrow in Figure 11a. This high-resistivity zone, and most of the resistivity section, is characterized by low-resistivity zones (low-irregularity zones), indicated by white dashed arrows. These irregular zones are considered fracture zones that connect surface water with deeper water and may be classified as fractures or lineaments displaying active mixing. These lineaments are further apparent in the MASW line in Figure 11b,c (indicated by dashed white arrows in Figure 11b) and correspond to a shear wave velocity zone(s) < 500 m/s extending from the surface to a depth of 12 m. Further, the lineaments that connect the surface to depth may represent evidence of possible water recycling along lineaments.

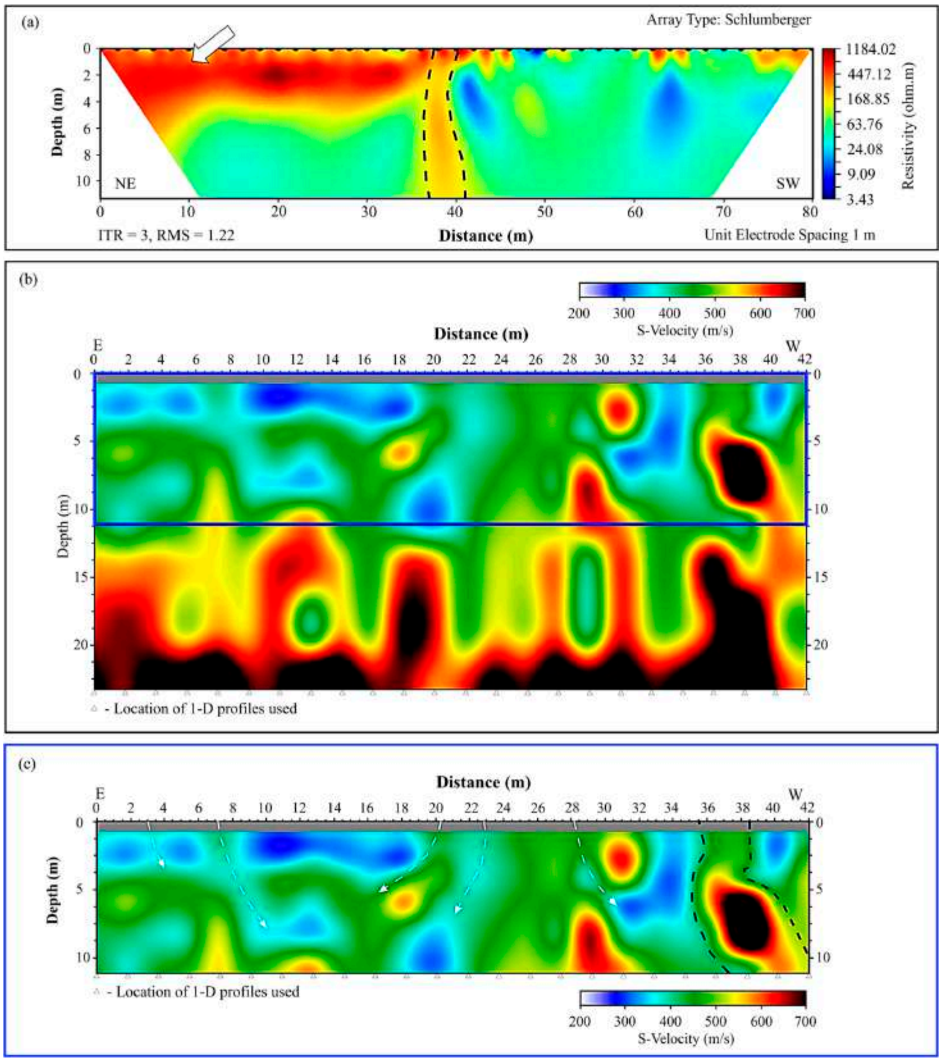

Figure 11. (**a**) Electrical resistivity tomography (ERT) Schlumberger array inversion results for Tailings Storage Facility (TSF) 1. The solid white arrow represents a high-resistivity zone with multiple irregularities suggestive of possible fractures in the less weathered zone of the profile (indicated by white dashed arrows). The black dashed lines delineate a high-resistivity zone and are classified as a less conductive and weathered zone. The solid red line delineates the location of the MASW line. (**b**) Multichannel analysis of surface waves (MASW) inversion results for TSF 1. The white dashed arrows delineate low-shear-wave-velocity zones or more weathered zones in the profile, which may allow for water migration. (**c**). Extension of the MASW line for TSF 1. The blue rectangle represents the section correlating to the MASW profile in image (**b**).

Along Tailings Storage Facility Line 2 (TSF L2; Figure 5c), the ERT (Figure 12a) and MASW (Figure 12b) survey results reveal the presence of a low-resistivity zone (21–64 ohm.m) and shear wave velocity zone (< 1000 m/s), interpreted as the upper weathered zone, extending from the surface to a depth of about 25 m. At various depths in the profile, discontinuous (probably fractured) high-resistivity (~191 ohm.m) and -shear-wave-velocity (~700 m/s) zones were observed and interpreted as less weathered zones within the upper weathered zone. Further, a lineament (indicated in Figure 12a,b as a dashed white arrow) of ~21 ohm.m and ~400 m/s connects the upper and lower weathered zones. It was interpreted as a possible fracture zone (allowing deep infiltration). Low-resistivity and low-shear-wave-velocity fractured and weathered zones (indicated by black dashed arrows in Figure 12b) may permit surface water migration to a greater depth within the subsurface. The evidence of surface waters mixing with deep water is thus depicted in Figure 12.

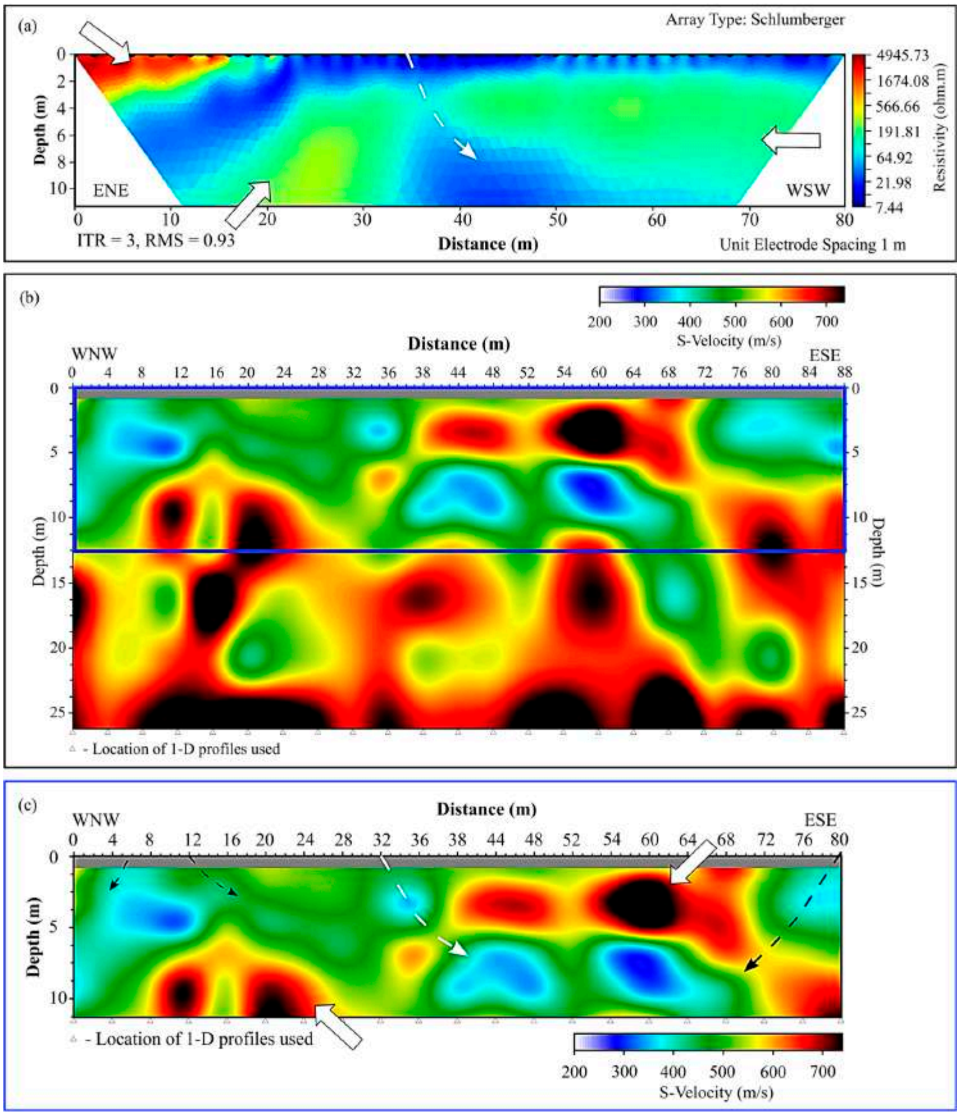

Figure 12. (**a**) Electrical resistivity tomography (ERT) Schlumberger array inversion results for Tailings Storage Facility (TSF) 2. The solid white arrows delineate high-resistivity zones and, therefore, less conductive zones. The dashed white arrow represents a low-resistivity zone which may allow for possible water migration. (**b**) Multichannel analysis of surface waves (MASW) inversion results for TSF 2. The white dashed arrow represents a low-shear-wave-velocity zone which may allow for water migration. The black dashed arrows represent other low-shear-wave-velocity zones. The solid white arrows indicate higher shear velocity areas and, therefore, less weathered rock. (**c**) Extension of the MASW line for TSF 1. The blue rectangle represents the section correlating to the MASW profile in image (**b**).

From the total magnetic intensity (TMI) magnetic grids (Figure 5d; M1, M2, M3, and M4), a vertical tilt angle was applied to enhance lineaments in the East Pit (Figure 13). On grid M2 (Figure 13b), a strong positive anomaly occurred on the southern edge and was characterized as a dyke. This anomaly is again delineated in Figure 13a,c and can be mapped as an E–W trending feature. This anomaly was correlated with the dyke in the East Pit (Figure 5d) as they followed the same trend. The negative magnetic anomalies may be linked to possible lineaments such as fracture zones. This was not unexpected as there is an enhancement of the dyke edges (high magnetic signature) associated with low magnetic signatures, possibly related to fracturing. The negative magnetic signatures attributed to fracturing are delineated in Figure 13 as black dashes.

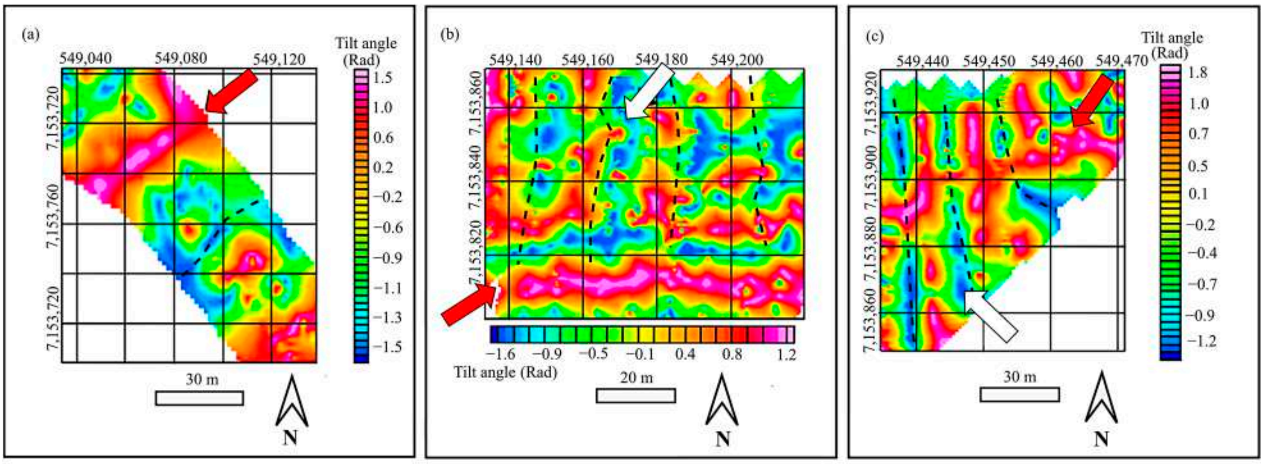

Figure 13. (**a**) Vertical tilt angle derivative map of the total magnetic intensity (TMI) for Magnetic Grid 1 (M1). (**b**) Vertical tilt angle derivative map of the TMI for Magnetic Grid 2 (M2). (**c**) Vertical tilt angle derivative map of the TMI for Magnetic Grid 3 (M3). The red arrows indicate positive magnetic anomalies, while the white arrows indicate negative magnetic anomalies. Some areas of negative magnetism show discontinuities (indicated by the black dashed lines) and are possible fracture systems/lineaments.

Seismic Profile 1 (SP1; Figure 5d) shows a disturbance at 30–40 m on the tomographic section along a reflector and is associated with depression in P-wave velocity (represented by a black dashed line in Figure 14a). This discontinuity is associated with the mapped fault within the East Pit (Figure 5d). This is further correlated with the resistivity discontinuity in Resistivity Profile 1 (RP1), interpreted as the slight decrease in resistivity at around 40–50 m into the profile (Figure 14b). RP1 (Figure 5d) is a W to E trending line and further intersects the mapped fault. An interpreted fault was further apparent in SP1.

Resistivity values between 89 and 213 ohm.m and P-wave velocities between 500 and 1300 m/s on SP1 (Figure 14a) describe the dark-blue to light-green zones on RP1 (Figure 14b). This area, thought to represent the top layer of highly fractured norite, may have been caused by blasting in the pit. Subsurface rocks exhibit an increase in resistivity and P-wave velocity with depth. A transitional region of intermediate resistance (light green to yellow: 213–3274 ohm.m.) is then present, along with P-wave velocities of 1300–2100 m/s. A zone of much greater resistivities (between 3274 and 20,000 ohm.m.) lies under the intermediate-resistivity zone; this zone appears as orange to red and may represent fresh bedrock. The Schlumberger model shows conductive layers (low-resistivity, blue-colored zone) with a thickness between 2.5 and 14 m across the profiles.

The electrical resistivity and seismic velocity models showed inhomogeneous horizons with sudden resistivity changes that may be attributed to fracturing.

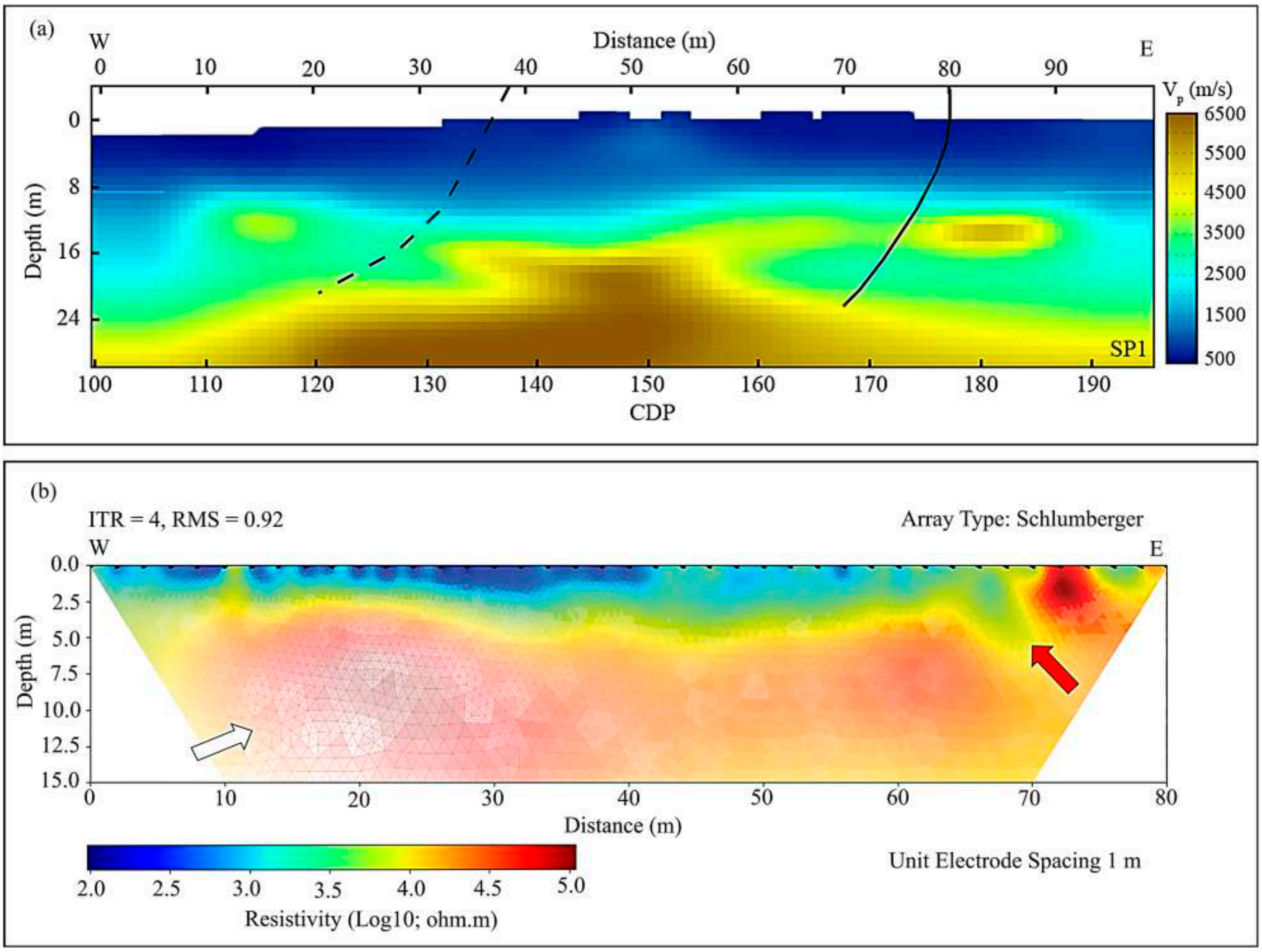

Figure 14. (**a**) Seismic tomogram for input Seismic Profile 1 (SP1). The dotted black line represents the mapped fault, whilst the solid black line indicates an interpreted fault. (**b**) Schlumberger electrical resistivity inverse sections for Resistivity Profile 1 (RP1). The red arrow indicates a low-resistivity zone, while the white arrow indicates a high-resistivity zone. Depth is on a logarithmic scale.

Seismic Profile 2 (SP2) was conducted on top of the dyke (Figure 5d), with the dyke covered by a highly fractured rock from mine workings (Figure 15b). The highly fractured rock's thickness increases towards the profile's center and creates a syncline structure that might result from the fault zone on the eastern part of the profile (indicated by a black dashed line in Figure 15b). This was evident on SP2, as it showed low-velocity regions towards the southwestern side of the profile at varying depths (Figure 15b). Multiple discontinuities were further noted in the profile and may have resulted from fracturing along the dyke edges. This fracturing along the dyke was further apparent on the southern edge of Magnetic Grid 2 (Figure 15a) and Resistivity Profile 2 (RP2; Figures 5d and 15c). RP2 has an S–N trend and was surveyed across the dyke to characterize the association with the dyke. Resistivity values over the dyke ranged from 3000 to ~4000 ohm.m. A notable discontinuity was observed at a distance of 25–36 m with resistivity values between 120 and 3900 ohm.m (Figure 15c). The average thickness of the dyke at the profile was 25 m, and the anomaly had a thickness of ~8 m. The discrepancy in thickness might be due to the edges of the dyke being fractured due to differential weathering of the host rock at the contacts with the dyke (Figure 15a; represented as black dashed lines). Such areas have potential for hosting groundwater and are supported by the Schlumberger results as they exhibit low-resistivity zones (Figure 15c at 30–40 m).

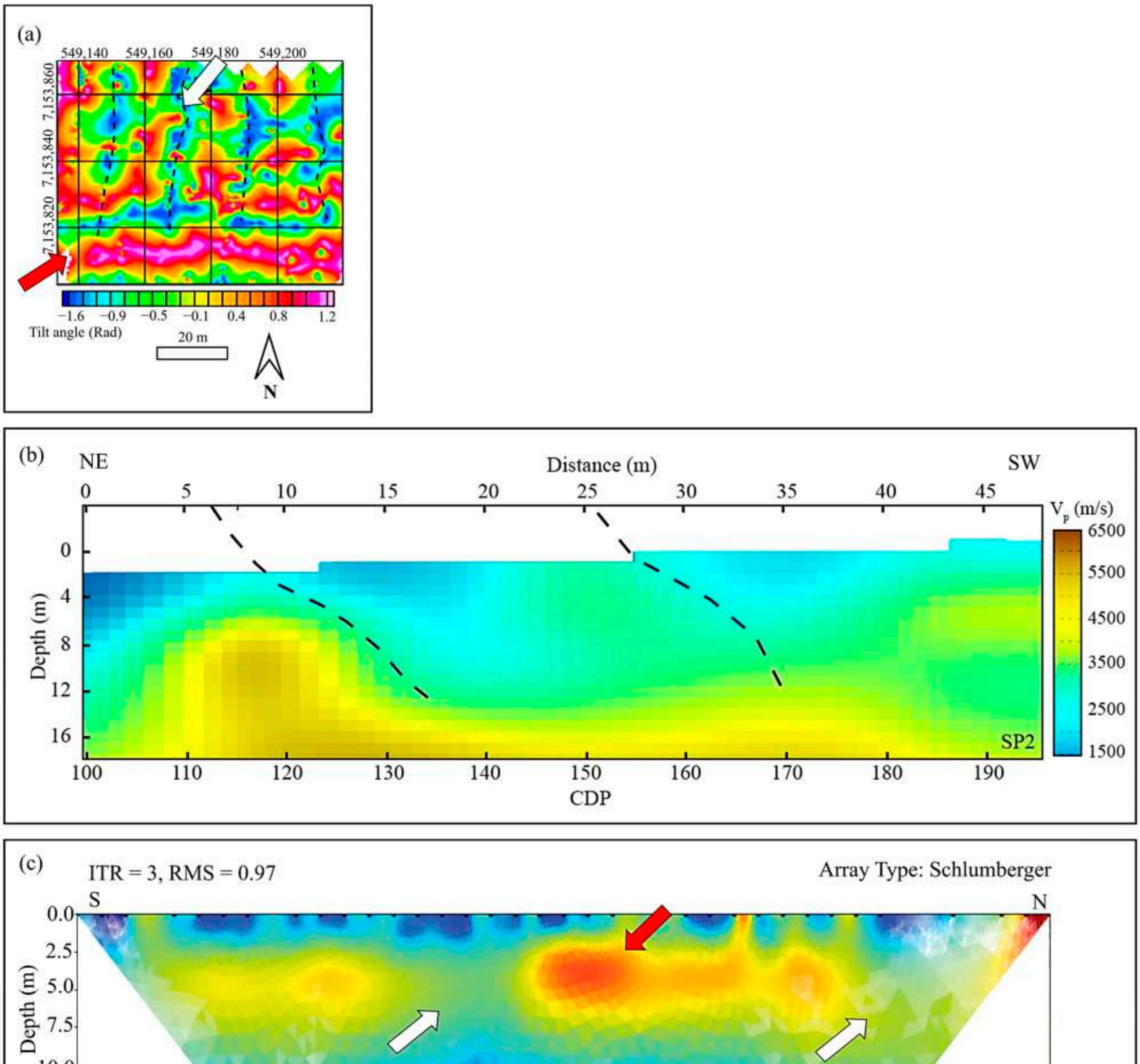

Figure 15. (**a**) Vertical tilt angle derivative map of the TMI for Magnetic Grid 2 (M2). The red arrow indicates areas of positive magnetic anomalies, while the white arrow indicates negative magnetic anomalies. Some areas of negative magnetism show discontinuities (indicated by the black dashed lines) and are possible fracture systems/lineaments. (**b**) Seismic tomogram for input Seismic Profile 2 (SP2). The dotted black lines represent the interpreted faults. (**c**) Schlumberger electrical resistivity inverse sections for Resistivity Profile 2 (RP2). The red arrow indicates high-resistivity areas, while the white arrows indicate low-resistivity areas. Depth is on a logarithmic scale.

4. Discussion

Based on the preliminary data presented, the weathered overburden has a very varied thickness ranging from 3 m to 25 m. The fine- to coarse-grained sandy soil that makes up this differentially weathered overburden in the area of Tharisa was created by the in situ breakdown of the underlying norites, anorthosites, and pyroxenites. Norites, anorthosites, and pyroxenites that are fractured and underlie the weathered aquifer are all parts of a deeper, unweathered, semi-confined bedrock aquifer. Open fracture systems that are linked to one another determine the material's effective permeability. However, these fracture structures may occasionally enable fast vertical groundwater flow from weathered overburden and surface water bodies to deeper levels of the fractured aquifer. While, generally speaking, there is limited connectivity between the lower fractured aquifer and the weathered aquifer, this is not the case for Tharisa Mine.

The geophysical data and ^{18}O and ^{2}H isotope groundwater data from the Tharisa Mine were combined to comprehend the recharge sources, processes, and isotopic variability. The findings show that the levels of ^{18}O and ^{2}H in the groundwater at the time of sampling did not always match the overall isotopic composition of the recharging water in the mine. Due to evaporation and mixing, the replenishing groundwater significantly altered the values of ^{18}O and ^{2}H. Through evaporation and mixing with the surface impoundments, the indirect recharge and recycling from surface water that predominates changes the composition of the ^{18}O and ^{2}H.

The mixing tendency is further supported by the observed alignment of the isotopic data along the meteoric water line. The very closely clustered data suggest the likelihood of a comparable source and homogeneous water mixing. These aquifers have a narrow range of maximum and lowest values. However, a large gap may indicate climatic control over recharging, fluctuation in the source of the recharge, and a reduced possibility of mixing. In addition, stable isotope data (^{2}H and ^{18}O) and tritium data show that a large amount of the mine water comprises relatively ancient (low ^{3}H value) and deep circulating water (low ^{18}O) in addition to relatively young (high ^{3}H value) and shallow circulating water (high ^{18}O). According to stable isotope data, the groundwater recharge to the region's bedrock aquifers may further be attributable to both diffuse and concentrated recharge mechanisms.

According to the study, the direct recharge in the high-elevation regions experiencing deep circulation through tectonically produced fractures may have been responsible for the depletion in some samples. Low-salinity fluids exist inside the aquifer system that contains depleted ^{18}O because rapid infiltration through fractures may lead to a low degree of water–rock interaction. Characterizing potential fracture systems in the mine was made attainable by Figures 14 and 15. Furthermore, samples T16, T17, and T22 (Figures 8 and 9), gathered in Figures 14 and 15, showed the isotope signatures of an active mixing zone, supporting the likelihood of mixing and rapid infiltration along these structures.

According to the study, diffuse recharging in high-elevation locations experiencing deep circulation through tectonically produced fractures may also be responsible for the mixing. An intermediate isotope value is produced when the depleted water combines with surface water, enhanced by evaporation. This also suggests that mixing might occur along lineaments such as faults or fractures. Figure 12 clearly shows this indication of mixing. T5, taken at TSF 2, shown in Figure 12, showed a mixing signature of depleted and enriched water (Figures 8 and 9), which accounts for potential mixing along the joint/fracture zones indicated.

According to the geophysical findings, the source of the dominating groundwater circulation is located about 20 m away from the possible recharge zone, close to the surface (Figures 11 and 12). A fairly recent and shallow-moving locally recharged water component combines with an older groundwater component that is slower moving (depleted in ^{18}O and low in ^{3}H) within the weathered crystalline aquifer. This further suggests the likelihood of an active groundwater and surface water mixing zone. Mixing shallow and deep water from different mine regions may be possible due to these fractures acting as groundwater conduits. Additionally, the permeability and porosity of the aquifer may rise due to the junction of many lineaments, enabling enhanced fluid movement due to higher hydraulic conductivity [67]. Groundwater migrates via linked conductive zones and through interconnected fracture systems, with the potential for fast vertical groundwater flow from weathered overburden (and surface water bodies) to increased depths [67,68].

Along the lines of SP1, SP1, RP1, and RP2, there are intersections of various lineaments (Figures 14 and 15).

The hydrogeological and geophysical studies for TSF 1 show the potential for tailings dam seepages, another noteworthy finding. Monitoring Borehole T29 may have leaked into TSF 1 sample T6 (sampled along the line shown in Figure 11; see Figure 8), shown by the deep infiltration zones in Figure 11 at TSF 1.

The early outputs of the groundwater inflow volumes into the open pit (East Pit) are as follows after integrating the findings:

1. The majority of groundwater influx volumes may come from different fracture systems or zones;
2. By continuously developing the mine, a bigger aquifer volume is reached, promoting rising groundwater inflows into the open pit;
3. During mining operations (such as unloading rock masses, blasting operations, and dewatering plans), the aquifer material's capacity to transfer and retain groundwater is significantly enhanced close to the open pit.

5. Conclusions

We demonstrated the use of hydrogeological and geophysical techniques to identify possible groundwater extraction zones for the Tharisa Mine and provided a qualitative interpretation. The underlying aquifers of the Tharisa Mine were delineated, and it is evident that there is variable connectivity between the lower fractured aquifer and the weathered aquifer. Further, the geological structure, including fluid movement channels and appropriate lineaments, was further revealed by integrating the hydrogeological and geophysical data. Additionally, the geophysical findings support the hydrogeological information in that the primary water sources in the mine include mixing surface/rain water with nearby deep water sources, possible water recycling through lineaments, and tailings dam seepages.

Based on the early data, it is advised that the mine upgrade its dewatering systems and make more appropriate storage facility investments. Seepages will also be reduced via techniques for managing boreholes and monitoring tailings dams. Lastly, it is argued that regular monitoring of the extraction from the open pit will precisely confirm the groundwater inflow rates.

Author Contributions: Conceptualization, M.S.D.M., T.A. and J.D.; methodology, J.D., S.G. and M.K.R.; software, J.D., S.G. and M.K.R.; validation, M.S.D.M., T.A. and J.D.; formal analysis, J.D.; investigation, J.D.; resources, M.S.D.M., T.A. and G.D.; data curation, J.D.; writing—original draft preparation, J.D.; writing—review and editing, J.D., M.S.D.M., T.A. and G.D.; visualization, J.D.; supervision, M.S.D.M., T.A. and G.D.; project administration, M.S.D.M. and J.D.; funding acquisition, M.S.D.M. All authors have read and agreed to the published version of the manuscript.

Funding: This research was funded by Tharisa Mine, Wits Seismic Research Centre, and Centre of Excellence for Integrated Mineral and Energy (CIMERA).

Data Availability Statement: The data are not publicly available due to privacy restrictions.

Acknowledgments: The authors would like to acknowledge Tharisa Mine and CIMERA for funding this research. Further recognition goes to Michael Butler from iThemba Labs, Gauteng, for providing the analysis of the tritium results. Lastly, appreciation is given to Tharisa Mine for providing access to the mine for this project and for allowing us to publish the results.

Conflicts of Interest: The authors declare no conflict of interest.

References

1. Lines, G.C. *The Ground-Water System and Possible Effects of Underground Coal Mining in the Trail Mountain Area, Central Utah*; Department of the Interior, US Geological Survey: Reston, WV, USA, 1985.
2. MINEO Consortium. *Review of Potential Environmental and Social Impact of Mining*; MINEO Consortium: Gela, Italy, 2000.
3. Environment Australia. *Overview of Best Practice Environmental Management in Mining*; Environment Australia: Canberra, Australia, 2002.

4. Mengistu, H.A.; Demlie, M.B.; Abiye, T.A.; Xu, Y.; Kanyerere, T. Conceptual Hydrogeological and Numerical Groundwater Flow Modelling around the Moab Khutsong Deep Gold Mine, South Africa. *Groundw. Sustain. Dev.* **2019**, *9*, 100266. [CrossRef]
5. Szczepiński, J. The Significance of Groundwater Flow Modeling Study for Simulation of Opencast Mine Dewatering, Flooding, and the Environmental Impact. *Water* **2019**, *11*, 848. [CrossRef]
6. Jhariya, D.C.; Khan, R.; Thakur, G.S. Impact of Mining Activity on Water Resource: An Overview Study. In Proceedings of the Recent Practices and Innovations in Mining Industry, Raipur, India, 19–20 February 2016; pp. 271–277.
7. Yang, Y.; Guo, T.; Jiao, W. Destruction Processes of Mining on Water Environment in the Mining Area Combining Isotopic and Hydrochemical Tracer. *Environ. Pollut.* **2018**, *237*, 356–365. [CrossRef] [PubMed]
8. Ruiz, F.; Gomis, V.; Blasco, P. Application of Factor Analysis to the Hydrogeochemical Study of a Coastal Aquifer. *J. Hydrol.* **1990**, *119*, 169–177. [CrossRef]
9. Subramani, T.; Rajmohan, N.; Elango, L. Groundwater Geochemistry and Identification of Hydrogeochemical Processes in a Hard Rock Region, Southern India. *Environ. Monit. Assess.* **2010**, *162*, 123–137. [CrossRef] [PubMed]
10. Al-Ahmadi, M.E. Hydrochemical Characterization of Groundwater in Wadi Sayyah, Western Saudi Arabia. *Appl. Water Sci.* **2013**, *3*, 721–732. [CrossRef]
11. Chebbah, M.; Allia, Z. Geochemistry and Hydrogeochemical Process of Groundwater in the Souf Valley of Low Septentrional Sahara, Algeria. *Afr. J. Environ. Sci. Technol.* **2015**, *9*, 261–273. [CrossRef]
12. Al-Hmani, A.; Jamaa, N.B.; Kharroubi, A.; Agoubi, B. Assessment of Groundwater in Sana'a Basin Aquifers, Yemen, Using Hydrogeochemical Modeling and Multivariate Statistical Analysis. *Arab. J. Geosci.* **2022**, *15*, 684. [CrossRef]
13. Yihdego, Y.; Webb, J.A.; Leahy, P. Modelling of Lake Level under Climate Change Conditions: Lake Purrumbete in Southeastern Australia. *Environ. Earth Sci.* **2015**, *73*, 3855–3872. [CrossRef]
14. Mogaji, K.A.; Omobude, O.B. Modeling of Geoelectric Parameters for Assessing Groundwater Potentiality in a Multifaceted Geologic Terrain, Ipinsa Southwest, Nigeria—A GIS-Based GODT Approach. *NRIAG J. Astron. Geophys.* **2017**, *6*, 434–451. [CrossRef]
15. Mohamaden, M.I.I.; Hamouda, A.Z.; Mansour, S. Application of Electrical Resistivity Method for Groundwater Exploration at the Moghra Area, Western Desert, Egypt. *Egypt. J. Aquat. Res.* **2016**, *42*, 261–268. [CrossRef]
16. Wattanasen, K.; Elming, S.-Å. Direct and Indirect Methods for Groundwater Investigations: A Case-Study of MRS and VES in the Southern Part of Sweden. *J. Appl. Geophys.* **2008**, *66*, 104–117. [CrossRef]
17. Younis, A.; Soliman, M.; Moussa, S.; Massoud, U.; ElNabi, S.A.; Attia, M. Integrated Geophysical Application to Investigate Groundwater Potentiality of the Shallow Nubian Aquifer at Northern Kharga, Western Desert, Egypt. *NRIAG J. Astron. Geophys.* **2016**, *5*, 186–198. [CrossRef]
18. Song, L.; Zhu, J.; Yan, Q.; Kang, H. Estimation of Groundwater Levels with Vertical Electrical Sounding in the Semiarid Area of South Keerqin Sandy Aquifer, China. *J. Appl. Geophys.* **2012**, *83*, 11–18. [CrossRef]
19. Lopes, D.D.; Silva, S.M.C.P.; Fernandes, F.; Teixeira, R.S.; Celligoi, A.; Dall'Antônia, L.H. Geophysical Technique and Groundwater Monitoring to Detect Leachate Contamination in the Surrounding Area of a Landfill—Londrina (PR—Brazil). *J. Environ. Manag.* **2012**, *113*, 481–487. [CrossRef] [PubMed]
20. Mohamaden, M.I.I.; Ehab, D. Application of Electrical Resistivity for Groundwater Exploration in Wadi Rahaba, Shalateen, Egypt. *NRIAG J. Astron. Geophys.* **2017**, *6*, 201–209. [CrossRef]
21. Ruthsatz, A.D.; Sarmiento Flores, A.; Diaz, D.; Reinoso, P.S.; Herrera, C.; Brasse, H. Joint TEM and MT Aquifer Study in the Atacama Desert, North Chile. *J. Appl. Geophys.* **2018**, *153*, 7–16. [CrossRef]
22. Helaly, A.S. Assessment of Groundwater Potentiality Using Geophysical Techniques in Wadi Allaqi Basin, Eastern Desert, Egypt—Case Study. *NRIAG J. Astron. Geophys.* **2017**, *6*, 408–421. [CrossRef]
23. Binley, A.; Hubbard, S.S.; Huisman, J.A.; Revil, A.; Robinson, D.A.; Singha, K.; Slater, L.D. The Emergence of Hydrogeophysics for Improved Understanding of Subsurface Processes over Multiple Scales. *Water Resour. Res.* **2015**, *51*, 3837–3866. [CrossRef]
24. McLachlan, P.J.; Chambers, J.E.; Uhlemann, S.S.; Binley, A. Geophysical Characterisation of the Groundwater–Surface Water Interface. *Adv. Water Resour.* **2017**, *109*, 302–319. [CrossRef]
25. Singha, K.; Day-Lewis, F.D.; Johnson, T.; Slater, L.D. Advances in Interpretation of Subsurface Processes with Time-Lapse Electrical Imaging: Time-Lapse Electrical Imaging. *Hydrol. Process.* **2015**, *29*, 1549–1576. [CrossRef]
26. Dailey, D.; Sauck, W.; Sultan, M.; Milewski, A.; Ahmed, M.; Laton, W.R.; Elkadiri, R.; Foster, J.; Schmidt, C.; Al Harbi, T. Geophysical, Remote Sensing, GIS, and Isotopic Applications for a Better Understanding of the Structural Controls on Groundwater Flow in the Mojave Desert, California. *J. Hydrol. Reg. Stud.* **2015**, *3*, 211–232. [CrossRef]
27. Wiederhold, H.; Kallesøe, A.J.; Kirsch, R.; Mecking, R.; Pechnig, R.; Skowronek, F. Geophysical Methods Help to Assess Potential Groundwater Extraction Sites. *Grund. Z. Fachsekt. Hydrogeol.* **2021**, *26*, 367–378. [CrossRef]
28. Polom, U.; Bagge, M.; Wadas, S.; Winsemann, J.; Brandes, C.; Binot, F.; Krawczyk, C.M. Surveying Near-Surface Depocentres by Means of Shear Wave Seismics. *First Break* **2013**, *31*, 67–79. [CrossRef]
29. Krawczyk, C.M.; Polom, U.; Trabs, S.; Dahm, T. Sinkholes in the City of Hamburg—New Urban Shear-Wave Reflection Seismic System Enables High-Resolution Imaging of Subrosion Structures. *J. Appl. Geophys.* **2012**, *78*, 133–143. [CrossRef]
30. Pugin, A.J.-M.; Pullan, S.E.; Hunter, J.A.; Oldenborger, G.A. Hydrogeological Prospecting Using P- and S-wave Landstreamer Seismic Reflection Methods. *Near Surf. Geophys.* **2009**, *7*, 315–328. [CrossRef]

31. Burschil, T.; Scheer, W.; Kirsch, R.; Wiederhold, H. Hydrogeological Characterisation of a Glacially Affected Barrier Island—The North Frisian Island of Föhr. *Groundw. Hydrol. Instrum. Obs. Tech.* **2012**, *9*, 5085–5119. [CrossRef]
32. Høyer, A.-S.; Jørgensen, F.; Piotrowski, J.A.; Jakobsen, P.R. Deeply Rooted Glaciotectonism in Western Denmark: Geological Composition, Structural Characteristics and the Origin of Varde Hill-Island: Deeply Rooted Glaciotectonism in Western Denmark. *J. Quat. Sci.* **2013**, *28*, 683–696. [CrossRef]
33. Tamiru, G.; Wiederhold, H. P- and S-Wave Reflection Profiling for near-Surface Investigation of Glacial Sediments. *J. Appl. Geophys.* **2020**, *183*, 104216. [CrossRef]
34. Hoffmann, S.; Beilecke, T.; Polom, U.; Werban, U.; Leven, C.; Engeser, B. Integrierter Einsatz von Scherwellenseismik und Direct-Push-Verfahren zur Erkundung eines urbanen Grundwasserleiters. *Grundwasser* **2008**, *13*, 78–90. [CrossRef]
35. Clarke, B.M. Intrusion Mechanisms of the Southwestern Rustenburg Layered Suite as Deduced from the Spruitfontein Inlier. *S. Afr. J. Geol.* **2000**, *103*, 120–127. [CrossRef]
36. Eales, H.V.; Reynolds, I.M. Cryptic Variations within Chromitites of the Upper Critical Zone, Northwestern Bushveld Complex. *Econ. Geol.* **1986**, *81*, 1056–1066. [CrossRef]
37. Eales, H.V.; Field, M.; De Klerk, W.J.; Scoon, R.N. Regional Trends of Chemical Variation and Thermal Erosion in the Upper Critical Zone, Western Bushveld Complex. *Mineral. Mag.* **1988**, *52*, 63–79. [CrossRef]
38. Eales, H.V.; De Klerk, W.J.; Butcher, A.R. The Cyclic Unit beneath the UG1 Chromitite (UGIFW Unit) at RPM Union Section Platinum Mine—Rosetta Stone of the Bushveld upper Critical Zone? *Mineral. Mag.* **1990**, *54*, 23–43. [CrossRef]
39. Teigler, B.; Eales, H.V.; Scoon, R.N. The Cumulate Succession in the Critical Zone of the Rustenburg Layered Suite at Brits, Western Bushveld Complex. *S. Afr. J. Geol.* **1992**, *95*, 17–28.
40. Cawthorn, R.G. Pressure Fluctuations and the Formation of the PGE-Rich Merensky and Chromitite Reefs, Bushveld Complex. *Min. Depos.* **2005**, *40*, 231–235. [CrossRef]
41. Taylor, C.D.; Schulz, K.J.; Doebrich, J.L.; Orris, G.; Denning, P.; Kirschbaum, M.J. *Geology and Nonfuel Mineral Deposits of Africa and the Middle East*; Open-File Report; US Geological Survey: Reston, WV, USA, 2009.
42. Zientek, M.L.; Causey, J.D.; Parks, H.L.; Miller, R.J. *Global Mineral Resource Assessment: Platinum-Group Elements in Southern Africa—Mineral Inventory and an Assessment of Undiscovered Mineral Resources*; Scientific Investigations Report; US Geological Survey: Reston, WV, USA, 2014.
43. Lourens, P. The Relation between South African Geology and Geohydrology. Ph.D. Thesis, University of the Free State, Bloemfontein, South Africa, 2013.
44. Titus, R.; Witthüser, K.; Walters, B. Groundwater and Mining in the Bushveld Complex. In Proceedings of the International Mine and Water Conference, Extended Abstracts, Pretoria, South Africa, 19–23 October 2009.
45. Loseby, B. *Tharisa Mine Dewatering Strategy*; SLR Consulting (Pty)Ltd.: Johannesburg, South Africa, 2021.
46. Lomberg, K.; Bornman, H.; Goldschmidt, A.D.; James, J.; Lotheringen, J.; Pheiffer, A.; Stobart, B.; Wiid, G. *Tharisa Chrome and PGM Mine*; South Africa Competent Persons Report; Coffey Mining(Pty)Ltd.: Johannesburg, South Africa, 2016.
47. Mazor, E. *Chemical and Isotopic Groundwater Hydrology*; Marcel Dekker Inc.: New York, NY, USA, 1997; Volume 413.
48. Dotsika, E.; Lykoudis, S.; Poutoukis, D. Spatial Distribution of the Isotopic Composition of Precipitation and Spring Water in Greece. *Glob. Planet. Chang.* **2010**, *71*, 141–149. [CrossRef]
49. Clark, I.; Fritz, P. *Environmental Isotopes in Hydrogeology*; CRC Press: Boca Raton, FL, USA, 2013; p. 328.
50. Abiye, T.A.; Mengistu, H.; Masindi, K.; Demlie, M. Surface Water and Groundwater Interaction in the upper Crocodile River Basin, Johannesburg, South Africa: Environmental Isotope Approach. *S. Afr. J. Geol.* **2015**, *118*, 109–118. [CrossRef]
51. Paz, M.; Alcalá, F.; Medeiros, A.; Martínez-Pagán, P.; Pérez-Cuevas, J.; Ribeiro, L. Integrated MASW and ERT Imaging for Geological Definition of an Unconfined Alluvial Aquifer Sustaining a Coastal Groundwater-Dependent Ecosystem in Southwest Portugal. *Appl. Sci.* **2020**, *10*, 5905. [CrossRef]
52. Rey, J.; Martínez, J.; Mendoza, R.; Sandoval, S.; Tarasov, V.; Kaminsky, A.; Hidalgo, M.C.; Morales, K. Geophysical Characterization of Aquifers in Southeast Spain Using ERT, TDEM, and Vertical Seismic Reflection. *Appl. Sci.* **2020**, *10*, 7365. [CrossRef]
53. Schoor, M.V.; Fourie, C.J.S. Introduction to the Geophysical Methods Applicable to Coal. In *A Guide for Applying Geophysics to Coal Mining Problems in South Africa*; Struik Nature: South Africa, Workflow;14822. [place unknown]: Coaltech; 2015; pp. 32–99. Available online: http://hdl.handle.net/10204/8280 (accessed on 31 July 2023).
54. Martínez-Segura, M.A.; Conesa-García, C.; Pérez-Cutillas, P.; Martínez-Pagán, P.; Vásconez-Maza, M.D. Identifying Changes in Sediment Texture along an Ephemeral Gravel-Bed Stream Using Electrical Resistivity Tomography 2D and 3D. *Appl. Sci.* **2021**, *11*, 3030. [CrossRef]
55. Sendrós, A.; Urruela, A.; Himi, M.; Alonso, C.; Lovera, R.; Tapias, J.C.; Rivero, L.; Garcia-Artigas, R.; Casas, A. Characterization of a Shallow Coastal Aquifer in the Framework of a Subsurface Storage and Soil Aquifer Treatment Project Using Electrical Resistivity Tomography (Port de La Selva, Spain). *Appl. Sci.* **2021**, *11*, 2448. [CrossRef]
56. Alcalá, F.J.; Martínez-Pagán, P.; Paz, M.C.; Navarro, M.; Pérez-Cuevas, J.; Domingo, F. Combining of MASW and GPR Imaging and Hydrogeological Surveys for the Groundwater Resource Evaluation in a Coastal Urban Area in Southern Spain. *Appl. Sci.* **2021**, *11*, 3154. [CrossRef]
57. Malehmir, A.; Durrheim, R.; Bellefleur, G.; Urosevic, M.; Juhlin, C.; White, D.J.; Milkereit, B.; Campbell, G. Seismic Methods in Mineral Exploration and Mine Planning: A General Overview of Past and Present Case Histories and a Look into the Future. *Geophysics* **2012**, *77*, WC173–WC190. [CrossRef]

58. Manzi, M.S.D.; Gibson, M.A.S.; Hein, K.A.A.; King, N.; Durrheim, R.J. Application of 3D Seismic Techniques to Evaluate Ore Resources in the West Wits Line Goldfield and Portions of the West Rand Goldfield, South Africa. *Geophysics* **2012**, *77*, WC163–WC171. [CrossRef]
59. Manzi, M.; Malehmir, A.; Durrheim, R.J. 3D Reflection Seismics for Deep Platinum Exploration in the Bushveld Complex, South Africa. In Proceedings of the 2nd Conference on Geophysics for Mineral Exploration and Mining, Porto, Portugal, 9–12 September 2018; European Association of Geoscientists & Engineers: Porto, Portugal, 2018; pp. 1–5. [CrossRef]
60. Manzi, M.S.D.; Durrheim, R.J.; Hein, K.A.A.; King, N. 3D Edge Detection Seismic Attributes Used to Map Potential Conduits for Water and Methane in Deep Gold Mines in the Witwatersrand Basin, South Africa. *Geophysics* **2012**, *77*, WC133–WC147. [CrossRef]
61. Pazzi, V.; Di Filippo, M.; Di Nezza, M.; Carlà, T.; Bardi, F.; Marini, F.; Fontanelli, K.; Intrieri, E.; Fanti, R. Integrated Geophysical Survey in a Sinkhole-Prone Area: Microgravity, Electrical Resistivity Tomographies, and Seismic Noise Measurements to Delimit Its Extension. *Eng. Geol.* **2018**, *243*, 282–293. [CrossRef]
62. Robinson, D.A.; Binley, A.; Crook, N.; Day-Lewis, F.D.; Ferré, T.P.A.; Grauch, V.J.S.; Knight, R.; Knoll, M.; Lakshmi, V.; Miller, R.; et al. Advancing Process-Based Watershed Hydrological Research Using near-Surface Geophysics: A Vision for, and Review of, Electrical and Magnetic Geophysical Methods. *Hydrol. Process.* **2008**, *22*, 3604–3635. [CrossRef]
63. Lubczynski, M.; Roy, J. Hydrogeological Interpretation and Potential of the New Magnetic Resonance Sounding (MRS) Method. *J. Hydrol.* **2003**, *283*, 19–40. [CrossRef]
64. World Health Organization. *The World Health Report 2007: A Safer Future: Global Public Health Security in the 21st Century*; World Health Organization: Geneva, Switzerland, 2007.
65. Rusydi, A.F. Correlation between Conductivity and Total Dissolved Solid in Various Type of Water: A Review. *IOP Conf. Ser. Earth Environ. Sci.* **2018**, *118*, 012019. [CrossRef]
66. Porowski, A. Isotopic Evidence of the Origin of Mineralized Waters from the Central Carpathian Synclinorium, SE Poland. *Environ. Geol.* **2004**, *46*, 661–669. [CrossRef]
67. Chilton, P.J.; Foster, S.S.D. Hydrogeological Characterisation and Water-Supply Potential of Basement Aquifers in Tropical Africa. *Hydrogeol. J.* **1995**, *3*, 36–49. [CrossRef]
68. Howard, R.T.K. A Tectono-Geomorphic Model of the Hydrogeology of Deeply Weathered Crystalline Rock: Evidence from Uganda. *Hydrogeol. J.* **2000**, *8*, 279–294.